HIERARCHICAL POROUS METAL-ORGANIC FRAMEWORKS (MOFS): DESIGN, SYNTHESIS, AND THEIR APPLICATION AS GAS ADSORPTION MATERIALS

by
AYSU YURDUŞEN

Submitted to the Graduate School of Engineering and Natural Sciences
in partial fulfillment of the requirements for the degree of
Doctor of Philosophy

Sabancı University
July 2020

HIERARCHICAL POROUS METAL-ORGANIC FRAMEWORKS (MOFS): DESIGN, SYNTHESIS, AND THEIR APPLICATION AS GAS ADSORPTION MATERIALS

APPROVED BY:

Prof. Dr. Selmiye Alkan Gürsel (Thesis Supervisor)

Dr. Alp Yürüm (Thesis Co-advisor)

Prof. Dr. Fatma Yüksel

Dr. Mustafa Kemal Bayazıt

Assoc. Prof. Dr. Emre Erdem

Assoc. Prof. Dr. Alper Uzun

DATE OF APPROVAL: 27/07/2020

© AYSU YURDUŞEN 2020
All Rights Reserved

ABSTRACT

HIERARCHICAL POROUS MOFS: DESIGN, SYNTHESIS, AND THEIR APPLICATIONS AS GAS ADSORPTION MATERIALS

AYSU YURDUŞEN

Materials Science and Engineering, Ph.D. Dissertation, July 2020

Thesis Supervisor: Prof. Dr. Selmiye Alkan Gürsel
Thesis Co-Advisor: Dr. Alp Yürüm

Keywords: Metal-organic frameworks, hierarchical porous MOFs, hierarchical pores, carbon dioxide adsorption, hydrogen adsorption

Climate change is a global concern and interacts with economics, energy, and environment. Alternative energy resources are necessary to act towards global climate change and to produce energy in a sustainable way. In this Ph.D. thesis, hierarchical porous MOFs were designed to enhance the CO_2 and H_2 adsorption capacities of traditional MOFs.

Hierarchical porous MOFs were synthesized via a perturbation assisted nanofusion synthesis strategy at which the sizes of textural pores were controlled by metal to linker ratio and synthesis temperature. Formation of hierarchical pores enhanced the BET surface areas and total pore volumes and the highest of all the reported BET surface areas and the pore volumes for MIL-88B and Fe-BTC are achieved. Introducing hierarchical porosity to the

pore structure enhanced the measured CO_2 and H_2 adsorption capacities at 298 K. The achieved CO_2 and H_2 adsorption capacities (298 K and 1 bar) are higher than those of previously reported ones for MIL-88Bs and Fe-BTCs. The enhanced gas adsorption capacities are attributed to the ultramicropores present in the pore structure which have higher binding energies than the wider pores. This Ph.D. study experimentally proves the necessity of ultramicropores in the gas adsorption studies (at 298 K), reports an effortless, and feasible synthesis strategy that can form hierarchical pores and enhance the textural properties and gas adsorption capacities measured at 298 K. This study paves the way for the design of hierarchical porous MOFs and leads the way for the use of hierarchical porous MOFs in gas adsorption studies.

ÖZET

HİYERARŞİK GÖZENEKLİ METAL KAFESLİ YAPILARIN TASARIMI, ÜRETİMİ VE GAZ ADSORPSİYON ÇALIŞMALARINDA ADSORBAN MALZEMELER OLARAK KULLANIMI

AYSU YURDUŞEN

Malzeme Bilimi ve Mühendisliği, Doktora Tezi, Temmuz 2020

Tez Danışmanı: Prof. Dr. Selmiye Alkan Gürsel
Tez Eş-Danışmanı: Dr. Alp Yürüm

Anahtar Kelimeler: Metal-kafesli yapılar, hiyerarşik gözenekli MOFlar, hiyerarşik gözenekler, karbon dioksit adsorpsiyonu, hidrojen adsorpsiyonu

İklim değişikliği, ekonomi, enerji ve çevre ile etkileşime giren küresel bir sorundur. Alternatif enerji kaynakları, küresel iklim değişikliğine karşı harekete geçmek ve sürdürülebilir enerji üretimi için gereklidir. Bu doktora tezinde, hiyerarşik gözenekli metal-kafesli yapılar (MOFlar) gaz adsorpsiyon çalışmalarında kullanılmak üzere ve oda sıcaklığında ölçülen CO_2 ve H_2 adsorpsiyon kapasitelerini arttırmak için tasarlanmıştır. Hyerarşik gözenekli bir yapı oluşturmak için şablonsuz, kolay uygulanabilir bir sentez stratejisi kullanılmıştır. Hiyerarşik gözenekli MOFlar dokusal gözenek boyutlarının metal

bağlayıcı oranı ile ve sentez sıcaklığı ile kontrol edilebildiği pertürbasyon destekli nanofüzyon sentez stratejisi ile sentezlenmiştir. Bu çalışmada sentezlenen hiyerarşik gözenekli MOFların BET yüzey alanları ve toplam gözenek hacimleri önemli miktarda artmış ve literatürde bugüne kadar MIL-88B ve Fe-BTC için rapor edilen en yüksek BET yüzey alanına ve toplam gözenek hacmine ulaşılmıştır.

Hiyerarşik gözenekler sentezlemek, 298 K'de ölçülen CO_2 ve H_2 adsorpsiyon kapasitelerini arttırmıştır. Ulaşılan CO_2 ve H_2 adsorpsiyon kapasiteleri (298 K ve 1 bar) MIL-88B ve Fe-BTC için daha önce bildirilen adsorpsiyon kapasitelerinden daha yüksektir. Artan gaz adsorpsiyon kapasiteleri, daha yüksek bağlanma enerjisine sahip ultramikro gözenek yapıları ile ilişkilendirilmiştir. Bu doktora tez çalışması ile gaz adsorpsiyon çalışmalarında ultramikro gözenek yapılarının gerekliliği deneysel olarak kanıtlanmış, hiyerarşik gözenek oluşturan ve 298 K'de ölçülen gaz adsorpsiyon kapasitelerini arttıran bir sentez yöntemi ve hiyerarşik gözeneklerin boyutlarının sentez parametreleri ile değiştirilme mekanizması rapor edilmiştir. Bu çalışma, hiyerarşik gözenekli MOFların tasarımına zemin hazırlamakta ve hiyerarşik gözenekli MOFların gaz adsorpsiyon çalışmalarında kullanılması için öncü olmaktadır.

This thesis has been dedicated to my beloved parents, Figen and Mustafa Yurduşen, who raised me to believe that anything was possible…

Acknowledgments

Ph.D. journey is an experience that you take it with several invaluable people, whom I would like to thank deeply. This journey had been the most exciting journey I have ever had. But also, with the loss of two people that I believed and loved the most, I felt the deep pain.

I would like to express my deepest gratitude to my advisor Prof. Dr. Yuda Yürüm for his support, encouragement, guidance and patience. It was Prof. Dr. Yuda Yürüm who gave me the opportunity to do my Ph.D. in Sabancı University and encouraged me every single day. He has always been more than an advisor. He made me believe that if I worked sufficient enough, I could success. I will never forget the day that I went to his office to show him our newly synthesized crystals. He was as excited as I was. It has been a real privilege to work with him.

I would like to express my sincere thanks to Prof. Selmiye Alkan Gürsel. During the toughest times, she was always there, supporting and helping me. Her guidance lighted my way.

I would like to express my deepest thanks to Prof. Alp Yürüm for his patience and constant support. He was always available and helped me with his inestimable scientific guidance and support.

I am grateful to my dissertation committee, Prof. Fatma Yüksel, Prof. Mustafa Kemal Bayazıt, Prof. Emre Erdem, and Prof. Alper Uzun for their time and consideration.

I would like to thank NS committee, Dr. Yuki Kaneko, Dr. Süphan Bakkal, Dr. Kerem Bora, and Dr. Aslıhan Ünsal, for their constant support, I owe the many things I have learned to them.

I would like to thank Nursel Karakaya and Sibel Pürçüklü for their constant support. Their fast solutions made me work faster.

I would like to thank Sinem Aydın and Banu Akıncı for their constant and endless support.

I would like to express my greatest thanks to Yürüm Research Group and Sabancı University Energy Storage and Conversion Research Group. Especially, Ezgi Dündar Tekkaya, Zahra Gohari, Buse Bulut, and Adnan Taşdemir.

I owe many thanks to my colleagues and friends who made these seven years fun: Tuğçe Akkaş, İpek Bilge, Senem Seven, Leila Haghighi, Kadriye Kahraman, İlayda Berktaş, Burçin Üstbaş, Gökşin Liu, Omid Moradi, Deniz Köken, Onur Zırhlı (I would definetly miss our camera and fountain pen talks!), Utku Seven and the remaining MAT-grad family.

The very first day I arrived in Sabancı University, I met with Tuğçe Akkaş who become a sister-like, life-long friend and a secret sharer. During my Ph.D. I found my sister-like, life-long friend. I would like to thank her for her constant support through these seven years.

I would like to thank deeply to my beloved family for their support, and patience during this journey. Mom and dad (Figen and Mustafa Yurduşen), they have always taught me to follow my dreams, and encouraged me to do so. Mom always taught me and "forced" me to be a strong and independent woman which daddy also helped me to be one. Their love and support always surrounded me. I owe all the things I earned till today to them.

I have always found myself very lucky to have a brother, Orçun Yurduşen, who is very successful, funny, and has sense of humor. He has always been my role model.

I would like to thank Yeşim Yurduşen for her support, kindness, and love, she has been a real sister to me.

Having a niece (Ela Rin Yurduşen), and a nephew (Tan Yurduşen) is awesome! I would like to thank them for making our lives even more colorful.

Lastly, I owe my loving's to my life-long partner, and husband Erdinç Öztürk. From the very first day we dated till to date, I had my thesis to be completed. I thank you for your patience, support, and understanding.

TABLE OF CONTENTS

ABSTRACT iv
ÖZET vi
Acknowledgments ..... *ix*
TABLE OF CONTENTS xi
LIST OF FIGURES ..... *xiv*
LIST OF TABLES ..... *xxi*
Chapter I Introduction *1*
1.1. Motivation 1
1.2. Challenges and research needs 2
1.3. Objective of thesis 4
1.4. Thesis outline 4
Chapter II Literature Survey *6*
2.1. Introduction 6
2.2. Carbon Dioxide Capture and Storage Technologies 8
2.2.1. Absorption 9
2.2.2. Membrane Contactors 12
2.2.3. Adsorption 18
2.3. Gas Adsorption 30
2.3.1. Thermodynamics of Adsorption 31
2.3.2. Adsorption Potential 31
2.4. Hydrogen Storage 34
2.4.1. Hydrogen Physisorption with Carbon-based Materials 37
2.4.2. Hydrogen Physisorption with Zeolites 39
2.5. Metal-organic Frameworks (MOFs) 40
2.5.1. Hydrogen Storage in MOFs 43
2.6. Hierarchical Porous MOFs 49
Chapter III Effect of iron to benzene-1,4-dicarboxylic acid ratio on and synthesis temperature on the textural properties of hierarchical porous MIL-88Bs *52*
3.1. Background 52
3.2. Experimental 54
3.2.1. Materials 55
3.2.2. Synthesis of Hierarchical Porous MIL-88Bs 55
3.2.3. Characterization of Hierarchical Porous MIL-88Bs 57
3.3. Results and Discussion 59
3.3.1. XRD Analysis 59
3.3.2. SEM Analysis 70
3.3.3. N_2 Sorption Isotherms 74
3.3.4. t-plot Method 77
3.3.5. NLDFT Method 82
3.3.6. FTIR Analysis 87
3.3.7. Thermogravimetric Analysis (TGA) 101

3.3.8. Possible Effect of Fe:TPA Ratio on the Textural Properties....107
3.3.9. Possible Effect of Synthesis Temperature on the Textural Properties....108
3.4. Comparison with Literature....108
3.5. Concluding Remarks....109

Chapter IV....*111*

Carbon dioxide adsorption capacity of hierarchically porous MIL-88Bs and the crucial role of narrow micropores....*111*
4.1. Background....111
4.2. Experimental....115
4.2.1. Materials....115
4.2.2. Synthesis of Hierarchically Porous MIL-88Bs....115
4.2.3. Characterization of Hierarchically Porous MIL-88Bs....116
4.3. Results and Discussion....118
4.3.1. XRD Analysis....118
4.3.2. SEM Imaging....119
4.3.3. Textural Properties....120
Hierarchically porous MIL-88Bs synthesized at 130 °C....128
Hierarchically porous MIL-88Bs synthesized at 150 °C....129
Hierarchically porous MIL-88Bs synthesized with an Fe:BDC ratio of 1....130
Hierarchically porous MIL-88Bs synthesized with an Fe:BDC ratio of 3....131
Hierarchically porous MIL-88Bs synthesized with an Fe:BDC ratio of 5....132
4.3.4. FTIR Analysis....135
4.3.5. TGA Analysis....138
4.3.6. CO_2 Adsorption Studies....140
4.4. Comparison with Literature....162
4.5. Concluding Remarks....163

Chapter V....*165*

Hydrogen adsorption capacity of hierarchically porous MIL-88Bs and the role of ultramicropores....*165*
5.1. Background....165
5.2. Experimental....167
5.2.1. Materials....167
5.2.2. Synthesis....167
5.2.3. Characterization Analysis....168
5.3. Results and Discussion....169
5.3.1. XRD Analysis....169
5.3.2. SEM Images....171
5.3.3. N_2 Sorption Isotherms....172
5.3.4. t-plot Method....175
5.3.5. NLDFT Method....177
A possible mechanism for the widened mesopores in MIL-88B-5....179
5.3.6. FTIR Analysis....180
5.3.7. Thermal Gravimetric Analysis (TGA)....182
5.3.8. H_2 Sorption Analysis....184
5.4. Comparison with Literature....194
5.5. Concluding Remarks....195

Chapter VI Carbon dioxide adsorption capacity of Basolite F300 like hierarchical porous Fe-BTCs and the role of ultramicropores *197*
6.1. Background 197
6.2. Experimental 199
6.2.1. Materials 199
6.2.2. Synthesis of Hierarchically Porous Fe-BTCs 200
6.2.3. Characterization of Hierarchically Porous Fe-BTCs 201
6.3. Results and Discussion 203
6.3.1. XRD Analysis 203
6.3.2. SEM Images 204
6.3.3. N_2 Sorption Isotherms 205
6.3.4. Pore Size Distribution Analysis 207
6.3.5. CO_2 Adsorption Studies 224
6.4. Comparison of the Properties of Fe-BTC Synthesized and Used in Other Studies with Fe-BTC Synthesized in This Study 250
6.5. Comparison with Literature 251
6.5.1. Comparison of the Properties of Fe-BTC Synthesized and Used in Other Studies with Hierarchically Porous Fe-BTCs 251
6.5.2. Comparison of the CO_2 Adsorption Studies of Hierarchically Porous Fe-BTCs and the other MOFs Reported in Literature 253
6.6. Concluding Remarks 255

Chapter VII Hydrogen adsorption capacity of hierarchically porous Fe-BTCs: influence of pore size distribution *257*
7.1. Background 257
7.2. Experimental 260
7.2.1. Materials 260
7.2.2. Synthesis of Hierarchically Porous Fe-BTCs 260
7.2.3. Characterization Analysis 261
7.3. Results and Discussion 263
7.3.1. XRD Analysis 263
7.3.2. SEM Images 264
7.3.3. N_2 Sorption Isotherms 265
7.3.4. t-plot Method 267
7.3.5. NLDFT Method 268
7.3.6. FTIR Analysis 269
7.3.7. TGA 272
7.3.8. H_2 Adsorption Studies 273
7.4. Comparison with Literature 283
7.5. Concluding Remarks 286

Chapter VIII *288*

Conclusion and future works *288*
8.1. Conclusion 288
8.2. Future work 290

BIBLIOGRAPHY *291*

LIST OF FIGURES

Figure 1. Temperature anomaly with respect to years ("Global Temperature | Vital Signs – Climate Change: Vital Signs of the Planet," n.d.) 6

Figure 2. Illustration of the adsorption potential graph of (a) macroporous, (b) mesoporous, and (c) microporous adsorbents (Lowell et al., 2004b). 32

Figure 3. Adsorption isotherms (Lowell et al., 2004b) 33

Figure 4. Schematic representation of experimental procedure. 56

Figure 5. Schematic of conventional crystallization process and nanofusion 57

Figure 6. XRD patterns of the simulated MIL-88B, and the hierarchical porous MIL-88Bs synthesized at 110 °C. 59

Figure 7. XRD patterns of the simulated MIL-88B, and the hierarchical porous MIL-88Bs synthesized at 130 °C. 60

Figure 8. XRD patterns of the simulated MIL-88B, and the hierarchical porous MIL-88Bs synthesized at 150 °C. 61

Figure 9. Comparison of XRD patterns of the simulated MIL-88B, MIL-101, and the hierarchical porous MIL-88Bs synthesized in this study. 62

Figure 10. Comparison of XRD patterns of the simulated MIL-88B, MIL-101, and the hierarchical porous MIL-88Bs synthesized in this study. 63

Figure 11. Comparison of XRD patterns of the simulated MIL-88B, MIL-101, and the hierarchical porous MIL-88Bs synthesized in this study. 64

Figure 12. Comparison of XRD patterns of the simulated MIL-88B, and the hierarchical porous MIL-88B-110-1 synthesized in this study. 65

Figure 13. Comparison of XRD patterns of the simulated MIL-88B, and the hierarchical porous MIL-88B-110-3 synthesized in this study. 65

Figure 14. Comparison of XRD patterns of the simulated MIL-88B, and the hierarchical porous MIL-88B-110-5 synthesized in this study. 66

Figure 15. Comparison of XRD patterns of the simulated MIL-88B, and the hierarchical porous MIL-88B-130-1 synthesized in this study. 66

Figure 16. Comparison of XRD patterns of the simulated MIL-88B, and the hierarchical porous MIL-88B-130-3 synthesized in this study. 67

Figure 17. Comparison of XRD patterns of the simulated MIL-88B, and the hierarchical porous MIL-88B-130-5 synthesized in this study. 67

Figure 18. Comparison of XRD patterns of the simulated MIL-88B, and the hierarchical porous MIL-88B-150-1 synthesized in this study. 68

Figure 19. Comparison of XRD patterns of the simulated MIL-88B, and the hierarchical porous MIL-88B-150-3 synthesized in this study. 68

Figure 20. Comparison of XRD patterns of the simulated MIL-88B, and the hierarchical porous MIL-88B-150-5 synthesized in this study. 69
Figure 21. SEM images of MIL-88B-110-1, MIL-88B-110-3, and MIL-88B-110-5. 71
Figure 22. SEM images of MIL-88B-130-1, MIL-88B-130-3, and MIL-88B-130-5. 72
Figure 23. SEM images of MIL-88B-150-1, MIL-88B-150-3, and MIL-88B-150-5. 73
Figure 24. N_2 sorption isotherms of hierarchically porous MIL-88Bs. 74
Figure 25. N_2 sorption isotherms of MIL-88B-110-1, MIL-88-110-3, and MIL-88B-110-5. 75
Figure 26. N_2 sorption isotherms of MIL-88B-130-1, MIL-88-130-3, and MIL-88B-130-5. 76
Figure 27. N_2 sorption isotherms of MIL-88B-150-1, MIL-88-150-3, and MIL-88B-150-5. 76
Figure 28. t-plots of hierarchically porous MIL-88Bs. 78
Figure 29. t-plots of MIL-88B-110-1, MIL-88B-110-3, and MIL-88B-110-5. 79
Figure 30. t-plots of MIL-88B-130-1, MIL-88B-130-3, and MIL-88B-130-5. 80
Figure 31. t-plots of MIL-88B-150-1, MIL-88B-150-3, and MIL-88B-150-5. 81
Figure 32. NLDFT plot of hierarchically porous MIL-88Bs synthesized at 110 °C. 83
Figure 33. NLDFT plot of MIL-88B-110-1, MIL-88B-110-3, and MIL-88B-110-5. 83
Figure 34. NLDFT plot hierarchically porous MIL-88Bs synthesized at 130 °C. 84
Figure 35. NLDFT plot of MIL-88B-130-1, MIL-88B-130-3, and MIL-88B-130-5. 84
Figure 36. NLDFT plot MIL-88B type MOF crystallites synthesized at 150 °C. 85
Figure 37. NLDFT plot of MIL-88B-150-1, MIL-88B-150-3, and MIL-88B-150-5. 85
Figure 38. FTIR spectra of hierarchically porous MIL-88Bs and the $FeCl_3.6H_2O$. 88
Figure 39. FTIR spectra of hierarchical porous MIL-88Bs synthesized with an Fe:BDC ratio of 1. 89
Figure 40. FTIR spectra of MIL-88B-110-3, MIL-88B-130-3, and MIL-88B-150-3. 93
Figure 41. FTIR spectra of MIL-88B-110-5, MIL-88B-130-5, and MIL-88-150-5. 97
Figure 42. TGA curves of MIL-88B-110-1, MIL-88B-110-3, and MIL-88B-110-5. 102
Figure 43. TGA curves of MIL-88B-130-1, MIL-88B-130-3, and MIL-88B-130-5. 104
Figure 44. TGA curves of MIL-88B-150-1, MIL-88B-150-3, and MIL-88B-150-5. 106
Figure 45. XRD pattern of hierarchically porous MIL-88Bs. 119
Figure 46. SEM images of hierarchically porous MIL-88Bs (a) MIL-88B-110-1, (b) MIL-88B-110-3, (c) MIL-88B-110-5, (d) MIL-88B-130-1, (e) MIL-88B-130-3, (f) MIL-88B-130-5, (g) MIL-88B-150-1, (h) MIL-88B-150-3, and (i) MIL-88B-150-5. 120
Figure 47. N_2 sorption isotherms of hierarchically porous MIL-88Bs. 122

Figure 48. N_2 sorption isotherms of MIL-88B-110-1, MIL-88-110-3, and MIL-88B-110-5. 122
Figure 49. N_2 sorption isotherms of MIL-88B-130-1, MIL-88-130-3, and MIL-88B-130-5. 123
Figure 50. N_2 sorption isotherms of MIL-88B-150-1, MIL-88-150-3, and MIL-88B-150-5. 123
Figure 51. t-plots of hierarchically porous MIL-88Bs 124
Figure 52. NLDFT plot of hierarchically porous MIL-88Bs synthesized at 110 °C..... 127
Figure 53. NLDFT plot of hierarchically porous MIL-88Bs synthesized at 130 °C..... 128
Figure 54. NLDFT plot of hierarchically porous MIL-88Bs synthesized at 150 °C..... 129
Figure 55. NLDFT plot of hierarchically porous MIL-88Bs synthesized with an Fe:BDC ratio of 1. 130
Figure 56. NLDFT plot of MIL-88B-110-1, MIL-88B-130-1, and MIL-88B-150-1. 130
Figure 57. NLDFT plot of hierarchically porous MIL-88Bs synthesized with an Fe:BDC ratio of 3. 131
Figure 58. NLDFT plot of MIL-88B-110-3, MIL-88B-130-3, and MIL-88B-150-3. 131
Figure 59. NLDFT plot of hierarchically porous MIL-88Bs synthesized with an Fe:BDC ratio of 5. 132
Figure 60. NLDFT plot of MIL-88B-110-5, MIL-88B-130-5, and MIL-88B-150-5. 133
Figure 61. FTIR spectra of hierarchically porous MIL-88Bs synthesized with an Fe:BDC ratio of 1. 135
Figure 62. FTIR spectra of hierarchically porous MIL-88Bs synthesized with an Fe:BDC ratio of 3. 136
Figure 63. FTIR spectra of hierarchically porous MIL-88Bs synthesized with an Fe:BDC ratio of 5. 137
Figure 64. TGA curves of hierarchically porous MIL-88Bs. 139
Figure 65. Comparison of experimental data and nonlinear fitting of Langmuir and Freundlich model of MIL-88B-110-1. 143
Figure 66. Comparison of experimental data and nonlinear fitting of Langmuir and Freundlich model of MIL-88B-110-3. 144
Figure 67. Comparison of experimental data and nonlinear fitting of Langmuir and Freundlich model of MIL-88B-110-5. 145
Figure 68. Comparison of experimental data and nonlinear fitting of Langmuir and Freundlich model of MIL-88B-130-1. 146
Figure 69. Comparison of experimental data and nonlinear fitting of Langmuir and Freundlich model of MIL-88B-130-3. 147
Figure 70. Comparison of experimental data and nonlinear fitting of Langmuir and Freundlich model of MIL-88B-130-5. 148

Figure 71. Comparison of experimental data and nonlinear fitting of Langmuir and Freundlich model of MIL-88B-150-1. 149
Figure 72. Comparison of experimental data and nonlinear fitting of Langmuir and Freundlich model of MIL-88B-150-3. 150
Figure 73. Comparison of experimental data and nonlinear fitting of Langmuir and Freundlich model of MIL-88B-150-5. 151
Figure 74. CO_2 adsorption isotherm of hierarchically porous MIL-88Bs measured at 298 K. 154
Figure 75. Dependence of CO_2 adsorption capacity on BET surface area. 155
Figure 76. Dependence of CO_2 adsorption capacity on volume of narrow micropores. 156
Figure 77. Dependence of CO_2 adsorption capacity on micropore volume. 156
Figure 78. Dependence of CO_2 adsorption capacity on mesopore volume. 157
Figure 79. Dependence of CO_2 adsorption capacity on total pore volume. 157
Figure 80. Volume of pores narrower than 1 and 2 nm reported with standard deviations. 160
Figure 81. CO_2 uptake capacity of some of the MOFs reported in literature and MIL-88B (shown in red) reported in this report (at 1 bar and 298 K). 163
Figure 82. XRD patterns of MIL-88B-1, MIL-88B-3, and MIL-88B-5. 170
Figure 83. Comparison of XRD patterns of simulated MIL-88B and synthesized hierarchically porous MIL-88Bs. 171
Figure 84. SEM images of hierarchically porous MIL-88Bs. 172
Figure 85. N_2 sorption isotherms of MIL-88B-1, MIL-88B-3, and MIL-88B-5. 173
Figure 86. N_2 sorption isotherm of MIL-88B-1. 173
Figure 87. N_2 sorption isotherm of MIL-88B-3. 174
Figure 88. N_2 sorption isotherm of MIL-88B-5. 174
Figure 89. t-plots of MIL-88B-1, MIL-88B-3, and MIL-88B-5. 175
Figure 90. t-plot of MIL-88B-1. 176
Figure 91. t-plot of MIL-88B-3. 176
Figure 92. t-plot of MIL-88B-5. 177
Figure 93. NLDFT plots of MIL-88B type MOF crystallites. 177
Figure 94. Schematic diagram of textural pore formation sequence. 179
Figure 95. Schematic diagram of textural pore formation mechanism. 179
Figure 96. FTIR spectra of MIL-88B-1, MIL-88B-3, and MIL-88B-5. 181
Figure 97. TGA curve of hierarchically porous MIL-88B. 183
Figure 98. H_2 sorption isotherms of MIL-88B-1, MIL-88B-3, and MIL-88B-5 measured at 298 K. 185

Figure 99. Comparison of experimental data and nonlinear fitting of Langmuir and Freundlich model of H_2 adsorption behavior on MIL-88B-1.....187
Figure 100. Comparison of experimental data and nonlinear fitting of Langmuir and Freundlich model of H_2 adsorption behavior on MIL-88B-3.....188
Figure 101. Comparison of experimental data and nonlinear fitting of Langmuir and Freundlich model of H_2 adsorption behavior on MIL-88B-5.....189
Figure 102. NLDFT plots of incremental pore volume versus pore width of hierarchical porous MIL-88Bs. 191
Figure 103. NLDFT plots of cumulative pore volume versus pore width of hierarchical porous MIL-88Bs. 192
Figure 104. NLDFT plots of cumulative pore volume versus pore width of MIL-88B crystallites.....192
Figure 105. XRD patterns of hierarchically porous Fe-BTCs.....203
Figure 106. SEM images of hierarchically porous Fe-BTCs. 204
Figure 107. N_2 sorption isotherms of hierarchically porous Fe-BTCs.....205
Figure 108. N_2 sorption isotherms of Fe-BTC-110-1, Fe-BTC-110-3, and Fe-BTC-110-5. 206
Figure 109. N_2 sorption isotherms of Fe-BTC-130-1, Fe-BTC-130-3, and Fe-BTC-130-5. 206
Figure 110. N_2 sorption isotherms of Fe-BTC-150-1, Fe-BTC-150-3, and Fe-BTC-150-5. 206
Figure 111. t-plots of hierarchically porous Fe-BTCs. 207
Figure 112. NLDFT plots of Fe-BTC type crystallites. 209
Figure 113. FTIR spectra of hierarchically porous Fe-BTCs and $FeCl_3.6H_2O$.....211
Figure 114. FTIR spectra of hierarchically porous Fe-BTCs.....212
Figure 115. FTIR spectra of Fe-BTC-110-1, Fe-BTC-110-3, and Fe-BTC-110-5. 213
Figure 116. FTIR spectra of Fe-BTC-130-1, Fe-BTC-130-3, and Fe-BTC-130-5. 214
Figure 117. FTIR spectra of Fe-BTC-150-1, Fe-BTC-150-3, and Fe-BTC-150-5. 215
Figure 118. TGA curves of Fe-BTCs.....217
Figure 119. TGA curve of Fe-BTC-110-1. 217
Figure 120. TGA curve of Fe-BTC-110-3. 218
Figure 121. TGA curve of Fe-BTC-110-5. 218
Figure 122. TGA curve of Fe-BTC-130-1. 219
Figure 123. TGA curve of Fe-BTC-130-3. 220
Figure 124. TGA curve of Fe-BTC-130-5. 220
Figure 125. TGA curve of Fe-BTC-150-1. 221

Figure 126. TGA curve of Fe-BTC-150-3. 222
Figure 127. TGA curve of Fe-BTC-150-5. 222
Figure 128. Comparison of experimental data and nonlinear fitting of Langmuir and Freundlich Model of Fe-BTC-110-1. 226
Figure 129. Comparison of experimental data and nonlinear fitting of Langmuir and Freundlich Model of Fe-BTC-110-3. 227
Figure 130. Comparison of experimental data and nonlinear fitting of Langmuir and Freundlich Model of Fe-BTC-110-5. 228
Figure 131. Comparison of experimental data and nonlinear fitting of Langmuir and Freundlich Model of Fe-BTC-130-1. 230
Figure 132. Comparison of experimental data and nonlinear fitting of Langmuir and Freundlich Model of Fe-BTC-130-3. 231
Figure 133. Comparison of experimental data and nonlinear fitting of Langmuir and Freundlich Model of Fe-BTC-130-5. 232
Figure 134. Comparison of experimental data and nonlinear fitting of Langmuir and Freundlich Model of Fe-BTC-150-1. 234
Figure 135. Comparison of experimental data and nonlinear fitting of Langmuir and Freundlich Model of Fe-BTC-150-3. 235
Figure 136. Comparison of experimental data and nonlinear fitting of Langmuir and Freundlich Model of Fe-BTC-150-5. 236
Figure 137. CO_2 adsorption isotherm of hierarchically porous Fe-BTCs. 237
Figure 138. Dependence of CO_2 adsorption capacity of hierarchically porous Fe-BTCs on narrow micropore volume. 239
Figure 139. Dependence of CO_2 adsorption capacity on micropore volume of hierarchically porous Fe-BTCs. 239
Figure 140. Dependence of CO_2 adsorption capacity on mesopore volume of hierarchically porous Fe-BTCs. 240
Figure 141. Dependence of CO_2 adsorption capacity on the BET surface area of hierarchically porous Fe-BTCs. 240
Figure 142. Dependence of CO_2 adsorption capacity on the BET surface area of hierarchically porous Fe-BTCs. 241
Figure 143. NLDFT plot of hierarchically porous Fe-BTCs. 242
Figure 144. Narrow micropore volumes of hierarchically porous Fe-BTCs. 243
Figure 145. Comparison of the CO_2 adsorption capacities (5 bar and 298 K) and the narrow micropore volumes of Fe-BTC-150-3 and Fe-BTC-150-5 244
Figure 146. CO_2 adsorption isotherm (298 K) of Fe-BTC-110-5, and Fe-BTC-150-5. 245
Figure 147. Comparison of the CO_2 adsorption capacities measured at 5 bar and 298 K and the narrow micropore volumes of Fe-BTC-110-5 and Fe-BTC-150-5. 246

Figure 148. CO_2 adsorption isotherm (298 K) of Fe-BTC-110-1, Fe-BTC-110-3, and Fe-BTC-110-5.....247
Figure 149. CO_2 adsorption isotherm (298 K) of Fe-BTC-130-1, Fe-BTC-130-3, and Fe-BTC-130-5.....248
Figure 150. CO_2 adsorption isotherm (298 K) of Fe-BTC-150-1, Fe-BTC-150-3, and Fe-BTC-150-5.....249
Figure 151. Schematic representation of experimental procedure. 261
Figure 152. XRD patterns of Fe-BTC-1, Fe-BTC-3, and Fe-BTC-5. 263
Figure 153. SEM images of Fe-BTC-1. 264
Figure 154. SEM images of Fe-BTC-3. 264
Figure 155. SEM images of Fe-BTC-5. 264
Figure 156. N_2 sorption isotherms of Fe-BTC-1, Fe-BTC-3, and Fe-BTC-5. 265
Figure 157. N_2 sorption isotherms of Fe-BTC-1, Fe-BTC-3, and Fe-BTC-5. 266
Figure 158. t-plots of Fe-BTC-1, Fe-BTC-3, and Fe-BTC-5. 267
Figure 159. NLDFT plots of Fe-BTC-1, Fe-BTC-3, and Fe-BTC-5. 268
Figure 160. FTIR spectra of Fe-BTC-1, Fe-BTC-3, and Fe-BTC-5. 270
Figure 161. TGA curve of Fe-BTC-1, Fe-BTC-3, and Fe-BTC-5. 272
Figure 162. H_2 sorption isotherms (298 K) of Fe-BTC-1, Fe-BTC-3, and Fe-BTC-5.....274
Figure 163. Comparison of the experimental and the estimated data (Fe-BTC-1). 276
Figure 164. Comparison of the experimental and the estimated data (Fe-BTC-3). 277
Figure 165. Comparison of the experimental and the estimated data (Fe-BTC-5). 278
Figure 166. Volume of narrow- and micropores of Fe-BTC-1, Fe-BTC-3, and Fe-BTC-5 279
Figure 167. H_2 adsorption capacity (7.6 bar and 298 K) and narrow micropore volume of Fe-BTC-1 and Fe-BTC-5 280
Figure 168. H_2 adsorption capacity (7.6 bar and 298 K) and the narrow micropore volume of Fe-BTCs 282
Figure 169. Comparison of H_2 adsorption capacities of Fe-BTC-3 and some of the MOFs reported in literature 285

LIST OF TABLES

Table 1. Abbreviations for the hierarchical porous MIL-88Bs synthesized at different temperatures with different Fe:BDC ratio. 56

Table 2. Micropore volume, slope, y-intercept, and correlation coefficient estimated by t-plot method. 78

Table 3. BET surface area(m^2/g), micropore volume (m^3/g) and total pore volume (cm^3/g) of hierarchically porous MIL-88Bs synthesized at 110, 130, 150 °C with different iron to TPA ratio. 87

Table 4. Representative assigned modes of hierarchical porous MIL-88Bs synthesized at 110°C. 90

Table 5. Representative assigned modes of hierarchically porous MIL-88Bs synthesized at 130°C. 94

Table 6. Representative assigned modes of MOF crystallites synthesized at 150°C. 98

Table 7. Percentage of residual mass left after TGA was completed, %. 101

Table 8. % mass loss during TGA analysis of MIL-88B-110-1, MIL-88B-110-3, and MIL-88B-110-5 103

Table 9. % mass loss during TGA analysis of MIL-88B-130-1, MIL-88B-130-3, and MIL-88B-130-5 105

Table 10. % mass loss during TGA analysis of MIL-88B-150-1, MIL-88B-150-3, and MIL-88B-150-5 107

Table 11. BET surface area and pore volume of MIL-88Bs reported in literature 109

Table 12. Abbreviations for the hierarchically porous MIL-88Bs synthesized at different temperatures with different Fe:BDC ratio. 116

Table 13. BET surface area, micropore area, micropore volume, and fraction of mesoporosity 121

Table 14. Micropore volume, slope, y-intercept, and correlation coefficient estimated by t-plot method. 125

Table 15. Micro- and mesopore volume, fraction of micro- and mesoporosity estimated by NLDFT method 126

Table 16. Volume of mesopores at the upper mesopore size range, and their distribution within mesopores and the whole pore size range. 127

Table 17. Percentage of residual mass, % 139

Table 18. Decomposition temperature, °C 140

Table 19. Respective equations obtained from models 141

Table 20. Langmuir and Freundlich isotherm parameters 142

Table 21. Respective model and monolayer capacity of the hierarchically porous MIL-88Bs 152
Table 22. CO_2 uptake capacities of hierarchically porous MIL-88Bs at 1, 3 and 5 bar and 25 °C 153
Table 23. Pore volumes, pore volume ratios, and CO_2 uptake capacity of hierarchically porous MIL-88Bs 159
Table 24. Sample Abbreviations 168
Table 25. Volume of ultramicropores, narrow micropores, micropores, and mesopores 178
Table 26. % mass loss during TGA 184
Table 27. Respective equations obtained from models 186
Table 28. Langmuir and Freundlich isotherm parameters 186
Table 29. Textural properties, H_2 sorption capacity (wt. % at 7.6 bar and 298 K), H_2 uptake per specific surface area (10^3 wt. % g/m^2) of MIL-88B-1, MIL-88B-3, and MIL-88B-5 190
Table 30. H_2 sorption capacities of MOFs 194
Table 31. Sample abbreviations for hierarchical porous Fe-BTCs 201
Table 32. Micro- and mesopore area (m^2/g), micropore volume of Fe-BTC type crystallites estimated by t-plot method. 208
Table 33. Volume of pores smaller than 1 nm, micro-, uppermeso-, mesopore and total pore volume, and fraction of micropores of Fe-BTCs estimated by NLDFT method. 210
Table 34. % mass loss during TGA of hierarchically porous Fe-BTCs synthesized at 110 °C. 219
Table 35. % mass loss during TGA analysis of hierarchically porous Fe-BTCs synthesized at 130 °C. 221
Table 36. % mass loss during TGA analysis of hierarchically porous Fe-BTCs synthesized at 150 °C. 223
Table 37. Percent residual mass at the end of TGA. 223
Table 38. Respective equations obtained from models 224
Table 39. Langmuir and Freundlich isotherm parameters 225
Table 40. Respective equations obtained from models 228
Table 41. Langmuir and Freundlich isotherm parameters 229
Table 42. Respective equations obtained from models 232
Table 43. Langmuir and Freundlich isotherm parameters 233
Table 44. Volume of ultramicropores (pore diameter < 0.7 nm), narrow micropores and micropores, and CO2 adsorption capacities of Fe-BTC type crytallites measured at 5 bar and 298 K. 238
Table 45. BET surface areas, total pore volume and decomposition temperature of Fe-BTCs synthesized in different studies 250

Table 46. BET surface areas, total pore volume and decomposition temperature of Fe-BTCs synthesized in different studies 252
Table 47. BET surface areas, and CO_2 uptake capacities of some of those reported MOFs 254
Table 48. Sample abbreviations of hierarchically porous Fe-BTCs synthesized with different Fe:BTC ratio 261
Table 49. BET surface area (m^2/g) and total pore volume (cm^3/g) of Fe-BTCs 266
Table 50. Micro-, and mesopore area, micropore to total pore area fraction and micropore volume estimated by t-plot method 267
Table 51. Narrow micro-, micro-, uppermeso-, meso- and total pore volume estimated by NLDFT method 269
Table 52. FTIR frequencies of Fe-BTCs 271
Table 53. % mass loss during TGA analysis of Fe-BTC synthesized at 150 °C 273
Table 54. Percent residual mass at the end of TGA. 273
Table 55. Respective equations obtained from models 275
Table 56. Langmuir and Freundlich isotherm parameters 275
Table 57. BET surface area, ultramicro-, narrow micro-, micropore volume, volume fraction of narrow micro- to micropores, and H_2 adsorption capacities of Fe-BTCs 279
Table 58. BET surface area, pore volume, and H_2 adsorption capacity of MOFs reported in literature 284

LIST OF SYMBOLS AND ABBREVIATIONS

ACs: Activated carbons

ACS: American Chemical Society

BTC: Benzene-1,3,5-tricarboxylic acid

CNTs: Carbon nanotubes

APTS: 3-aminopropyl-triethoxysilane

BET: Brunauer Emmett Teller

CCS: Carbon capture and storage

CO_2: Carbon dioxide

DMF: N, N-Dimethylformamide

DOE: U.S. Department of Energy

DMAB: (dimethylamino)-2-butanol

$FeCl_3.6H_2O$: Iron(III) chloride hexahydrate

FTIR: Fourier Transformed Infrared Spectroscopy

HEEBAB: 4-((2-hydroxyethyl)(ethyl)amino)-2-butanol

HEMAB: 4-((2 hydroxyethyl)(methyl)amino)-2-butanol

HPLC: High performance liquid chromatography

IEA: International Energy Agency

IGA: Intelligent Gravimetric Analyzer

ILs: Ionic liquids

IUPAC: International Union of Pure and Applied Chemistry

IPCC: Intergovernmental Panel on Climate Change

MEA: Monoethanolamine

MeOH: Methanol

MOFs: Metal-organic frameworks

NH_3: Ammonia

NLDFT: Non-Local Density Functional Theory

PDMS: Polydimethylsiloxane

PE: Polyethylene

PP: Polypropylene

PTFE: Polytetrafluoroethylyene

PVDF: Polyvinylidene fluoride

PXRD: Powder x-ray diffraction

rGO: Reduced graphene oxide

SBUs: Secondary building units

SEM: Scanning Electron Microscopy

STP: Standard temperature and pressure

TEA: Triethanolamine

TGA: Thermal Gravimetric Analyzer

TPA: Benzene-1,4-dicarboxylic acid

XRD: X-ray Diffraction

C_e: Adsorbate concentration in equilibrium (mg/L)

K_a: Langmuir adsorption constant (L/mg)

K_F: Freundlich constant (mg/g)

1/n: Measure of intensity (Freundlich isotherm)

Q_e: Solute amount adsorbed per unit weight of adsorbent (mg/g)

Q_m: Capacity at monolayer coverage (mg/g)

Q_o: Maximum monolayer coverage capacity(mg/g)

R^2: Coefficient of determination value

ΔG: Free energy change

ΔH: Ethalphy change (kJ/ mol)

ΔS: Entropy change (kJ/mol)

Chapter I
Introduction

"I'd put my money on the sun and solar energy, what a source of power. I hope we don't have to wait until oil and coal run out, before we tackle that".
Thomas Edison, 1931

1.1. Motivation

We, humanity, are the richest of all times, have prolonged life times, we have developed technology, we have machines that can solve even the most difficult problems that we cannot solve. However, we still cannot figure out a solution for climate change which poses a direct threat on our rights to access clean, safe, and cheap water, clean air, food, energy, our health, and our communities' development.

Climate change is a global concern, at which a vision has to be shared globally, and a world-wide cooperation has to be established. Climate change interacts with economics, energy and environment. While trying to find out a solution, we should always keep in mind that economics, energy and environment cannot be separated from each other. Energy is necessary for the development of the society but also it is the major contributor to the anthropogenic greenhouse gas emissions. We do need alternative energy resources to act towards global climate change and resupply the depleted hydrocarbon reserves. Moreover, the development of alternative energy sources has to be fast enough to keep the depletion pace of hydrocarbon sources while switching our conventional energy sources into alternative energy sources.

1.2. Challenges and research needs

10% of the CO_2 produced today remains in the atmosphere for ten thousand years, which makes CO_2 come to the front. To reduce the risks and the magnitude of the impacts of climate change, a target has been set by Intergovernmental Panel on Climate Change (IPCC) which limits the global temperature rise to 1.5 °C. However, none of the mitigation measures are able to decrease the CO_2 emissions to zero, unless all of them, together applied.

Carbon capture and storage (CCS) is one of the measures that can decrease the CO_2 emissions by 80 to 90% in power plants. Absorption process which is the mostly used CO_2 capture technology is limited by its high energy demand, energy intensive regeneration processes, by-product formation (ammonia and salts), and decreased absorption capacities due to absorption of end-products. In the meanwhile, the use of membrane contactors is limited by membrane degradation, membrane fouling, and membrane wetting. For the commercial use of membrane contactors, these limitations should be overcome and chemically and thermally stable membranes should be developed at industrial scale.

Adsorption comes to front with its low-cost, less energy intensive regeneration processes, feasibility, and easy applicability. However, for the commercial use of adsorbents, there is still room for improvement. For instance, carbon-based materials show low CO_2 adsorption performances, and low selectivity; zeolites show low CO_2 adsorption performances. CO_2 adsorption capacities of silica-based materials decrease at high temperatures. Polymer-based materials show promising CO_2 adsorption capacities. However, after several adsorption and desorption cycles, CO_2 adsorption capacities of polymer-based materials decrease, drastically. Alkali-metal carbonate-based materials are also investigated for their use in CO_2 adsorption studies. However, the low durability, and slow carbonation reaction rates limits the use of these materials in practical applications. The CO_2 adsorption capacities of MgO and CaO based materials are also investigated. However, the use of MgO based sorbents are limited with the long regeneration processes while the use of CaO based sorbents are limited with the low durability, and short-life cycle of these materials.

MOFs get ahead of the above-mentioned adsorbents owing to their tunable topology, high BET surface area, and high porosity. However, due to weak van der Waals interactions between CO_2 molecules and MOFs, adsorption capacity of MOFs decreases drastically at

ambient temperature. Despite all the strategies developed and the progresses made, it is still a challenge to achieve an optimum CO_2 adsorption capacity at 298 K. There remains a big room to develop MOFs with larger isosteric heat of adsorption values.

Transport sector contribute to the overall greenhouse gas emissions by 14%. Hydrogen is a promising alternative to fossil fuels since it is abundant, and no by-product is formed. However, storing hydrogen in a safe, light and economic way still remains as a challenge which is necessary for the practical use of on-board hydrogen storage systems. Among the hydrogen storage methods investigated to date, physisorption comes to front owing to its low cost and feasibility. However, physisorption is limited by the weak van der Waals forces and despite the high H_2 adsorption capacities measured at 77 K, the measured H_2 adsorption capacities decrease dramatically at room temperature and atmospheric pressure.

Carbon-based materials were considered as promising H_2 storage materials owing to their availability, low-cost, high BET surface areas, and high porosities. However, when the H_2 adsorption studies are conducted at 298 K, the measured H_2 adsorption capacities decrease drastically. Despite the developed strategies and enhancements achieved, the measured H_2 adsorption capacities are far from meeting the U.S. DOE target of on-board hydrogen storage.

Zeolites are another family of materials that were considered as promising candidates as on-board hydrogen storage materials. Despite all the strategies developed, H_2 adsorption capacities of zeolite-based materials are also far from achieving the U.S. DOE target of on-board hydrogen storage.

MOFs are considered as promising candidates for hydrogen storage studies and get ahead of other materials owing to their high porosity, tunability and promising results obtained from H_2 adsorption measurements at 77 K. Despite the very high H_2 adsorption capacities measured at 77 K and high pressures, H_2 adsorption capacities of MOFs decrease drastically at 298 K and atmospheric pressure. It is still a challenge to design a MOF with a high H_2 adsorption capacity that meets the U.S. DOE target of on-board hydrogen storage.

The low H_2 adsorption capacities of MOFs at 298 K are attributed to the very weak van der Waals interactions between MOFs and H_2 molecules. The very weak van der Waals interactions result isosteric heat of adsorption values of MOFs to vary in between 4 to 7 kJ/mol while to adsorb considerable amount of H_2 at ambient temperature 15 kJ/mol of

energy is needed. In order to develop MOFs that function optimally at 298 K, binding energies between the H_2 molecules and MOFs should be enhanced and a MOF that possesses an adsorption enthalpy of 15 kJ/mol should be developed.

1.3. Objective of thesis

The overall objective of this Ph.D. study is to develop hierarchical porous MOFs, enhance their gas adsorption capacities measured at 298 K, and show the influence of pore size and pore size distribution on the gas adsorption capacities measured at 298 K.

The scope is to synthesize hierarchical porous MOFs with different pore size and pore size distributions, and characterize these materials, analyze their pore size and pore size distribution extensively, and measure and evaluate the CO_2 and H_2 adsorption capacities. The CO_2 and H_2 adsorption behaviors of these materials are further studied by analyzing their pore size distributions, in detail. The findings are used to develop adsorbents with enhanced gas adsorption capacities. The objectives of this study are listed as follows:

(1) To synthesize hierarchically porous MOFs with different pore size distributions,
(2) To optimize synthesis parameters to form textural pores with different pore diameters,
(3) To investigate CO_2 and H_2 adsorption capacities of hierarchical porous MOFs,
(4) To evaluate the CO_2 and H_2 adsorption behaviors of the hierarchical porous MOFs with pore size distribution analysis,
(5) To develop a hierarchical porous MOF with enhanced CO_2 and H_2 adsorption capacity.

1.4. Thesis outline

This thesis is divided into eight chapters. You can find the content of the chapters as listed below:

- Chapter I presents the motivation, challenges and research needs, objectives, and outline of thesis,

- Chapter II provides a brief literature survey of climate change, mitigation measures, gas adsorption theory, materials used for CO_2 adsorption studies, metal-organic frameworks (MOFs), and hierarchical porous MOFs,
- Chapter III describes the synthesis method and the characterization analyses of hierarchical porous MIL-88Bs, and discusses the effect of iron to benzene-1,4-dicarboxylic acid ratio and synthesis temperature on the textural properties of hierarchical porous MIL-88Bs,
- Chapter IV investigates the CO_2 adsorption capacity of hierarchically porous MIL-88Bs and discusses the crucial role of narrow micropores on the CO_2 adsorption capacity of hierarchically porous MIL-88Bs,
- Chapter V examines the H_2 adsorption capacity of hierarchically porous MIL-88Bs and discusses the role of ultramicropores on the H_2 adsorption capacity of hierarchically porous MIL-88Bs,
- Chapter VI describes the synthesis and the characterization analyses of hierarchical porous Fe-BTCs, and investigates the CO_2 adsorption capacity of Basolite F300 like hierarchical porous Fe-BTCs,
- Chapter VII presents the results of H_2 adsorption studies conducted with hierarchically porous Fe-BTCs and discusses the influence of pore size distribution on the H_2 adsorption capacity,
- Chapter VIII summarizes the conclusions of the study and discusses the possible further work.

Chapter II

Literature Survey

2.1. Introduction

The impact of carbon dioxide (CO_2) on the Earth's surface temperature was firstly mentioned by Arrhenius (Svante, 1896). From the pre-industrial period (1850 to 1900) till today, the global surface temperature has increased by 1 °C (IPCC, 2018). Moreover, the five warmest years were recorded since 2010 (NASA, 2019) and the year 2016 has been reported as the warmest year since 1880 (NASA/GISS, 2019). The following graph (Figure 1) shows the temperature anomaly with respect to years.

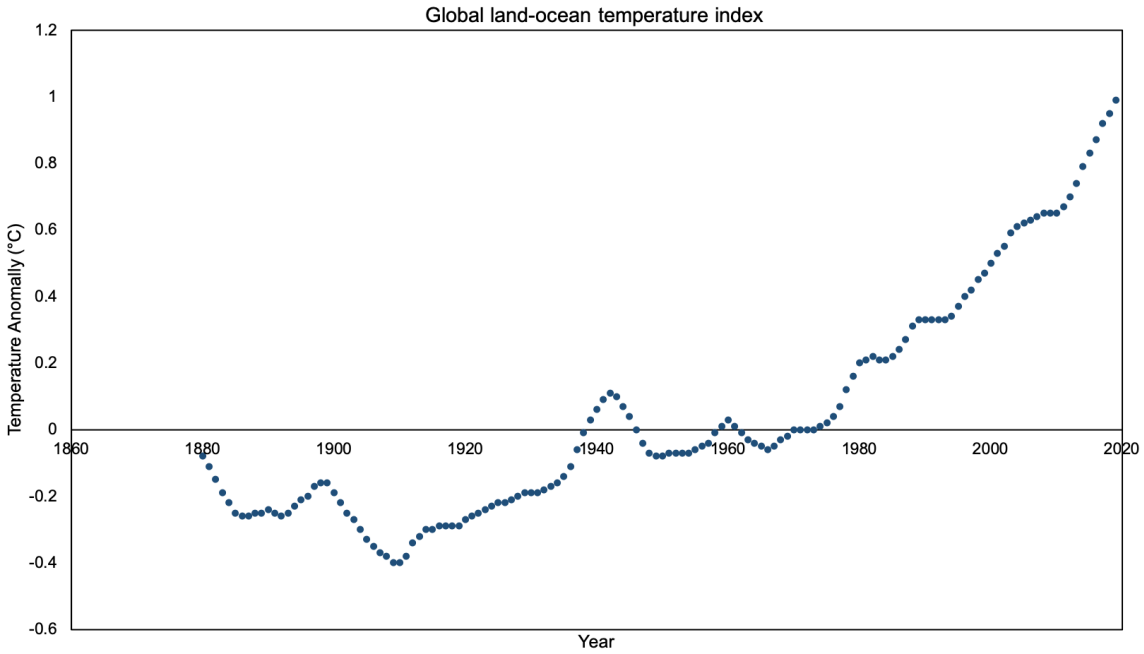

Figure 1. Temperature anomaly with respect to years ("Global Temperature | Vital Signs – Climate Change: Vital Signs of the Planet," n.d.)

Since the mid 20th century, a significant rise is observed in the annual mean temperatures. This significant rise is attributed to the anthropogenic greenhouse gas emissions. Recently conducted investigations pointed out the substantial increase in CO_2

levels. From preindustrial period till today CO_2 concentrations increased from 280 to 413 ppm and the measured CO_2 concentration of today is the highest of all the measured CO_2 concentrations for 650 thousand years (NASA, 2020). Scientists associated the increase in the surface temperatures of the late 21st century to the increase in the cumulative CO_2 emissions.

Among the greenhouse gases, CO_2 plays a key role (Ciais et al., 2013). Particularly, water vapor, methane, and nitrous oxides leave the atmosphere in 10 days, 10 years, and 100 years, respectively while 10% of the CO_2 emitted today, remains in the atmosphere for ten thousand years, past our lifetimes (Ciais et al., 2013). Within the last forty years, the cumulative CO_2 concentrations have reached 50% of the measured CO_2 concentrations and the greenhouse gas emissions have increased from 27 to 49 gigatons of CO_2 equivalent (Adger & Coauthors including Fischlin, 2007; Intergovernmental Panel on Climate Change, 2014). Fossil fuel combustion and the industrial processes contribute to the total greenhouse gas emissions by 78% (Adger & Coauthors including Fischlin, 2007; Intergovernmental Panel on Climate Change & Intergovernmental Panel on Climate Change, 2015). Our activities caused surface temperatures to increase by 1 °C from pre-industrial period till today. However, if no precautions are taken and the warming continues to rise at the same rate global warming would reach 1.5 °C in between 2030 and 2052 (Masson-Delmotte et al., 2018).

The Intergovernmental Panel on Climate Change (IPCC) points out that further increase in surface temperatures will increase the irreversible effects of climate change. As climate system changes, the magnitude of the risks rises. These risks include extinction of some species, food insecurity, difficulty in finding accessible surface and groundwaters in dry regions, increases in illnesses, and extreme weather events. However, it is foreseen that even if the greenhouse gas emissions are totally cut now, the impacts of climate change will be issued for centuries and reducing the greenhouse gas emissions will only reduce the magnitude of the impacts of climate change (Stocker et al., 2013).

Within the framework of the Paris Agreement, a target has been set to decrease the greenhouse gas emissions, by this way risks and the magnitude of the impacts of climate change can be reduced. According to Paris Agreement, to decrease the risks and impacts of climate change, considerable efforts will be put to limit the global temperature rise to 1.5 °C above the pre-industrial levels (United Nations, 2015). Thereby, several strategies have been

suggested to decrease CO_2 emissions: (i) developing energy systems that decrease energy intensity; (ii) decreasing carbon intensity by using low carbon fuels; (iii) developing renewable energy sources; and last (iv) developing technologies for CO_2 capture. These strategies will all contribute to stabilize and decrease greenhouse gas emissions. However, none of them will decrease the greenhouse gas emissions to zero by itself, all the mitigation measures should be improved and applied together.

2.2. Carbon Dioxide Capture and Storage Technologies

IPCC estimates that CO_2 emissions can only be decreased by 80 to 90% if power plants use carbon dioxide capture and storage (CCS) technologies (IPCC, 2005a). CCS involves the separation of CO_2 from its source, and transportation to a location where the separated CO_2 can be stored without being emitted to the atmosphere. CCS can be used in large point sources such as heat and energy production facilities and then the CO_2 captured can be transferred either to storage areas or to industries that can re-use the captured CO_2 (IPCC, 2005b). There are three main CO_2 capture methods: (i) post-combustion, (ii) oxy-fuel combustion, and (iii) pre-combustion. It has been 80 years that CO_2 is captured from industrial process steams. However, the captured CO_2 was charged directly to atmosphere (Metz, Davidson, de Coninck, Loos, & Meyer, 2005).

In the post-combustion capture systems, CO_2 formed during fossil fuel combustion is captured and separated from the flue gas. Separated CO_2 is transferred to a storage area and the flue gas is emitted to the atmosphere. Combustion processes contribute significantly to the anthropogenic CO_2 emissions. Combustion chambers have been used for centuries owing to their low-cost and high efficiency. Cement kilns, iron and steel production plants, and power plants are some of the examples of the processes or the industries that use combustion systems. To decrease the anthropogenic CO_2 emissions, post-combustion CO_2 capture systems should be used in industries that have combustion processes. Post-combustion process comes a head of the other CO_2 capture processes since the existing facilities can be easily converted into facilities that can imply post-combustion CO_2 capture process for very low cost (Rochelle, 2009; Singh, Croiset, Douglas, & Douglas, 2003). Post-combustion systems can be used for any type of flue gas. However, as the combustion

products become more complicated, the process becomes more energy intensive and expensive.

In the oxy-fuel combustion systems, combustion process is conducted under oxygen environment at which CO_2 and H_2O are produced as final products.

In pre-combustion capture systems, fuel reacts either with oxygen or air which produces carbon monoxide and hydrogen as a final product. Produced carbon monoxide is reacted in a catalytic reactor with steam to produce CO_2 and hydrogen. Then the produced CO_2 is separated by an absorption process which forms a hydrogen-rich fuel.

To separate CO_2 from the CO_2 capture systems different separation techniques are used. CO_2 can be separated with sorbents/solvents, with membranes and by distillation. When CO_2 is separated with sorbents or solvents, a liquid or a solid sorbent is used to capture CO_2 from the flue gas. The main limitation of sorbents is the energy requirement of regeneration process. Moreover, the sorbents should be cost-effective, should be used for several cycles, and the residues should be environmentally friendly. Another method to separate CO_2 from the flue gas is membrane separation. By the selective permittivity of the membrane, CO_2 can be separated from the flue gas. However, reliability and the cost of membrane systems still limit the commercial use of these membranes in large scale systems. The last method to separate CO_2 from the flue gas is distillation. In distillation method, by compressing, cooling and expanding the gas a liquid is obtained and CO_2 is separated from this gas in a distillation column. This method is used commercially.

2.2.1. Absorption

Absorption is the mostly preferred CO_2 capture technology (Riemer & Ormerod, 1995). It has several advantages such as high capture efficiency, selectivity, low energy requirement, and low cost. However, it also has limitations. These limitations are: (i) the high energy demand; (ii) by-product formation (ammonia, and salts), and (iii) absorption of gasses that are produced at the end of the combustion process which decreases the absorption capacity of the solvent.

Flue gas combustion processes are conducted at atmospheric pressure and therefore, CO_2 present in the flue gas is diluted and possesses a very low pressure. Moreover, flue gas does not only contain CO_2, but it also contains other gasses which makes the separation more

difficult and the use of a highly selective absorbent necessary. For instance, in natural gas combustion processes NO_x, and in coal combustion processes NO_x and SO_x are produced besides CO_2. These by-products also interact with the alkaline solvent which form heat stable salts and decrease the absorption capacity of the solvent. As the absorption capacity of the solvent decreases, the regeneration cycle and the cost increases. Therefore, it is necessary to remove other gasses (NO_x and SO_x) prior to CO_2 capture process. Last but not least, the heat of desorption should be low to decrease the energy consumption during the absorption process.

Among the various absorbents (amines, ammonia, aqueous solvents, blends, and ionic liquids) used, the most effective ones are the aqueous amine solutions (Kohl & Nielsen, 1997). It has been more than 50 years that a primary amine, monoethanolamine (MEA) is used for post combustion CO_2 capture systems (Jones, 2011; S. Zhang et al., 2018). This primary amine, MEA has many advantages over other amine solutions such that it is cost-effective, highly reactive with CO_2, and has an easy synthesis procedure. However, it also has its own drawbacks. Regeneration process demands for high energy, it is highly corrosive, and has poor thermal stability besides its low CO_2 absorption capacity (Aroonwilas & Veawab, 2004; Davidson, 2007; Dawodu & Meisen, 1994; Lepaumier, Picq, & Carrette, 2009; Olajire, 2010; A. B. Rao & Rubin, 2002; Van Der Zwaan & Smekens, 2009). When compared with MEA, ammonia (NH_3) possesses a greater absorption capacity, and NH_3 can remove NO_x and SO_x from the flue gas. However, being highly volatile and having a slow absorption rate, NH_3 is expensive to be used in CO_2 absorption processes.

Recently, some amines come to front with their high absorption capacities and rates, low heats of absorption and fast regeneration rates. These amines are 4-(dimethylamino)-2-butanol (DMAB), 4-((2-hydroxyethyl)(ethyl)amino)-2-butanol (HEEBAB), and 4-((2 hydroxyethyl)(methyl)amino)-2-butanol (HEMAB) (Singto et al., 2016) which were investigated for their CO_2 absorption performances. Despite their high absorption capacities, and selectivity, higher corrosion resistances and cost-effective regeneration processes, they have low absorption rates (Aboudheir, Tontiwachwuthikul, & Idem, 2006; Y. E. Kim et al., 2013; Mandal & Bandyopadhyay, 2005; Sartorl & Savage, 1983; Sherman, Ciftja, & Rochelle, 2016). By blending tertiary amines with secondary-tertiary amines a new class of absorbents with improved features are introduced. Secondary-tertiary amines with high reaction rates are blended with tertiary amines that possess high equilibrium capacities (J. H.

Choi et al., 2016; Dash, Samanta, & Bandyopadhyay, 2014; D. Fu, Wang, Mi, & Zhang, 2016; K. Fu et al., 2012; J. Gao et al., 2016; Hairul, Shariff, & Bustam, 2017; W. Luo, Guo, Zheng, Gao, & Chen, 2016; Shuangchen Ma et al., 2016; Nwaoha et al., 2016; Ramazani, Samsami, Jahanmiri, Van der Bruggen, & Mazinani, 2016; Shamiri et al., 2016; Svendsen, Hessen, & Mejdell, 2011; Vaidya & Kenig, 2008; X. Zhang et al., 2014; Z. Zhang, 2016).

Aqueous ammonia (NH_3) is another absorbent that has been used in post-combustion CO_2 capture processes (Guo et al., 2011). It is easily available, cost-effective, has high CO_2 absorption capacity and can remove NO_x and SO_x (W. J. Choi, Min, Seo, Park, & Oh, 2009; Gouedard, Picq, Launay, & Carrette, 2012; Olajire, 2010; Pellegrini, Strube, & Manfrida, 2010; Puxty, Rowland, & Attalla, 2010; Yeh & Bai, 1999; B. Zhao, Su, Tao, Li, & Peng, 2012). However, due to ammonia slip, the use of aqueous ammonia in CO_2 capture processes becomes limited.

Ionic liquids (ILs) come to front with their low vapor pressure, high thermal stability, high selectivity, and easy regeneration processes (Dai & Deng, 2016). Imidazolium based ionic liquids are used in CO_2 capture processes. Inflammability, high selectivity, high reaction rates, chemical and thermal durability, and low cost make imidazolium based ionic liquids promising candidates for CO_2 capture processes (Rogers, 2007; Sreenivasulu, Gayatri, Sreedhar, & Raghavan, 2015; Wappel, Gronald, Kalb, & Draxler, 2010). To enhance the absorption capacity of ionic liquids, they were blended with amines. However, these blends were not applicable to be used commercially due to the fact that they were expensive, and they had high viscosities. To decrease the costs, and to lower the viscosity, solutions of non-ionic surfactants and ionic liquids were investigated. It was observed that viscosity decreased, the cost was reduced, and the absorbent can be used after regeneration (A. B. Rao & Rubin, 2002). Despite the many advantages of ILs, the contradictory effects of absorbent concentration and viscosity on the absorption performance (absorption capacity and rate) limits the use of ILs at commercial scale (Z. Feng, Jing-Wen, Zheng, You-Ting, & Zhi-Bing, 2012; D. Fu, Zhang, & Mi, 2016; Y. Gao et al., 2013; Xue, Zhang, Han, Chen, & Mu, 2011).

Some solvents have been used commercially in post-combustion CO_2 capture processes (Sreedhar, Nahar, Venugopal, & Srinivas, 2017). However, several limitations exist. Using solvents in CO_2 capture processes demands for high energy due to energy intensive regeneration process, and degradation of the solvents results in corrosion which is

not environmentally friendly. To be used commercially, novel solvents should be developed which possess high absorption capacities and absorption rates, low heats of absorption/desorption, and low viscosities while being non-toxic, and easily regenerable.

In conclusion, from the perspective of absorbents, solvents that have easy synthesis procedures and easy regeneration processes; solvents that possess low viscosity, and faster mass transport properties; solvents that are chemically and thermally stable, and non-toxic should be developed to be used commercially. Researchers should give considerable attention to regeneration process which should be environmentally friendly, and cost-effective.

2.2.2. Membrane Contactors

Amine-based absorption is the mostly used CO_2 capture technology. However, it is energy intensive, and faces corrosion and degradation issues. Membrane contactor is one of the promising alternatives to CO_2 absorption which was firstly used in 1980s (Qi & Cussler, 1985a). In a membrane contactor, a porous membrane separates liquid and gas phases. Without the dispersion of phases, these two phases (liquid and gas) flow at different sides of the membrane which prevents flooding and foaming. Mass transfer occurs at three steps. Firstly, diffusion occurs from bulk gas to gas-membrane interface, and then diffuses through the membrane pores to liquid-membrane interface, and transfers to the bulk liquid and lastly, physical or chemical absorption occurs (S. Zhao et al., 2016).

In a membrane contactor, flue gas passes through a selective membrane at which CO_2 is separated. CO_2 flows through a nonselective porous membrane and then, absorbed by a liquid absorbent. To separate CO_2 from the flue gas, a high CO_2 permeance and a high CO_2 to N_2 selectivity is necessary. By this way, the advantages of absorption (high selectivity) and membrane separation (compact structure) can be combined.

Membrane contactors have some advantages over absorption systems (Cui & Demontigny, 2013; Gabelman & Hwang, 1999; J. L. Li & Chen, 2005; A. Mansourizadeh & Ismail, 2009). Membrane contactors are easy to operate; their surface area per contactor volume is high; the flow rates of liquid and gas phases can be controlled independently and thereby, foaming and flooding can be prevented; independent of the flow rates of each phase, the membrane surface area is available to both phases; membrane contactors are compact so

that much more gas-liquid interfaces can be achieved; they are less energy intensive; cost-effective; and efficient (Demontigny, Tontiwachwuthikul, & Chakma, 2005; Drioli, Stankiewicz, & Macedonio, 2011; Karoor & Sirkar, 1993; J. L. Li & Chen, 2005; Qi & Cussler, 1985b). However, membranes face several challenges. These are: (i) membrane degradation; (ii) membrane fouling; and (iii) membrane wetting (Lu, Wang, Sun, Li, & Liu, 2005; Mosadegh-Sedghi, Rodrigue, Brisson, & Iliuta, 2014; Rangwala, 1996; H.-Y. Zhang, Wang, Liang, & Tay, 2008). For long-term use, membrane systems should be chemically and thermally stable since they can be degraded by the absorbent or the solvents (Barbe, Hogan, & Johnson, 2000; R. Wang, Li, Zhou, Liu, & Liang, 2004).

Absorbents, especially the ones with higher CO_2 absorption capacities, are found to be even more corrosive which can cause changes in the chemical structure, morphology, and properties of the membranes (Barbe et al., 2000; Kladkaew, Idem, Tontiwachwuthikul, & Saiwan, 2011; Saiwan, Supap, Idem, & Tontiwachwuthikul, 2011). Not only the absorbents or the chemical solvents, but also the degradation products of solvents can cause damages. Moreover, fine particles lower the performance of membrane contactors. Depositing on the surface and the pores of the membrane, fine particles plug the pores. This deposition that occurs on the surface and the pores of the membrane is irreversible causing mass transfer resistance to increase and membrane performance to decrease (Xia Wang et al., 2014; L. Zhang, Qu, Sha, Wang, & Yang, 2015). To achieve better separation efficiencies, flue gas has to be treated prior to membrane separation. Membrane wetting results in significant increases in mass transfer resistance which causes CO_2 absorption capacity to decrease (Kreulen, Smolders, Versteeg, & van Swaaij, 1993; Lu et al., 2005; Mosadegh-Sedghi et al., 2014; Rangwala, 1996; H.-Y. Zhang et al., 2008).

Membrane resistance is found to be dependent on the textural properties of the membrane, membrane hydrophobicity, surface roughness, surface tension of the absorbent, and operation conditions (J. L. Li & Chen, 2005; A. Mansourizadeh & Ismail, 2009; R. Wang, Zhang, Feron, & Liang, 2005). There are three different modes that membranes are operated: (i) non-wetted; (ii) partially wetted; and (iii) fully wetted (A. Mansourizadeh & Ismail, 2009; Y. Zhang & Wang, 2013b). Non-wetting mode is the mostly used mode in membrane contactors since a minimum diffusion is achieved (Boributh, Rongwong, Assabumrungrat, Laosiripojana, & Jiraratananon, 2012; Dindore, Brilman, Geuzebroek, & Versteeg, 2004; J. L. Li & Chen, 2005; A. Mansourizadeh & Ismail, 2009; Mavroudi, Kaldis,

& Sakellaropoulos, 2006). However, achieving a complete non-wetted mode is practically not possible. Solutions of absorbents can fill the membrane pores causing partial wetting. Moreover, in the long-term uses, membrane pores get wetted which increases mass transfer resistance (Malek, Li, & Teo, 1997; A. Mansourizadeh & Ismail, 2009; Mavroudi, Kaldis, & Sakellaropoulos, 2003; R. Wang et al., 2005; H.-Y. Zhang et al., 2008). In order to minimize membrane wetting hydrophobic membranes or composite membranes should be preferred, high surface tension liquids and absorbents that are less corrosive should be used, and operating conditions should be optimized (J. L. Li & Chen, 2005; Mosadegh-Sedghi et al., 2014). In the long-term uses, absorbent (absorbent operating conditions (Boributh, Assabumrungrat, Laosiripojana, & Jiraratananon, 2011; Boributh et al., 2012; Dindore et al., 2004; J.-G. Lu, Zheng, & Cheng, 2008; A Mansourizadeh, Ismail, & Matsuura, 2010; Rongwong, Jiraratananon, & Atchariyawut, 2009; R. Wang, Li, Zhou, et al., 2004; H.-Y. Zhang et al., 2008; Q.-S. Zheng, Yu, & Zhao, 2005), absorbent type (Bougie & Iliuta, 2010b, 2010a, 2011; Bougie, Lauzon-Gauthier, & Iliuta, 2009; S.-C. Chen, Lin, Chien, Wang, & Hsiao, 2011; Dindore et al., 2004; García-Payo, Izquierdo-Gil, & Fernández-Pineda, 2000; S.-H. Lin, Hsieh, Li, & Tung, 2009; S.-H. Lin, Tung, Chen, & Chang, 2009; J.-G. Lu et al., 2008; Ma'mun, Svendsen, Hoff, & Juliussen, 2007; Mosadegh-Sedghi, Brisson, Rodrigue, & Iliuta, 2012; Portugal, Sousa, Magalhães, & Mendes, 2009; Rangwala, 1996; R. Wang, Li, & Liang, 2004; S. Yan et al., 2007; H.-Y. Zhang et al., 2008) and absorbent concentration (J.-G. Lu et al., 2008; Rongwong et al., 2009; Yeon, Lee, Sea, Park, & Lee, 2005)) influence membrane wetting, significantly. Membrane wetting is affected by absorbent flow rate, and pressure, significantly. Several researchers reported that pore wetting was enhanced, when liquid flow rates were increased (Boributh et al., 2012; Mavroudi et al., 2006; H.-Y. Zhang et al., 2008). The higher flow rates cause liquid boundary to decrease and thereby, the resistance inside the membrane pores increases which results mass transfer resistance to increase. Additionally, operating pressure was observed to effect pore wetting, considerably (Boributh et al., 2011; J.-G. Lu et al., 2008; R. Wang, Li, & Liang, 2004; Q.-S. Zheng et al., 2005). Several researchers reported that when high absorbent pressures are applied, membrane wetting increases (Boributh et al., 2011; J.-G. Lu et al., 2008; Rongwong et al., 2009; R. Wang, Li, & Liang, 2004). The increase in liquid pressure cause transmembrane pressure to increase which therefore increases the pore wetness (J.-G. Lu et al., 2008). Absorbent properties (surface tension and viscosity) have considerable effects on membrane

wetting. For instance, as the surface tension increases, the tendency to observe membrane wetting decreases (Dindore et al., 2004). For CO_2 capture processes, aqueous amines are the mostly used absorbents. However, the tendency of wetting increases when single and mixed alkanolamine solutions are used (Dindore et al., 2004; Rangwala, 1996; Rongwong et al., 2009; R. Wang, Li, & Liang, 2004; H.-Y. Zhang et al., 2008). It was concluded that when the surface tension of the solution is low, it has a low contact angle with the membrane surface which causes the tendency of wetting to increase (Dindore et al., 2004; J. L. Li & Chen, 2005; S.-H. Lin, Chiang, Hsieh, Li, & Tung, 2008). Viscosity is another parameter that effects membrane wetting. Absorbents that have lower viscosities can flow into pores more easily (S.-H. Lin et al., 2008). For instance, when pure water is used as an absorbent, CO_2 flux stays constant whereas when aqueous amines are used flux decreases. Surface tension and viscosity influences membrane wetting, simultaneously. In order to minimize or eliminate membrane wetting, absorbents that lowers the tendency of wetting should be developed. Researchers worked on amino acid salts (Kumar, Hogendoorn, Feron, & Versteeg, 2002; J.-G. Lu, Ji, Zhang, & Chen, 2010; J.-G. Lu et al., 2008; Ma'mun et al., 2007; Portugal et al., 2009), potassium glycinate (S. Yan et al., 2007), mixed piperazine/amine absorbents (Bougie & Iliuta, 2010a, 2010b; Bougie et al., 2009; S.-C. Chen et al., 2011; S.-H. Lin, Hsieh, et al., 2009; S.-H. Lin, Tung, et al., 2009; Mosadegh-Sedghi et al., 2012), and mixed aqueous absorbent of MEA and triethanolamine (TEA) and obtained promising results. It was observed that with the increasing concentrations of amino acid salts, surface tension increases and thereby, breakthrough pressure increases (Kumar et al., 2002). In the case of potassium glycinate, the surface tension increases with increasing potassium glycinate concentration which decreases the tendency of wetting (S. Yan et al., 2007). Increasing piperazine/amine concentrations in a mixed absorbent increases absorbent viscosity which decreases the tendency of wetting (S.-H. Lin, Tung, et al., 2009). Studies showed that to decrease wetting tendency, significant effort has to be put on the surface tension and the viscosity of the absorbent. Several researches showed that absorbent concentration is another parameter that influences wetting tendency, significantly (Boributh et al., 2012; Franken, Nolten, Mulder, Bargeman, & Smolders, 1987; S.-H. Lin et al., 2008). However, the effect of absorbent concentration on its surface tension depends on its type. For instance, for absorbents that are formed of organic compounds, surface tension decreases with increasing organic compound concentration which increases the tendency of wetting

and therefore, increases the mass transfer resistance (Franken et al., 1987; Rongwong et al., 2009). Membrane surface energy is related with the surface hydrophobicity and thus the contact angle between the liquid drop and the membrane surface. For contact angles greater than 90 °, tendency of wetting decreases. However, for contact angles lower than 90 °, tendency of wetting increases. Thus, a membrane with a lower surface energy would have a lower tendency of wetting while a membrane with a higher surface energy would have a higher tendency of wetting. Pore size has a key role in membrane wetting tendency. Several studies showed that as pore size increases, the critical entry pressure also increases which therefore enhances the tendency of wetting (Keshavarz, Fathikalajahi, & Ayatollahi, 2008; Malek et al., 1997; Amir Mansourizadeh, 2012; H.-Y. Zhang et al., 2008). Membrane wettability depends on both the absorbent and the membrane. Using absorbents that have high surface tensions, increases the contact angle between the liquid drop and the membrane or using a membrane with a low surface energy, and using a membrane with a small pore size minimize the tendency of wetting and therefore, the mass transfer resistance decreases.

In conclusion, membrane degradation, membrane fouling and membrane wetting are the main challenges issued in membrane contactors. To overcome these limitations the following has to be taken into account. In order to increase the contact angle greater than 90 °, either hydrophobic membranes have to be used or hydrophobic modifications have to be made. A composite membrane formed of dense layers should be used, liquid absorbents with high surface tension should be preferred, in order to avoid membrane degradation, significant effort has to be given to absorbent and membrane compatibility and operation conditions should be optimized.

Another important parameter that influences absorption capacity is membranes. Membranes behave as barriers which are not selective to CO_2. Most of the membrane contactors use hollow fibers. The outside layer of these membranes is selective. To achieve high performances from membrane contactors, membranes with the following properties should be used: (i) thermally stable; (ii) chemically stable; (iii) highly hydrophobic; and (iv) highly porous. Using a thermally and chemically stable membrane would minimize the probability of membrane degradation, using a highly hydrophobic membrane would minimize the tendency of membrane wetting, and lastly, using a highly porous membrane would decrease the mass transfer resistance. Different polymers are used as membrane materials for hydrophobic membranes. For instance, polypropylene (PP) (deMontigny,

Tontiwachwuthikul, & Chakma, 2006; Khaisri, deMontigny, Tontiwachwuthikul, & Jiraratananon, 2009; S.-H. Lin, Hsieh, et al., 2009; S.-H. Lin, Tung, et al., 2009; Mavroudi et al., 2006; H.-Y. Zhang et al., 2008), polyvinylidene fluoride (PVDF) (Atchariyawut, Feng, Wang, Jiraratananon, & Liang, 2006; C. Feng, Wang, Zhang, & Shi, 2011; Khaisri et al., 2009; S.-H. Lin, Hsieh, et al., 2009; A Mansourizadeh & Ismail, 2010; A Mansourizadeh et al., 2010; Amir Mansourizadeh & Ismail, 2011; H. H. Park, Deshwal, Kim, & Lee, 2008; A. Xu, Yang, Young, deMontigny, & Tontiwachwuthikul, 2008; H.-Y. Zhang et al., 2008), polytetrafluoroethylyene (PTFE) (Chabanon, Roizard, & Favre, 2011; S.-C. Chen, Lin, Chien, & Hsu, 2010; deMontigny et al., 2006; Falk-Pedersen, Grønvold, Nøkleby, Bjerve, & Svendsen, 2005; Hoff, Juliussen, Falk-Pedersen, & Svendsen, 2004; Khaisri et al., 2009), and polyethylene (PE) (Mosadegh-Sedghi et al., 2012; Sedghi, Brisson, Rodrigue, & Iliuta, 2011). Membranes constructed of different materials show different CO_2 absorption performances which is attributed to different wetting tendencies of the membranes (Khaisri et al., 2009). For instance, it is found that PTFE membranes have better absorption performances and lower wetting tendencies than PP membranes (Chabanon et al., 2011; deMontigny et al., 2006). Thermal stabilities of these polymers have critical role in the absorption studies since desorption studies are conducted in between 100 and 150 °C. PTFE and PEEK are found to be promising candidates to be used in membrane contactors due to their high dimensional stability. Moreover, several factors are found to affect membrane performance, considerably. For instance, additives can be used to decrease the pore size, and to enhance hydrophobicity; polymer concentrations can be increased to have smaller pore size; and coagulant concentrations can be set accordingly to construct membranes that do not have an inner skin to decrease the mass transfer resistance. Liquid absorbents cause wetting in the membranes. Therefore, dense skin layer composite membranes are used. By this way, wetting tendency decreases and the chemical resistance of the membrane increases (Kreulen et al., 1993). However, to minimize the mass transfer resistance the dense layer should be very thin; the dense layer should be chemically and thermally stable; and the dense layer has to possess a high CO_2 permeability. Non-porous membrane contactors are investigated for their CO_2 absorption performance (Al-saffar, Ozturk, & Hughes, 1997; Heile, Rosenberger, Parker, Jefferson, & McAdam, 2014; McLeod, Buzatu, Autin, Jefferson, & McAdam, 2015; Scholes, Qader, Stevens, & Kentish, 2014). These membranes either of silicone rubber or polydimethylsiloxane (PDMS) are found to be promising candidates that minimize

membrane wetting. However, their high mass transfer resistances cause significant decrease in their CO_2 absorption capacities (Scholes et al., 2014).

Several researchers worked on nanoparticle incorporation to decrease mass transfer resistance and enhance membrane hydrophobicity. By adding fluorinated SiO_2 nanoparticles and surface hydrophobilization, hydrophobicity was enhanced and absorption flux was increased (Y. Zhang & Wang, 2013a, 2014). Moreover, another researcher added clay particles to PVDF which showed promising results. A mixed matrix membrane was obtained with lower wetting tendency and higher CO_2 absorption performance (Rezaei, Ismail, Bakeri, Hashemifard, & Matsuura, 2015; Rezaei, Ismail, Hashemifard, Bakeri, & Matsuura, 2014).

In conclusion, membrane contactors come to front in CO_2 capture studies by combining the advantages of absorption and membrane separation: Membrane contactors are highly selective and compact. However, researchers have to put significant effort to develop membrane contractors to be commercially used. Membrane wetting is one of the crucial challenges that has to be worked on since it affects CO_2 absorption capacity and performance, considerably. Moreover, some more effort has to be put on solvents, especially green solvents should be developed. Lastly, in order to use membrane contactors at industrial scale, robust, chemically and thermally stable membrane materials should be developed.

2.2.3. Adsorption

Even though amine-based absorption is the most commonly used CO_2 capture technology, it has several drawbacks. Particularly, solvents are corrosive, and the regeneration processes are highly energy intensive (D'Alessandro, Smit, & Long, 2010; Haszeldine, 2009; Leci, 1996). Therefore, studies were conducted to find a cost-effective and less energy intensive alternative to amine-based CO_2 capture process.

In 1990s adsorption process come to front as a promising alternative to amine based solvents (Chue, Kim, Yoo, Cho, & Yang, 1995; Ishibashi et al., 1996; Kikkinides, Yang, & Cho, 1993). For instance, an adsorption process can be retrofitted to any facility easily; adsorbents can be designed to work at a variety of pressures and temperatures; adsorption process is so environmentally friendly that by-product formation is minimized while amine-based solvents form toxic by-products; adsorption process is cost-effective; and the

regeneration step of adsorption process is less energy intensive since the heat capacity of an adsorbent is lower than the heat capacity of an amine based solvent.

Adsorption is the adhesion of atoms, ions or molecules to a surface (Lowell, Shields, Thomas, & Thommes, 2004a). Adsorbent is the material that the molecules are attached on while adsorbate is the atoms, ions or molecules that attach to a surface. Absorption and adsorption differ from each other since only the surface of the adsorbent is involved. Chemical and physical adsorption differ from each other by the type of bonding involved during adsorption. For instance, if adsorption occurs physically, van der Waals forces are involved. However, if adsorption occurs chemically, covalent bonds are involved.

From 1990s till today, researchers worked on adsorbents to increase their adsorption capacity, and selectivity. Theoretical studies show that an adsorbent with a CO_2 adsorption capacity equal to and/or greater than 3 mmol/g would decrease the energy demand of post-combustion CO_2 capture systems by 30 to 50% (Gray, Champagne, Fauth, Baltrus, & Pennline, 2008). However, it is also crucial to take into account that the flue gas contains impurities that would decrease the CO_2 adsorption capacity of the adsorbent.

To achieve the targets set by US Department of Energy and European Union SET plan, researchers focused on alternative technologies that are cost-effective, and less energy intensive. The National Energy Laboratory in the U.S. set some targets for the adsorbent materials. The targets are as follows:

i) The energy requirement of an adsorbent for post-combustion carbon capture process should be 30 to 50% lower than the energy requirement of an amine-based absorbent,

ii) Under flue gas conditions, the adsorbent should have a minimum CO_2 adsorption capacity of 3.0. mmol/g,

iii) The temperature to adsorb and desorb should be within a narrow temperature range (40 to 110 °C) and the adsorbent should be able to adsorb and desorb at atmospheric pressure,

iv) The adsorbent should work in the presence of water vapor,

v) The adsorbent should be chemically and thermally stable,

vi) The adsorbent should have a high adsorption capacity even after regeneration, and

vii) The adsorbent should maintain its high adsorption capacity even after several adsorption and regeneration cycles.

CO_2 adsorption capacity, CO_2 selectivity, adsorption/desorption kinetics, chemical stability, mechanical strength, regeneration process and the cost of sorbent are crucial parameters for the commercial use of adsorbents. For instance, adsorption capacity defines the quantity of adsorbent that will be used and determines the volume of the adsorbent containers. An adsorbent with a high CO_2 adsorption capacity would require lower amounts of adsorbent and thus, the size of the container would be reduced which will decrease the capital cost of the overall process.

An adsorbent has to be highly selective towards CO_2. The high or the low selectivity of an adsorbent influences the transportation and sequestration processes, thus effects the cost of the system.

The adsorption/desorption kinetics determines the cycle time of an adsorption process. An ideal adsorbent would have fast CO_2 adsorption/desorption kinetics which would decrease the amount of adsorbent necessary to capture CO_2 from a certain amount of flue gas.

An ideal adsorbent should be chemically stable towards flue gasses and flue gas contaminants. An ideal adsorbent should be stable microstructurally and morphologically. Even if, the adsorbent goes through several adsorption and regeneration cycles it should maintain its CO_2 adsorption capacity. Operating conditions (high flow rates) should not lower the CO_2 adsorption capacity of an ideal adsorbent.

An ideal adsorbent should possess a low heat of adsorption (the energy needed for regeneration) and should maintain its CO_2 adsorption capacity even after several absorption-regeneration cycles. By this way, regeneration costs can be reduced. Carbon based materials, zeolites, silica-based materials, polymer-based materials, clay-based materials, alkali metal carbonate-based materials, immobilized ionic liquid-based materials, MgO, CaO, and metal-organic frameworks (MOFs) are some of the materials used in CO_2 adsorption studies.

2.2.3.1.Carbon-based materials

Carbon based adsorbents come to front with their high BET surface area, high porosity, low cost, easiness to modify the pore structure and easy regeneration processes. However, they possess poor selectivity towards CO_2 and low CO_2 adsorption capacities at

temperatures above 273 K (Arenillas, Smith, Drage, & Snape, 2005). Researchers focused their studies on the influence of BET surface area on the CO_2 adsorption capacity of the adsorbents. However, they have changed their direction towards the effect of pore size and pore structure. Several researchers showed that pore size influences CO_2 adsorption capacity of carbon-based materials, considerably (Environ, Sevilla, & Fuertes, 2011; S.-Y. Lee & Park, 2013; Marco-Lozar, Kunowsky, Suárez-García, & Linares-Solano, 2014; Wickramaratne & Jaroniec, 2013). Researchers put significant effort to develop methods and/or synthesis strategies to increase the CO_2 adsorption capacities of carbon-based adsorbents.

One of these methods is to introduce nitrogen groups which can be done in several ways (Arenillas et al., 2005; Drage et al., 2007; Gray et al., 2004; H. Y. Huang, Yang, Chinn, & Munson, 2003; Maroto-Valer, Tang, & Zhang, 2005; Plaza, Pevida, Arenillas, Rubiera, & Pis, 2007; Przepiórski, Skrodzewicz, & Morawski, 2004). First one is the carbonization of nitrogen-rich precursors. Some of the investigated precursors are dicyandiamide (J. Wei et al., 2013), chitosan (Fan, Zhang, Zhang, Shu, & Shi, 2013), HNO_3 (Xiaoyu Ma, Cao, & Hu, 2013), porous polyimine (J. Wang et al., 2013), polypyrrole (Meng, Meng, Chen, & Jin, 2014; Sevilla, Valle-Vigón, & Fuertes, 2011; Juhyon Yu et al., 2014), and ionic liquids (Sethia & Sayari, 2014).

Another method to introduce amine groups to the surface of these materials is surface modification which can be done by: i) impregnation with amine based polymers (Franchi, Harlick, & Sayari, 2005; Xiaoliang Ma, Wang, & Song, 2009; Satyapal, Filburn, Trela, & Strange, 2001; Son, Choi, & Ahn, 2008; Xingrui Wang, Li, Liu, & Hou, 2011; M. B. Yue, Chun, Cao, Dong, & Zhu, 2006); and ii) grafting (Harlick & Sayari, 2007; Hiyoshi, Yogo, & Yashima, 2005; Knowles, Delaney, & Chaffee, 2006; Serna-Guerrero, Belmabkhout, & Sayari, 2010a). All these methods involve the dispersion of amine-functionalities in the pores of a mesoporous carbon-based material which increases the amount of CO_2 captured by these mesoporous carbon-based materials. Among the above-mentioned surface modifications, grafting provides the highest stability to carbon-based materials even after the regeneration process.

Fluorination (B.-C. Bai, Kim, Im, Jung, & Lee, 2011), oxidation (Plaza et al., 2013), metal doping and metal loading are alternative methods that can be used to modify the surface of carbon-based materials. Fluorination method is reported to be a cost-effective,

easy, and efficient method that increases the CO_2 adsorption capacity. The increase in the CO_2 adsorption capacity is attributed to the interaction of the CO_2 molecules with oxygen functional groups (B.-C. Bai et al., 2011).

Some of the studies conducted in literature shows that increasing the oxygen content increases the CO_2 adsorption capacity of these carbon-based materials (Plaza et al., 2013).

Moreover, several studies investigated the effect of metal doping and metal loading on carbon-based materials. CuO (B.-J. Kim, Cho, & Park, 2010), and NiO (Jang & Park, 2012) are several examples of the metals doped/loaded.

Lastly, synthesis of hybrid composites can be an alternative way to enhance the CO_2 adsorption capacity and the performance of the carbon-based materials. The reported hybrid materials are: i) carbon/carbon; ii) carbon/carbon nitride (Y. Kong, Jin, & Qiu, 2013); and iii)carbon/MOF (Anbia & Hoseini, 2012).

2.2.3.2.Graphite/graphene-based materials

Graphite/graphene-based materials are low-cost materials which possess high specific surface areas. The low-cost and the high BET surface areas of these materials draw the attention of researchers and several researchers investigated the CO_2 adsorption capacity and CO_2 adsorption performance of these materials.

Prior to CO_2 adsorption studies, researchers exfoliated, functionalized, and synthesized the hybrids of graphite/graphene-based materials and then tested their respective CO_2 adsorption performances.

Graphene nanoplates prepared by exfoliation method achieve a high CO_2 adsorption capacity at 25 °C and 30 bar. This high CO_2 adsorption capacity is attributed to the enlarged inter-layer spacing and increased void volume (Meng & Park, 2012).

Despite its low cost, the low BET surface area and the low CO_2 adsorption capacity limit the use of graphite in CO_2 adsorption studies. In order to increase the CO_2 adsorption capacity of graphite, its surface was modified with 3-aminopropyl-triethoxysilane (APTS). The CO_2 adsorption capacity of graphite was still low (0.074 mmol/g) while the CO_2 adsorption capacity of graphene oxide increased, significantly (S.-M. Hong, Kim, & Lee, 2013).

Synthesizing graphene-inorganic hybrid materials is a promising alternative to enhance the CO_2 adsorption capacity (Yanwu Zhu et al., 2010). Several studies showed that

incorporation of nanoparticles in between graphene sheets enhanced the CO_2 adsorption capacity of graphene (Alhwaige, Agag, Ishida, & Qutubuddin, 2013; Mishra & Ramaprabhu, 2012; S. Yang et al., 2013). The enhanced CO_2 adsorption capacity is attributed to the nanoparticle incorporation which avoided graphene sheets to aggregate (Yanwu Zhu et al., 2010).

2.2.3.3.Zeolites

Zeolites adsorb CO_2 molecules either by ion-dipole interaction or bi-coordination of carbonate species (Qiang Wang, Luo, Zhong, & Borgna, 2011). Even though zeolites possess high BET surface areas, and pore volumes, they show low CO_2 adsorption capacities at high temperatures (200 °C). There have been several zeolites investigated for their CO_2 adsorption performances (Araki, Kiyohara, Tanaka, & Miyake, 2012; Bezerra, Oliveira, Vieira, Cavalcante, & Azevedo, 2011; Bonelli, Onida, Fubini, Areán, & Garrone, 2000; Díaz, Muñoz, Vega, & Ordóñez, 2008; Hernández-Huesca, Díaz, & Aguilar-Armenta, 1999; P. Li & Handan Tezel, 2007; Z. Liang, Marshall, & Chaffee, 2009; Merel, Clausse, & Meunier, 2008; Pires, de Carvalho, Ribeiro, & Derouane, 1993; Su & Lu, 2012; Wirawan & Creaser, 2006; Xiao et al., 2008; J. Zhang, Singh, & Webley, 2008; Zukal et al., 2010). Several researchers showed that by applying cation exchange, CO_2 adsorption capacity was increased, significantly (Arévalo-Hidalgo, Almodóvar-Arbelo, & Hernández-Maldonado, 2011; T.-H. Bae et al., 2013; S.-H. Hong, Jang, Cho, & Ahn, 2014; K.-M. Lee, Lim, Park, & Jo, 2012; Lozinska et al., 2012; Ridha, Yang, & Webley, 2009; Walton, Abney, & Douglas LeVan, 2006).

Researchers figured out that modifying the surfaces of zeolites with amine groups enhanced the CO_2 adsorption capacity of these materials. It was observed that modifying the surfaces of zeolites by impregnation method increased the CO_2 adsorption capacity of several zeolites (Jadhav et al., 2007; Jing, Wei, Wang, & Yu, 2014; L.-Y. Lin, Kuo, & Bai, 2011; Su, Lu, Kuo, & Zeng, 2010). This enhancement in the adsorption capacities is attributed to the higher amount of nitrogen atoms present in the alkyl chains. As the temperature rises above 100 °C, the CO_2 adsorption capacities of zeolites decrease, significantly. To overcome this limitation, zeolites were grafted with aminosilanes (K. K. Han et al., 2012; Sanz, Calleja, Arencibia, & Sanz-Pérez, 2012; Serna-Guerrero et al., 2010a; Serna-Guerrero, Belmabkhout, & Sayari, 2010b). It was concluded that the distribution of amines through the pore channels

has a key role in enhancing the CO_2 adsorption capacity (Sanz et al., 2012). Moreover, moisture is found to be a factor that lower the CO_2 adsorption capacity of zeolites. Several researchers reported that water competes with CO_2 for the adsorption sites which results in a decreased CO_2 adsorption capacity (Brandani & Ruthven, 2004; Gallei & Stumpf, 1976; Jänchen, Möhlmann, & Stach, 2007; K.-M. Lee, Lim, & Jo, 2012; Rege & Yang, 2001).

2.2.3.4.Silica-based materials

Silica based materials possess high BET surface areas and pore volumes, and high chemical stability which make these materials promising support materials in CO_2 capture studies (S. Bai, Liu, Gao, Yang, & Li, 2012; Y. Du et al., 2013; Fauth et al., 2012; Goeppert et al., 2014; Ko, Lee, Oh, & Choi, 2013; Leal, Bolívar, Ovalles, García, & Espidel, 1995; J.-L. Liu & Lin, 2013; D. Wang, Sentorun-Shalaby, Ma, & Song, 2011; K. Wang et al., 2012; Jiaguo Yu, Le, & Cheng, 2012; H. Zhang, Goeppert, Czaun, Prakash, & Olah, 2014). To enhance the CO_2 adsorption capacity, surface of the silica-based materials is functionalized with amines. Studies showed that functionalizing the surface of silica-based materials with amine or loading them with amine enhanced their CO_2 adsorption capacity (S. Bai et al., 2012; Y. Du et al., 2013; Goeppert et al., 2014; Ko et al., 2013; J.-L. Liu & Lin, 2013; Jiaguo Yu et al., 2012).

Thermal stability is a material property that limits the commercial use of any material. In the case of CO_2 adsorption studies, a material that is thermally stable at temperatures above 100 °C is necessary. Several amine functionalized silica-based materials were investigated for their CO_2 adsorption performances above 100 °C and researchers developed strategies to improve their thermal stability (Jiao, Cao, Xia, & Zhao, 2016). Impregnation with amines enhanced the thermal stability of silicas and even after several adsorption-regeneration cycles, amine functionalized silicas were found to be chemically and thermally stable (W. Zhao, Zhang, Li, & Cai, 2013). Grafting is used as an alternative method to impregnation method for enhancing thermal stability. However, not all the grafted silicas show high CO_2 adsorption capacities (Leal et al., 1995).

2.2.3.5.Polymer-based materials

Porous polymers can be easily modified, they are light in weight, and they are chemically and thermally stable and cost-effective. Moreover, porous polymers show high CO_2 adsorption performances and selectivity. These properties make porous polymers come to front in adsorption studies (D'Alessandro et al., 2010; Dawson, Stöckel, Holst, Adams, & Cooper, 2011; Liebl & Senker, 2013).

Several polymers have been investigated for their CO_2 adsorption performances (Ben et al., 2012, 2011; X. Chen, Qiao, Du, Zhou, & Yang, 2013; Dawson, Adams, & Cooper, 2011; N. Du et al., 2011; H. J. Jeon et al., 2012; Kaliva, Armatas, & Vamvakaki, 2012; H. Lim, Cha, & Chang, 2012; W. Lu, Sculley, Yuan, Krishna, & Zhou, 2013; Y. Luo, Li, Liang, & Tan, 2011; Y. Luo, Li, Wang, Wu, & Tan, 2012; Martín et al., 2011; Rabbani & El-Kaderi, 2011; K. V. Rao, Mohapatra, Kulkarni, Maji, & George, 2011; Ritter, Senkovska, Kaskel, & Weber, 2011; Wilke & Weber, 2011; Xie & Suh, 2013; Yi Zhao, Shen, Bai, Hao, & Dong, 2012; X. Zhu et al., 2014). For instance, melamine-formaldehyde. It was observed that presence of porosity was necessary for this polymer to efficiently capture CO_2 (Wilke & Weber, 2011).

Hyper-crosslinked polymers were also investigated for their CO_2 adsorption performances. Their high surface areas, chemical stabilities, large-scale and low-cost productions, and high CO_2 adsorption capacities at 1 atm make these materials promising candidates for CO_2 adsorption studies (J.-H. Ahn et al., 2006; Germain, Svec, & Fréchet, 2008; Y. Luo et al., 2012; Martín et al., 2011).

Conjugated microporous polymers show promising CO_2 adsorption capacities which may be attributed to their high flexibility in structural modifications, tunable and high porosities, microporous pore structures, and high isosteric heats of adsorption (X. Chen et al., 2013; Dawson, Adams, et al., 2011; Xie & Suh, 2013).

Polymers with porous aromatic frameworks come to front with their very high surface areas, high stabilities in the presence of water, high isosteric heats of adsorption, high thermal stabilities, and high CO_2 selectivity towards CO_2/N_2 and CO_2/CH_4. In addition to all these promising features, these porous aromatic frameworks show high CO_2 uptake capacities at room temperatures (Ben et al., 2012, 2011; Wenliang Li, Shi, & Zhang, 2014).

In conclusion, polymer-based materials show promising results in CO_2 adsorption studies owing to their high flexibility in structural modifications and high porosity. However,

further research has to be conducted to improve the stability of these materials after several cycles of adsorption and desorption.

2.2.3.6.Clay-based materials

Clay-based materials are low-cost, chemically and thermally stable and abundant materials (Swartzen-Allen & Matijevic, 1974). Two types of clays, montmorillonite and bentonite, take particular attention of researchers in CO_2 adsorption studies (Azzouz et al., 2013; C. Chen, Park, & Ahn, 2013; Gil, Vicente, & Korili, 2005; Leliveld, Ros, van Dillen, Geus, & Koningsberger, 1999; Roth, Agarwal, & Gupta, 2013; Stevens et al., 2013; Weilong Wang et al., 2013).

In order to be used in CO_2 adsorption studies, researchers modified bentonites and montmorillonites with amines since the non-modified ones show low CO_2 adsorption capacities. However, when modified, these materials show high chemical and thermal stabilities with enhanced CO_2 adsorption capacities.

2.2.3.7.Alkali metal carbonate-based materials

Alkali metal carbonate based materials (K_2CO_3 and Na_2CO_3) have been used in CO_2 adsorption studies which possess high CO_2 uptake capacities (S. C. Lee et al., 2006; Y. Liang, Harrison, Gupta, Green, & McMichael, 2004; Y. Seo, Jo, Ryu, & Yi, 2007; C. Zhao, Chen, & Zhao, 2010a). However, these materials possess low durability, and slow reaction rates. Moreover, the adsorption and the regeneration processes can be conducted within a very limited temperature range (J. B. Lee et al., 2008; Y. Liang et al., 2004; C.-K. Yi et al., 2006; C. Zhao, Chen, & Zhao, 2010b).

To fasten the carbonation reaction rate, these alkali metal carbonate-based materials are loaded on a support material (Derevschikov, Veselovskaya, Kardash, Trubitsyn, & Okunev, 2014; W. Dong, Chen, & Wu, 2014; Harrison, 2005; S. C. Lee et al., 2009; Y. Liang et al., 2004; Sharonov, Okunev, & Aristov, 2004; Ye Wu et al., 2013; C.-K. Yi, Jo, Seo, Lee, & Ryu, 2007). Studies show that loading alkali metal carbonate-based materials on support materials improve their CO_2 adsorption capacities. However, loading these materials on support materials increases the regeneration temperatures which later on causes a significant decrease in the CO_2 adsorption capacities.

In conclusion, the commercial use of alkali metal carbonate-based materials is limited with the low durability, slow carbonation reaction rates and limited reaction temperatures of alkali metal carbonate-based materials.

2.2.3.8.Immobilized ionic liquid-based materials

Easy tunability, high CO_2 solubility, low volatility and high thermal stability of immobilized ionic liquid based materials (IL based materials) attract the attention of various researchers (Bara et al., 2009; Blanchard, Hancu, Beckman, & Brennecke, 1999; Hasib-ur-Rahman, Siaj, & Larachi, 2010; Jie Ren, Wu, & Li, 2012; Wappel et al., 2010). However, the hyper viscosity of IL based materials causes these materials to possess low sorption capacities.

Even if less viscous IL based materials are used, the increase in sorption capacities is not sufficient enough to be used in commercial applications (Blanchard et al., 1999; Blasig et al., 2007; Goodrich et al., 2011; Gutowski & Maginn, 2008; Tang, Sun, Tang, Radosz, & Shen, 2005; H. Yu, Wu, Jiang, Zhou, & Zhang, 2009; Qichao Zhao, Wajert, & Anderson, 2010). In order to overcome the above mentioned limitations and enhance the CO_2 adsorption capacities, IL based materials materials were: i) loaded on a support material (metal-organic frameworks, nanoporous polymers); ii) functionalized with pyridine containing-anion; and iii) synthesized as polymers (Bara et al., 2008; Y. Chen, Hu, Gupta, & Jiang, 2011; Eddaoudi et al., 2002; K. M. Gupta, Chen, Hu, & Jiang, 2012; Hasib-ur-Rahman et al., 2010; Kato, Tsujita, Yoshimizu, Kinoshita, & Higgins, 1997; X. Luo et al., 2014; Mogri & Paul, 2001; Privalova et al., 2013; Supasitmongkol & Styring, 2010; Tang, Sun, et al., 2005; Tang, Tang, Sun, Radosz, & Shen, 2005; Xianfeng Wang, Akhmedov, Duan, Luebke, & Li, 2013).

2.2.3.9.MgO based materials

Metal oxides have abundant basic sites at their surface which make them promising candidates in CO_2 adsorption studies. When MgO and CaO based sorbents are compared, it is found that MgO based sorbents can be regenerated at lower temperatures, and thus their energy needs for the regeneration process is lower than CaO based sorbents (S. Choi, Drese, & Jones, 2009b; B. Feng, An, & Tan, 2007; Philipp & Fujimoto, 1992). However, the very long regeneration processes or the necessity to conduct the regeneration processes at high

temperatures limit the use of MgO based sorbents, commercially (Bhagiyalakshmi, Lee, & Jang, 2010). In addition to the energy intensive regeneration processes, MgO based sorbents possess relatively low CO_2 adsorption capacities (Bhagiyalakshmi et al., 2010). To enhance the CO_2 sorption capacities, particle size was reduced, porous MgO based materials were synthesized, and MgO was dispersed on a porous material (Bhagiyalakshmi, Hemalatha, Ganesh, Mei, & Jang, 2011; Bian, Baltrusaitis, Galhotra, & Grassian, 2010; K. K. Han, Zhou, Lin, & Zhu, 2013; H. Jeon et al., 2012; T. K. Kim, Lee, Yuh, Kwak, & Moon, 2014; Lei Li et al., 2010; Y. Y. Li et al., 2013; W.-J. Liu, Jiang, Tian, Ding, & Yu, 2013; Ruminski, Jeon, & Urban, 2011; She et al., 2011).

2.2.3.10. CaO based materials

CaO based materials are cost-effective materials. The high theoretical CO_2 sorption capacities of CaO based materials make them promising candidates in CO_2 sorption studies (H. Gupta & Fan, 2002; Salvador, Lu, Anthony, & Abanades, 2003). However, durability of these sorbents suffer due to the sintering process at which the carbonation process is highly exothermic and the volume of CaO decreases while the volume of $CaCO_3$ increases (J Carlos Abanades & Alvarez, 2003; J Carlos Abanades, Anthony, Lu, Salvador, & Alvarez, 2004; Juan Carlos Abanades, 2002; Barker, 1973; Salvador et al., 2003; P Sun, Grace, Lim, & Anthony, 2007; Ping Sun, Grace, Lim, & Anthony, 2007). Therefore, to improve the durability of CaO based sorbents, researchers changed the morphology and the microstructure, modified the surface, synthesized mixed oxides, and investigated the effect of SO_2. A study shows that synthesizing a CaO based sorbent as $CaO/Ca_{12}Al_{14}O_{33}$ hollow nanospheres with relatively high surface area, narrow pore size distribution, and with inert $Ca_{12}Al_{14}O_{33}$ binders enhances the CO_2 adsorption capacity and the life cycle performance of the sorbent (F.-Q. Liu, Li, Liu, & Li, 2013).

Introducing inert materials into CaO particles is found to be the most effective and the feasible way to improve the life cycle performance of CaO based sorbents (B. Feng, Liu, Li, & An, 2006; Gruene, Belova, Yegulalp, Farrauto, & Castaldi, 2011; C.-H. Huang, Chang, Yu, Chiang, & Wang, 2010; Kierzkowska, Poulikakos, Broda, & Müller, 2013; Liyu Li, King, Nie, & Howard, 2009; Yingjie Li, Zhao, Chen, Duan, & Chen, 2010; Z. Li, Cai, Huang, & Han, 2005; W. Liu, Low, Feng, Wang, & Diniz da Costa, 2010; C. Luo et al., 2010; Manovic & Anthony, 2010; Martavaltzi & Lemonidou, 2008; S. F. Wu & Zhu, 2010; K. B.

Yi, Ko, Park, & Kim, 2009; C.-T. Yu & Chen, 2014; M. Zhao et al., 2014; Z. Zhou, Qi, Xie, Cheng, & Yuan, 2012). The inert materials act as supports and thereby, the sorbent possesses improved resistance properties and thereby, life cycle performance of the sorbent increases. Reactivation of the degraded CaO based sorbents is crucial for the commercial use of these sorbents (Barker, 1973; Iyer, Gupta, Sakadjian, & Fan, 2004; Phalak, Deshpande, & Fan, 2012; P Sun et al., 2007; Valverde, Sanchez-Jimenez, & Perez-Maqueda, 2014). It was reported by several researchers that by steam hydration, degraded CaO based sorbents can be reactivated (Coppola, Salatino, Montagnaro, & Scala, 2014; Kuramoto et al., 2003; Y Wu, Blamey, Anthony, & Fennell, 2010; Yin et al., 2012; F.-C. Yu, Phalak, Sun, & Fan, 2012).

In conclusion, for the commercial use of CaO based sorbents the life-cycle performance and the degradation problem of the CaO based sorbents should be solved. Increasing the surface area of the sorbent, having high and accessible porosity would enhance the CO_2 adsorption performance of the sorbents while introducing inert particles into CaO based particles would improve the life cycle performance of the sorbent, considerably.

2.2.3.11. Metal-Organic Frameworks (MOFs)

MOFs are highly porous crystalline materials that are formed of an organic and an inorganic part. MOFs come to front in gas storage and separation studies with their high BET surface areas, and high and tunable porosities (Furukawa et al., 2010; Mueller et al., 2006). Their high porosities and high surface areas provide these materials to achieve very high CO_2 adsorption capacities at 77 K and high pressures. For instance, at 50 bar and 30 °C CO_2 adsorption capacities of MOF-177 and MIL-101 were found to be 33.5 mmol/g, and 40 mmol/g, respectively (Llewellyn et al., 2008; Millward & Yaghi, 2005c). However, at low pressures the CO_2 adsorption capacity of MOFs decreases, drastically (Demessence, D'Alessandro, Foo, & Long, 2009). Therefore, to enhance the CO_2 adsorption capacity of MOFs at low pressures, researchers focused on several approaches.

One of these strategies is to remove solvent molecules that are bound to terminals and thereby, open metal sites would be created (Britt, Furukawa, Wang, Glover, & Yaghi, 2009; B. Chen et al., 2000; Dietzel, Besikiotis, & Blom, 2009; Dietzel et al., 2008; Millward & Yaghi, 2005c). By this way, coordinatively unsaturated metal would act as adsorption sites for CO_2 molecule (Caskey, Wong-Foy, & Matzger, 2008; Mu, Li, Huang, & Walton, 2012; Sanz, Martínez, Orcajo, Wojtas, & Briones, 2013; Wade & Dincă, 2012; H. Wu, Simmons,

Srinivas, Zhou, & Yildirim, 2010). Several other researchers enhanced the achieved CO_2 uptake capacities by changing the organic linker which increases both the surface area and the CO_2 uptake capacity (H.-S. Choi & Suh, 2009; Farha et al., 2010, 2012; Henke, Schneemann, Wütscher, & Fischer, 2012; Masoomi, Stylianou, Morsali, Retailleau, & Maspoch, 2014; B. Zheng, Yun, et al., 2013). Moreover, some other researchers synthesized MOFs with different morphologies to increase the CO_2 adsorption performances (Bataille et al., 2012; T. Li, Sullivan, & Rosi, 2013; Sarawade, Tan, & Polshettiwar, 2013; Q. Yan et al., 2013). Another strategy to enhance the CO_2 uptake capacities of MOFs at low pressures is to functionalize MOFs with amines. However, amine functionalized MOFs did not show promising results in CO_2 capture studies (Duan et al., 2012; Montoro et al., 2012; Qingfei Wang et al., 2013; B. Zheng, Liu, et al., 2013). Several researchers investigated the effect of PEI, alkylamine and carboxyl group incorporation to the MOF structure which showed enhanced CO_2 adsorption capacity and performance (Yingli Hu, Verdegaal, Yu, & Jiang, 2014; Y. Lin, Yan, Kong, & Chen, 2013; Si et al., 2012; Xiang, Leng, & Cao, 2012).

Despite all the enhancements achieved, it is still a challenge to have optimum CO_2 adsorption capacity at 1 bar and 298 K. Researchers should focus on alternative methods that would develop low-cost, environmentally friendly, regenerable, chemically and thermally stable MOFs with high CO_2 adsorption capacities measured at 298 K and 1 bar.

2.3. Gas Adsorption

In adsorption processes, the solid that is used to adsorb the gas is called the adsorbent while the gas that is being adsorbed is called the adsorptive and the vapor that is in the adsorbed state is the adsorbate (Lowell, Shields, Thomas, & Thommes, 2004b). The amount of gas adsorbed on the adsorbent depends on temperature, pressure, and the interaction potential between the adsorbate and the adsorbent. There are two types of adsorption processes: Physisorption and chemisorption. Interaction strength between the adsorbate and the adsorbent defines whether physisorption or chemisorption occur.

In chemisorption the adsorbate is strongly and chemically bonded to the surface and the adsorbate can be chemically adsorbed on a specific site which is due to the chemical bonds form between the site and the adsorbate. The very characteristic feature of

chemisorption is the large interaction potentials which results in high heats of adsorption (Lowell et al., 2004b).

Physisorption is a completely reversible process. Unlike chemisorption, it is very typical of physisorption to possess low heats of adsorption. Moreover, during the adsorption process no changes occur in the surface of the adsorbent and unlike in chemisorption, adsorbate covers the whole surface rather than being adsorbed on specific sites. In physisorption, surface of the adsorbent can be covered with more than a single layer of adsorbate. Despite the small pores, no activation energy is necessary for the adsorption equilibrium to be achieved (Lowell et al., 2004b).

2.3.1. Thermodynamics of Adsorption

During the adsorption process, entropy of the adsorbate decreases since the degree of multiplicity of the adsorbate is lower than the degree of multiplicity of the adsorptive. It is assumed for physisorption that the entropy of the adsorbent does not change during adsorption. However, there may be cases where the entropy of the adsorbent increases. Even if it increases, this increase will be lower than the decrease in the adsorbate's entropy which makes the entropy change of the whole system lower than zero.

The spontaneity of the system depends on the change in Gibbs free energy. For a system to be spontaneous, the change in the Gibbs free energy *(*ΔG*)* should be negative. Physisorption processes are spontaneous processes. Gibbs free energy is defined by the the following formula at constant temperatures where ΔG is the change in the Gibbs free energy, ΔH is the change in enthalpy, and ΔS is the change in entropy:

$$\Delta G = \Delta H - T\Delta S$$

For the negative value of ΔG and the negative value of ΔS, ΔH becomes a negative value which means that physisorption processes are always exothermic (Lowell et al., 2004b).

2.3.2. Adsorption Potential

International Union of Pure and Applied Chemistry (IUPAC) defined pore width as the pore diameter of the cylindrical pores or the distance between the pore walls of slit pores

(Lowell et al., 2004b). In accordance with the size of the pore widths, pores are divided into three categories: Micropores, mesopores, and macropores. The pore widths of micropores are smaller than 2 nm, the pore widths of mesopores range in between 2 to 50 nm and lastly, the pore width of macropores are greater than 50 nm (Lowell et al., 2004b). The following figure (Figure 2) illustrates the adsorption potential graphs of macro-, meso- and microporous adsorbents.

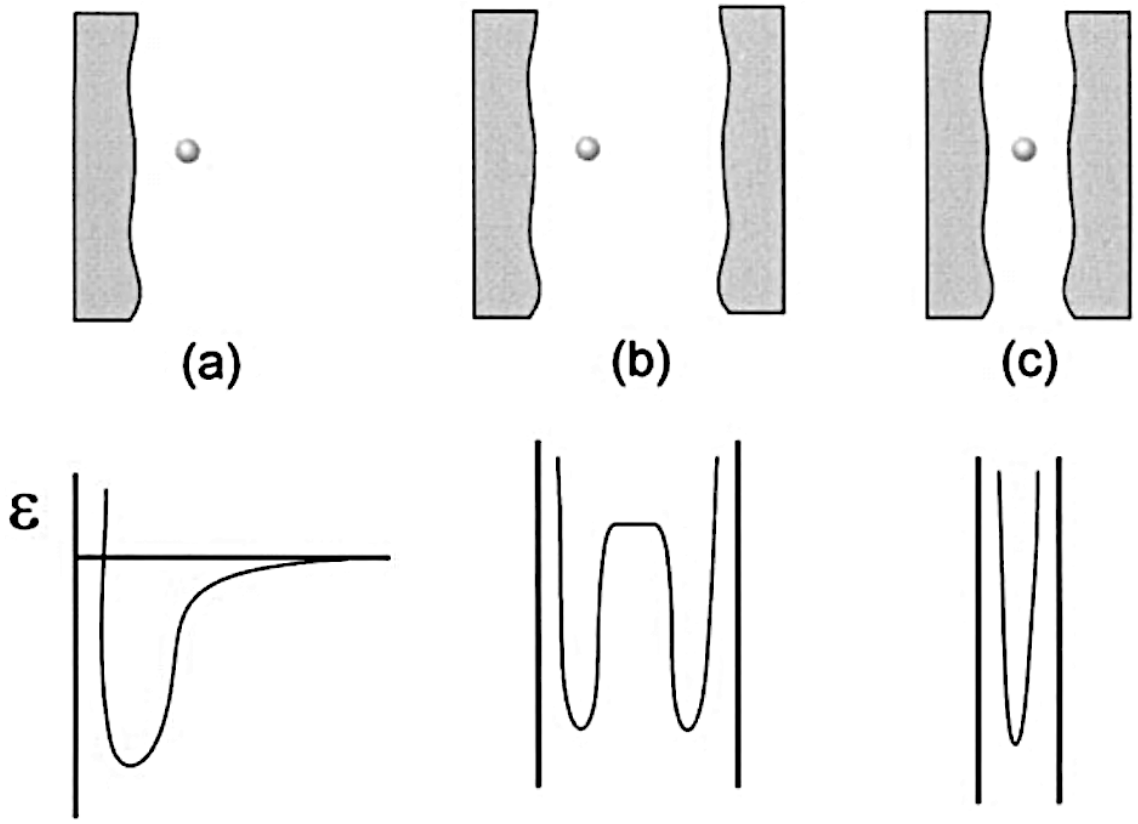

Figure 2. Illustration of the adsorption potential graph of (a) macroporous, (b) mesoporous, and (c) microporous adsorbents (Lowell et al., 2004b).

Figure 2 (a) illustrates the adsorption potential graph of a macropore. The pore width of a macropore is greater than 50 nm. The pore width is too large that a macropore is considered as a flat surface. Figure 2 (b) shows that in the middle of a mesopore, the adsorption potential is negligible. Therefore, the adsorption behavior of mesopores depends on both the attractive interactions between fluid molecules and the interactions between the wall and the fluid. Figure 2 (c) illustrates the adsorption potential of micropores. In the case of micropores, the adsorption behavior is mostly depended on the interactions between the pore walls and the fluid molecules.

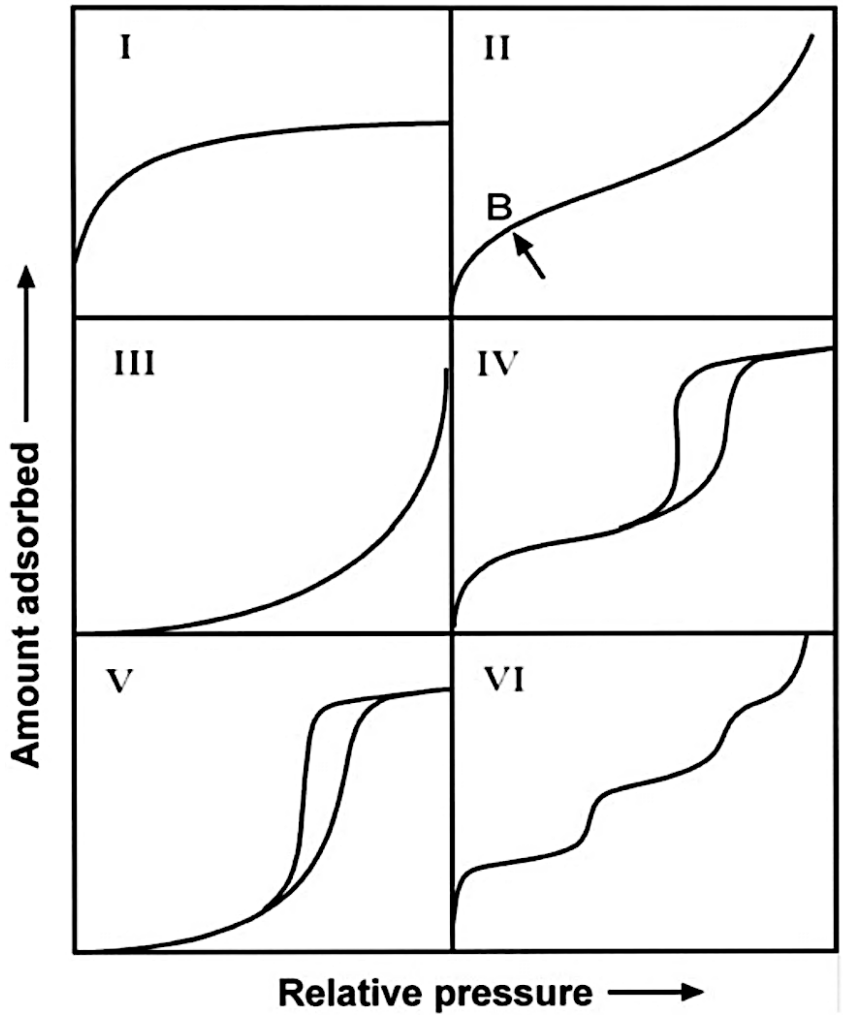

Figure 3. Adsorption isotherms (Lowell et al., 2004b)

Figure 3 shows the adsorption isotherms classified by IUPAC. In 1985, IUPAC classified the adsorption isotherms in six groups (Union, Pure, & Chemistry, 1985). Figure 3 I illustrates Type I isotherms at which micropores dominate the pore structure. High N_2 uptakes obtained at low pressures ($P/P_0 < 0.2$) illustrate the presence of micropores. Figure 3 II represents Type II isotherms which are the characteristic isotherms of macro- and/or nonporous materials. Point B shown on the graph (Figure 3 II) is the point where monolayer coverage is completed and multilayer adsorption starts. Figure 3 III illustrates Type III isotherms. These types of isotherms are rarely observed at which adsorbate-adsorbate interactions dominate. Type IV isotherms (Figure 3 IV) are the characteristic isotherms of mesoporous materials with hysteresis loop present. At the first part of the isotherm a monolayer-multilayer adsorption occurs and then a plateau is achieved which is associated

with limited N_2 uptake and thus, pore filling. Similar to Type IV isotherms, Type V isotherms (Figure 3 V) possess a hysteresis loop. However, the initial part of Type V isotherms is different from Type IV isotherms. The initial part of the Type V isotherms illustrates the presence of weak adsorbate-adsorbent interactions. Type VI isotherms (Figure 3 VI) shows the typical features of a non-porous adsorbent. The several steps of multilayer adsorption can be observed in the isotherm (Hill, 1955).

2.4. Hydrogen Storage

Energy has a crucial role on society's economic development. Rising energy demand results in excessive fossil fuel consumption, and more importantly, adversely influences the ecosystem and human health (Fakioğlu, Yürüm, & Veziroğlu, 2004). A fuel that can meet the necessary energy demand should be developed before fossil fuel reserves are depleted (Andreas Züttel, Remhof, Borgschulte, & Friedrichs, 2010a).

Hydrogen is an abundant element that is a that is a clean alternative to fossil fuels (Khan, Kang, Seok, & Jhung, 2011; L. Schlapbach & Züttel, 2001). Hydrogen has the following advantages over fossil fuels: i) CO_2 does not form during its combustion; and ii) hydrogen possesses a high energy density (energy per kilogram) which is three times greater than the energy density of the hydrocarbon based fuels (Mazloomi & Gomes, 2012; L. Schlapbach & Züttel, 2001).

Hydrogen fuel-based technologies are promising alternatives to fossil fuel-based technologies in the transportation sector since combustion of fossil fuels contribute by 24% to the overall CO_2 emissions ("Aviation – Tracking Transport 2019 – Analysis - IEA," n.d.). However, storing hydrogen in a safe, light and economic way still remains as a challenge which is necessary for the practical use of on-board hydrogen storage systems (Mazloomi & Gomes, 2012; Andreas Züttel, 2004).

Hydrogen is stored as: i) compressed gas in high pressure gas cylinders; ii) liquid hydrogen in cryogenic tanks; iii) absorbed hydrogen (metal hydrides); and iv) adsorbed hydrogen (Andreas Züttel, 2004). However, each method has its own drawbacks.

Being a widely used hydrogen storage technology, compressed hydrogen storage systems are used in various prototype fuel cell vehicles (J. Zheng et al., 2012). High pressures are necessary for the use of highly pressurized gas cylinders since compressed hydrogen gas

possesses a low volumetric density (Abe, Popoola, Ajenifuja, & Popoola, 2019; J. Yang, Sudik, Wolverton, & Siegel, 2010). However, having highly pressurized compressed gas cylinders in the vehicles is risky for safe transportation (Durbin & Malardier-Jugroot, 2013). Moreover, it is very expensive to store a highly pressurized hydrogen gas in a vessel that can safely store hydrogen under high pressure (O'Malley et al., 2015). Recently, DOE has made some suggestions: i) decreasing the cost of carbon fiber and carbon fiber composites; and ii) development of cost-effective alternative composites to carbon fiber. Lastly, in the case of large vehicles, the large volumes of the storage tanks may not have significant effect. However, the size of the storage tanks has particular importance in light-duty vehicles. Despite the progresses made, the use of compressed hydrogen gas at light-duty platforms remains as a challenge (Office-of-Energy-Efficiency-&-Renewable-Energy, 2015).

The energy content of liquid hydrogen storage systems is greater than the energy content of its compressed state. However, liquefication temperature of hydrogen increases the power necessary for the liquifying process which makes hydrogen storage in cryogenic tanks even more expensive than its pressurized gas form (Carpetis, 1982; Sakintuna, Lamari-Darkrim, & Hirscher, 2007; Andreas Züttel et al., 2010a). Moreover, the cryogenic storage tanks should be thermally insulated to avoid boiling-off of the hydrogen. The energy necessary for the liquefaction process, and the thermal insulation necessary to avoid boil-off of hydrogen increase the cost of the process which limit the practical use of liquid hydrogen (Andreas Züttel, 2004).

At high temperatures transition metals and metal alloys react with hydrogen gas to form metal hydrides (Andreas Züttel, 2004). As hydrogen molecules come close to the metal surface these molecules experience an attractive force, van der Waals forces. In order to form a hydrogen metal bond, hydrogen molecules should overcome the necessary activation barrier. When hydrogen molecules overcome this activation barrier, they will be chemisorbed on the metal surface sharing their electrons with the metal atoms (Andreas Züttel, 2004). During the absorption process, phase transition occurs which offers metal hydrides to absorb large quantities of hydrogen at constant pressure. The chemical bonds formed between hydrogen and metal hydrides are stronger than the bonds formed in physisorption. Therefore, it requires higher amount of energy for hydrogen to be desorbed (Andersson & Grönkvist, 2019). Elemental metal hydrides, intermetallic hydrides, and complex metal hydrides are used in hydrogen storage studies. Most of the elemental metal

hydrides cannot be used practically in hydrogen storage applications owing to the thermodynamics of the process and/or the low hydrogen storage capacities (Sandrock, 1999). For instance, high temperatures are required for the hydrogenation and dehydrogenation process of magnesium hydrides, it is very difficult to regenerate aluminum unless the regeneration process is conducted at very high temperatures (Aguey-Zinsou & Ares-Fernández, 2010; de Rango, Marty, & Fruchart, 2016; Fabian San Francisco, CA (United States)], Petrie Menlo Park, CA (United States)], Crouch-Baker Menlo Park, CA (United States)], & Fong Menlo Park, CA (United States)], 2017; J Graetz et al., 2011; Jason Graetz & Hauback, 2013; Hua & Ahluwalia, 2011; Shao, He, Lin, & Li, 2018; Y. Sun et al., 2018; Yartys et al., 2019). In the case of intermetallic hydrides, they possess low gravimetric hydrogen storage capacities and the process is not cost-effective (Bellosta von Colbe et al., 2019; Harries, Paskevicius, Sheppard, Price, & Buckley, 2012; Sandrock, 1999; Wenger, Polifke, Schmidt-Ihn, Abdel-Baset, & Maus, 2009). However, intermetallic hydrides are used in several applications at which the weight of the storage system is not important such as mining vehicles and forklifts (Bevan, Züttel, Book, & Harris, 2011; Lototskyy et al., 2016; Sandrock & Bowman, 2003). The practical use of complex metal hydrides is limited with their high dehydrogenation temperatures (Felderhoff, Weidenthaler, von Helmolt, & Eberle, 2007; Møller et al., 2017; Puszkiel et al., 2017). Moreover, most of the complex metal hydrides cannot be reversibly dehydrogenated (Pommerin, Weidenthaler, Schüth, & Felderhoff, 2010; Puszkiel et al., 2017). The regeneration process is energy intensive and expensive (Ouyang, Zhong, Li, & Zhu, 2018). Metal hydrides can absorb large amounts of hydrogen (Andreas Züttel, 2004). However, the measured gravimetric hydrogen storage densities of reversible transition metals are lower than 3 wt.% (at room temperature and atmospheric pressure) (Mazloomi & Gomes, 2012; Andreas Züttel, 2004). There rises the necessity of the use of heavy tanks which fails the practical use of metal hydrides (Andreas Züttel, 2003a).

Lastly, hydrogen molecules can be adsorbed on the surface of porous sorbents reversibly by the weak van der Waals forces. Physisorption is the reversible hydrogen adsorption process at which van der Waals interactions dominate (Andreas Züttel, 2003a). Physisorption has the advantage over the other methods by its low cost and feasibility (Andreas Züttel, 2004). However, it is limited by the weak van der Waals forces. Despite the high H_2 adsorption capacities of adsorbents measured at 77 K, the measured H_2 adsorption

capacities decrease drastically at room temperature and atmospheric pressure (L. Schlapbach & Züttel, 2001; Andreas Züttel, 2004). Therefore, researchers have put extensive effort to develop porous sorbents that can store high amounts of hydrogen at ambient conditions (Attia, Menemparabath, Arepalli, & Geckeler, 2013; A. Gupta et al., 2019; Pareek, Rohan, Chen, Zhao, & Cheng, 2017; H. Zhou et al., 2015b). Porous materials with high BET surfaces areas have been investigated for their H_2 adsorption capacities (Dündar-Tekkaya & Yürüm, 2016; Durbin & Malardier-Jugroot, 2013; A. G. Klechikov et al., 2015a; A. Klechikov et al., 2015; Barbara Panella, Hirscher, & Roth, 2005a; L. Schlapbach & Züttel, 2001). Despite the achievements and enhancements obtained in H_2 adsorption studies, it is still a challenge to achieve the target set by DOE at ambient conditions (Broom et al., 2019; Moradi & Groth, 2019; Pyle, Gray, & Webb, 2016; Yürüm, Taralp, & Veziroglu, 2009a; Qiang Zhao, Yuan, Liang, & Li, 2013).

2.4.1. Hydrogen Physisorption with Carbon-based Materials

Carbon-based materials are considered as promising candidates in gas adsorption studies owing to their availability, low-cost, low densities, high BET surface areas and large pore volumes, high chemical stabilities and tunable structures (H.-M. Cheng, Yang, & Liu, 2001; Ritschel et al., 2002; Yürüm, Taralp, & Veziroglu, 2009b). Activated carbons (ACs), carbon nanotubes (CNTs), and graphene and graphene-based, graphene-like materials, are several carbon-based materials investigated for their H_2 adsorption capacities (C. C. Ahn et al., 1998; Baughman, Zakhidov, & de Heer, 2002; Bénard & Chahine, 2007; Chambers, Park, Baker, & Rodriguez, 1998; P. Chen, Wu, Lin, & Tan, 1999; H.-M. Cheng et al., 2001; Dillon et al., 1997; Gadiou et al., 2005; Gangu, Maddila, Mukkamala, & Jonnalagadda, 2019; Gohari-Bajestani, Akhlaghi, Yürüm, & Yürüm, 2017; Gohari Bajestani, Yürüm, & Yürüm, 2016; B. K. Gupta & Srivastava, 2000, 2001; M Hirscher et al., 2002; Kayiran, Lamari, & Levesque, 2004; C Liu et al., 1999; Lueking & Yang, 2003; Nijkamp, Raaymakers, van Dillen, & de Jong, 2001; Barbara Panella, Hirscher, & Roth, 2005b; Ritschel et al., 2002; Schimmel et al., 2004; Shiraz & Tavakoli, 2017; Takagi, Hatori, Soneda, Yoshizawa, & Yamada, 2004; Takagi, Hatori, Yamada, Matsuo, & Shiraishi, 2004; Texier-Mandoki et al., 2004; Thomas, 2007; Tozzini & Pellegrini, 2013; X. B. Wu, Chen, Lin, & Tan, 2000; Ye et

al., 1999; Yürüm et al., 2009b; X. B. Zhao, Xiao, Fletcher, & Thomas, 2005; Y. Zhou, Feng, Sun, & Zhou, 2003).

The fast adsorption desorption kinetics, high reversibility, high BET surface area, wide range of pore size make ACs promising candidates in gas adsorption studies (Y. Xia, Yang, & Zhu, 2013; Yürüm et al., 2009b). Studies show that the measured H_2 adsorption capacities (77 K) of ACs range in between 0.2 to 5.5 wt.% (Bénard & Chahine, 2007; Kayiran et al., 2004). However, when the H_2 adsorption studies are conducted at 298 K, the measured adsorption capacities decrease, drastically (Chahine & Bose, 1994; de la Casa-Lillo, Lamari-Darkrim, Cazorla-Amorós, & Linares-Solano, 2002; Thomas, 2007; L. Zhou, Zhou, & Sun, 2004). To enhance the measured H_2 adsorption capacities at 298 K, researchers prepared chemically activated carbons which showed an enhanced H_2 adsorption capacity of 3.2 wt.% at 298 K and 200 bar (Jordá-Beneyto, Suárez-García, Lozano-Castelló, Cazorla-Amorós, & Linares-Solano, 2007).

Studies show that CNTs possess H_2 adsorption capacities lower than 1 wt.% at 298 K and 1 bar (Ansón et al., 2004; M Hirscher et al., 2002; A Züttel et al., 2002). To enhance the measured H_2 adsorption capacities, researchers conducted acid treatment process which enhanced the measured H_2 adsorption capacities at 77 K to 1.7 wt.% (Takagi, Hatori, Soneda, et al., 2004). In the meanwhile, theoretical studies showed that neither the H_2 adsorption capacities at 77 K nor the H_2 adsorption capacities at 298 K are sufficient enough to meet the U.S. DOE target (Frankland & Brenner, 2001; Guay, Stansfield, & Rochefort, 2004).

H_2 storage capacities of graphene and graphene based materials are investigated by various researchers and research groups owing to their high BET surface areas, high pore volumes, light weight and high abundancies (Jin et al., 2011; Kaur & Pal, 2016; A. G. Klechikov et al., 2015b; Kostoglou et al., 2016; Qin et al., 2015; C. N. R. Rao, Sood, Subrahmanyam, & Govindaraj, 2009; Srinivas et al., 2010; Tozzini & Pellegrini, 2013; Vinayan, Nagar, & Ramaprabhu, 2013; L. Wang, Stuckert, & Yang, 2011; L. Wei & Mao, 2016; Q. Zhang et al., 2016; C. Zhou & Szpunar, 2016; C. Zhou, Szpunar, & Cui, 2016; H. Zhou et al., 2015a; Yu Zhu, James, & Tour, 2012). Researchers figured out that at 298 K and 120 bar the H_2 adsorption capacities of bulk graphene powders were at most 1 wt.% (A. G. Klechikov et al., 2015b). To enhance the measured H_2 adsorption capacities at 298 K, researchers used hydrogen spillover mechanism. For instance, researchers synthesized Ni/reduced graphene oxide (rGO), Ni/Pd/rGO, and Ni/Pd/Ag/rGO hybrid materials. The

measured H_2 adsorption capacities (293 K and 800 mm Hg) of Ni/rGO, Ni/Pd/rGO, and Ni/Pd/Ag/rGO hybrid materials were enhanced to 0.007 wt.%, 0.13 wt.% and 0.055 wt.%, respectively (L. Wei & Mao, 2016). Some other researchers developed hybrid rGO nanocomposites. The measured H_2 adsorption capacity (298 K and 10 bar) of Pd/Al_2O_3-rGO hybrid nanocomposite was enhanced to 0.31 wt.% (Gohari Bajestani et al., 2016). Another researcher synthesized Pt-doped HKUST-1/GO composite whose H_2 adsorption capacity was enhanced to 0.250 mmol/g at 298 K and 860 mm Hg (H. Zhou et al., 2015a). Researchers decorated graphene with Ni nanoparticles and formed a Ni-graphene composite. The measured H_2 adsorption capacities of Ni-graphene composite at 298 K are 0.14 wt.%, and 1.18 wt.% at 1 bar and 60 bar, respectively (C. Zhou et al., 2016). In conclusion, studies show that bulk graphene does not show an optimal H_2 adsorption capacity at 298 K that can meet the U.S. DOE target. Significant enhancements are achieved by spillover mechanism provided by metal catalysts and the hybrid nanocomposites. However, despite the all efforts spent, the measured optimal H_2 adsorption capacities at 298 K are far from meeting U.S. DOE target.

2.4.2. Hydrogen Physisorption with Zeolites

The high BET surface areas, high pore volumes, chemical and thermal stabilities of zeolites led researchers investigate the hydrogen storage performances of zeolites (Carraro et al., 2014; X. Du & Wu, 2006; Dündar-Tekkaya & Yürüm, 2015; J. Edler, A. Reynolds, J. Branton, R. Trouw, & W. White, 1997; H W Langmi et al., 2003; S.-J. Park & Lee, 2010; Ramachandran, Ha, & Kim, 2007; Sheppard, Maitland, & Buckley, 2005; Weitkamp, Fritz, & Ernst, 1995; C. Wu, Gao, Hu, Chen, & Shi, 2009; Andreas Züttel, 2003b). Theoretical studies show that the maximum H_2 adsorption capacity (77 K) of a zeolite can range in between 2.6 to 2.9 wt.% (Vitillo, Ricchiardi, Spoto, & Zecchina, 2005). In line with the theoretical studies, a maximum of 2.1 wt.% H_2 adsorption capacity was achieved at 77 K, experimentally (J. Dong, Wang, Xu, Zhao, & Li, 2007; H W Langmi et al., 2003; Sheppard & Buckley, 2008). In order to enhance the measured H_2 adsorption capacities, researchers incorporated transition metals into the frameworks of zeolites (Carraro et al., 2014; Dündar-Tekkaya & Yürüm, 2015; S.-J. Park & Lee, 2010; Prasanth, Raj, Bajaj, Kim, & Jasra, 2010; Ramachandran et al., 2007; Yamamoto et al., 2011). For instance, a Ni doped MCM-41

showed a H_2 adsorption capacity of 0.68 wt.% at 298 K and 65 bar. The enhancement in the H_2 adsorption capacity was attributed to the spillover effect owing to the presence of Ni particles (S.-J. Park & Lee, 2010). In order to enhance the H_2 adsorption capacity of MCM-41, researchers loaded it with Pd and Ni metal mixtures. Pd-Ni loaded MCM-41 showed a H_2 adsorption capacity of 0.98 wt.% at 298 K and 10 bar (Dündar-Tekkaya & Yürüm, 2015). Studies showed that doping zeolites with transition metals enhanced the H_2 adsorption capacities of zeolites measured at 298 K thanks to the spillover effect. However, the reported H_2 adsorption capacities cannot meet the DOE target (Carraro et al., 2014; Dündar-Tekkaya & Yürüm, 2015; S.-J. Park & Lee, 2010; Prasanth et al., 2010; Ramachandran et al., 2007; Yamamoto et al., 2011).

2.5. Metal-organic Frameworks (MOFs)

MOFs, a new family of porous materials, were firstly introduced by Yaghi in 1995 (O M Yaghi, Li, & Li, 1995). These crystalline porous frameworks are constructed by linking metal ions or metal ion clusters (secondary building units) with organic ligands ("Emergence of Metal-Organic Frameworks," 2019). Bridging ligands link neighboring secondary building units (SBUs) to each other.

Secondary building units (SBUs) define the final topology of the MOF framework. Moreover, the geometry of SBU depends on: i) the type of the ligand; ii) the type of the metal; and iii) metal to ligand ratio. Thus, depending on the choice of the starting materials, structural and textural properties of MOFs can be arranged which offers a wide variety of MOFs with different chemical and textural properties to be synthesized.

Most commonly, MOFs are synthesized via a solvothermal synthesis route. Metal salt, organic ligand and solvent are placed in a glass vial tube which is properly sealed, and the reaction takes place at elevated temperatures. Solvothermal synthesis follows the working principle of Lewis acid-base reactions at which the metal salt and the organic ligand are mixed in a solvent and heated in an oven at high temperatures. Metal ions act as Lewis acids while the deprotonated ligands act as Lewis bases. Considerable attention has to be given to the synthesis conditions which possess significant role on the produced MOF structures and determine whether a bulk precipitate or a single crystal will form (D. Zhao, Timmons, Yuan, & Zhou, 2011a).

Solvothermal synthesis produces high quality crystals while reaction duration lasts from hours to days. It is important to consider pH, temperature, concentrations of the metal salt, the ligand, and the solvent since all these parameters influence the final product, considerably.

Another method to synthesize MOFs is microwave-assisted method which accelerates the rates of the reactions (Biswas et al., 2009; Bux et al., 2009; Centrone, Harada, Speakman, & Hatton, 2010; Centrone, Yang, et al., 2010; Chalati, Horcajada, Gref, Couvreur, & Serre, 2011; J.-S. Choi, Son, Kim, & Ahn, 2008; Denysenko et al., 2011; Horcajada et al., 2010b; Jae et al., 2006; S. H. Jhung et al., 2007; Sung Hwa Jhung et al., 2006; Jung, Yang, Kim, Kim, & Ahn, 2010; Khan, Haque, & Jhung, 2010a; Khan et al., 2011; D. O. Kim et al., 2011; J. S. Lee et al., 2010; Wei Li, Jin, Huang, & Chen, 2010; B. Liu et al., 2008; H.-K. Liu, Tsao, Zhang, & Lin, 2009; C.-M. Lu, Liu, Xiao, & Harris, 2010; Ni & Masel, 2006; J. H. Park, Park, & Jhung, 2009; Sabouni, Kazemian, & Rohani, 2010; Schlesinger, Schulze, Hietschold, & Mehring, 2010; Y.-K. Seo et al., 2009; Silva, Valente, Rocha, & Almeida Paz, 2010; Taylor-Pashow, Della Rocca, Xie, Tran, & Lin, 2009; Tonigold et al., 2009; X.-F. Wang, Zhang, Huang, Zhang, & Chen, 2008; Xiang et al., 2010). In the microwave-assisted method, synthesis depends on the interaction of electric charges with electromagnetic waves at which the orientations of molecules change permanently. As molecules collide, kinetic energy of the system increases. Therefore, reaction durations are shortened.

In the electrochemical synthesis, an electrode that contains the metal ions and a solution that contains the linker are present (Ameloot et al., 2010, 2009; Hartmann et al., 2008; Mueller et al., 2006; Schlesinger et al., 2010). When voltage is applied, metal ions move through the reaction medium. Metal ions and linkers react and then form MOFs (Al-Kutubi, Gascon, Sudhölter, & Rassaei, 2015; Mueller et al., 2005).

Another synthesis method is mechanochemical synthesis at which a mechanical force induces chemical reactivity (Beldon et al., 2010; Beyer & Clausen-Schaumann, 2005; Friščić, 2010; Friščić & Fábián, 2009; Friščić et al., 2010; Fujii et al., 2010; Garay, Pichon, & James, 2007; Klimakow, Klobes, Thünemann, Rademann, & Emmerling, 2010; Pichon & James, 2008; Schlesinger et al., 2010; Willans et al., 2011; Hongwei Yang, Orefuwa, & Goudy, 2011; W. Yuan, Friščić, Apperley, & James, 2010; W. Yuan, Garay, et al., 2010).

Mechanochemical reactions benefit from the short reaction times, and solvent-free synthesis environments.

In sonochemical synthesis, reaction occurs as high-energy ultrasound is applied. Bubbles firstly form and then collapse which provide high local temperatures and pressures to be achieved. By this way, reactions occur faster. Sonocohemical synthesis is used to scale-up MOF synthesis which decreases reaction durations while forming small MOF crystals (Chalati et al., 2011; Jung et al., 2010; Khan, Haque, & Jhung, 2010b; Khan & Jhung, 2009; J. Kim et al., 2011; Z.-Q. Li et al., 2009; Qiu, Li, et al., 2008; Sabouni et al., 2010; Schlesinger et al., 2010; Tranchemontagne, Hunt, & Yaghi, 2008).

MOFs significantly benefit from their highly porous and crystalline structure, high surface area, tunable pore structure, and their ability to be loaded with other elements and components without any changes in their topology (Rowsell & Yaghi, 2004b). These properties make MOFs promising candidates in many application areas such as adsorption and separation studies, catalysis, chemical separations, degradation of toxic substances, drug delivery, gas storage and release, light and water harvesting, and sensor studies (Adams, Carson, Ward, Tannenbaum, & Koros, 2010; T.-H. Bae et al., 2013; Y. S. Bae & Snurr, 2011; Corma, García, & Llabrés I Xamena, 2010; García-García, Moreno, Díaz, Bruix, & Corma, 2016; Hanikel et al., 2019; Hanikel, Prévot, & Yaghi, 2020; Horcajada et al., 2006; Katz et al., 2014, 2015; Jeongyong Lee et al., 2009; J. R. Li, Kuppler, & Zhou, 2009; J. R. Li et al., 2011; Jiewei Liu et al., 2014; López-Maya et al., 2015; Nguyen et al., 2020; Nunes, Gomes, Pillinger, Gonçalves, & Abrantes, 2015; Y. Peng et al., 2013; Rieth, Yang, Wang, & Dincă, 2017; J. S. Seo et al., 2000; So, Wiederrecht, Mondloch, Hupp, & Farha, 2015; Taylor-Pashow, Della Rocca, Huxford, & Lin, 2010; J.-L. Wang, Wang, & Lin, 2012).

Micropores make microporous materials promising candidates in gas storage and separation studies since the interactions between the pores and the pore walls are very strong. The high microporosity and large surface areas of MOFs make these materials promising in gas adsorption, storage and separation studies (Dincă & Long, 2008; Kitagawa, Kitaura, & Noro, 2004; JeongYong Lee et al., 2009; Mueller et al., 2006; Omar M Yaghi et al., 2003; X. Zhao et al., 2004). To enhance the adsorbed gas amount, the number of active adsorption sites within the porous framework should be increased which can be achieved by ligand expansion method. However, ligand expansion method was not as effective as it was thought: MOFs synthesized with expanded ligands were fragile, and had higher tendency to self-

interpenetrate (B. Chen, Eddaoudi, Hyde, O'Keeffe, & Yaghi, 2001; Furukawa et al., 2010; X. Lin, Jia, Hubberstey, Schröder, & Champness, 2007).

2.5.1. Hydrogen Storage in MOFs

MOFs are highly crystalline and highly porous materials that possess high BET surface areas, tunable pore size and pore structure, and found to be promising candidates in various application areas including adsorption/desorption, gas storage and separation studies.

After the promising results obtained from the very first study conducted in 2003, many researchers and research groups spent particular attention on hydrogen storage performances of MOFs (Rosi et al., 2003). MOFs are promising candidates for hydrogen storage studies and get ahead of other materials since: i) pore sizes and structure of MOFs can be designed to enhance the H_2 adsorption performances, and ii) the specific hydrogen adsorption sites can be identified in a MOF. From 2003 till now, many studies have been conducted to enhance hydrogen storage performances of MOFs. MOFs possess very high H_2 adsorption capacities at 77 K and high pressures. However, when the studies are conducted at 298 K, H_2 adsorption capacities of MOFs decrease, dramatically. It is still a challenge to design a MOF with a H_2 adsorption capacity that meet the DOE target of hydrogen storage.

While conducting H_2 adsorption studies, one has to be careful about the excess and total H_2 adsorption capacities. At 1 bar the excess and total H_2 adsorption values are found to be the same while as the pressure increases to 100 bar, these two values differ from each other (Murray, Dincă, & Long, 2009). Excess adsorption is an approximation of the amount of H_2 that can be adsorbed on the surface of the material. In a microporous material, the excess adsorption would first reach its maximum, and then start to decrease with increasing pressure. Depending on the material, the maximum adsorption capacity would be achieved in between 20 to 40 bars. In the meanwhile, total uptake considers both the surface adsorbed H_2 and the compressed H_2 gas within the pores.

To understand the H_2 adsorption behavior in MOFs, several researchers worked on computational models. It was found that H_2 adsorption capacity measured at 77 K is correlated with surface area. Moreover, very low H_2 adsorption capacities can be achieved at 298 K. This correlation between H_2 adsorption capacity measured at 77 K and the surface

area and the low H_2 adsorption capacities achieved at 298 K are attributed to weak van der Waals interactions between MOFs and the H_2 molecules. The very weak van der Waals interactions result isosteric heats of adsorption values to vary in between 4 to 7 kJ/mol (Düren & Snurr, 2004; Frost, Düren, & Snurr, 2006b; Frost & Snurr, 2007; S. S. Han, Deng, & Goddard III, 2007; S. S. Han & Goddard, 2007; E Klontzas, Mavrandonakis, Froudakis, Carissan, & Klopper, 2007; Emmanouel Klontzas, Mavrandonakis, Tylianakis, & Froudakis, 2008; Emmanouel Klontzas, Tylianakis, & Froudakis, 2008; Lochan & Head-Gordon, 2006; Mavrandonakis, Tylianakis, Stubos, & Froudakis, 2008).

In order to develop MOFs that function optimally at 298 K, the binding energies between the H_2 molecules and MOFs have to be increased and a MOF that possesses an adsorption enthalpy of 20 kJ/mol should be developed (Bhatia & Myers, 2006b; Garrone, Bonelli, & Otero Areán, 2008; Murray, Dincă, et al., 2009). Several studies showed that partial charges on the surface of MOFs strengthen the H_2 binding via dipole-induced dipole interactions (Lochan & Head-Gordon, 2006; Lochan, Khaliullin, & Head-Gordon, 2008).

H_2 adsorption studies conducted on microporous materials show that adsorption capacity depends on the pore size, considerably. For graphitic carbons, and carbon nanotubes calculations show that having pores with pore diameters of 7 Å would increase the H_2 adsorption capacity of the material to the maximum adsorption capacity at 298 K. Moreover, regardless of the pore shape, a pore size of 10 Å would provide the maximum H_2 adsorption capacity to be achieved at 100 bar (Rzepka, Lamp, & de la Casa-Lillo, 1998).

2.5.1.1.Strategies to increase hydrogen adsorption enthalpy of MOFs

Introducing open metal sites on the surface of MOFs is found to enhance the H_2 adsorption capacity of MOFs. However, strong metal-H_2 bonds should be avoided and charge-induced dipole interactions should be formed. However, it is challenging to form highly concentrated open metal sites (Dincă & Long, 2008). Strategies that are used to form open metal sites include thermally-assisted solvent molecule evacuation, photolysis, guest metal cation exchange, and use of reactive bridging ligands (Dincă et al., 2006; Dincă et al., 2007; Dincă & Long, 2007; Kaye, Dailly, Yaghi, & Long, 2007a; Kaye & Long, 2005, 2007; Mulfort & Hupp, 2007; Prestipino et al., 2006).

Catenation/interpenetration is a method to enhance H_2 adsorption capacity of MOFs. It is found that as the pore diameters increase, the attraction felt by H_2 molecules at the center

of the pore walls decreases which decreases the measured H_2 adsorption capacities. Therefore, microporous MOFs with smaller pore sizes would be more efficient in H_2 adsorption studies (Belof, Stern, Eddaoudi, & Space, 2007; Kabbour, Baumann, Satcher Joe H., Saulnier, & Ahn, 2006).

Framework interpenetration is a method to increase the amount of narrow pores present in the pore structure of the framework (Shengqian Ma et al., 2007; D. Sun, Ma, Ke, Collins, & Zhou, 2006). However, practically, it is not easy to control. Moreover, computational studies show that even though the heat of adsorption increases when framework interpenetration is issued, the decrease in the surface area, and the pore volume would decrease the total H_2 uptake (Frost & Snurr, 2007).

Hydrogen spillover is another method that can enhance the total H_2 uptake of the framework at which H_2 molecules dissociate into $H^{\bullet}$ on a metal surface while hydrogen atoms migrate towards the pores of the material (Christmann, Ertl, & Pignet, 1976; Gee, Hayden, Mormiche, & Nunney, 2000; Khoobiar, 1964; Pasteur, Dixon-Warren, Ge, & King, 1997; Somorjai, 1994). However, hydrogenation should be reversible and the packing density of $H^{\bullet}$ should be greater than the packing density of H_2 (H. Cheng, Chen, Cooper, Sha, & Pez, 2008; L. Wang & Yang, 2008). The effect of hydrogen spillover phenomenon was tested on several MOFs and encouraging results were obtained, the measured H_2 adsorption capacities of the frameworks increased (Yingwei Li, Yang, & Yang, 2007; Yingwei Li & Yang, 2006b, 2006a, 2007, 2008; Y.-Y. Liu, Zeng, Zhang, Xu, & Sun, 2007). However, there is still room for improvement. For instance, long-time recyclability and reproducibility of the materials should be investigated, and the H_2 adsorption performance of cheaper metals or metal clusters should be tested.

2.5.1.2.Hydrogen adsorption capacities of several MOFs

$Zn_4O(BDC)_3$ is one of the MOFs whose H_2 adsorption capacity was reported for the first time in literature (Rosi et al., 2003). The H_2 adsorption capacity of $Zn_4O(BDC)_3$ was measured at 77 K and found to be 1.3 wt. %, 5.1 wt.%, and 10.0 wt.% at 1 bar, 50 bar and 100 bar, respectively (Kaye, Dailly, Yaghi, & Long, 2007b; B Panella, Hirscher, Pütter, & Müller, 2006; Rowsell, Millward, Park, & Yaghi, 2004). However, it was observed that depending on the synthesis procedure reported, H_2 adsorption capacities of $Zn_4O(BDC)_3$ vary (Dybtsev, Chun, & Kim, 2004; J. Y. Lee, Olson, Pan, Emge, & Li, 2007; Jinchen Liu

et al., 2008; Pan et al., 2004; B Panella & Hirscher, 2005; B Panella et al., 2006; Rosi et al., 2003; Rowsell et al., 2004; Sabo, Henschel, Fröde, Klemm, & Kaskel, 2007; Wong-Foy, Matzger, & Yaghi, 2006). Moreover, $Zn_4O(BDC)_3$ can be used for 24 cycles without the loss of its adsorption capacity (Kaye et al., 2007b). Researchers investigated the influence of Pd loading on the H_2 adsorption performance of MOF-5 and found that H_2 adsorption capacity (at 77 K and 1 bar) of Pd loaded MOF-5 increases from 1.15 to 1.86 wt.% (Sabo et al., 2007).

HKUST-1 is one of the first Cu based MOFs reported in literature (Chui, Lo, Charmant, Orpen, & Williams, 1999). HKUST-1 has a higher isosteric heat of adsorption at low coverage than MOF-5 which provides HKUST-1 to achieve a higher H_2 adsorption capacity at 77 K and 1 bar (Batten & Robson, 1998; B Panella et al., 2006; Rowsell & Yaghi, 2006a). It was observed that removal of gust molecules and solvent molecules affect the measured H_2 adsorption capacities, considerably; by a complete solvent removal process, the H_2 adsorption capacity of HKUST-1 was enhanced to 4.1 wt.% (77 K and 26 bar) (Jinchen Liu et al., 2007).

A Mn based MOF possesses a BET surface area of 2100 m^2/g, an isosteric heat of adsorption of 10.1 kJ/mol and achieved a H_2 adsorption capacity of 6.9 wt.% (77 K and 90 bar). This relatively high H_2 adsorption capacity of Mn based MOF is attributed to its high isosteric heat of adsorption and the unsaturated Mn^{2+} sites present in its framework (Dincă et al., 2006).

MIL-53 that possesses 1D channels with large pore sizes and a BET surface area of 1100 m^2/g was investigated for its H_2 adsorption capacity. The measured H_2 adsorption capacities of MIL-53 formed of chromium and MIL-53 formed of aluminum are 3.1 wt.%, and 3.8 wt.% (77 K and 16 bar), respectively (Férey et al., 2003).

MIL-100 and MIL-101 were investigated for their H_2 adsorption performances at 77 K. The measured maximum H_2 adsorption capacity of MIL-100 is 3.28 wt.% at 77 K and 26.5 bar while MIL-101a achieved a maximum capacity of 4.5 wt.% (77 K and above 40 bar) and MIL-101b achieved a maximum capacity of 6.1 wt.% (77 K and 80 bar). The differences in the H_2 adsorption capacities of MIL-100 and MIL-101 were attributed to their different isosteric heat of adsorption values. MIL-101b possesses an isosteric heat of adsorption value greater than MIL-100. Moreover, evacuating $BDCH_2$ from the pores of MIL-101b provided MIL-101b to possess a higher H_2 adsorption capacity than MIL-101a (Latroche, Surblé, Serre, Mellot-Draznieks, Llewellyn, Lee, Chang, Jhung, et al., 2006).

MOFs possess very high H_2 adsorption capacities at 77 K. However, at 298 K their H_2 adsorption capacities decrease, drastically. Those lower H_2 adsorption capacities measured at 298 K are attributed to the weak van der Waals interactions between H_2 molecules and MOFs (Dincă et al., 2006; S. S. Han & Goddard, 2007; Kesanli et al., 2004; Latroche, Surblé, Serre, Mellot-Draznieks, Llewellyn, Lee, Chang, Jhung, et al., 2006; Yingwei Li & Yang, 2007; X. Lin et al., 2006; Y.-Y. Liu et al., 2007; Pan et al., 2004; Rosi et al., 2003). For instance, the H_2 adsorption capacities of HKUST-1 and MIL-101 were measured as 0.35 wt.%, and 0.51 wt.% (298 K 10 MPa), respectively (Yingwei Li & Yang, 2008). MIL-53(Al) attained its maximum H_2 adsorption capacity of 1.7 wt.% at 35 MPa (298 K) while MOF-177 which possesses a specific surface area of 4126 m^2/g achieved its maximum H_2 adsorption capacity of 0.94 wt.% at 45 MPa (298 K) (Voskuilen, Pourpoint, & Dailly, 2012).

Researchers investigated the effect of interconnected channels on the H_2 adsorption capacity of MOFs measured at 298 K. $[Co_3(ndc)_3(dabco)]$ achieves a higher H_2 adsorption capacity than $[Co_3(bdc)_3(dabco)]$ which is attributed to the interconnected channels of $[Co_3(ndc)_3(dabco)]$ and achieved a H_2 adsorption capacity of 0.89 wt.% at 298 K and 17.2 bar (Chun, Jung, Koo, Jeong, & Kim, 2008).

Researchers investigated the influence of spillover on the H_2 adsorption capacities of MOF-5, and IRMOF-8 at 298 K. It was observed that H_2 adsorption capacities of MOF-5 and IRMOF-8 were increased by a factor of 3.3 and 3.1, and a H_2 adsorption capacity of 1.32 wt.% and 1.8 wt.% were achieved, respectively (Yingwei Li & Yang, 2006b). Researchers investigated the effect of platinum doping on activated carbon/MOF-5 hybrid composites. By introducing hydrogen, favorable sites on the activated carbon/MOF-5 composite was created and the H_2 adsorption capacity was enhanced by a factor of 3 to 2.3 wt.% at 298 K and 100 bar (S.-Y. Lee & Park, 2011).

In order to obtain better performances from hydrogen spillover, researchers suggested to use a carbon precursor as a bridge that would enhance the contact between the spillover source and the MOF. Researchers used active carbon as the carbon precursor and enhanced the H_2 adsorption capacities of MOF-5 and IRMOF-8 by a factor of 2, and 8 to 3 wt.% and 4 wt.% at 298 K and 100 bar, respectively (Lachawiec, Qi, & Yang, 2005). Researchers tested the strategy of using a catalyst and a carbon bridge on MOF-177 and found that using a H_2 dissociation catalyst, Pt, and a carbon bridge enhanced the H_2 adsorption capacity of

MOF-177 by 2.5 to 1.5 wt.% at 298 K and 10 MPa. Researchers attributed the enhanced H_2 adsorption capacity to the contact between Pt and activated carbon which ensured a secondary spillover effect on the surface of AC/MOF-177 hybrid composite (Yingwei Li & Yang, 2007). However, some other researchers found contradictory results showing no enhancement in the H_2 adsorption capacities of the bridged composites (Campesi, Cuevas, Latroche, & Hirscher, 2010; Luzan & Talyzin, 2010). In the meanwhile, the bridged spillover strategy enhanced the H_2 adsorption capacities of HKUST-1 and MIL-101 by a factor of 3.2 and 2.8 to 1.12 wt.% and 1.4 wt.% (298 K and 10 MPa), respectively (Yingwei Li & Yang, 2008).

Researchers investigated the influence of doping metal supported carbon catalyst through a carbon bridge on the H_2 adsorption capacities of MIL-101, and MIL-53, and significant enhancements were achieved. H_2 adsorption capacities of MIL-101, and MIL-53 were measured as 1.14 wt.% and 0.63 wt.% at 293 K and 5 MPa, respectively (Y.-Y. Liu et al., 2007).

Researchers investigated the influence of Pt incorporation into MOF-177 framework. The H_2 adsorption capacity of Pt incorporated MOF-177 increased to 2.5 wt.% at 144 bar and 298 K. However, after several cycles of adsorption-desorption, its H_2 adsorption capacity decreased, drastically (Proch et al., 2008). Moreover, researchers tested the influence of Pt doping on the H_2 adsorption capacity of IRMOF-8. Pt-doped IRMOF-8 achieved a H_2 adsorption capacity of 0.85 wt.% at 10 MPa and 298 K while IRMOF-8 possessed a H_2 adsorption capacity of 0.44 wt.% at 298 K and 100 bar (Henrietta W Langmi, Ren, North, Mathe, & Bessarabov, 2014). Researchers examined the influence of embedding Pd nanoparticles into the pores of MIL-100(Al). Embedding Pd nanoparticles enhanced the H_2 adsorption capacity of MIL-100(Al) by a factor of 1.8 to 0.35 wt.% (298 K and 40 bar) (Zlotea et al., 2010).

Researchers incorporated metal hydrides into the pores of MOF framework to increase the achieved H_2 adsorption capacities. For instance, Mg nanocrystals were embedded into SNU-90' which enhanced the H_2 adsorption capacity of SNU-90' to 0.54 wt.%. (298 K and 90 bar). The enhanced H_2 adsorption capacity was due to the synergistic effect of physisorption and chemisorption (D.-W. Lim, Yoon, Ryu, & Suh, 2012).

In conclusion, MOFs possess high H_2 adsorption capacities (6 to 15 wt.%) at 77 K and high pressures with fast hydrogen release kinetics. However, for MOFs to the used as

hydrogen storage systems in light-duty fuel cell vehicles, the DOE target of hydrogen storage should be met at 298 K and lower pressures. Studies show that H_2 adsorption capacities of MOFs decrease drastically when the H_2 adsorption studies are conducted at 298 K. The reported H_2 adsorption capacities at 298 K (0.5 wt.% to 1 wt. % 298) are lower than the DOE targets. Therefore, researchers put significant effort on the strategies that can enhance the H_2 adsorption capacities of MOFs measured at 298. K. For instance, open metal sites were introduced, strategies that involve framework catenation/interpenetration were tested, effects of hydrogen spillover were investigated, guest metal ions that can provide unsaturated metal sites were introduced, Pd or Pt nanoparticles were loaded, bridged spillover was tested, and hybrid MOF composites were synthesized. All these strategies show promising results with an enhancement in H_2 adsorption capacities. However, the proposed strategies are not sufficient enough to synthesize MOFs that can achieve the DOE target of hydrogen storage. Despite the given effort by various researchers, there is still room for improvement for the H_2 adsorption capacities of MOFs measured at 298 K. Researchers should focus on to develop a strategy that would form cost-effective MOFs with high specific surface areas, and large pore volumes with high isosteric heats of adsorption that can show optimal H_2 adsorption performances at 298 K.

2.6. Hierarchical Porous MOFs

Hierarchical porous MOFs are developed to obtain enhanced performances and superior properties. Hierarchical porous MOFs can be used in various application areas, including adsorption, batteries, catalysis, electrocatalysts, energy storage and conversion, separation, sensors, solar cells and supercapacitor electrodes (Yue Hu et al., 2015; G. Huang et al., 2014; Jing Jiang, Zhang, & Ai, 2016; X.-J. Kong, Lin, Zhang, Zhang, & Lin, 2016; Q. Lin et al., 2015; T. Liu et al., 2015; Salunkhe, Kaneti, Kim, Kim, & Yamauchi, 2016; Wenjing Wang & Yuan, 2014; Xin Wang et al., 2016; Xi et al., 2013; L. Yan et al., 2017). By synthesizing hierarchical porous MOFs, a wide range of benefits such as high surface area, high pore volume, accessible space, shortened diffusion paths, low density, and interconnected porosity can be achieved.

Having only micropores on the pore structure is considered as a crucial disadvantage since micropores limit the mass transfer and diffusion properties of the material while having

a two-pore system offers the advantages of both micro- and mesopores. For instance, while micropores provide a high surface area and high pore volume; mesopores enhance the mass transport and diffusion properties, thus guest molecules can reach the active sites, easily (Vallet-Regi, Rámila, del Real, & Pérez-Pariente, 2001). Therefore, researchers put significant effort to develop strategies to increase the pore size and have mesoporosity in the pore structure. The strategies to increase the pore size are: i) ligand extension (Chong Liu, Li, & Rosi, 2012; Lykourinou et al., 2011); ii) surfactant templating (Pal & Bhaumik, 2013; Qiu, Xu, et al., 2008); iii) microwave-assisted synthesis (D.-Y. Hong, Hwang, Serre, Férey, & Chang, 2009); iv) solvent evaporation diffusion (Fang et al., 2007); v) ionic liquid emulsion route (Yueju Zhao et al., 2011); and vi) CO_2 expanded liquids (L. Peng et al., 2014b). However, a stable porosity cannot be achieved.

Ligand extension method has several disadvantages such that it is limited with synthesis conditions, pore size cannot be increased more than a certain size, framework collapses as the guest molecules are removed, and a close packed structure is formed. Moreover, some frameworks issue interpenetration which in turn results in decreased pore sizes and surface areas (D. Zhao et al., 2011a).

Researchers investigated a modulator-induced strategy that forms hierarchical pores. A metal, insufficient amount of ligand and a modulator are used in the synthesis. The main principle behind the use of a modulator is to form mesopores by the structural defects formed by the coordination of the modulator with the metal ions (G. Cai & Jiang, 2017a).

In the case of surfactant templating method, a chelating agent is used whose removal cause collapse of the framework.

Another method to introduce mesopores to the pore structure of MOFs is by the nanoparticle encapsulation and etching process which show promising results (W. Zhang et al., 2015).

In brief, hierarchical porous MOFs benefit from their high surface areas and high pore volumes. Moreover, their high porosity is available for the large molecules to diffuse and tunable pore sizes and pore shapes offer various advantages while enhancing the commercialization of MOFs. However, it is still a great challenge to control the synthesis of hierarchical porous MOFs, and there is limited knowledge of the influence of the synthesis parameters. Moreover, for the commercialization of MOFs, a template-free, easy, low-cost, reproducible and scalable synthesis procedure is necessary.

In conclusion, as the amount of micropores increases, a larger surface area will be achieved and there will be more active sites for adsorption while as the amount of mesopores increases, mass transport properties will be enhanced. Thus, combining the benefits of micro- and mesopores, hierarchical porous MOFs are promising candidates for a wide range of application and the commercialization of MOFs.

Chapter III

Effect of iron to benzene-1,4-dicarboxylic acid ratio on and synthesis temperature on the textural properties of hierarchical porous MIL-88Bs

In this chapter, a surfactant and template-free synthesis strategy to synthesize hierarchically porous MIL-88Bs is reported. The aggregated MIL-88B nanorods form textural mesoporosity whose size can be finely controlled by iron to benzene-1,4-dicarboxylic acid ratio (Fe:TPA) and synthesis temperature. For the first time in the literature, we report a detailed pore size distribution analysis and a mechanism that controls the size of textural pores by utilizing Fe:TPA ratio and synthesis temperature. Last but not least, by introducing hierarchical pores to the pore structure, a BET surface area (enhanced by 2.7 times), and total pore volume (enhanced by 4.1 times) that is higher than those of reported BET surface area, and total pore volume for MIL-88B are reported.

3.1. Background

Highly crystalline and porous metal-organic frameworks (MOFs) are firstly reported by Yaghi and his coworkers in 1995. These highly porous materials are formed by linking metal ion or metal ion clusters with an organic linker (O M Yaghi et al., 1995). Length and the functionality of the linkers determine pore size and structure (Rowsell & Yaghi, 2004a). MOFs significantly benefit and come to forefront with their easy synthesis routes, highly porous and crystalline structure, high surface area, tunable pore structure, and their ability to be loaded with other elements and components without any changes in their topology (Rowsell & Yaghi, 2004a). Depending on the starting materials, structure of MOFs varies, and pore size and shape can be easily tuned specific to the application area. This makes MOFs promising in various applications such as energy storage, adsorption and separation studies, catalysis, sensors, drug delivery and luminescence (Adams et al., 2010; Y. S. Bae & Snurr, 2011; Corma et al., 2010; García-García et al., 2016; Latroche, Surblé, Serre, Mellot-Draznieks, Llewellyn, Lee, Chang, Sung, et al., 2006a; Jeongyong Lee et al., 2009; J. R. Li

et al., 2009, 2011; Jiewei Liu et al., 2014; Rieth et al., 2017; Saha, Chandra, Garai, & Banerjee, 2012; Jung Soo Seo et al., 2000; Taylor-Pashow et al., 2010; T. Zhang & Lin, 2014).

Solvothermal synthesis follows the working principle of Lewis acid-base reactions at which metal salts and organic ligands are mixed in a solvent and heated in an oven at high temperatures. Metal ions act as Lewis acids and deprotonated ligands are considered as Lewis bases. Solvothermal reactions are conducted at high temperatures to form amines which will deprotonate carboxylic acids. Synthesis conditions possess significant role on the produced MOF structures which determine whether bulk precipitation or single crystals will be formed (D. Zhao, Timmons, Yuan, & Zhou, 2011b).

MOFs that are considered as open structures are microporous crystalline materials. The short diffusion pathway of mesopores extend the use of MOFs in various application areas. In the presence of mesopores, molecules can diffuse faster and reach to the storage site easier (Y. Yue, Fulvio, & Dai, 2015). Therefore, even though micropores contribute to the surface area, it is necessary to have mesopores in the pore structure as well as the micropores (Y. Yue, Fulvio, et al., 2015).

To synthesize MOFs that consist both micro- and mesopores several synthesis strategies: i) ligand extension; ii) template directing strategy have been investigated. However, the challenges that methods possess, limited their use. Apparently, ligand extension method caused MOFs that are synthesized from large ligands to collapse after the removal of guest molecules which decreases the pore size of MOFs (Reineke, Eddaoudi, Moler, O'Keeffe, & Yaghi, 2000; Omar M. Yaghi, Li, Davis, Richardson, & Groy, 1998; Y. Yue et al., 2014, 2013a; Y. Yue, Fulvio, et al., 2015). In the meanwhile, even though hierarchical porous MOF structures can be formed by the template directing strategy, the necessity to remove the template makes this strategy challenging (Y. Yue et al., 2014, 2013a; Y. Yue, Fulvio, et al., 2015). Therefore, several researches have been conducted to overcome the challenges of these methods. A template free synthesis strategy that creates hierarchical pores has been investigated by several studies (X. Liu et al., 2015; L. Peng et al., 2014a; Y. Yue et al., 2013a) and found to be a facile alternative to ligand extension method and template directing synthesis strategy that creates hierarchical pores.

In this study, MIL-88B type MOF crystallites were synthesized by a perturbation assisted nanofusion synthesis strategy and the effect of iron to benzene-1,4-dicarboxylic acid

ratio (Fe:TPA) on the morphology and the textural properties of MIL-88B type MOF crystallites were investigated. To the best of our knowledge there has been no report showing the effect of Fe:TPA ratio on the morphology and textural properties of MIL-88B type MOF crystallites. With the aim of filling the missing gap in the literature, we have investigated and imaged the changes in the morphology and textural properties of MIL-88B type MOF crystallites when these crystallites were synthesized with different Fe:TPA ratio, determined the effect of Fe:TPA ratio on textural porosity, pore size distribution, and percentage of textural mesoporosity quantitatively. Pore volumes were estimated by t-plot method, and NLDFT method and pore size distribution analysis was conducted by NLDFT method. Structural changes were shown by XRD and FTIR analysis and morphology of the synthesized MIL-88B type MOF crystallites were imaged by SEM.

In conclusion, MIL-88B type MOF crystallites were synthesized successfully by a perturbation assisted nanofusion synthesis strategy that forms hierarchical pores. It is found that Fe:TPA ratio has control over the morphology and the textural porosity of MIL-88B type MOF crystallites. A high Fe:TPA ratio causes interparticle voids to widen and fraction of textural mesopores to increase. By the perturbation assisted nanofusion synthesis strategy, a BET surface area and a total pore volume that is higher than those of reported MIL-88B is achieved. Once and for all, the perturbation assisted nanofusion synthesis strategy is a cost effective and facile alternative to synthesize MIL-88B type MOF crystallites that consist both micro- and mesopores within their pore structure with enhanced BET surface area (by 2.7 times) (C. Gao, Chen, Quan, Yu, & Zhang, 2017), and total pore volume (by 4.05 times) (C. Gao et al., 2017).

3.2. Experimental

Reproducibility of our method was tested by the repetitive synthesis and characterization analysis. Each hierarchical porous MIL-88B was synthesized for five times. The characterization analyses were repeated for five times. Average results of BET surface area, ultramicro-, micro-, uppermeso-, mesopore, and total pore volumes with calculated standard deviations were reported. The fractions of micro- and mesoporosity were estimated by the ratio of micro- and mesopore volume (NLDFT method) to total pore volume estimated by NLDFT method.

3.2.1. Materials

Chemicals were used as received, no further purification was required. Chemicals were purchased from Merck Millipore and Sigma Aldrich. As the metal source 98% pure, ACS Reagent grade, iron(III) chloride hexahydrate was used; 99.9% pure, HPLC grade, N, N-Dimethylformamide (DMF) was the main solvent used during the synthesis and 99.8% pure methanol was used during solvent exchange processes.

3.2.2. Synthesis of Hierarchical Porous MIL-88Bs

A template and surfactant-free synthesis strategy was used in the synthesis of hierarchical porous MIL-88Bs (Cao et al., 2016; Y. Yue et al., 2013a). An iron source ($FeCl_3.6H_2O$) (3.4 mmol) and benzene-1,4-dicarboxylic acid (TPA) were dissolved in 80 mL of *N, N*-dimethylformamide (DMF). Quantity of $FeCl_3.6H_2O$ and benzene-1,4-dicarboxylic acid used during the synthesis can be found in Table 1. Prepared solution was mixed vigorously via a magnetic stirrer with a stirring rate of 800 rpm for an hour at 25 °C and the solution was then distributed into glass vials. Glass vials were heated for 2 days in an isothermal oven. Then the mother liquor was poured into falcon tubes (50 mL). Solutions and the precipitates were firstly, washed with DMF (3 times) and then washed with methanol (3 times). At the end of each washing step, products were centrifuged and then washed again. Later the products were heated at 100 °C under vacuum for 30 hours. Figure 4 illustrates the synthesis procedure.

Table 1. Abbreviations for the hierarchical porous MIL-88Bs synthesized at different temperatures with different Fe:BDC ratio.

Hierarchical porous MIL-88Bs	Heating temperature (°C)	$FeCl_3.6H_2O$ (mmol)	Benzene-1,4-dicarboxylic acid (mmol)
MIL-88B-110-1	110	3.4	3.4
MIL-88B-110-3	110	3.4	1.13
MIL-88B-110-5	110	3.4	0.68
MIL-88B-130-1	130	3.4	3.4
MIL-88B-130-3	130	3.4	1.13
MIL-88B-130-5	130	3.4	0.68
MIL-88B-150-1	150	3.4	3.4
MIL-88B-150-3	150	3.4	1.13
MIL-88B-150-5	150	3.4	0.68

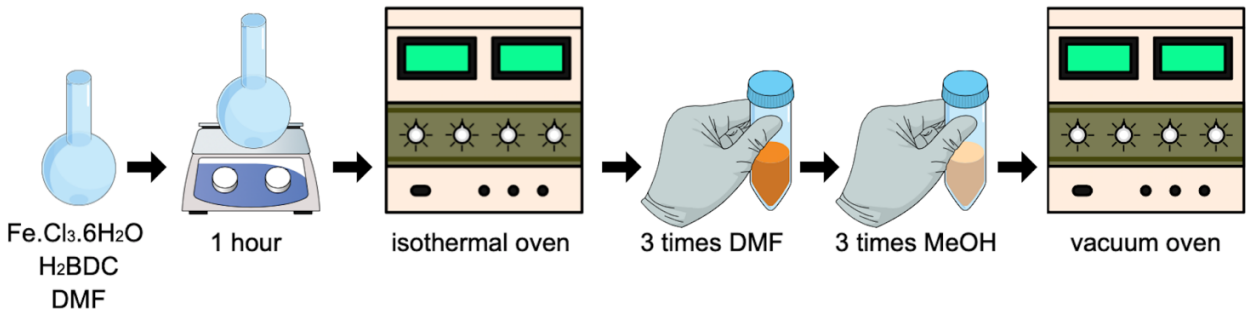

Figure 4. Schematic representation of experimental procedure.

3.2.2.1.Our approach

Different from the conventional crystallization process, a perturbation assisted nanofusion synthesis strategy was used in the synthesis of hierarchical porous MIL-88Bs. In a classic crystallization process a nuclei would form and then the unit-cell would replicate resulting in single crystal formation (Carné-Sánchez, Imaz, Stylianou, & Maspoch, 2014). However, different from the conventional crystallization process $FeCl_3.6H_2O$, TPA and DMF

were vigorously stirred which prevented the single crystal growth. From the coordination of $FeCl_3.6H_2O$ and TPA, secondary building units (SBUs) form which later aggregate into nanosized MIL-88B type MOF crystallites (Cao et al., 2016; McNamara & Hicks, 2015; S. Yuan et al., 2017; Y. Yue et al., 2014, 2013a; Y. Yue, Fulvio, et al., 2015; Y. Yue, Zhang, et al., 2015). Interparticle voids present in between the aggregated nanosized MIL-88B type MOF crystallites form the textural mesoporosity. Figure 5 is a schematic of conventional crystallization process and nanofusion process.

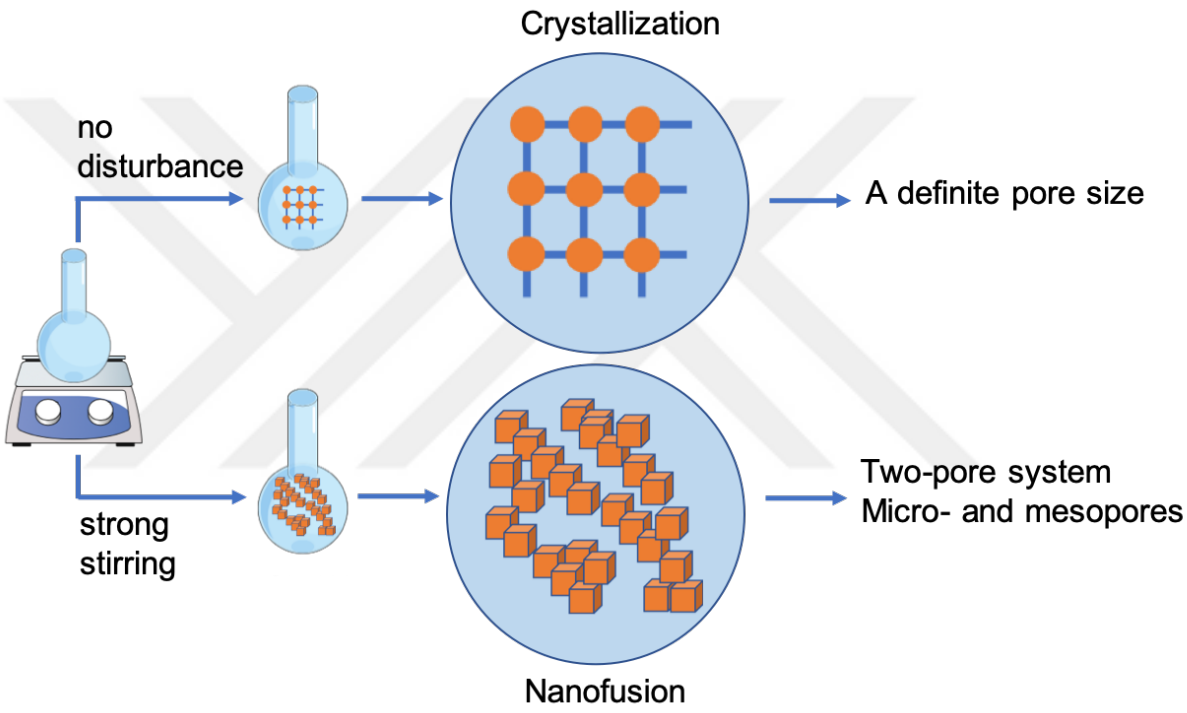

Figure 5. Schematic of conventional crystallization process and nanofusion

3.2.3. Characterization of Hierarchical Porous MIL-88Bs

N_2 sorption isotherms, pore size distribution analysis, powder x-ray diffraction (PXRD), thermogravimetric analysis (TGA), Fourier transform infrared spectroscopy (FTIR), and scanning electron microscopy (SEM) were used to characterize hierarchical porous MIL-88Bs. Gas sorption measurements were conducted by Intelligent Gravimetric Analyzer (IGA).

3.2.3.1.X-Ray diffraction

X-ray diffraction (XRD) analysis was performed at room temperature with a Bruker D8 Diffractometer (XRD Bruker AXS GmbH D8 Advance, Karlsruhe, Germany). Analysis was held with 0.15406 nm Cu Kα radiation. During the analysis X-ray generator voltage and current were set to 40 kV and 5 mA, respectively. A scan range of 2 to 90° in 2θ range was used while the step size was set to 0.02° and counter-time was adjusted to 2 seconds per step.

3.2.3.2.Scanning Electron Microscopy (SEM)

Leo Supra 35VP field emission scanning electron microscope was used for imaging. Voltage was kept constant in between 2 to 4 keV depending on the hierarchical porous MIL-88Bs and the analysis was conducted with secondary electron imaging technique.

3.2.3.3.Brunauer-Emmett-Teller (BET) surface area and pore size distribution analysis

Surface area and pore size distribution analysis were performed by Micromeritics 3Flex Instrument. N_2 adsorption isotherms were obtained at 77 K. Prior to each analysis, samples were degassed to remove the present impurities at 120 °C for 6 hours. For each analysis 0.10 to 0.20 grams of sample was used. Surface area and pore size distribution analysis were performed by measuring liquid N_2 adsorption capacity at 77 K with a relative pressure range of 0.05 to 1 which monolayer coverage is assumed to be complete. For the measurement of surface area, BET model at which the main assumption is surface area is associated with the monolayer capacity, was used.

3.2.3.4.Fourier Transform Infrared Spectroscopy (FT-IR) Analysis

FTIR analysis was conducted via Thermo Scientific Nicolet Is10 with a spectral resolution of 4 cm-1 over a wavelength range of 600 to 4000 cm-1. Scans were repeated for 32 times and spectrum were corrected for the background noise.

3.2.3.5.Thermogravimetric Analysis (TGA)

Hierarchical porous MIL-88Bs were thermally analysed by Shimadzu DTG-60H simultaneous thermal analysis TG-DTA equipment. Hierarchical porous MIL-88Bs were kept under a continuous flow of 20 mL/min N_2 gas. Heating rate was set to 10 K/min and TGA curves were obtained by heating the samples from 25 °C to 1200 °C under 20 mL/min continuous flow of N_2 gas.

3.3. Results and Discussion

3.3.1. XRD Analysis

XRD patterns of hierarchical porous MIL-88Bs can be found below in Figure 6-20.

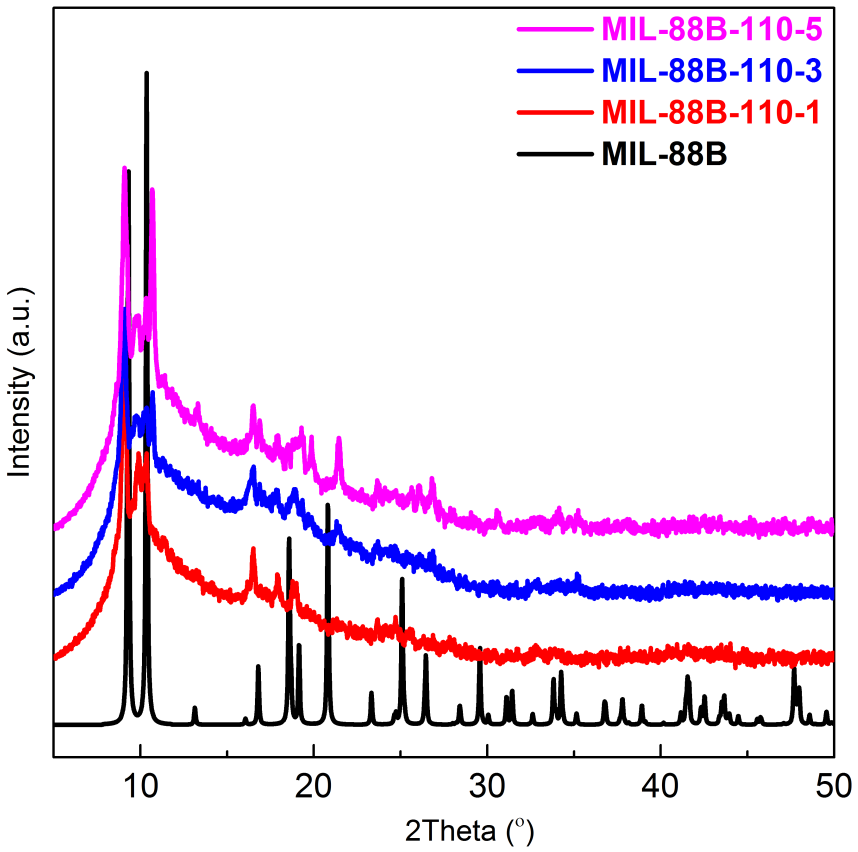

Figure 6. XRD patterns of the simulated MIL-88B, and the hierarchical porous MIL-88Bs synthesized at 110 °C.

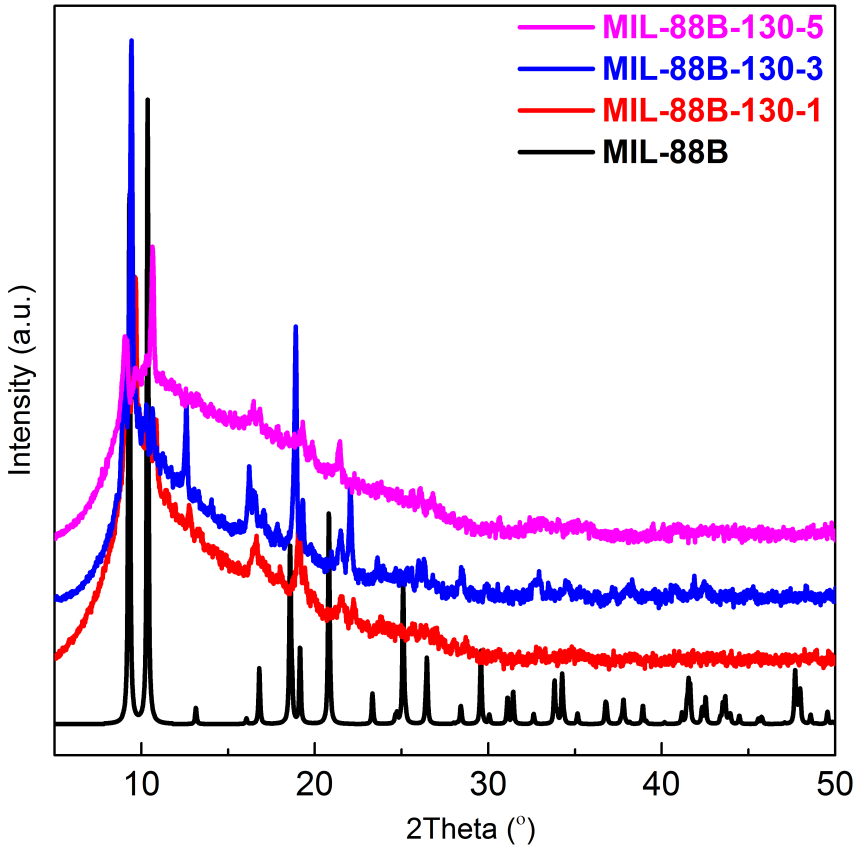

Figure 7. XRD patterns of the simulated MIL-88B, and the hierarchical porous MIL-88Bs synthesized at 130 °C.

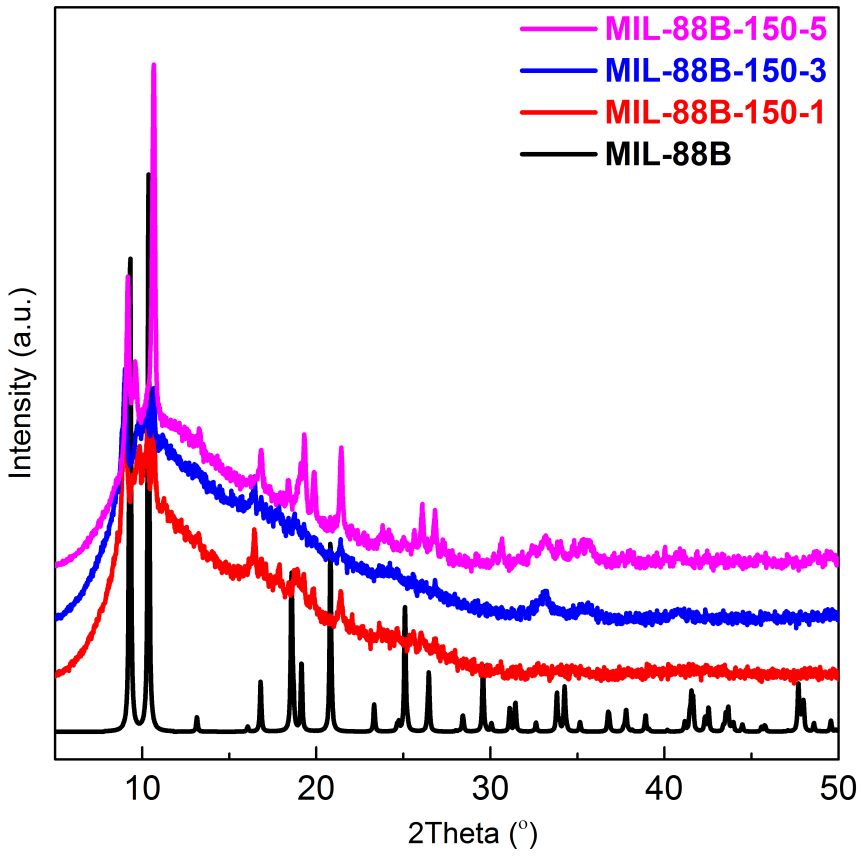

Figure 8. XRD patterns of the simulated MIL-88B, and the hierarchical porous MIL-88Bs synthesized at 150 °C.

3D crystal model of MIL-88B was simulated to obtain the powder XRD pattern of MIL-88B. XRD patterns of hierarchical porous MIL-88Bs synthesized via a perturbation assisted nanofusion strategy matched well with the XRD pattern of MIL-88B. Comparison of XRD patterns of the synthesized hierarchical porous MIL-88Bs and the XRD pattern of the simulated MIL-88B can be found below in Figure 9-20.

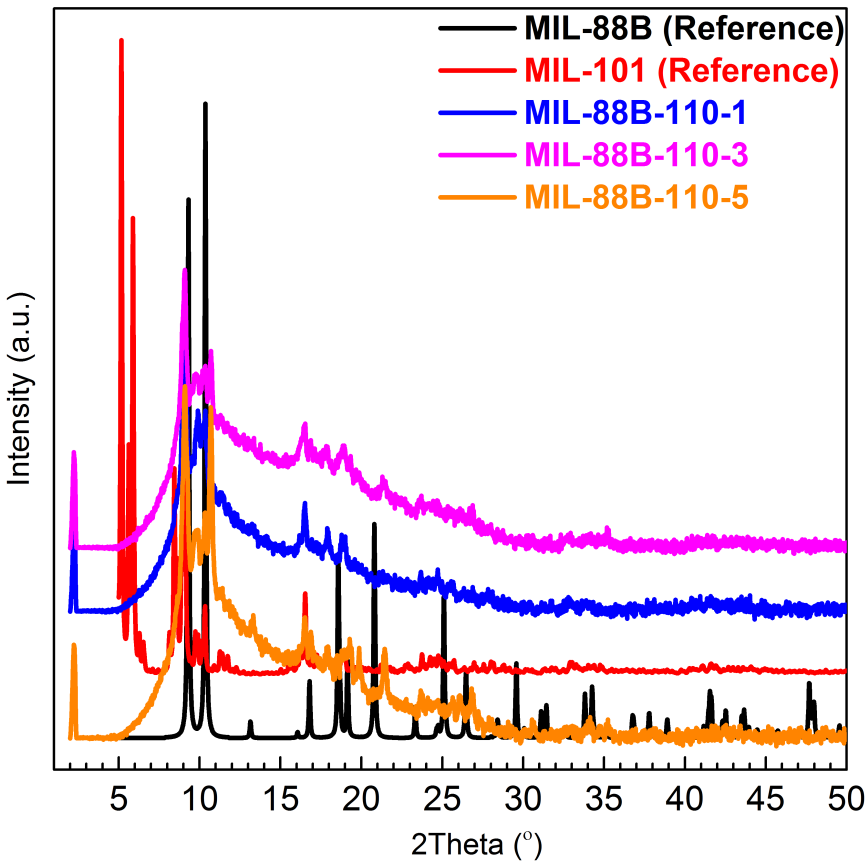

Figure 9. Comparison of XRD patterns of the simulated MIL-88B, MIL-101, and the hierarchical porous MIL-88Bs synthesized in this study.

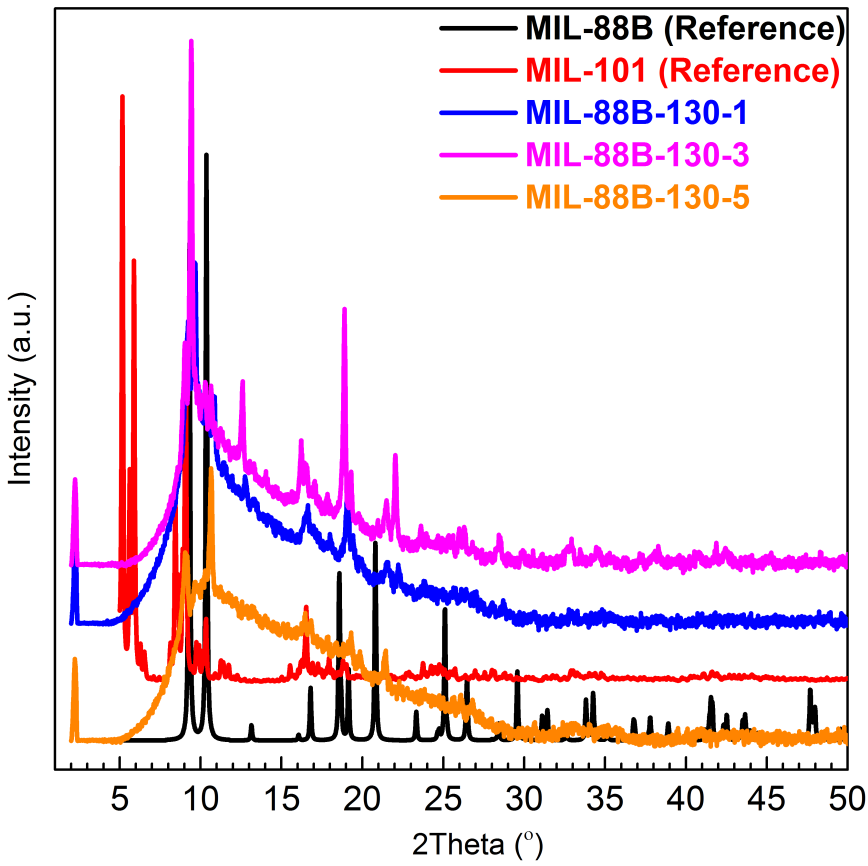

Figure 10. Comparison of XRD patterns of the simulated MIL-88B, MIL-101, and the hierarchical porous MIL-88Bs synthesized in this study.

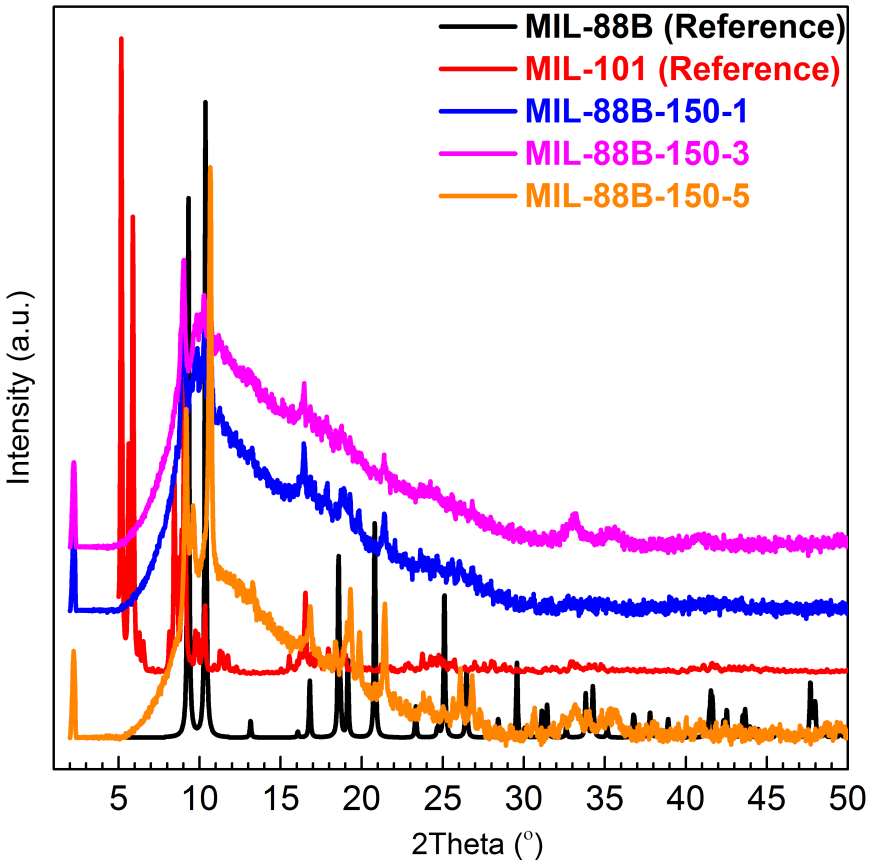

Figure 11. Comparison of XRD patterns of the simulated MIL-88B, MIL-101, and the hierarchical porous MIL-88Bs synthesized in this study.

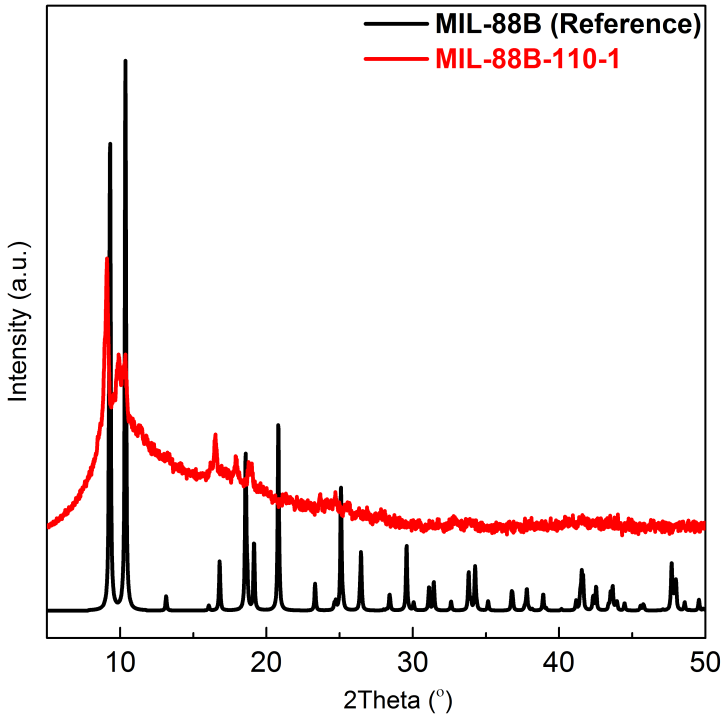

Figure 12. Comparison of XRD patterns of the simulated MIL-88B, and the hierarchical porous MIL-88B-110-1 synthesized in this study.

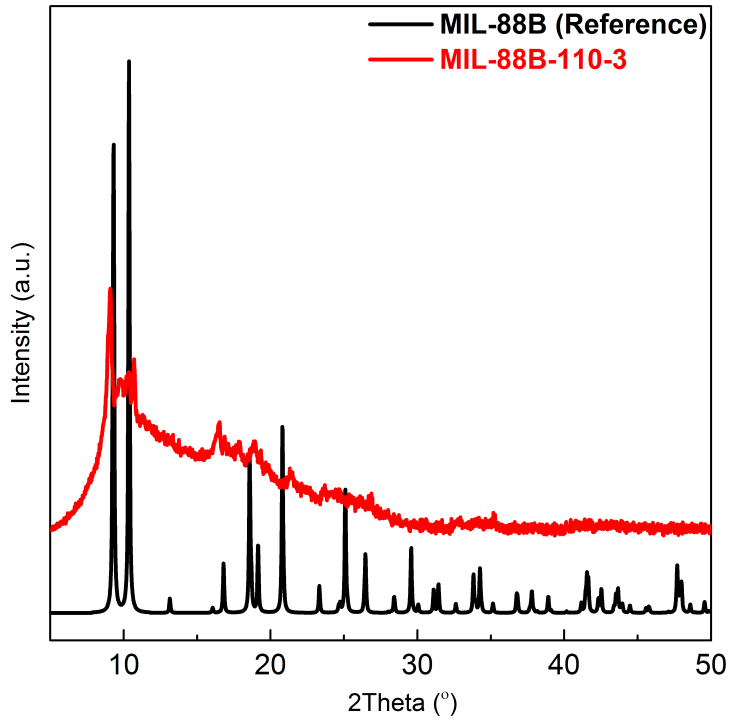

Figure 13. Comparison of XRD patterns of the simulated MIL-88B, and the hierarchical porous MIL-88B-110-3 synthesized in this study.

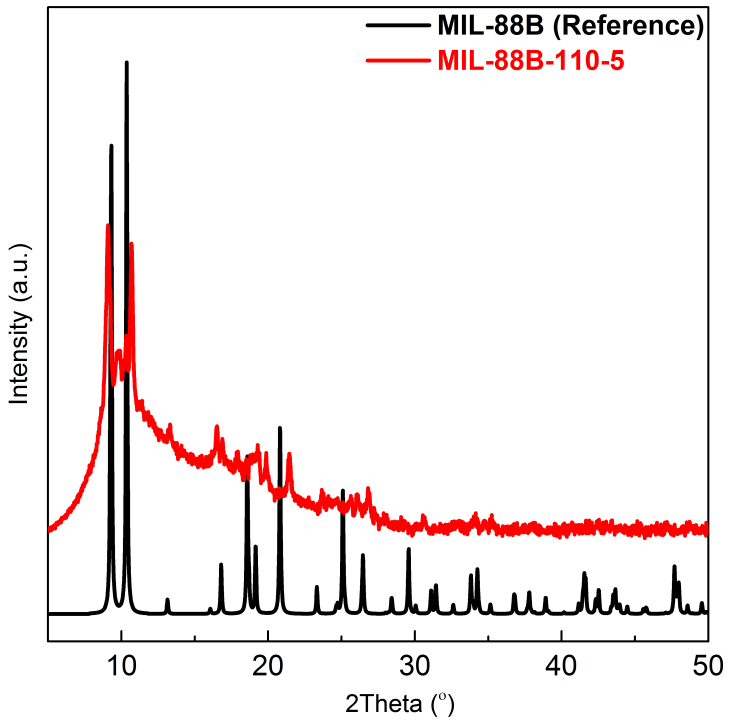

Figure 14. Comparison of XRD patterns of the simulated MIL-88B, and the hierarchical porous MIL-88B-110-5 synthesized in this study.

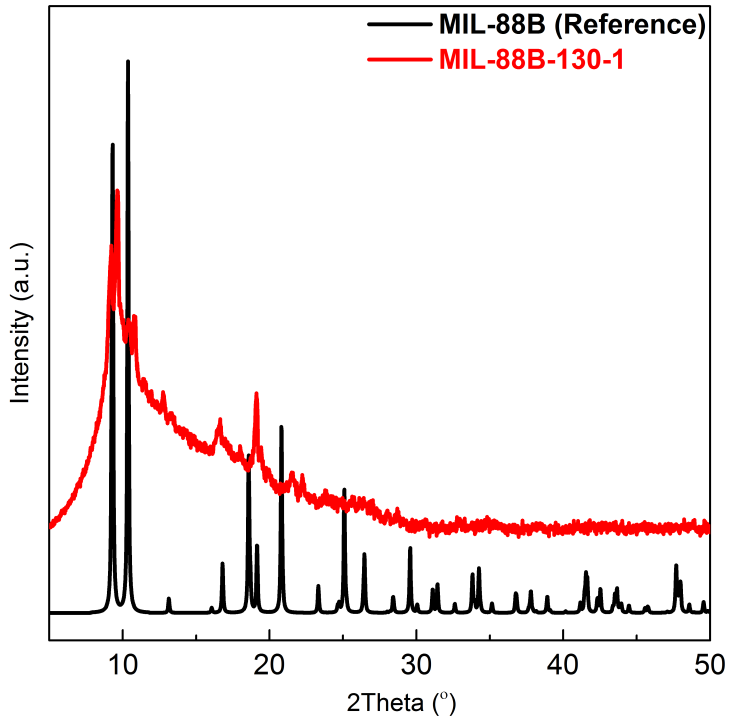

Figure 15. Comparison of XRD patterns of the simulated MIL-88B, and the hierarchical porous MIL-88B-130-1 synthesized in this study.

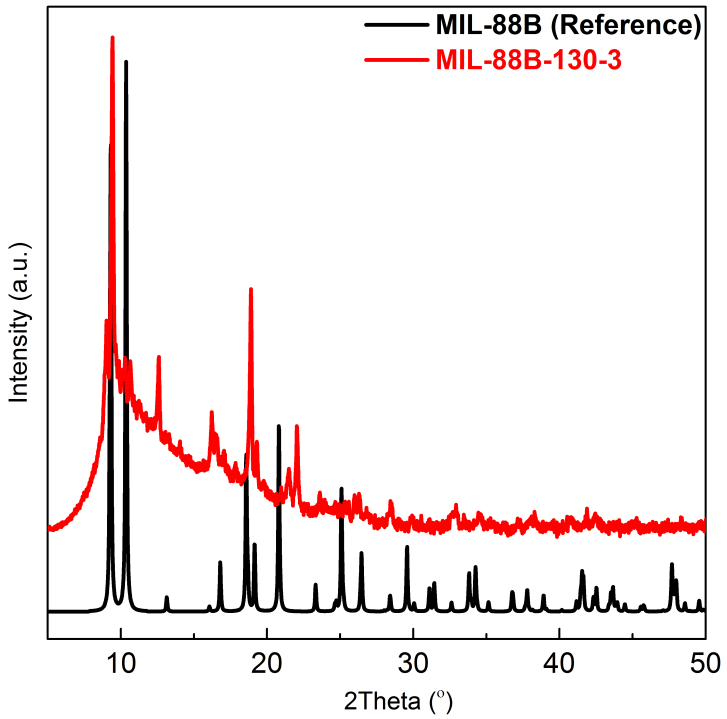

Figure 16. Comparison of XRD patterns of the simulated MIL-88B, and the hierarchical porous MIL-88B-130-3 synthesized in this study.

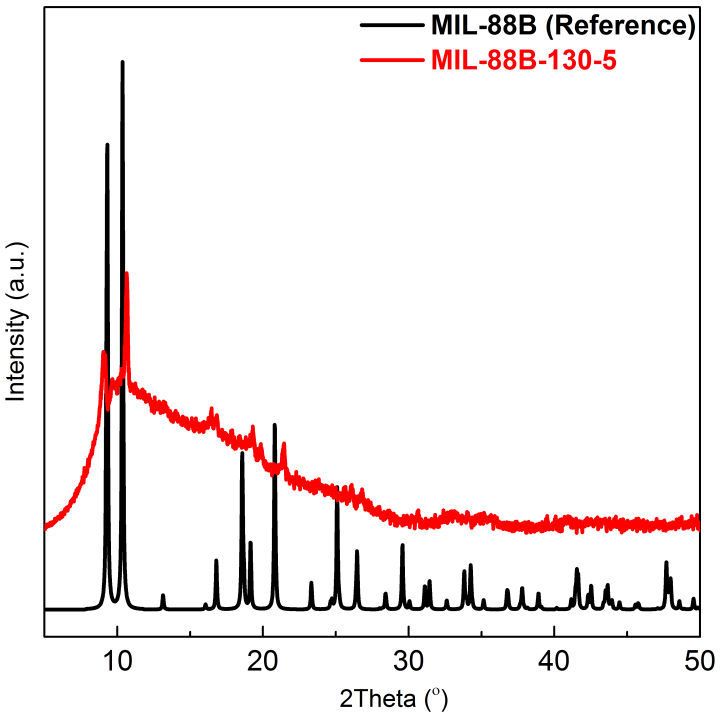

Figure 17. Comparison of XRD patterns of the simulated MIL-88B, and the hierarchical porous MIL-88B-130-5 synthesized in this study.

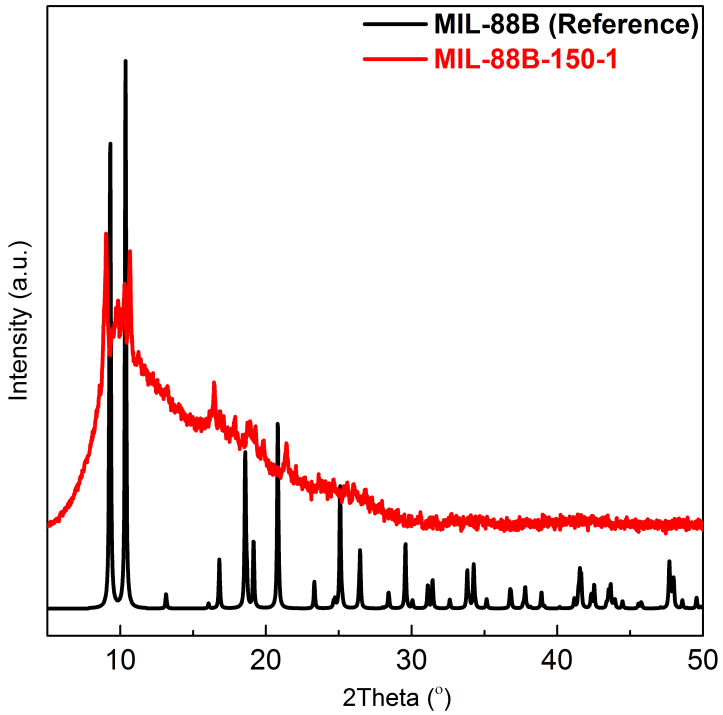

Figure 18. Comparison of XRD patterns of the simulated MIL-88B, and the hierarchical porous MIL-88B-150-1 synthesized in this study.

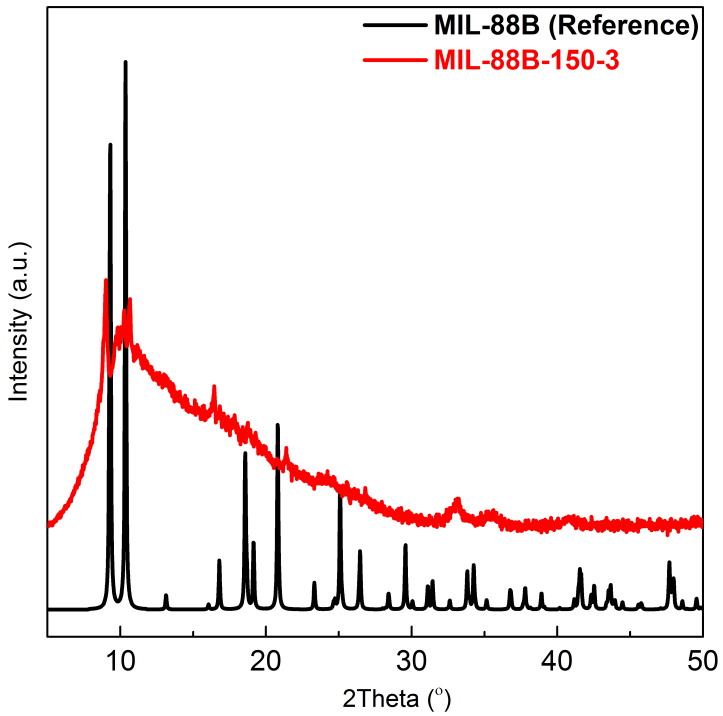

Figure 19. Comparison of XRD patterns of the simulated MIL-88B, and the hierarchical porous MIL-88B-150-3 synthesized in this study.

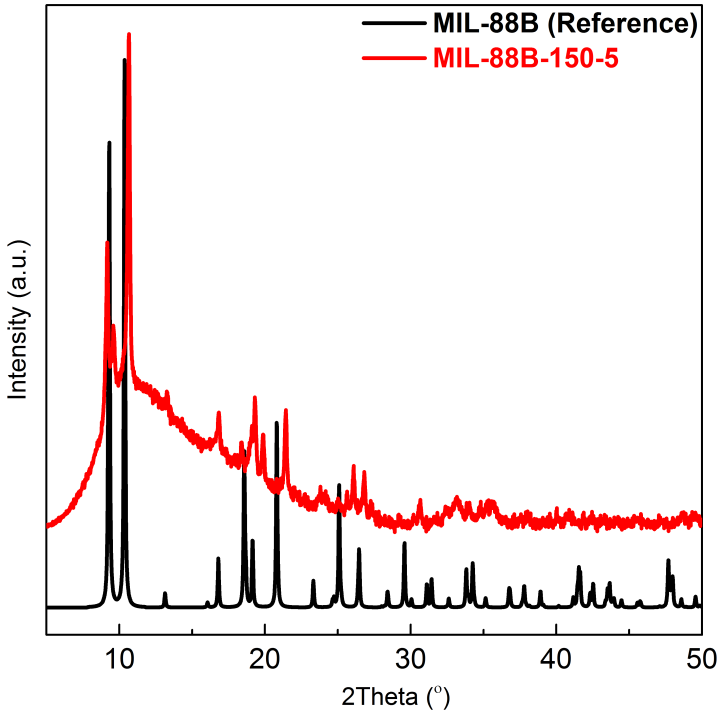

Figure 20. Comparison of XRD patterns of the simulated MIL-88B, and the hierarchical porous MIL-88B-150-5 synthesized in this study.

The well matched XRD patterns of hierarchical porous MIL-88Bs synthesized by the perturbation assisted nanofusion synthesis strategy and XRD pattern of the simulated MIL-88B confirm that by the perturbation assisted nanofusion synthesis strategy MIL-88B type MOF crystallites with hierarchical pores were synthesized successfully.

XRD patterns of hierarchical porous MIL-88Bs do not possess sharp peaks. Rather than sharp peaks, broadened Bragg peaks are observed. The perturbation assisted nanofusion synthesis strategy avoided the single crystal growth. Vigorous stirring of $FeCl_3.6H_2O$, TPA and DMF formed SBUs which later aggregated into nanosized MIL-88B type MOF crystallites. Broadening observed in Bragg peaks are attributed to the presence of nanosized MIL-88B rods which were embedded in an amorphous matrix (Cao et al., 2016).

A remarkable broadening was observed in the Bragg peaks of hierarchical porous MIL-88Bs synthesized with an Fe:TPA ratio of 5. This broadening is attributed to excess amount of iron salt present in the solution. By vigorously stirring $FeCl_3.6H_2O$, TPA and DMF, SBUs were formed. Presence of excess amount of iron salt cause more iron oxide clusters to form which compete for TPA.

Hierarchically porous MIL-88Bs are formed by the aggregation of nanosized MIL-88B rods. Using a high Fe:TPA ratio cause more iron clusters to form which results in widened interparticle voids (textural mesopores). We have attributed the broadened Bragg peaks of hierarchically porous MIL-88Bs synthesized with an Fe:TPA ratio of 5 to the excess amount of iron salt present in the solution which causes more iron clusters to form and result in widened textural mesopores.

Moreover, single crystal X-ray crystallography analyses were conducted with a Bruker APEXII Quazar Diffractometer. Analyses showed that micro-sized single crystals were not formed and there were no metallic-iron present.

3.3.2. SEM Analysis

SEM images of hierarchically porous MIL-88Bs can be found below in Figure 21-23. It is found that Fe:TPA ratio has control over the morphology of the hierarchically porous MIL-88Bs. Hierarchically porous MIL-88Bs are formed by the agglomeration of nanosized MIL-88B rods. The vigorous stirring of $FeCl_3.6H_2O$, TPA, and DMF formed nanosized MIL-88B rods. The amorphous matrix is formed by the Fe TPA coordination. SEM images clearly show the aggregated nanosized MIL-88Bs and the textural mesopores formed in between the aggregated particles.

As Fe:TPA ratio increases, higher number of iron oxide clusters form which aggregate into MIL-88B nanorods, and the interparticle voids (textural pores) widen. Particularly, interparticle voids created by the agglomeration of the MIL-88B nanorods are wider in H-150-5 which is attributed to the excess amount of iron salt present in the solution. Iron oxide clusters form just before the formation of SBUs and cause widened textural mesopores to form.

Figure 21 shows the SEM images of MIL-88B-110-1, MIL-88B-110-3, and MIL-88B-110-5. Figure 22 illustrates the SEM images of MIL-88B-130-1, MIL-88B-130-3, and MIL-88B-130-5 and figure 23 represents the SEM images of MIL-88B-150-1, MIL-88B-150-3, and MIL-88B-150-5.

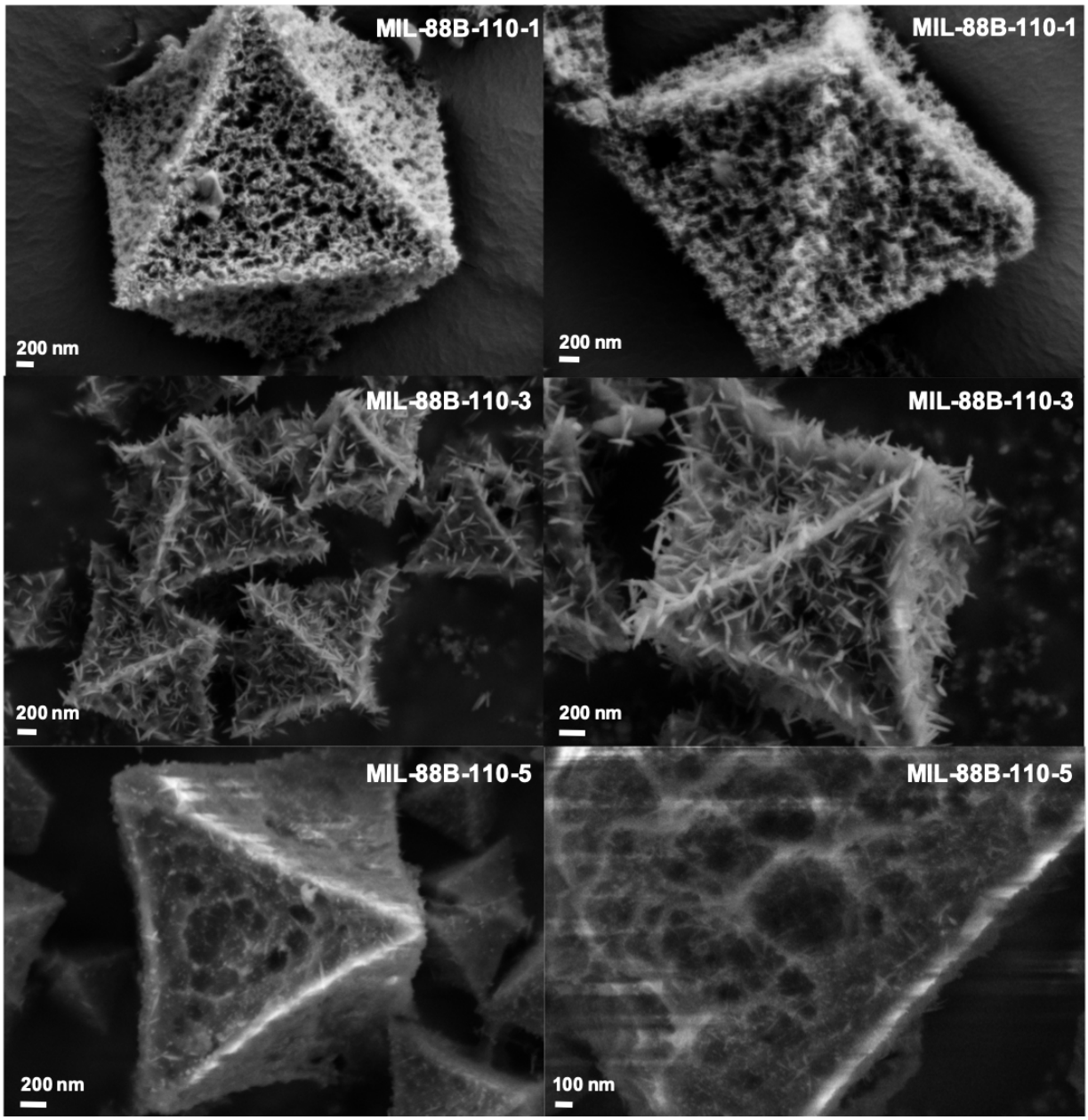

Figure 21. SEM images of MIL-88B-110-1, MIL-88B-110-3, and MIL-88B-110-5.

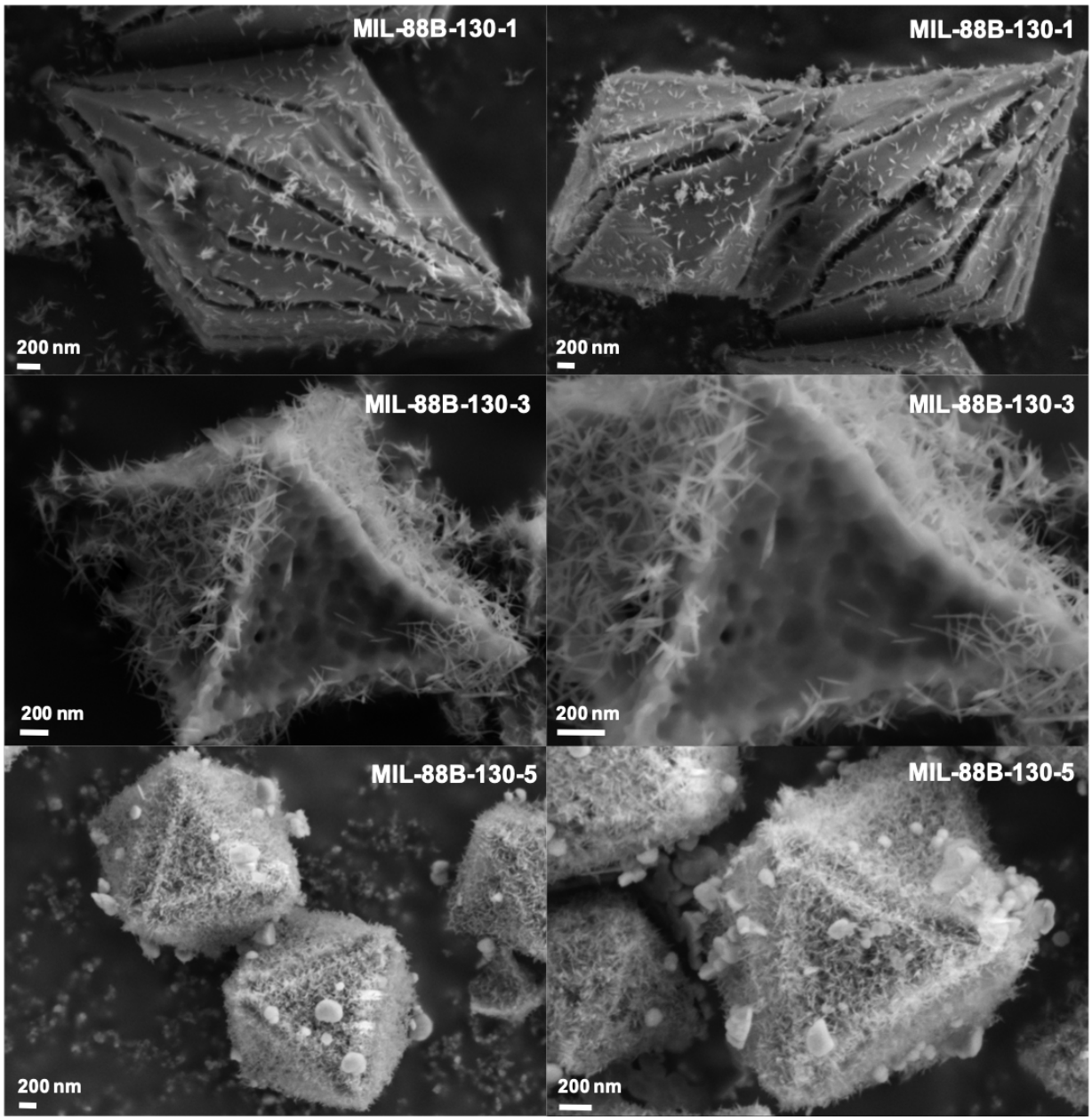

Figure 22. SEM images of MIL-88B-130-1, MIL-88B-130-3, and MIL-88B-130-5.

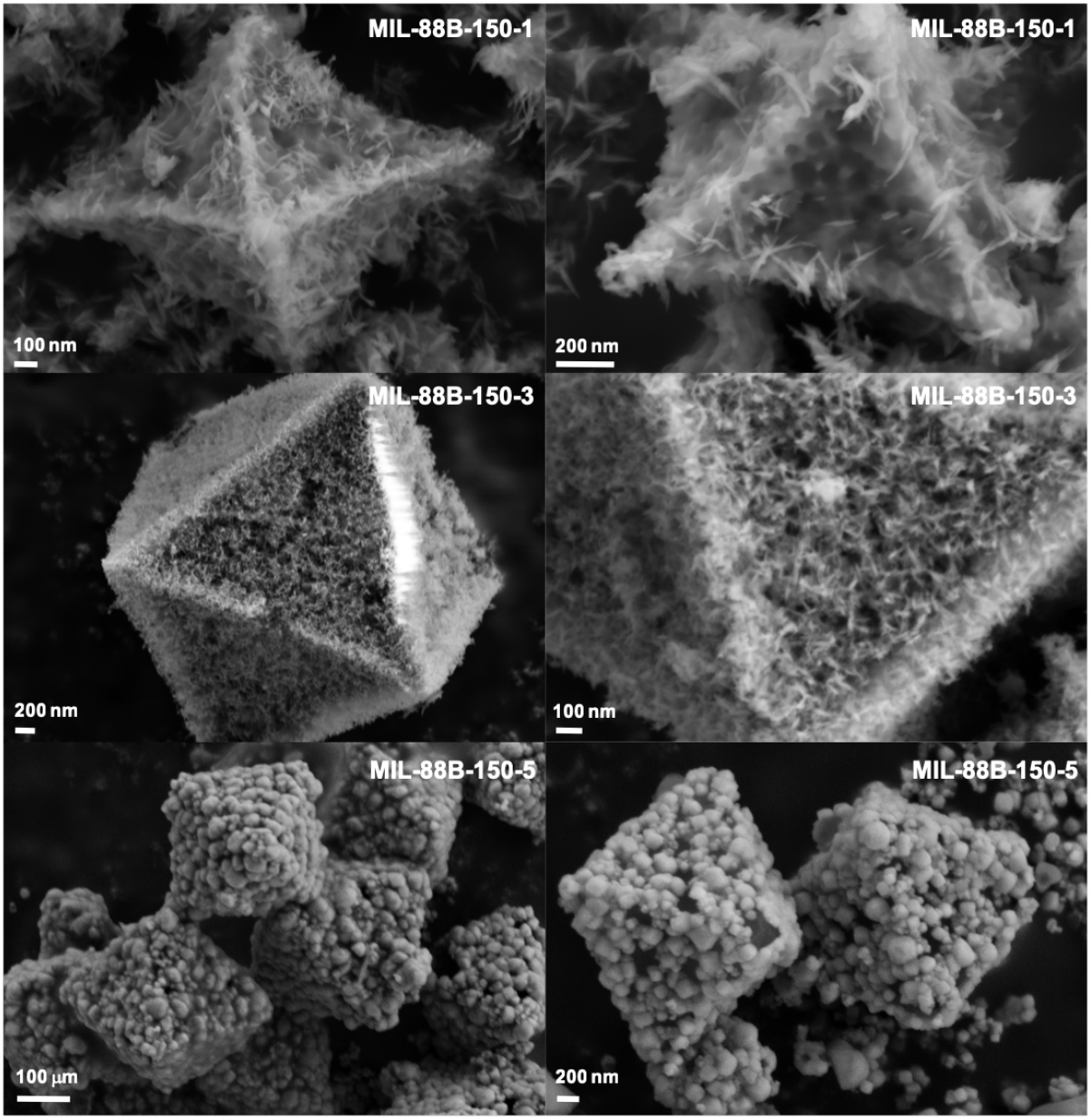

Figure 23. SEM images of MIL-88B-150-1, MIL-88B-150-3, and MIL-88B-150-5.

SEM images show the amorphous matrix at which nanosized MIL-88B nanorods were embedded in and the interparticle voids (textural mesopores) created in between the aggregated nanosized MIL-88Bs.

As Fe:TPA ratio increases, more iron clusters form which aggregates into nanosized MIL-88B rods, and the interparticle voids (textural pores) widen. Particularly, interparticle voids created by the agglomeration of nanosized MIL-88B rods are wider in MIL-88B-150-5 which is attributed to the excess amount of iron salt present in the solution. Iron oxide

clusters form just before the formation of SBUs and cause widened textural mesopores to form.

3.3.3. N_2 Sorption Isotherms

BET surface area estimations are made by the N_2 sorption analysis conducted at 77 K within the relative pressure range of 0.05 to 0.2. IUPAC classification of physisorption isotherms were used to classify the N_2 sorption isotherms (Thommes et al., 2015). N_2 sorption isotherms of hierarchically porous MIL-88Bs synthesized at different temperatures with different Fe:TPA ratio are shown below in Figure 24.

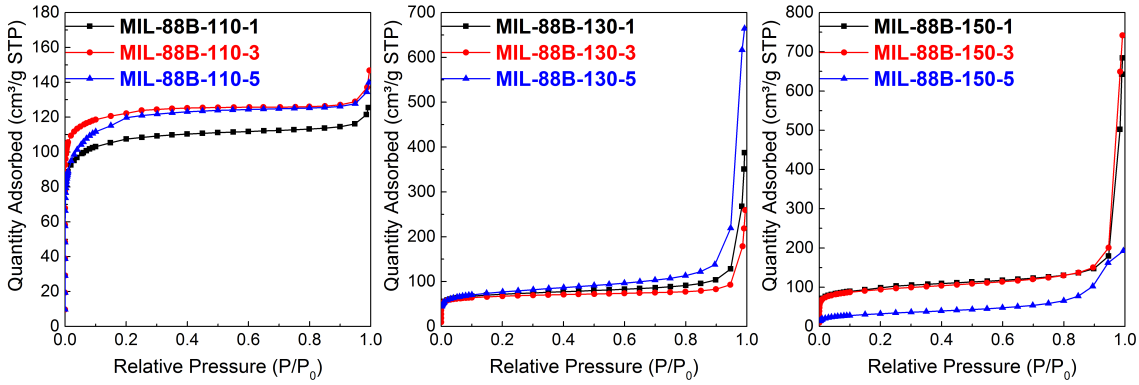

Figure 24. N_2 sorption isotherms of hierarchically porous MIL-88Bs.

Hierarchically porous MIL-88Bs synthesized at different temperatures with different Fe:TPA ratio show differences in their N_2 sorption behaviors. For a better analysis, we have divided the isotherm into following regions: (i) $P/P_0 < 0.2$, (ii) $0.2 < P/P_0 < 0.9$, and (iii) $0.9 < P/P_0 < 1$.

N_2 sorption isotherms of hierarchically porous MIL-88Bs synthesized at 110 °C with Fe:TPA ratio of 1, 3, and 5 represents typical features of IUPAC type I isotherms with some mesoporosity present. Figure 25 illustrates the N_2 sorption isotherms of MIL-88B-110-1, MIL-88B-110-3, and MIL-88B-110-5.

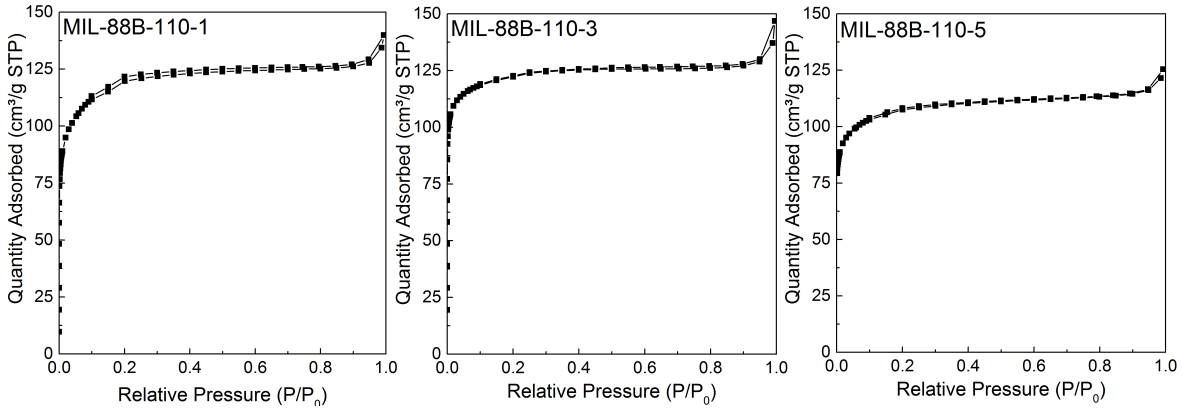

Figure 25. N_2 sorption isotherms of MIL-88B-110-1, MIL-88-110-3, and MIL-88B-110-5.

N_2 sorption isotherms of hierarchically porous MIL-88Bs synthesized at 110 °C with an Fe:TPA ratio of 1, 3, and 5 differ from each other by their knee shapes, initial point of plateau, and amount of N_2 uptake at low relative pressures. At low relative pressures (i) $P/P_0 < 0.1$, N_2 uptake has a sharp increase which is a consequence of micropore filling. The sharpest increase is observed in MIL-88B-110-3, while MIL-88B-110-5 shows the lowest one. This steeper uptake is attributed to presence of narrower micropores. At region (ii) where relative pressure ranges between 0.2 and 0.9, isotherms become almost flat. Particularly, MIL-88B-110-3, has a flat horizontal plateau which confirms that micropores are completely filled and further N_2 uptake becomes limited. The isotherms of MIL-88B-110-1, and MIL-88B-110-5 still possess a relatively small slope within the region (ii) which is associated with mesopore filling. At region (iii) where relative pressure is close to saturation pressure, rise observed in N_2 uptake is attributed to presence of mesopores. Figure 26 shows the N_2 sorption isotherms of MIL-88B-130-1, MIL-88B-130-3, and MIL-88B-130-5.

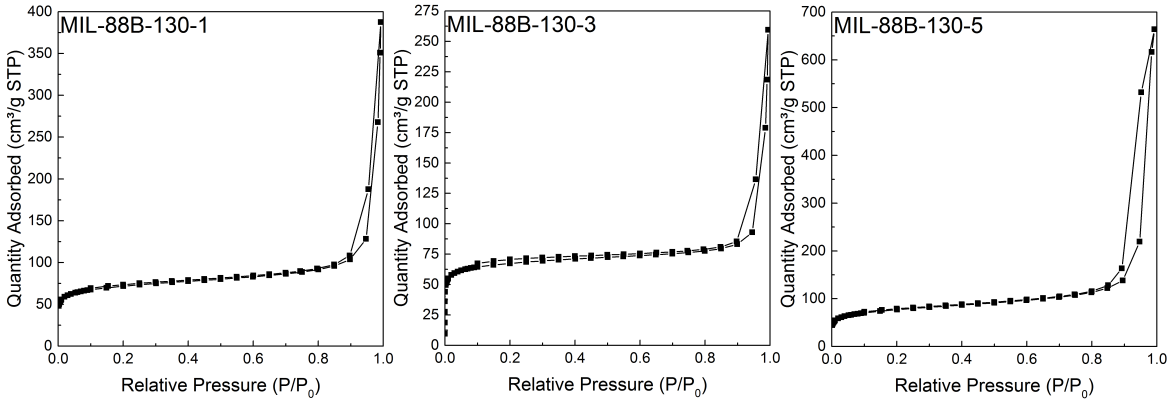

Figure 26. N_2 sorption isotherms of MIL-88B-130-1, MIL-88-130-3, and MIL-88B-130-5.

At low relative pressures, hierarchically porous MIL-88Bs synthesized at 130 °C possess sharp N_2 uptakes indicating the presence of micropores. MIL-88B-130-3 shows the steepest N_2 uptake which indicates the enhanced adsorbate-adsorbent interactions. At region (ii) N_2 sorption isotherm of MIL-88B-130-3 possesses a horizontal plateau which is neither observed in MIL-88B-130-1 nor observed in MIL-88B-130-5. Amount of N_2 uptake increases with increasing relative pressure which is a consequence of mesopore filling. At region (iii) steep increase observed in N_2 uptake is thought to be associated with interparticle capillary condensation. MIL-88B type MOF crystallites synthesized at 130 °C with Fe:TPA ratio of 1, 3, and 5 represents the major characteristics of IUPAC type IV isotherms with some micropores present. N_2 sorption isotherms of MIL-88B-150-1, MIL-88B-150-3, and MIL-88B-150-5 can be found in Figure 27.

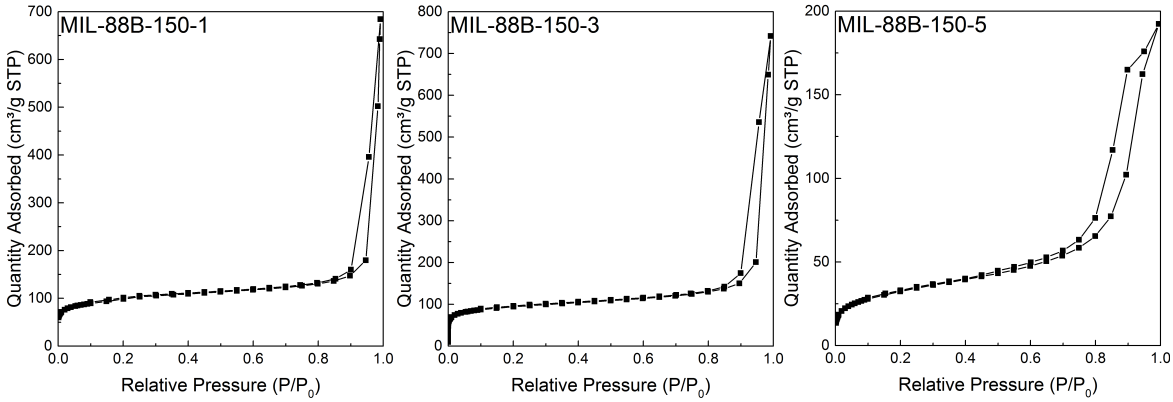

Figure 27. N_2 sorption isotherms of MIL-88B-150-1, MIL-88-150-3, and MIL-88B-150-5.

N_2 sorption isotherms of MIL-88B-150-1, MIL-88B-150-3, and MIL-88B-150-5 show the major characteristics of IUPAC type IV isotherms with some microporosity present. MIL-88B-150-1 and MIL-88B-150-3 have considerably higher N_2 uptakes at region

(i). These high nitrogen uptake capacities are associated with micropore filling suggesting the presence of micropores within the pore structure. At region (ii) N_2 sorption isotherms of hierarchically porous MIL-88Bs synthesized with an Fe to TPA ratio of 1, 3, and 5 become nearly flat. However, a true horizontal plateau cannot be achieved. As relative pressure increases, a slope is observed which is associated with mesopore filling. At region (iii) a drastic increase in the amount of N_2 adsorbed is observed in the N_2 sorption isotherms of MIL-88B-150-1, and MIL-88B-150-3. This drastic increase at region (iii) is associated with interparticle capillary condensation and thereby confirms the presence of mesopores that possess sizes at the upper mesopore size range. The N_2 sorption isotherm of MIL-88B-150-5 is very typical of mesoporous materials. At low pressures, monolayer-multilayer adsorption is observed. Then a plateau is achieved. This plateau is a consequence of limiting N_2 uptake over a broad range of high relative pressure. At relative pressures lower than 0.6, a linear trend in N_2 sorption isotherm is observed. A very significant hysteresis loop, which is associated with pore condensation, is observed as relative pressure increases from 0.4 to 1. Finally, a true horizontal plateau is achieved.

3.3.4. t-plot Method

t-plot given below (Figure 28-31) belongs to hierarchically porous MIL-88Bs synthesized at 110, 130, and 150 °C with different Fe:TPA ratio and represents the volume of N_2 adsorbed with various statistical thickness.

Table 2. Micropore volume, slope, y-intercept, and correlation coefficient estimated by t-plot method.

MOF	Micropore Volume (cm^3/g)	Slope ($cm^3/g.nm$)[a]	Y intercept ($cm^3/g.nm$)[a]	Correlation Coefficient
MIL-88B-110-1	0.13±1.4E-2	58.2±3.9	81.6±1.8	0.991
MIL-88B-110-3	0.15±3.4E-2	54.9±2.0	98.2±8.0E-1	0.997
MIL-88B-110-5	0.114±3.2E-2	101.6±7.5	74.1±3.0	0.989
MIL-88B-130-1	0.069±1.9E-2	61.6±2.1	44.7±8.4E-1	0.998
MIL-88B-130-3	0.076±1.7E-2	42.0±1.6	48.98±6.4E-1	0.997
MIL-88B-130-5	0.055±1.7E-2	94.3±2.5	35.6±1.0	0.999
MIL-88B-150-1	0.063±1.7E-2	131.8±1.8	40.9±7.0E-1	0.999
MIL-88B-150-3	0.077±1.7E-2	101.5±2.5	49.5±1.0	0.999
MIL-88B-150-5	0.0054±1.0E-3	13.0±6.3E-1	3.5±2.5E-1	0.995

[a] At standard temperature and pressure (STP)

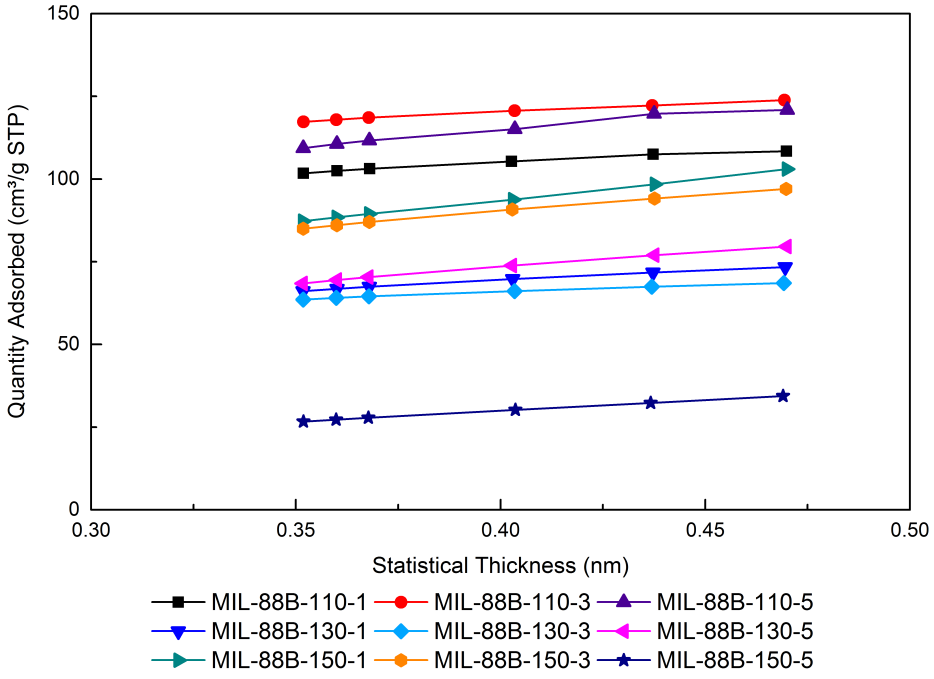

Figure 28. t-plots of hierarchically porous MIL-88Bs.

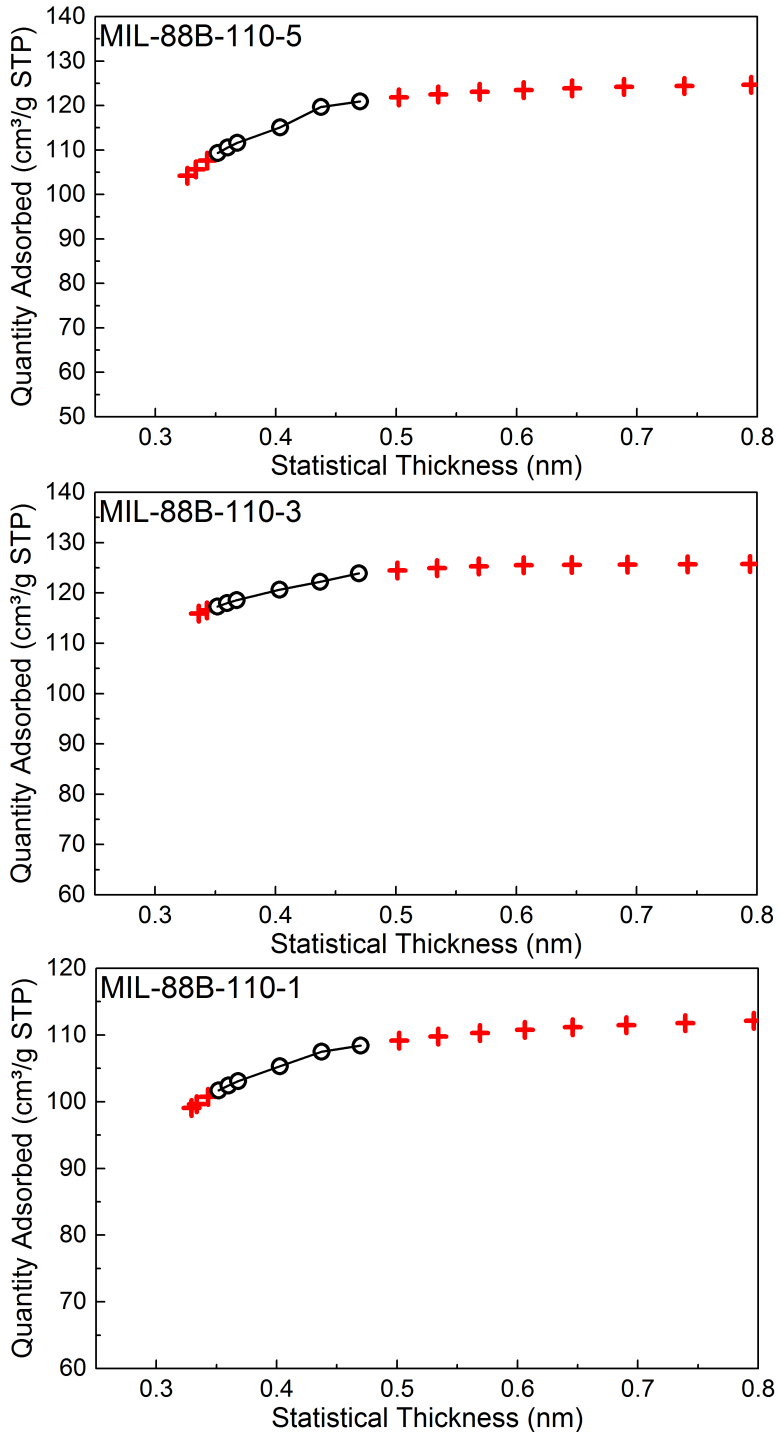

Figure 29. t-plots of MIL-88B-110-1, MIL-88B-110-3, and MIL-88B-110-5.

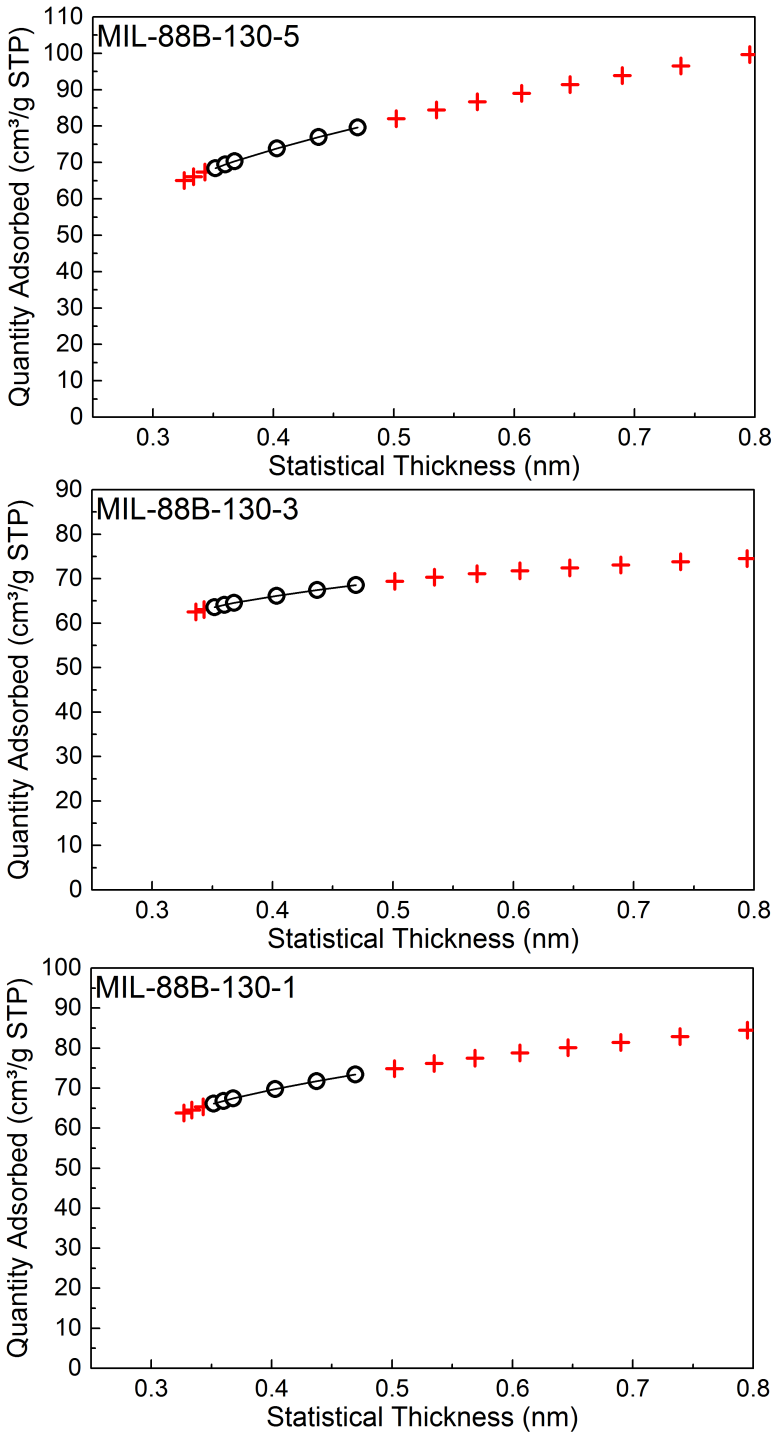

Figure 30. t-plots of MIL-88B-130-1, MIL-88B-130-3, and MIL-88B-130-5.

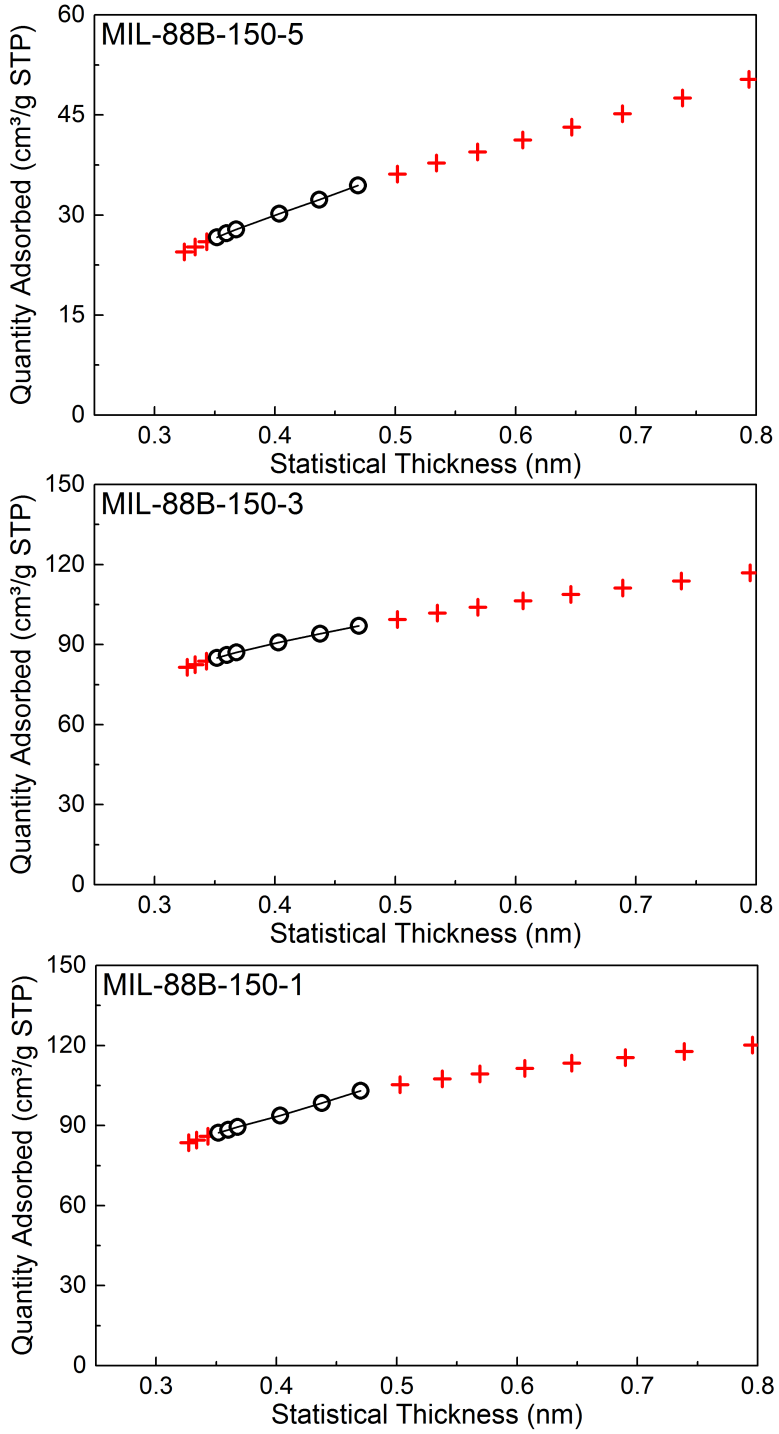

Figure 31. t-plots of MIL-88B-150-1, MIL-88B-150-3, and MIL-88B-150-5.

t-plots show significant differences in the micropore volumes of hierarchically porous MIL-88Bs synthesized at different temperatures with different Fe:TPA ratios. Hierarchically porous MIL-88Bs possess t-plots with positive intercepts which suggest that

micropores are present in the pore structure of these hierarchically porous MIL-88Bs. Dots deviate from the linear regime in the t-plots of hierarchically porous MIL-88Bs synthesized with an Fe:TPA ratio of 1, and 5 while t-plots of MIL-88B type MOF crystallites synthesized with an Fe:TPA ratio of 3 show a linear regime indicating that hierarchically porous MIL-88Bs synthesized with an Fe:TPA ratio of 3 are dominantly formed of micropores.

t-plots of hierarchically porous MIL-88Bs synthesized with an Fe:TPA ratio of 1, and 5 are formed of two linear parts which prove that mesopores are present as well as micropores. Intercept of hierarchically porous MIL-88Bs synthesized with an Fe:TPA ratio of 3 is significantly higher than the intercept of hierarchically porous MIL-88Bs synthesized with an Fe:TPA ratio of 1 and 5 indicating that hierarchically porous MIL-88Bs synthesized with an Fe:TPA ratio of 3 possess the highest micropore volume among the hierarchically porous MIL-88Bs synthesized with an Fe:TPA ratio of 1, 3, and 5. It is shown that textural mesoporosity increased drastically when the amount of linker used decreased.

3.3.5. NLDFT Method

NLDFT method has a better description of the thermodynamics of the confined fluid and thereby, has the highest precision in pore size estimations (Lowell et al., 2004a). NLDFT plots of hierarchically porous MIL-88Bs show several increases within micro- and mesoporous region. In addition to the wide mesopores observed at 44.8 nm, some narrow mesopores are also tracked. Figure 32 and 33 illustrate the NLDFT plot of hierarchically porous MIL-88Bs synthesized at 110 °C.

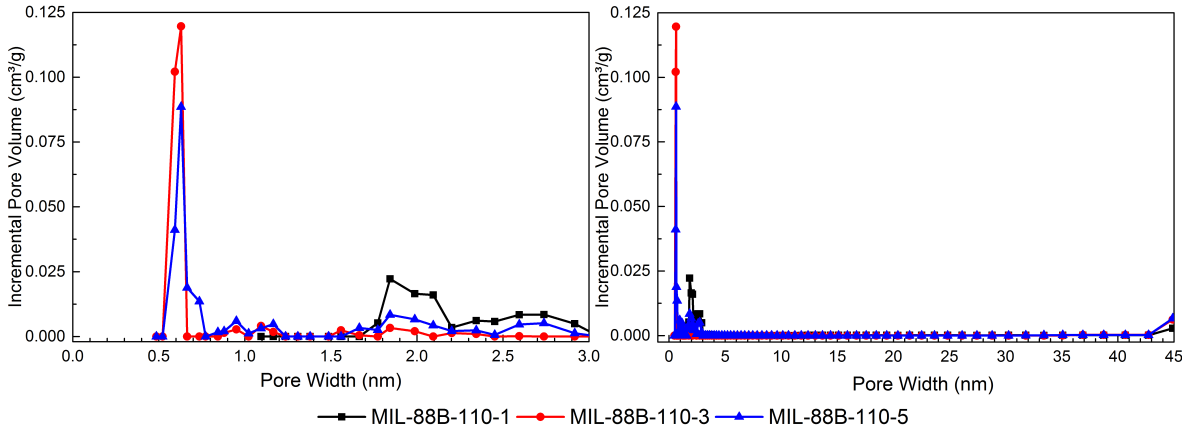

Figure 32. NLDFT plot of hierarchically porous MIL-88Bs synthesized at 110 °C.

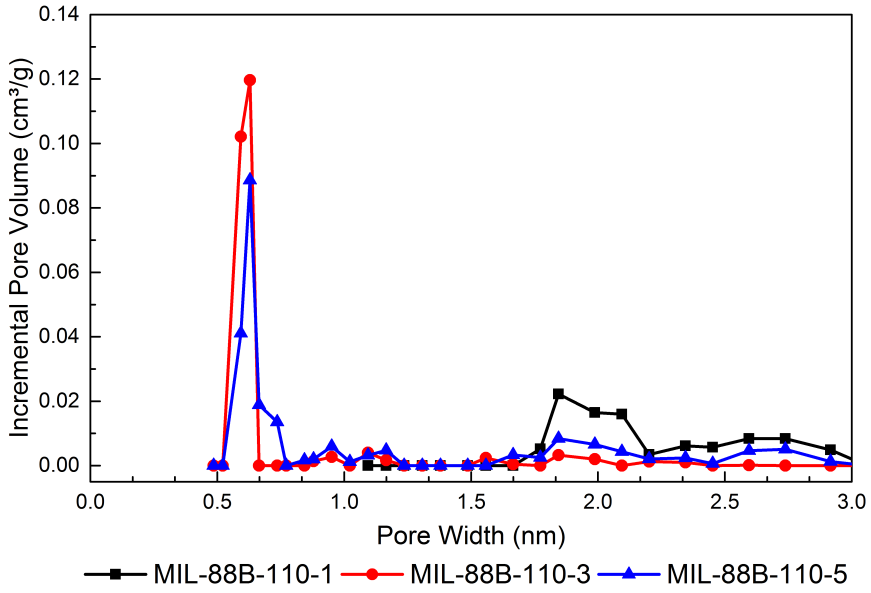

Figure 33. NLDFT plot of MIL-88B-110-1, MIL-88B-110-3, and MIL-88B-110-5.

NLDFT plots of hierarchically porous MIL-88Bs synthesized at 110 °C show sharp increases in microporous region while the increase in mesoporous region remains insignificant. The highest volume increase in microporous region is observed in MIL-88B-110-3 at which micropores contribute significantly to the total pore volume (96.1%). Total pore volume of MIL-88B-110-1 is measured to be 0.199 cm^3 in which micropores occupy 0.182 cm^3/g of volume. Identical to MIL-88B-110-3, MIL-88B-110-5 has no pores narrower than 0.593 nm. Micropores present in MIL-88B-110-5 occupy a volume of 0.202 cm^3/g which corresponds to 87.8% of the total pore volume while micropores of MIL-88B-110-3

possess 0.24 cm^3/g of volume that corresponds to 96.1% of the total pore volume. Figure 34 and 35 show the NLDFT plot of hierarchically porous MIL-88Bs synthesized at 130 °C.

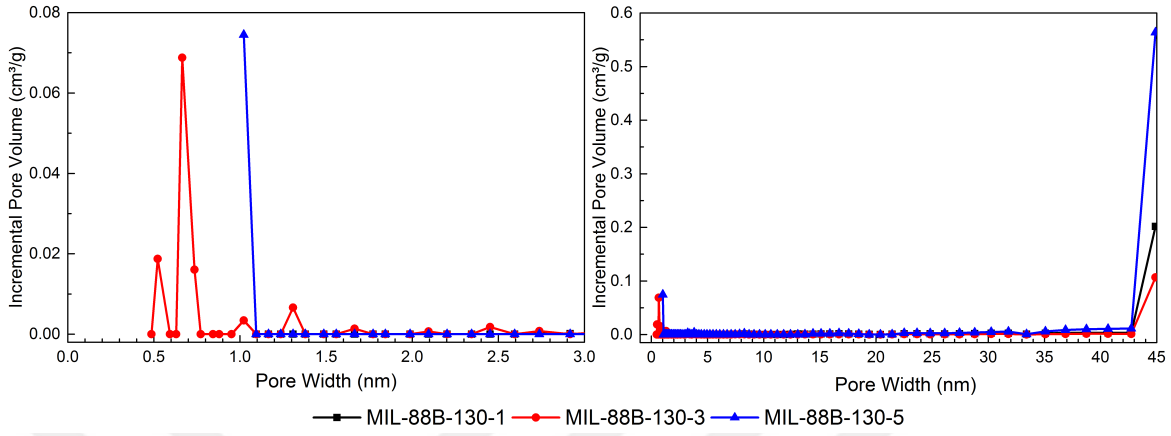

Figure 34. NLDFT plot hierarchically porous MIL-88Bs synthesized at 130 °C.

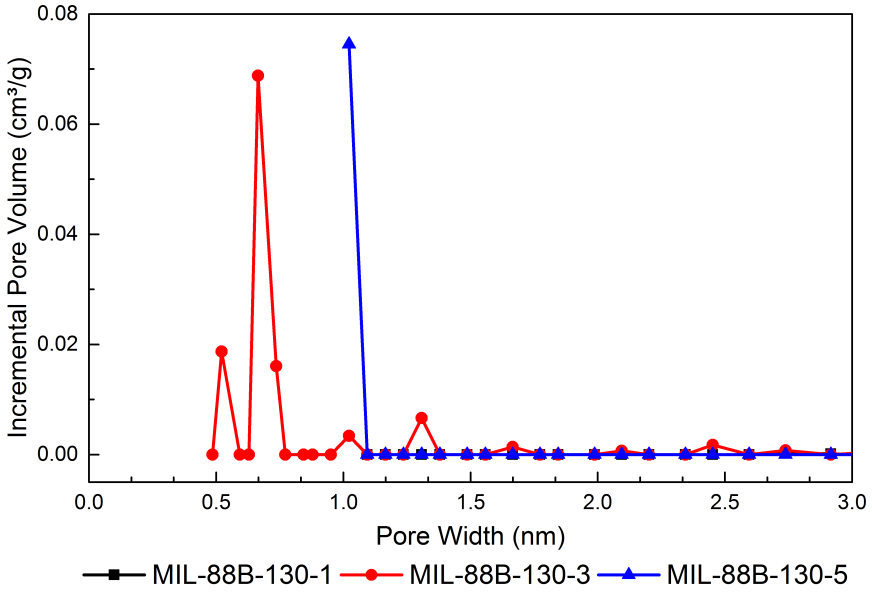

Figure 35. NLDFT plot of MIL-88B-130-1, MIL-88B-130-3, and MIL-88B-130-5.

MIL-88B-130-1 has no micropores wider than 1.094 nm which possess a volume of 0.114 cm^3/g and corresponds to 31.3% of the total pore volume. The highest volume increase which corresponds to 55.5% of the total pore volume belongs to pores with pore diameters of 44.8 nm. MIL-88B-130-3 has no pores narrower than 0.522 nm and pores with pore diameters of 0.629 nm possess the highest volume increase in the microporous region which corresponds to 11.6% of the total pore volume. MIL-88B-130-5 has the highest volume contribution from the pores with pore diameters of 44.8 nm which corresponds to 80.4% of the total pore volume and illustrates that MIL-88B-130-5 has uniform micropores. Contrary

to this, MIL-88B-130-3 has micropores with pore sizes ranging between 0.665 nm and 1.666 nm. The highest volume belongs to pores with pore diameters of 0.665 nm in MIL-88B-130-3 while MIL-88B-130-5 has the highest contribution from micropores with pore diameters of 1.022 nm. NLDFT plots of MIL-88B-150-1, MIL-88B-150-3, and MIL-88B-150-5 can be found below in Figure 36 and 37.

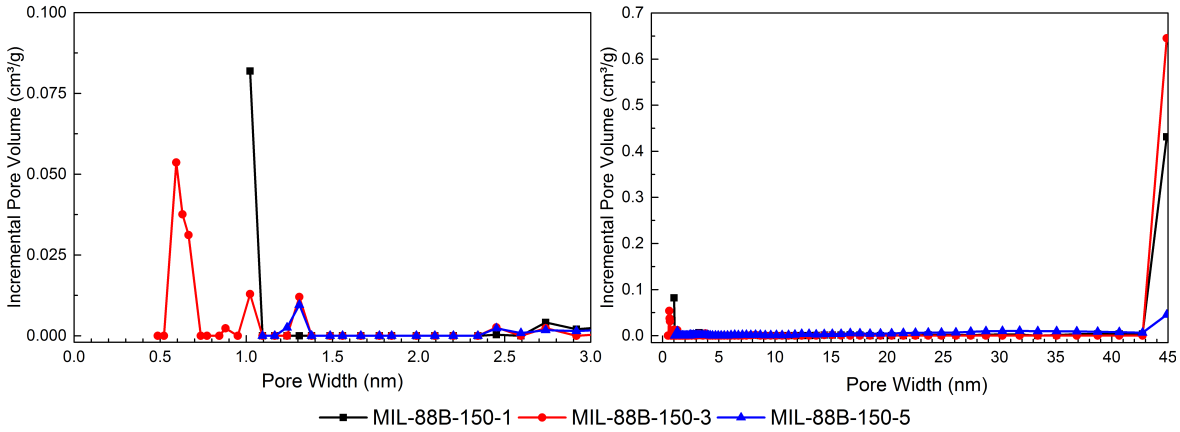

Figure 36. NLDFT plot MIL-88B type MOF crystallites synthesized at 150 °C.

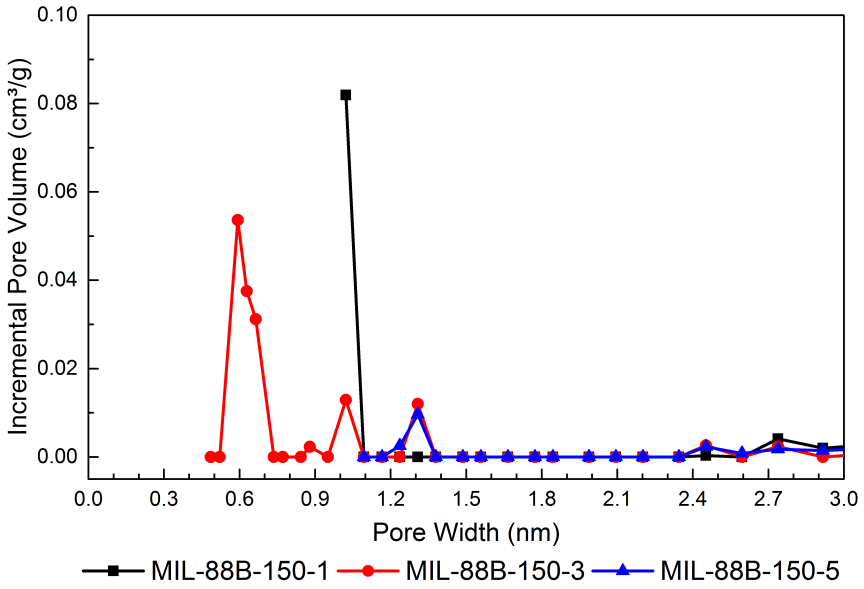

Figure 37. NLDFT plot of MIL-88B-150-1, MIL-88B-150-3, and MIL-88B-150-5.

MIL-88B-150-1 and MIL-88B-150-3 show considerable increase in their pore volumes at the upper mesoporous range. MIL-88B-150-1 possess 0.43 cm^3/g of volume increase that corresponds to 68.1% of the total pore volume while MIL-88B-150-3 has 0.65 cm^3/g of volume increase at the upper mesopore size range which corresponds to 79% of the

total pore volume. Total pore volume of MIL-88B-150-5 (0.28 cm^3/g) is considerably lower than MIL-88B-150-1 (0.634 cm^3/g) and MIL-88B-150-3 (0.82 cm^3/g). In the case of MIL-88B-150-1 micropores that contributes to micropore and total pore volume have diameters lower than 1.0 nm and their overall contribution to the total pore volume is as low as 12.9%. MIL-88B-150-3 has pores as narrow as 0.593 nm and there are no pores narrower than 0.593 nm. Apparently, MIL-88B-150-3 possess either micropores which have pore widths lower than 1.38 nm or mesopores at the upper mesoporous range.

MIL-88B-150-5 has a micropore volume of 0.0355 cm^3/g which corresponds to 12.6% of the total pore volume. Identical to MIL-88B-150-1 and MIL-88B-150-3, the highest volume increase is observed in pores with pore diameters of 44.8 nm. In addition, mesopores that contributes to the total pore volume occupies 87.4% of the total pore volume which is considerably higher than the contribution of micropores. Total pore volume of MIL-88B-150-3 is 2.9 times higher than the total pore volume of MIL-88B-150-5.

NLDFT analysis confirms that the surfactant and template-free synthesis strategy forms hierarchical porosity. The hierarchical porous MIL-88Bs possess a two-pore system. In line with N2 sorption isotherms and t-plot method, NLDFT analysis shows that Fe:TPA ratio has significant effect on the textural porosity. When hierarchically porous MIL-88Bs are synthesized with excess amount of iron salt, volume occupied by textural mesopores at the upper mesoporous range increases, fraction of the textural porosity increases. Table 3 presents the measured and calculated BET surface areas, micropore volume and total pore volume of hierarchically porous MIL-88Bs synthesized at 110, 130, 150 °C with different TPA amount.

Table 3. BET surface area(m^2/g), micropore volume (m^3/g) and total pore volume (cm^3/g) of hierarchically porous MIL-88Bs synthesized at 110, 130, 150 °C with different iron to TPA ratio.

	BET Surface Area (m^2/g)	Micropore Volume (cm^3/g)	Mesopore Volume (cm^3/g)	Total Pore Volume (cm^3/g)	Textural Mesoporosity (%)
MIL-88B-110-1	400.4±1.1E01	0.18±1.4E-02	0.017±1.4E-2	0.19±2.0E-2	8.3
MIL-88B-110-3	452.4±1.9E01	0.24±3.2E-02	0.0096±7.0E-3	0.25±1.2E-2	3.9
MIL-88B-110-5	445.9±1.9E01	0.20±3.2E-02	0.028±1.7E-2	0.23±2.2E-2	12.3
MIL-88B-130-1	265.4±2.6E01	0.11±6.5E-03	0.25±9.7E-3	0.36±1.1E-1	68.8
MIL-88B-130-3	249.4±1.6E01	0.12±1.6E-02	0.13±5.5E-2	0.24±8.5E-2	52.8
MIL-88B-130-5	283.1±2.6E01	0.11±2.8E-03	0.66±4.3E-2	0.77±2.0E-2	86.0
MIL-88B-150-1	357.1±7.8E01	0.14±4.6E-02	0.49±3.1E-1	0.63±2.6E-1	77.4
MIL-88B-150-3	346.3±1.7E01	0.15±2.3E-02	0.67±3.6E-1	0.81±3.0E-1	81.7
MIL-88B-150-5	117.7±1.9E01	0.036±9.0E-03	0.25±2.7E-2	0.28±1.8E-2	87.4

3.3.6. FTIR Analysis

Assigning vibrational modes has crucial importance on the determination of the structure and structural changes of these frameworks. FTIR spectra of hierarchical porous MIL-88Bs synthesized at different temperatures with different Fe:TPA ratio, and observed bands and representative assigned modes are provided below.

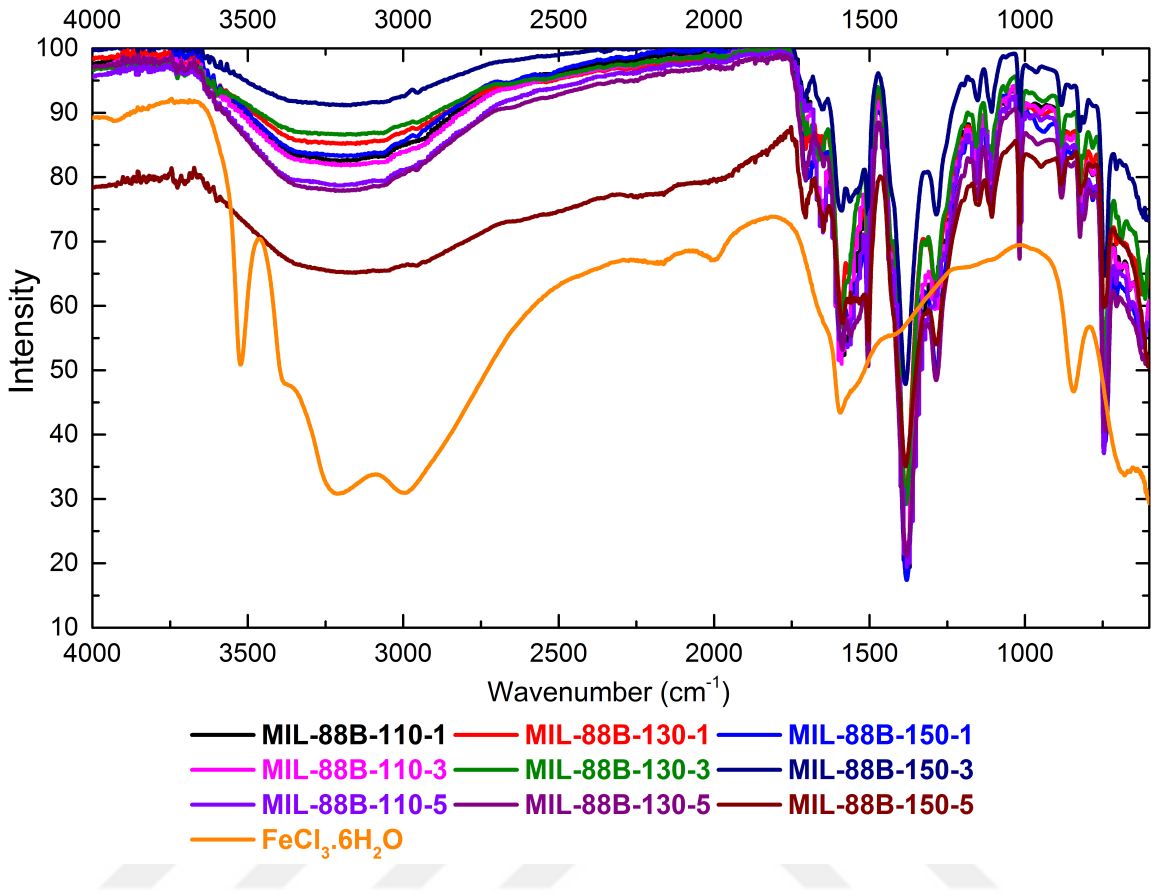

Figure 38. FTIR spectra of hierarchically porous MIL-88Bs and the $FeCl_3.6H_2O$.

FTIR spectrum is divided into following regions: (i) 3000-3600 cm^{-1} (ii) 1650-2800 cm^{-1} (iii) 1300-1650 cm^{-1} and, (iv) 800-1300 cm^{-1}. Three important conclusions are drawn: (I) None of the hierarchical porous MIL-88Bs synthesized at 110 °C possess peaks attributed to free TPA. (II) Firm hierarchical porous MIL-88Bs which possess successfully attached TPAs to metal center, were formed, and lastly (III) Bands attributed to H_2O is present.

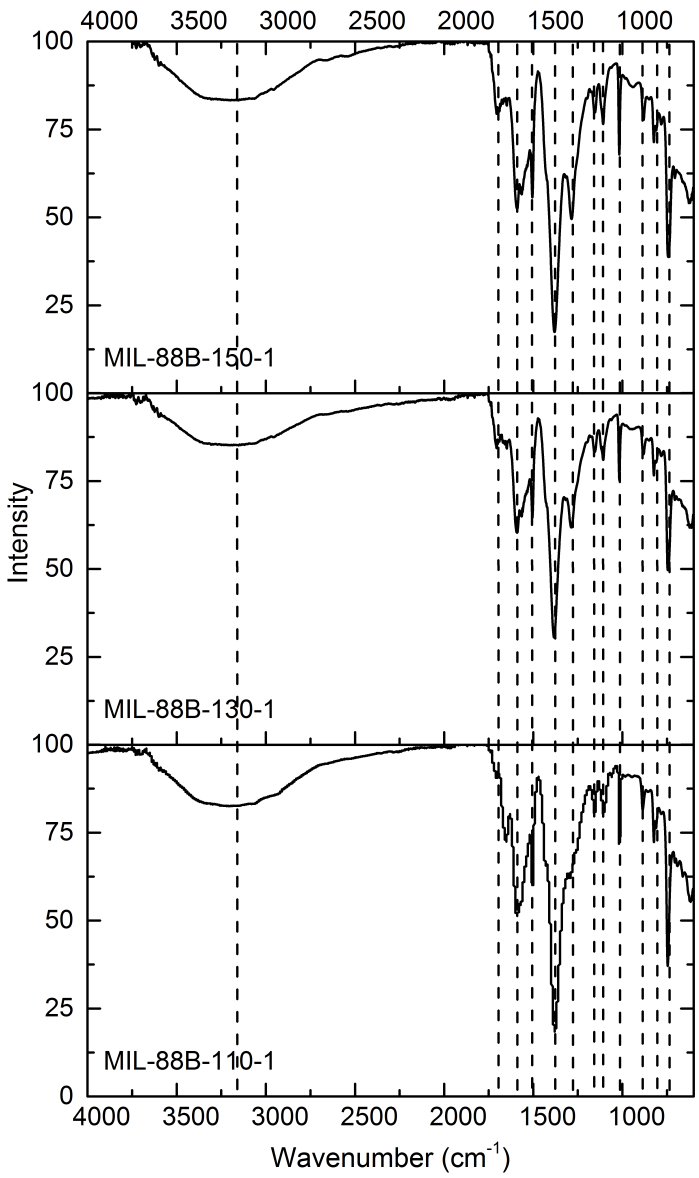

Figure 39. FTIR spectra of hierarchical porous MIL-88Bs synthesized with an Fe:BDC ratio of 1.

Table 4. Representative assigned modes of hierarchical porous MIL-88Bs synthesized at 110°C.

	MIL-88B-110-1	MIL-88B-110-3	MIL-88B-110-5	Assigned mode	References
1st	3207 cm^{-1}	3197 cm^{-1}	3197 cm^{-1}	O-H bond stretching	(Torres et al., 2018)
2nd	1650 cm^{-1}	1650 cm^{-1}	1649 cm^{-1}	C=O asymmetric stretching mode of DMF	(Dhumal, Singh, Anderson, Kiefer, & Kim, 2016)
3rd	1589 cm^{-1}	1591 cm^{-1}	1569 cm^{-1}	19b phenyl modes of H_2BDC (skelatal modes of MIL-88B)	(Arenas & Marcos, 1979; Benbellat et al., 2006; Rowsell & Yaghi, 2006a; Tafipolsky, Amirjalayer, & Schmid, 2010; Téllez S., Hollauer, Mondragon, & Castaño, 2001; Tripathi & Sheng, 1979)
4th	1503 cm^{-1}	1504 cm^{-1}	1503 cm^{-1}	19a phenyl modes of H_2BDC (skelatal modes of MIL-88B)	(Arenas & Marcos, 1979; Téllez S. et al., 2001; Tripathi & Sheng, 1979)
5th	1378 cm^{-1}	1380 cm^{-1}	1378 cm^{-1}	Skelatal modes of MIL-88B	(Benbellat et al., 2006; Rowsell & Yaghi, 2006a;

					Tafipolsky et al., 2010)
6th	1156 cm^{-1}	1156 cm^{-1}	1156 cm^{-1}	skelatal modes of MIL-88B	(Arenas & Marcos, 1979; Téllez S. et al., 2001; Tripathi & Sheng, 1979)
7th	1106 cm^{-1}	1106 cm^{-1}	1106 cm^{-1}	C-O-Fe stretching, skelatal modes of MIL-88B	(Arenas & Marcos, 1979; Téllez S. et al., 2001; Tripathi & Sheng, 1979)
8th	1016 cm^{-1}	1016 cm^{-1}	1016 cm^{-1}	υ_{18a} ring mode of terephthalate	(Arenas & Marcos, 1979; Téllez S. et al., 2001; Tripathi & Sheng, 1979)
9th	823 cm^{-1}	823 cm^{-1}	823 cm^{-1}	Fe-O stretching mode	(Ye Li et al., 2015)
10th	746 cm^{-1}	745 cm^{-1}	745 cm^{-1}	Fe-O stretching mode	(Ye Li et al., 2015)
11th	617 cm^{-1}	621 cm^{-1}	624 cm^{-1}	Central oxygen in single Fe_3O	(Vuong, Pham, & Do, 2013a)

Broad bands observed in between 3000 to 3600 cm^{-1} are assigned to OH groups of O-H bond stretching. The broadest band within region (i) belongs to MIL-88-110-5. We have attributed the observed broadening in region (i) to statistical distribution of OH over the available sites. In a study of Jacobs et. al. (Jacobs & Mortier, 1982), OH band broadening in zeolites was associated with the greater pore sizes. In line with the other characterization methods conducted so far, we suggest that the broadened band represents a larger pore size at which more OH groups are adsorbed. Having the broadest OH band with the lowest

intensity, hierarchically porous MIL-88Bs synthesized with an Fe:TPA ratio of 5 are thought to be formed of larger textural pores in comparison to hierarchically porous MIL-88Bs synthesized at 110 °C.

The band in between 3000 to 3100 cm^{-1} deduces that a stable MOF structure was formed. DMF spectra consisted C–H (cis-methyl) stretching and symmetric C–H (cis-methyl) stretching mode within the wavelength range of 2500 to 3000 cm^{-1}. Hierarchically porous MIL-88Bs synthesized at 110 °C do not consist peaks that are assigned to DMF within this wavelength range. Additionally, no other peaks are observed at 1063 cm^{-1}. Having no peaks either at 1063 or at 2861 cm^{-1} confirms the successful removal of DMF molecules from the pores.

The peaks in the wavelength range of 1650 and 2800 cm^{-1} are assigned to the characteristic modes of iron-based MOFs. None of the hierarchically porous MIL-88Bs consist the peaks at 1704 cm^{-1} illustrating that there were no free TPA left and most of the H_2BDC was deprotonated. A lower TPA amount used in the synthesis causes the band width to increase while the peak intensity decreases. None of the hierarchically porous MIL-88Bs synthesized at 110 °C consist the peak at 1704 cm^{-1} which is an indicator of the free TPA linker. Having no peaks at 1704 cm^{-1} suggests that most of the H_2BDC used during the synthesis was deprotonated. More importantly, using a Cl^- based metal salt provides a promising result as linker was deprotonated and there was no need to remove free acid present in the sample. Without any further treatment, hierarchically porous MIL-88Bs were synthesized acid free.

The peak at 1659 cm^{-1} is assigned to C=O asymmetric stretching mode of DMF molecule and is present in the FTIR spectra of all hierarchically porous MIL-88Bs synthesized at 110 °C. We have confirmed that we have formed the skeletal of our hierarchically porous MIL-88Bs by the peaks obtained at region (iii) at which wavelength ranges between 1300 and 1650 cm^{-1}. Peaks obtained at this region are typical of crystalline state carboxylic acids and are a confirmation of the successfully formed MOF structure.

Peaks observed at 1385 and 1589 cm^{-1} illustrate the successful attachment of TPA to metal centre. Random distribution of DMF that was used as the main solvent during the heating process can be proved by the peaks at 1285 and 1504 cm^{-1} in the FTIR spectra of all hierarchically porous MIL-88Bs. Peaks at 1017 cm^{-1}, 1155 cm^{-1}, 1504 cm^{-1}, 1589 cm^{-1} are

associated with a form of TPA and present in the FTIR spectra of all hierarchically porous MIL-88Bs.

We have proved that TPA is attached to the metal by C-O-Fe stretching by the peak at 1107 cm^{-1}. In addition, the peaks at 742 and 823 cm^{-1} are assigned to Fe-O stretching and prove that Fe was coordinated with TPA. Finally, the peak in between the wavelength range of 600 and 626 cm^{-1} is assigned to central oxygen in single Fe_3O and is present in the FTIR spectra of all the hierarchically porous MIL-88Bs synthesized at 110 ˚C. Table 5 shows the representative assigned modes of hierarchically porous MIL-88Bs synthesized at 130 °C.

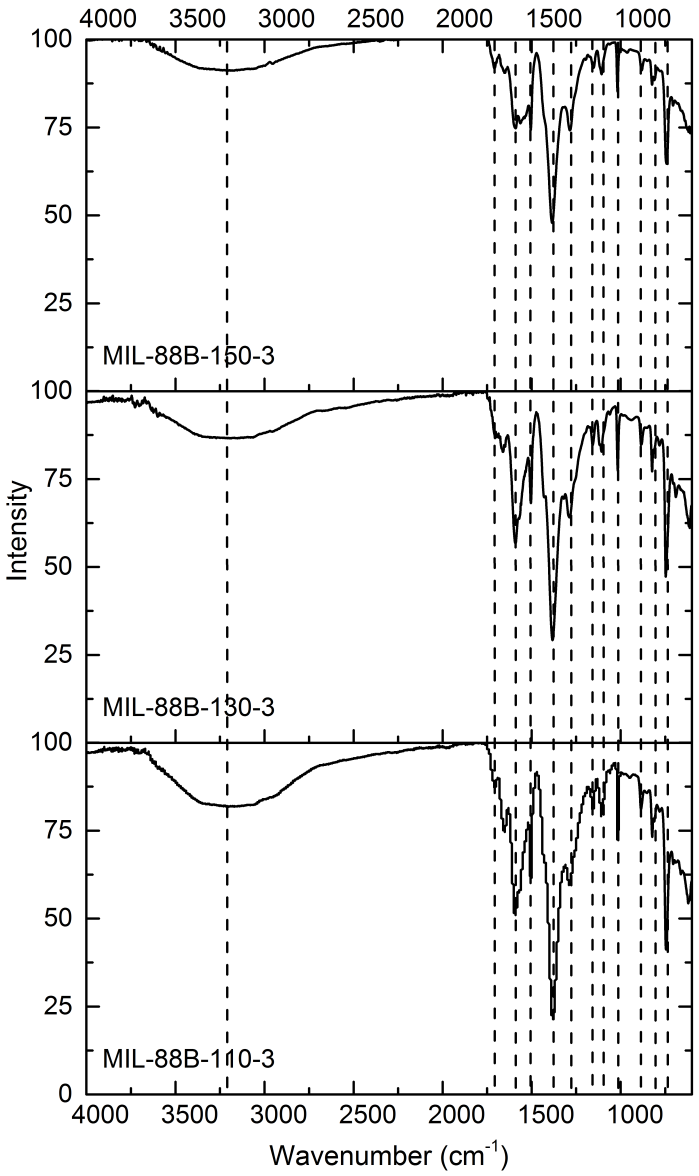

Figure 40. FTIR spectra of MIL-88B-110-3, MIL-88B-130-3, and MIL-88B-150-3.

Table 5. Representative assigned modes of hierarchically porous MIL-88Bs synthesized at 130°C.

	MIL-88B-130-1	MIL-88B-130-3	MIL-88B-130-5	Assigned mode	References
1st	3152 cm^{-1}	3188 cm^{-1}	3217 cm^{-1}	O-H bond stretching	(Torres et al., 2018)
2nd	1705 cm^{-1}	-	1705 cm^{-1}	C=O band of carboxylic acid	(Aysu Yurduşen, Yürüm, & Yürüm, 2019)
3rd	1647 cm^{-1}	1661 cm^{-1}		C=O asymmetric stretching mode of DMF	(Dhumal et al., 2016)
4th	1590 cm^{-1}	1590 cm^{-1}	1587cm^{-1}	19b phenyl modes of H_2BDC (skelatal modes of MIL-88B)	(Arenas & Marcos, 1979; Benbellat et al., 2006; Rowsell & Yaghi, 2006a; Tafipolsky et al., 2010; Téllez S. et al., 2001; Tripathi & Sheng, 1979)
5th	1504 cm^{-1}	1503 cm^{-1}	1504 cm^{-1}	19a phenyl modes of H_2BDC (skelatal modes of MIL-88B)	(Arenas & Marcos, 1979; Téllez S. et al., 2001; Tripathi & Sheng, 1979)
6th	1383 cm^{-1}	1382 cm^{-1}	1380 cm^{-1}	skelatal modes of MIL-88B	(Benbellat et al., 2006; Rowsell & Yaghi, 2006a; Tafipolsky et al., 2010)
7th	1156 cm^{-1}	1156 cm^{-1}	1155 cm^{-1}	skelatal modes of MIL-88B	(Arenas & Marcos, 1979; Téllez S. et al., 2001; Tripathi

					& Sheng, 1979)
8th	1107 cm^{-1}	1107 cm^{-1}	1107 cm^{-1}	C-O-Fe stretching, skelatal modes of MIL-88B	(Arenas & Marcos, 1979; Téllez S. et al., 2001; Tripathi & Sheng, 1979)
9th	1017 cm^{-1}	1016 cm^{-1}	1017 cm^{-1}	υ_{18a} ring mode of terephthalate	(Arenas & Marcos, 1979; Téllez S. et al., 2001; Tripathi & Sheng, 1979)
10th	823 cm^{-1}	823 cm^{-1}	823 cm^{-1}	Fe-O stretching mode	(Ye Li et al., 2015)
11th	745 cm^{-1}	746 cm^{-1}	740 cm^{-1}	Fe-O stretching mode	(Ye Li et al., 2015)
12th	612 cm^{-1}	612 cm^{-1}	-	Central oxygen in single Fe_3O	(Vuong et al., 2013a)

A broad band is observed within the first region. This broad band is attributed to OH groups with O-H bond stretching. In the case of hierarchically porous MIL-88Bs synthesized at 130 °C, no peaks that belong to DMF is observed. Furthermore, there are no peaks traced at 1063 cm^{-1}. No peaks observed at 1063, 2861, or 2931 cm^{-1} confirm the successful removal of DMF molecules from the pores. We have confirmed our stable hierarchically porous MIL-88B structures with the band in between 3000 to 3100 cm^{-1}. In between the wavelengths of 1650 to 2800 cm^{-1} characteristic modes of iron-based MOFs are traced. MIL-88B type MOF crystallites synthesized with an Fe:TPA ratio of 1 and 5 possess peaks at 1704 cm^{-1} showing that free TPA linker was still present in the structure. However, there are no peaks at 1704 cm^{-1} in MIL-88B-130-3. The peak at 1659 cm-1 represents the C=O asymmetric stretching mode of DMF molecule. MIL-88B-130-1 and MIL-88B-130-3 consist the peaks at 1647 cm^{-1} while MOFs synthesized with an Fe:TPA ratio of 5 do not.

At region (iii) where wavelength ranges between 1300 and 1650 cm^{-1} characteristic peaks of crystalline state carboxylic acids are observed and confirm that the skeletal of the hierarchically porous MIL-88Bs were formed successfully. We proved that TPA is successfully attached to metal centre by the peaks present at 1385 and 1589 cm^{-1}. The peaks

at 1285 and 1504 cm^{-1} confirmed the randomly distributed DMF molecules. Besides, bands which are assigned to a form of TPA are observed at 1017 cm^{-1}, 1155 cm^{-1}, 1504 cm^{-1}, 1589 cm^{-1}. We showed the successful attachment of TPA to metal by the C-O-Fe stretching by the peak at 1107 cm^{-1}. Additionally, the peaks obtained at 742 and 823 cm^{-1} are assigned to Fe-O stretching mode which prove the successful coordination of Fe and TPA.

Different from hierarchically porous MIL-88Bs synthesized with an Fe:TPA ratio of 1 and 5, MIL-88B-130-3 possesses a peak at 690 cm^{-1} which is also present in the FTIR spectra of neat TPA. Lastly, the peak at 612 cm^{-1} is attributed to central oxygen in single Fe_3O which is only observed in MIL-88B-130-1, and MIL-88B-130-3. Table 6 illustrates the representative assigned modes of hierarchically porous MIL-88Bs synthesized at 150 °C. In the case of hierarchically porous MIL-88Bs synthesized at 150 °C, the following conclusions are drawn: (I) Free TPA is present in the samples, (II) Carboxylate ligand attaches successfully to metal center, and (III) Bands typical of H_2O is observed.

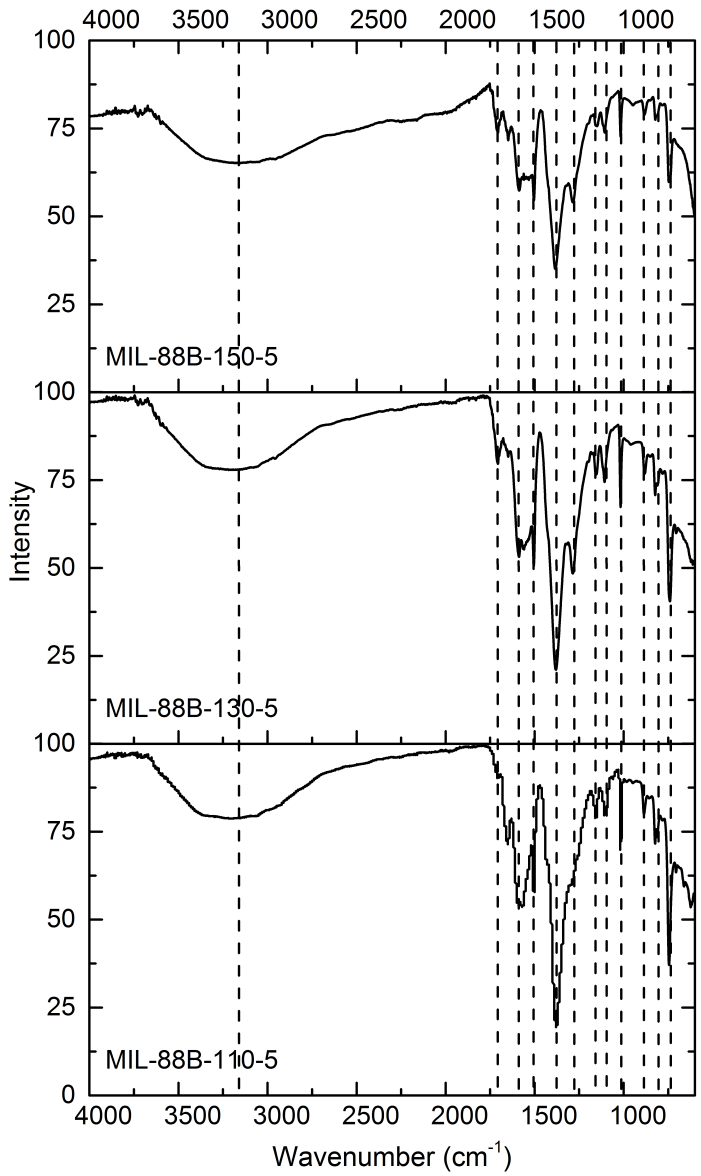

Figure 41. FTIR spectra of MIL-88B-110-5, MIL-88B-130-5, and MIL-88-150-5.

Table 6. Representative assigned modes of MOF crystallites synthesized at 150°C.

	MIL-88B-150-1	MIL-88B-150-3	MIL-88B-150-5	Assigned mode	References
1st	3152 cm^{-1}	3170 cm^{-1}	3153 cm^{-1}	O-H bond stretching	(Torres et al., 2018)
2nd	1704 cm^{-1}	1708 cm^{-1}	1705 cm^{-1}	C=O band of carboxylic acid	(Aysu Yurduşen et al., 2019)
3rd			1647cm^{-1}	C=O asymmetric stretching mode of DMF	(Dhumal et al., 2016)
4th	1589 cm^{-1}	1589 cm^{-1}	1586 cm^{-1}	19b phenyl modes of H_2BDC (skelatal modes of MIL-88B)	(Arenas & Marcos, 1979; Benbellat et al., 2006; Rowsell & Yaghi, 2006a; Tafipolsky et al., 2010; Téllez S. et al., 2001; Tripathi & Sheng, 1979)
5th	1504 cm^{-1}	1504 cm^{-1}	1503 cm^{-1}	19a phenyl modes of H_2BDC (skelatal modes of MIL-88B)	(Arenas & Marcos, 1979; Téllez S. et al., 2001; Tripathi & Sheng, 1979)
6th	1380 cm^{-1}	1384 cm^{-1}	1384 cm^{-1}	Skelatal modes of MIL-88B	(Arenas & Marcos, 1979; Benbellat et al., 2006; Rowsell & Yaghi, 2006a; Tafipolsky et al., 2010; Téllez S. et al., 2001; Tripathi & Sheng, 1979)
7th	1155 cm^{-1}	1152 cm^{-1}	1149 cm^{-1}	Skelatal modes of MIL-88B	(Arenas & Marcos, 1979;

					Téllez S. et al., 2001; Tripathi & Sheng, 1979)
8th	1107 cm^{-1}	1107 cm^{-1}	1106 cm^{-1}	C-O-Fe stretching	(Arenas & Marcos, 1979; Téllez S. et al., 2001; Tripathi & Sheng, 1979)
9th	1017 cm^{-1}	1017 cm^{-1}	1017 cm^{-1}	υ_{18a} ring mode of terephthalate	(Arenas & Marcos, 1979; Téllez S. et al., 2001; Tripathi & Sheng, 1979)
10th	823 cm^{-1}	823 cm^{-1}		Fe-O stretching mode	(Ye Li et al., 2015)
11th	742 cm^{-1}	742 cm^{-1}	746 cm^{-1}	Fe-O stretching mode	(Ye Li et al., 2015)
12th	626 cm^{-1}			Central oxygen in single Fe_3O	(Vuong et al., 2013a)

Within the region (i) observed bands are attributed to OH groups involved in H-bonds. For an Fe:TPA ratio greater than 3, the band intensity decreases. Besides the decreased intensity, broadening in band width is observed. MIL-88B-150-3 has the narrowest band with the highest intensity within region (i). As already reported for zeolites, OH band broadens with increasing pore size (Jacobs & Mortier, 1982). Thus, a more broadened band can be attributed to a larger pore size at which more OH groups are adsorbed whereas the band would be narrower for a smaller pore diameter.

Even though neither MIL-88B-150-1 nor MIL-88B-150-3 consist the peak at 1647 cm^{-1}, it is attributed to C=O asymmetric stretching mode of DMF. Having no peaks at 1647 cm^{-1} is a consequence of the successful removal of DMF molecules from the pores of MIL-88B-150-1 and MIL-88B-150-3. However, MIL-88B-150-5 had some residual DMF molecule left in the pores of. Peak at 1659 cm^{-1} is a typical peak of DMF molecules. MIL-88B-150-1 achieves the sharpest peak at 1380 cm^{-1} with the lowest intensity. 1380 cm^{-1} is within region (iii) and it is attributed to the symmetric stretching vibration of carboxylates.

Three of the hierarchically porous MIL-88Bs synthesized with different TPA amounts obtained different peak intensities for the peak at 1380 cm^{-1}. Additional to 1380 cm^{-1}, intensities of the peak at 1017 cm^{-1} varies in accordance with the TPA amount used during the synthesis. The peak at 1017 cm^{-1} has been previously attributed to υ_{18a} ring mode of terephthalate. Thus, signifies the structural changes present in hierarchically porous MIL-88Bs (Leclerc et al., 2011; Serre et al., 2007). Another noticeable difference is observed in the intensity of the band at 742 cm^{-1}. Hierarchically porous MIL-88Bs synthesized with an Fe:TPA ratio of 1 possess the sharpest peak with the lowest intensity. Additionally, peak intensity increases by the decreasing the linker amount used during synthesis. We have previously assigned the peak at 742 cm^{-1} to Fe-O stretching mode as a consequence of the Fe and TPA coordination. Hierarchically porous MIL-88Bs synthesized with an Fe:TPA ratio of 1 possess the highest TPA amount among the hierarchically porous MIL-88Bs synthesized at 150 °C. For one Fe atom hierarchically porous MIL-88Bs synthesized with an Fe:TPA ratio of 5 has the lowest amount of TPA which we attribute the intensity of the peak at 742 cm^{-1} for hierarchically porous MIL-88Bs synthesized with an Fe:TPA of 5 to be the most intense.

Although all the hierarchically porous MIL-88Bs are exposed to same heating and thermal activation procedure, band widths and peak intensities of their OH band vary significantly. In line with other characterization methods, FTIR analysis shows that MIL-88B type MOF crystallites synthesized with an Fe.TPA ratio of 3 are formed of smaller textural pores among the hierarchically porous MIL-88Bs synthesized with different Fe:TPA ratios. Additionally, we have shown that DMF is removed successfully from the pores of hierarchically porous MIL-88Bs synthesized with an Fe:TPA ratio of 1 and 3. Presence of peaks characteristic to TPA confirms the successful attachment of TPA to the metal centre. By using a Cl^- based metal salt, hierarchically porous MIL-88Bs that are free of TPA were synthesized, successfully. Lastly, FTIR spectrum of hierarchically porous MIL-88Bs were compared with the FTIR spectra of $FeCl_3.6H_2O$. None of the peaks observed in the FTIR spectra of $FeCl_3.6H_2O$ (842 cm^-1, 1594 cm^-1, 2993 cm^-1, 3212 cm^-1, and 3523 cm^{-1}) were observed in the FTIR spectrum of hierarchically porous MIL-88Bs which proves that there are no metallic iron present.

3.3.7. Thermogravimetric Analysis (TGA)

TGA curves of hierarchically porous MIL-88Bs synthesized at 110, 130, and 150 °C with different Fe:TPA ratio can be found below in Figure 42, 43 and 44 and Table 7-10 show the percentage of mass loss during TGA.

TGA analysis demonstrates that MIL-88B type MOF crystallites synthesized with different Fe:TPA ratio are thermally stable. Table 7 shows the percentage of residual mass left after TGA was completed. Differences were observed in the residual masses left after analysis and decomposition temperature differ with TPA amount. Percent residual masses left after the analysis can be found in Table 7. Remaining residual masses are attributed to remaining metal oxides.

Table 7. Percentage of residual mass left after TGA was completed, %.

	Fe:TPA 1	Fe:TPA 3	Fe:TPA 5
110 °C	31.0	28.1	25.7
130 °C	30.5	28.1	31.3
150 °C	33.8	33.6	56.3

The first step of TGA curve corresponds to adsorbed and coordinated water and DMF molecules. The second step is associated with solvent molecules trapped in pores. The third step which forms the main step of TGA curve is attributed to linker decomposition and lastly, the last step corresponds to CO_2 release by decomposition of carboxylates.

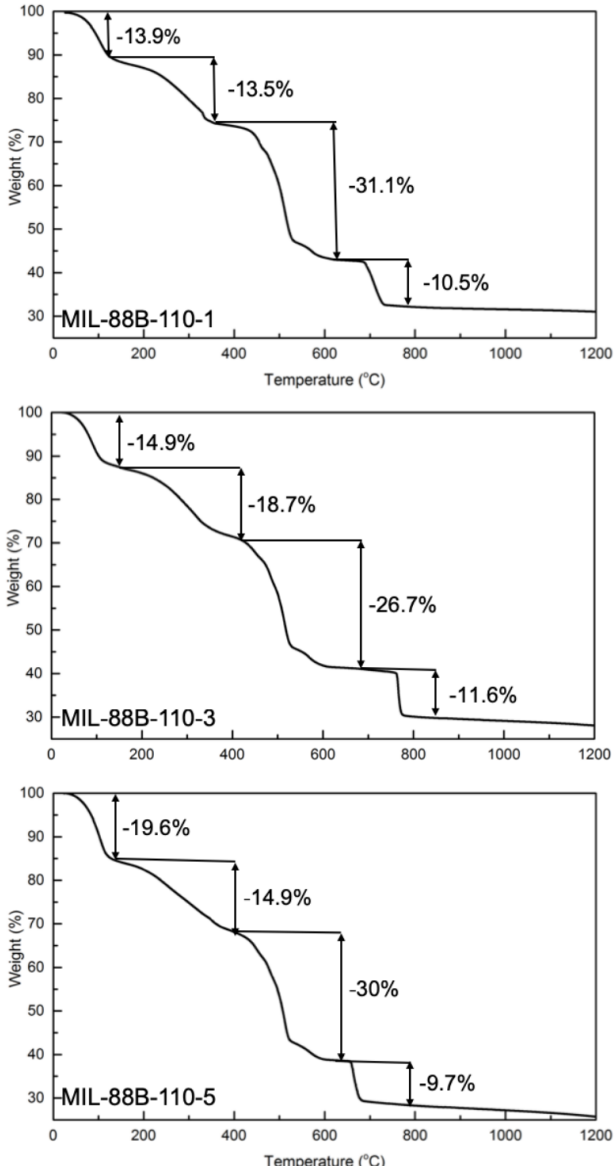

Figure 42. TGA curves of MIL-88B-110-1, MIL-88B-110-3, and MIL-88B-110-5.

MIL-88B-110-5 has the highest amount of mass loss in the first step. The highest fraction of mass loss at the second step is issued by MIL-88B-110-3.

Table 8. % mass loss during TGA analysis of MIL-88B-110-1, MIL-88B-110-3, and MIL-88B-110-5

Temperature Range (°C)	MIL-88B-110-1 (%)	Temperature Range (°C)	MIL-88B-110-3 (%)	Temperature Range (°C)	MIL-88B-110-5 (%)
25-185	-13.9	25-175	-14.9	25-169	-19.6
185-380	-13.5	175-448	-18.7	169-387	-14.9
380-642	-31.1	448-638	-26.7	387-625	-30
642-757	-10.5	638-850	-11.6	625-716	-9.7

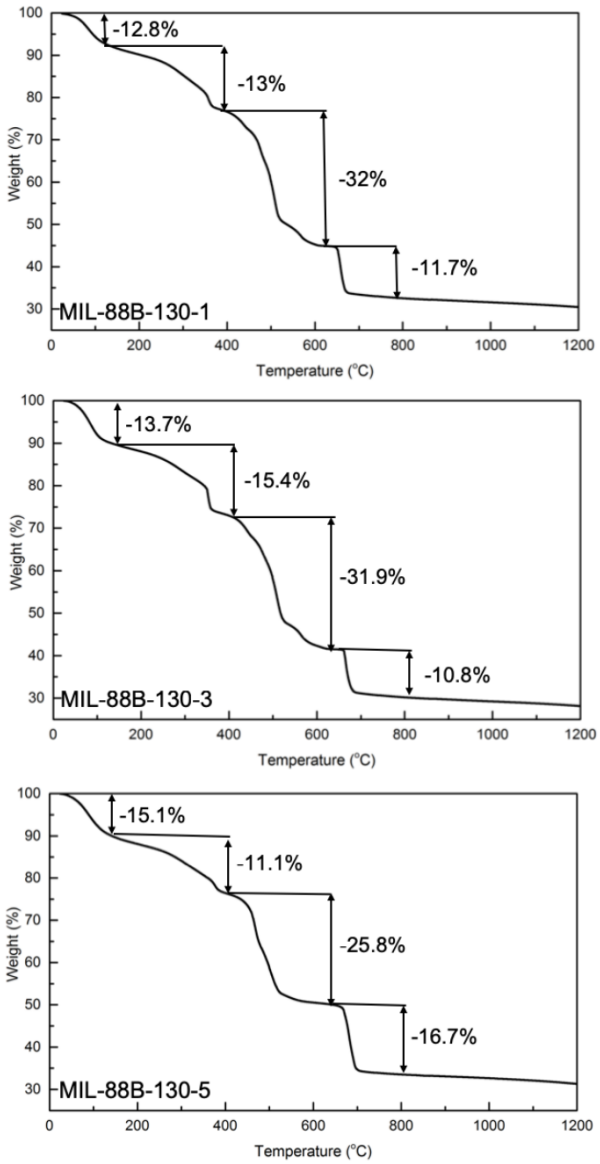

Figure 43. TGA curves of MIL-88B-130-1, MIL-88B-130-3, and MIL-88B-130-5.

Decomposition temperature of MIL-88B-130-5 is higher than MIL-88B-130-1, and MIL-88B-130-3. Percentage of mass lost by MIL-88B-130-5 is the least which may be attributed to the low amount of TPA used during synthesis.

Table 9. % mass loss during TGA analysis of MIL-88B-130-1, MIL-88B-130-3, and MIL-88B-130-5

Temperature Range (°C)	MIL-88B-130-1 (%)	Temperature Range (°C)	MIL-88B-130-3 (%)	Temperature Range (°C)	MIL-88B-130-5 (%)
25-208	-12.8	25-169	-13.7	25-226	-15.1
208-392	-13	169-384	-15.4	226-405	-11.1
392-624	-32	384-633	-31.9	405-602	-25.8
624-720	-11.7	633-732	-10.8	602-759	-16.7

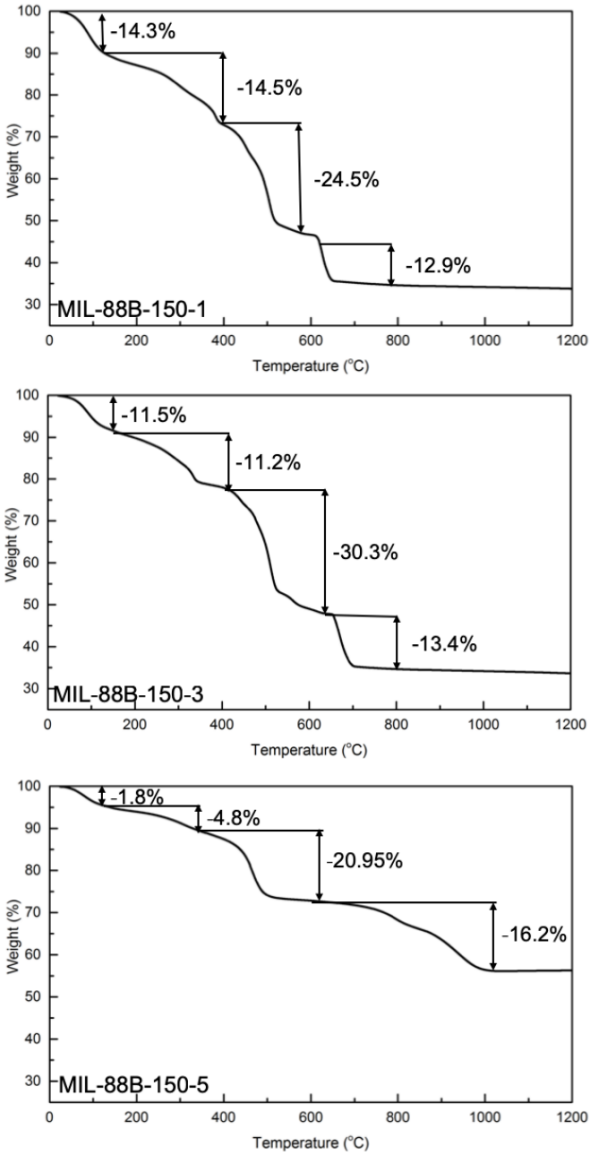

Figure 44. TGA curves of MIL-88B-150-1, MIL-88B-150-3, and MIL-88B-150-5.

Decomposition temperature of MIL-88B-150-3 is the highest among the hierarchically porous MIL-88Bs synthesized at 150 °C indicating its higher thermal stability. MIL-88B-150-1 possesses the highest residual mass left within the hierarchically porous MIL-88Bs synthesized at 150 °C.

Table 10. % mass loss during TGA analysis of MIL-88B-150-1, MIL-88B-150-3, and MIL-88B-150-5

Temperature Range (°C)	MIL-88B-150-1 (%)	Temperature Range (°C)	MIL-88B-150-3 (%)	Temperature Range (°C)	MIL-88B-150-5 (%)
25-201	-14.3	25-203	-11.5	25-236	-6.5
201-404	-14.5	203-442.4	-11.2	236-652	-20.95
404-548	-24.5	442.4-623	-30.3	652-1070	-10.6
548-698	-12.9	623-759	-13.4		

Changing Fe:TPA ratio by varying the amount of linker used not only controlled the textural porosity but also changed the thermal stability of hierarchically porous MIL-88Bs. Hierarchically porous MIL-88Bs synthesized with different linker amounts possess different decomposition temperatures. By adjusting Fe:TPA ratio to 3, a higher thermal stability is achieved.

3.3.8. Possible Effect of Fe:TPA Ratio on the Textural Properties

MIL-88Bs are synthesized by the vigorous stirring of $FeCl_3.6H_2O$, TPA, and DMF. The vigorous stirring of $FeCl_3.6H_2O$, TPA, and DMF limited the growth of single crystals leading SBUs to aggregate and form nanosized MIL-88Bs. By the self-assembly of nanosized MIL-88Bs and Fe-TPA coordination, textural mesopores are formed spontaneously.

Moreover, to enhance the control over textural porosity during the synthesis of hierarchical porous MIL-88Bs, different Fe:TPA ratios are used. It is observed that textural properties of MIL-88Bs differ with Fe:TPA ratio used during the synthesis.

Hierarchical porous MIL-88Bs are synthesized by the aggregation of nanosized MIL-88B rods. In the presence of excess iron salt (a high Fe:TPA ratio), iron oxide clusters form prior to SBU formation. The interparticle voids (textural mesopores) in between the SBU aggregates widen which widens the textural mesopores. SEM images (Figure 21-23) clearly show the widened textural mesopores of MIL-88B-110-5, MIL-88B -130-5, and MIL-88B-150-5.

3.3.9. Possible Effect of Synthesis Temperature on the Textural Properties

Hierarchical porous MIL-88Bs are synthesized by the aggregation of nanosized MIL-88B rods. Vigorous stirring of iron salt, TPA and DMF limits the growth of single crystals. The vigorous stirring forms SBUs which aggregate into MIL-88B nanorods. MIL-88B nanorods aggregate and form mesostructures.

In order to have control over textural porosity, the effect of synthesis temperature is investigated. It is shown that by utilizing the synthesis temperature the size of the textural mesopores can be finely controlled. At a synthesis temperature of 110 °C, pore structure of hierarchical porous MIL-88Bs are found to be formed dominantly of micropores, while at synthesis temperatures above 130 °C, textural mesopores dominate the pore structure. We have attributed this change in textural porosity to the influence of synthesis temperature on the size and the packing of the nanoparticles. When hierarchical porous MIL-88Bs are synthesized at 110 °C, smaller MIL-88B nanorods form. These smaller MIL-88B nanorods pack tightly and form narrower pores26. However, when hierarchical porous MIL-88Bs are synthesized at temperatures above 130 °C, larger MIL-88B nanorods form and then pack loosely which result wider pores to form.

3.4. Comparison with Literature

Table 11 illustrates the BET surface area and total pore volume of MIL-88B that has been reported in the literature. Not only hierarchical pores are formed, but also a BET surface area higher than those of reported MIL-88Bs is achieved by the perturbation assisted nanofusion synthesis strategy. By the synthesis strategy used, we increased the BET surface area, and the total pore volume of hierarchical porous MIL-88Bs (MIL-88B-110-3) by 2.7, and 4.05 times, respectively.

Table 11. BET surface area and pore volume of MIL-88Bs reported in literature

Heating temperature and duration	Solvent used in the synthesis	Drying temperature	BET Surface Area (m^2/g)	Pore Volume (cm^3/g)	Reference
145 °C 1.5 hour	DMF	-	209.8	0.42	(X. Cai, Lin, & Pang, 2016)
100 °C 12 hour	DMF	110 °C	165.4	0.2	(C. Gao et al., 2017)
170 °C 24 hour	DMF	Room temperature	355	0.14	(Vuong, Pham, & Do, 2013b)
Room temperature	EtOH	80 °C	214		(Hou et al., 2018)
110 °C 48 hour	DMF	100 °C	452.4	0.25	This Study (MIL-88B-110-3)
150 °C 48 hour	DMF	100 °C	346.3	0.81	This Study (MIL-88B-150-3)

3.5. Concluding Remarks

In this chapter the effect of Fe:TPA ratio and synthesis temperature on the textural porosity of hierarchically porous MIL-88Bs were investigated. Hierarchically porous MIL-88Bs with different pore size distribution were synthesized by a perturbation assisted nanofusion synthesis strategy that forms hierarchical pores. The perturbation assisted nanofusion synthesis strategy is a cost effective and a facile alternative to the synthesis of mesoporous materials with micropores. Vigorous stirring of $FeCl_3.6H_2O$, TPA, and DMF formed nanosized MIL-88B and embedded the formed nanosized MIL-88B into an

amorphous matrix. Interparticle voids were formed in between the aggregates of nanosized MIL-88B crystals which formed the textural mesopores.

It is found that Fe:TPA ratio controls the morphology and the textural porosity of hierarchically porous MIL-88Bs synthesized by a perturbation assisted nanofusion synthesis strategy. When synthesized at 110 °C with an Fe:TPA ratio of 3, micropore volume of MIL-88B-110-3 increases by a factor of 1.3 and a highly microporous pore structure (96%) is formed. In the meantime, synthesizing hierarchically porous MIL-88Bs with an Fe:TPA ratio of 5 provides a higher fraction of textural mesoporosity to hierarchically porous MIL-88Bs (MIL-88B-110-5: 12.3%, MIL-88B-130-5: 86%, and MIL-88B-150-5: 87.4%) providing hierarchically porous MIL-88Bs to consist both micro- and mesopores in their pore structure. In addition, by the perturbation assisted nanofusion synthesis strategy, a BET surface area and total pore volume that is higher than those of reported for MIL-88Bs are achieved. By the perturbation assisted nanofusion synthesis strategy, the BET surface area and total pore volume is enhanced by 2.7 and 4.05 times, respectively (C. Gao et al., 2017).

The increased fraction of textural mesoporosity of hierarchically porous MIL-88Bs synthesized with a high Fe:TPA ratio is due to excess iron salt present in the solution. Just before the formation of SBUs, iron oxide clusters form. Then in between the aggregates of nanosized MIL-88B, interparticle voids (textural mesopores) form spontaneously. These interparticle voids (textural mesopores) in between the SBU aggregates widen which increase the fraction of textural mesoporosity.

By this surfactant and template free synthesis strategy, this study reports an effortless way to produce hierarchical MOFs that consists both micro- and mesopores. The presence of micro- and mesopores in the pore structure will provide a great deal of opportunities in catalysis, and gas adsorption studies

Chapter IV

Carbon dioxide adsorption capacity of hierarchically porous MIL-88Bs and the crucial role of narrow micropores

In this chapter, we report a synthesis strategy that enhances the CO_2 adsorption capacity of hierarchically porous MIL-88Bs by the control of hierarchical pores via Fe/BDC ratio and synthesis temperature. Hierarchically porous MIL-88Bs synthesized at different temperatures with different Fe/BDC ratios are investigated for their CO_2 adsorption capacities. The crucial role of narrow micropores (pores with pore sizes smaaller than 1 nm) on CO_2 adsorption capacity is shown. The highest CO_2 adsorption capacity of 5.58 wt.% (at 1 bar and 298 K) is achieved by hierarchically porous MIL-88Bs with a BET surface area of 400.4 m^2/g. This CO_2 adsorption capacity is greater than those of reported commercially available MOFs (MOF-5 CO_2 adsorption capacity, 4.5 wt. %, and ZIF-8 CO_2 adsorption capacity, 4.3 wt. %. By the formation of hierarchical pores and control of textural mesoporosity via the Fe/BDC ratio and synthesis temperature, this research paves the way for the synthesis of hierarchically porous MOFs with enhanced CO_2 adsorption capacity (A. Yurduşen & Yürüm, 2019).

4.1. Background

The Intergovernmental Panel on Climate Change reported that the increase in CO_2 concentrations is a consequence of excessive consumption of fossil fuels and deforestation (M. Gupta, Coyle, & Thambimuthu, 2003). From the preindustrial period until today CO_2 concentrations have increased to 412 ppm, which was the highest CO_2 concentration measured in the last 650 years (Bachu, 2000; IEA & OECD, 2004). Reaching its highest concentration level and very long lifetime of CO_2, has brought this gas into the spotlight. Particularly, water vapor can only stay in the atmosphere for 10 days, methane leaves the atmosphere in 10 years, and it takes 100 years for nitrous oxides to leave. However, in the case of CO_2, 40% of CO_2 emissions remain in the atmosphere for 100 years while 10% of

the emissions remain even after 10 thousand years (Ciais et al., 2013). The CO_2 emissions we produce today cannot be removed completely which means CO_2 remains in the atmosphere past our lifetimes. Therefore, the need for alternative technologies to eliminate the increase in CO_2 concentrations and technologies that decrease CO_2 emissions has become crucial. Several strategies have been suggested to decrease CO_2 emissions: (i) developing energy systems that decrease energy intensity; (ii) decreasing carbon intensity by using low carbon fuels; (iii) developing renewable energy sources; and lastly (iv) developing technologies for CO_2 sequestration and capture (CCS) (Hongqun Yang et al., 2008). The Intergovernmental Panel on Climate Change has emphasized on the need for the development and improvement of technologies for CCS and highlighted that CO_2 emissions can only be decreased by 80 to 90% if power plants use carbon dioxide capture and storage technologies (Metz et al., 2005). Accordingly, researchers have focused their research on the development and improvement of CCS technologies which are formed from three different processes: (i) carbon dioxide capture; (ii) carbon dioxide separation; and (iii) transportation to its permanent storage site. The last step of CCS technologies has already been improved to pilot scale (Wilson, E. ; Gerard, 2007). However, carbon dioxide capture (i), and carbon dioxide separation (ii) still require further research. To decrease the cost of CCS, a considerable amount of effort has to be given to carbon dioxide capture and separation processes, and the most effective scenario would be achieved only if a material used in carbon dioxide capture achieves maximum separation efficiency.

Post-combustion CO_2 capture by amine solvents, oxyfuel combustion and calcium looping (D'Alessandro et al., 2010), membrane based separation, and adsorption are the most commonly used processes in carbon dioxide capture technologies. All of the processes involving absorption and chemical adsorption form CO_2 based products, while the temperature increases during the regeneration of CO_2 and results in increased separation costs (Force, 2009). In order to lower the cost, the formation of by-products should be minimized and in the long run should be eliminated. At that point, physical sorbents come to the forefront with their lower energy requirement and lack of by-product formation (S. Choi, Drese, & Jones, 2009a). Among the physical sorbents, those with high CO_2/N_2 selectivity with high CO_2 uptake capacity have emerged. For instance, activated carbon is the most commonly used physical sorbent with a high surface area and pore volume. However, the low CO_2/N_2 selectivity of this material limits its performance. Zeolites with a high BET

surface area and pore volume possess high CO_2/N_2 selectivity. However, their low CO_2 uptake capacity limits their use in carbon dioxide capture technologies (S. Choi et al., 2009a; Force, 2009). Similar to activated carbons, polymer membranes possess high CO_2 sorption capacities. However, their low CO_2/N_2 selectivity limits their use in CCS technologies (Force, 2009).

Metal-organic frameworks (MOFs) are formed by linking a metal ion or metal ion cluster with an organic linker. The combination of the metal part with the organic linker provides one-, two-, or three- dimensional networks. Depending on how building blocks are chosen, the structure of MOF crystallites varies, and pores can be easily tuned specific to the application that will be used (D. Yuan, Zhao, Sun, & Zhou, 2010; D. Zhao, Yuan, Sun, & Zhou, 2009). In addition to their tunability, their high surface area and pore volume make these materials promising in various applications such as drug delivery, gas storage and separation, catalysis, and molecular separation (Y. S. Bae & Snurr, 2011; Chughtai, Ahmad, Younus, Laypkov, & Verpoort, 2015; Corma et al., 2010; Farrusseng, Aguado, & Pinel, 2009; Jeongyong Lee et al., 2009; J. R. Li et al., 2009; Jiewei Liu et al., 2014; J. S. Seo et al., 2000; Taylor-Pashow et al., 2010; Yoon, Srirambalaji, & Kim, 2012; T. Zhang & Lin, 2014). Their high surface areas, high pore volumes, and easy tunability have brought MOFs to the fore among the porous materials. When compared to porous inorganic solids such as zeolites, MOFs possess lower chemical and thermal stability as a consequence of their coordination bonds. High selectivity and reduced heat capacity provide MOFs an edge over other sorbent materials such that the volumetric CO_2 adsorption capacity of MOF-177 at 35 bar have been measured to be 9 times greater than that of zeolite 13X (Millward & Yaghi, 2005b). Additionally, high CO_2 uptake capacities can only be achieved at low pressures when the surface of the pores has been functionalized accordingly. Therefore, synthesizing MOFs with moderate or high surface areas, high CO_2 selectivity and high CO_2 uptake capacities with decreased regeneration energy would provide a promising sorbent material for CCS technologies.

Constructed from oxo centered corner-sharing trimers of iron (III) (Horcajada et al., 2011), MIL-88B is a nontoxic, biodegradable MOF whose CO_2 uptake capacity has not been reported yet. Additionally, researchers mainly focused either on BET surface area or functional groups to enhance measured CO_2 uptake capacities. However, there is a few

efforts spent to understand the effect of narrow micropores (pore sizes < 1 nm) and pore size distribution on the adsorbed CO_2 amount.

In this study, we report of the role of narrow micropores (pore diameters < 1 nm) on CO_2 adsorption capacity. Hierarchical pores were formed by vigorously stirring iron salt, linker and DMF prior to solvothermal synthesis. Textural porosity of hierarchically porous MIL-88Bs is systematically tuned via Fe:BDC ratio and synthesis temperature. With the control of Fe:BDC ratio and synthesis temperature hierarchically porous MIL-88Bs with different pore size distribution were synthesized. CO_2 uptake measurements were conducted in between 0 and 5 bar at 298 K gravimetrically. The results were correlated with BET surface area, narrow micropore (pore diameter < 1 nm), micropore, mesopore and total pore volume. CO_2 adsorption capacity of hierarchically porous MIL-88Bs synthesized in our laboratories (BET: 400.4 m^2/g, narrow micropore volume: 0.177 cm^3/g) was compared with the CO_2 uptake capacities of commercially available MOFs. With our controlled synthesis strategy, the volume of narrow micropores was increased by 1.3 times (0.177 cm^3/g) and the CO_2 uptake capacity was enhanced by a factor of 1.3.

Hierarchically porous MIL-88Bs synthesized in our laboratories (BET surface area: 400.4 m^2/g) achieved a 5.58 wt.% of CO_2 uptake capacity (at 298 K and 1 bar), which is greater than the CO_2 adsorption capacities of commercially available MOFs and ZIFs. For instance, MOF-5 (BET surface area: 2833 m^2/g CO_2 uptake capacity: 4.5 wt.% (Millward & Yaghi, 2005b)), MOF-177 (BET surface area: 5400 m^2/g CO_2 uptake capacity: 3.6 wt.% (Mason, Sumida, Herm, Krishna, & Long, 2011a)) and lastly UMCM-1 (BET surface area: 4034 m^2/g CO_2 uptake capacity: 3.8 wt.% (A. Ö. Yazaydin et al., 2009)), IRMOF-6 (Millward & Yaghi, 2005b), MIL-101(Cr) (B. Wang, Côté, Furukawa, O'Keeffe, & Yaghi, 2008), MIL-102 (Phan et al., 2010), MOF-2 (Millward & Yaghi, 2005b), ZIF-8 (Mason et al., 2011a), ZIF-71 (A. O. Yazaydin et al., 2009), ZIF-95 (Frost, Düren, & Snurr, 2006a), ZIF-97 (Frost et al., 2006a), and ZIF-100 (Trickett et al., 2017). The enhanced CO_2 adsorption capacity of hierarchically porous MIL-88Bs obtained in this study is attributed to relatively high fraction and volume of narrow micropores provided by the controlled synthesis strategy that tunes the textural mesoporosity of hierarchically porous MIL-88Bs via Fe:BDC ratio and synthesis temperature.

Here we report a controlled synthesis strategy that tunes the textural porosity and thereby, enhances the CO_2 adsorption capacity of hierarchically porous MIL-88Bs. Our

results are an experimental evidence that CO_2 uptake capacities can be controlled by the volume and distribution of narrow micropores (pore diameter < 1 nm).

4.2. Experimental

Reproducibility of hierarchically porous MIL-88Bs was tested by the repetitive synthesis and characterization analysis. Each hierarchically porous MIL-88Bs was synthesized for five times. The characterization analysis of each synthesized hierarchically porous MIL-88Bs was repeated for five times. Average results of BET surface area, ultramicro-, micro-, uppermeso-, mesopore, and total pore volumes with calculated standard deviations were reported. The fractions of micro- and mesoporosity were estimated by the ratio of micro- and mesopore volume (NLDFT method) to total pore volume estimated by NLDFT method.

4.2.1. Materials

All chemicals were used without the need of further purification. 98% pure (ACS Reagent grade) iron(III) chloride hexahydrate ($FeCl_3.6H_2O$) was purchased from Merck Millipore while 99.9% pure N, N-Dimethylformamide (DMF) (HPLC grade), and 99.8% pure methanol were purchased from Sigma Aldrich.

4.2.2. Synthesis of Hierarchically Porous MIL-88Bs

Different from the regular MIL-88B synthesis (Bazin et al., 2013; C. Gao et al., 2017; Horcajada et al., 2011), NaOH was not used. 3.1 mmoles of $FeCl_3.6H_2O$ and (3.1 mmoles, 1 mmoles, 0.62 mmoles) terephthalic acid were stirred vigorously via a magnetic stirrer with a stirring rate of 800 rpm in 80 mL of N, N-dimethylformamide (DMF) for an hour at 25 °C. Prepared solution and the precipitate were poured into 20 mL glass vials capped with Teflon caps. The prepared solutions were heated at 110, 130, and 150 °C in an isothermal oven for 2 days and then washed with DMF and methanol. Washing procedure lasted for 6 days and at the end of each 24-hour solvent was changed. After completing the solvent exchange

process, samples were thermally activated in vacuum oven at 100 °C for 30 hours. The following abbreviations listed in Table 12 are used for hierarchically porous MIL-88Bs synthesized at different temperatures with different Fe:BDC ratio.

Table 12. Abbreviations for the hierarchically porous MIL-88Bs synthesized at different temperatures with different Fe:BDC ratio.

Sample Abbreviation	Synthesis Temperature (°C)	Fe:BDC ratio
MIL-88B-110-1	110	1
MIL-88B-110-3	110	3
MIL-88B-110-5	110	5
MIL-88B-130-1	130	1
MIL-88B-130-3	130	3
MIL-88B-130-5	130	5
MIL-88B-150-1	150	1
MIL-88B-150-3	150	3
MIL-88B-150-5	150	5

4.2.3. Characterization of Hierarchically Porous MIL-88Bs

N_2 sorption isotherms, pore size distribution analysis, powder x-ray diffraction (PXRD), thermogravimetric analysis (TGA), Fourier transform infrared spectroscopy (FTIR), and scanning electron microscopy (SEM) were used to characterize MIL-88B type MOF crystallites. Gas sorption measurements were conducted by Intelligent Gravimetric Analyzer (IGA).

4.2.3.1.X-Ray diffraction

X-ray diffraction (XRD Bruker AXS GmbH D8 Advance, Karlsruhe, Germany) analysis was conducted with a 0.15406 nm Cu Kα radiation, under a 40 kV X-ray generator voltage and 5 mA current in between a 2θ range of 2 to 90° with a step size of 0.02°.

4.2.3.2.Scanning Electron Microscopy (SEM)

Leo Supra 35VP field emission scanning electron microscope was used for imaging. Voltage and working distance vary with the MIL-88B type MOF crystallite imaged.

4.2.3.3.Brunauer-Emmett-Teller (BET) surface area and pore size distribution analysis

Surface area and pore size distribution analysis were conducted by Micromeritics 3Flex Instrument. Prior to each analysis, hierarchically porous MIL-88Bs were degassed at 120 °C for 6 hours. For each analysis, 0.10 to 0.15 grams (g) of MIL-88B type MOF crystallites were used. N2 sorption isotherms were obtained in between a relative pressure of 0 to 1 while for surface area analysis, BET model was used at which relative pressure ranged between 0.05 and 0.2. Pore size distribution analysis was conducted by NLDFT method.

4.2.3.4.Fourier Transform Infrared Spectroscopy (FT-IR) Analysis

FTIR analysis was conducted via Thermo Scientific Nicolet Is10 with a spectral resolution of 4 cm-1 over a wavelength range of 600 to 4000 cm^{-1}. Scans were repeated for 32 times and spectrum were corrected for background noise.

4.2.3.5.Thermogravimetric Analysis (TGA)

TGA was conducted with Shimadzu DTG-60H simultaneous thermal analysis TG-DTA equipment. A heating rate of 10 K was used, and analysis was conducted under a continuous flow of 20 mL/min N2 gas in between 25 and 1200 °C.

4.2.3.6.CO_2 Uptake Capacity Measurement

Gravimetric gas sorption capacities were measured with Intelligent Gravimetric Analyzer (IGA). For accuracy, a microbalance head with ± 1.0 μg sensitivity was placed in a stainless-steel vacuum pressure reactor. The CO_2 sorption studies were conducted for hierarchically porous MIL-88Bs with tuned pore sizes. Prior to each analysis, 25 to 30 mg of sample was outgassed at 120 °C for 6 hours. Static CO_2 sorption isotherms were measured at 25 °C within a relative pressure range of 0 to 5 bar.

4.3. Results and Discussion

4.3.1. XRD Analysis

XRD patterns of hierarchically porous MIL-88Bs can be found below in Figure 45. Sharp peaks obtained at low angles match well with the characteristic peaks of MIL-88B. By vigorously stirring metal salt, linker and DMF prior to solvothermal synthesis, hierarchical pores were introduced by the aggregation of small sized crystallites. Aggregation of small sized crystallites show themselves by the broadened PXRD patterns.

PXRD patterns of hierarchically porous MIL-88Bs synthesized at different temperatures with different Fe:BDC ratio consist peaks located at similar peak positions. However, intensities of the peaks differed with Fe:BDC ratio and synthesis temperature. A high Fe:BDC ratio results in broadened Bragg peaks and synthesizing hierarchically porous MIL-88Bs with an Fe:BDC ratio of 1 result in decreased peak intensity. The differences observed in Bragg peak intensities are attributed to the changes in textural porosity.

Lastly, single crystal X-ray crystallography analyses confirmed that micro-sized single crystals were not formed and there were no metallic-iron present.

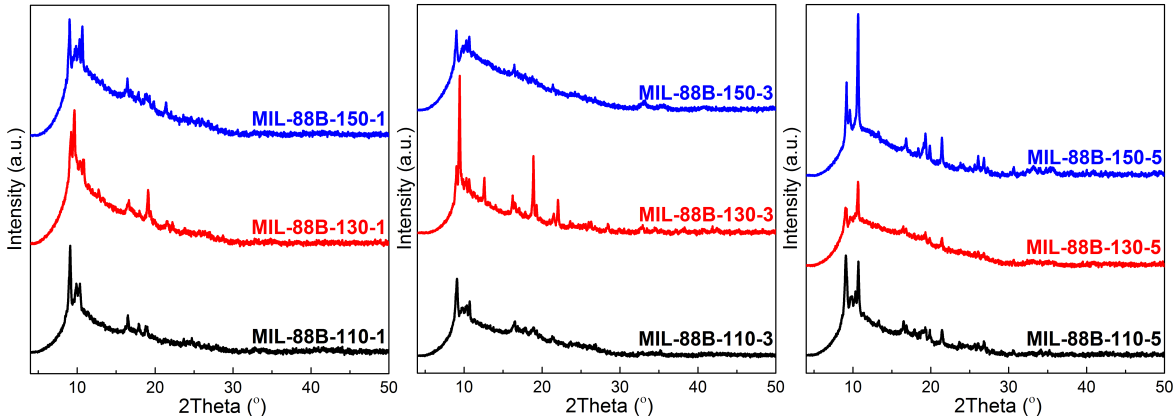

Figure 45. XRD pattern of hierarchically porous MIL-88Bs.

4.3.2. SEM Imaging

Representative SEM images can be found in Figure 46. It is observed that morphology of hierarchically porous MIL-88Bs differs with Fe:BDC ratio and synthesis temperature. MIL-88B-110-1 possesses a rough surface while MIL-88B-130-1 has some cracks. By vigorously stirring the metal salt, linker and DMF, textural mesopores are formed. These textural mesopores are formed by the aggregation of small MOF crystallites. The nanosized rods of MIL-88B can be seen in the SEM images. Aggregated nanosized MIL-88Bs formed a hierarchical structure at which textural mesopores are present. The aggregated MOF crystallites can be seen clearly in the SEM images of MIL-88B-150-5. Formed majorly of organic linkers, MOF crystallites was not be imaged by TEM analysis.

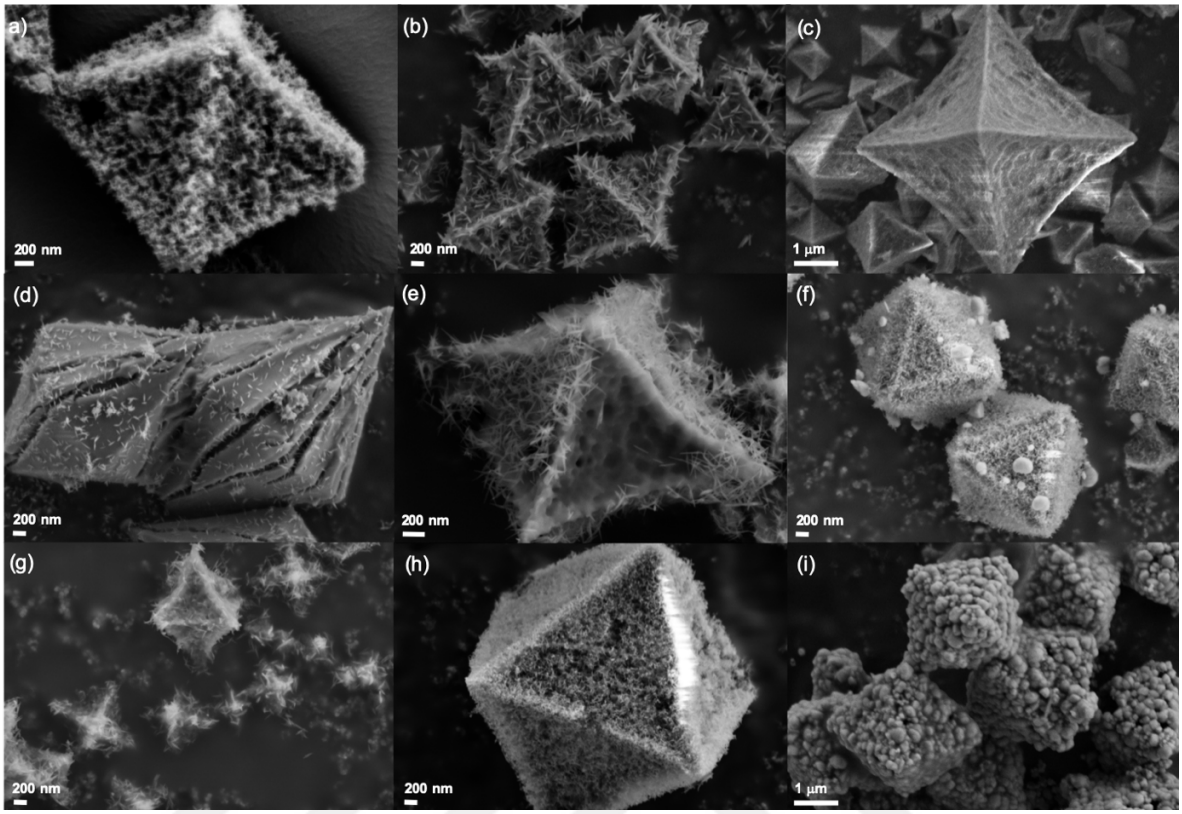

Figure 46. SEM images of hierarchically porous MIL-88Bs (a) MIL-88B-110-1, (b) MIL-88B-110-3, (c) MIL-88B-110-5, (d) MIL-88B-130-1, (e) MIL-88B-130-3, (f) MIL-88B-130-5, (g) MIL-88B-150-1, (h) MIL-88B-150-3, and (i) MIL-88B-150-5.

4.3.3. Textural Properties

Different synthesis temperatures and different Fe:BDC ratios result differences in BET surface area, and textural porosity to be observed. Representative BET surface area, micro- and mesopore volume, total pore volume, and mesopore fraction are presented at Table 13.

Table 13. BET surface area, micropore area, micropore volume, and fraction of mesoporosity

MOF	BET Surface Area (m^2/g)	Micropore Volume (cm^3/g)	Mesopore Volume (cm^3/g)	Total Pore Volume (cm^3/g)	Vmeso (%)
MIL-88B-110-1	400.4±1.1E1	0.182±1.4E-2	0.017±1.4E-2	0.19±2.0E-2	8.3
MIL-88B-110-3	452.4±1.9E1	0.239±3.2E-2	0.0096±7.0E-3	0.25±1.2E-2	3.9
MIL-88B-110-5	445.9±1.9E1	0.202±3.2E-2	0.028±1.7E-2	0.23±2.2E-2	12.3
MIL-88B-130-1	265.4±2.6E1	0.114±6.5E-3	0.25±9.7E-3	0.36±1.1E-1	68.8
MIL-88B-130-3	249.4±1.6E1	0.115±1.6E-2	0.13±5.5E-2	0.24±8.5E-2	52.8
MIL-88B-130-5	283.1±2.6E1	0.108±2.8E-3	0.66±4.3E-2	0.77±2.0E-2	86.0
MIL-88B-150-1	357.1±7.8E1	0.143±4.6E-2	0.49±3.1E-1	0.63±2.6E-1	77.4
MIL-88B-150-3	346.3±1.7E1	0.149±2.3E-2	0.67±3.6E-1	0.81±3.0E-1	81.7
MIL-88B-150-5	117.7±1.9	0.0355±9.0E-3	0.25±2.7E-2	0.28±1.8E-2	87.4

4.3.3.1. N_2 sorption isotherms

Representative N_2 sorption isotherms of hierarchically porous MIL-88Bs are illustrated at Figure 47-50. Hierarchically porous MIL-88Bs synthesized at different temperatures with different Fe:BDC ratio show significant changes in their N_2 sorption isotherms.

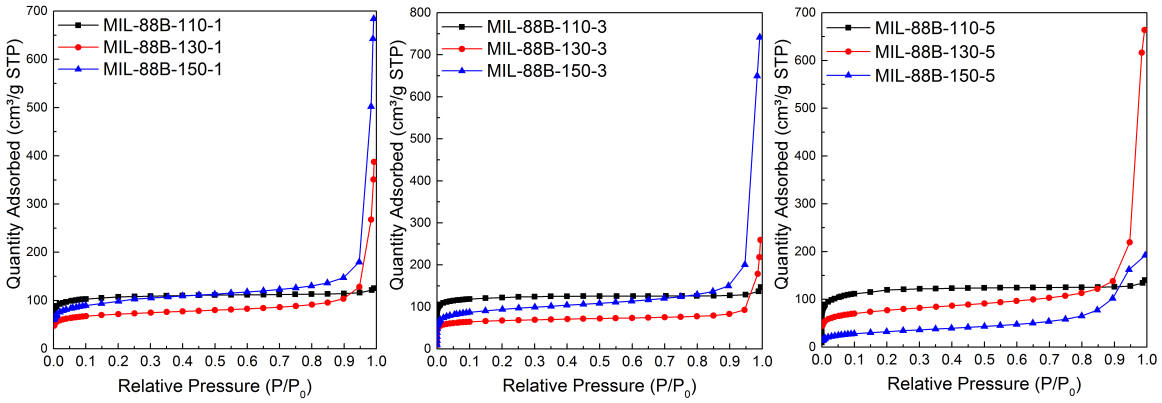

Figure 47. N_2 sorption isotherms of hierarchically porous MIL-88Bs.

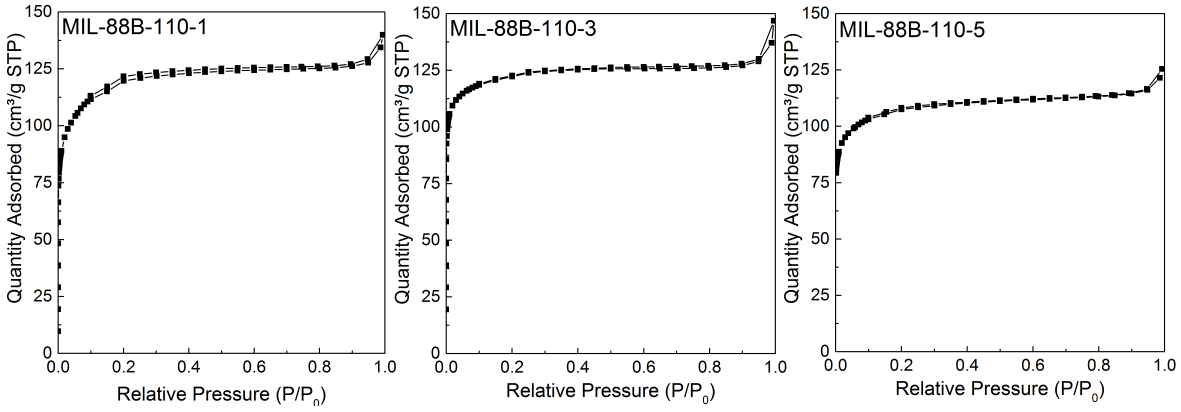

Figure 48. N_2 sorption isotherms of MIL-88B-110-1, MIL-88-110-3, and MIL-88B-110-5.

N_2 sorption isotherms of MIL-88B-110-1, MIL-88B-110-3, and MIL-88B-110-5 (Figure 48) follow characteristic features of IUPAC type I isotherms with some amount of mesoporosity present. N_2 sorption isotherms possess high N_2 uptakes at low relative pressures. For relative pressures ranging between 0.2 and 0.9 almost horizontal plateau parallel to relative pressure axis is achieved. Lastly, at pressures close to saturation pressure a steep N_2 uptake is observed.

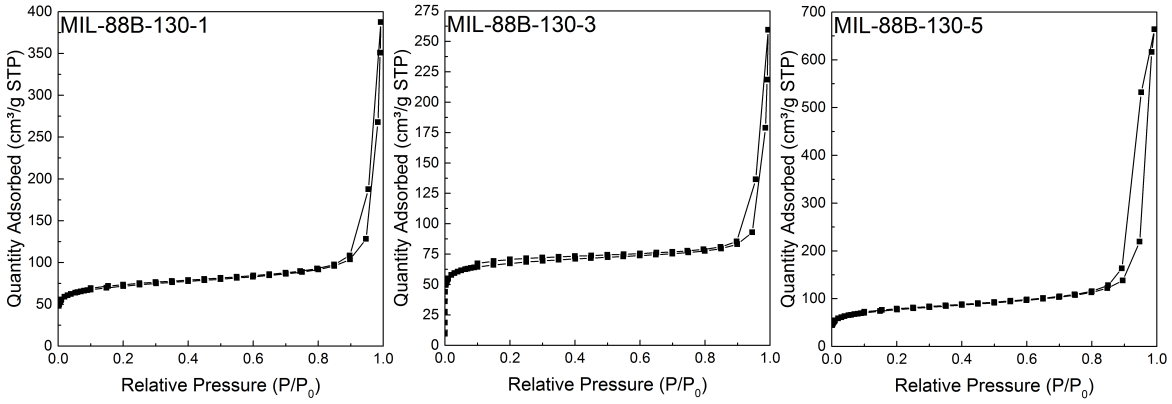

Figure 49. N_2 sorption isotherms of MIL-88B-130-1, MIL-88-130-3, and MIL-88B-130-5.

MIL-88B-130-1, MIL-88B-130-3, and MIL-88B-130-5 possess the characteristic IUPAC type IV isotherms with some microporosity present (Figure 49). Presence of hysteresis loop points out the presence of mesopores. The high N_2 sorption capacities at low relative pressures reveals that micropores are present in the pore structure of MIL-88B-130-1, MIL-88B-130-3, and MIL-88B-130-5. Slope observed in between the relative pressure range of 0.2 and 0.9 is associated with mesopore filling. The steep increase observed close to saturation pressure is associated with mesopores at the upper mesopore size range.

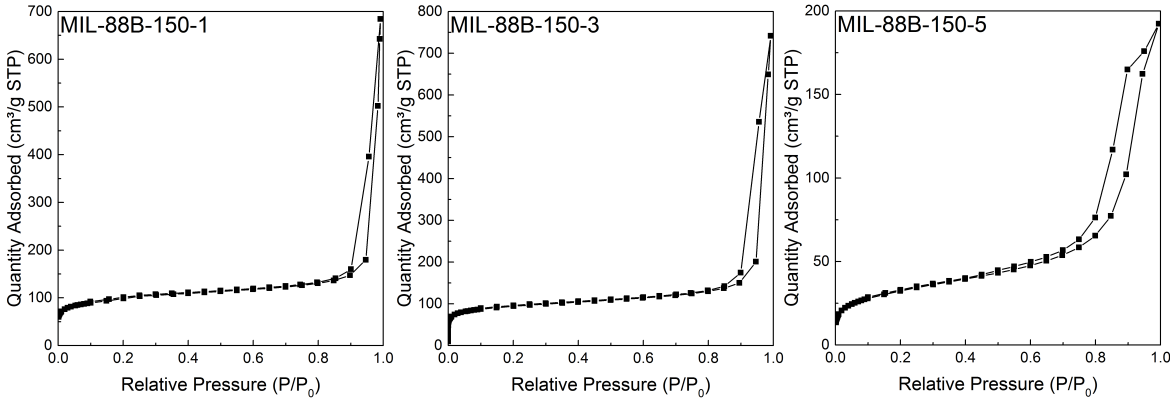

Figure 50. N_2 sorption isotherms of MIL-88B-150-1, MIL-88-150-3, and MIL-88B-150-5.

Hierarchically porous MIL-88Bs synthesized at 150 °C show the typical features of IUPAC type IV isotherms with some microporosity present (Figure 50). Hysteresis loops present in the N_2 sorption isotherms are due to pore condensation and therefore is attributed to the presence of mesopores. Steep N_2 uptake at low relative pressures illustrates that the micropores are present. Slope obtained in between the relative pressure range of 0.2 and 0.9

and the steep uptake close to saturation pressure demonstrates that MIL-88B-150-1, MIL-88B-150-3, and MIL-88B-150-5 are formed of mesopores.

As synthesis temperature and Fe:BDC ratio differ, significant changes in N_2 sorption isotherms are observed. These changes are attributed to changes occurred in textural mesoporosity. N_2 sorption isotherms show some typical features of mesopores when hierarchically porous MIL-88Bs were synthesized at temperatures higher than 110 °C illustrating the developed textural mesoporosity. In order to assess micropore volumes, t-plot method is used at which amount of N_2 adsorbed is plotted with respective to statistical thickness. Representative t-plots are shown in Figure 51.

4.3.3.2.t-plot method

For micropore volume estimations statistical thickness is used. Harkins and Jura thickness equation is used at which *"t"* represents statistical thickness and *"P/P_0"* stands for relative pressure (Lowell et al., 2004a). Table 14 illustrates micropore volumes, slope, y-intercept values and correlation coefficients for respective t-plot method estimations.

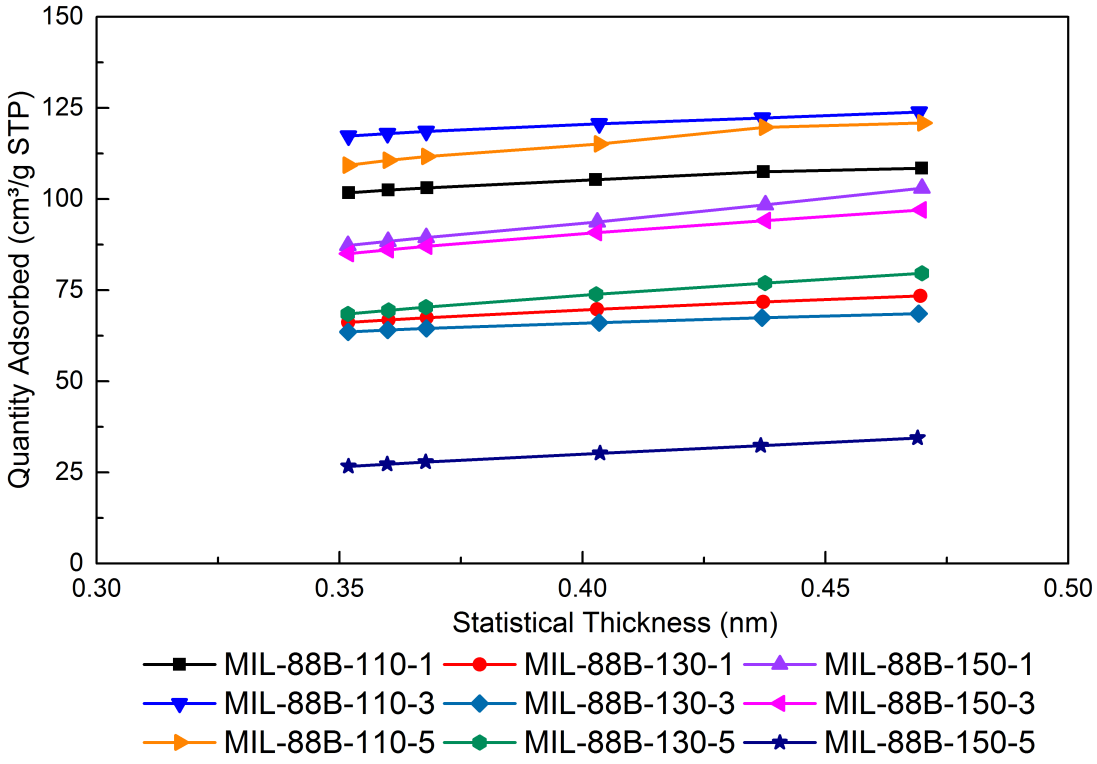

Figure 51. t-plots of hierarchically porous MIL-88Bs

Table 14. Micropore volume, slope, y-intercept, and correlation coefficient estimated by t-plot method.

MOF	Micropore Volume (cm^3/g)	Slope ($cm^3/g.nm$)[a]	Y intercept ($cm^3/g.nm$)[a]	Correlation Coefficient
MIL-88B-110-1	0.13±1.4E-2	58.2±3.9	81.6±1.8	0.991
MIL-88B-110-3	0.15±3.4E-2	54.9±2.0	98.2±8.0E-1	0.997
MIL-88B-110-5	0.114±3.2E-2	101.6±7.5	74.1±3.0	0.989
MIL-88B-130-1	0.069±1.9E-2	61.6±2.1	44.7±8.4E-1	0.998
MIL-88B-130-3	0.076±1.7E-2	42.0±1.6	48.98±6.4E-1	0.997
MIL-88B-130-5	0.055±1.7E-2	94.3±2.5	35.6±1.0	0.999
MIL-88B-150-1	0.063±1.7E-2	131.8±1.8	40.9±7.0E-1	0.999
MIL-88B-150-3	0.077±1.7E-2	101.5±2.5	49.5±1.0	0.999
MIL-88B-150-5	0.0054±1.0E-3	13.0±6.3E-1	3.5±2.5E-1	0.995

[a] At standard temperature and pressure (STP)

Dots that deviated towards downwards illustrate the presence of micropores. In the meantime, deviations from the linear regime reveal the presence of mesopores. Presence of two linear parts confirm both micro- and mesopores exist in pore structure. The highest intercept value belongs to MIL-88B-110-3.

4.3.3.3.NLDFT method

Figure 52 to 60 represents NLDFT plots of hierarchically porous MIL-88Bs. Volume of narrow micropores (pore diameters < 1 nm), micro-, and mesopores can be found below at Table 15. Additionally, volume of mesopores at the upper mesopore size range and their distribution within mesopores and the whole pore size range are illustrated at Table 16.

Table 15. Micro- and mesopore volume, fraction of micro- and mesoporosity estimated by NLDFT method

MOF	Volume of pores < 1 nm (cm^3/g)	Micropore Volume (cm^3/g)	Mesopore Volume (cm^3/g)	Vmicro (%)	Vmeso (%)
MIL-88B-110-1	0.177±1.7E-2	0.182±1.4E-2	0.016±1.4E-2	91.7	8.3
MIL-88B-110-3	0.226±1.2E-2	0.239±3.2E-2	0.0096±7.0E-3	96.1	3.9
MIL-88B-110-5	0.172±1.7E-2	0.202±3.2E-2	0.028±1.7E-2	87.7	12.3
MIL-88B-130-1	0.113±1.6E-2	0.1137±6.5E-3	0.25±9.7E-3	31.2	68.8
MIL-88B-130-3	0.107±2.6E-2	0.115±1.6E-2	0.13±5.5E-2	47.2	52.8
MIL-88B-130-5	0.108±1.1E-2	0.108±2.8E-3	0.66±4.3E-2	14.0	86.0
MIL-88B-150-1	0.142±3.7E-2	0.143±4.6E-2	0.49±3.0E-1	22.6	77.4
MIL-88B-150-3	0.137±3.2E-2	0.149±2.2E-2	0.67±3.6E-1	18.3	81.7
MIL-88B-150-5	0.023±1.8E-2	0.0355±9.0E-3	0.25±2.7E-2	12.6	87.4

Table 16. Volume of mesopores at the upper mesopore size range, and their distribution within mesopores and the whole pore size range.

MOF	Vupper (cm^3/g) [a]	Vmesopore (cm^3/g)	Vupper/ Vmeso[b]	Vupper/ Vtotal[c]
MIL-88B-110-1	0.0060±5.7E-05	0.017±1.4E-2	0.36	0.030
MIL-88B-110-3	0.0062±5.0E-3	0.0096±7.0E-3	0.64	0.024
MIL-88B-110-5	0.0066±1.2E-3	0.028±1.7E-2	0.23	0.029
MIL-88B-130-1	0.20 ±1.3E-1	0.25±9.7E-3	0.81	0.55
MIL-88B-130-3	0.11±7.0E-2	0.13±5.5E-2	0.83	0.43
MIL-88B-130-5	0.56 ±5.0E-3	0.66±4.3E-2	0.85	0.73
MIL-88B-150-1	0.43 ±2.9E-1	0.49±3.1E-1	0.87	0.68
MIL-88B-150-3	0.65 ±3.4E-1	0.67±3.6E-1	0.96	0.79
MIL-88B-150-5	0.045±2.0E-2	0.25±2.7E-2	0.185	0.16

[a] Volume of mesopores at the upper mesopore size range (cm^3/g)

[b] Volume ratio of mesopores at the upper mesopore size range to mesopores

[c] Volume ratio of mesopores at the upper mesopore size range to total pore volume

Hierarchically porous MIL-88Bs synthesized at 110 °C

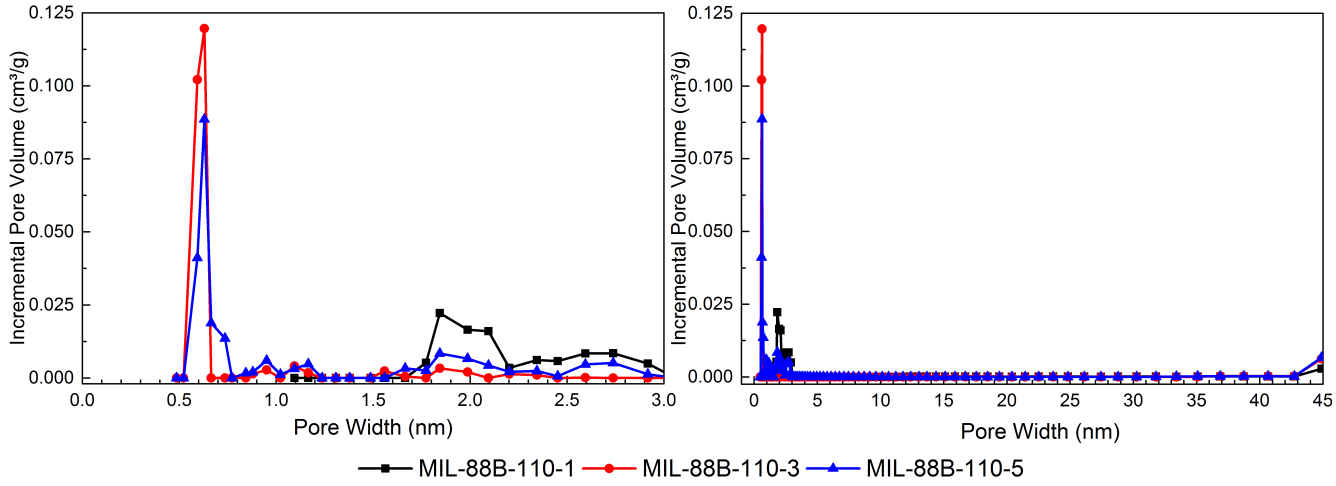

Figure 52. NLDFT plot of hierarchically porous MIL-88Bs synthesized at 110 °C.

Hierarchically porous MIL-88Bs synthesized at 110 °C are formed mostly of micropores. The lowest fraction of textural mesoporosity belongs to MIL-88B-110-3. The volume of narrow micropores and their distribution through the micropore size distribution differ with Fe:BDC ratio. Fraction of narrow micropores (Vpores < 1nm / Vpores < 2 nm) is the highest in MIL-88B-110-1 and the lowest in MIL-88B-110-5. In the meantime, mesopore volume increases by a factor 2.9 when MIL-88B type MOF crystallites were synthesized with an Fe:BDC ratio of 5.

Hierarchically porous MIL-88Bs synthesized at 130 °C

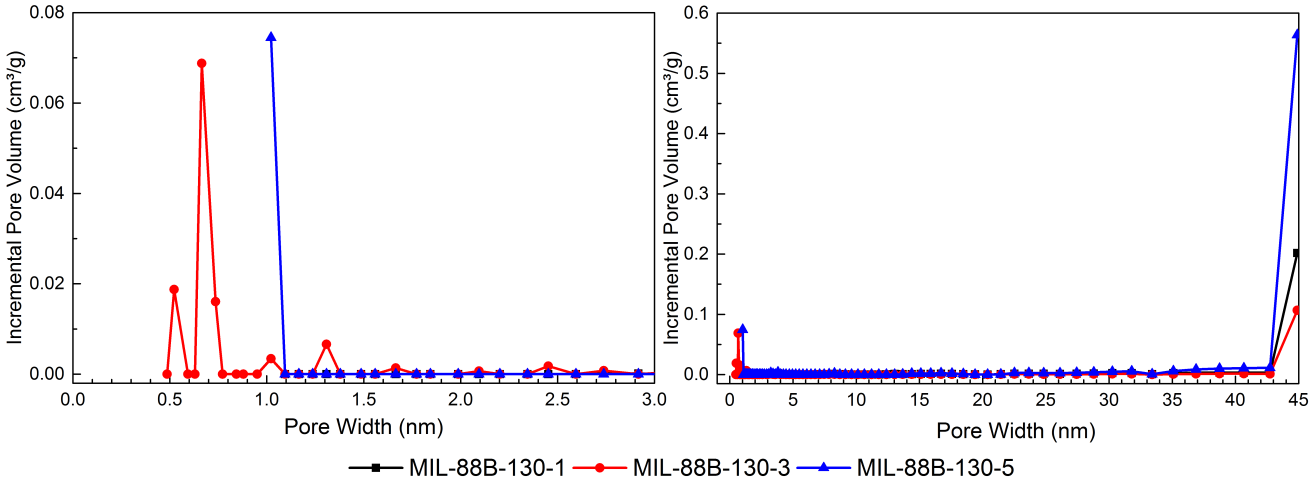

Figure 53. NLDFT plot of hierarchically porous MIL-88Bs synthesized at 130 °C.

The highest volume increase in the upper mesopore size range is attained by MIL-88B-130-5 while MIL-88B-130-3 obtained the lowest. Mesopore volume of MIL-88B-130-5 is 5.1 and 2.9 times higher than the mesopore volume of MIL-88B-130-1 and MIL-88B-130-3, respectively.

The fraction of pores with pore diameters narrower than 1.0 nm corresponds to 31.3% of the total pore volume in MIL-88B-130-1. Additionally, mesopore volume of MIL-88B-130-1 is 15 times higher than the mesopore volume of MIL-88B-110-1 illustrating that the synthesis temperatures higher than 110 °C resulted in pore widening.

Hierarchically porous MIL-88Bs synthesized at 150 °C

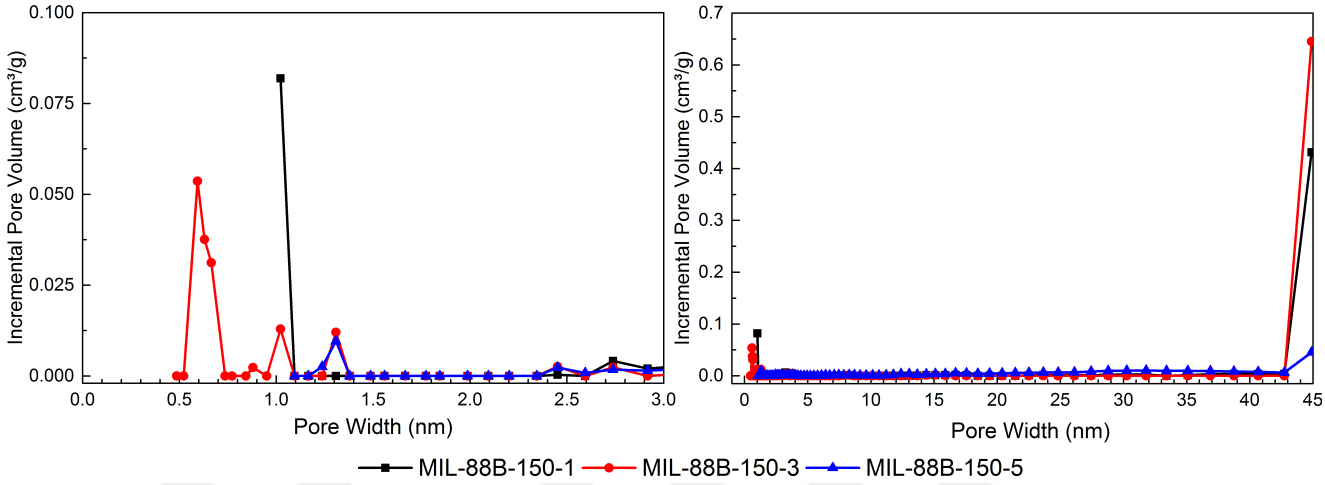

Figure 54. NLDFT plot of hierarchically porous MIL-88Bs synthesized at 150 °C.

MIL-88B-150-1, MIL-88B-150-3, and MIL-88B-150-5 are formed mostly of mesopores, 77.4%, 81.7%, and 87.4%, respectively. Volume of narrow micropores (pore diameter < 1 nm) corresponds to 22.5% of the total pore volume in MIL-88B-150-1 while mesopores at the upper mesopore size range (42 nm < pore diameter < 44 nm) occupy 0.43 cm^3/g of volume and form 68.1% of the total pore volume. Similar to MIL-88B-150-1, the volume increment in the upper mesopore size range corresponds to 79% of the total pore volume which make us conclude that the major volume contribution of pores arises from mesopores at the upper mesopore size range. Even though mesopores form 87.4% of the total pore volume in MIL-88B-150-5, volume contribution of mesopores at the upper mesopore range is relatively low.

Similar to the trend observed in hierarchically porous MIL-88Bs synthesized at 110, and 130 °C, among the hierarchically porous MIL-88Bs synthesized at 150 °C, MIL-88B-150-5 possesses the highest fraction of textural mesoporosity. Micropore volume of MIL-88B-150-5 is 4.0, and 4.2 times lower than the micropore volume of MIL-88B-150-1, and MIL-88B-150-3, respectively.

Hierarchically porous MIL-88Bs synthesized with an Fe:BDC ratio of 1

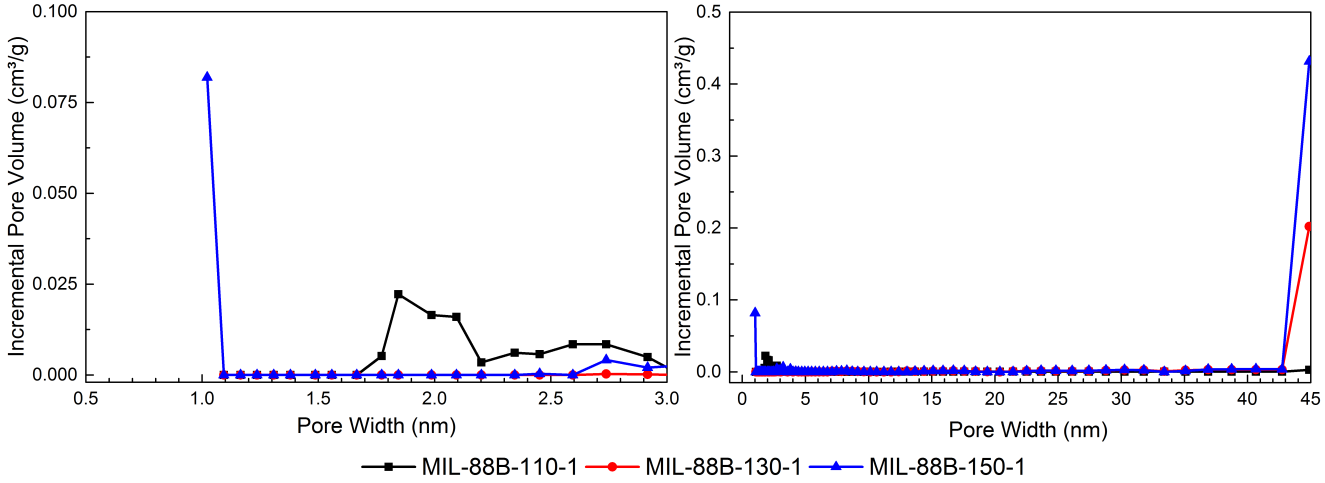

Figure 55. NLDFT plot of hierarchically porous MIL-88Bs synthesized with an Fe:BDC ratio of 1.

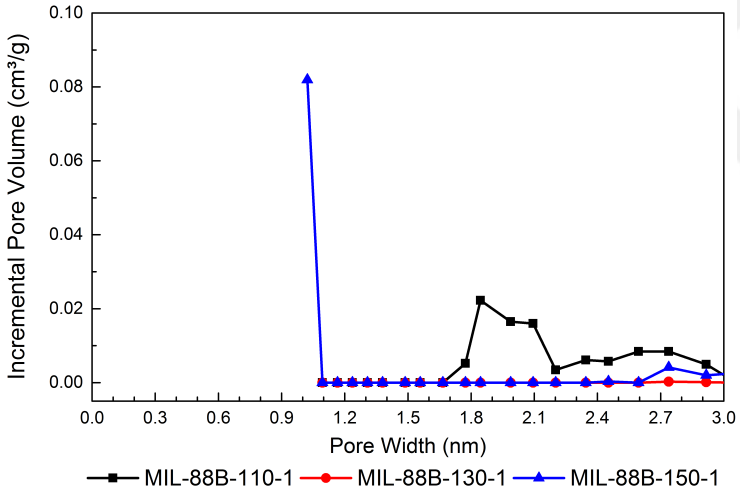

Figure 56. NLDFT plot of MIL-88B-110-1, MIL-88B-130-1, and MIL-88B-150-1.

The highest total pore volume belongs to MIL-88B-150-1. However, its micropore fraction is significantly lower than MIL-88B-110-1. Higher pore volume of MIL-88B-150-1 is associated with its relatively high mesopore volume. MIL-88B-110-1 is formed 91.7% of micropores while MIL-88B-130-1, and MIL-88B-150-1 possess 31.3% and 22.5% microporosity, respectively. A remarkable decrease in textural mesopore volume occurs when hierarchically porous MIL-88Bs were synthesized at lower synthesis temperatures (110 °C). This drastic decrease in mesopore fraction indicates that mesopore formation is promoted at temperatures higher than 110 °C. Mesopore volume of MIL-88B-110-1 is 30

times lower than the mesopore volume of MIL-88B-150-1. MIL-88B-110-1 possesses 8.3% of mesoporosity which is significantly lower than the mesopore fraction of MIL-88B-130-1, and MIL-88B-150-1. It is found that mesopores are the main contributors to the total pore volume in MIL-88B-130-1, MIL-88B-150-1 while micropores dominated the pore structure in MIL-88B-110-1.

Hierarchically porous MIL-88Bs synthesized with an Fe:BDC ratio of 3

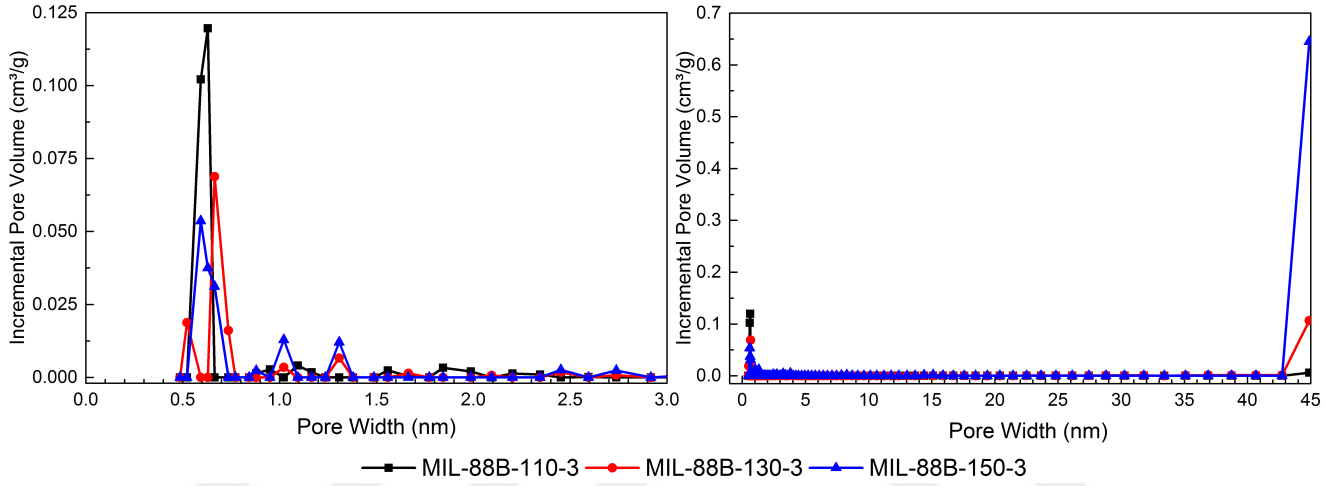

Figure 57. NLDFT plot of hierarchically porous MIL-88Bs synthesized with an Fe:BDC ratio of 3.

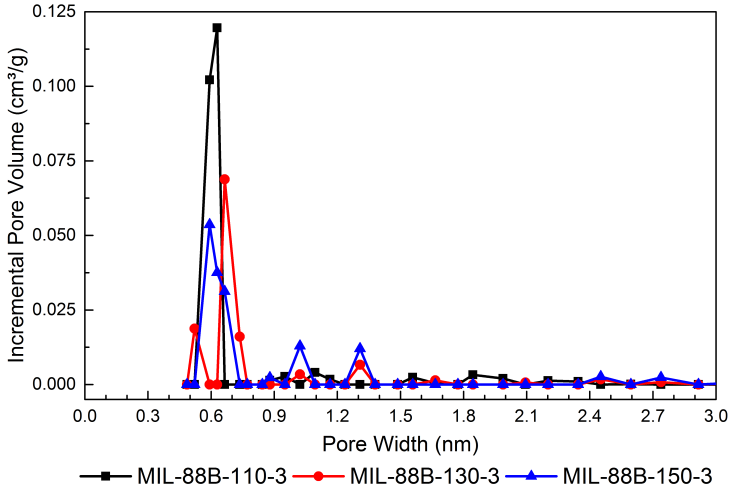

Figure 58. NLDFT plot of MIL-88B-110-3, MIL-88B-130-3, and MIL-88B-150-3.

Hierarchically porous MIL-88Bs synthesized with an Fe:BDC ratio of 3 are formed of pores as small as 0.59 nm. Pores smaller than 0.59 nm contribute to 40.9, 10.2, and 6.6%

increase in total pore volume in MIL-88B-110-3, MIL-88B-130-3, and MIL-88B-150-3, respectively. MIL-88B-110-3, MIL-88B-130-3, and MIL-88B-150-3 are formed 96.1, 36.7, and 18.3% of micropores, respectively. MIL-88B-130-3, and MIL-88B-150-3 are dominantly formed of mesopores and show remarkable increase in their pore volume within mesoporous pore size range. Particularly, MIL-88B-130-3, and MIL-88B-150-3 are formed 52.8% and 81.7% of mesopores, respectively. The highest volume increase in the mesoporous range occurs at the upper mesopore size range (42 nm < pore diameter < 44 nm). For instance, the highest volume increase which corresponds to 79% of the total pore volume of MIL-88B-150-3 belongs to pores with pore diameters ranging between 42.7 and 44.9 nm. Identical to MIL-88B-150-3, MIL-88B-130-3 experiences a volume increase at the upper mesopore range that corresponds to 43.0% of the total pore volume while volume increase in upper mesopore size range of MIL-88B-10-3 is insignificant in comparison to the volume increase observed in MIL-88B-130-3, and MIL-88B-150-3. In conclusion, when hierarchically porous MIL-88Bs were synthesized at temperatures higher than 110 °C, pore widening is observed, mesopore volume and fraction of mesopores at the upper mesopore size range increases.

Hierarchically porous MIL-88Bs synthesized with an Fe:BDC ratio of 5

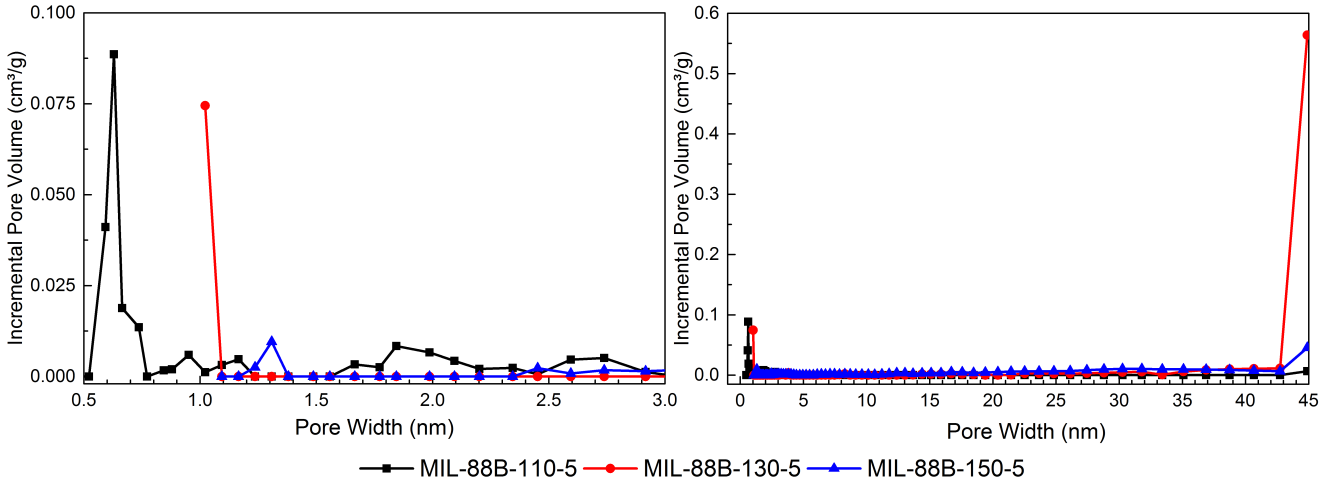

Figure 59. NLDFT plot of hierarchically porous MIL-88Bs synthesized with an Fe:BDC ratio of 5.

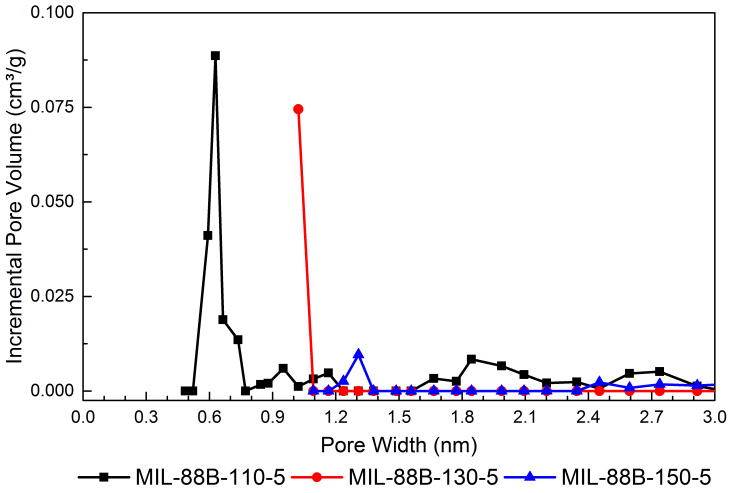

Figure 60. NLDFT plot of MIL-88B-110-5, MIL-88B-130-5, and MIL-88B-150-5.

The highest volume increase in microporous range belongs to MIL-88B-110-5 which is 0.20 cm^3/g. The micropore volume of MIL-88B-110-5 is 2 and 5.7 times more than the micropore volume of MIL-88B-130-5, and MIL-88B-150-5, respectively. In the same manner of hierarchically porous MIL-88Bs synthesized at 110, and 130 °C, the highest fraction of mesopores (87.4%) belongs to MIL-88B-150-5.

4.3.3.4.Impact of Fe/BDC ratio on the pore size distribution

Pore size distribution analysis shows that fraction of mesopores increases with increasing Fe:BDC ratio. Among the MIL-88B type MOF crystallites synthesized at three different temperatures (110, 130, and 150 °C), MOF crystallites synthesized with an Fe:BDC ratio of 5 possess the highest fraction of textural mesoporosity. We have attributed the increased mesoporosity to the presence of excess amount of iron salt which competes for BDC. In a study conducted by Choi et al., it was shown that excess Zn clusters compete for the ligand that has already played a role in MOF-5 crystal formation which results in decreased crystallinity and decreased BET surface area (J. S. Choi, Son, Kim, & Ahn, 2008). In another study conducted by Wu et. al., it was showed that in the absence of the linkers, positively charged vacancy sites would be balanced by -OH groups (H. Wu et al., 2013). From this point of view, we have attributed the increased textural mesoporosity to the presence of excess iron salts competing for BDC. As the iron amount increases, iron oxide clusters start to form which would later compete for BDC.

4.3.3.5.Impact of synthesis temperature on pore size distribution

Prouzet and Pinnavaia showed the temperature dependence of pore structures in MSU-X silicas. Synthesizing MSU-X silicas at high temperatures resulted pore sizes to increase, and disorganized pore structures with broader pore size distribution to form (Prouzet & Pinnavaia, 1997). Similarly, Mahata et. al. showed that synthesizing MOFs at high temperatures cause number of water molecules present in the MOF structure (coordinated and uncoordinated) to decrease and coordination around the central metal ions to change (Mahata et al., 2008).

In another study conducted by Cao et. al., the size of mesopores were found to be dependent on the synthesis temperature. High synthesis temperatures resulted nanoparticles to pack loosely and larger mesopores to form. On the contrary, conducting the synthesis at relatively low synthesis temperatures resulted nanoparticles to pack tightly and smaller pores to form (Cao et al., 2016).

In line with what has been reported in the literature, NLDFT pore size distribution analysis illustrates that conducting the synthesis at relatively low temperatures (110 °C) limited the growth of mesopores, cause nanoparticles to pack tightly leading to an increase in the fraction of microporosity whereas synthesizing hierarchically porous MIL-88Bs at high synthesis temperatures (temperatures greater than 130 °C) results nanoparticles to pack loosely, pores to widen and fraction of mesopores to increase.

By synthesizing hierarchically porous MIL-88Bs at 110°C, the lowest fraction of textural mesoporosity is achieved. In the meantime, synthesizing hierarchically porous MIL-88Bs at temperatures higher than 110 °C formed MOF crystallites with increased fraction of mesoporosity with wider pores dominating the pore structure.

NLDFT analysis reveals that synthesis temperature plays a key role in the textural porosity formation mechanism in MIL-88B type MOF crystallites. Synthesizing MIL-88B type MOF crystallites at high temperatures (synthesis temperature > 130 °C) increased the fraction of textural mesoporosity.

4.3.4. FTIR Analysis

Changes in wavelength intensities reveals the structural changes in hierarchically porous MIL-88Bs. FTIR spectra of hierarchically porous MIL-88Bs can be found in Figure 61, 62, and 63.

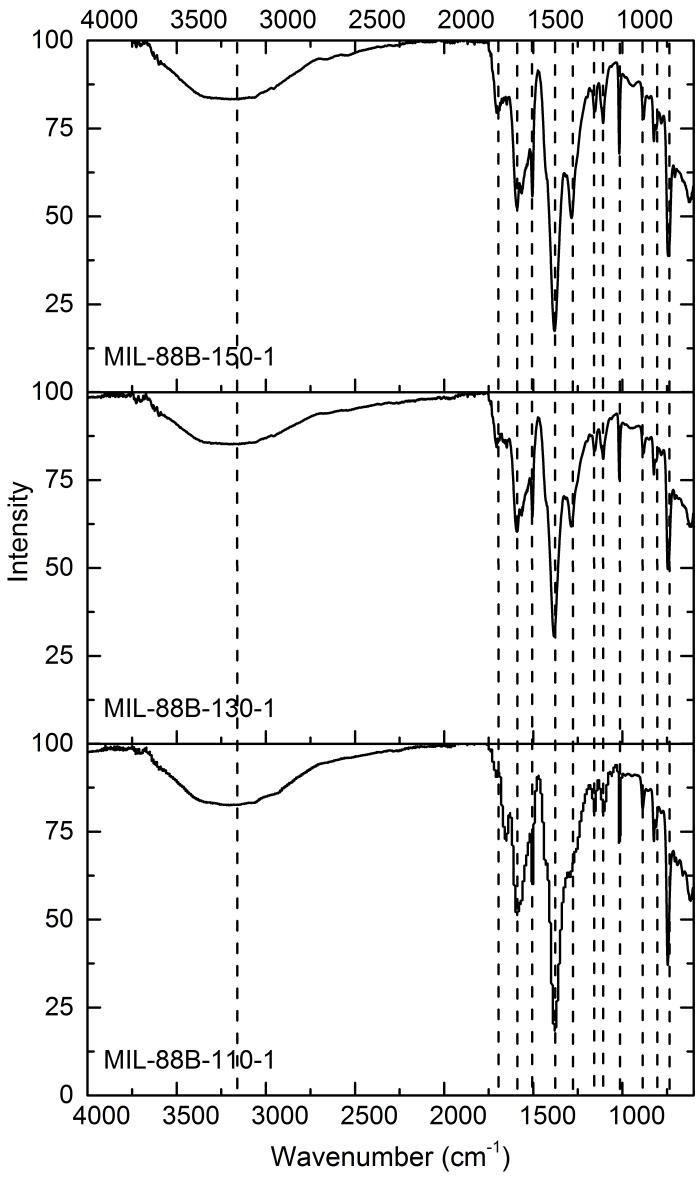

Figure 61. FTIR spectra of hierarchically porous MIL-88Bs synthesized with an Fe:BDC ratio of 1.

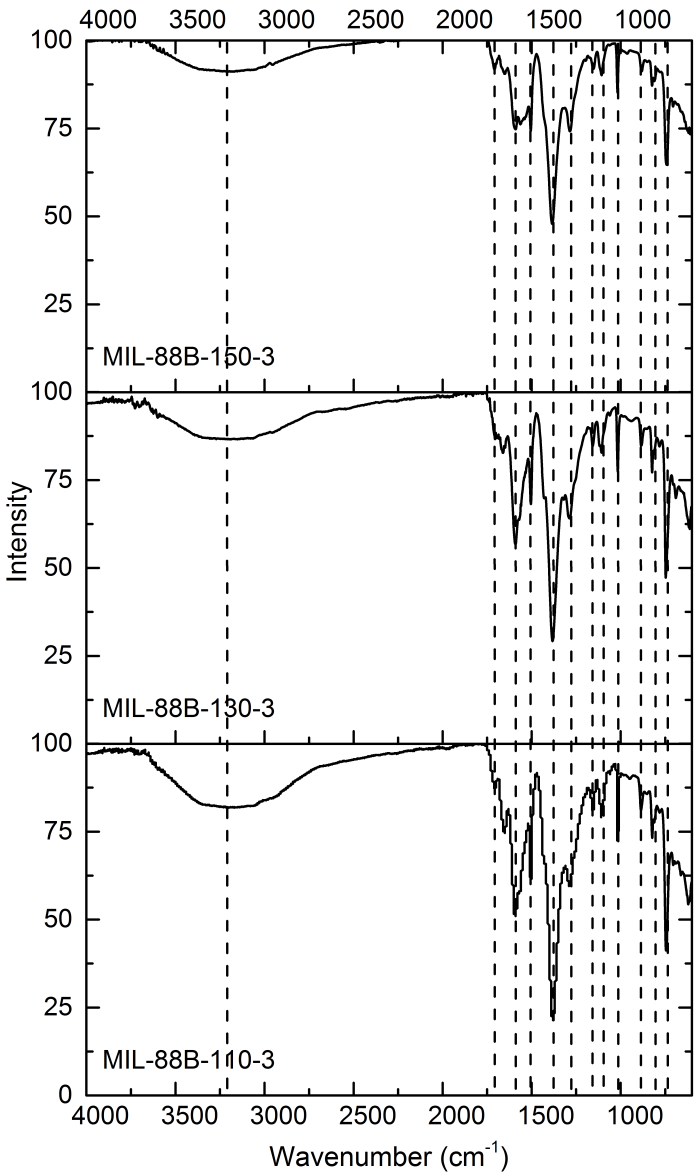

Figure 62. FTIR spectra of hierarchically porous MIL-88Bs synthesized with an Fe:BDC ratio of 3.

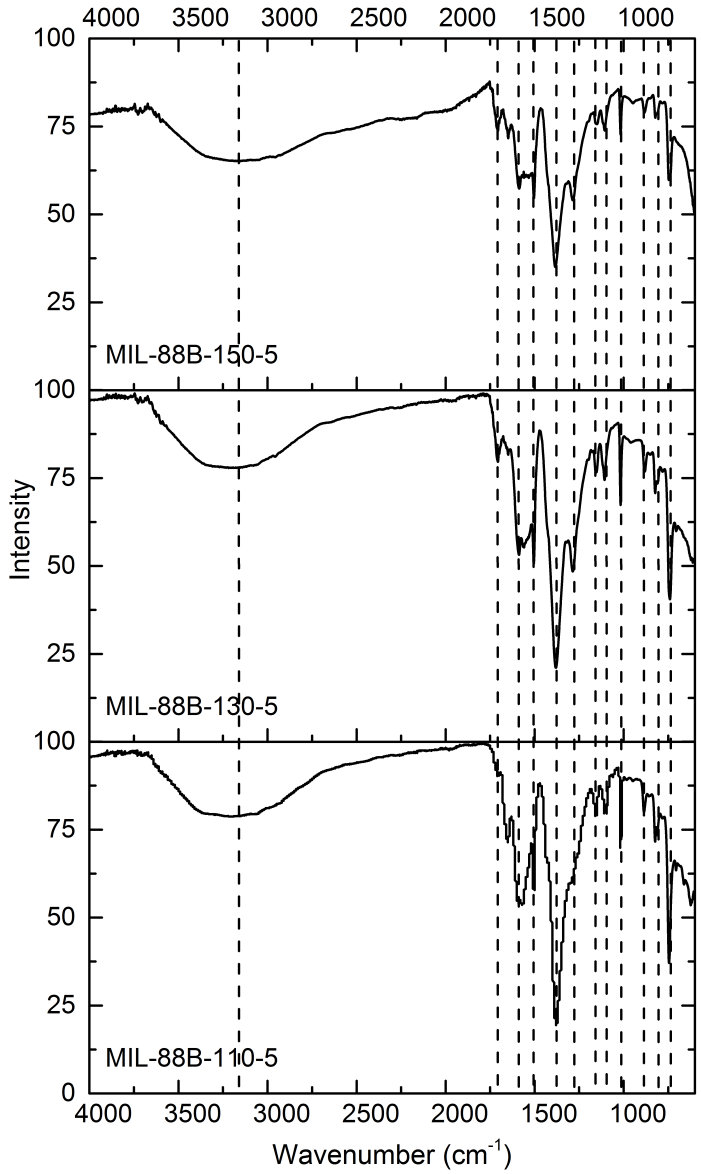

Figure 63. FTIR spectra of hierarchically porous MIL-88Bs synthesized with an Fe:BDC ratio of 5.

Differences in Fe:BDC ratio result band widths and peak intensities to differ. More importantly, the peak at 1704 cm^{-1} points out the structural changes occurred with Fe:BDC ratio and synthesis temperature. The broad band in between 3000 and 3600 cm^{-1} is assigned to OH groups involved in H-bonds. Hierarchically porous MIL-88Bs synthesized with an Fe:BDC ratio of 5 possess broader OH band in between 3000 and 3600 cm^{-1}. In the meantime, peak intensity of the broadened OH band is lower than the OH band peak intensity of hierarchically porous MIL-88Bs synthesized with lower Fe:BDC ratios. A broadened OH band is a consequence of increased number of unsaturated metal sites and widened pores and

expectedly, hierarchically porous MIL-88Bs synthesized with an Fe:BDC ratio of 3 have the narrowest band width which is in line with our conclusions. Peaks neither at 1063 nor at 2861 cm^{-1} are present which proved that DMF molecules are successfully removed from the pores. There are no peaks at 1704 cm^{-1} in the FTIR spectra of hierarchically porous MIL-88Bs synthesized at 110 °C which is attributed to free BDC acid and absence of this peak indicates that almost all H_2BDC is deprotonated. In the meantime, FTIR spectra of hierarchically porous MIL-88Bs synthesized at 130 °C and 150 °C consist the peak at 1704 cm^{-1} which indicates that there are some free BDC acid left in the structure and complete deprotonation of H_2BDC cannot be achieved. Different from MIL-88B-150-1 and MIL-88B-150-3, MIL-88B-150-5 has peaks at 1647 cm^{-1} which is associated with C=O asymmetric stretching mode of DMF. Having no peak at 1647 cm^{-1} confirms the successful removal of DMF molecules from the pores of MIL-88B-150-1 and MIL-88B-150-3. Peaks in between the wavelength range of 1300 and 1650 cm^{-1} are the characteristic peaks of crystalline state carboxylic acids and proves that the skeletal of hierarchically porous MIL-88Bs are formed successfully. Peaks at 1385 and 1589 cm^{-1} prove terephthalic acid is attached to metal center. Additionally, the peak at 1107 cm^{-1} is assigned to C-O-Fe stretching mode and confirms the attachment of terephthalic acid to iron. Lastly, the peaks at 742 and 823 cm^{-1} prove Fe is successfully coordinated with BDC. Lastly, by comparing the FTIR spectrum of hierarchically porous MIL-88Bs with FTIR spectra of $FeCl_3.6H_2O$ we have shown that there are no metallic iron present. None of the peaks (842 cm^{-1}, 1594 cm^{-1}, 2993 cm^{-1}, 3212 cm^{-1}, and 3523 cm^{-1}) characteristic of $FeCl_3.6H_2O$ were observed in the FTIR spectrum of hierarchically porous MIL-88Bs.

4.3.5. TGA Analysis

Figure 64 shows the TGA curves of hierarchically porous MIL-88Bs. TGA analysis reveals that thermally stable hierarchically porous MIL-88Bs are formed. Percentage of residual mass left at the end of TGA and decomposition temperatures are illustrated at Table 17 and 18, respectively.

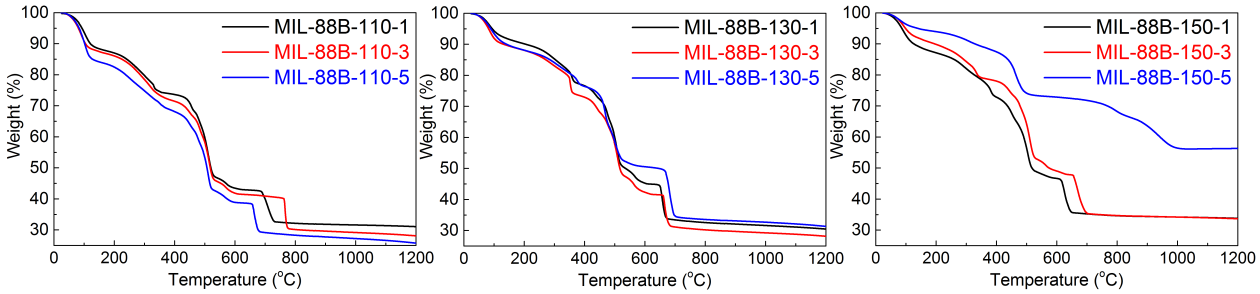

Figure 64. TGA curves of hierarchically porous MIL-88Bs.

Several mass losses occur as temperature increases from 25 °C to 1200 °C. The first mass loss is attributed to adsorbed and coordinated water and DMF molecules. The second mass loss is attributed to trapped solvent molecules inside the pores. Third mass loss is due to decomposition of terephthalic acid which results in structure collapse. And, lastly the fourth step is attributed to CO_2 release as a consequence of carboxylate decomposition. Hierarchically porous MIL-88Bs synthesized with an Fe:BDC ratio of 1 and 5 decompose nearly at the same temperature while MIL-88B-110-3 achieves the highest thermal stability. Fraction of mass left at the end of TGA is almost similar in hierarchically porous MIL-88Bs synthesized with an Fe:BDC ratio of 1 and 3 whereas residual mass increases drastically in MIL-88B-150-5.

Table 17. Percentage of residual mass, %

Hierarchically porous MIL-88Bs [a]	110 °C	130 °C	150 °C
M/L 1	31.0	30.5	33.8
M/L 3	28.1	28.1	33.6
M/L 5	25.7	31.3	56.3

[a] Synthesis temperature, metal to linker ratio (M/L)

Table 18. Decomposition temperature, °C

Hierarchically porous MIL-88Bs [a]	110 °C	130 °C	150 °C
M/L 1	380	392	404
M/L 3	448	384	442.4
M/L 5	387	405	-

[a] Synthesis temperature, metal to linker ratio (M/L)

Moreover, TGA analysis show that hierarchically porous MIL-88Bs synthesized in this study are thermally stable under adsorption process conditions.

4.3.6. CO_2 Adsorption Studies

Differently synthesized hierarchically porous MIL-88Bs show differences in their CO_2 uptake capacities. Isotherms illustrate the rapidly increased CO_2 uptake capacities in between 0 and 3 bars. For pressures greater than 3 bar, CO_2 adsorption rate decreases, which can be attributed to the relatively low pore volume of the synthesized hierarchically porous MIL-88Bs. Calculated Langmuir and Freundlich isotherm parameters, respective equations of the fitted experimental data, coefficient of determination value (R^2) and respective comparison of experimental data and nonlinear fitting of the Langmuir and Freundlich models can be found below.

Langmuir Model:

$$\frac{C_e}{q_e} = \frac{1}{KQ^0} + \frac{C_e}{Q^0} \tag{4.1}$$

Freundlich Model:

$$logq_e = logK_F + \frac{1}{n} logC_e \tag{4.2}$$

Table 19. Respective equations obtained from models

Hierarchically porous MIL-88Bs	Langmuir Model	Freundlich Model
MIL-88B-110-1	$y = 0.2396x+586.96$ $R^2 = 0.9986$	$y = 0.5429x-1.5641$ $R^2 = 0.9588$
MIL-88B-110-3	$y = 0.2714x+627.75$ $R^2 = 0.9989$	$y = 0.5883x-1.749$ $R^2 = 0.9642$
MIL-88B-110-5	$y = 0.2758x+740.17$ $R^2 = 0.998$	$y = 0.559x-1.6988$ $R^2 = 0.9657$
MIL-88B-130-1	$y = 0.4109x+820.32$ $R^2 = 0.9972$	$y = 0.5708x-1.8328$ $R^2 = 0.9638$
MIL-88B-130-3	$y = 0.4216x+733.36$ $R^2 = 0.9979$	$y = 1.3041x-4.3203$ $R^2 = 0.8474$
MIL-88B-130-5	$y = 0.5134x+1110.4$ $R^2 = 0.996$	$y = 0.5372x-1.8407$ $R^2 = 0.9989$
MIL-88B-150-1	$y = 0.3062x+705.14$ $R^2 = 0.9986$	$y = 0.5332x-1.6231$ $R^2 = 0.9578$
MIL-88B-150-3	$y = 0.3774x+935.51$ $R^2 = 0.997$	$y = 0.9251x-3.0943$ $R^2 = 0.9206$
MIL-88B-150-5	$y = 0.3776x+1095.3$ $R^2 = 0.9977$	$y = 0.5639x-1.871$ $R^2 = 0.9663$

Table 20. Langmuir and Freundlich isotherm parameters

MOF	Langmuir	Freundlich
MIL-88B-110-1	Q_m= 4.17 mmol/g	K_F= 0.0273
	K_a= 4.082E-04	η_F= 1.842
	R^2= 0.9986	R^2= 0.9588
MIL-88B-110-3	Q_m= 3.68 mmol/g	K_F= 0.0178
	K_a= 4.3E-04	η_F= 1.699
	R^2= 0.9989	R^2= 0.9642
MIL-88B-110-5	Q_m= 3.63 mmol/g	K_F= 0.020
	K_a= 3.7E-04	η_F= 1.789
	R^2= 0.998	R^2=0.9657
MIL-88B-130-1	Q_m= 2.43 mmol/g	K_F= 0.0147
	K_a= 5.01E-04	η_F= 1.752
	R^2= 0.9972	R^2= 0.9638
MIL-88B-130-3	Q_m= 2.37 mmol/g	K_F= 4.78E-05
	K_a= 5.7E-04	η_F= 0.766
	R^2= 0.9979	R^2= 0.8474
MIL-88B-130-5	Q_m= 1.95 mmol/g	K_F= 0.0144
	K_a= 4.6E-04	η_F= 1.862
	R^2= 0.996	R^2= 0.9731
MIL-88B-150-1	Q_m= 3.27 mmol/g	K_F=0.0238
	K_a= 4.34E-04	η_F=1.875
	R^2= 0.9986	R^2=0.9578
MIL-88B-150-3	Q_m= 2.649 mmol/g	K_F= 8.05E-04
	K_a= 4.03E-04	η_F= 1.081
	R^2= 0.997	R^2= 0.9206
MIL-88B-150-5	Q_m= 2.648 mmol/g	K_F= 0.0135
	K_a= 3.44E-04	η_F= 1.77
	R^2= 0.9977	R^2= 0.9663

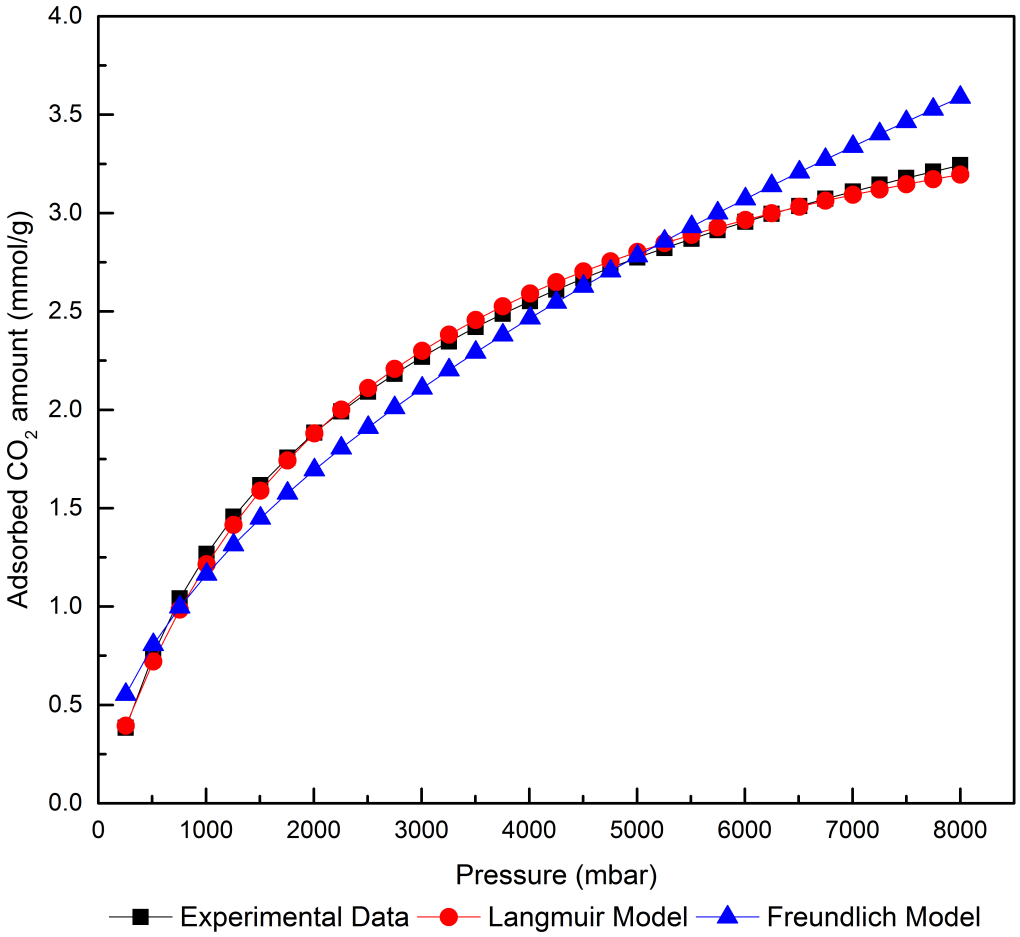

Figure 65. Comparison of experimental data and nonlinear fitting of Langmuir and Freundlich model of MIL-88B-110-1.

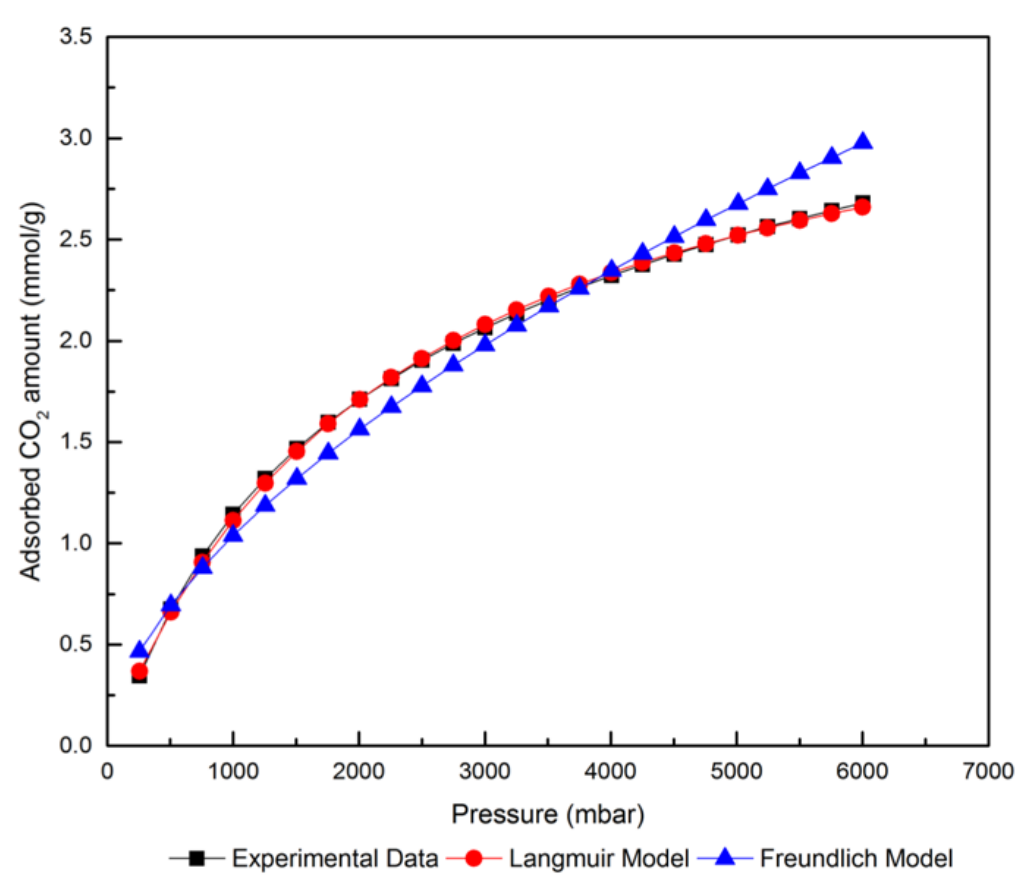

Figure 66. Comparison of experimental data and nonlinear fitting of Langmuir and Freundlich model of MIL-88B-110-3.

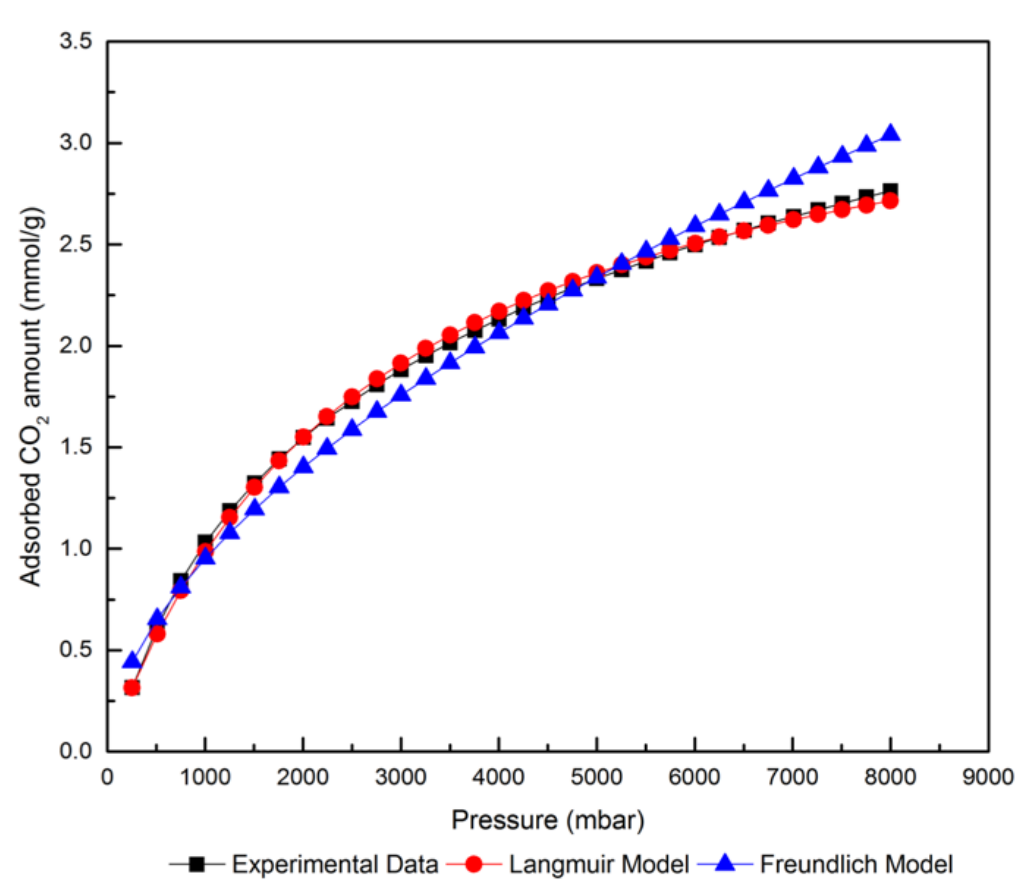

Figure 67. Comparison of experimental data and nonlinear fitting of Langmuir and Freundlich model of MIL-88B-110-5.

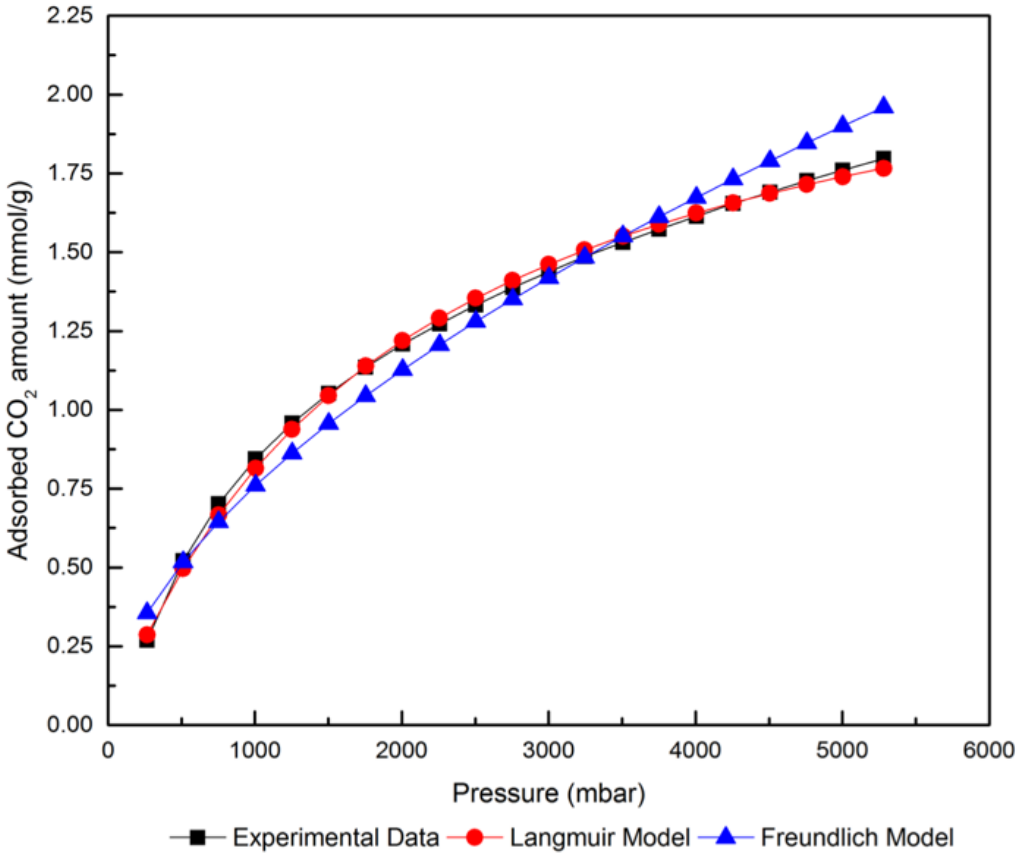

Figure 68. Comparison of experimental data and nonlinear fitting of Langmuir and Freundlich model of MIL-88B-130-1.

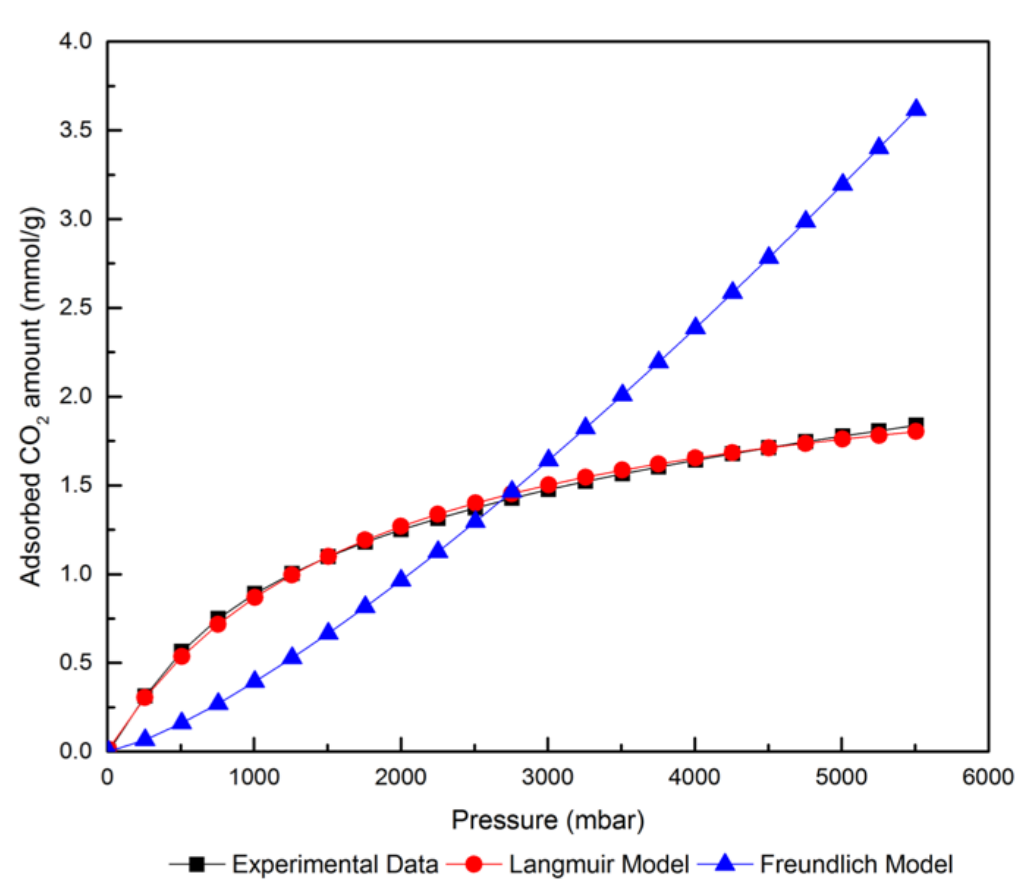

Figure 69. Comparison of experimental data and nonlinear fitting of Langmuir and Freundlich model of MIL-88B-130-3.

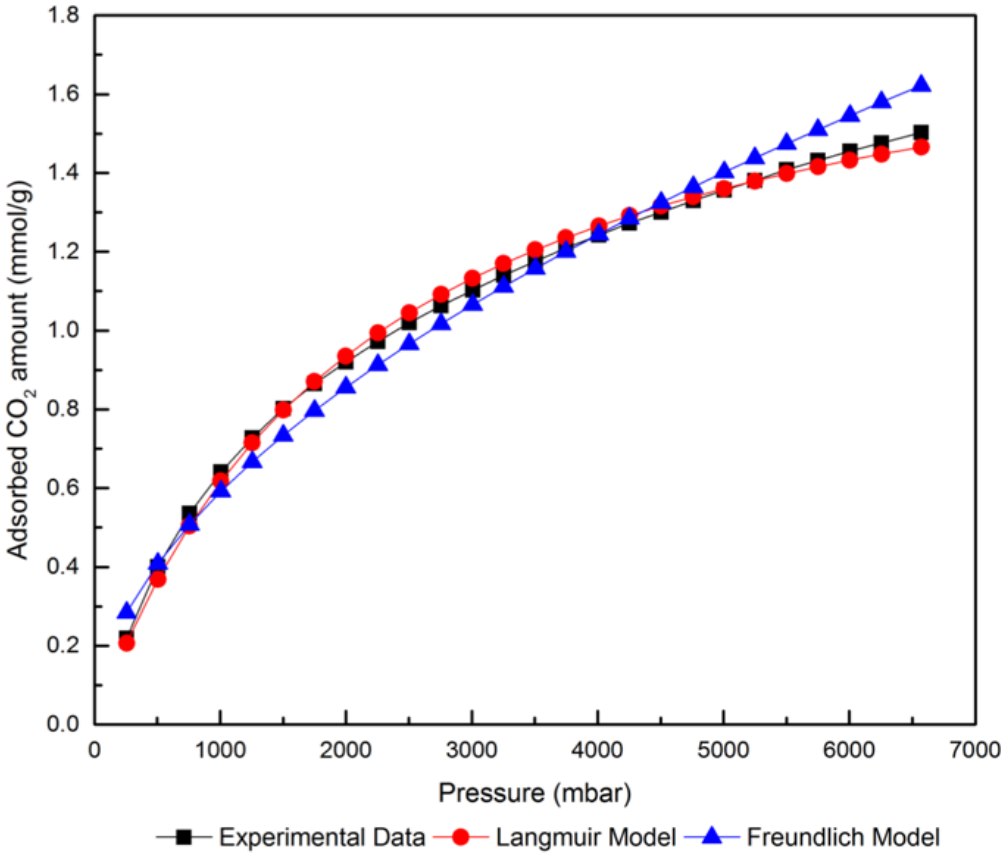

Figure 70. Comparison of experimental data and nonlinear fitting of Langmuir and Freundlich model of MIL-88B-130-5.

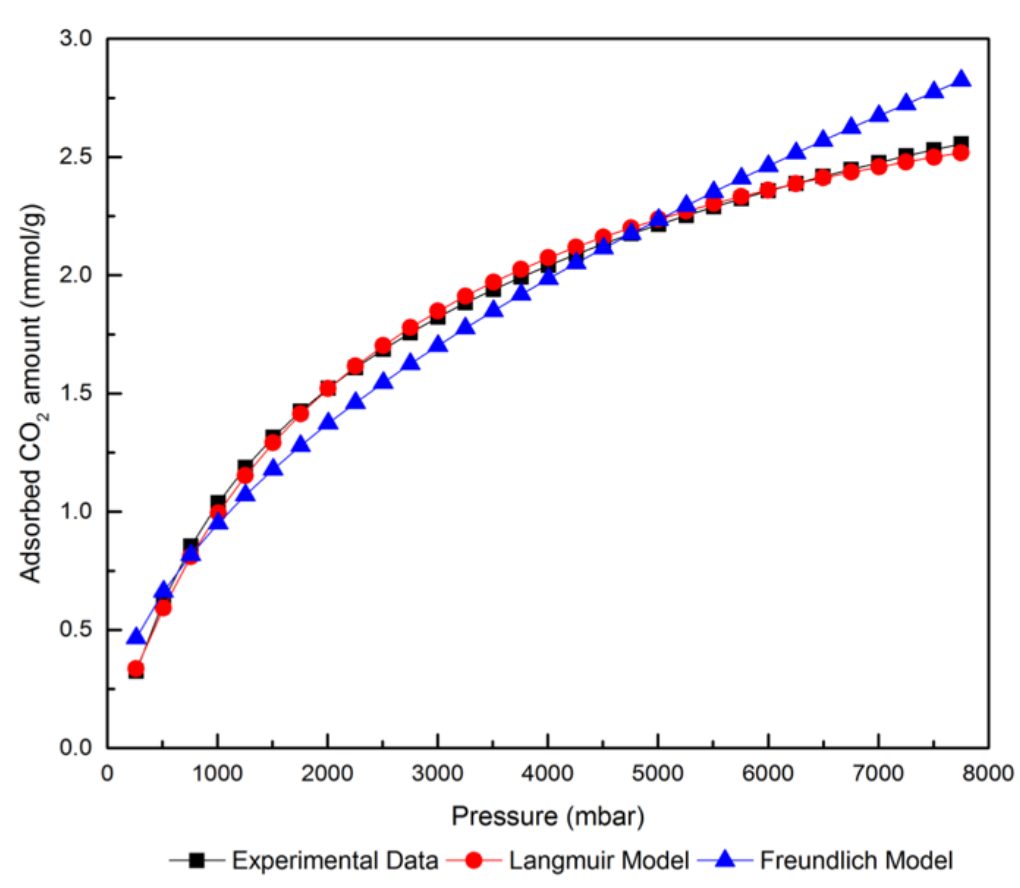

Figure 71. Comparison of experimental data and nonlinear fitting of Langmuir and Freundlich model of MIL-88B-150-1.

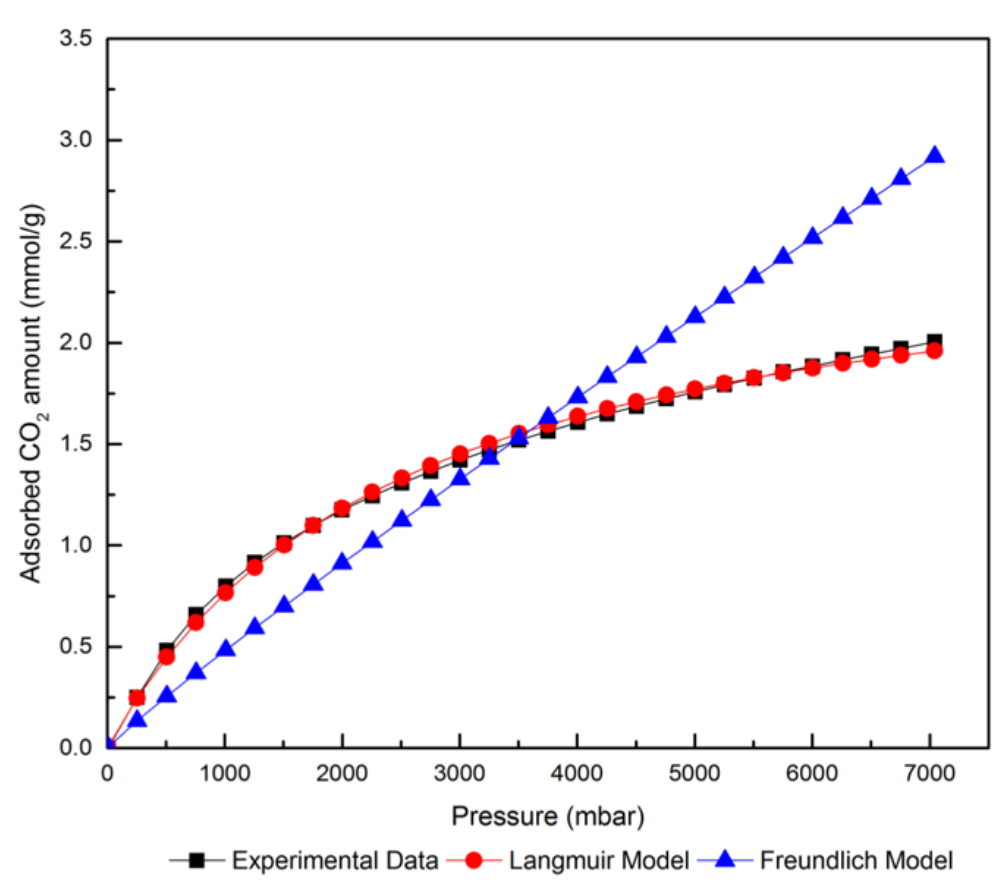

Figure 72. Comparison of experimental data and nonlinear fitting of Langmuir and Freundlich model of MIL-88B-150-3.

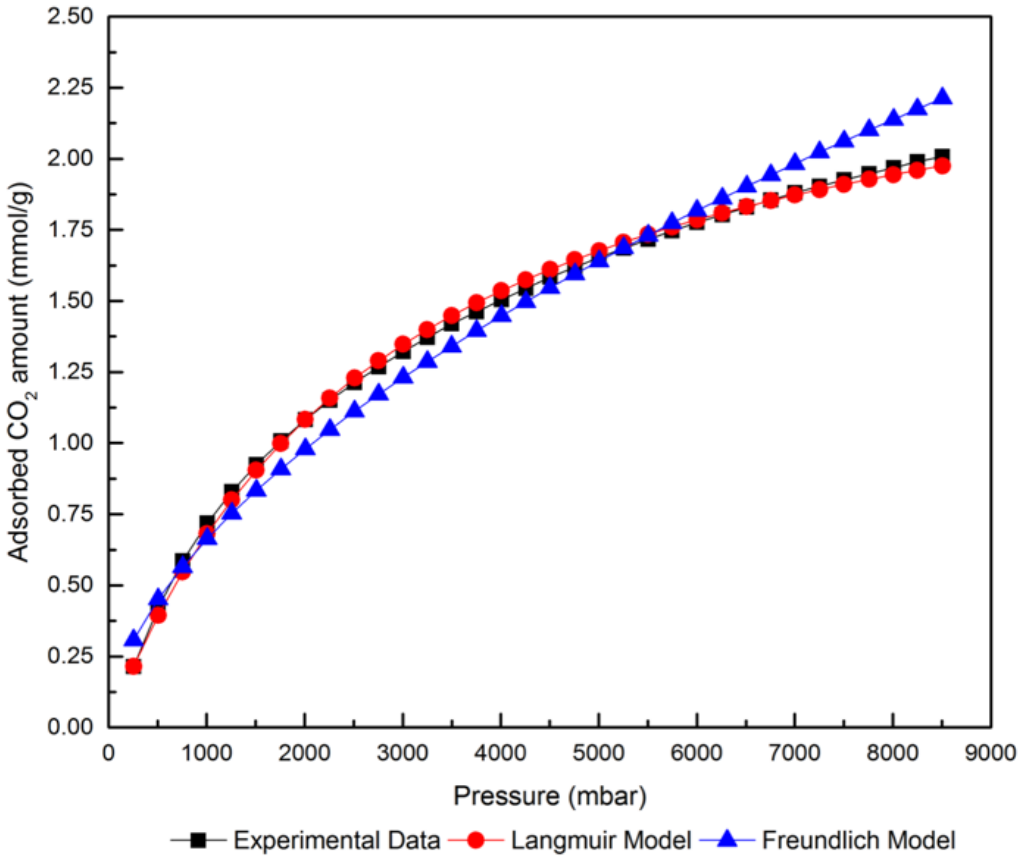

Figure 73. Comparison of experimental data and nonlinear fitting of Langmuir and Freundlich model of MIL-88B-150-5.

Table 21. Respective model and monolayer capacity of the hierarchically porous MIL-88Bs

Hierarchically porous MIL-88Bs	Model	Monolayer Capacity (mol/kg)
MIL-88B-110-1	Langmuir	4.17
MIL-88B-110-3	Langmuir	3.68
MIL-88B-110-5	Langmuir	3.63
MIL-88B-130-1	Langmuir	2.43
MIL-88B-130-3	Langmuir	2.37
MIL-88B-130-5	Langmuir	1.95
MIL-88B-150-1	Langmuir	3.27
MIL-88B-150-3	Langmuir	2.65
MIL-88B-150-5	Langmuir	2.64

The best fit is obtained with the Langmuir model with a relatively high coefficient of determination value. Hierarchically porous MIL-88Bs follow the Langmuir adsorption model, at which adsorption of CO_2 molecules on the surface is homogeneous and monolayer coverage is obtained (Lowell et al., 2004a). Estimated monolayer capacities of hierarchically porous MIL-88Bs and the adsorption model of the synthesized hierarchically porous MIL-88Bs are presented. Hierarchically porous MIL-88Bs show different monolayer capacities. It is certain that Fe:BDC ratio and synthesis temperature have significant effect on the textural porosity of hierarchically porous MIL-88Bs, which in turn affect the CO_2 adsorption capacities. Table 22 presents measured CO_2 uptake capacities at 298 K and 1, 3, and 5 bar, respectively. The CO_2 adsorption isotherms of hierarchically porous MIL-88Bs can be found in Figure 74.

Table 22. CO_2 uptake capacities of hierarchically porous MIL-88Bs at 1, 3 and 5 bar and 25 °C

MOF	CO_2 uptake capacity at 1 bar (mol/kg)	CO_2 uptake capacity at 3 bar (mol/kg)	CO_2 uptake capacity at 5 bar (mol/kg)	BET Surface Area (m^2/g)	Micropore Volume
MIL-88B-110-1	1.27	2.27	2.77	400.4±1.1E1	0.182±1.4E-2
MIL-88B-110-3	1.14	2.07	2.52	452.4±1.9E1	0.239±3.2E-2
MIL-88B-110-5	1.03	1.88	2.33	445.9±1.9E1	0.202±3.2E-2
MIL-88B-130-1	0.84	1.44	1.76	265.4±2.6E1	0.113±6.5E-3
MIL-88B-130-3	0.89	1.48	1.78	249.4±1.6E1	0.115±1.6E-2
MIL-88B-130-5	0.64	1.10	1.36	283.1±2.6E1	0.108±2.8E-3
MIL-88B-150-1	1.04	1.82	2.21	357.1±7.8E1	0.143±4.6E-2
MIL-88B-150-3	0.80	1.42	1.76	346.3±1.7E1	0.140±2.2E-2
MIL-88B-150-5	0.72	1.32	1.65	117.7±1.9	0.0350±9.0E-3

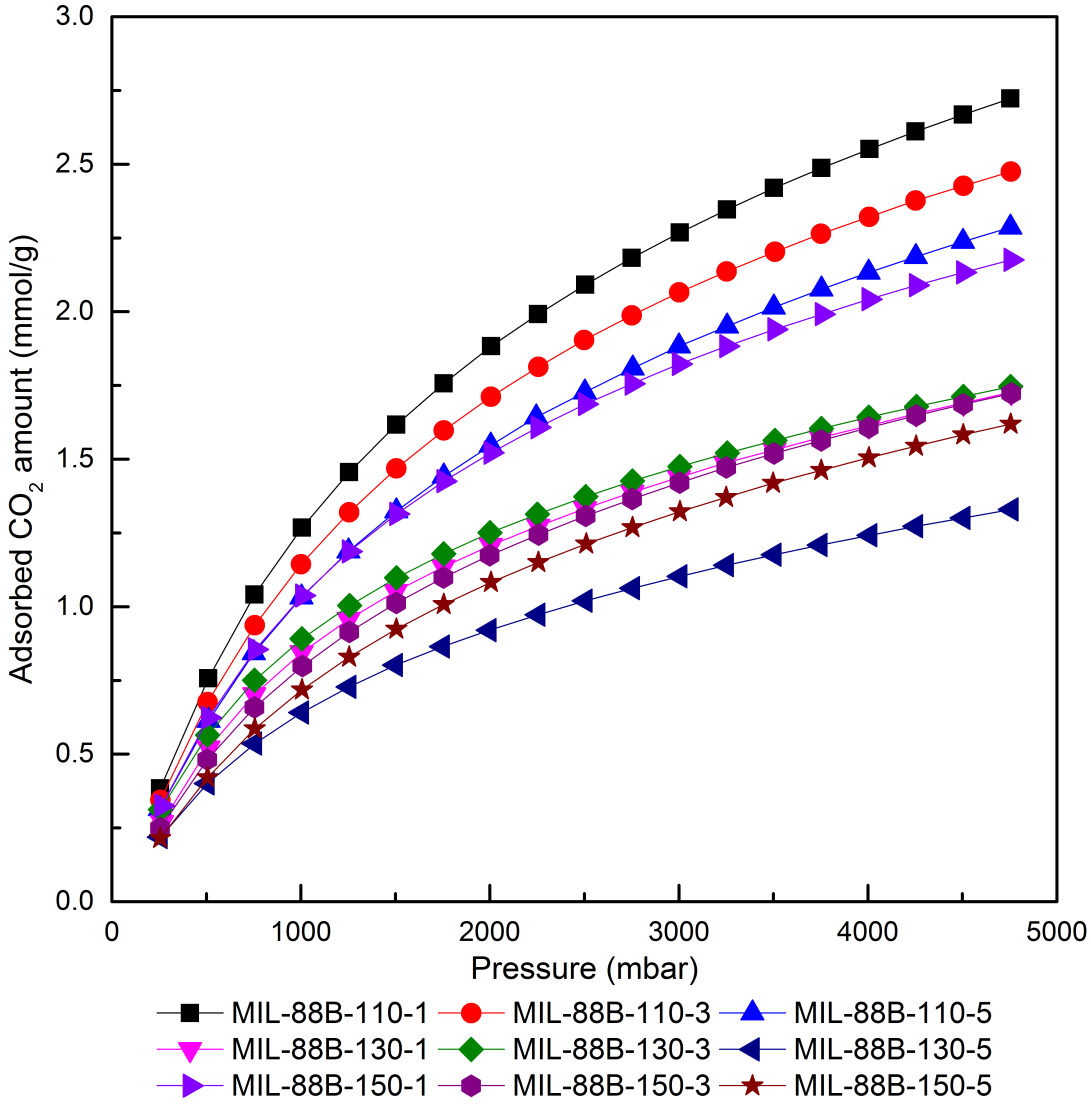

Figure 74. CO_2 adsorption isotherm of hierarchically porous MIL-88Bs measured at 298 K.

At 1, 3, and 5 bar and 298 K, the highest CO_2 uptake capacity is achieved by MIL-88B-110-1 while the lowest CO_2 uptake capacity belongs to MIL-88B-130-5. Even though MIL-88B-110-3 possesses the highest micropore volume (0.239 cm^3/g) and BET surface area (452.4 m^2/g), its CO_2 adsorption capacity (2.52 mol/kg) is lower than the CO_2 uptake capacity of MIL-88B-110-1(2.77 mol/kg) measured at 5 bar and 298 K.

In addition, the lowest micropore volume (0.0355 cm^3/g) and the lowest BET surface area (117.7 m^2/g) belongs to MIL-88B-150-5. However, MIL-88B-150-5 possesses a CO_2 adsorption capacity higher (1.65 mol/kg, measured at 5 bar and 298 K) than MIL-88B-130-

5 (1.36 mol/kg, measured at 5 bar and 298 K) which reveals that there is no direct relation between the micropore volume and the CO_2 uptake capacity exists.

To investigate the relation between the CO_2 adsorption capacity with BET surface area, narrow micro-, micro-, meso- and total pore volume, adsorbed CO_2 amount is plotted with respect to BET surface area, narrow micro-, micro-, meso- and total pore volume which can be found below in Figure 75-79. Mesopore volume (R^2: 0.32), total pore volume (R^2: 0.1975) and BET surface area (R^2: 0.5171) are found out to be weakly correlated with the CO_2 adsorption capacity which illustrates that there is no direct relation between these parameters and the CO_2 uptake capacity of hierarchically porous MIL-88Bs.

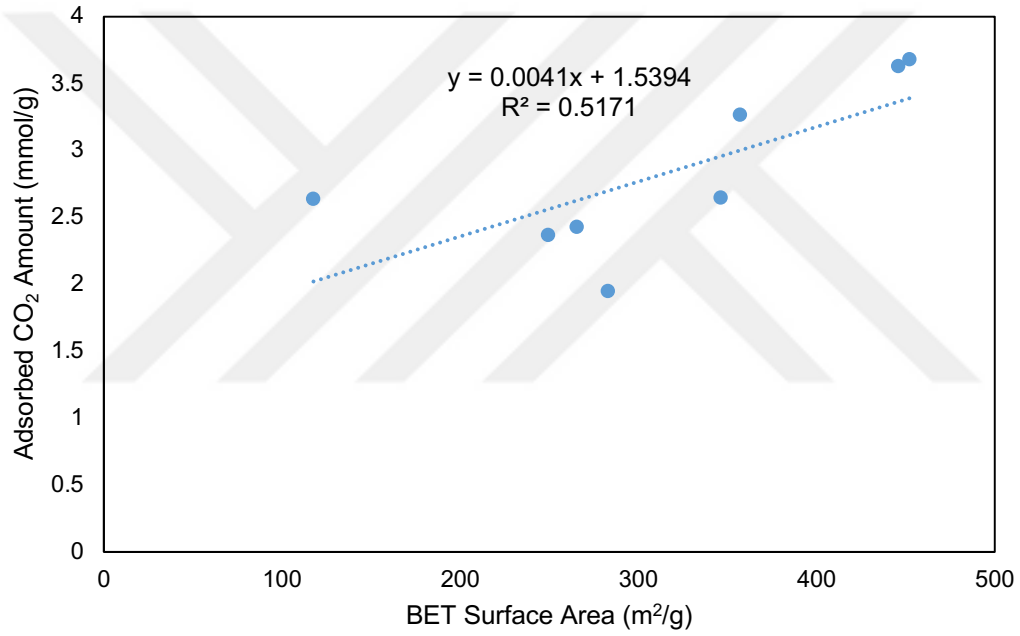

Figure 75. Dependence of CO_2 adsorption capacity on BET surface area.

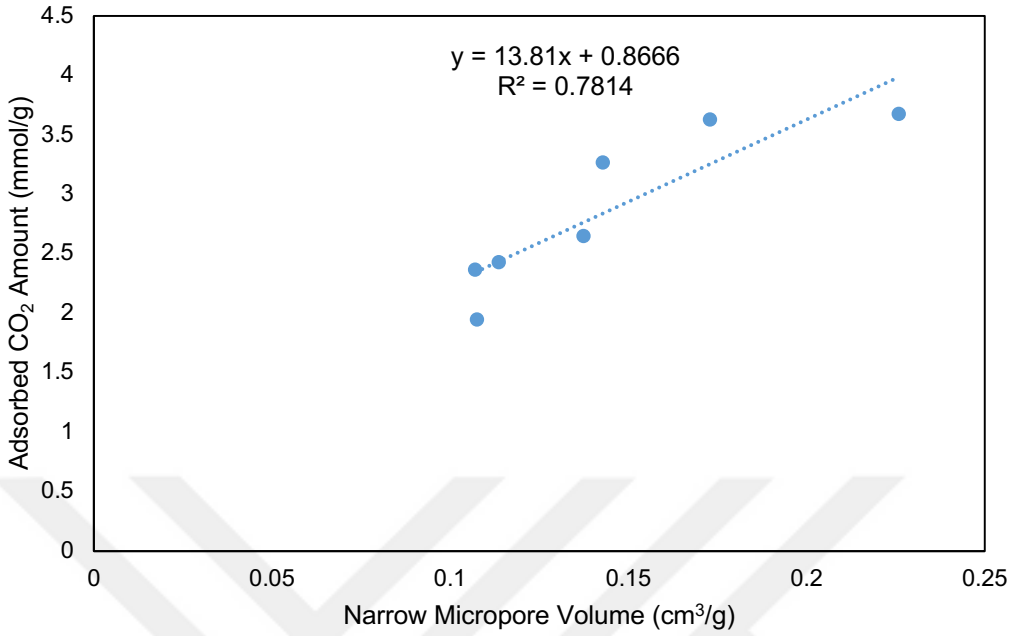

Figure 76. Dependence of CO_2 adsorption capacity on volume of narrow micropores.

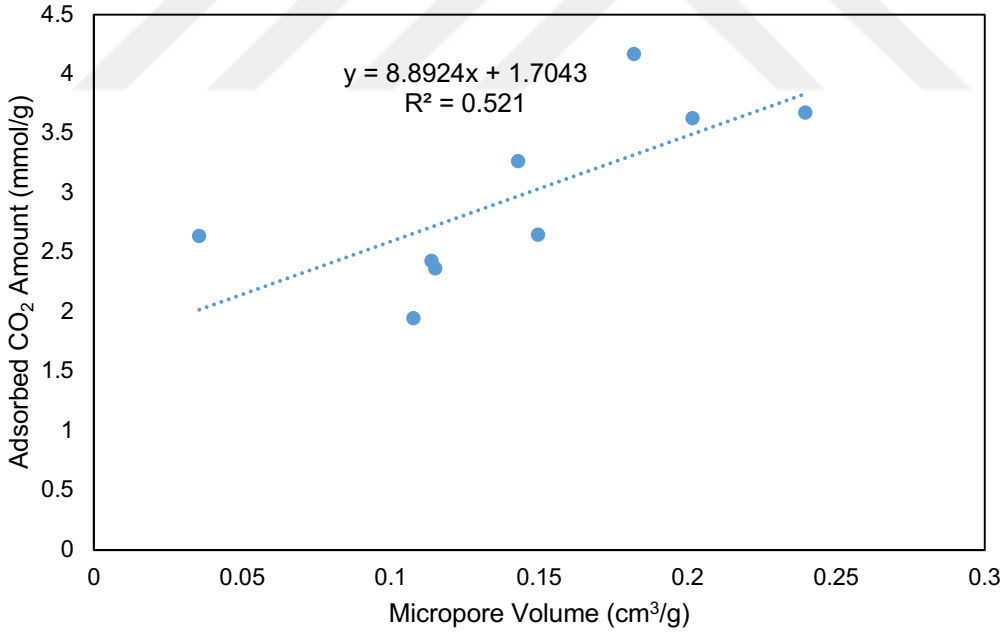

Figure 77. Dependence of CO_2 adsorption capacity on micropore volume.

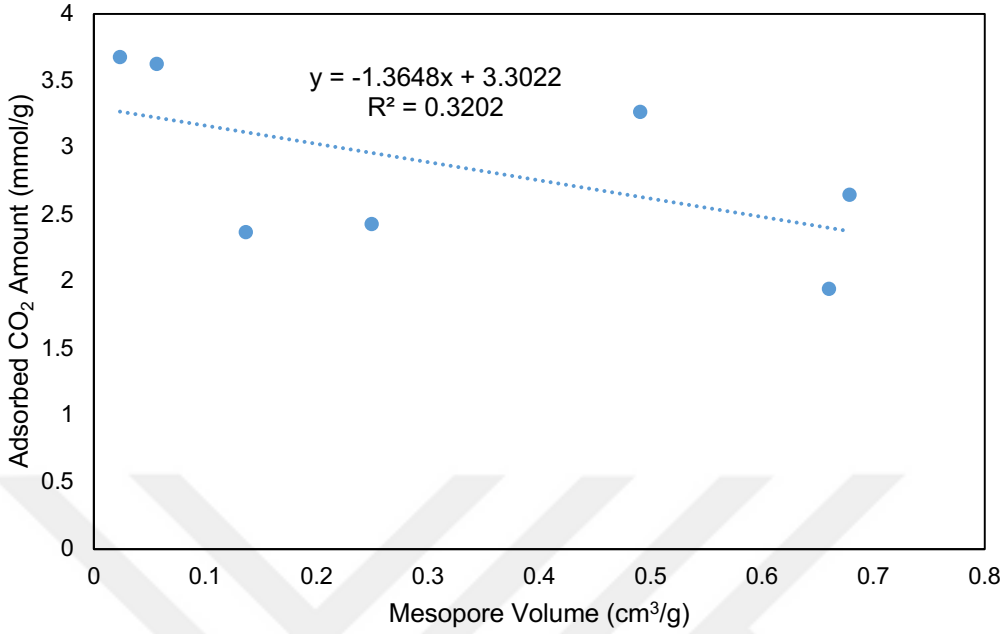

Figure 78. Dependence of CO_2 adsorption capacity on mesopore volume.

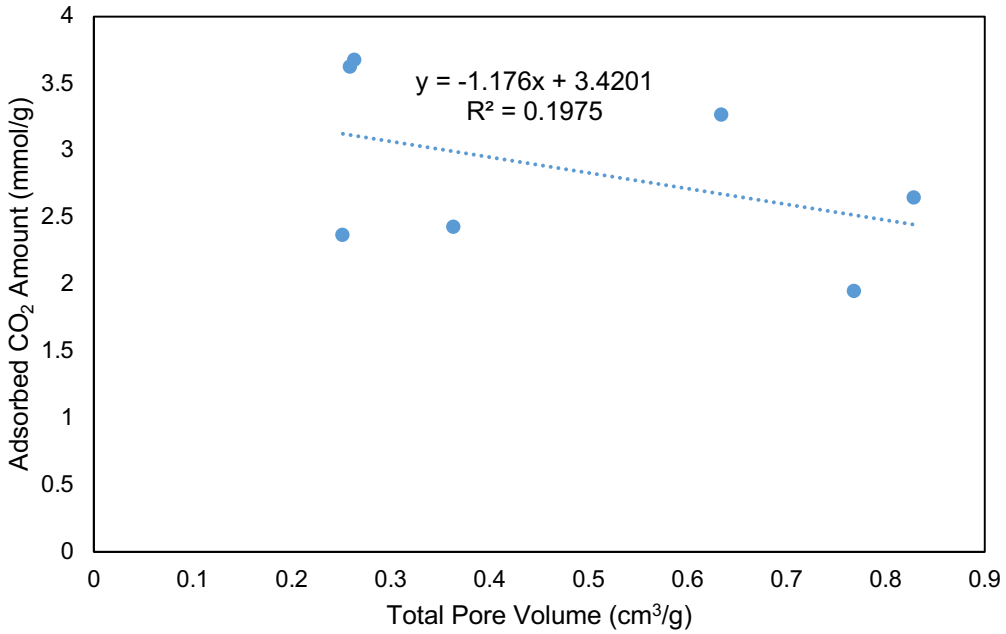

Figure 79. Dependence of CO_2 adsorption capacity on total pore volume.

Among the various parameters examined, the strongest correlation is in between the CO_2 adsorption capacity and the volume of narrow micropores (R^2: 0.78). However, a R^2 value very close to 1 cannot be achieved which reveals that there may be some other

parameters affecting the CO_2 uptake capacity in addition to the volume of pores narrower than 1 nm.

The highest fraction of microporosity is achieved when hierarchically porous MIL-88Bs were synthesized at 110 °C. However, when synthesis was conducted at temperatures higher than 110 °C, textural mesopores widen and the fraction of textural mesoporosity increases. In accordance with the increased pore diameter, CO_2 uptake capacity is expected to decrease. However, MIL-88B-150-1 shows a greater CO_2 uptake capacity (2.21 mol/kg, measured at 5 bar and 298 K) than MIL-88B-130-1 (1.76 mol/kg, measured at 5 bar and 298 K).

Even though the highest micropore volume is achieved by MIL-88B-110-3 (0.239 cm3/g), its sorption capacity (2.52 mol/kg, measured at 5 bar and 298 K) is lower than the sorption capacity of MIL-88B-110-1 (2.77 mol/kg, measured at 5 bar and 298 K) which makes us focus on the micropore size distribution of MIL-88B type MOF crystallites. Table 23 illustrates volume of pores narrower than 1 and 2 nm, ratio of pore volumes of pores narrower than 1 nm to 2 nm, and CO2 uptake capacity of MIL-88B type MOF crystallites at 5 bar.

Table 23. Pore volumes, pore volume ratios, and CO_2 uptake capacity of hierarchically porous MIL-88Bs

Hierarchically porous MIL-88Bs	Vpores < 1 nm (cm^3/g)	Vpores < 2 nm (cm^3/g)	Ratio of Vpores < 1 nm to Vpores < 2 nm[a]	CO_2 uptake capacity at 5 bar (mol/kg)
MIL-88B-110-1	0.177±1.7E-2	0.182±1.4E-2	0.97	2.77
MIL-88B-110-3	0.226±1.2E-2	0.239±3.2E-2	0.94	2.52
MIL-88B-110-5	0.172±1.7E-2	0.202±3.2E-2	0.85	2.33
MIL-88B-130-1	0.113±1.6E-2	0.1137±6.5E-3		1.76
MIL-88B-130-3	0.107±2.6E-2	0.115±1.6E-2	0.93	1.78
MIL-88B-130-5	0.108±1.1E-2	0.108±2.8E-3		1.36
MIL-88B-150-1	0.142±3.7E-2	0.143±4.6E-2		2.21
MIL-88B-150-3	0.137±3.2E-2	0.149±2.2E-2	0.916	1.76
MIL-88B-150-5	0.023±1.8E-2	0.0355±9.0E-3	0.65	1.65

[a] Volume ratio of pores smaller than 1 nm to 2 nm

The highest pore volume of 0.82 cm^3/g belongs to MIL-88B-150-3 while its CO_2 uptake capacity (1.76 mol/kg) is lower than MIL-88B-110-1 (2.77 mol/kg, measured at 5 bar and 298 K) which has considerably lower pore volume (0.20 cm^3/g). A similar trend is observed for MIL-88B-110-3 (2.52 mol/kg, measured at 5 bar and 298 K). Despite its high micropore volume (0.239 cm^3/g) and total pore volume (0.249 cm^3/g), the CO_2 uptake capacity of MIL-88B-110-3 (2.52 mol/kg, measured at 5 bar and 298 K) is lower than the CO_2 adsorption capacity of MIL-88B-110-1 (2.77 mol/kg, measured at 5 bar and 298 K). Apparently, hierarchically porous MIL-88Bs that possess higher pore volumes for pores narrower than 1 nm achieve higher CO_2 uptake capacities. This enhanced adsorption capacity is attributed to high CO_2 adsorption potential of narrow micropores (pore diameters < 1 nm) (Fonseca, Gutierrez, & Lueking, 2008; Romanos et al., 2012).

Among the hierarchically porous MIL-88Bs synthesized at different temperatures with different Fe:BDC ratios, hierarchically porous MIL-88Bs synthesized at 110 °C show higher CO_2 adsorption capacities than hierarchically porous MIL-88Bs synthesized at 130

and 150 °C. As mentioned above, synthesizing hierarchically porous MIL-88Bs at 110 °C leads to highly microporous hierarchically porous MIL-88Bs to form. Pores narrower than 1 nm dominate the micropore size distribution whose volumes correspond to 97, 94 and 85% of the micropore volume of MIL-88B-110-1, MIL-88B-110-3, and MIL-88B-110-5, respectively. Surprisingly, MIL-88B-110-1 achieves a CO_2 adsorption capacity (2.77 mol/kg, measured at 5 bar and 298 K) higher than MIL-88B-110-3 (2.52 mol/kg, measured at 5 bar and 298 K) whose volume of narrow micropores (0.177 cm^3/g) is lower than the volume of narrow micropores of MIL-88B-110-3 (0.226 cm^3/g). This high CO_2 adsorption capacity of MIL-88B-110-1 is attributed to its high fraction of narrow micropores (97%) present in its micropore size distribution. Pore volumes narrower than 1 nm and 2 nm are illustrated at Figure 80.

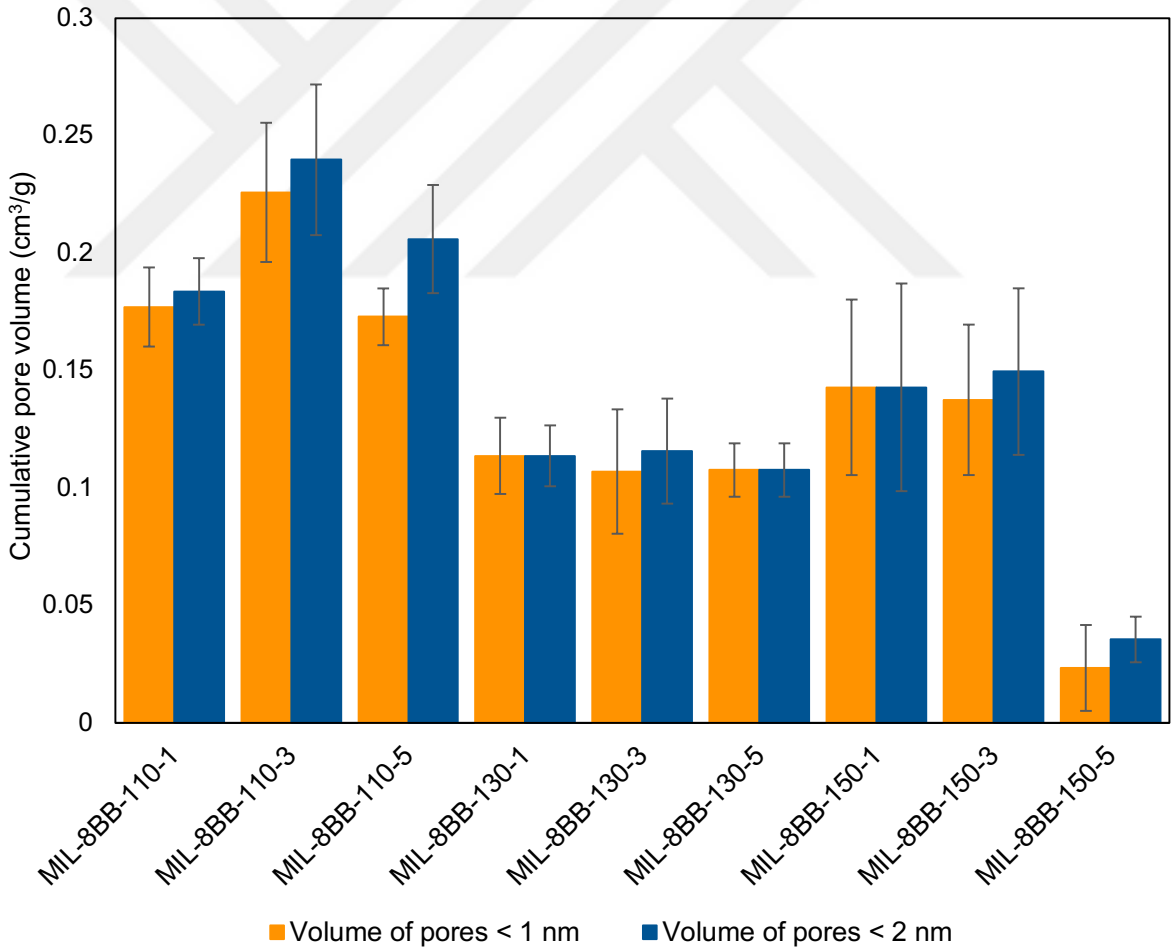

Figure 80. Volume of pores narrower than 1 and 2 nm reported with standard deviations.

Order of CO_2 uptake capacity from the highest to the lowest is in the order of the highest to the lowest volume of pores narrower than 1 nm. CO_2 adsorption capacity increases as the volume of narrow micropores increase. The volume of narrow micropores present in hierarchically porous MIL-88Bs synthesized at 110 °C is higher than the volumes of narrow micropores present in hierarchically porous MIL-88Bs synthesized at 130 and 150 °C. Meanwhile, the CO_2 uptake capacities of hierarchically porous MIL-88Bs synthesized at 150 °C are lower than the CO_2 uptake capacities of hierarchically porous MIL-88Bs synthesized at 110 °C. It is important to note that, even though, MIL-88B-150-3 possesses a greater micropore volume (0.149 cm^3/g) than MIL-88B-150-1 (0.142 cm^3/g), narrow micropores present in MIL-88B-150-1 provide these crystallites achieve a higher CO_2 uptake capacity (2.21 mol/kg) than MIL-88B-150-3 (1.76 mol/kg) at 5 bar and 298 K. Volume of the pores narrower than 1 nm is almost equal in MIL-88B-130-3 and MIL-88B-130-5. However, MIL-88B-130-3 possesses a CO_2 adsorption capacity higher (1.78 mol/kg) than MIL-88B-130-5 (1.36 mol/kg) at 5 bar and 298 K. When examined in more detail, it is observed that MIL-88B-130-3 has a cumulative pore volume of 0.104 cm^3/g for pores narrower than 0.7 nm. Meanwhile, the cumulative pore volume of pores narrower than 1 nm in MIL-88B-130-5 is 0.108 cm^3/g. Although, MIL-88B-130-3 and MIL-88B-130-5 possess similar pore volumes for pores narrower than 1 nm, the CO_2 uptake capacity of MIL-88B-130-3 is 1.31 times higher than the CO_2 uptake capacity of MIL-88B-130-5. Thereby, we concluded that it is not only the volume of micropores narrower than 1 nm affecting the CO_2 adsorption capacity, but also the volume of pores with pore diameters ranging in between 0.5 and 0.7 nm that heavily influences the CO_2 adsorption capacity.

These results simply indicate that as opposed to BET surface area, mesopore volume and total pore volume, volume of pores narrower than 1 nm and their distribution within the micropore size range affect the CO_2 uptake capacity.

The significance of pores being narrower than 1 nm lies behind their increased binding energies. As pore sizes decrease, their binding energies increase (Fonseca et al., 2008; Romanos et al., 2012). The overlapped adsorption potentials cause ultramicropores to attract CO_2 molecules stronger. In fact, deep well potential is created when the interaction potentials of opposite ultramicropore walls overlap, which attracts CO2 molecules more strongly (Ello et al., 2013). Thus, a narrower micropore size distribution and higher fraction of narrow micropores enables higher CO2 uptake capacities to be attained.

4.4. Comparison with Literature

Several MOFs with high BET surface areas have been investigated for their CO_2 uptake capacities. In line with our results, in this study BET surface area was not the main factor enhancing CO_2 adsorption capacities. For instance, at 1 bar and 298 K MOF-177 with 5400 m^2/g of BET surface area possessed 3.6 wt.% CO_2 uptake capacity (Mason et al., 2011a); MOF-5 with 2833 m^2/g BET surface area possessed 4.5 wt.% CO_2 uptake capacity (Millward & Yaghi, 2005b); IRMOF-3 with 2160 m^2/g BET surface area had 5.1 wt.% CO_2 uptake capacity (Millward & Yaghi, 2005b); IRMOF-6 with 2516 m^2/g BET surface area had 5.1 wt.% CO_2 uptake capacity (Millward & Yaghi, 2005b); ZIF-8 with 1135 m^2/g BET surface area possessed 4.3 wt.% CO_2 uptake capacity (A. O. Yazaydin et al., 2009); MIL-101(Cr) with 2674 m^2/g BET surface area had 4.2 wt.% CO_2 adsorption capacity (Chowdhury, Bikkina, & Gumma, 2009); and lastly UMCM-1 with 4034 m^2/g BET surface area had 3.8 wt.% CO_2 adsorption capacity (A. O. Yazaydin et al., 2009). Additionally, to the best of our knowledge the obtained CO_2 adsorption capacity of MIL-88B type MOF crystallites in the present study is greater than those of IRMOF-6 (Millward & Yaghi, 2005b), MIL-101(Cr) (B. Wang et al., 2008), MIL-102 (Phan et al., 2010), MOF-2 (Millward & Yaghi, 2005b), ZIF-8 (Mason et al., 2011a), ZIF-71 (A. O. Yazaydin et al., 2009), ZIF-95 (Frost et al., 2006a), ZIF-97 (Frost et al., 2006a) and ZIF-100 (Trickett et al., 2017). Figure 81 illustrates the CO_2 adsorption capacity (wt. %) of several reported MOFs.

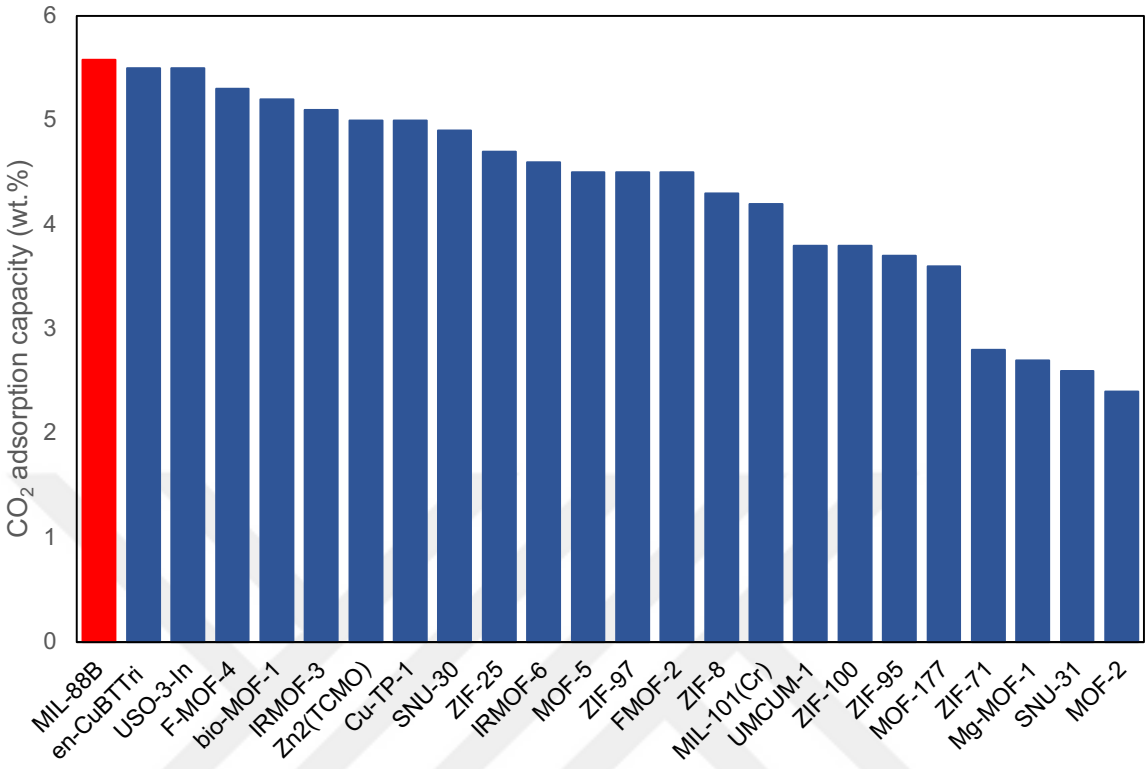

Figure 81. CO_2 uptake capacity of some of the MOFs reported in literature and MIL-88B (shown in red) reported in this report (at 1 bar and 298 K).

In comparison to the mentioned MOFs, hierarchically porous MIL-88Bs synthesized with a relatively short linker (BET surface area: 400.4 m^2/g) possess a relatively higher CO_2 uptake capacity than the reported ones (the CO_2 uptake capacity of hierarchically porous MIL-88Bs synthesized in the present study is represented by red in Figure 81). By forming hierarchical pores via stirring metal salt, linker and DMF vigorously and tuning the pore size and pore size distribution of textural mesoporosity via synthesis temperature and Fe:BDC ratio, the CO_2 uptake capacity of hierarchically porous MIL-88Bs is increased by a factor of 2.1 (5.58 wt.% at 298 K and 1 bar) which is relatively higher than those of listed MOF structures.

4.5. Concluding Remarks

The CO_2 uptake capacities of hierarchically porous MIL-88Bs were found to be dependent on the fraction and volume of narrow micropores (pore diameter < 1 nm). Textural

pores were strategically controlled by Fe:BDC ratio and synthesis temperature. Volume of narrow micropores (pore diameter < 1 nm) increased by a factor of 1.65, and the highest volume of narrow micropores were achieved (MIL-88B-110-3, 0.226 cm^3/g). Among the hierarchically porous MIL-88Bs synthesized at different temperatures with different Fe:BDC ratios, the highest CO_2 adsorption capacity (5.58 wt.% at 298 K and 1 bar) was attained by those with the highest fraction (97%) and volume of narrow micropores (0.177 cm^3/g).

As pore sizes become narrower than 1 nm, adsorption potentials overlapped, which in turn results in higher binding energies (Fonseca et al., 2008; Romanos et al., 2012) and thereby, the amount of CO_2 adsorbed increases to 5.58 wt.% at 298 K and 1 bar. Our results demonstrate that CO_2 adsorption capacity is heavily dependent on: (i) the volume of micropores narrower than 1 nm; (ii) the cumulative volume of pores narrower than 0.7 nm; and lastly (iii) the distribution of narrow micropores (pore diameters < 1 nm) within the micropore size distribution (Vpores < 1 nm / Vpores < 2 nm).

This study reports a controlled synthesis strategy at which hierarchical pores are controlled by Fe:BDC ratio and synthesis temperature. The CO_2 adsorption capacity of hierarchically porous MIL-88Bs were enhanced by a factor of 2.1, and a CO_2 adsorption capacity (5.58 wt.% at 298 K and 1 bar) higher than those of commercially available MOFs is achieved. To move beyond the CO_2 uptake capacities achieved today, strategies to synthesize porous sorbents that are majorly formed of ultramicropores should be considered. The present study suggests that hierarchically porous MIL-88Bs synthesized in this work can be a promising and novel candidate in gas adsorption studies while our controlled synthesis strategy paves the way for the design of hierarchically porous MOFs with increased fraction and volume of micropores narrower than 1 nm.

Chapter V

Hydrogen adsorption capacity of hierarchically porous MIL-88Bs and the role of ultramicropores

5.1. Background

Energy plays a crucial role in society's economic development (Mao & Chen, 2007). Rising energy demand results in excessive fossil fuel consumption, and more importantly, adversely influences the ecosystem and human health (Fakioğlu et al., 2004). Hydrogen comes to the fore as a clean alternative to fossil fuels (Fakioğlu et al., 2004). Therefore, the use of hydrogen in energy and transportation applications is a key to decrease pollutant emissions (U.S. Department of Energy, 2015). In 2011, the U.S. Department of Energy (DOE) set a target to develop safe and cost-effective onboard vehicle hydrogen storage systems that can provide 300 miles of driving (U.S. Department of Energy, 2015). More than 180 fuel cell light-duty vehicles and 20 fuel cell buses using compressed hydrogen have been reported (U.S. Department of Energy, 2015). However, the high energy density demands and DOE target for 2020 (5.5 wt.% H_2) limited the use of hydrogen in energy and transportation applications (U.S. Department of Energy, 2015).

Physisorption of hydrogen on porous materials is a cost-effective, efficient and safe way of storing hydrogen (K. C. Kim, 2018; Jianwei Ren, Langmi, North, & Mathe, 2014a; Jianwei Ren, Musyoka, Langmi, Mathe, & Liao, 2017; Louis Schlapbach, Schlapbach, & Züttel, 2001; U.S. Department of Energy, 2015). Porous materials show very promising results at 77 K and high pressures (Beckner & Dailly, 2016). However, their H_2 adsorption capacities decrease drastically at 298 K and low pressures (0-100 bar) which limit the practical use of porous materials, economically (Broom et al., 2016; Kaskun & Kayfeci, 2018). The hydrogen adsorption capacity of a porous material changes with the surface area, pore volume, pressure, and temperature at which hydrogen storage studies are carried on (Jianwei Ren et al., 2017). Materials with high surface area and low density (i.e. carbon materials, activated carbons, zeolites, and metal-organic frameworks) tend to adsorb more

H_2 molecules (A. Züttel, 2003). Particularly, carbon materials have been used widely in H_2 sorption studies (Andersson & Grönkvist, 2019; Blankenship, Balahmar, & Mokaya, 2017; Broom et al., 2016; Yürüm et al., 2009a). However, theoretical studies illustrated their limited H_2 sorption capacities (only a few wt.%) (Becher et al., 2003; Barbara Panella et al., 2005a; Rzepka, Lamp, & de la Casa-Lillo, 2002; Yürüm et al., 2009a).

In 1995 a new family of porous materials, metal-organic frameworks (MOFs), formed of an organic and inorganic part was introduced (O M Yaghi et al., 1995). Controllable synthesis conditions, designable organic ligands, tuneable pore sizes, high specific surface area, and the highly porous nature make MOFs attractive in H_2 storage applications (Andersson & Grönkvist, 2019; Balderas-Xicohténcatl, Schlichtenmayer, & Hirscher, 2018; García-Holley et al., 2018; Jianwei Ren et al., 2014a; G. Xu et al., 2019).

MOFs possess incredibly high H_2 adsorption capacities at high pressures and cryogenic temperatures (Abdalla et al., 2018; Kaye et al., 2007a; Jianwei Ren, Langmi, North, & Mathe, 2014b; Rowsell & Yaghi, 2004a). However, very low H_2 sorption capacities can be achieved at 298 K and low pressures (Klyamkin et al., 2014; Murray, Dincă, & Long, 2009). These low H_2 sorption capacities have been due to weak van der Waals interactions between H_2 molecules and the surface (Latroche, Surblé, Serre, Mellot-Draznieks, Llewellyn, Lee, Chang, Sung, et al., 2006a; Barbara Panella, Hirscher, Pütter, & Müller, 2006; Surblé, Millange, et al., 2006). In order to enhance the H_2 sorption capacities measured at 298 K, researchers have focused on increasing the surface area of MOFs. However, the effect of pore size has remained understudied. To the best of our knowledge, there are scarcely any reports that investigates the relation between the pore size and the adsorbed H_2 amount.

In this work, the effect of pore size on the adsorbed H_2 amount has been reported. Hierarchically porous MIL-88Bs were synthesized via a perturbation assisted nanofusion synthesis strategy and the fraction and the volume of textural pores were controlled by the iron to terephthalic acid (TPA) ratio (1, 3, and 5). By the control over textural porosity via Fe:TPA ratio, an ultramicroporous MOF structure (pores with pore diameters of 0.6 nm dominated the pore structure) with a BET surface area 2.11 and 2.74 times higher than those of reported MIL-88B's have been achieved (C. Gao et al., 2017; Hou et al., 2018). More importantly, the measured H_2 adsorption capacity at 298 K has been enhanced by a factor of 1.96. Our results reveal that H_2 adsorption capacity of porous structures (at 298 K and

pressures lower than 10 bar) are highly dependent on: i) the presence of ultramicropores; ii) high fraction of ultramicropores through the whole pore size distribution; and iii) the volume of ultramicropores (Aysu Yurduşen et al., 2019).

5.2. Experimental

Synthesis and characterization analyses were conducted for five times. BET specific surface area, ultramicro-, micro-, upper meso-, and mesopore and total pore volumes were reported with calculated standard deviations.

5.2.1. Materials

98% pure, ACS Reagent grade, iron(III) chloride hexahydrate ($FeCl_3 \cdot 6H_2O$) (Merck Millipore); and HPLC grade 98% pure terephthalic acid, 99.9% pure N, N-Dimethylformamide (DMF), and 99.8% pure methanol (MeOH) was used (Sigma Aldrich). Chemicals were used as they were received. An isothermal oven (Protherm Furnace), Teflon capped glass vials (ISOLAB) and a vacuum oven (Nüve, EV 018) was used during the synthesis of MIL-88B type MOF crystallites.

5.2.2. Synthesis

3.1 mmoles of $FeCl_3.6H_2O$, TPA (3.1 mmoles or 1 mmoles or 0.62 mmoles) and 80 mL of DMF were vigorously stirred via a magnetic stirrer with a stirring rate of 800 rpm for an hour at 25 °C. Prepared clear solution was then distributed into glass vials capped with Teflon caps (20 mL). An isothermal oven was used to heat the samples for two days at 110 °C. Then the precipitates and the solution were distributed into 50 mL falcon tubes. A solvent exchange process was used for the washing procedure. Precipitates and the solution were washed with DMF (three times) and methanol (three times). Lastly, the precipitates were dried under vacuum at 100 °C for 30 hours. The abbreviations of hierarchically porous MIL-88Bs can be found below in Table 24. For the samples prepared with 3.1 mmoles of $FeCl_3.6H_2O$, 3.1 mmoles of TPA and 80 mL of DMF the sample abbreviation of MIL-88B-

1; for the samples synthesized with 3.1 mmoles of $FeCl_3.6H_2O$, 1.03 mmoles of TPA and 80 mL of DMF the sample abbreviation of MIL-88B-3; and for the samples prepared with 3.1 mmoles of $FeCl_3.6H_2O$, 0.62 mmoles of TPA and 80 mL of DMF the sample abbreviation of MIL-88B-5 have been used through the manuscript.

Table 24. Sample Abbreviations

Sample Abbreviation	Fe:TPA ratio
MIL-88B-1	1
MIL-88B-3	3
MIL-88B-5	5

5.2.3. Characterization Analysis

Powder x-ray diffraction (XRD), scanning electron microscopy (SEM) analysis, N_2 sorption isotherms, pore size distribution analysis, nitrogen gas adsorption measurements, Fourier Transform Infrared Spectroscopy (FTIR), and thermogravimetric analysis (TGA) were used for structural characterization of the synthesized hierarchically porous MIL-88Bs. Each characterization analysis was repeated for five times and the results are reported with their respective standard deviations.

5.2.3.1.X-Ray diffraction

X-ray diffraction analysis was carried out with a Bruker D2 Phaser XRD. The analysis was carried with a step size of 0.02° in between a 2θ range of 2 to 90°.

5.2.3.2.Scanning electron microscopy (SEM)

Imaging was conducted with a Leo Supra 35VP field emission scanning electron microscope. Voltage and working distance were set in accordance with the MOF imaged.

5.2.3.3. Brunauer-Emmett-Teller (BET) surface area and pore size distribution analysis

BET surface area and pore size distribution analysis was conducted with a Micromeritics 3Flex Instrument. 0.35±0.05 grams (g) of MOF was used. Before each analysis, hierarchically porous MIL-88Bs were degassed at 120 °C for 6 hours. BET was used for surface area analysis and NLDFT model was used for pore size distribution analysis.

5.2.3.4. Fourier Transform Infrared Spectroscopy (FT-IR) Analysis

Thermo Scientific Nicolet Is10 was used for the FTIR analysis. A wavelength range of 600 to 4000 cm-1 with a spectral resolution of 4 cm-1 was used. Scans were repeated for 32 times and each spectrum was corrected for background noise.

5.2.3.5. Thermogravimetric analysis

Shimadzu DTG-60H simultaneous thermal analysis TG-DTA was used. 49±5 mg MOF was analyzed under an N_2 flow of 20 mL/min. A heating rate of 10 K was used.

5.2.3.6. H_2 sorption isotherm measurement

H_2 uptake capacities were measured gravimetrically via Intelligent Gravimetric Analyzer (IGA) from very low (vacuum) to high pressures. Hydrogen adsorption studies were conducted in between 0 and 8 bar and at 298 K. A microbalance head placed in a stainless-steel vacuum-pressure reactor with ± 1.0 μg sensitivity was used for accuracy. Hierarchically porous MIL-88Bs samples were outgassed at 120 °C for 6 hours.

5.3. Results and Discussion

5.3.1. XRD Analysis

A perturbation assisted nanofusion synthesis strategy that forms hierarchical pores were used in the synthesis of hierarchically porous MIL-88Bs. Vigorously stirring iron salt, linker and DMF caused secondary building units (SBUs) to aggregate into nanosized MOF

crystallites which were later embedded in an amorphous matrix. Single crystal X-ray crystallography analyses proved that micro-sized single crystals were not formed and there were no metallic-iron present. Figure 82 illustrates the XRD patterns of hierarchically porous MIL-88Bs.

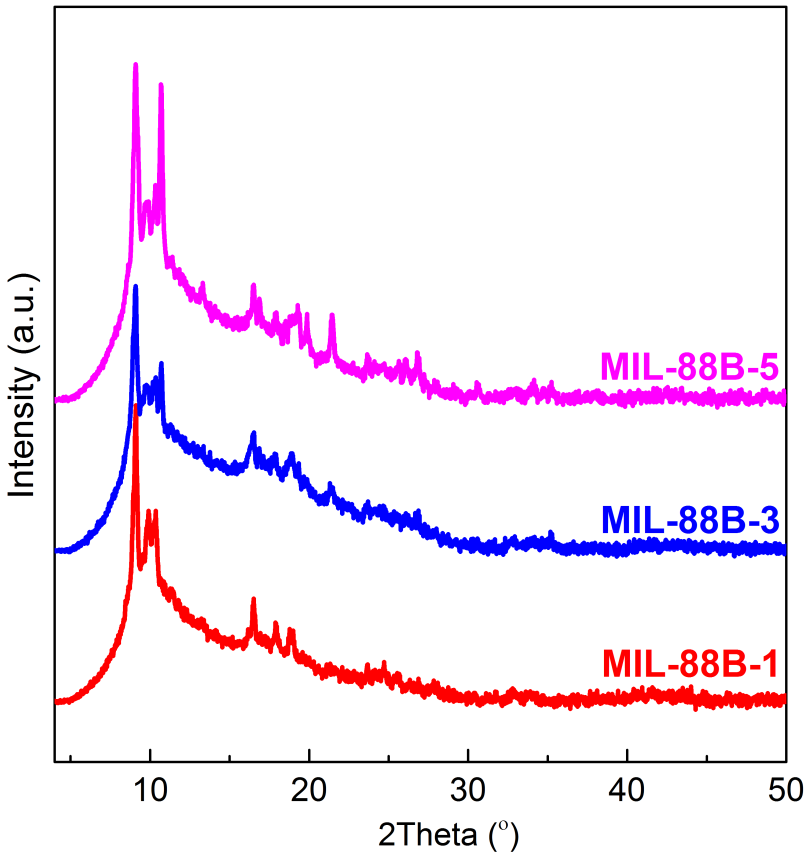

Figure 82. XRD patterns of MIL-88B-1, MIL-88B-3, and MIL-88B-5.

XRD patterns of the hierarchically porous MIL-88Bs agree well with the XRD pattern of the simulated MIL-88B (Surblé, Serre, Mellot-Draznieks, Millange, & Férey, 2006). Single crystal X-ray crystallography analyses demonstrated that micro-sized single crystals were not formed and there were no metallic-iron present. A comparison of the XRD pattern of the reference MIL-88B with the XRD patterns of the synthesized hierarchically porous MIL-88Bs can be found below in Figure 83.

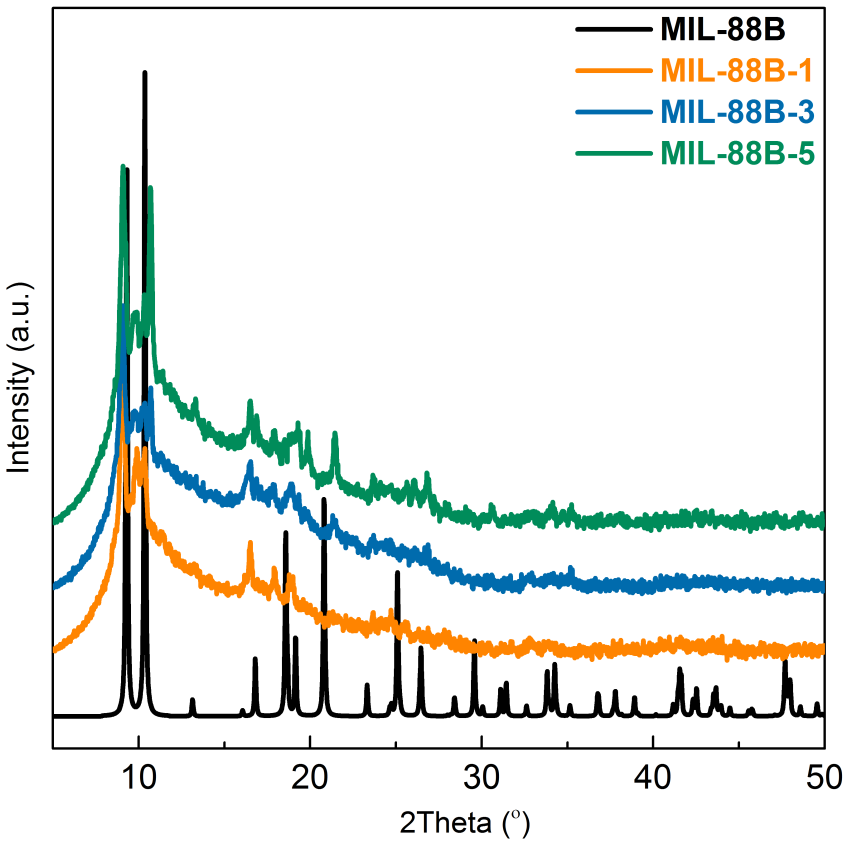

Figure 83. Comparison of XRD patterns of simulated MIL-88B and synthesized hierarchically porous MIL-88Bs.

Both the MIL-88B nanorods and the amorphous matrix at which MIL-88B nanorods were embedded in, cause the observed broadening in the XRD patterns as well as the amorphous nature of the XRD patterns.

In the case of MIL-88B-5, Bragg peaks were even more broadened. The broadened Bragg peaks are attributed to the excess amount of iron salt used during the synthesis. Excess amount of iron salt causes more iron oxide clusters to form which competes for TPA. Aggregates of excess iron oxide clusters form the MIL-88B nanorods.

5.3.2. SEM Images

Figure 84 illustrates the SEM images of MIL-88B-1, MIL-88B-3, and MIL-88-5.

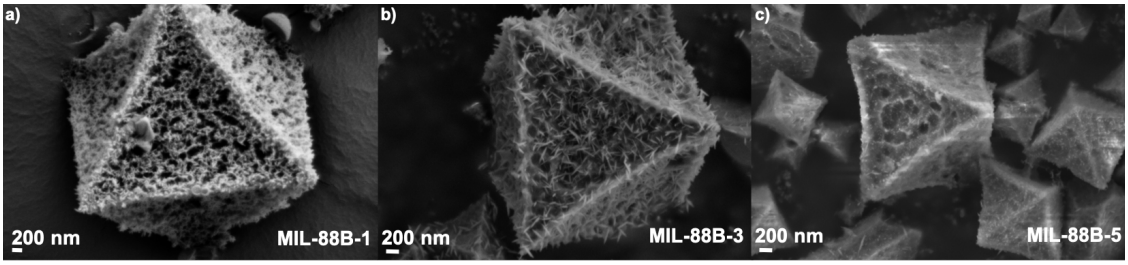

Figure 84. SEM images of hierarchically porous MIL-88Bs.

SEM images show the MIL-88B nanorods and the amorphous matrix at which the nanosized MIL-88B rods were embedded in. Hierarchically porous MIL-88Bs were formed by the precipitation of aggregated MIL-88B nanorods. Aggregated MIL-88B nanorods were precipitated on the amorphous matrix at which the interparticle voids formed the textural porosity. Textural pores with pore diameters ranging in between 2 to 50 nm can be seen as dark spots in Figure 84 a), b), and c).

5.3.3. N_2 Sorption Isotherms

BET surface areas of MIL-88B crystallites (MIL-88B-1: 400.4 m^2/g; MIL-88B-3: 452.4 m^2/g; MIL-88B-5: 445.9 m^2/g) are higher than those of reported MIL-88B structures (C. Gao et al., 2017; Vuong et al., 2013a). The enhancement in the BET surface area is a consequence of the hierarchical pores introduced to the pore structure. Textural pores were formed by the coordination, nucleation and nanoparticle aggregation mechanism. MIL-88B nanocrystallites were embedded in an amorphous matrix at which the textural pores were formed. Introducing textural pores to the pore structure enhances BET surface areas and the pore volumes of the crystallites which are found to be higher than those of reported BET surface areas and pore volumes of MIL-88B (C. Gao et al., 2017; Vuong et al., 2013b). Figure 85-88 illustrates the respective N_2 sorption isotherms.

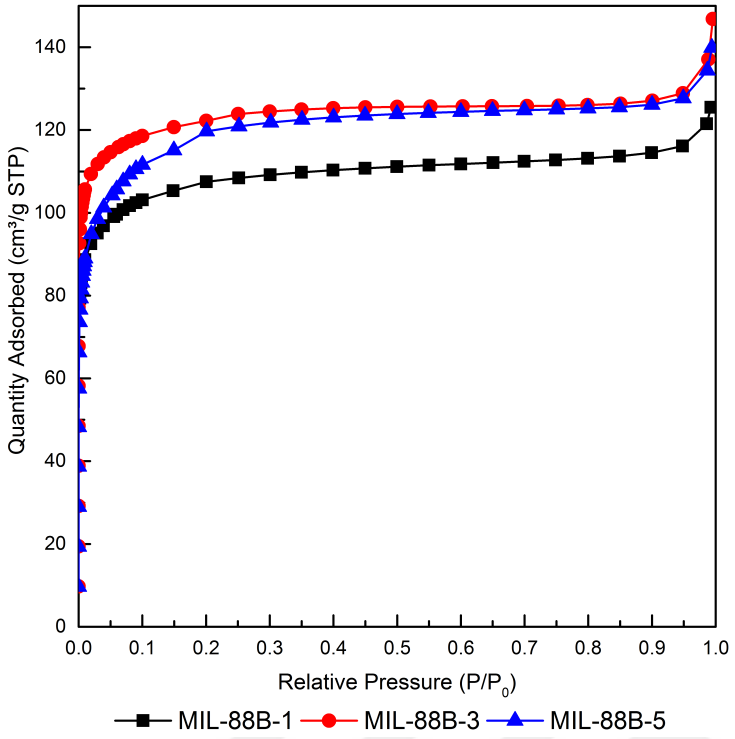

Figure 85. N_2 sorption isotherms of MIL-88B-1, MIL-88B-3, and MIL-88B-5.

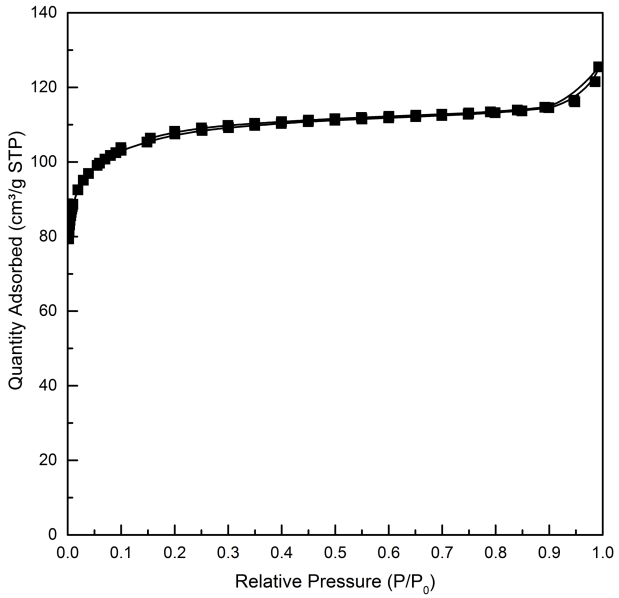

Figure 86. N_2 sorption isotherm of MIL-88B-1.

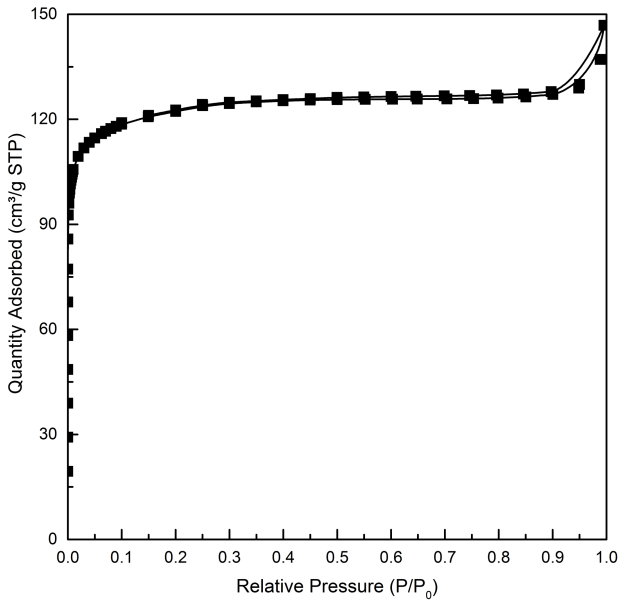

Figure 87. N_2 sorption isotherm of MIL-88B-3.

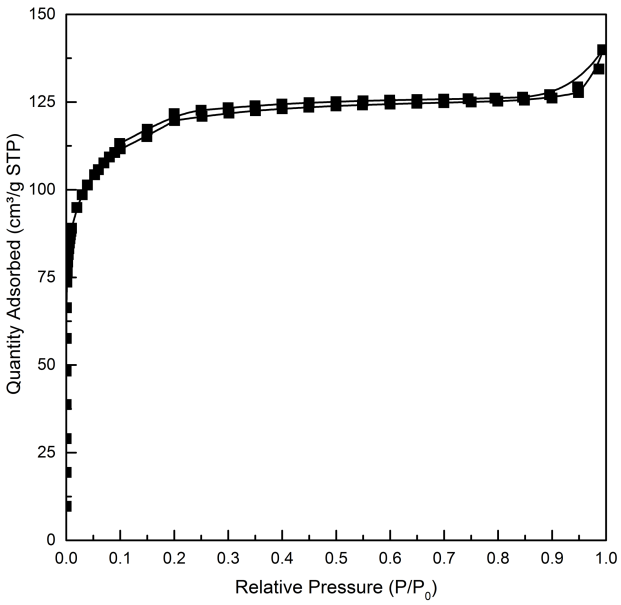

Figure 88. N_2 sorption isotherm of MIL-88B-5.

N_2 sorption isotherms of MIL-88B-1, MIL-88BB-3, and MIL-88B-5 have the features of IUPAC type I isotherms with some mesoporosity. At low relative pressures ($P/P_0 < 0.1$) hierarchical porous MIL-88Bs show sharp increases in the adsorbed N_2 amount. In between the relative pressure ranges of 0.2 and 0.9 N_2 sorption isotherm of MIL-88B-3 possesses a horizontal plateau while a relatively small slope is observed in the N_2 sorption

isotherms of MIL-88B-1, and MIL-88B-5. This relatively small slope is associated with mesopore filling which is due to the presence of mesopores. At pressures close to saturation pressure ($P/P_0 > 0.9$), the amount of N_2 adsorbed increases which reveals that there are some mesopores present. Lastly, neither of the isotherms possess hysteresis. In order to compare the micropore volume, t-plot method is used.

5.3.4. t-plot Method

t-plot method is used to estimate the micropore volumes of MIL-88B-1, MIL-88B-3, and MIL-88B-5. Respective t-plots of MIL-88B-1, MIL-88B-3, and MIL-88B-5 can be found in Figure 89-92.

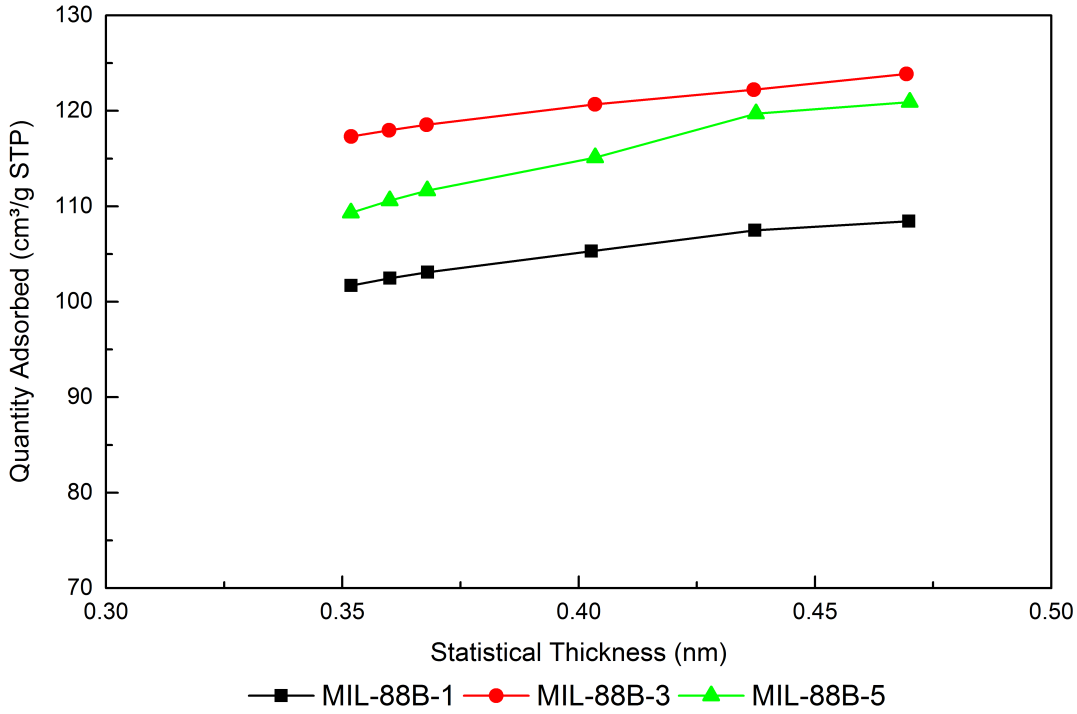

Figure 89. t-plots of MIL-88B-1, MIL-88B-3, and MIL-88B-5.

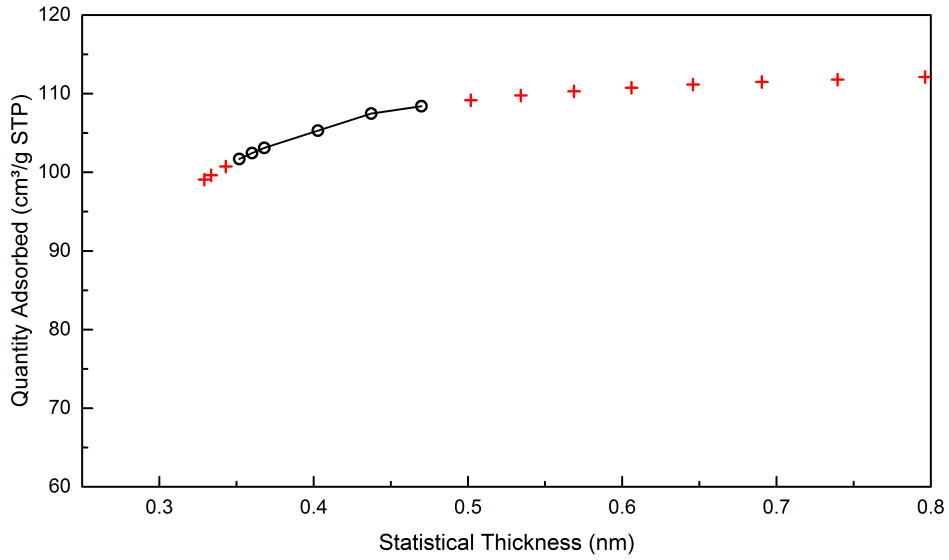

Figure 90. t-plot of MIL-88B-1.

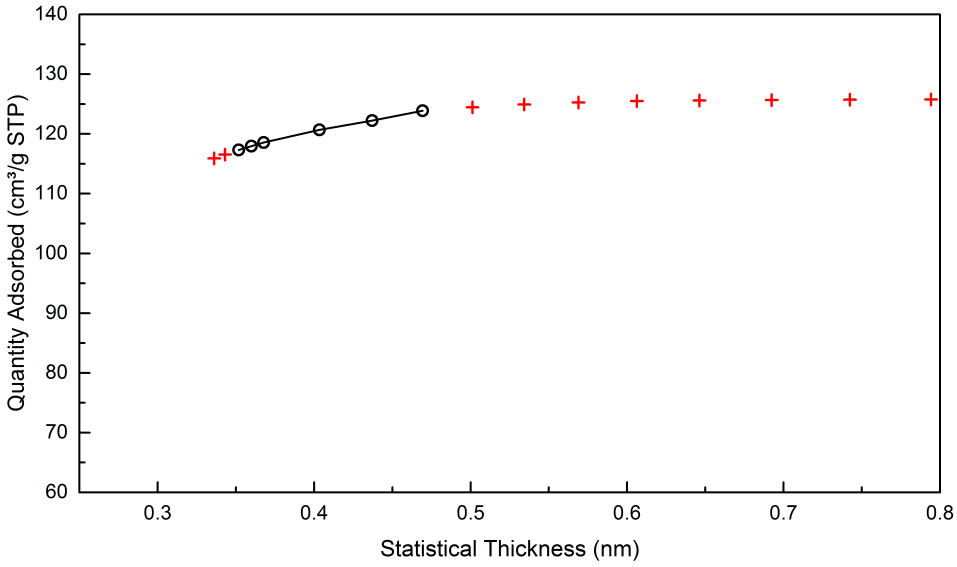

Figure 91. t-plot of MIL-88B-3.

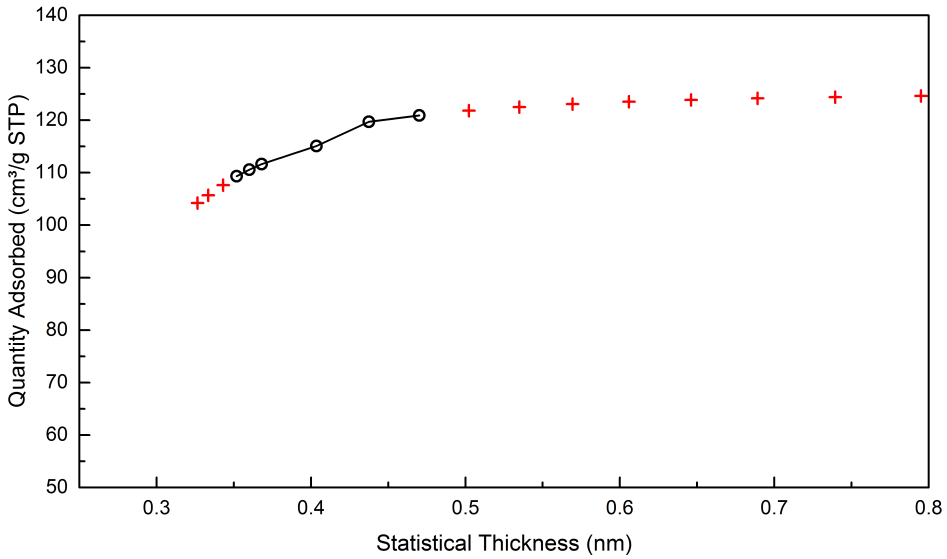

Figure 92. t-plot of MIL-88B-5.

MIL-88B-3 intersects y-axis at a considerably higher value than MIL-88B-1, and MIL-88B-5 evidencing that MIL-88B-3 possesses a relatively higher micropore volume than MIL-88B-1, and MIL-88B-5. For a better pore volume estimation NLDFT method has been used. Figure 93 illustrates the NLDFT plots of MIL-88B-1, MIL-88B-3, and MIL-88B-5.

5.3.5. NLDFT Method

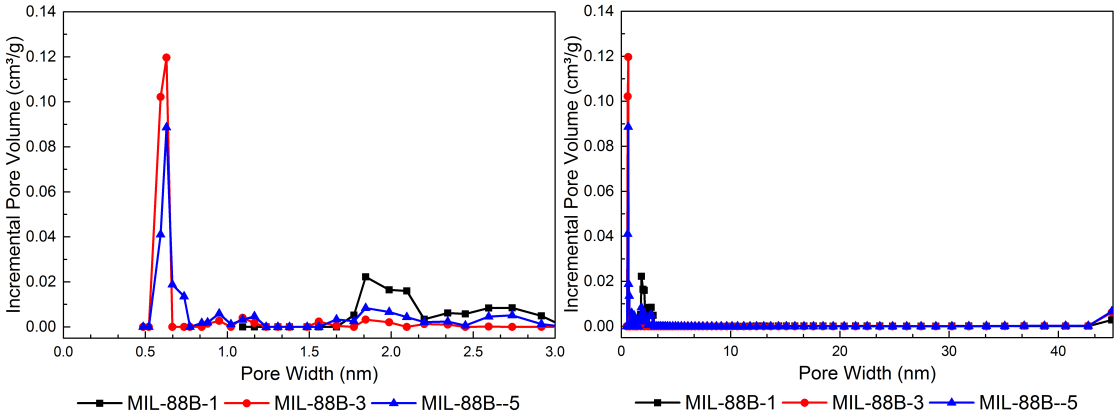

Figure 93. NLDFT plots of MIL-88B type MOF crystallites.

NLDFT plots of incremental pore volume-pore width show several increases within micro- and mesopore size range. In addition to the wide mesopores at 44.8 nm, some narrow

mesopores are also tracked. MIL-88B-1 is mainly formed of micropores (92%) while volume of mesopores contribute by 7.5%. NLDFT analysis shows that MIL-88B-1 has no pores with pore diameters ranging in between 3 to 11.2 nm. Pores within the mesopore size range occupy a volume of 0.01481 cm^3/g which corresponds to 7.5% of the total pore volume. Pores with the pore diameters of 44.8 nm form 40% of the mesopores.

MIL-88B-3 does not have any pores narrower than 0.59 nm. The volume increase associated with micropores narrower than 0.62 nm corresponds to 89% of the total pore volume while micropores form 96.1% of the total pore volume. NLDFT analysis shows that there are no pores with pore diameters ranging in between 2.7 and 33.4 nm. In between 35 and 44.8 nm a relatively small increase in pore volume is observed. Within the mesoporous range, a volume increase of 0.0096 cm^3/g which corresponds to 3.9% of the total pore volume is issued.

NLDFT plot of MIL-88B-5 shows a steep increase in the microporous region which is then followed by large and small volume increases till a pore diameter of 3 nm. The highest volume increase of 0.13 cm^3/g is observed for pore diameters ranging between 0.59 nm and 0.62 nm which corresponds to 56.4% of the total pores. In brief, the volume increase in the microporous region corresponds to 87.8% of the total pore volume. There are no pores with pore diameters ranging between 3.1 to 30.3 nm. In the meanwhile, in between the pores with pore diameters of 31.8 and 44.8 nm a volume increase of 0.00768 cm^3/g is observed. Table 25 illustrates the volume of ultramicropores, narrow micropores, micropores, and mesopores.

Table 25. Volume of ultramicropores, narrow micropores, micropores, and mesopores

Hierarchical porous MIL-88Bs	Volume of ultramicropores (cm^3/g)	Volume of narrow micropores (cm^3/g)	Volume of micropores (cm^3/g)	Volume of mesopores (cm^3/g)
MIL-88B-1	-	0.177±1.7E-2	0.182±1.4E-2	0.0165±1.4E-2
MIL-88B-3	0.22	0.226±1.2E-2	0.239±3.2E-2	0.0096±7.0E-3
MIL-88B-5	0.16	0.172±1.7E-2	0.202±3.2E-2	0.0281±1.7E-2

A possible mechanism for the widened mesopores in MIL-88B-5

The following mechanism is suggested for the widened mesopores in MIL-88B-5. To introduce textural pores, MIL-88B-1, MIL-88B-3, and MIL-88B-5 were synthesized by a perturbation assisted nanofusion synthesis strategy. By this way, single crystal growth would be prevented, and amount and fraction of textural pores can be controlled. Strongly stirring iron salt, TPA and DMF, prevented the single crystal growth. The vigorous stirring of iron salt, TPA and DMF, formed SBUs which aggregate into nanosized MIL-88B rods. The high Fe:TPA ratio used in the synthesis of MIL-88B-5 caused iron oxide clusters to form that compete for the limited amount of TPA present in the solution. Aggregated nanosized MIL-88Bs were embedded in the amorphous matrix at which interparticle voids formed the textural mesoporosity. We suggest that using a high Fe:TPA ratio caused more nanosized MIL-88B type MOF crystallites to aggregate which widens the interparticle voids (textural mesopores). Figure 94 shows the sequence of textural pore formation and Figure 95 illustrates the textural pore formation mechanism

Figure 94. Schematic diagram of textural pore formation sequence.

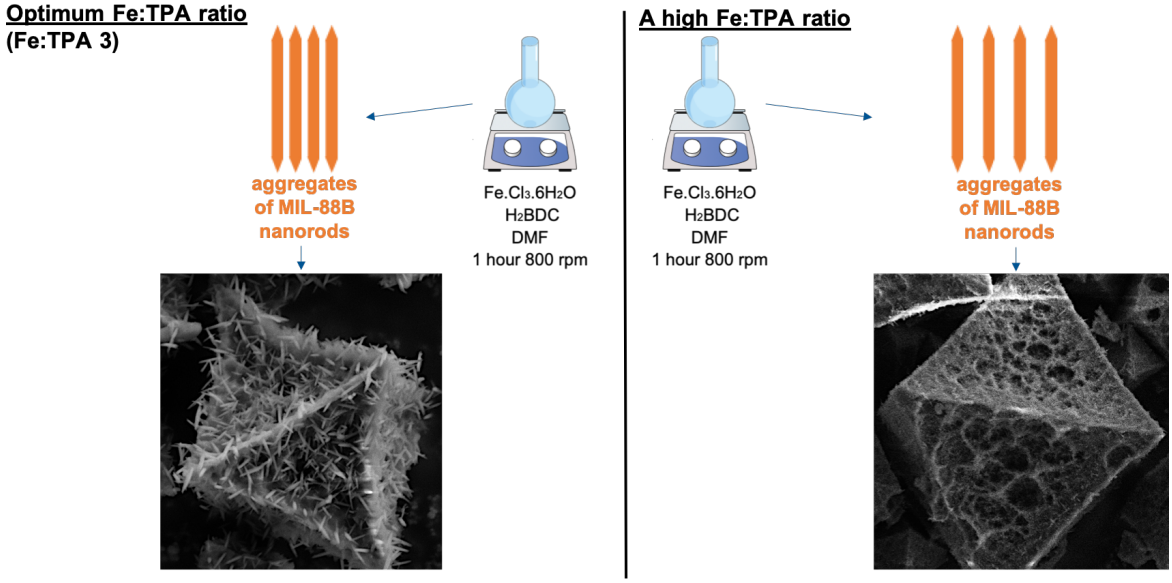

Figure 95. Schematic diagram of textural pore formation mechanism.

Our results show that in the presence of insufficient amount of terephthalic acid (a high Fe:TPA ratio), pore diameters widen, and the volume occupied by the pores at the upper mesoporous range increases. We have attributed the observed increase in the mesopore fraction to the formation of iron oxide clusters and aggregation of the nanosized MIL-88B-5 crystallites. Thereby, interparticle voids (textural mesopores) widen and the fraction of textural mesopores increases.

5.3.6. FTIR Analysis

Figure 96 illustrates FTIR spectra of hierarchical porous MIL-88Bs. FTIR spectra agree well with each other with some small changes in band shapes and peak intensities.

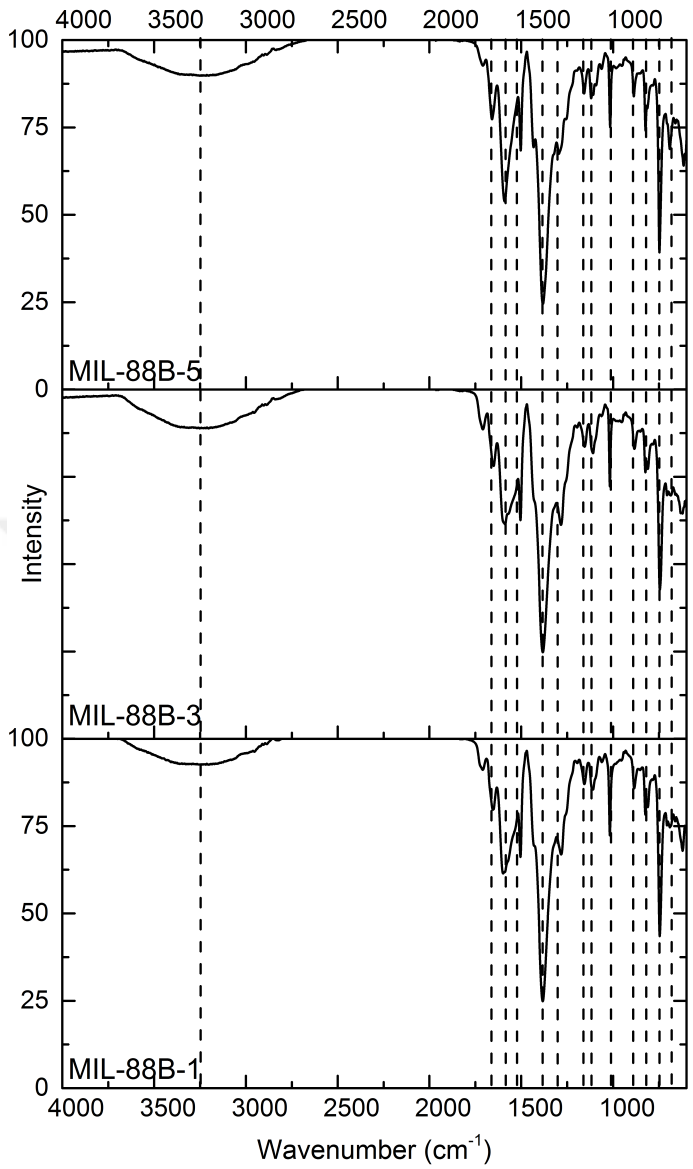

Figure 96. FTIR spectra of MIL-88B-1, MIL-88B-3, and MIL-88B-5.

In between the wavelengths of 3000 to 3600 cm^{-1} broad bands typical of OH groups are observed. MIL-88B-5 possesses a wider band width with lower peak intensity than MIL-88B-1 and MIL-88B-3 In a study of Jacobs et. al., broadened OH bands were attributed to widened pore widths (Jacobs & Mortier, 1982). Having the broadest OH band with the lowest intensity, it is concluded that MIL-88B-5 possess larger pores in comparison to MIL-88B-1, and MIL-88B-3.

There is no peak at 1704 cm^{-1} suggesting that most of the H_2BDC used during the synthesis are deprotonated. More importantly, using a Cl^- based metal salt eliminates the necessity to remove free terephthalic acid present in the sample.

Presence of peaks at 1647 cm^{-1} illustrates that there is still some residual DMF left in the pores (1659 cm-1; C=O asymmetric stretching mode) (Sharma, Kaur, Mahajan, Tripathi, & Saini, 2007).

We have confirmed that we have formed the skeletal of our hierarchical porous MIL-88Bs by the peaks obtained in between the wavelengths 1300 and 1650 cm^{-1}. Peaks at 1385 and 1589 cm^{-1} illustrate that TPA was attached successfully to the metal center (Benbellat et al., 2006; Rowsell & Yaghi, 2006b; Tafipolsky et al., 2010).

The peaks obtained at 1017 cm^{-1}, 1155 cm^{-1}, 1504 cm^{-1}, and 1589 cm^{-1} are associated with a form of TPA (Arenas & Marcos, 1979; Téllez S. et al., 2001; Tripathi & Sheng, 1979). The peak at 1017 cm^{-1} (C-O-Fe stretching mode) illustrates TPA was successfully attached to the metal center. In addition, the peaks obtained at 742 and 823 cm^{-1} are assigned to Fe-O stretching mode proving that Fe is coordinated with TPA (Ye Li et al., 2015). Finally, the peak in between 600 and 626 cm^{-1} is assigned to central oxygen in single Fe_3O and observed in the FTIR spectra of all the crystallites (Vuong et al., 2013a). Moreover, FTIR spectrum of hierarchically porous MIL-88Bs were compared with the FTIR spectra of $FeCl_3.6H_2O$. Having no peaks at 842 cm^{-1}, 1594 cm^{-1}, 2993 cm^{-1}, 3212 cm^{-1}, and 3523 cm^{-1} which are the characteristic peaks of $FeCl_3.6H_2O$ showed that there are no metallic iron present.

5.3.7. Thermal Gravimetric Analysis (TGA)

Figure 97 illustrates the respective TGA curves. Similar TGA curves were obtained for the synthesized hierarchically porous MIL-88Bs. Detailed TGA results with percentage of mass losses is provided in Table 26.

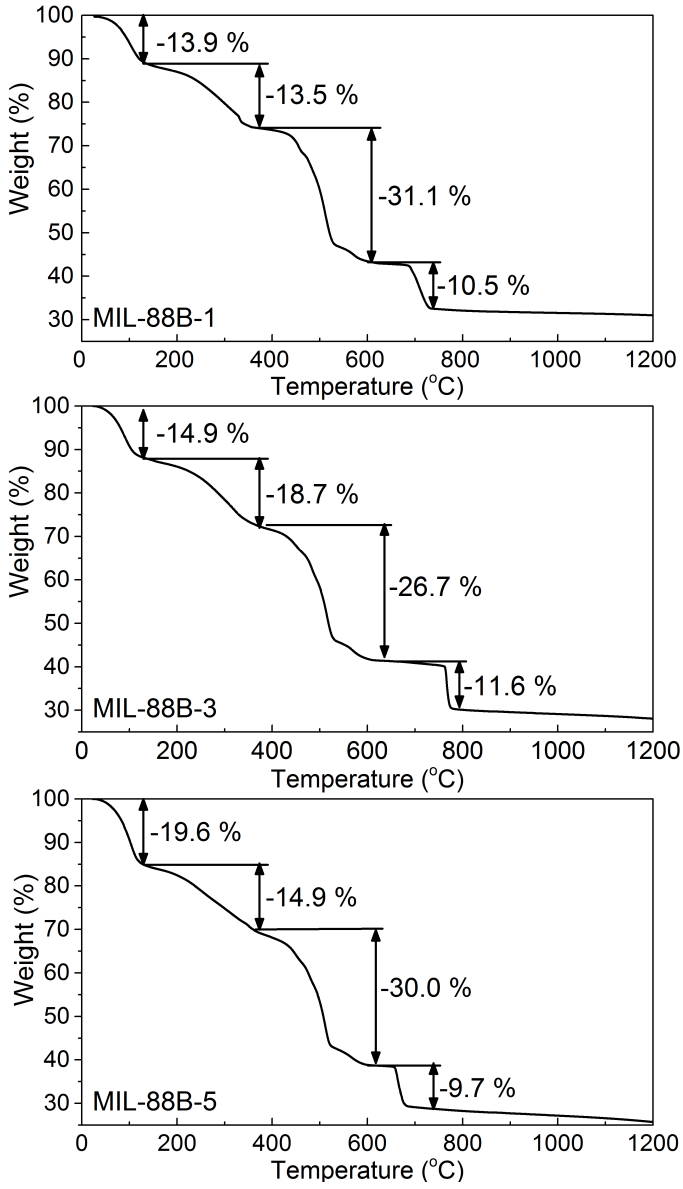

Figure 97. TGA curve of hierarchically porous MIL-88B.

Table 26. % mass loss during TGA

Temperature Range (°C)	MIL-88B-1 (%)	Temperature Range (°C)	MIL-88B-3 (%)	Temperature Range (°C)	MIL-88B-5 (%)
25-185	-13.9	25-175	-14.9	25-169	-19.6
185-380	-13.5	175-448	-18.7	169-387	-14.9
380-642	-31.1	448-638	-26.7	387-625	-30
642-757	-10.5	638-850	-11.6	625-716	-9.7

At the first step adsorbed and coordinated water and DMF molecules are lost. MIL-88B-5 has the highest amount of mass loss in the first step. The second step is associated with solvent molecules trapped in the pores. The third step occurs due to linker decomposition and MIL-88B-3 is found to decompose at a temperature higher than MIL-88B-1, and MIL-88B-5. Finally, the last step corresponds to CO_2 release during the decomposition of carboxylates. Additionally, TGA analysis shows that hierarchically porous MIL-88Bs are thermally stable under adsorption process conditions.

5.3.8. H_2 Sorption Analysis

Hierarchically porous MIL-88Bs synthesized with different Fe:TPA ratio (1, 3, and 5) possess different H_2 sorption capacities. Figure 98 illustrates H_2 adsorption isotherms.

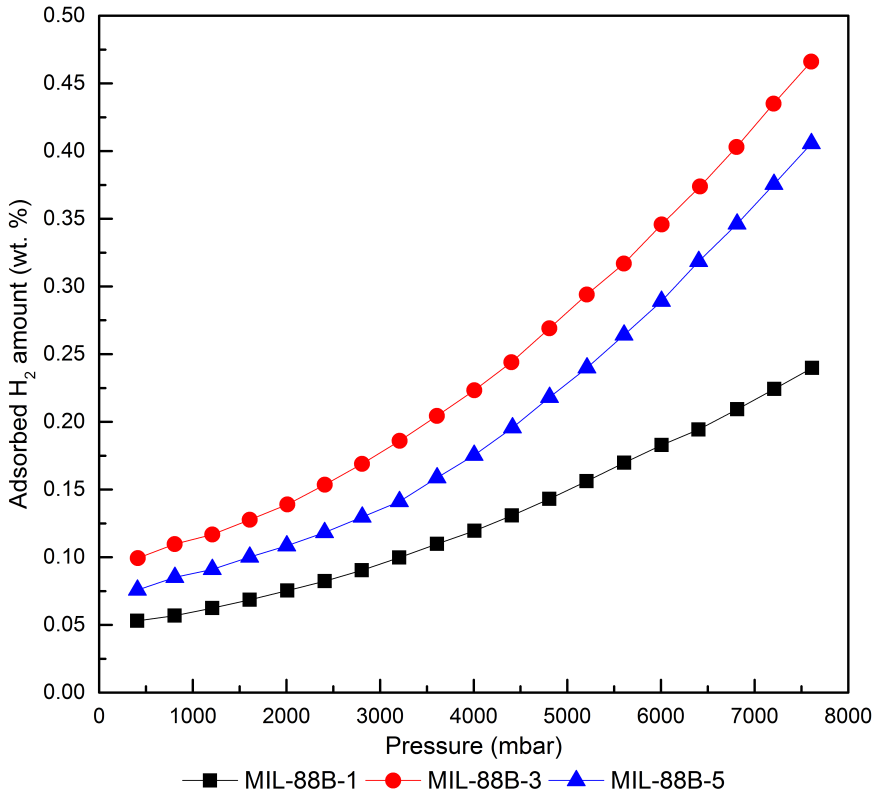

Figure 98. H_2 sorption isotherms of MIL-88B-1, MIL-88B-3, and MIL-88B-5 measured at 298 K.

Calculated Langmuir and Freundlich isotherm parameters and the representative plots comparing experimental data with the nonlinear fitting of Langmuir and Freundlich model can be found below. The Freundlich model describes H_2 adsorption behavior of MIL-88B type MOF crystallites measured at 298 K, better. However, as the adsorption studies were conducted till 8 bars, the shape of the isotherm may be misleading. Table 27-28 illustrate the respective coefficient of determination, R^2, values for MIL-88B-1, MIL-88B-3, and MIL-88B-5. Table 29 presents the textural properties, H_2 sorption capacities (at 7.6 bar) and adsorbed H_2 amount per specific surface area of MIL-88B-1, MIL-88B-3, and MIL-88B-5.

Langmuir Model:

$$\frac{C_e}{q_e} = \frac{1}{KQ^0} + \frac{C_e}{Q^0} \tag{5.1}$$

Freundlich Model:

$$logq_e = logK_F + \frac{1}{n} logC_e \quad (5.2)$$

Table 27. Respective equations obtained from models

Hierarchically porous MIL-88Bs	Langmuir Model	Freundlich Model
MIL-88B-1	y = 0.5001 x+3790.4	y = 0.8398x-3.2216
	R^2 = 0.5676	R^2 = 0.9759
MIL-88B-3	y = 0.2509x+2068.1	y = 0.8673x-3.0457
	R^2 = 0.5104	R^2 = 0.9716
MIL-88B-5	y = 0.2926x+2697.3	y = 0.9502x-3.4377
	R^2 = 0.4014	R^2 = 0.9588

Table 28. Langmuir and Freundlich isotherm parameters

Hierarchically porous MIL-88Bs	Langmuir Model	Freundlich Model
	Q_m= 1.99 mg/g	K_F= 6.0E-04
MIL-88B-1	K_a= 1.32E-04 mg^{-1}	η_F= 1.19
	R^2= 0.5676	R^2= 0.9759
	Q_m= 3.99 mg/g	K_F= 9.0E-04
MIL-88B-3	K_a= 1.21E-04 mg^{-1}	η_F= 1.15
	R^2= 0.51	R^2= 0.9716
	Q_m= 3.42 mg/g	K_F= 3.65E-04
MIL-88B-5	K_a= 1.0851E-04 mg^{-1}	η_F= 1.05
	R^2= 0.4014	R^2=0.9588

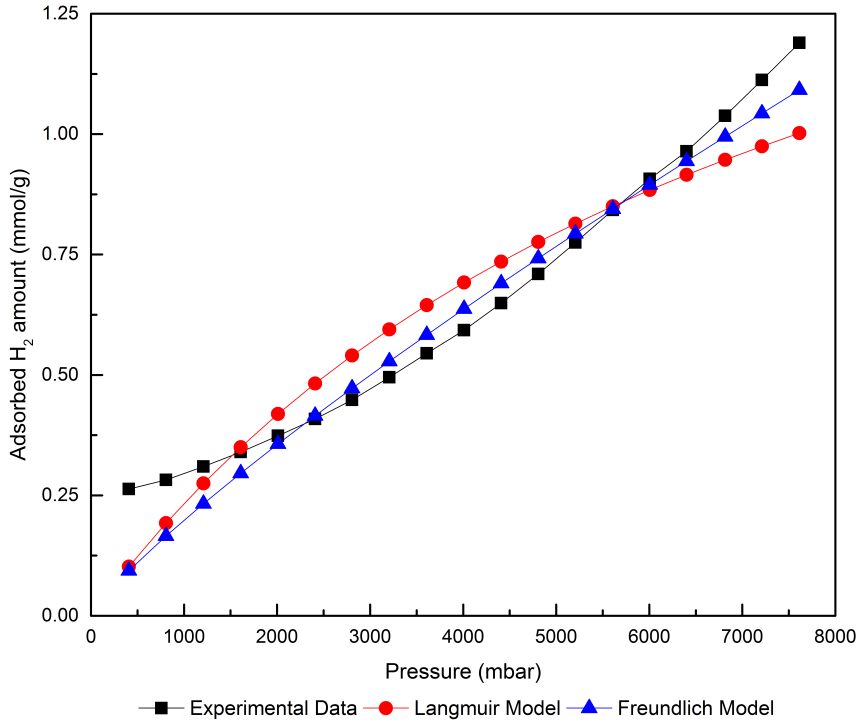

Figure 99. Comparison of experimental data and nonlinear fitting of Langmuir and Freundlich model of H_2 adsorption behavior on MIL-88B-1.

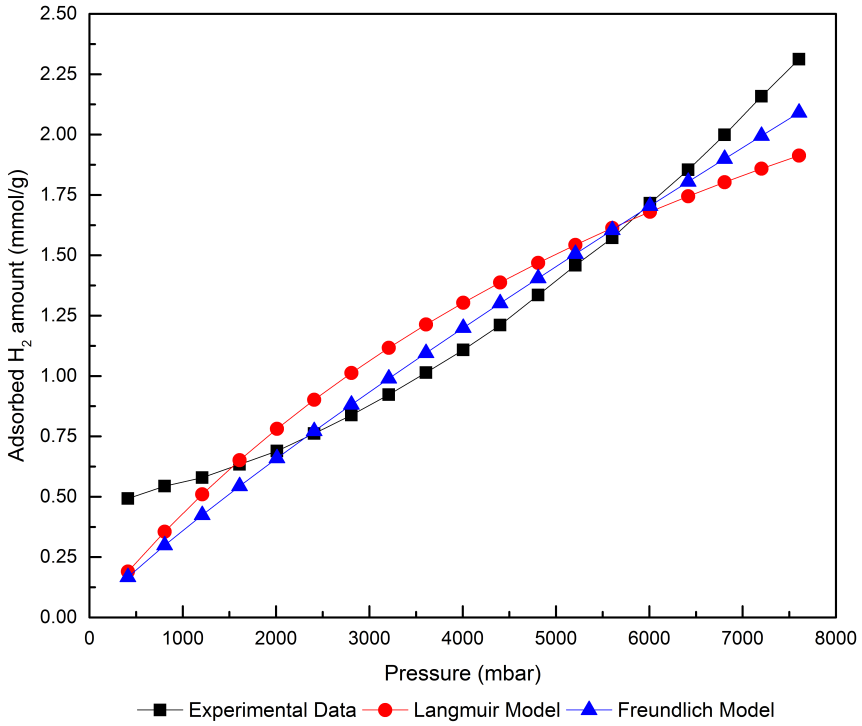

Figure 100. Comparison of experimental data and nonlinear fitting of Langmuir and Freundlich model of H_2 adsorption behavior on MIL-88B-3.

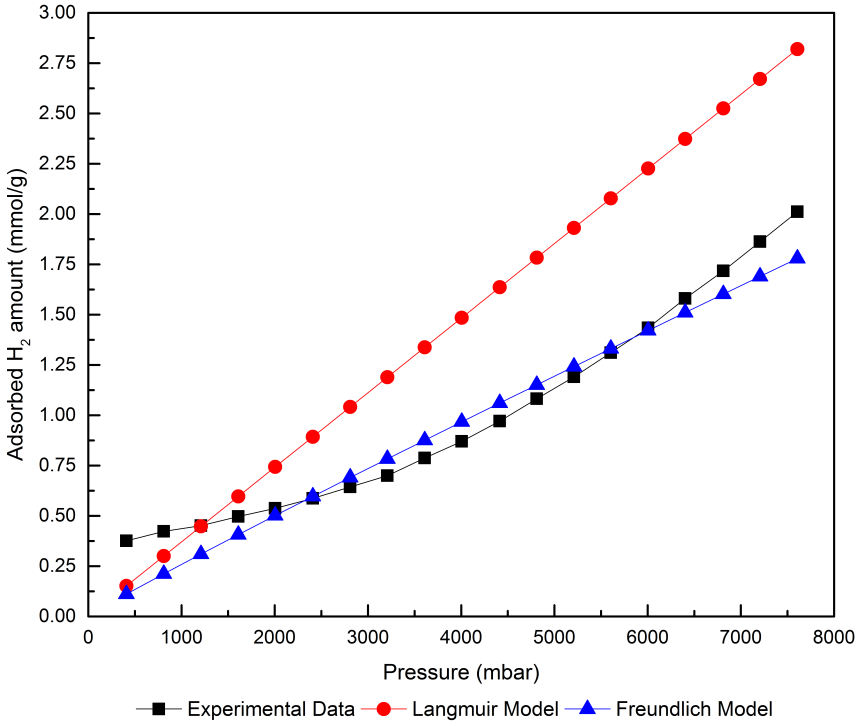

Figure 101. Comparison of experimental data and nonlinear fitting of Langmuir and Freundlich model of H_2 adsorption behavior on MIL-88B-5.

Table 29. Textural properties, H_2 sorption capacity (wt. % at 7.6 bar and 298 K), H_2 uptake per specific surface area (10^3 wt. % g/m^2) of MIL-88B-1, MIL-88B-3, and MIL-88B-5

Hierarchical porous MIL-88Bs	Vmicro (cm^3/g) [a]	Vmeso (cm^3/g) [b]	Vnarrow micro (cm^3/g) [c]	Vultra micro (cm^3/g) [d]	Vultramicro / Vnarrow micro [e]	H_2 sorption capacity (wt. %) [f]	H_2 uptake per SSA (10^3 wt.% g/m^2) [g]
MIL-88B-1	0.182±1.4E-2	0.0165±1.4E-2	0.177±1.7E-2	-	-	0.24	0.599
MIL-88B-3	0.239±3.2E-2	0.0096±7E-3	0.226±1.2E-2	0.221	0.98	0.47	1.03
MIL-88B-5	0.202±3.2E-2	0.0281±1.7E-2	0.172±1.7E-2	0.162	0.94	0.41	0.909

[a] Micropore volume (cm^3/g)
[b] Mesopore volume (cm^3/g)
[c] Narrow micropore volume (cm^3/g)
[d] Ultramicropore volume (cm^3/g)
[e] Fraction of ultramicropore volume to narrow micropore volume
[f] at 7.6 bar and 298 K
[g] H_2 uptake per specific surface area

MIL-88B-3 whose BET surface area and the ultramicropore volume (0.22 cm^3/g) are the highest among the synthesized hierarchical porous MIL-88Bs, possesses the highest H_2 adsorption capacity (0.47 wt.% at 7.6 bar and 298 K). at which ultramicropores possess a volume of 0.22 cm^3/g (98% of the narrow micropore volume) and narrow micropores possess a volume of 0.226 cm^3/g.

MIL-88B-5 that is formed of ultramicropores (0.162 cm^3/g) possesses a H_2 adsorption capacity 1.69 times greater than MIL-88B-1. Despite the low narrow micropore volume of MIL-88B-5, MIL-88B-5 possesses ultramicropores in its pore structure, whereas there are no ultramicropores in the pore structure of MIL-88B-1. Therefore, the higher (1.69 times) H_2 adsorption capacity of MIL-88B-5 is attributed to: i) the presence of ultramicropores; and ii) the relatively narrower micropore size distribution. Figure 102 illustrates the different micropores size distribution of MIL-88B-1, MIL-88B-3, and MIL-88B-5 and Figure 103 and 104 illustrate the different pore size distributions of MIL-88B-1, MIL-88B-3, and MIL-88B-5.

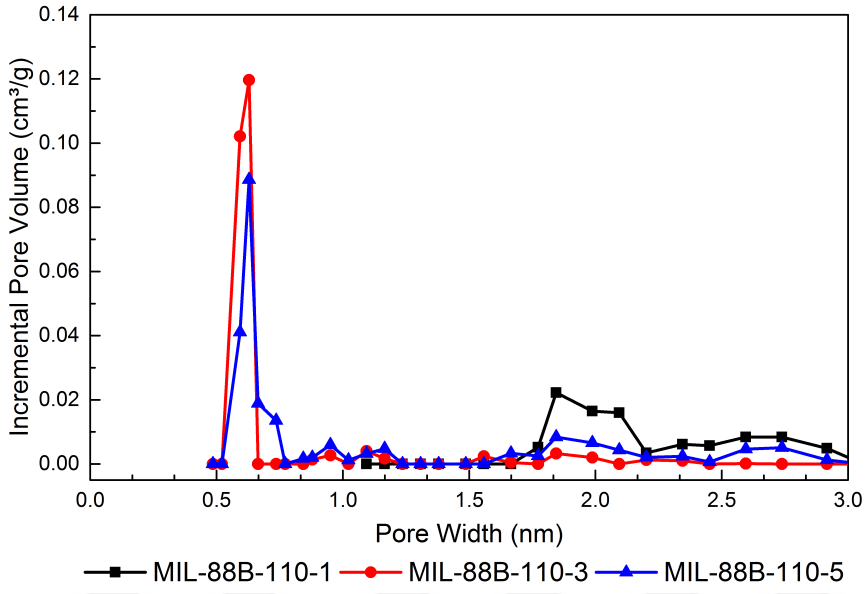

Figure 102. NLDFT plots of incremental pore volume versus pore width of hierarchical porous MIL-88Bs.

Vigorously stirring $FeCl_3.6H_2O$, TPA and DMF formed textural pores and differences in Fe:TPA ratio resulted in differences in textural porosity. NLDFT plot of MIL-88B-3 shows a sharp peak in 0.6 nm while MIL-88B-5 has a broadened peak centered at 0.65 nm with a lower volume increase with some small peaks located within the microporous range. In the case of MIL-88B-1, two peaks: i) one centred at the upper microporous range; and ii) the other centred at lower mesoporous range are observed. Different from MIL-88B-1 and MIL-88B-5, MIL-88B-3 is mainly formed of pores with identical pore sizes (0.6 nm). In the meantime, MIL-88B-1 and MIL-88B-5 possess a broader pore size range. Apparently, MIL-88B-5 is formed of micropores at the upper micropore size range and lower mesopore size range (pore diameter < 5 nm).

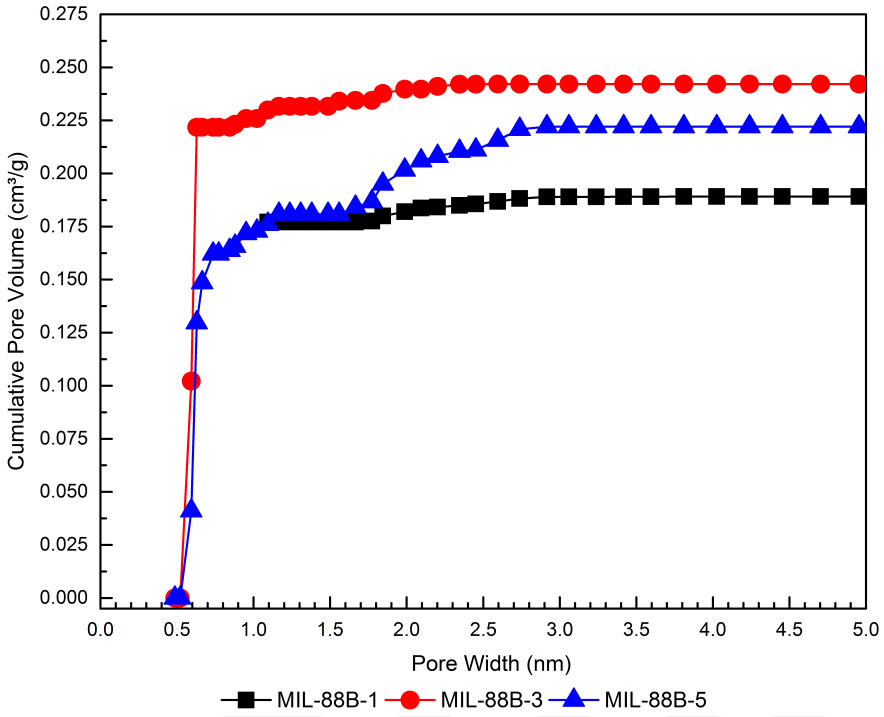

Figure 103. NLDFT plots of cumulative pore volume versus pore width of hierarchical porous MIL-88Bs.

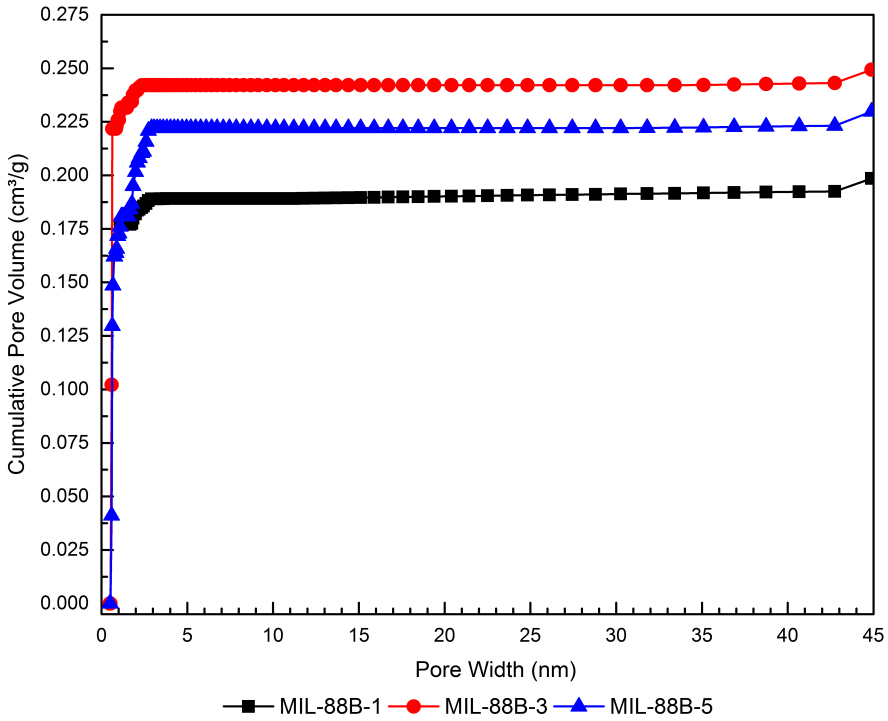

Figure 104. NLDFT plots of cumulative pore volume versus pore width of MIL-88B crystallites.

Unlike MIL-88B-1, and MIL-88B-5, MIL-88B-3 is mainly formed of pores with identical pore sizes (0.6 nm) and volume of these pores correspond to 89% of the overall pore volume. It is known that physisorption mechanism dominates adsorption in MOFs, and pore size influences the storage density heavily (Murray, Dincă, et al., 2009). More importantly, it is reported that at room temperature, pores that possess pore diameters of 6 to 8 Å achieves the highest van der Waals potential which can be explained by Lenard-Jones potential (Schlichtenmayer & Hirscher, 2012). Attractive forces dominate when the adsorbent and the hydrogen molecule is separated by a long distance whereas repulsion forces dominate when the adsorbent and the hydrogen molecule is separated by a short distance (Schlichtenmayer & Hirscher, 2012). Interestingly, theoretical studies show that when H_2 molecules are adsorbed on the wide pores, a hydrogen layer would be formed on the wells located close to the pore walls and a less dense layer of hydrogen would be adsorbed on the center of the pore which minimizes the attraction force felt by the pore walls and thereby, H_2 adsorption capacity decreases (Becher et al., 2003; Broom et al., 2019; Murray, Dincă, et al., 2009; Barbara Panella et al., 2005a; Schlichtenmayer & Hirscher, 2012, 2016; Schlichtenmayer, Streppel, & Hirscher, 2011).

In line with literature, we have found that the order of H_2 sorption capacity is from the highest to the lowest in accordance with the highest to the lowest volume of ultramicropores. Volume of ultramicropores present in MIL-88B-5 (0.162 cm^3/g) is 1.4 times less than the volume of ultramicropores present in MIL-88B-3 (0.221 cm^3/g). The significant increase in the adsorbed H_2 amount is attributed to: i) the presence of pores with pore sizes smaller than 0.7 nm which have stronger van der Waals interactions between the pore walls and H_2 molecules, ii) the higher volume of ultramicropores, and iii) the narrower pore size distribution (Rehman & Park, 2019a, 2019b; Schlichtenmayer & Hirscher, 2012; Schlichtenmayer et al., 2011; Qinyu Wang & Johnson, 1999).

Our results reveal that the volume of ultramicropores and their distribution within the microporous range influence the adsorbed H_2 amount heavily. MIL-88B-3 that is formed mainly of pores with pore diameters of 0.6 nm (89%) possesses an H_2 adsorption capacity 1.96 and 1.15 times greater than the measured H_2 sorption capacity of MIL-88B-1, and MIL-88B-5, respectively.

5.4. Comparison with Literature

Highly porous MOFs come to fore with their high surface area and low density in H_2 sorption studies (Murray, Dincă, et al., 2009). MIL-88B-3 possesses the highest H_2 sorption capacity among the synthesized hierarchical porous MIL-88Bs. Table 30 shows the reported H_2 sorption capacities of some of the MOFs.

Table 30. H_2 sorption capacities of MOFs

MOF	Pressure (bar)	Temperature (K)	H_2 sorption capacity (wt. %)	Reference
MIL-88B type MOF crystallites (this study)	7.6	298	0.47	
MIL-100	73.3	298	0.15	(Latroche, Surblé, Serre, Mellot-Draznieks, Llewellyn, Lee, Chang, Sung, et al., 2006b)
MIL-101 (Cr)	80	298	0.43	(Latroche, Surblé, Serre, Mellot-Draznieks, Llewellyn, Lee, Chang, Sung, et al., 2006b)
$Co_2(BDC)_2dabco$	10	298	0.03	(L. G. Zhu & Xiao, 2008)
HKUST-1	65	298	0.35	(Barbara Panella et al., 2006)
ZIF-8	60	298	0.13	(W. Zhou, Wu, Hartman, & Yildirim, 2007)
MOF-5	65	298	0.28	(Barbara Panella et al., 2006)
IRMOF-8	30	298	0.4	(Dailly, Vajo, & Ahn, 2006)
ZIF-8	60	298	0.13	(W. Zhou et al., 2007)

By introducing textural pores to the pore structure of MIL-88Bs and the control of textural porosity via Fe:TPA ratio, a H_2 adsorption capacity higher than some of those reported MOFs has been achieved. For instance, MIL-100 with a Langmuir surface area of

2700 m^2/g possesses an H_2 sorption capacity of 0.15 wt.% at 73.3 bar and 298 K (Latroche, Surblé, Serre, Mellot-Draznieks, Llewellyn, Lee, Chang, Sung, et al., 2006a); MIL-101(Cr) with a Langmuir surface area of 5500 m^2/g possesses an H_2 sorption capacity of 0.43 wt.% at 80 bar and 298 K (Latroche, Surblé, Serre, Mellot-Draznieks, Llewellyn, Lee, Chang, Sung, et al., 2006a); $Co_2(BDC)_2$dabco with a BET surface area of 1595 m^2/g possesses an H_2 sorption capacity of 0.03 wt.% at 10 bar and 298 K (L. G. Zhu & Xiao, 2008); HKUST-1 $(Cu_3BTC)_2$ with a BET surface area of 1154 m^2/g possesses an H_2 sorption capacity of 0.35 wt.% at 65 bar and 298 K (Barbara Panella et al., 2006); ZIF-8 with a BET surface area of 1630 m^2/g possesses an H_2 sorption capacity of 0.13 wt.% at 60 bar and 298 K (W. Zhou et al., 2007); MOF-5 with a BET surface area of 2296 m^2/g possesses an H_2 sorption capacity of 0.28 wt.% at 65 bar and 298 K (Barbara Panella et al., 2006); IRMOF-1 with a BET surface area of 572 m^2/g possesses an H_2 sorption capacity of 0.2 wt.% at 67 bar and 298 K; and IRMOF-8 with a Langmuir surface area of 1818 m^2/g possesses an H_2 sorption capacity of 0.4 wt.% at 30 bar and 298 K (Dailly et al., 2006); and ZIF-8 with a BET surface area of 1630 m^2/g possesses an H_2 sorption capacity of 0.13 wt.% at 60 bar and 298 K (W. Zhou et al., 2007).

Despite the relatively low BET surface area (452.4 m^2/g) of the hierarchically porous MIL-88Bs, their measured H_2 sorption capacity of 0.47 wt.% (298 K, 7.6 bar) is higher than the above-mentioned MOFs (Table 30). By the formation and control of textural porosity, a highly ultramicroporous MIL-88B is synthesized at which ultramicropores with pore diameters of 0.6 nm (89% of the total pore volume) dominate the pore structure and an H_2 adsorption capacity (0.47 wt.% at 7.6 bar and 298 K) that is greater than those of reported MOFs is attained.

5.5. Concluding Remarks

This study reveals the significant effect of ultramicropores on the adsorbed H_2 amount. Hierarchical porous MIL-88Bs were synthesized by a perturbation assisted nanofusion synthesis strategy that forms textural pores. The fraction and volume of textural mesoporosity were controlled by Fe:TPA ratio. MIL-88B-1, MIL-88B-3, and MIL-88B-5 with different pore size distributions show different H2 sorption capacities (0.24, 0.47, and 0.405 wt.%, respectively at 7.6 bar and 298 K). The highest H_2 adsorption capacity (0.47

wt.% H_2 sorption capacity at 7.6 bar and 298 K) belongs to MIL-88B-3 (MIL-88B-3) which possesses the highest fraction (89%) and volume (0.22 cm3/g) of ultramicropores. Additionally, a BET surface area 2.11 and 2.74 times higher than those of reported MIL-88B's has been achieved (C. Gao et al., 2017; Hou et al., 2018). Moreover, by the formation and control of hierarchical pores, the fraction of ultramicropores was increased to 89% which results measured H_2 adsorption capacities to increase by a factor of 1.96 (0.47 wt.% at 7.6 bar and 298 K).This measured H_2 adsorption capacity (at 7.6 bar and 298 K) of MIL-88B-3 is higher than some of those reported and commercially available MOFs which is thought to be a consequence of its high fraction of pores with pore diameters of 0.6 nm (89% of the total pore volume was formed of pores with 0.6 nm diameter) (Murray, Dincă, et al., 2009; Qinyu Wang & Johnson, 1999).

Our results show that H_2 adsorption capacity measured at 298 K is dependent on: i) the pore size of the porous sorbents (H_2 favors ultramicropores); and ii) the narrow distribution of ultramicropores through the micropore size distribution (high fraction of ultramicropores). This study is an experimental proof of the critical role of fraction and volume of ultramicropores on the adsorbed H_2 amount. The control of textural porosity via Fe:TPA ratio leads the way to increase the fraction of ultramicropores and thereby, enhances H_2 adsorption capacities at 298 K. Further studies should be focused on synthesizing MOFs formed of high fraction and volume of ultramicropores with pore diameters of 0.6 nm which would be the key to enhance H_2 sorption capacities measured at 298 K.

Chapter VI

Carbon dioxide adsorption capacity of Basolite F300 like hierarchical porous Fe-BTCs and the role of ultramicropores

6.1. Background

From pre-industrial period (1850 to 1900) till today, global mean surface temperature has increased by 1 °C (IPCC, 2018). In the evidence of increased global mean surface temperature, climate and weather extremes become more apparent (IPCC, 2018). The greenhouse gas emissions measured in 2010 were the highest of those measured greenhouse gas emissions through the human history.

Within the framework of Paris Agreement, a target has been set to decrease the greenhouse gas emissions. Among the greenhouse gasses CO_2 is the one that plays the key role in climate change (Ciais et al., 2013). Particularly, water vapor, methane, and nitrous oxides leave the atmosphere in 10 days, 10 years, and 100 years, respectively, while 10% of the CO_2 produced today remains in the atmosphere for 10 thousand years (Ciais et al., 2013). Within the last forty years, cumulative CO_2 concentrations reached the 50% of the cumulative CO_2 concentrations measured in between 1750 and 2010 (Intergovernmental Panel on Climate Change, 2014) and Intergovernmental Panel on Climate Change pointed out the necessity to develop and improve technologies to decrease CO_2 emissions (Metz et al., 2005). CO_2 capture and storage (CCS) technologies come to the fore with its ability to decrease CO_2 emissions by 80 to 90% (Metz et al., 2005) at which CO_2 is first separated from its source, then transported and stored at a site.

In order to increase the efficiency and the practical use of CCS technologies, researchers pointed out the need of cost-effective functional materials that will decrease the energy requirements and eliminate the by-product formation (S. Choi et al., 2009a; Cuéllar-Franca & Azapagic, 2015).

MOFs are highly crystalline materials that are introduced in 1995 (O M Yaghi et al., 1995). MOFs are formed of an organic and an inorganic part (O M Yaghi et al., 1995) and

come to the fore among the porous materials with their designable organic ligands, tunable pore structure, and high chemical stability (Rowsell & Yaghi, 2004a). MOFs have the listed advantages over other porous sorbents: i) reticular chemistry allow MOFs to be designed with the desired properties (Furukawa, Cordova, O'Keeffe, & Yaghi, 2013); ii) MOFs can be controlled at molecular level (Juncong Jiang, Zhao, & Yaghi, 2016); and iii) high and tuneable porosity allow MOFs to store large amounts of gases. Particularly, activated carbons with high BET surface areas and pore volumes have limited use in CO_2 capture studies due to their low CO_2/N_2 selectivity. Similarly, despite their high BET surface areas, the low CO_2 uptake capacities of zeolites decrease their use in CCS studies. To illustrate, CO_2 adsorption capacity of MOF-177 is 9 times higher than zeolite 13X at 35 bar (S. Choi et al., 2009a). Thereby, synthesizing MOFs with high BET surface for high CO_2 adsorption capacity has drawn particular attention.

The conventional MOF synthesis lasts for days to weeks and only a few milligrams of MOF can be produced. However, a large quantity of MOF is needed for industrial and commercial uses. Researchers have been searching for synthesis methods that produce high yields of MOF. MIL-53(Al) (Basolite A100), HKUST-1 (Basolite C100), Fe-BTC (Basolite F300), ZIF-8 (Basolite Z1200), MOF-177 (Basolite Z377), and magnesium formate (Basosiv M050) have been commercialized under the name of Basolite. Among the commercialized MOFs, Fe-BTC (Basolite F300) stands out among the others with its high thermal stability and low toxicity (Horcajada et al., 2012). Additionally, the high BET surface area and the high porosity of Fe-BTC (Basolite F300), increases its possibility to be used in CO_2 capture studies.

Fe-BTC (Basolite F300) is formed of Fe(III) and BTC (benzene-1,3,5-tricarboxylic acid). Interestingly, there is another MOF structure formed of the same starting chemicals, MIL-100(Fe). But these two MOFs differ from each other by their relative crystallinities, and BET surface areas. MIL-100(Fe) is a highly crystalline MOF while Fe-BTC (Basolite F300) has a disordered nature. Even though the crystal structure of Fe-BTC (Basolite F300) has been a mystery, its structure is thought to be similar of MIL-100(Fe), at which trimers of iron octahedra share a common vertex and linked by benzene-1,3,5-tricarboxylic acid.

To the best of our knowledge, despite its high BET surface area and porosity, there has been a study that has reported the CO_2 adsorption capacity of Fe-BTC (Basolite F300) (M. Du, Li, Li, & Si, 2016).

Herein, we report the CO_2 adsorption capacity of a series of Fe-BTC synthesized by a perturbation assisted nanofusion synthesis strategy that forms hierarchical pores. By the perturbation assisted nanofusion synthesis strategy, BET surface area, and total pore volume are increased by a factor of 1.6 and 3.1 times, respectively (Dhakshinamoorthy, Alvaro, Chevreau, et al., 2012; Dhakshinamoorthy, Alvaro, & Garcia, 2011; Dhakshinamoorthy, Alvaro, Horcajada, et al., 2012) and a Fe-BTC that possesses ultramicropores were formed. The reported BET surface area, and total pore volume are the highest of the BET surface area, and total pore volume reported for Fe-BTC, so far (Dhakshinamoorthy et al., 2011; Dhakshinamoorthy, Alvaro, & Garcia, 2012; M. Du et al., 2016; X. Hu et al., 2016; Opanasenko et al., 2013; Zukal, Opanasenko, Rubeš, Nachtigall, & Jagiello, 2015).

Among the synthesized Fe-BTCs, the highest CO_2 uptake capacity (5.20 wt.% at 1 bar and 298 K, 27.5 wt.% at 8.5 bar and 298 K) belongs to Fe-BTC-150-3 which is also higher than those of MOFs reported in literature (Gumma, Chowdhury, & Bikkina, 2009; Loiseau et al., 2006; Mallick, Saha, Pachfule, Roy, & Banerjee, 2010; Mason, Sumida, Herm, Krishna, & Long, 2011b; Millward & Yaghi, 2005a; W. Morris et al., 2010; H. J. Park, Cheon, & Suh, 2010; Phan et al., 2010; Surblé, Millange, et al., 2006; Wiersum et al., 2011; A. Ö. Yazaydin et al., 2009).

Our results demonstrate the critical role of ultramicropores on the adsorbed CO_2 amount and show that adsorbed CO_2 amount depends on: i) the presence of ultramicropores; ii) narrow micropore volume; and iii) the narrow distribution of narrow micropores through the micropores (Aysu Yurduşen, Yürüm, & Yürüm, 2020b).

6.2. Experimental

Fe-BTCs were repetitively synthesized for five times and characterization analyses were conducted for five times.

6.2.1. Materials

All the chemicals were used as received. 98% pure (ACS Reagent grade) iron(III) chloride hexahydrate ($FeCl_3.6H_2O$) was supplied from Merck Millipore. 95% pure benzene-

1,3,5-tricarboxylic acid, 99.9% pure (HPLC grade) *N,N*-Dimethylformamide (DMF), and 99.8% pure methanol were supplied from Sigma Aldrich.

6.2.2. Synthesis of Hierarchically Porous Fe-BTCs

A perturbation assisted nanofusion mechanism was used to form hierarchical pores. 3.1 mmoles of $FeCl_3.6H_2O$, (0.62 mmoles, 1 mmoles, or 3.1 mmoles) benzene-1,3,5-tricarboxylic acid, and 80 mL of DMF was mixed vigorously via a magnetic stirrer with a stirring rate of 800 rpm for an hour at room temperature (298 K). By vigorously stirring metal salt, benzene-1,3,5-tricarboxylic acid, and DMF, the growth of large single crystals was prevented. At the end of stirring, a clear solution was obtained which was then poured into glass vials (20 mL) capped with Teflon caps. Glass vials filled with clear solutions were heated in an isothermal oven at 110, 130, and 150 °C for 2 days. Obtained precipitates and the solutions were transferred into 50 mL falcon tubes. Solvent exchange process was carried out for 6 days (three times with DMF and three times with methanol) and each solvent was changed at the end of 24 hours. At the end of the washing process, samples were dried under vacuum at 100 °C for 30 hours. Table 31 illustrates the sample abbreviations for hierarchically porous Fe-BTCs.

Table 31. Sample abbreviations for hierarchical porous Fe-BTCs

Sample Abbreviation	Synthesis Temperature (°C)	Fe:BTC ratio
Fe-BTC-110-1	110	1
Fe-BTC-110-3	110	3
Fe-BTC-110-5	110	5
Fe-BTC-130-1	130	1
Fe-BTC-130-3	130	3
Fe-BTC-130-5	130	5
Fe-BTC-150-1	150	1
Fe-BTC-150-3	150	3
Fe-BTC-150-5	150	5

6.2.3. Characterization of Hierarchically Porous Fe-BTCs

Characterization analyses were repeated for five times. Characterization analyses were performed by powder x-ray diffraction (PXRD) analysis, scanning electron microscopy (SEM), Brunauer-Emmett-Teller (BET) surface area and pore size distribution analysis, Fourier Transform Infrared Spectroscopy (FT-IR) analysis, and thermogravimetric analysis (TGA). CO_2 uptake capacities were measured at 298 K by an Intelligent Gravimetric Analyzer (IGA).

6.2.3.1. X-ray diffraction

0.15406 nm Cu Kα radiation, 40 kV was used as X-ray generator voltage and 5 mA current was used in X-ray diffraction analysis. X-ray diffraction analysis were performed with a step size of 0.02° in between 2 and 90°.

6.2.3.2. Scanning electron microscopy (SEM)

A Leo Supra 35 VP field emission scanning electron microscope was used in SEM imaging. A working distance of 8 to 9 mm was used, and the voltage was set depending on the Fe-BTC imaged.

6.2.3.3. Brunauer-Emmett-Teller (BET) surface area and pore size distribution analyses

A Micromeritics 3Flex Instrument were used for BET surface area measurements and pore size distribution analysis. 100 to 150 milligrams (mg) of Fe-BTC weighed for each BET analysis. Fe-BTC were degassed for 6 hours at 120 °C and NLDFT method was used for pore volume estimations. BET surface areas were calculated in between the relative pressure(P/P_0) range of 0.05 and 0.099.

6.2.3.4. Fourier transform infrared spectroscopy (FTIR) analyses

Thermo Scientific Nicolet Is10 was used for FTIR analysis. Analyses were conducted with a spectral resolution of 4 cm^{-1} for the wavelengths ranging between 600 to 4000 cm^{-1}. Scans were repeated for 32 times and background noise was corrected.

6.2.3.5. Thermogravimetric analysis (TGA)

Shimadzu DTG-60H simultaneous thermal analysis (TG-DTA) was used in thermogravimetric analysis. Under a continuous flow of N_2 (20 mL/min) samples were heated from 25 to 1200 °C with a heating rate of 10 K. For each TGA test 32±5 mg of Fe-BTC was used.

6.3. Results and Discussion

6.3.1. XRD Analysis

XRD patterns of hierarchically porous Fe-BTCs are illustrated at Figure 105. Poor crystallinity observed in the XRD patterns is a consequence of the semiamorphous nature of Fe-BTC.

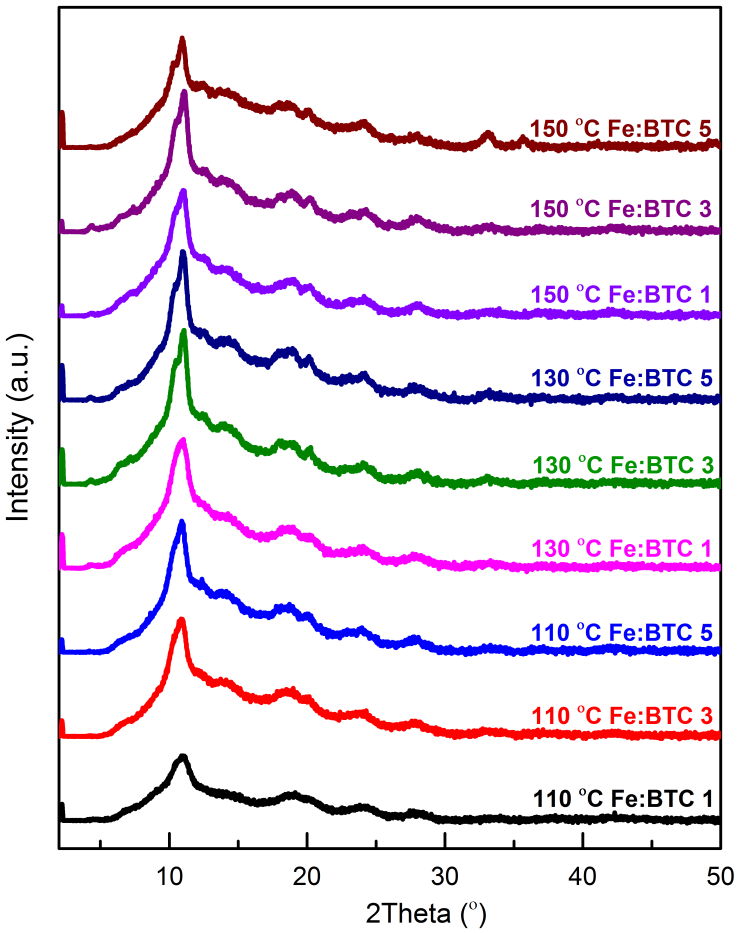

Figure 105. XRD patterns of hierarchically porous Fe-BTCs.

Similarities in Bragg peak positions and similar Bragg peak intensities reveal that Fe-BTC was synthesized successfully by the perturbation assisted nanofusion synthesis strategy.

XRD patterns consist broad bands with relatively weak intensities which illustrates the disordered nature of Fe-BTC. Additionally, synthesizing Fe-BTC via a perturbation

assisted nanofusion synthesis strategy caused nanosized MOF crystallites to be embedded in an amorphous matrix which caused broadening in bands (Cao et al., 2016).

XRD patterns of Fe-BTC type crystallites agree well with each other having Bragg reflections located at the same peak positions. XRD patterns comparing the peak positions of Fe-BTC synthesized at 110, 130, and 150 °C can be found in Supplementary Information. Moreover, it was proved by single crystal X-ray crystallography analyses that micro-sized single crystals were not formed and there were no metallic-iron present.

6.3.2. SEM Images

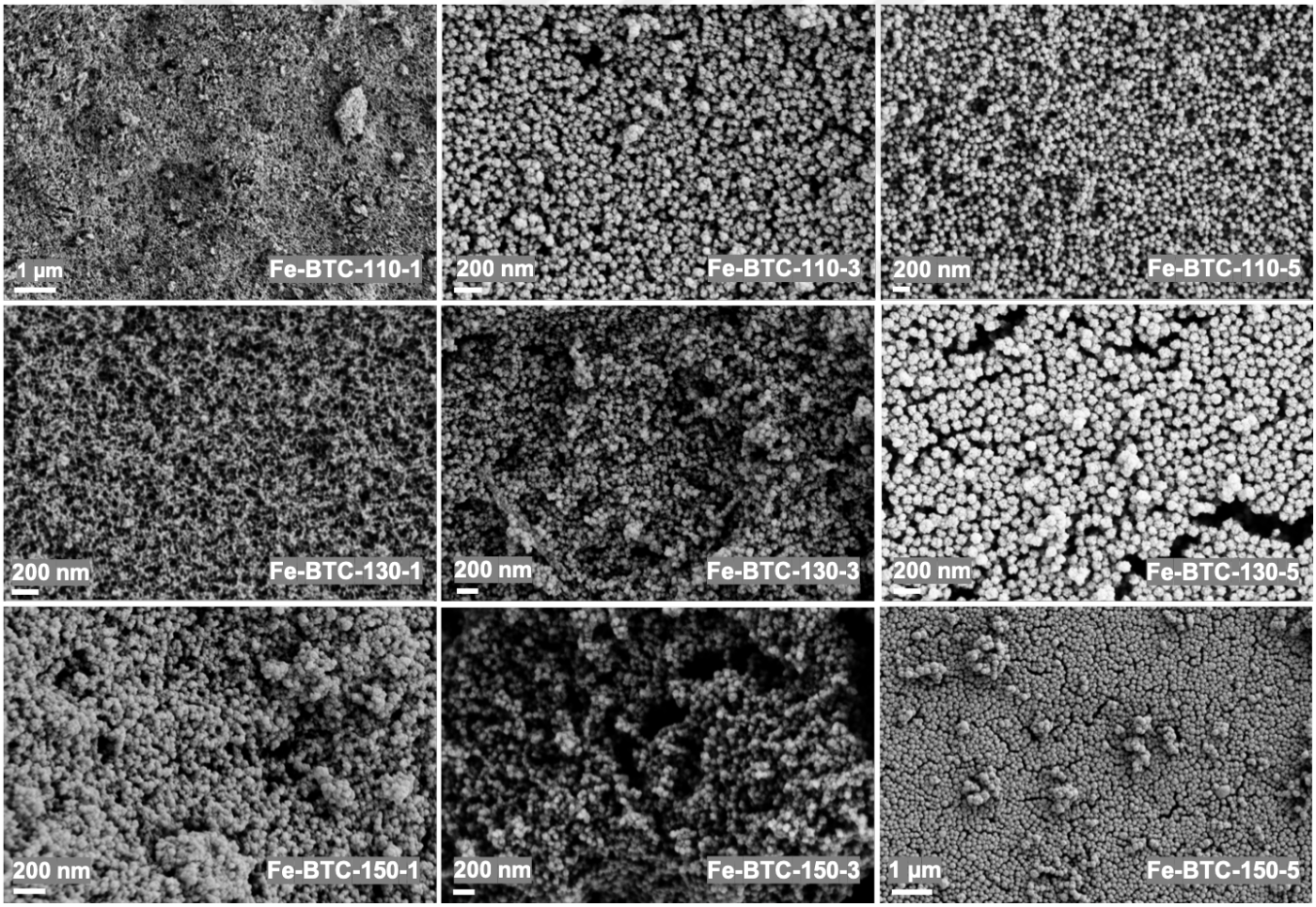

Figure 106. SEM images of hierarchically porous Fe-BTCs.

Figure 106 shows the SEM images hierarchically porous Fe-BTCs. SEM images illustrates the highly porous nature of Fe-BTC. Synthesizing Fe-BTC with a perturbation assisted nanofusion synthesis strategy resulted SBUs (secondary building units) to aggregate into nanosized Fe-BTC crystals which were embedded in an amorphous matrix. The aggregated SBUs, nanosized Fe-BTC crystals and the interconnected porous network can be visibly seen in the SEM images (Figure 106).

6.3.3. N_2 Sorption Isotherms

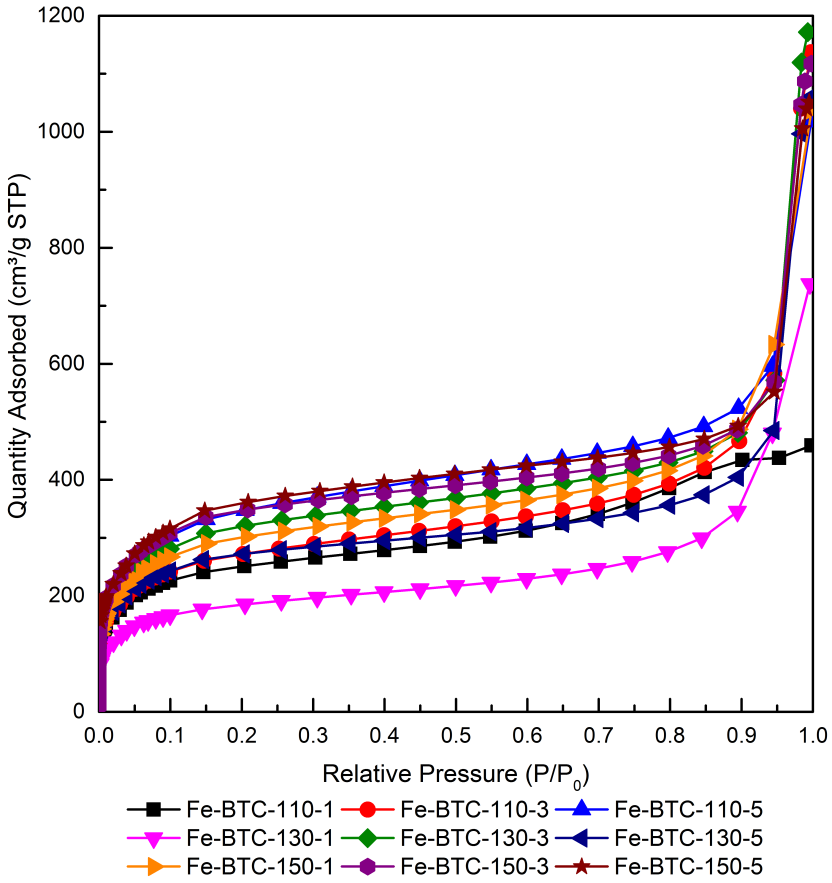

Figure 107. N_2 sorption isotherms of hierarchically porous Fe-BTCs.

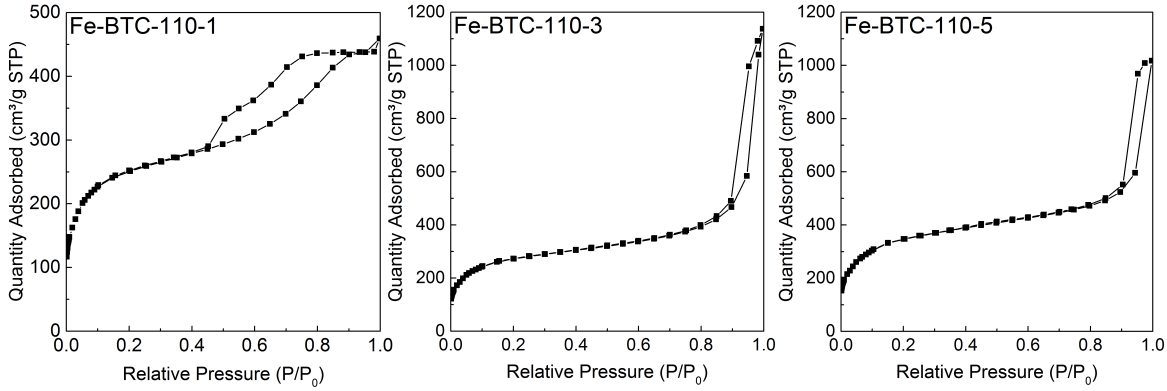

Figure 108. N_2 sorption isotherms of Fe-BTC-110-1, Fe-BTC-110-3, and Fe-BTC-110-5.

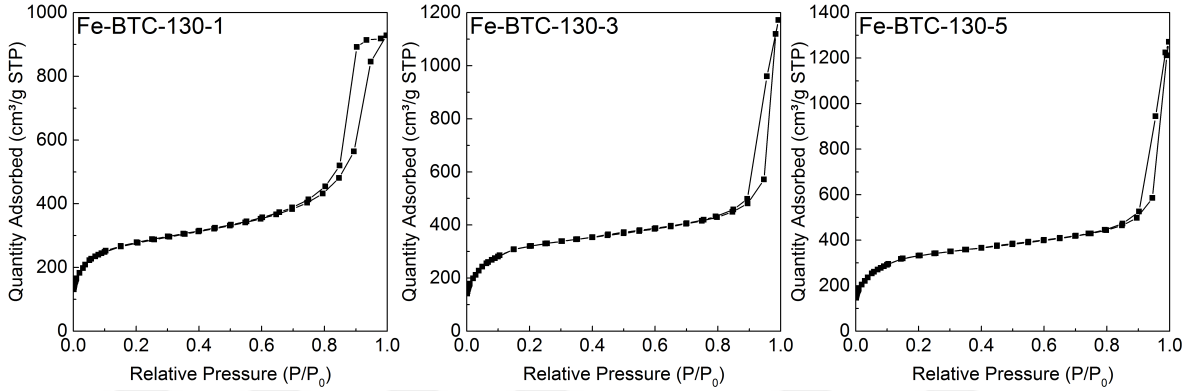

Figure 109. N_2 sorption isotherms of Fe-BTC-130-1, Fe-BTC-130-3, and Fe-BTC-130-5.

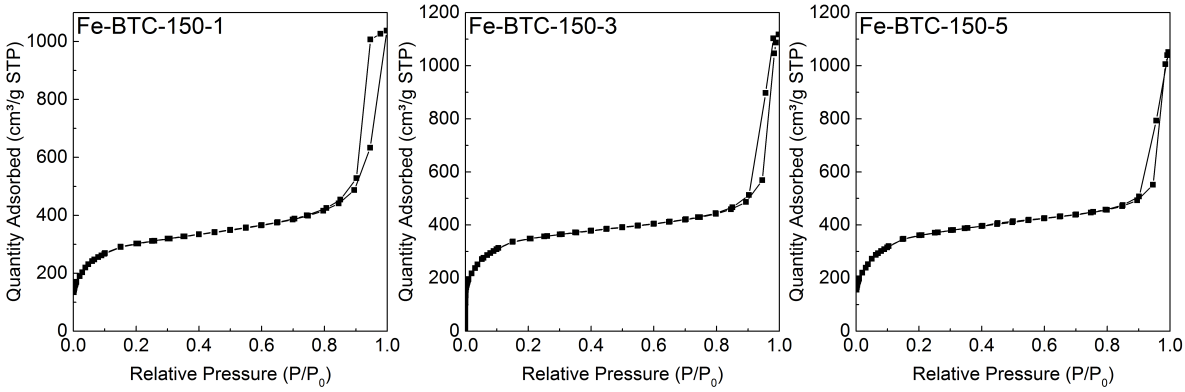

Figure 110. N_2 sorption isotherms of Fe-BTC-150-1, Fe-BTC-150-3, and Fe-BTC-150-5.

Figure 107-110 illustrate N_2 sorption isotherms hierarchically porous Fe-BTCs. N_2 sorption isotherms followed typical IUPAC type IV isotherms with some microporosity present. At low pressures ($P/P_0 < 0.1$), high N_2 uptakes are observed. These high N_2 uptakes are attributed to micropores present in the pore structure. In between relative pressures of 0.2 and 0.9, a true horizontal plateau cannot be achieved, and the observed slope is associated

with mesopore filling. At pressures close to saturation pressure ($0.9 < P/P_0 < 1$), the amount of N_2 adsorbed increased drastically which illustrates that pores with pore diameters at the upper mesopore size range is present.

6.3.4. Pore Size Distribution Analysis

6.3.4.1.t-plot method

t-plots of Fe-BTCs can be found below at Figure 111. t-plots show the amount of N_2 adsorbed at standard temperature and pressure with respect to statistical thickness (Lowell et al., 2004a).

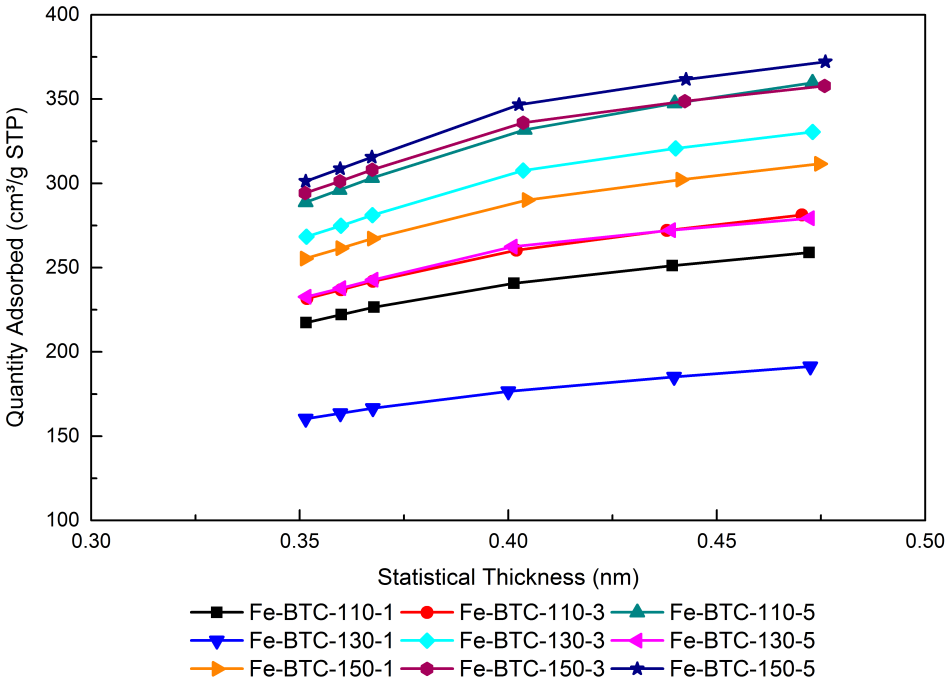

Figure 111. t-plots of hierarchically porous Fe-BTCs.

t-plots show deviations from the straight line. Deviations are towards downwards and t-plots held positive intercepts which suggest the presence of micropores (Lowell et al., 2004a). The highest micropore volume (0.181 cm^3/g) belongs to Fe-BTC-150-3 while the lowest micropore volume belongs to Fe-BTC-130-1 (0.112 cm^3/g). Respective micropore

volumes, micro- and mesopore areas estimated by t-plot method can be found below at Table 32.

Table 32. Micro- and mesopore area (m^2/g), micropore volume of Fe-BTC type crystallites estimated by t-plot method.

Hierarchically porous Fe-BTCs	Smicro (m^2/g)	Smeso (m^2/g)	Smicro (%)	Vmicro (cm^3/g)
Fe-BTC-110-1	419.4±3.2E1	531±1.2E2	44.9	0.154±1.6E-2
Fe-BTC-110-3	374.1±3.7E1	650±1.8E2	36.5	0.135±1.0E-2
Fe-BTC-110-5	388.8±8.9E1	913.8±1.6E2	29.8	0.133±4.0E-2
Fe-BTC-130-1	298.2±7.1E1	394.7±1.9E2	43.1	0.112±2.5E-2
Fe-BTC-130-3	400.7±6.0E1	806.4	33.2	0.139±2.3E-2
Fe-BTC-130-5	418.9±4.4E1	605.7±1.2E2	40.8	0.146±1.6E-2
Fe-BTC-150-1	425.5±5.3E1	713.6±7.4E1	37.4	0.151±2.6-2
Fe-BTC-150-3	509.6±6.0E-1	803.2±1.2E1	38.8	0.181
Fe-BTC-150-5	458.7±1.5E2	897.2±7.7	33.8	0.159±7.8E-2

6.3.4.2.NLDFT method

Figure 112 represents the NLDFT plots of Fe-BTC type crystallites.

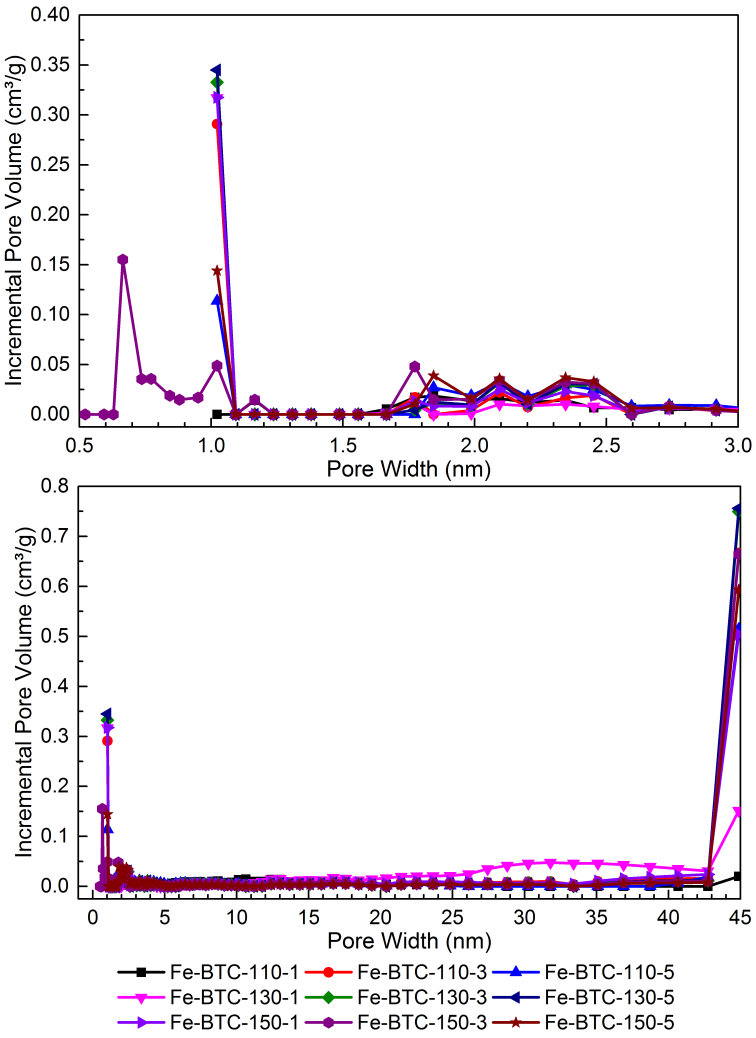

Figure 112. NLDFT plots of Fe-BTC type crystallites.

NLDFT plots (Figure 112) illustrate the different pore size distributions of Fe:BTCs. Remarkably, it is Fe-BTC-150-3 that has ultramicropores in its pore structure while the others have contributions from pores with pore diameters greater than 1 nm. Table 33 summarizes the pore volumes of narrow micropores, micropores, upper mesopores and mesopores, total pore volumes estimated by NLDFT method.

Table 33. Volume of pores smaller than 1 nm, micro-, uppermeso-, mesopore and total pore volume, and fraction of micropores of Fe-BTCs estimated by NLDFT method.

	Vpores <1 nm (cm^3/g)	Vmicro (cm^3/g)	Vuppermeso (cm^3/g)	Vmeso (cm^3/g)	Vtotal (cm^3/g)	Vmicro (%)
Fe-BTC-110-1	0.265±0.019	0.350±0.019	0.020±0.005	0.367±0.043	0.717±0.053	48.8
Fe-BTC-110-3	0.291±0.063	0.334±0.075	0.667±0.135	1.056±0.102	1.390±0.051	24.0
Fe-BTC-110-5	0.365±0.033	0.444±0.052	0.510±0.062	0.856±0.071	1.300±0.110	34.2
Fe-BTC-130-1	0.198±0.074	0.234±0.077	0.332±0.093	0.725±0.204	0.959±0.281	23.9
Fe-BTC-130-3	0.333±0.007	0.389±0.038	0.750±0.125	1.065±0.159	1.454±0.121	26.8
Fe-BTC-130-5	0.292±0.027	0.348±0.050	0.698±0.074	0.942±0.099	1.289±0.100	26.9
Fe-BTC-150-1	0.318±0.008	0.373±0.008	0.504±0.087	0.917±0.065	1.290±0.064	28.9
Fe-BTC-150-3	0.326±0.004	0.453±0.006	0.664±0.044	0.957±0.063	1.410±0.057	32.1
Fe-BTC-150-5	0.367±0.015	0.468±0.030	0.590±0.280	0.872±0.287	1.340±0.257	34.9

It is observed that volume of narrow micropores, micropores, upper mesopores, and mesopores differ with synthesis temperature and Fe:BTC ratio. It is notable that, Fe-BTC-110-1 possesses a relatively lower mesopore volume (0.0201±0.005 cm3/g) than Fe-BTC-110-3, and Fe-BTC-110-5. Mesopore volume of Fe-BTC-110-1 is 2.88 and 2.33 times lower than the mesopore volumes of Fe-BTC-110-3, and Fe-BTC-110-5, respectively and the total pore volume of Fe-BTC-110-1 is 1.94 and 1.8 times lower than the total pore volume of Fe-BTC-110-3, and Fe-BTC-110-5, respectively. These differences observed in pore size distribution reveal that textural porosity differ with synthesis temperature and Fe:BTC ratio. Within the synthesized Fe-BTCs, the highest micropore volume belongs to Fe-BTC-150-5 (0.468±0.0296 cm^3/g) and the highest total pore volume (1.45±0.12 cm^3/g) belongs to Fe-

BTC-130-3. Remarkably, it is Fe-BTC-150-3 that possess ultramicropores (0.19 cm^3/g) in its pore size distribution while none of the Fe-BTCs synthesized in this study possess ultramicropores.

6.3.4.3.FTIR analysis

FTIR spectra of hierarchically porous Fe-BTCs can be found below in Figure 113-117.

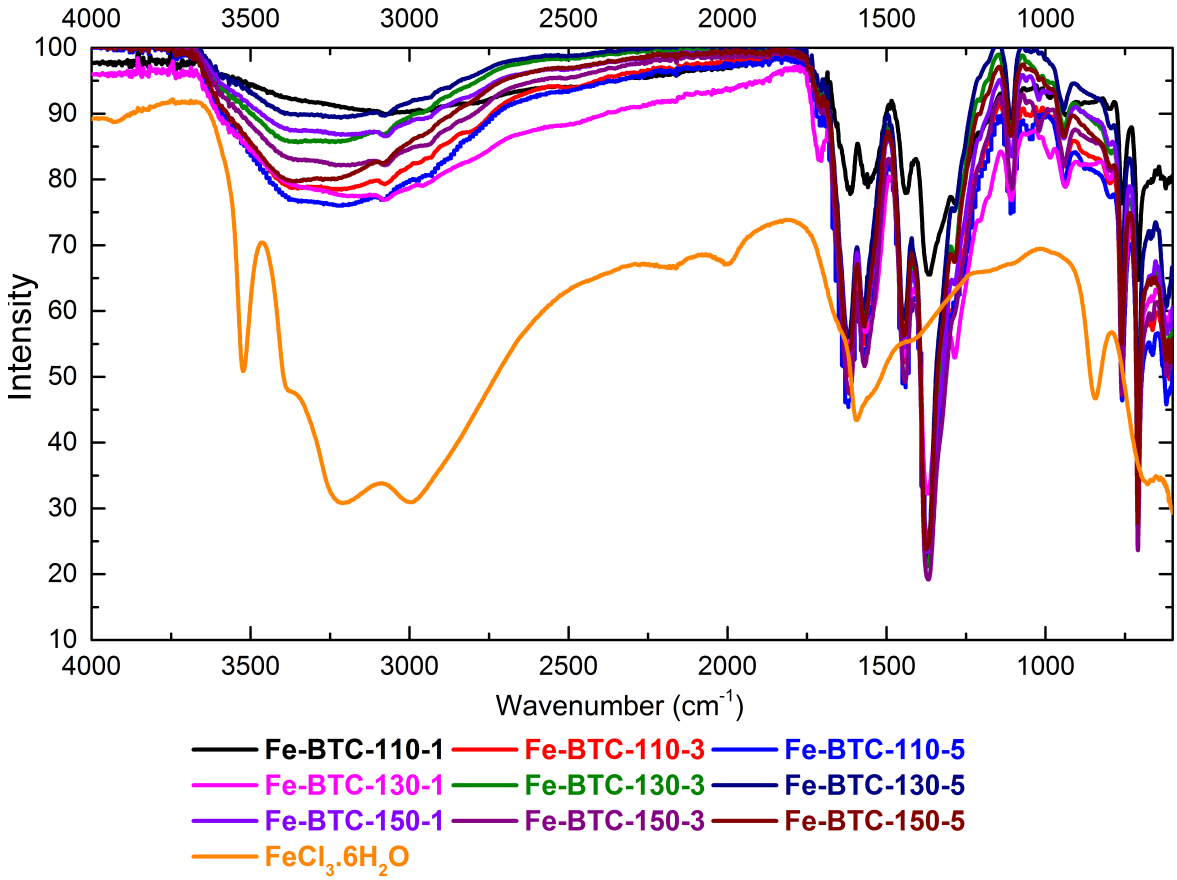

Figure 113. FTIR spectra of hierarchically porous Fe-BTCs and $FeCl_3.6H_2O$.

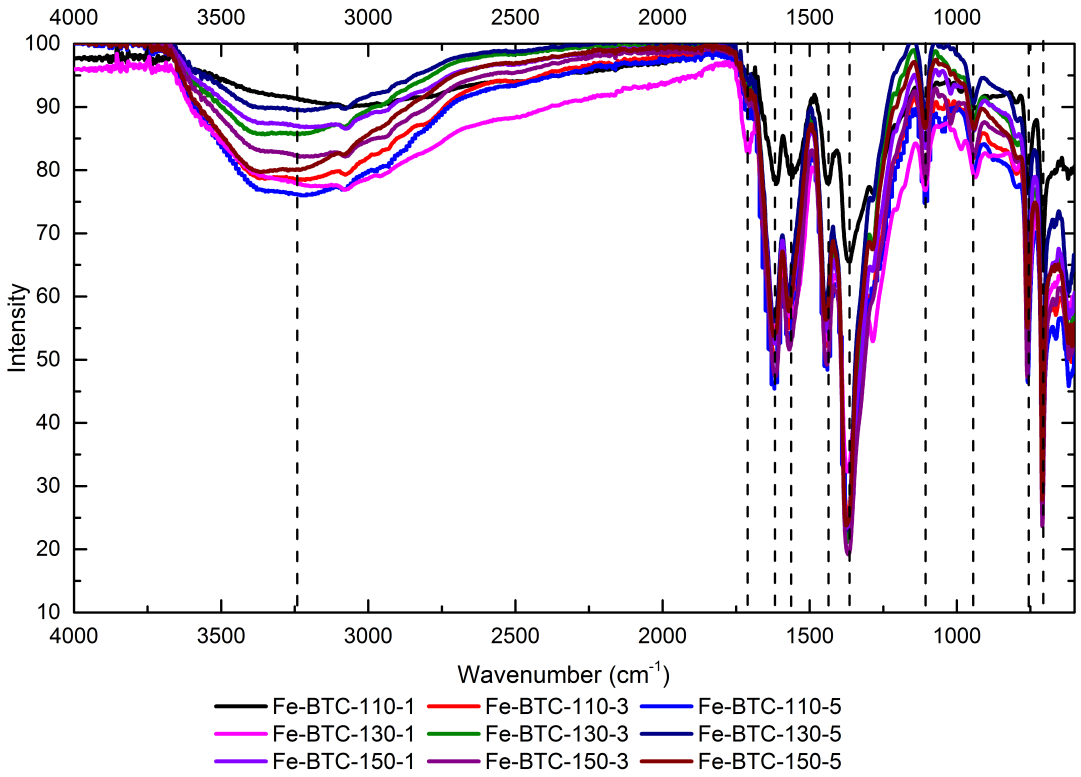

Figure 114. FTIR spectra of hierarchically porous Fe-BTCs.

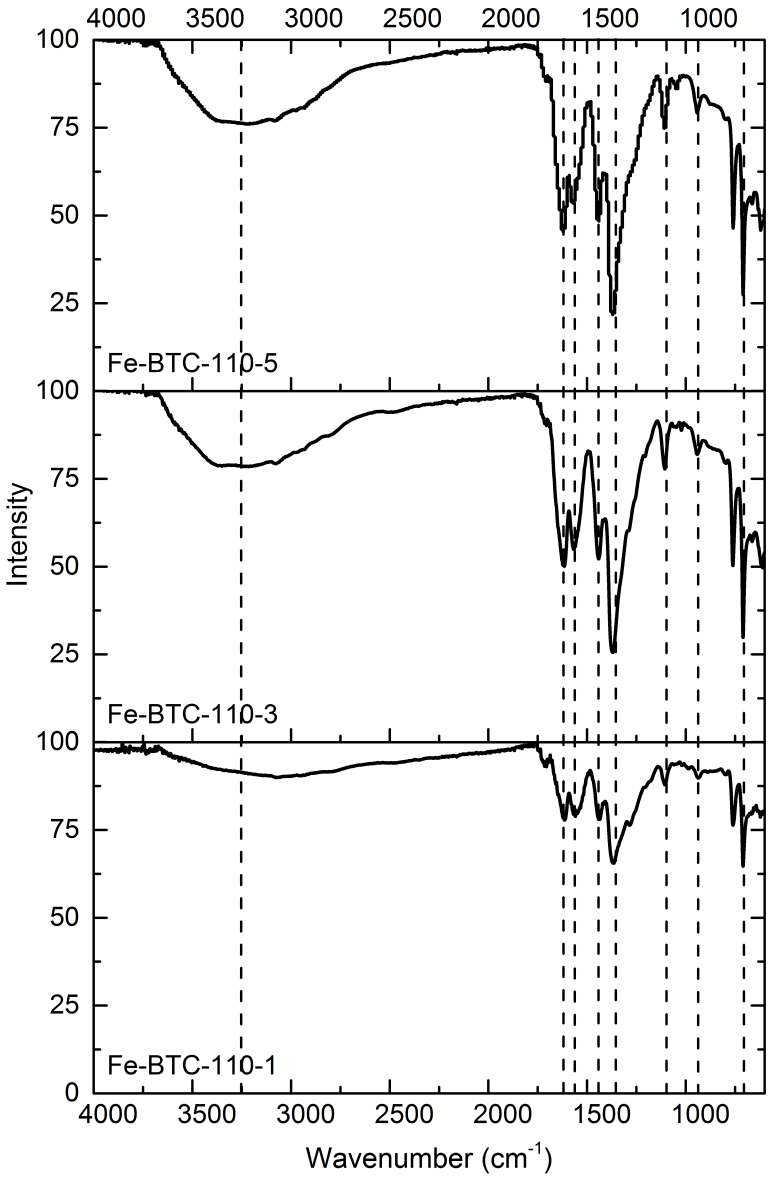

Figure 115. FTIR spectra of Fe-BTC-110-1, Fe-BTC-110-3, and Fe-BTC-110-5.

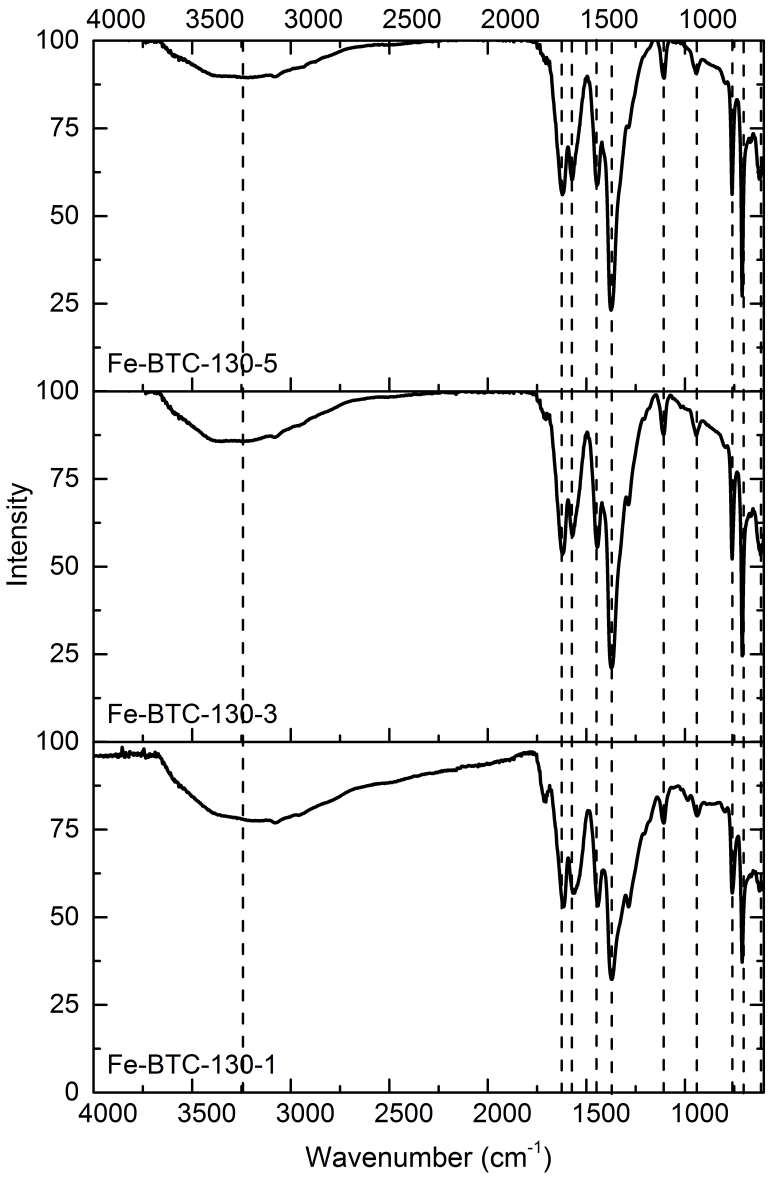

Figure 116. FTIR spectra of Fe-BTC-130-1, Fe-BTC-130-3, and Fe-BTC-130-5.

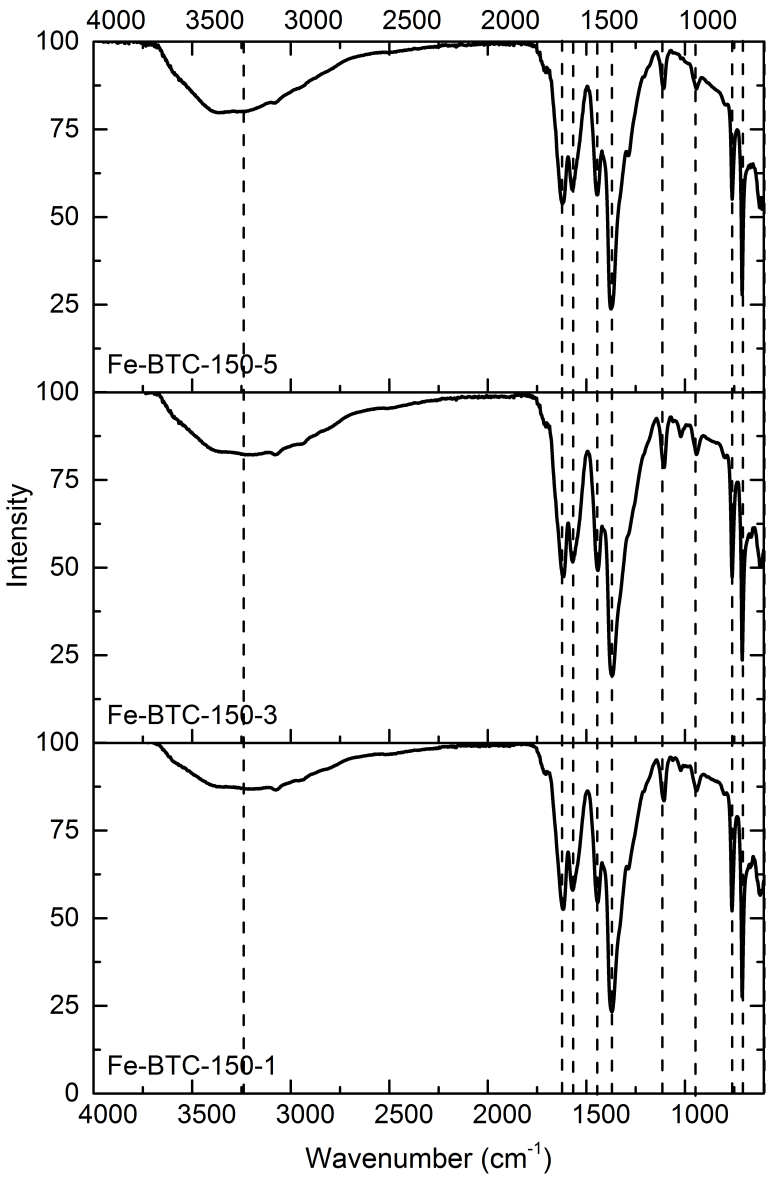

Figure 117. FTIR spectra of Fe-BTC-150-1, Fe-BTC-150-3, and Fe-BTC-150-5.

FTIR spectra of the hierarchically porous Fe-BTCs synthesized in this study, agree well with the FTIR spectra of the reported Fe-BTCs (Basolite F300) (Dhakshinamoorthy, Alvaro, Horcajada, et al., 2012; X. Hu et al., 2016; Oveisi, Khorramabadi-Zad, & Daliran, 2016). Fe-BTCs show broad bands in between 3000 and 3400 cm^{-1}. Observed broad bands are assigned to OH groups that are hydrogen-bonded water molecules which are adsorbed during FTIR analysis conducted under air environment. The broadened OH bands demonstrate the increase in the number of adsorbed water molecules at the open metal sites which is due to the increased number of unsaturated metal sites. Presence of the peaks at

1370, 1441, 1569, and 1621 cm^{-1} prove that -COOFe metallic esters are present in the synthesized Fe-BTC structure and BTC is successfully attached to Fe. The peaks at 1569 and 1621 cm^{-1} are assigned to bending modes of molecular water which reveals that Fe sites are coordinated with water. A remarkable shift to lower frequencies (1369 and 1440 cm^{-1}) occurred in the characteristic peaks (1375 and 1450 cm^{-1}) of carboxylate symmetric stretching mode. This remarkable shift is attributed to elongated bonds. The peaks at 941 and 1105 cm^{-1} are assigned to C-H in-plane and out-of-plane bending modes. The peaks at 709 and 760 cm^{-1} are assigned to C-C ring out-of-plane bending mode and characteristic of Fe-BTC structure. Lastly, the peak at 612 cm^{-1} is assigned to central oxygen in single Fe_3O.

Lastly, FTIR spectrum of hierarchically porous Fe-BTCs were compared with the FTIR spectra of $FeCl_3.6H_2O$. None of the peaks observed in the FTIR spectra of $FeCl_3.6H_2O$ (842 cm^{-1}, 1594 cm^{-1}, 2993 cm^{-1}, 3212 cm^{-1}, and 3523 cm^{-1}) were observed in the FTIR spectrum of hierarchically porous Fe-BTCs which proves that there are no metallic iron present.

6.3.4.4.TGA

TGA curves of Fe-BTCs are presented below at Figure 118-127 and Table 34-36 show the percentage of mass loss during TGA.

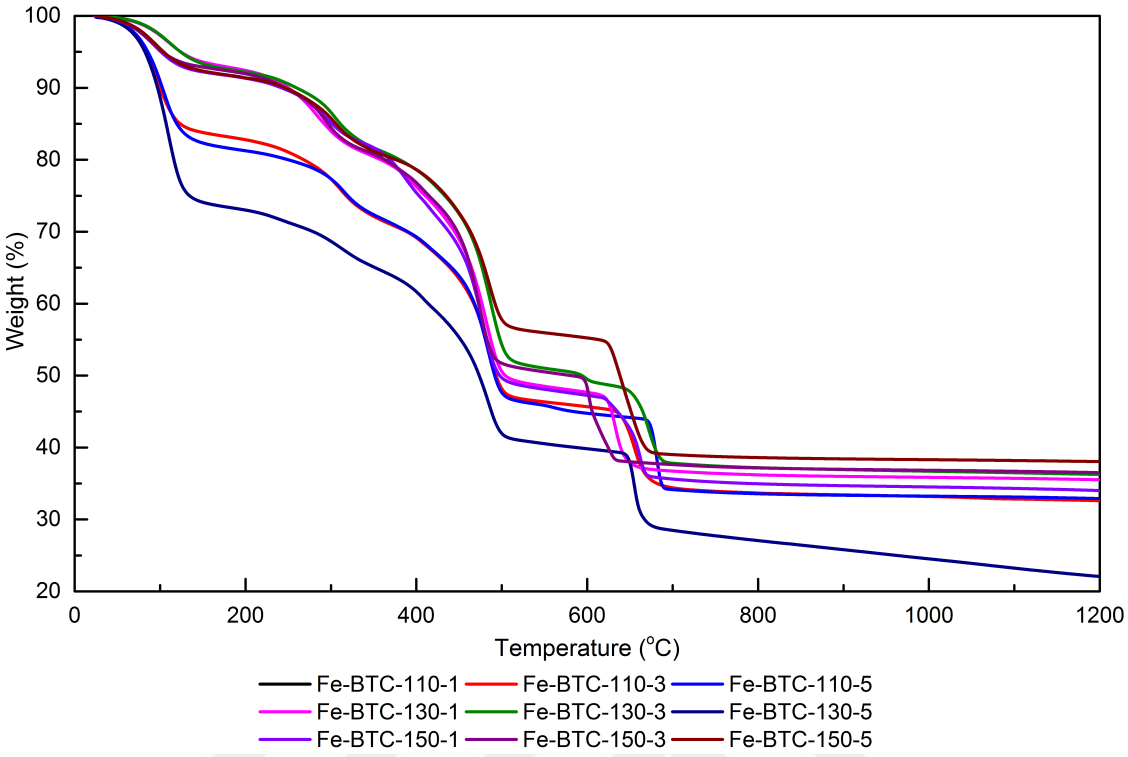

Figure 118. TGA curves of Fe-BTCs.

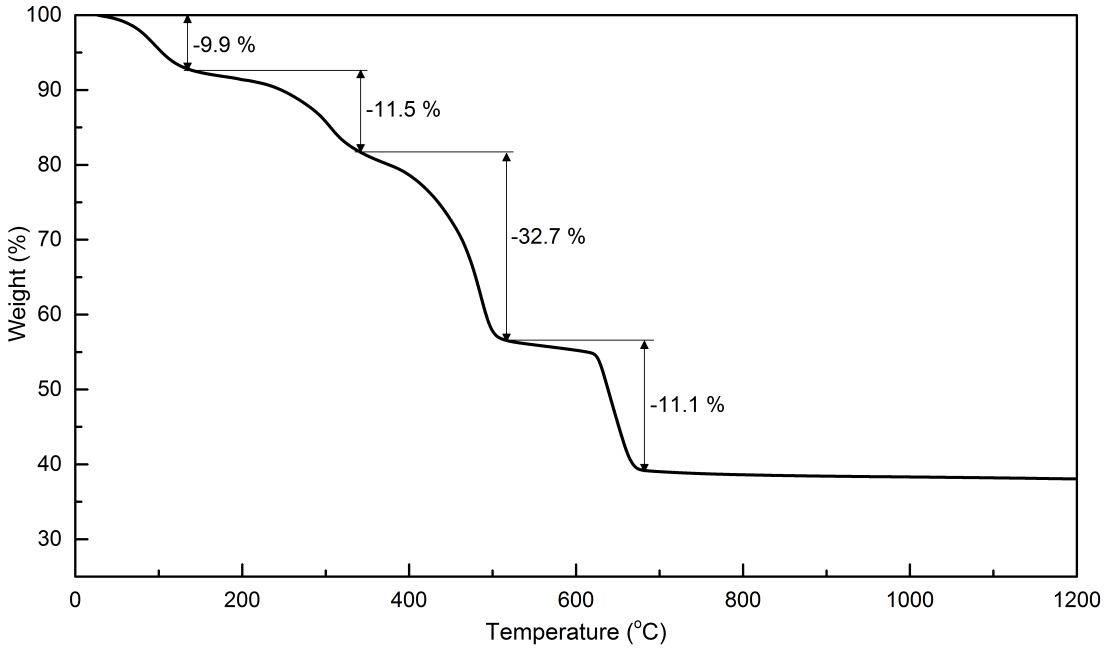

Figure 119. TGA curve of Fe-BTC-110-1.

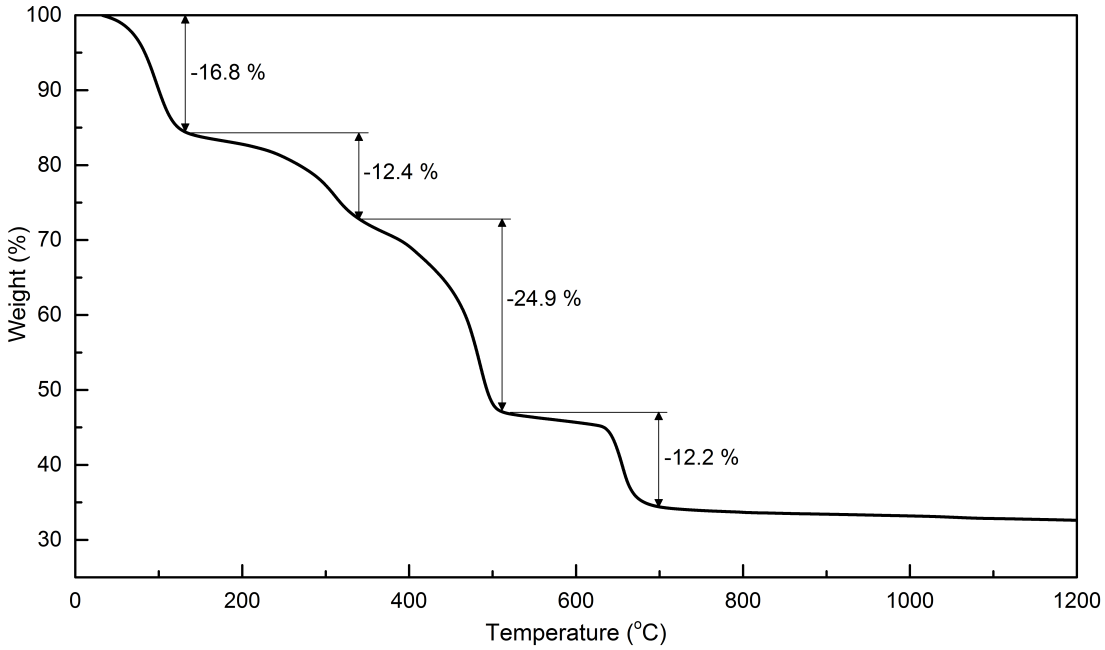

Figure 120. TGA curve of Fe-BTC-110-3.

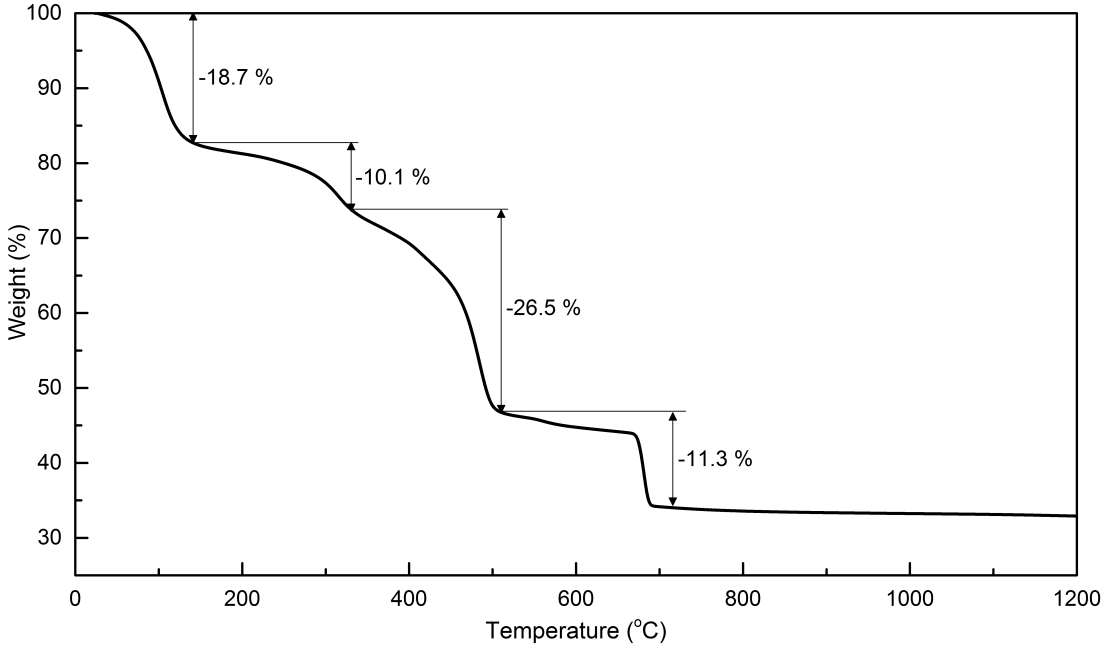

Figure 121. TGA curve of Fe-BTC-110-5.

Table 34. % mass loss during TGA of hierarchically porous Fe-BTCs synthesized at 110 °C.

Temperature Range (°C)	Fe-BTC-110-1 (%)	Temperature Range (°C)	Fe-BTC-110-3 (%)	Temperature Range (°C)	Fe-BTC-110-5 (%)
25-189	-9.9	25-178	-16.8	25-195	-18.7
189-342	-11.5	178-373	-12.4	195-371	-10.1
342-570	-32.7	373-577	-24.9	371-599	-26.5
570-717	-11.1	577-781	-12.2	599-829	-11.3

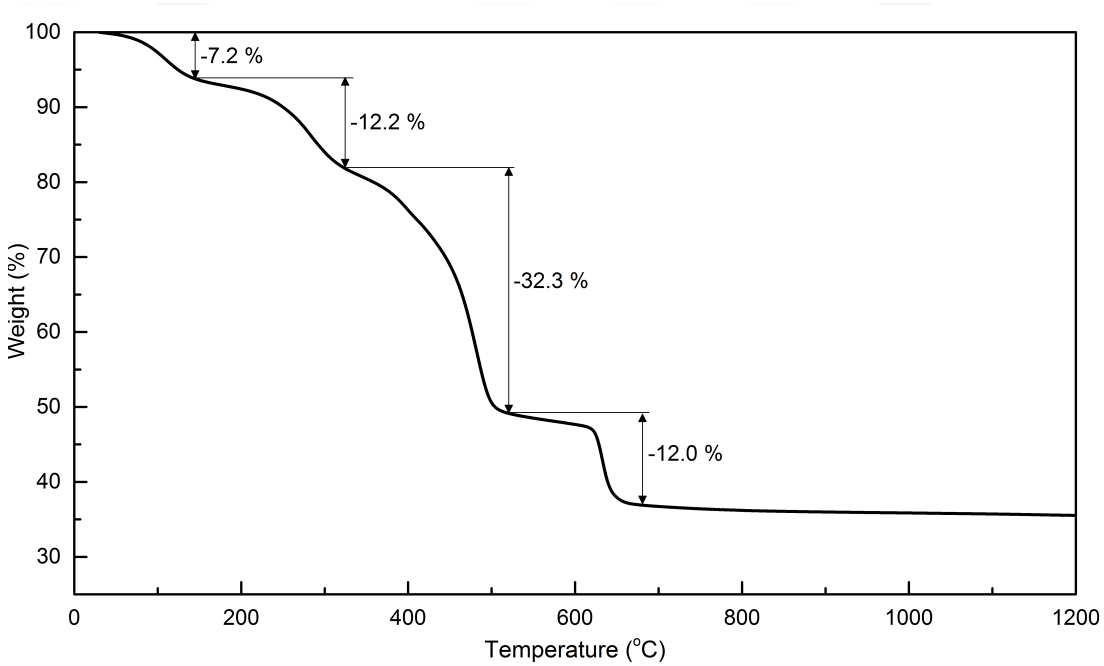

Figure 122. TGA curve of Fe-BTC-130-1.

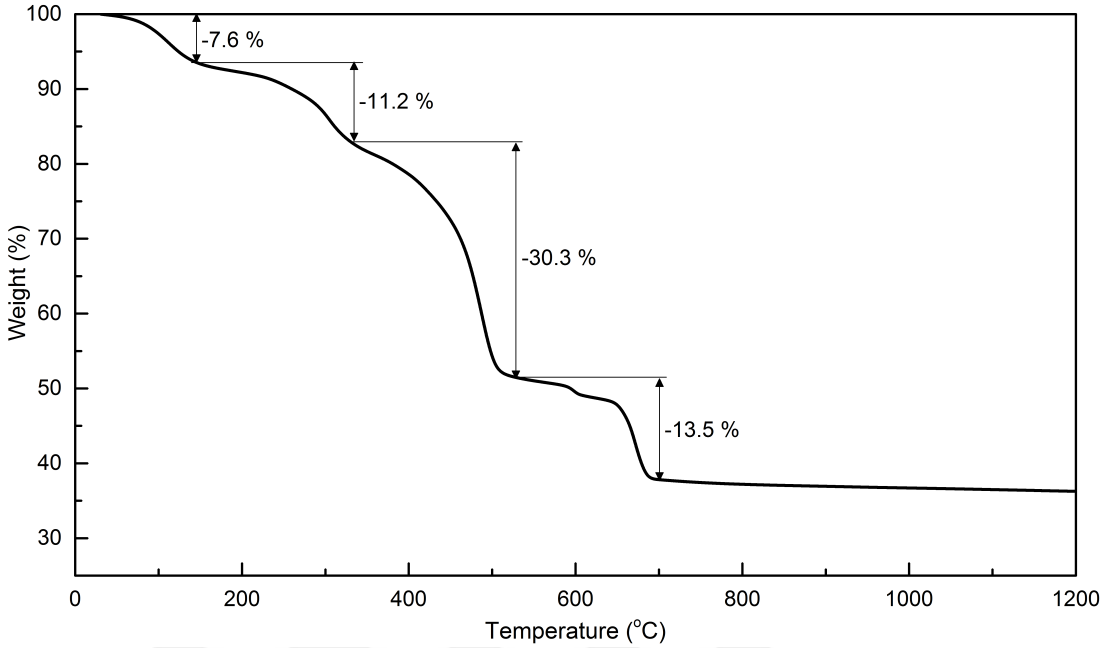

Figure 123. TGA curve of Fe-BTC-130-3.

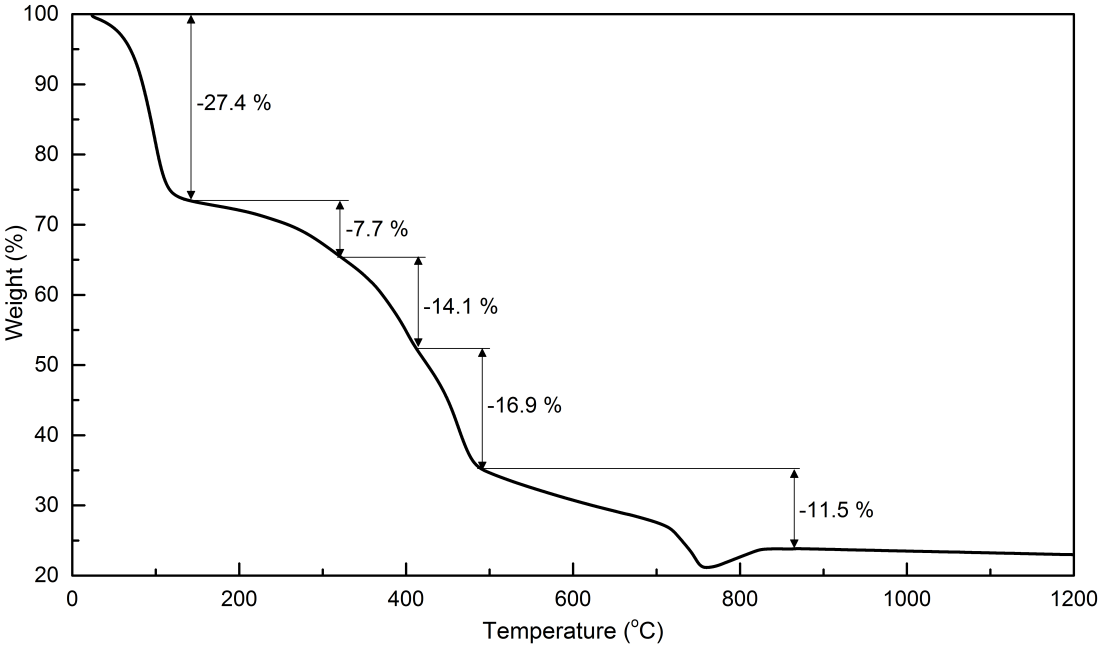

Figure 124. TGA curve of Fe-BTC-130-5.

Table 35. % mass loss during TGA analysis of hierarchically porous Fe-BTCs synthesized at 130 °C.

Temperature Range (°C)	Fe-BTC-130-1 (%)	Temperature Range (°C)	Fe-BTC-130-3 (%)	Temperature Range (°C)	Fe-BTC-130-5 (%)
25-182	-7.2	25-191	-7.6	25-177	-27.4
182-347	-12.2	191-359	-11.2	177-327	-7.7
347-564	-32.3	359-554	-30.3	327-421	-14.1
564-781	-12.0	554-623	-13.5	421-515	-16.9
				515-796	-11.5

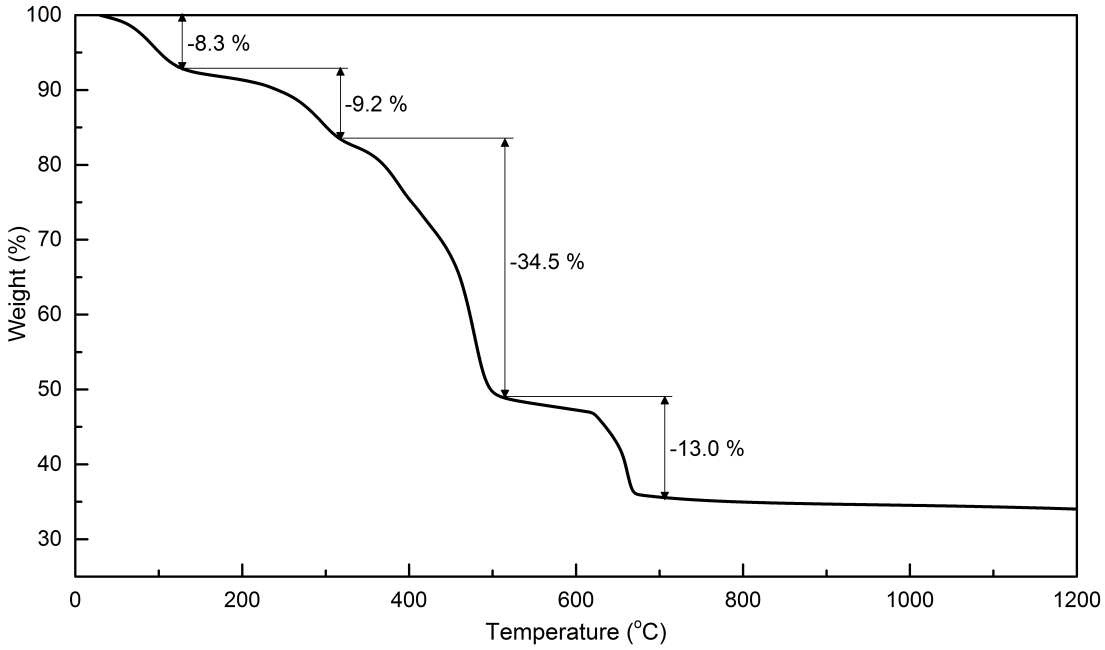

Figure 125. TGA curve of Fe-BTC-150-1.

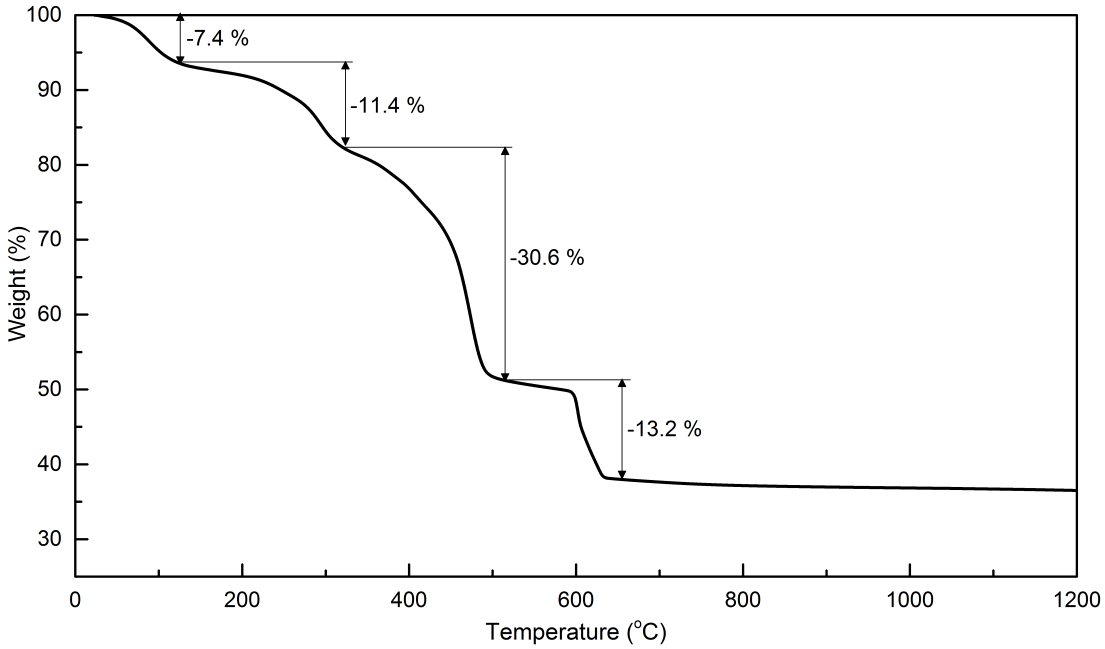

Figure 126. TGA curve of Fe-BTC-150-3.

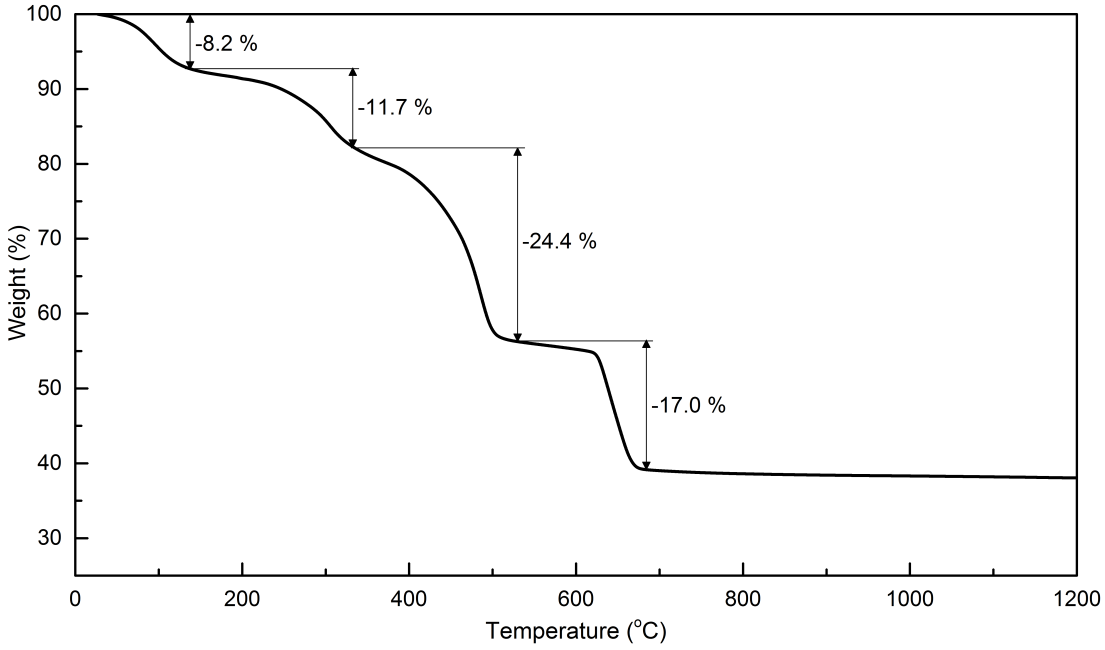

Figure 127. TGA curve of Fe-BTC-150-5.

Table 36. % mass loss during TGA analysis of hierarchically porous Fe-BTCs synthesized at 150 °C.

Temperature Range (°C)	Fe-BTC-150-1 (%)	Temperature Range (°C)	Fe-BTC-150-3 (%)	Temperature Range (°C)	Fe-BTC-150-5 (%)
25-179	-8.3	25-168	-7.4	25-178	-8.2
179-334	-9.2	168-342	-11.4	178-374	-11.7
334-556	-34.5	342-547	-30.6	374-570	-24.4
556-776	-13.0	547-754	-13.2	570-766	-17.0

Four major losses are issued. The first mass loss occurred in between 25 and 190 °C which is a consequence of the removal of adsorbed and coordinated water molecules. The second step (168-374 °C) is attributed to the loss of solvent molecules trapped in the pores. The third step illustrates the temperature at which BTC decomposes and structure collapse starts which thereby determines the stability of the synthesized Fe-BTC. Decomposition temperature of Fe-BTC varies with the synthesis conditions. The highest thermal stability is achieved by Fe-BTC-150-5 which decomposes at 374 °C while Fe-BTC-130-5 decomposes at a relatively lower temperature, 327 °C. By the perturbation assisted nanofusion synthesis strategy, an Fe-BTC that has higher thermal stability than those of reported Fe-BTCs and Basolite F300 is synthesized (X. Hu et al., 2016; Majano, Ingold, Yulikov, Jeschke, & Pérez-Ramírez, 2013). TGA analysis demonstrates that hierarchically porous MIL-88Bs are thermally stable under adsorption process conditions. Percentage of mass remains at the end of TGA can be found in Table 37.

Table 37. Percent residual mass at the end of TGA.

Residual Mass (%)	110 °C	130 °C	150 °C
Fe:BTC 1	34.7	36.3	35
Fe:BTC 3	33.7	37.4	37.4
Fe:BTC 5	33.6	22.4	38.7

6.3.5. CO_2 Adsorption Studies

Hierarchically porous Fe-BTCs are investigated for their CO_2 uptake capacities. Different CO_2 uptake capacities are obtained for hierarchically porous Fe-BTCs. These differences in CO_2 uptake capacities are attributed to the different pore size distribution of hierarchically porous Fe-BTCs. Langmuir and Freundlich isotherm models are investigated for the best fit. The calculated Langmuir and Freundlich isotherm parameters, respective equations, and R^2 values can be found below.

Langmuir Model:

$$\frac{C_e}{q_e} = \frac{1}{KQ^0} + \frac{C_e}{Q^0} \tag{6.1}$$

Freundlich Model:

$$logq_e = logK_F + \frac{1}{n} logC_e \tag{6.2}$$

Table 38. Respective equations obtained from models

Hierarchically porous Fe-BTCs	Langmuir Model	Freundlich Model
Fe-BTC-110-1	*y = 0.1686x+669.57*	*y = 0.639x-1.8419*
	R^2 = 0.9791	*R^2 = 0.9969*
Fe-BTC-110-3	*y = 0.0821x+796.06*	*y = 0.7741x-2.2584*
	R^2 = 0.9944	*R^2 = 0.9952*
Fe-BTC-110-5	*y = 0.0828x+719.25*	*y = 0.7741x-2.2584*
	R^2 = 0.9876	*R^2 = 0.9952*

Table 39. Langmuir and Freundlich isotherm parameters

Hierarchically porous Fe-BTCs	Langmuir Model	Freundlich Model
Fe-BTC-110-1	Q_m= 5.93 mg/g	K_F=1.44E-02 mg/g
	K_a= 2.5E-04 mg-1	η_F= 1.56
	R^2 = 0.9791	R^2= 0.9969
Fe-BTC-110-3	Q_m= 12.2 mg/g	K_F= 5.5E-03 mg/g
	K_a= 1.03E-04 mg-1	η_F= 1.29
	R^2= 0.9944	R^2= 0.9952
Fe-BTC-110-5	Q_m= 12.1 mg/g	K_F= 5.52E-03 mg/g
	K_a= 1.25E-04 mg-1	η_F = 1.29
	R^2= 0.9622	R^2=0.9952

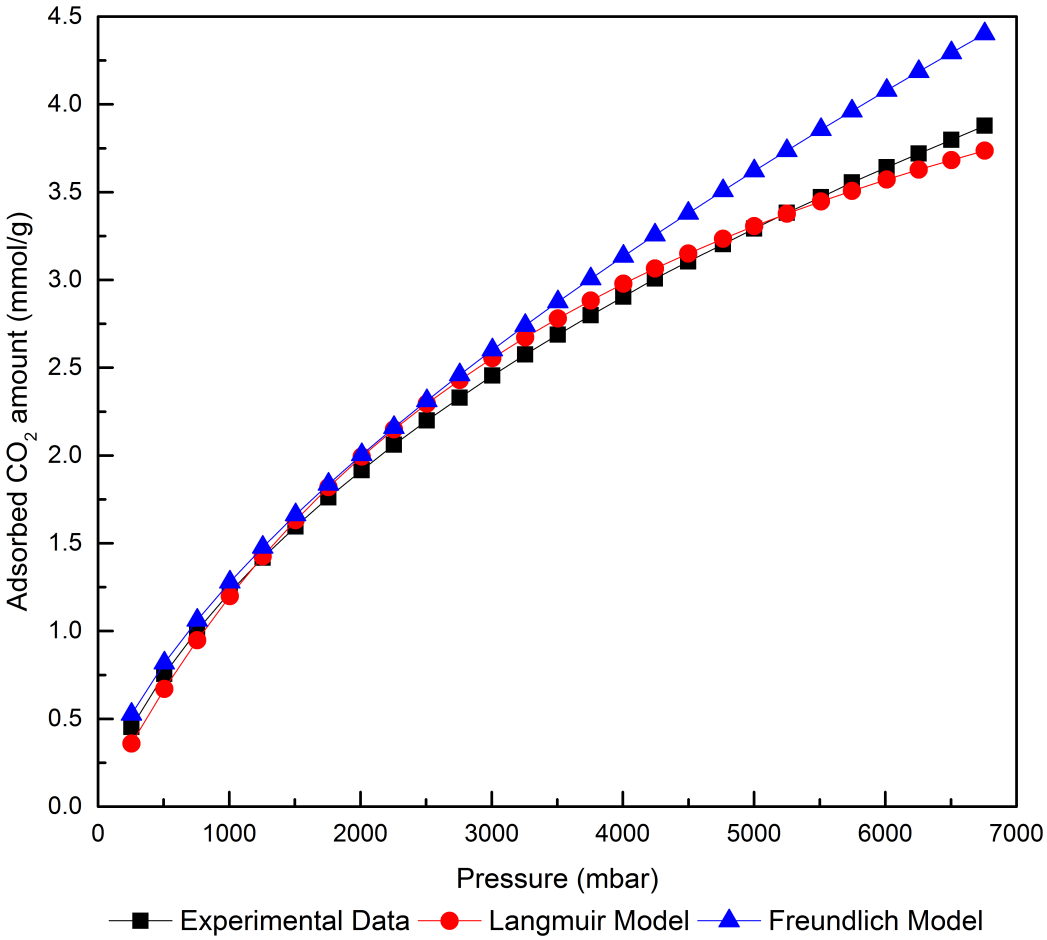

Figure 128. Comparison of experimental data and nonlinear fitting of Langmuir and Freundlich Model of Fe-BTC-110-1.

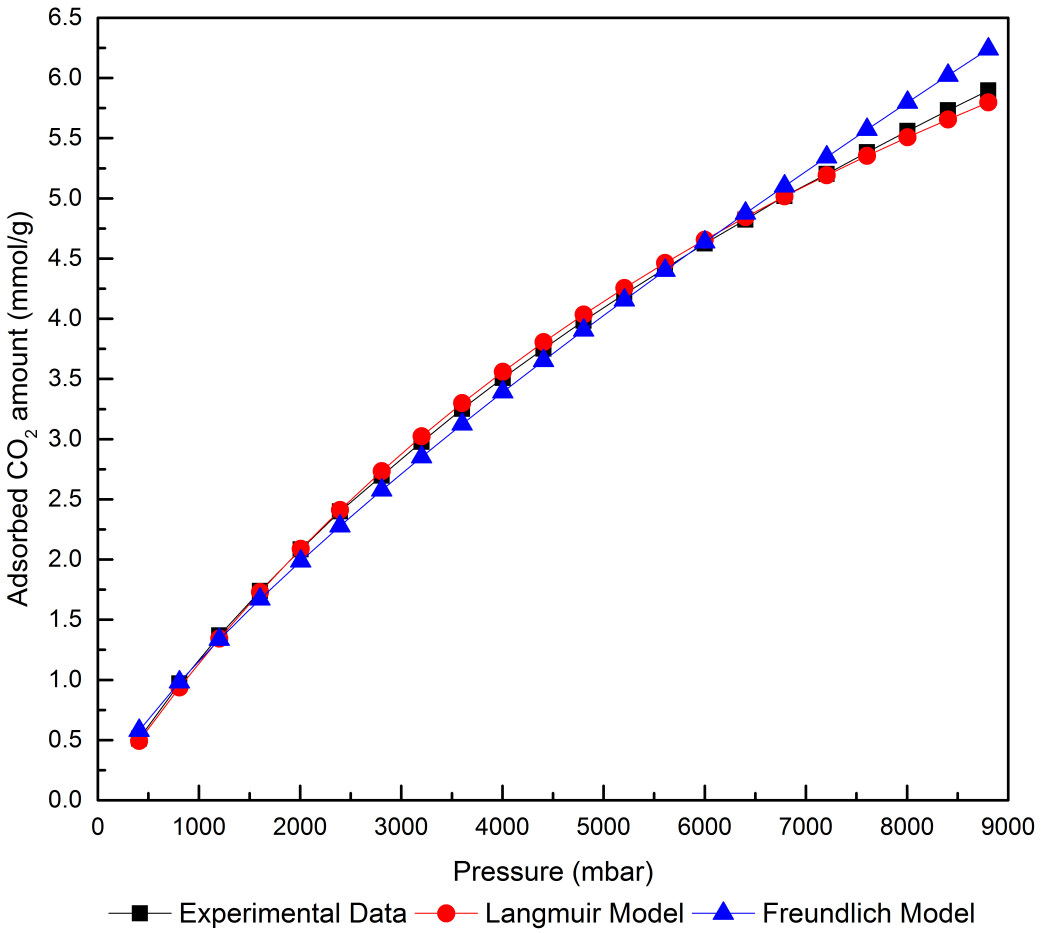

Figure 129. Comparison of experimental data and nonlinear fitting of Langmuir and Freundlich Model of Fe-BTC-110-3.

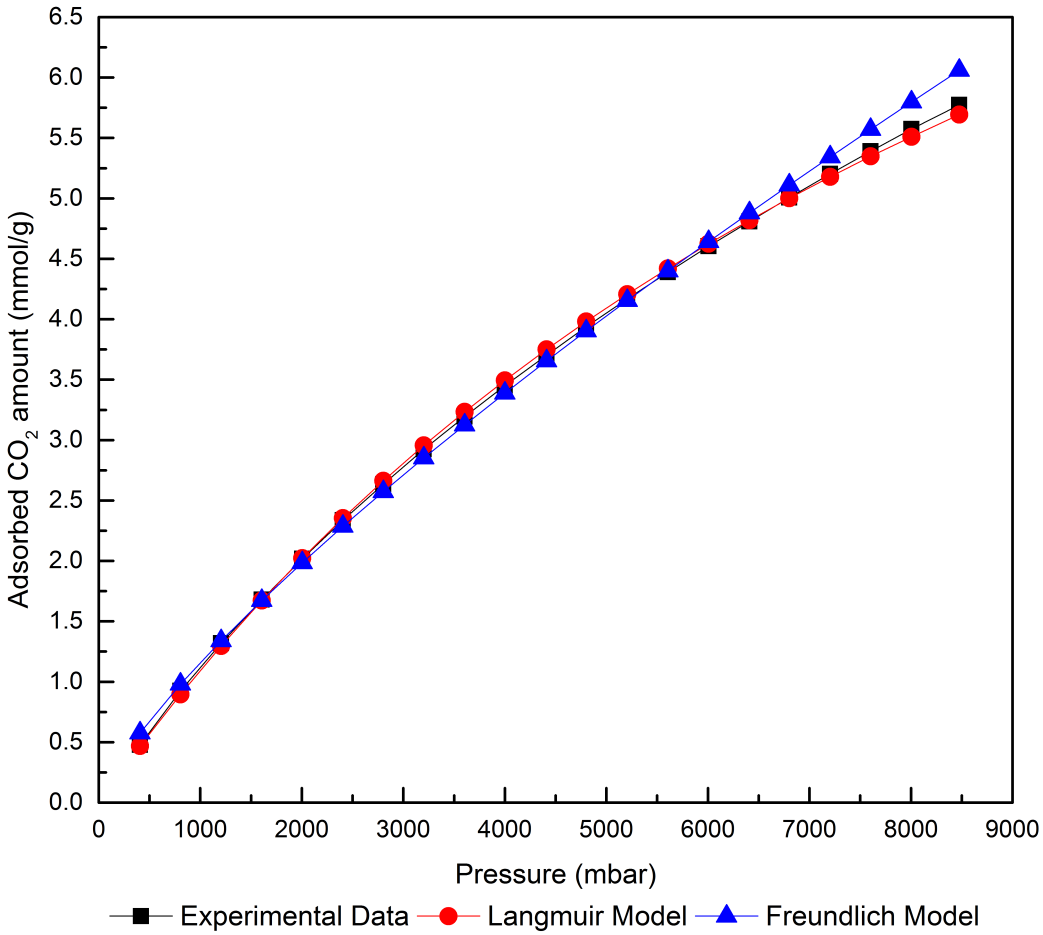

Figure 130. Comparison of experimental data and nonlinear fitting of Langmuir and Freundlich Model of Fe-BTC-110-5.

Table 40. Respective equations obtained from models

Hierarchical porous Fe-BTCs	Langmuir Model	Freundlich Model
Fe-BTC-130-1	y = 0.1153x+946.06	y = 0.7736x-2.35
	R^2 = 0.9921	R^2 = 0.9931
Fe-BTC-130-3	y = 0.1107x+656.9	y = 0.7458x-2.1252
	R^2 = 0.9704	R^2 = 0.9995
Fe-BTC-130-5	y = 0.0806x+855.78	y = 0.8119x-2.4075
	R^2 = 0.9967	R^2 = 0.9951

Table 41. Langmuir and Freundlich isotherm parameters

Hierarchical porous Fe-BTCs	Langmuir Model	Freundlich Model
Fe-BTC-130-1	Q_m= 8.67 mg/g	K_F=4.45E-03 mg/g
	K_a= 1.2E-04 mg^{-1}	η_F= 1.29
	R^2= 0.9921	R^2= 0.9931
Fe-BTC-130-3	Q_m= 9.03 mg/g	K_F= 7.5E-03 mg/g
	K_a= 1.69E-04 mg^{-1}	η_F= 1.34
	R^2= 0.9704	R^2= 0.9995
Fe-BTC-130-5	Q_m= 12.4 mg/g	K_F= 3.91E-03 mg/g
	K_a= 9.42E-05 mg^{-1}	η_F= 1.23
	R^2= 0.9967	R^2=0.9951

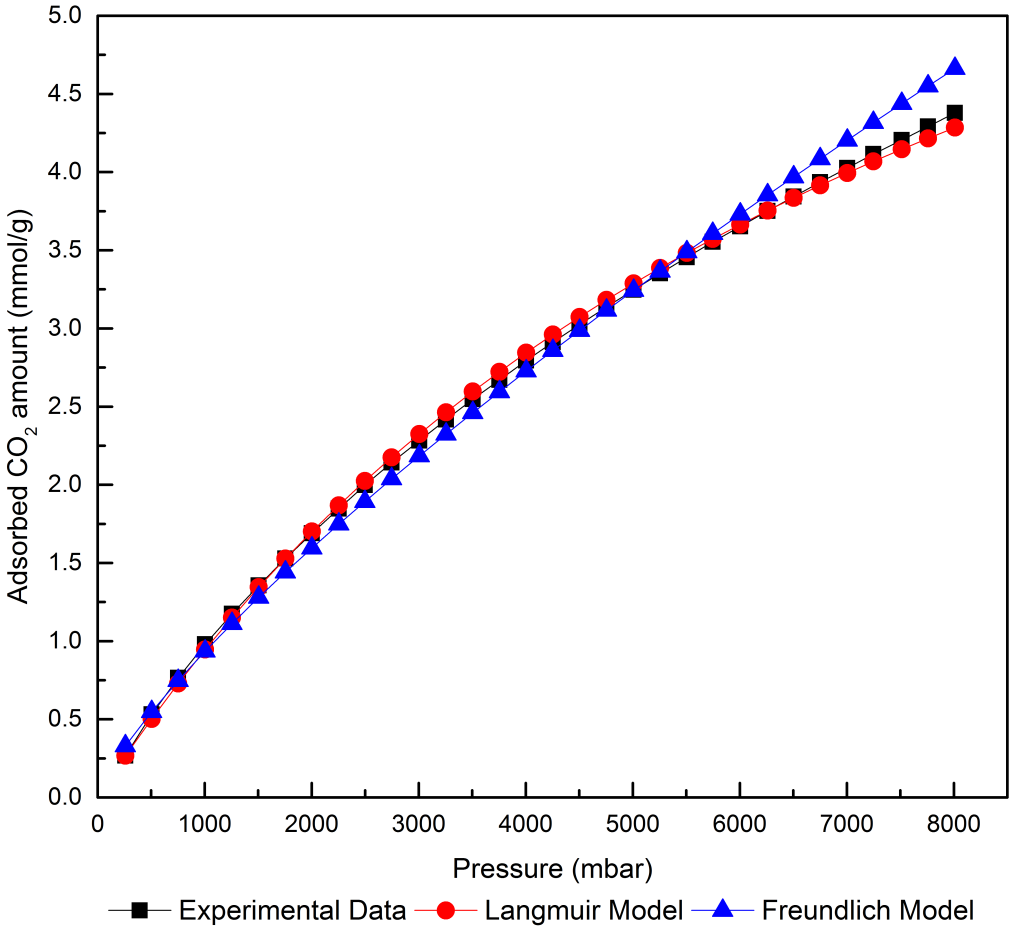

Figure 131. Comparison of experimental data and nonlinear fitting of Langmuir and Freundlich Model of Fe-BTC-130-1.

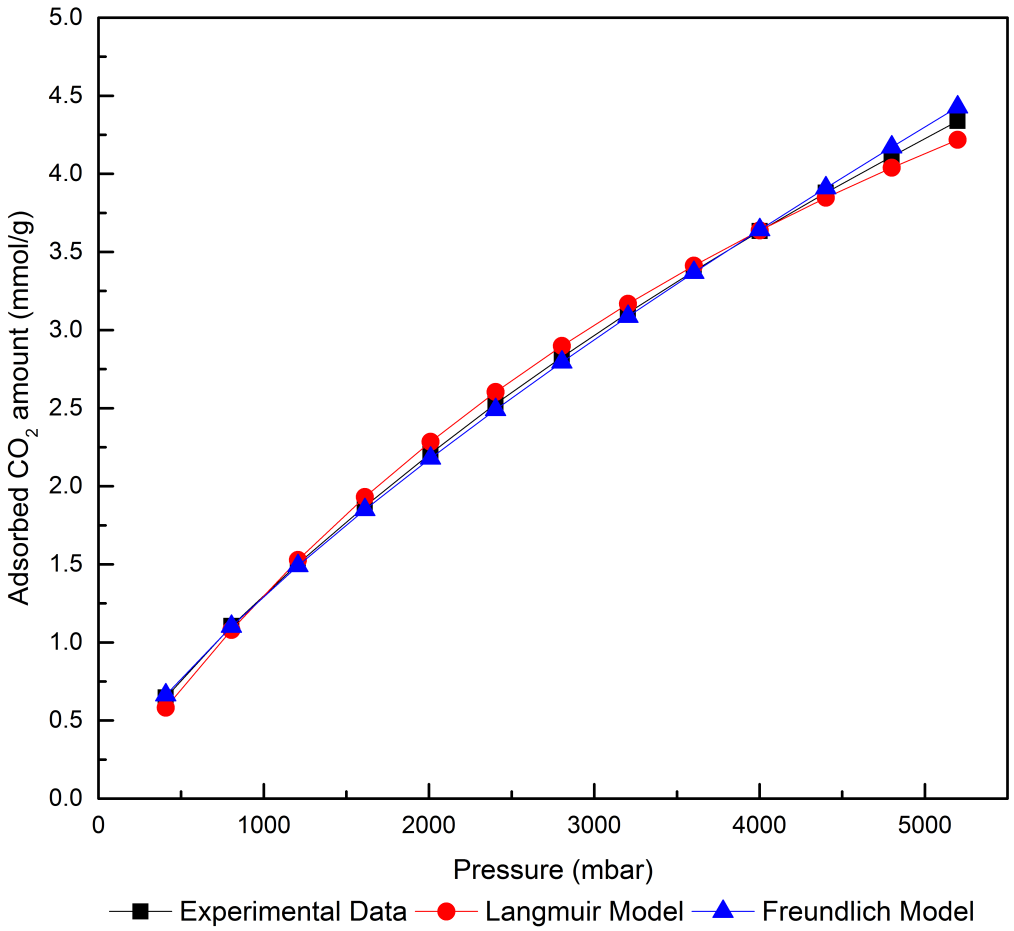

Figure 132. Comparison of experimental data and nonlinear fitting of Langmuir and Freundlich Model of Fe-BTC-130-3.

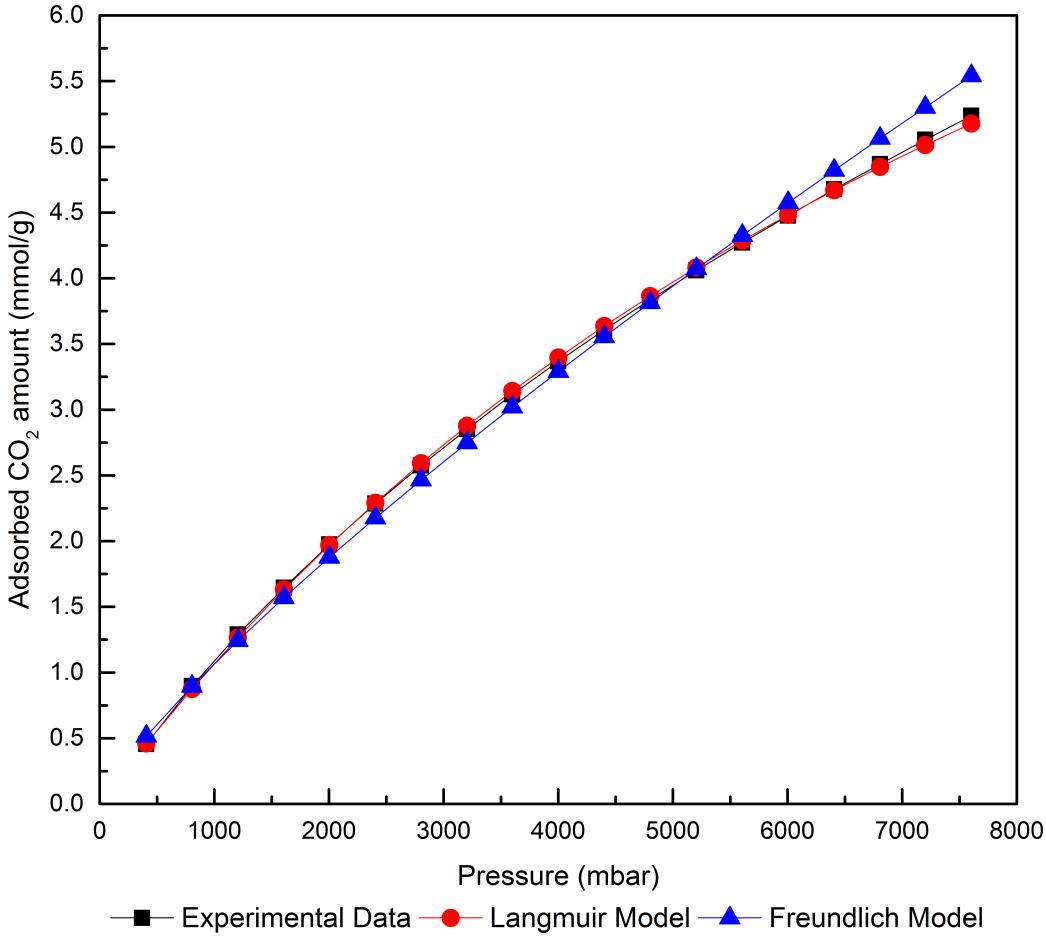

Figure 133. Comparison of experimental data and nonlinear fitting of Langmuir and Freundlich Model of Fe-BTC-130-5.

Table 42. Respective equations obtained from models

Hierarchically porous Fe-BTCs	Langmuir Model	Freundlich Model
Fe-BTC-150-1	$y = 0.0846x+785.5$	$y = 0.7708x-2.24$
	$R^2 = 0.9931$	$R^2 = 0.9965$
Fe-BTC-150-3	$y = 0.0683x+797.35$	$y = 0.8044x-2.3425$
	$R^2 = 0.9974$	$R^2 = 0.996$
Fe-BTC-150-5	$y = 0.09x+972.86$	$y = 0.781x-2.3546$
	$R^2 = 0.982$	$R^2 = 0.9984$

Table 43. Langmuir and Freundlich isotherm parameters

Hierarchically porous Fe-BTCs	Langmuir	Freundlich
Fe-BTC-150-1	Q_m= 11.82 mg/g	K_F= 5.7E-03
	K_a= 1.08E-04 mg^{-1}	η_F= 1.29
	R^2= 0.9931	R^2= 0.9965
Fe-BTC-150-3	Q_m= 14.64 mg/g	K_F= 4.5E-03
	K_a= 8.57E-05 mg^{-1}	η_F= 1.24
	R^2= 0.9974	R^2= 0.996
Fe-BTC-150-5	Q_m= 11.1 mg/g	K_F= 4.42E-03
	K_a= 9.25E-05 mg^{-1}	η_F= 1.28
	R^2= 0.982	R^2=0.9984

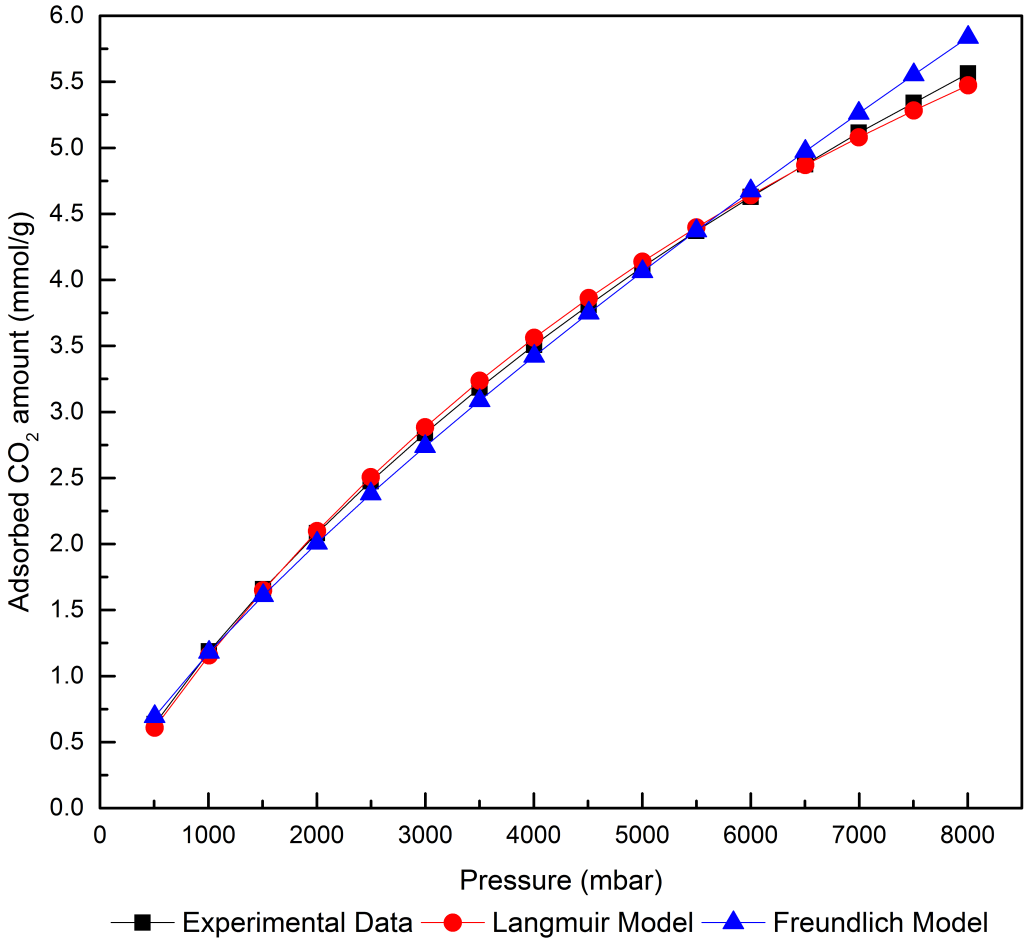

Figure 134. Comparison of experimental data and nonlinear fitting of Langmuir and Freundlich Model of Fe-BTC-150-1.

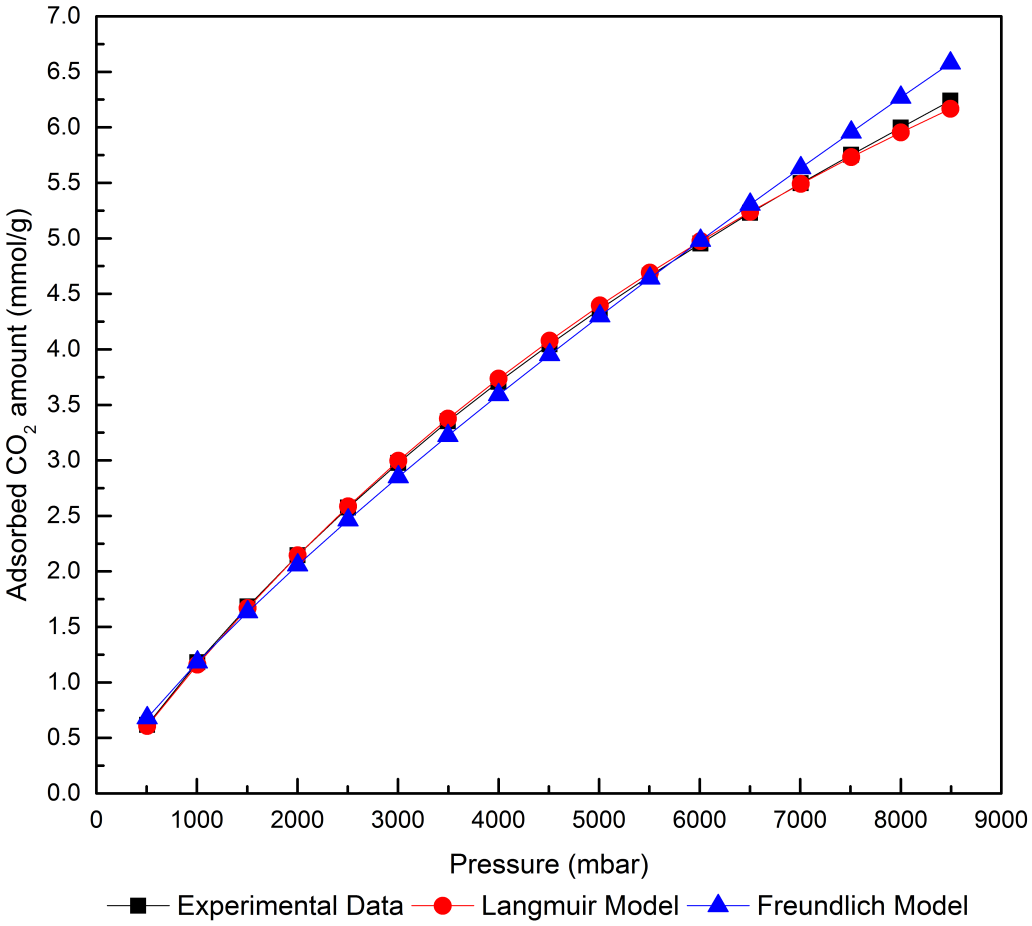

Figure 135. Comparison of experimental data and nonlinear fitting of Langmuir and Freundlich Model of Fe-BTC-150-3.

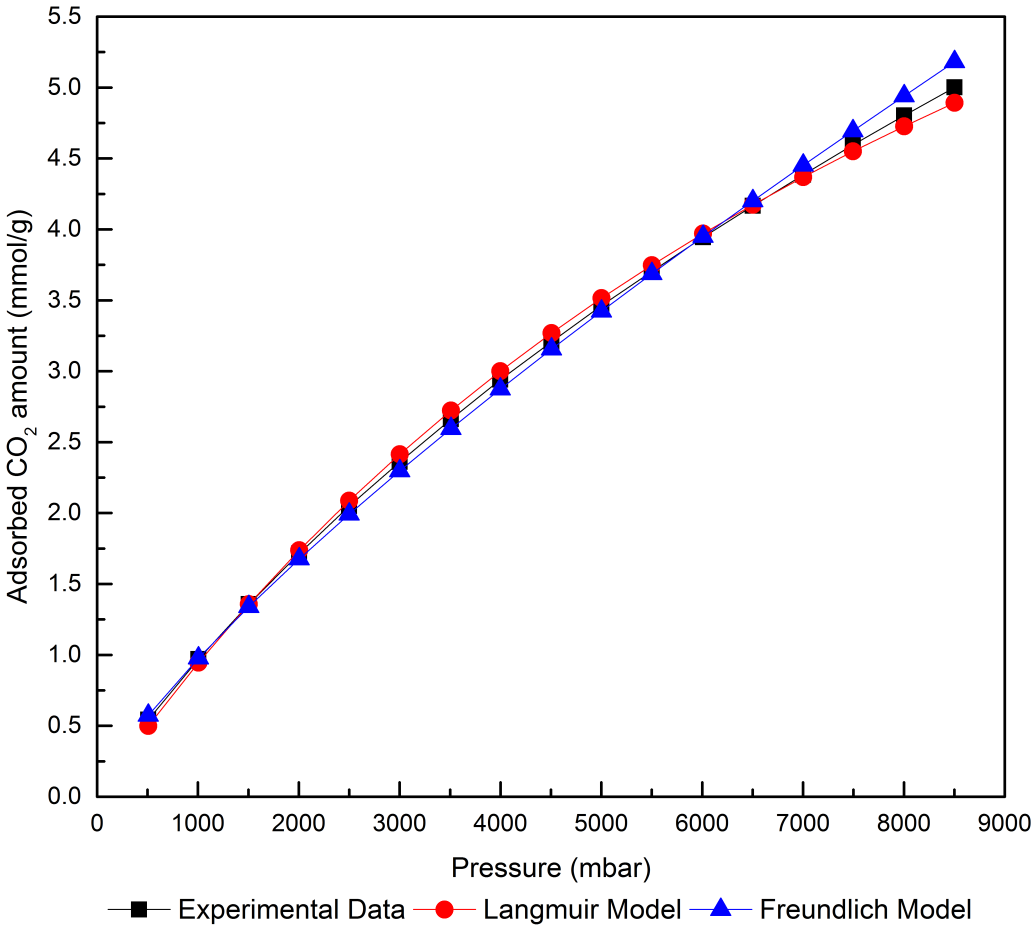

Figure 136. Comparison of experimental data and nonlinear fitting of Langmuir and Freundlich Model of Fe-BTC-150-5.

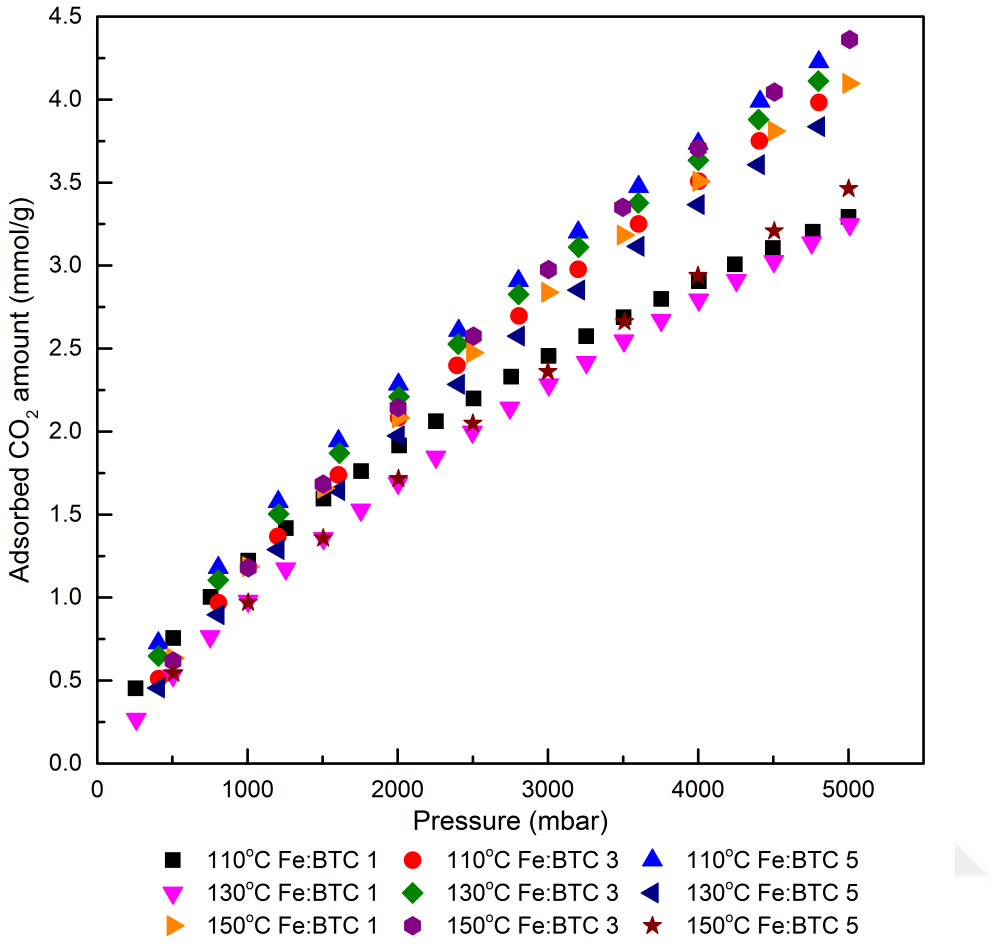

Figure 137. CO_2 adsorption isotherm of hierarchically porous Fe-BTCs.

Langmuir and Freundlich isotherm parameters show that Freundlich model describes the CO_2 adsorption (298 K) behavior of hierarchically porous Fe-BTCs better. However, as the adsorption studies were conducted till 5 bar, the shape of the isotherm may be misleading.

Among the synthesized hierarchically porous Fe-BTCs the highest CO_2 adsorption capacity is attained by Fe-BTC-150-3 while Fe-BTC-130-1 possesses the lowest CO_2 adsorption capacity. This differences in CO_2 adsorption capacities are attributed to their different pore size distributions. Figure 137 illustrates the amount of CO_2 adsorbed in between 0 and 5 bar and Table 44 shows the volume of ultramicropores, narrow micropores, fraction of narrow micropores to micropores and the CO_2 adsorption capacities (mmol/g) measured at 5 bar and 298 K. Figure 138-142 show the dependence of CO_2 adsorption capacity on the textural properties (narrow micropore, micropore, mesopore volume, total pore volume and BET surface area) of Fe-BTCs.

Table 44. Volume of ultramicropores (pore diameter < 0.7 nm), narrow micropores and micropores, and CO2 adsorption capacities of Fe-BTC type crytallites measured at 5 bar and 298 K.

	BET Surface Area (m^2/g)	Vpores < 0.7nm (cm^3/g)	Vpores <1 nm (cm^3/g)	Vpores <2 nm (cm^3/g)	V<1nm/ V<2nm	CO_2 adsorption capacity (mmol/g) [a]
Fe-BTC-110-1	950.4±9.1E1	-	0.265±1.9E-2	0.35±1.9E-2	75.7	3.29
Fe-BTC-110-3	1024.1±1.8E2	-	0.291±6.3E-2	0.334±7.5E-2	87.1	4.09
Fe-BTC-110-5	1302.6±1.5E2	-	0.365±3.3E-2	0.444±5.2E-2	82.2	4.34
Fe-BTC-130-1	692.9±1.1E2	-	0.198±7.0E-2	0.23±7.7E-2	86.0	3.25
Fe-BTC-130-3	1207.1±6.0E1	-	0.33±7.0E-3	0.389±3.8E-2	85.6	4.22
Fe-BTC-130-5	1024.6±1.5E2	-	0.292±2.6E-2	0.348±5.0E-2	83.9	3.95
Fe-BTC-150-1	1139.1±2.1E1	-	0.318±8.3E-3	0.373±8.1E-3	85.3	4.10
Fe-BTC-150-3	1312.7±1.1E1	0.19	0.326±4.0E-3	0.453±6.3E-3	71.9	4.36
Fe-BTC-150-5	1355.9±4.2E1	-	0.367±0.0148	0.468±3.0E-2	78.4	3.46

[a] *Measured at 5 bar and 298 K.*

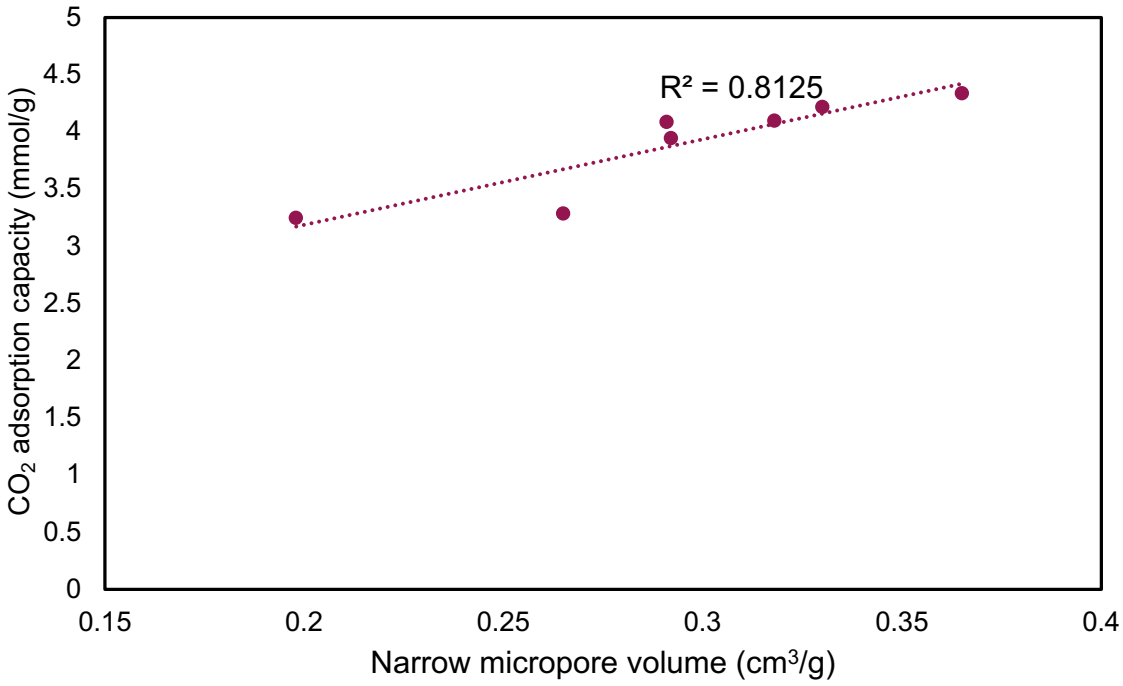

Figure 138. Dependence of CO_2 adsorption capacity of hierarchically porous Fe-BTCs on narrow micropore volume.

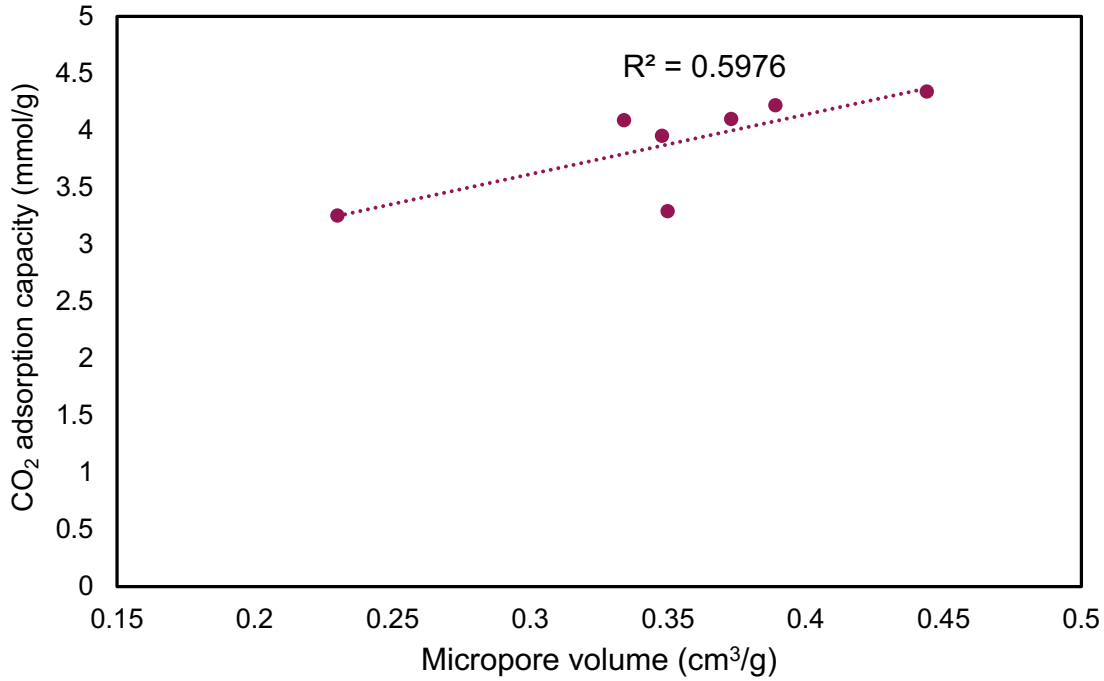

Figure 139. Dependence of CO_2 adsorption capacity on micropore volume of hierarchically porous Fe-BTCs.

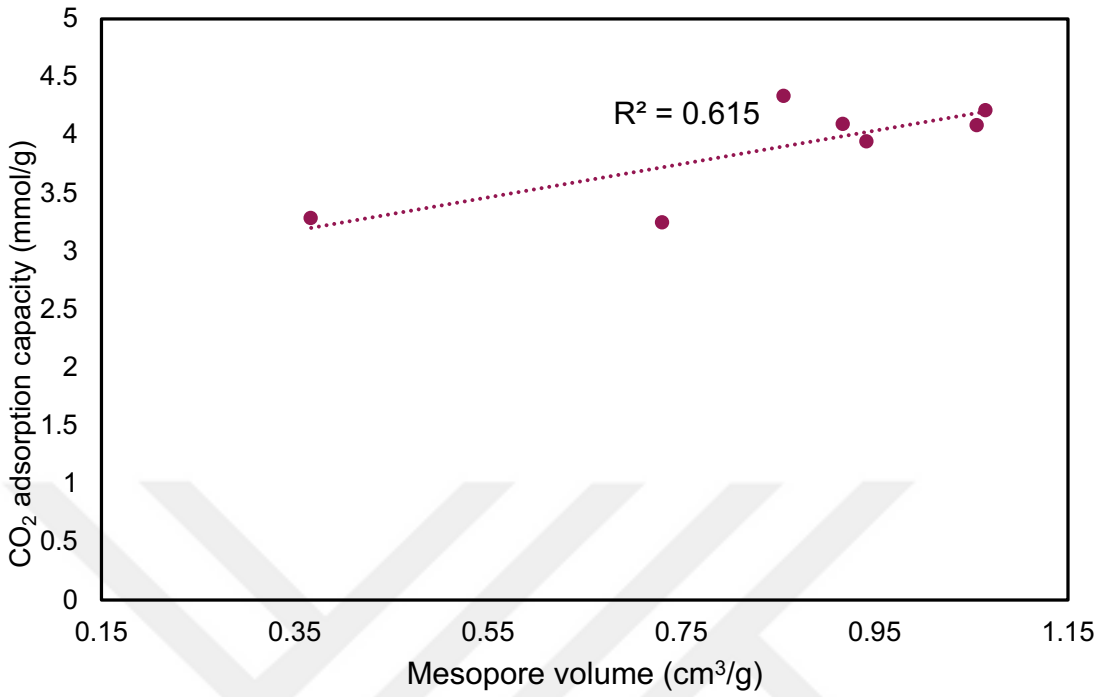

Figure 140. Dependence of CO_2 adsorption capacity on mesopore volume of hierarchically porous Fe-BTCs.

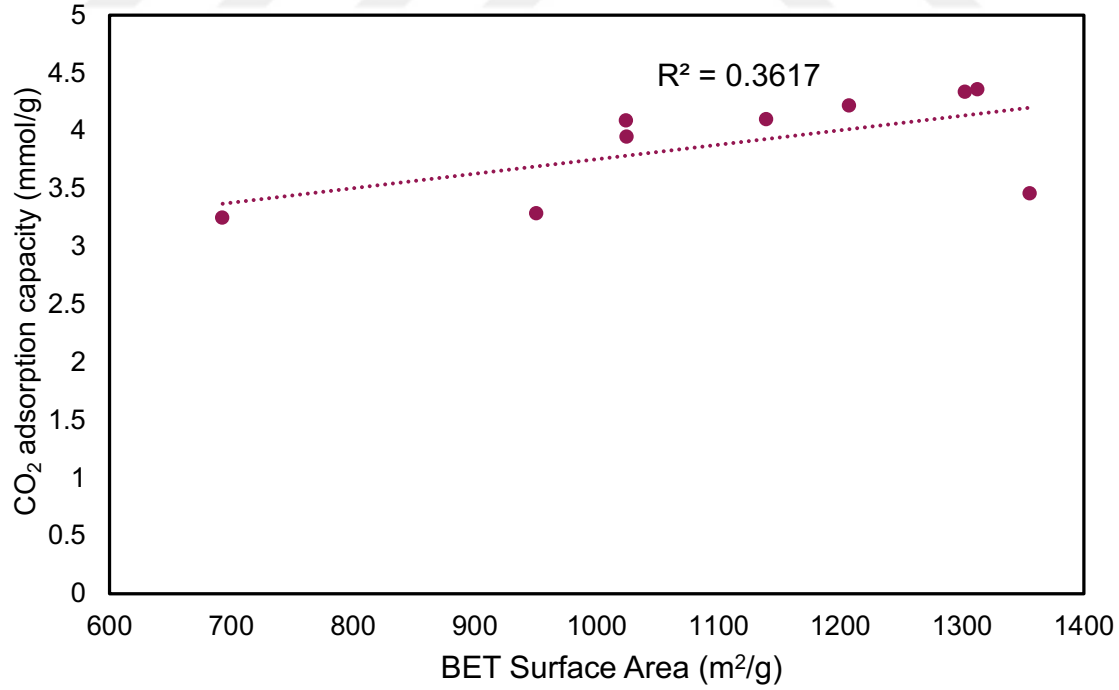

Figure 141. Dependence of CO_2 adsorption capacity on the BET surface area of hierarchically porous Fe-BTCs.

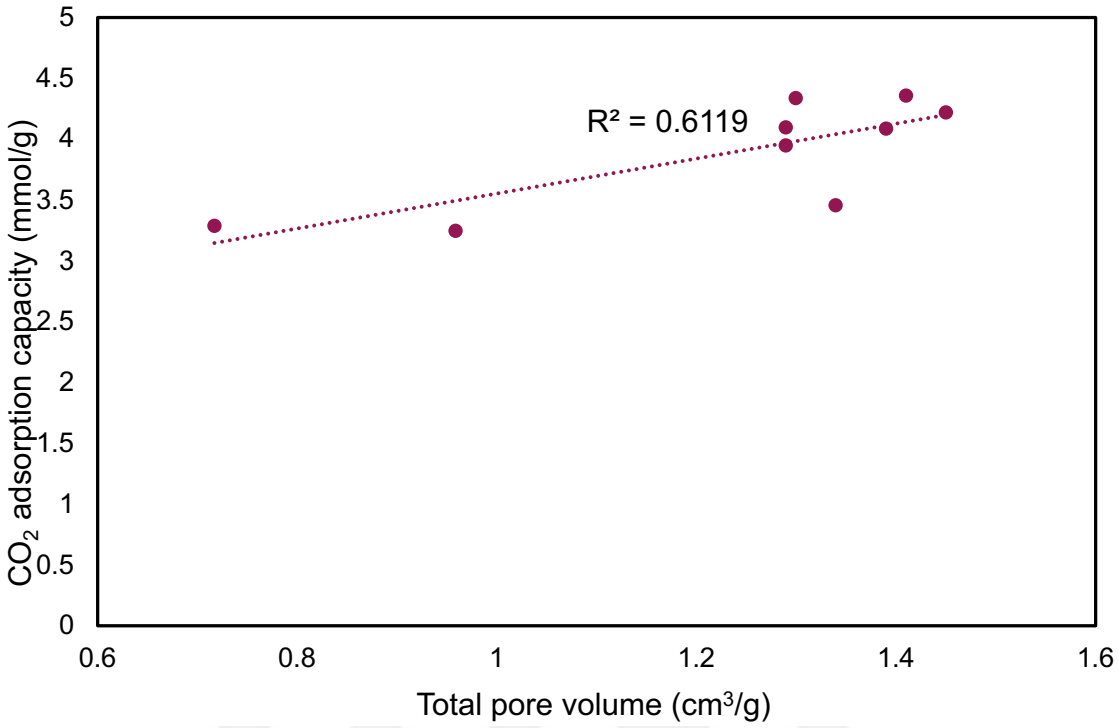

Figure 142. Dependence of CO_2 adsorption capacity on the BET surface area of hierarchically porous Fe-BTCs.

BET surface area (R^2, 0.36), micropore volume (R^2, 0.59), mesopore volume (R^2, 0.61), and total pore volume (R^2, 0.61), are found to be weakly correlated with the CO_2 adsorption capacity of Fe-BTCs. It is the narrow micropore volume (R^2, 0.81) that is strongly correlated with the CO_2 adsorption capacity of Fe-BTCs. Correlation coefficients indicate that among the various parameters (BET surface area, micro-, mesopore volume and total pore volume) investigated, narrow micropore volume affect the adsorbed CO_2 amount the most. Figure 143 illustrates the NLDFT plot of Fe-BTC in between the pore diameters of 0 and 3 nm and Figure 144 illustrates the narrow micropore volumes of hierarchically porous Fe-BTCs.

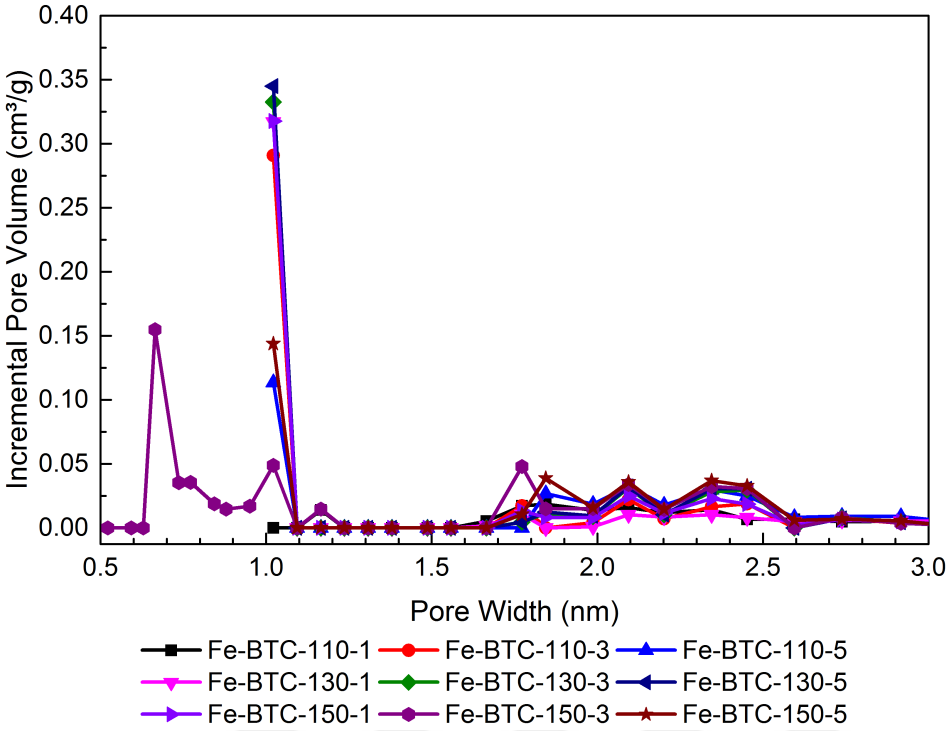

Figure 143. NLDFT plot of hierarchically porous Fe-BTCs.

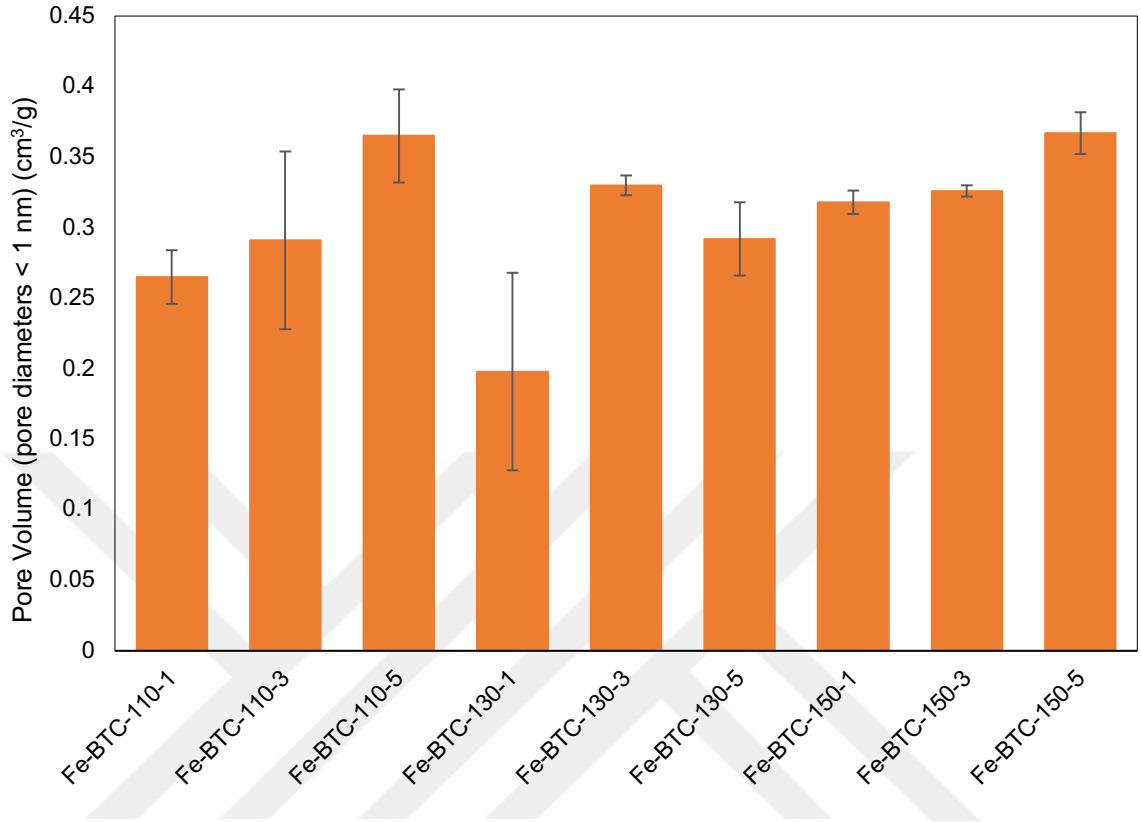

Figure 144. Narrow micropore volumes of hierarchically porous Fe-BTCs.

NLDFT plots show that Fe-BTC-150-3 is the only Fe-BTC that possesses ultramicropores in its pore structure. The volume of ultramicropores (pore diameters smaller than 0.7 nm) form 58.2% of the volume of narrow micropores and the highest CO_2 uptake capacity belongs to Fe-BTC-150-3. Even though the volume of narrow micropores is higher in Fe-BTC-150-5 (0.367 cm3/g), its CO_2 adsorption capacity (3.46 mmol/g) is 1.3 times lower than the CO_2 adsorption capacity of Fe-BTC-150-3 (4.36 mmol/g). Figure 145 illustrates the CO_2 adsorption capacities and the narrow micropore volumes of Fe-BTC-150-3 and Fe-BTC-150-5.

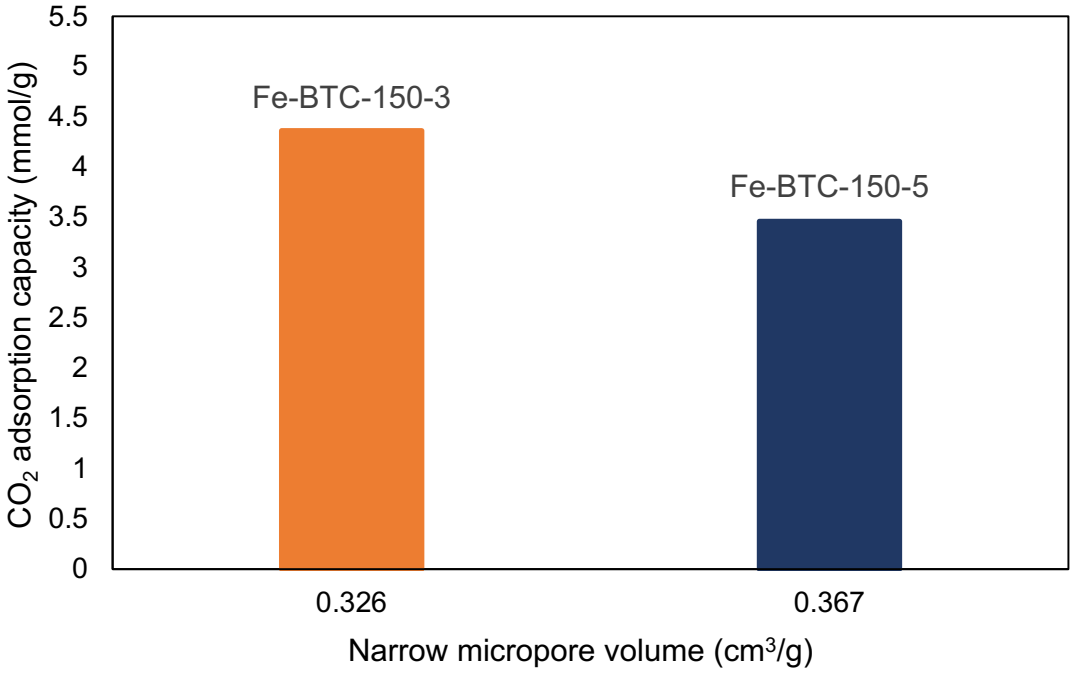

Figure 145. Comparison of the CO_2 adsorption capacities (5 bar and 298 K) and the narrow micropore volumes of Fe-BTC-150-3 and Fe-BTC-150-5

A similar trend is observed for Fe-BTC-110-5 and Fe-BTC-150-5. Fe-BTC-110-5 and Fe-BTC-150-5 possess similar narrow micropore volumes. However, their CO_2 adsorption capacities differ, considerably. Figure 146 illustrates the CO_2 adsorption isotherms of Fe-BTC-110-5 and Fe-BTC-150-5 and Figure 147 illustrates the CO_2 adsorption capacities and the narrow micropore volumes of Fe-BTC-110-5 and Fe-BTC-150-5.

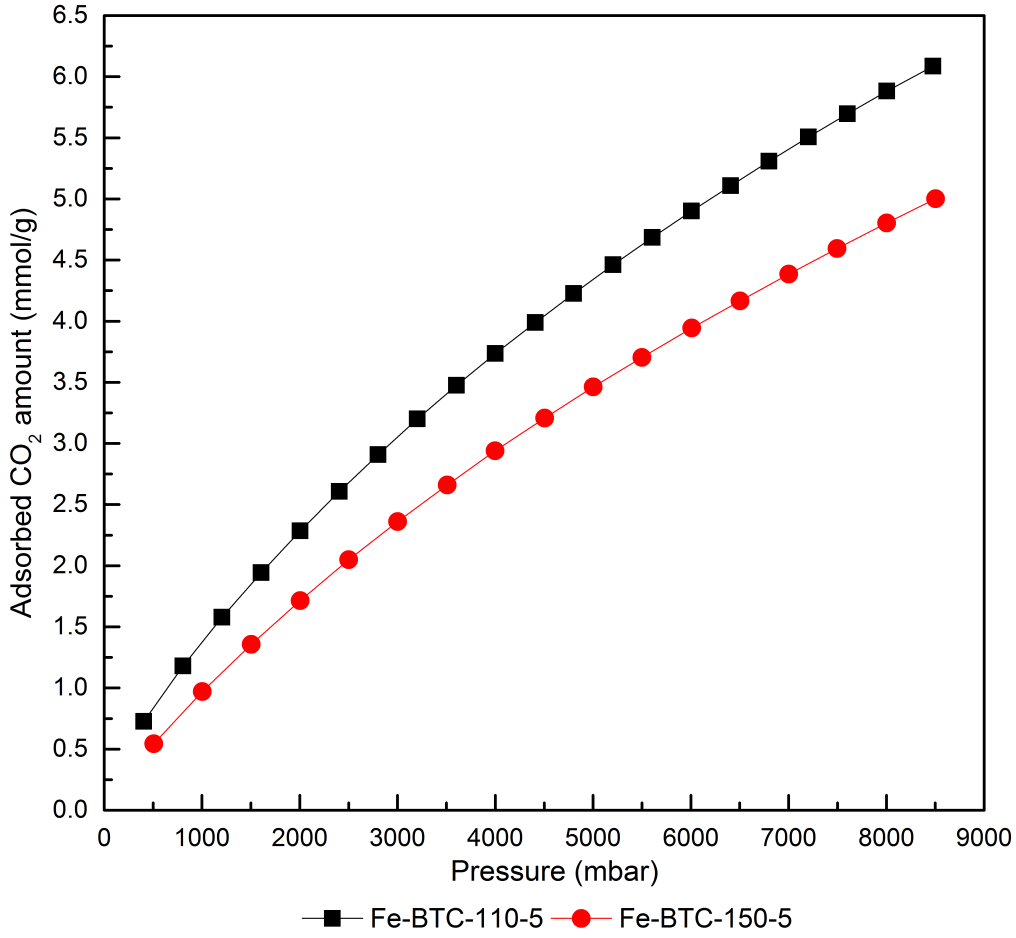

Figure 146. CO_2 adsorption isotherm (298 K) of Fe-BTC-110-5, and Fe-BTC-150-5.

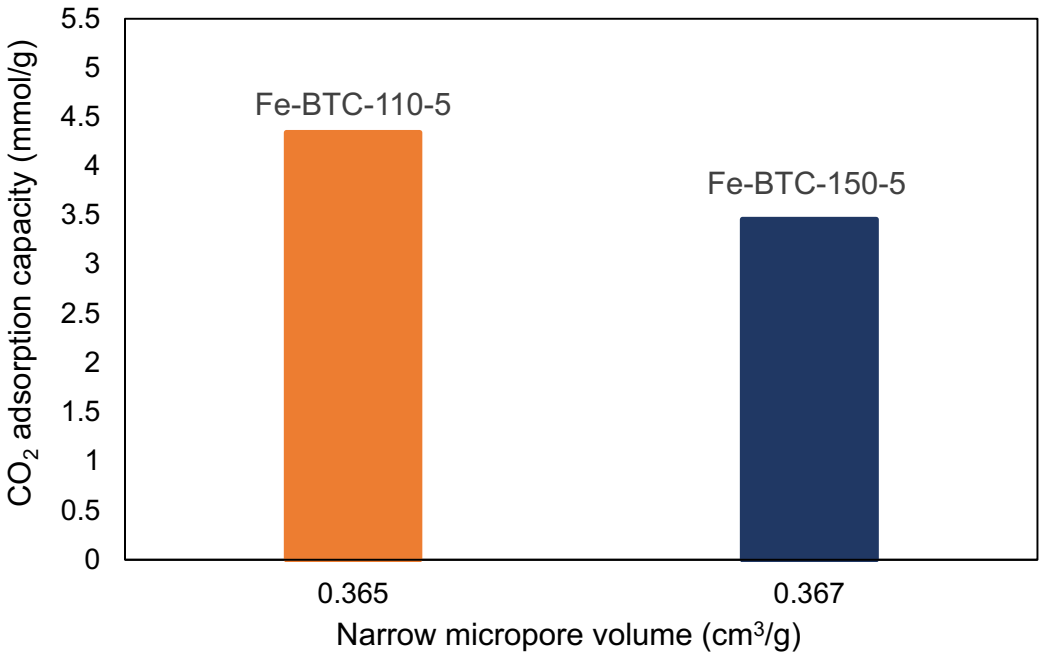

Figure 147. Comparison of the CO_2 adsorption capacities measured at 5 bar and 298 K and the narrow micropore volumes of Fe-BTC-110-5 and Fe-BTC-150-5.

The higher CO_2 adsorption capacity of Fe-BTC-110-5 is attributed to the narrow distribution of the narrow micropores through the micropore size range. The volume of narrow micropores corresponds to 82.2% of the volume of micropores in Fe-BTC-110-5 while the volume of narrow micropores corresponds to 78.4% of the volume of micropores in Fe-BTC-150-5. Thereby, we conclude that it is not only the volume of narrow micropores, but their distribution through the micropore size range that has significant effect on the adsorbed CO_2 amount. Figure 148 shows the CO_2 adsorption isotherms of Fe-BTC synthesized at 110, 130 and 150 °C.

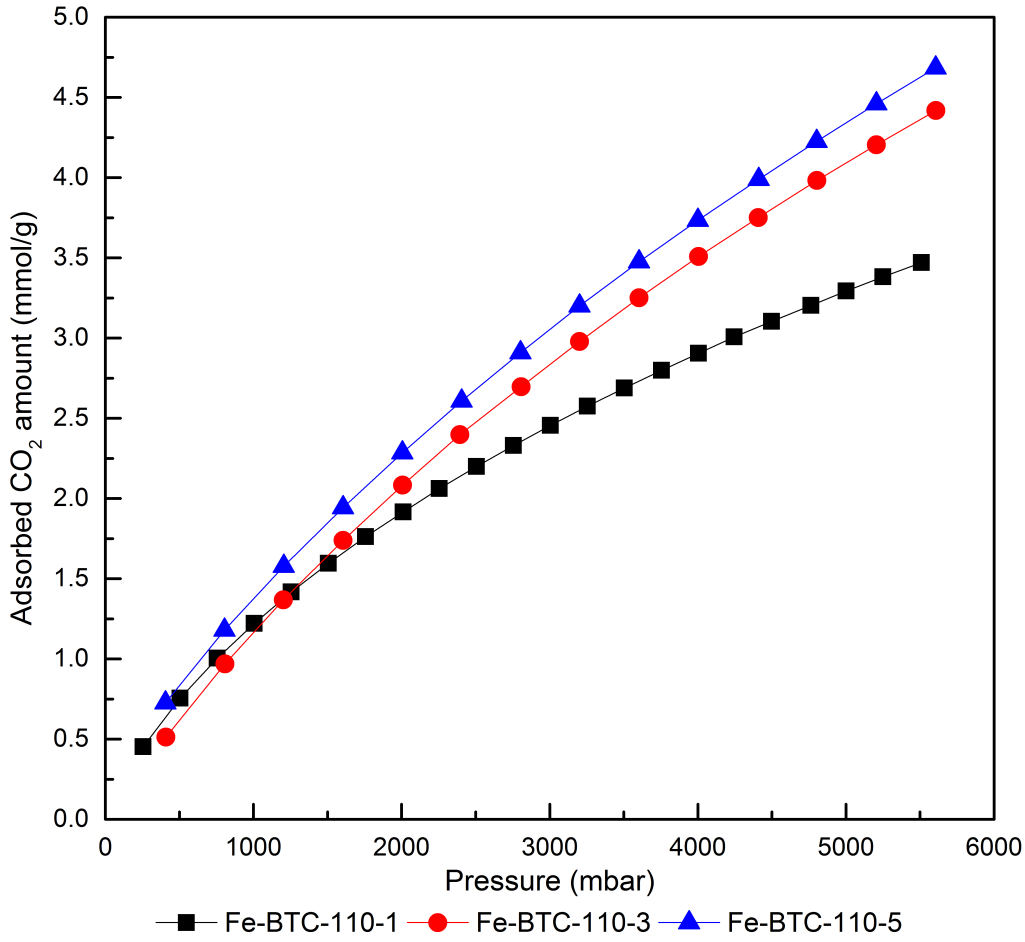

Figure 148. CO_2 adsorption isotherm (298 K) of Fe-BTC-110-1, Fe-BTC-110-3, and Fe-BTC-110-5.

Among the hierarchically porous Fe-BTCs synthesized at 110 °C, Fe-BTC-110-5 adsorbed the highest amount of CO_2 at 5 bar and 298 K. This higher CO_2 adsorption capacity of Fe-BTC-110-5 is attributed to its higher narrow micropore volume (0.365 cm^3/g). Fe-BTC-110-1 has a relatively lower CO_2 adsorption capacity than Fe-BTC-110-3 and Fe-BTC-110-5. This lower CO_2 adsorption capacity is due to its relatively lower narrow micropore volume (0.265 cm^3/g) and the broader micropore size distribution (75.7% of the micropores are formed of narrow micropores). As the narrow micropore volume increases and a narrower micropore size distribution is achieved, the adsorbed CO_2 amount increases.

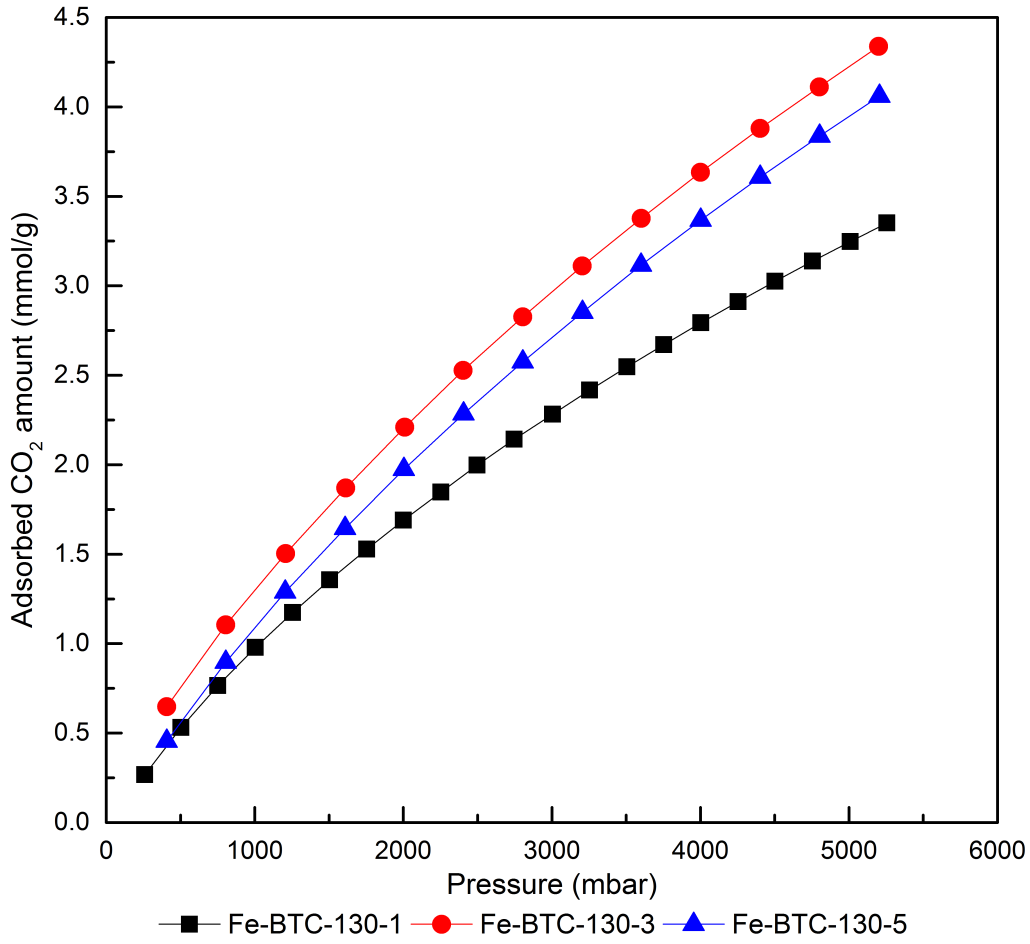

Figure 149. CO_2 adsorption isotherm (298 K) of Fe-BTC-130-1, Fe-BTC-130-3, and Fe-BTC-130-5.

Among the Fe-BTCs synthesized at 130 °C, the lowest CO_2 uptake capacity is achieved by Fe-BTC-130-1. This lower CO_2 uptake capacity is attributed to its lower narrow micropore volume (0.198 cm^3/g). In the meantime, among the Fe-BTCs synthesized at 130 °C, the highest CO_2 adsorption capacity belongs to Fe-BTC-130-3 (4.22 mmol/g) which is attributed to its relatively high volume (0.33 cm^3/g) of narrow micropores.

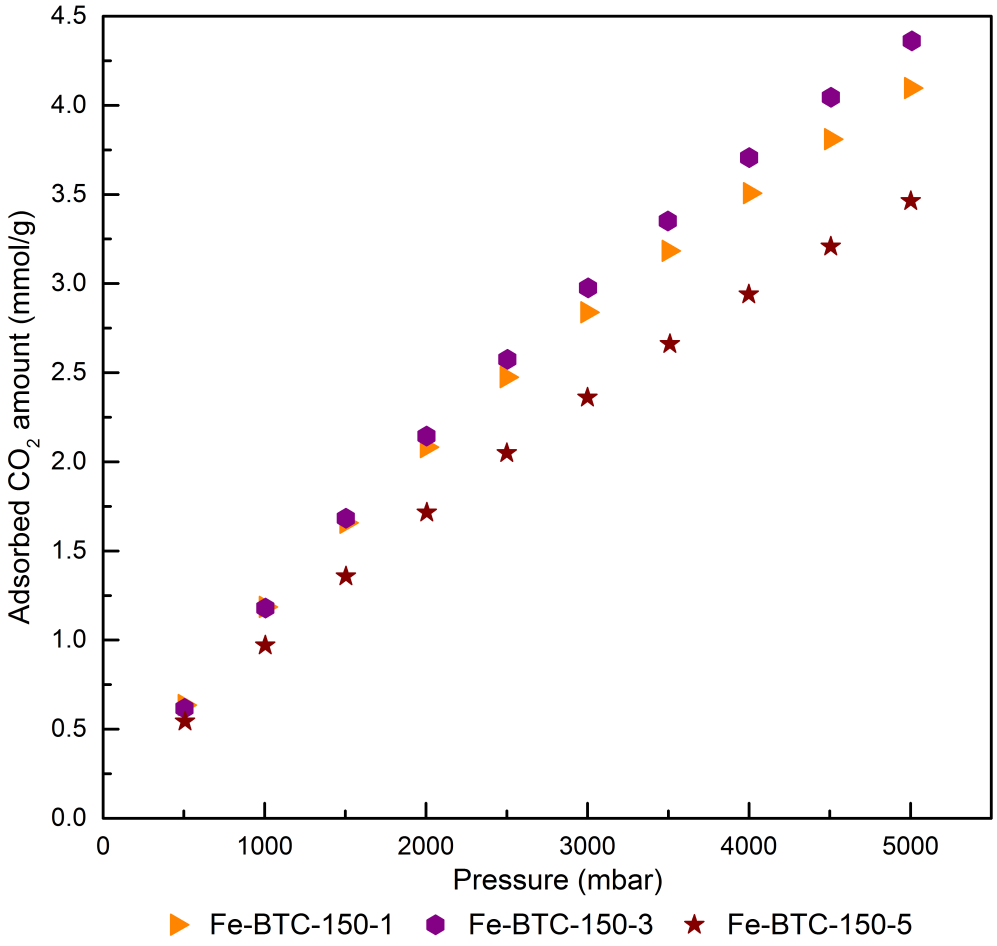

Figure 150. CO_2 adsorption isotherm (298 K) of Fe-BTC-150-1, Fe-BTC-150-3, and Fe-BTC-150-5.

The narrow distribution of the narrow micropores of Fe-BTC-150-1 has remarkable contribution on the CO_2 uptake capacity of Fe-BTC-150-1. Fe-BTC-150-1 (0.373 cm^3/g) possesses a lower micropore volume than Fe-BTC-150-5 (0.468 cm^3/g). However, its CO_2 adsorption capacity is 1.18 times greater than the CO_2 adsorption capacity of Fe-BTC-150-5. This higher CO_2 adsorption capacity of Fe-BTC-150-5 is attributed to its narrower micropore size distribution.

Fe-BTC-150-3 achieves a CO_2 uptake capacity 1.06 and 1.26 times greater than Fe-BTC-150-1 and Fe-BTC-150-5, respectively. As pointed earlier, Fe-BTC-150-3 is the only Fe-BTC that possesses ultramicropores (0.19 cm^3/g) in its pore structure. In line with the studies conducted in literature, we have attributed the enhanced CO_2 adsorption capacity of Fe-BTC-150-3 to the presence of ultramicropores. Theoretical studies show that as the pore size decreases below 0.7 nm, adsorption potential of opposite ultramicropore walls overlap

and a stronger binding energy is achieved (Ello et al., 2013) and thereby, ultramicropores can attract more CO_2 molecules.

In conclusion, obtained results reveal that CO_2 adsorption capacity depends on: i) the volume of ultramicropores (pore diameter < 0.7 nm); ii) the volume of narrow micropores; and iii) the the narrow distribution of narrow micropores through the micropores.

6.4.Comparison of the Properties of Fe-BTC Synthesized and Used in Other Studies with Fe-BTC Synthesized in This Study

Table 45 illustrates the BET surface areas, total pore volumes, and decomposition temperatures of Fe-BTCs synthesized in different studies. The BET surface area and the total pore volume reported in this study is the highest of those reported for Fe-BTC (Basolite F300).

Table 45. BET surface areas, total pore volume and decomposition temperature of Fe-BTCs synthesized in different studies

BET Surface Area (m^2/g)	Total Pore Volume (cm^3/g)	Decomposition Temperature (° C)	Reference
687.0	-	350	(Majano et al., 2013)
840.0	0.45	-	(Dhakshinamoorthy, Alvaro, Chevreau, et al., 2012; Dhakshinamoorthy et al., 2011; Dhakshinamoorthy, Alvaro, Horcajada, et al., 2012)
1010.0	0.90	341	
1024.3	0.60	348	(Torres et al., 2018)
1060.0	-	-	(Opanasenko et al., 2013)
1116.0	-	-	(Zukal et al., 2015)
1125.0	0.61	307	(X. Hu et al., 2016)
1312.0	1.41	342	This Study

The perturbation assisted nanofusion synthesis strategy resulted BET surface area and total pore volume to increase by a factor of 1.6 and 3.1, respectively13–15. More importantly, by controlling the Fe:BTC ratio and synthesis temperature, an Fe-BTC that consists ultramicropores in its pore structure has been synthesized.

6.5. Comparison with Literature

6.5.1. Comparison of the Properties of Fe-BTC Synthesized and Used in Other Studies with Hierarchically Porous Fe-BTCs

Table 46 illustrates the BET surface areas, total pore volumes, and decomposition temperatures of Fe-BTCs synthesized in different studies. The BET surface area and the total pore volume reported in this study is the highest of those reported for Fe-BTC (Basolite F300).

Table 46. BET surface areas, total pore volume and decomposition temperature of Fe-BTCs synthesized in different studies

BET Surface Area (m^2/g)	Total Pore Volume (cm^3/g)	Decomposition Temperature (° C)	Reference
687.0	-	350	(Majano et al., 2013)
840.0	0.45	-	(Dhakshinamoorthy, Alvaro, Chevreau, et al., 2012; Dhakshinamoorthy et al., 2011; Dhakshinamoorthy, Alvaro, Horcajada, et al., 2012)
1010.0	0.90	341	
1024.3	0.60	348	(Torres et al., 2018)
1060.0	-	-	(Opanasenko et al., 2013)
1116.0	-	-	(Zukal et al., 2015)
1125.0	0.61	307	(X. Hu et al., 2016)
1312.0	1.41	342	This Study

The perturbation assisted nanofusion synthesis strategy resulted BET surface area and total pore volume to increase by a factor of 1.6 and 3.1, respectively (Dhakshinamoorthy, Alvaro, Chevreau, et al., 2012; Dhakshinamoorthy et al., 2011; Dhakshinamoorthy, Alvaro, Horcajada, et al., 2012). More importantly, by controlling the Fe:BTC ratio and synthesis temperature, an Fe-BTC that consists ultramicropores in its pore structure has been synthesized.

6.5.2. Comparison of the CO_2 Adsorption Studies of Hierarchically Porous Fe-BTCs and the other MOFs Reported in Literature

Highly porous MOFs have been investigated for their gas adsorption capacities. Table 47 represents the CO_2 adsorption capacities of several MOFs. Our results indicate that BET surface area is not the only parameter effecting CO_2 a capacity. But volume of narrow micropores and the distribution of narrow micropores through micropore size distribution and ultramicropores have significant effect on the amount of CO_2 adsorbed. Among the Fe-BTCs synthesized in this study, the highest CO_2 adsorption capacity belongs to Fe-BTC-150-3 (5.2 wt. % or 1.18 mmol/g at 1 bar and 298 K). CO_2 uptake capacity of Fe-BTC-150-3 is found to be higher than those of reported MOFs listed below.

Table 47. BET surface areas, and CO_2 uptake capacities of some of those reported MOFs

MOF	BET Surface Area (m^2/g)	Pressure (bar)	Temperature (K)	CO_2 Uptake Capacity
Fe-BTC-150-3 (This study)	1312.7	1	298	5.20 wt. %; 1.18 mmol/g
Fe-BTC	1009.0	1	298	0.71 mmol/g (M. Du et al., 2016)
MOF-177	5400.0	1	298	3.6 wt. % (Mason et al., 2011b)
UMCM-1	4034.0	1	298	3.8 wt. % (A. Ö. Yazaydin et al., 2009)
MIL-101(Cr)	2674.0	1	298	4.2 wt. % (Gumma et al., 2009)
ZIF-8	1135.0	1	298	4.3 wt. % (A. Ö. Yazaydin et al., 2009)
MOF-5	2833.0	1	298	4.5 wt. % (Millward & Yaghi, 2005a)
IRMOF-3	2160.0	1	298	5.1 wt. % (Millward & Yaghi, 2005a)
ZIF-25	1110.0	1	298	4.7 wt. % (W. Morris et al., 2010)
IRMOF-6	2516.0	1.2	298	4.6 wt. % (Millward & Yaghi, 2005a)
ZIF-97	564.0	1.1	298	4.5 wt. % (W. Morris et al., 2010)
ZIF-100	595.0	1	298	3.8 wt. % (Phan et al., 2010)
ZIF-95	1050.0	1	298	3.7 wt. % (Phan et al., 2010)
ZIF-71	652.0	1	298	2.8 wt. % (W. Morris et al., 2010)
Mg-MOF-1		1	298	2.7 wt. % (Mallick et al., 2010)
SNU-31		1	298	2.6 wt. % (H. J. Park et al., 2010)
MOF-2	345.0	1	298	2.4 wt. % (Millward & Yaghi, 2005a)

6.6. Concluding Remarks

Here, we report the CO_2 adsorption capacities of hierarchically porous Fe-BTCs synthesized by a perturbation assisted nanofusion synthesis strategy that limits the growth of single crystal MOFs, and enhances BET surface area, micropore volume, total pore volume and thermal stability. The reported synthesis strategy increases the BET surface area and total pore volume by 1.6, and 3.1 times, respectively. A BET surface area of 1312 m^2/g and a total pore volume of 1.41 cm^3/g is achieved which are the highest BET surface area and total pore volume that have been reported for Fe-BTC, to date.

Among the synthesized hierarchically porous Fe-BTCs, Fe-BTC that possesses ultramicropores (58.2% of the micropore volume is formed of ultramicropores) in its pore structure achieves the highest CO_2 adsorption capacity (5.2 wt. % or 1.18 mmol/g at 1 bar and 298 K; 27.5 wt.% or 6.24 mmol/g at 8.5 bar and 298 K) which points out the significant contribution of ultramicropores on the CO_2 adsorption capacity.

By this study, we experimentally show the crucial role of ultramicropores on the adsorbed CO_2 amount. As pore size decreases below 0.7 nm, adsorption potential of opposite ultramicropore walls overlap and a stronger binding energy is achieved (Ello et al., 2013) and ultramicropores attract more CO_2 molecules. In addition, hierarchically porous Fe-BTCs with higher narrow micropore volumes and narrower micropore size distributions possess higher CO_2 adsorption capacities than the hierarchically porous Fe-BTCs that possess lower micropore volumes or the hierarchically porous Fe-BTCs that possess higher narrow micropore volumes but broader micropore size distributions.

Our results reveal that adsorbed CO_2 amount is controlled by: i) the presence of ultramicropores; ii) the volume of narrow micropores; and iii) the narrow distribution of narrow micropores through the micropore size range.

By synthesizing Fe-BTCs via the perturbation assisted nanofusion synthesis strategy, we report a BET surface area, pore volume, and CO_2 uptake capacity that is the highest of all those BET surface areas, pore volume, and CO_2 uptake capacities reported for hierarchically porous Fe-BTC, to date. We clearly showed that synthesizing a MOF that is formed of ultramicropores with a high ultramicropore volume and a narrow micropore size distribution would be the key factor to enhance the adsorbed CO_2 amount. Last but not least, considerable efforts have to be spent on the development of porous materials that are formed

mainly of ultramicropores with high pore volumes to increase the measured CO_2 uptake capacities at 1 bar and 298 K.

Chapter VII

Hydrogen adsorption capacity of hierarchically porous Fe-BTCs: influence of pore size distribution

7.1. Background

The energy consumption rate in 2018 has been the highest since 2010 (Teter, Cazzola, & Petropoulos, n.d.) and the energy consumption by the transportation sector corresponds to 21% ("Energy demand by sector | Energy economics | Home," n.d.). The International Energy Agency (IEA) has reported that transportation sector contributes by 24% to the CO_2 emissions (Teter et al., n.d.) which originates from fuel combustion and road vehicles contribute by three quarters (Teter et al., n.d.). There rises the necessity to develop and improve technologies alternative to fossil fuels which would decrease or eliminate CO_2 emissions (Fakioğlu et al., 2004; Louis Schlapbach & Züttel, 2002; Wilberforce et al., 2017; Yürüm et al., 2009a; Fan Zhang, Zhao, Niu, & Maddy, 2016; Zuo, E, & Lin, 2018; Zuo, Li, Zhang, & Li, 2019; Zuo, Jiaqiang, Liu, Peng, Zhao, et al., 2016; Zuo, Jiaqiang, Liu, Peng, Deng, et al., 2016; Andreas Züttel, Remhof, Borgschulte, & Friedrichs, 2010b).

Metal-organic frameworks (MOFs) are highly crystalline and porous materials formed of an organic and an inorganic part (O M Yaghi et al., 1995). Their high BET surface areas, and pore volumes make these materials promising in various application areas: adsorption/desorption studies, separation studies, and catalysis (H. C. Zhou, Long, & Yaghi, 2012). MOFs are found to be promising in H_2 adsorption studies (Moradi & Groth, 2019; Murray, Dincă, et al., 2009; Yürüm et al., 2009a). Fe-BTC is one of the five MOFs that has been commercialized by BASF ("basolite | Sigma-Aldrich," n.d.). Basolite F300 (Fe-BTC) and MIL-100(Fe) are formed by the reaction of the same starting materials: Fe(III) and BTC (benzene-1,3,5-tricarboxylic acid). However, Basolite F300 and MIL-100(Fe) have different properties. For instance, Basolite F300 has a disordered nature whilst MIL-100(Fe) is a highly crystallite material (Dhakshinamoorthy, Alvaro, Horcajada, et al., 2012). BET surface area (1600 to 1900 m^2/g) and pore volume (0.79 to 1.0 cm^3/g) of MIL-100(Fe) (Huo & Yan,

2012; Jeremias, Khutia, Henninger, & Janiak, 2012; Fumin Zhang et al., 2015) is greater than the BET surface area (800 to 1300 m^2/g) and pore volume (0.4 to 0.6 cm^3/g) of Basolite F300 (Dhakshinamoorthy, Alvaro, Chevreau, et al., 2012; Dhakshinamoorthy et al., 2011; Dhakshinamoorthy, Alvaro, Horcajada, et al., 2012; X. Hu et al., 2016; Majano et al., 2013; Opanasenko et al., 2013; Torres et al., 2018; Zukal et al., 2015). Even though Fe-BTC is as non-toxic and highly porous as MIL-100(Fe) (Horcajada et al., 2010a), there are a few reports investigating the potential application areas of Basolite F300.

Despite the very high H_2 adsorption capacities of MOFs at cryogenic temperatures and high pressures (Moradi & Groth, 2019; Murray, Dincă, et al., 2009), H_2 adsorption capacities of MOFs decrease drastically at ambient conditions (Henrietta W Langmi, Ren, North, Mathe, & Bessarabov, 2017; Murray, Dincă, et al., 2009; Rowsell & Yaghi, 2005). To achieve higher H_2 adsorption capacities at 298 K, significant amount of effort has to be put on to figure out ways that enhance the interactions of H_2 molecules with the surface of MOFs. Two strategies have been suggested to enhance the binding energies of H_2 molecules to the surface of MOFs at ambient temperatures: i) formation of narrow micropores (Dinča et al., 2006; Michael Hirscher & Panella, 2007; Michael Hirscher, Panella, & Schmitz, 2010; Y. H. Hu & Zhang, 2010; Latroche, Surblé, Serre, Mellot-Draznieks, Llewellyn, Lee, Chang, Sung, et al., 2006b; R. E. Morris & Wheatley, 2008; Barbara Panella et al., 2008; Schmitz et al., 2008); and ii) introducing unsaturated metal sites to the framework. (Dinča et al., 2006; Dincă & Long, 2005). In line with what has been suggested, researchers showed that hydrogen adsorbed in the narrower pores were desorbed at higher temperatures and illustrated the direct correlation of the desorption temperature and the pore size (Michael Hirscher et al., 2010; Barbara Panella et al., 2008). Based on the thermal desorption studies and temperature dependent adsorption isotherm measurements, it has been concluded that the pore size determines the heat of adsorption of H_2 and emphasized on the necessity to develop frameworks with high specific surface areas and narrow pores which has been a great challenge (Michael Hirscher et al., 2010; Barbara Panella et al., 2008; Schmitz et al., 2008).

To date, there have been several strategies used in MOF synthesis to enhance BET surface area, pore volume and gas adsorption efficiencies (Topologies, Stock, & Biswas, 2012). However, formation of hierarchical porous MOFs has not drawn particular attention as a consequence of the complicated synthesis procedures and the formation of unstable

mesoporous MOF structures (Bradshaw, El-Hankari, & Lupica-Spagnolo, 2014; G. Cai & Jiang, 2017b; L. Peng et al., 2014a; S. Yuan et al., 2017; Y. Yue, Fulvio, et al., 2015; Y. Yue et al., 2013b). Perturbation assisted nanofusion synthesis strategy come to the fore with its easy, template free and relatively environmentally friendly synthesis procedure (Cao et al., 2016; Y. Yue, Fulvio, et al., 2015; Y. Yue et al., 2013a). By the perturbation assisted nanofusion synthesis strategy textural mesopores are introduced to the pore structure. By this way, both micro- and mesopores would be present and the synthesized material would benefit from the two-pore system (Bradshaw et al., 2014; Cao et al., 2016). In a pore structure at which micro- and mesopores are present, micropores increases the surface area and provide benefits in gas adsorption studies and catalysis reactions mesopores provide larger molecules diffuse easily and enhance the mass transport (Groen, Peffer, Moulijn, & Pérez-Ramírez, 2005; Yueju Zhao et al., 2011). Additionally, one can easily tune the textural porosity via synthesis parameters which provides the opportunity to tune the textural pores with respect to the application area used.

In our study, free of a template, just by vigorously stirring, hierarchical pores were formed. We showed that introducing textural pores enhances the BET surface area and total pore volume, 1.6 and 3.1 times, respectively and a BET surface area and total pore volume higher than those of reported Fe-BTCs have been achieved. With its easy and relatively environmentally friendly synthesis procedure, Fe-BTCs with a BET surface area, and total pore volume higher than those of reported Fe-BTCs have been reported.

Herein, we report the i) synthesis; ii) H_2 adsorption capacity; and iii) role of ultramicropores on the H_2 adsorption capacity of Fe-BTC. To the best of our knowledge, this is the first study to report the H_2 adsorption capacity of Fe-BTC measured at 298 K. By the perturbation assisted nanofusion synthesis strategy, hierarchical pores are formed; BET surface area, and total pore volume are increased by 1.6 and 3.1 times, respectively. Fe-BTC-1, Fe-BTC-3, and Fe-BTC-5 synthesized with different Fe-BTC ratios and different pore size distributions possess different H_2 adsorption capacities. The highest H_2 adsorption capacity belongs to the hierarchically porous Fe-BTC that possesses ultramicropores in its pore structure (1.10 wt.% at 7.6 bar and 298 K). The presence of ultramicropores increases the H_2 adsorption capacity by 2.6 times which signifies the role of ultramicropores on the adsorbed H_2 amount. Here we report a study that suggests a way to enhance H_2 adsorption capacity of Fe-BTC via forming ultramicropores in its pore structure. By this study, not only the H_2

adsorption capacity of Fe-BTC has been increased, but also the role of ultramicropores on the H_2 adsorption capacity has been shown experimentally (Aysu Yurduşen, Yürüm, & Yürüm, 2020a).

7.2. Experimental

7.2.1. Materials

Purchased chemicals were not further treated prior to their use. Iron(III) chloride hexahydrate ($FeCl_36H_2O$) (ACS Reagent Grade, 98% pure) was purchased from Merck Millipore, benzene-1,3,5-tricarboxylic acid (95% pure), N,N-Dimethylformamide (DMF) (99% pure, HPLC grade), and methanol (99.8% pure) were purchased from Sigma Aldrich.

7.2.2. Synthesis of Hierarchically Porous Fe-BTCs

3.1 mmoles of $FeCl_3.6H_2O$, benzene-1,3,5-tricarboxylic acid (3.1 mmoles or 1.03 mmoles or 0.62 mmoles) and 80 mL of N, N-Dimethylformamide (DMF) were mixed vigorously via a magnetic stirrer with a stirring rate of 800 rpm for an hour at 25 °C. A clear solution of $FeCl_3.6H_2O$, benzene-1,3,5-tricarboxylic acid and DMF was obtained at the end of the first hour. Prepared clear solution was poured into glass vials (20 mL) capped with Teflon caps and then heated in an isothermal oven for 2 days at 150 °C. After two days of heating, precipitates were formed. Precipitates and the solution were transferred into falcon tubes (50 mL). Precipitates and the solution were washed with DMF (3 days) and methanol (3 days) for 6 days. Finally, the precipitates were dried under vacuum for 30 hours at 100 °C. Figure 151 is the schematic representation of the experimental procedure and Table 48 represents the sample abbreviations of Fe-BTC synthesized with different Fe:BTC ratio.

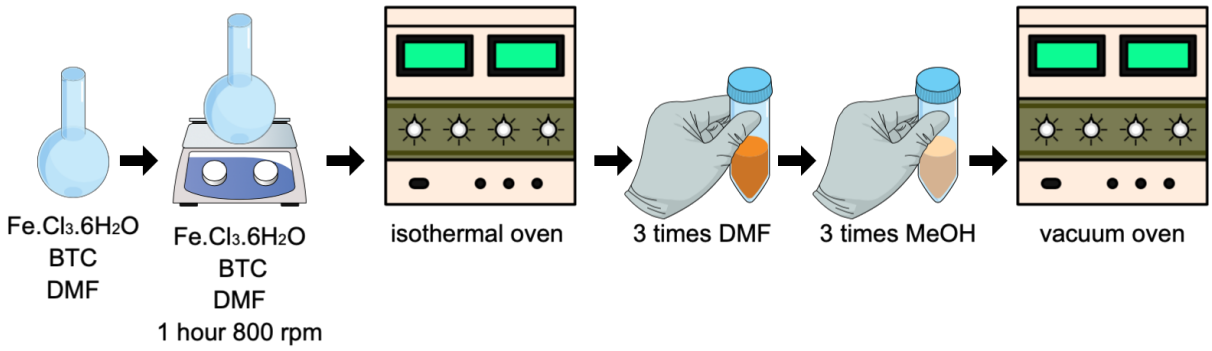

Figure 151. Schematic representation of experimental procedure.

Table 48. Sample abbreviations of hierarchically porous Fe-BTCs synthesized with different Fe:BTC ratio

Sample Abbreviation	Fe:BTC ratio (mmol/mmol)[a]
Fe-BTC-1	1:1
Fe-BTC-3	3:1
Fe-BTC-5	5:1

[a] *(mmol $FeCl_3.6H_2O$) (mmol BTC)*

7.2.3. Characterization Analysis

7.2.3.1.X-Ray diffraction

A Bruker D2 Phaser XRD was used in X-ray diffraction analysis. X-ray diffraction analysis was conducted in between a 2θ range of 2 to 90° with a step size of 0.02°.

7.2.3.2.Scanning electron microscopy (SEM)

For SEM analysis a Leo Supra 35VP field emission scanning electron microscope was used. Fe-BTC-1, and Fe-BTC-3 were imaged while the voltage value was set to 3 kV and working distance was set to 8.1 mm. In the meanwhile, Fe-BTC-5 was imaged while the voltage was set to 1.5 kV and working distance was set to 8.3 mm.

7.2.3.3. Brunauer-Emmett-Teller (BET) surface area and pore size distribution analysis

A Micromeritics 3Flex Instrument was used in BET surface area and pore size distribution analysis. Prior to each analysis 0.35±0.05 grams (g) of Fe-BTC was degassed at 120 °C for 6 hours. For surface area measurements BET model; for micropore volume estimations t-plot method and NLDFT method, and for pore size distribution analysis NLDFT method was used.

7.2.3.4. Fourier transform infrared spectroscopy (FT-IR) analysis

FTIR analysis was conducted with A Thermo Scientific Nicolet Is10 in between the wavelengths of 600 to 4000 cm^{-1}. Background noise was corrected, and scans were repeated for 32 times.

7.2.3.5. Thermogravimetric analysis (TGA)

A TG-DTA (Shimadzu DTG-60H simultaneous thermal analysis) was used to measure the mass losses. Fe-BTCs were heated from 25 °C to 1200 °C under a N_2 flow (20 mL/min) with the step size of 10 K/min.

7.2.3.6. H_2 sorption studies

An Intelligent Gravimetric Analyzer (IGA) was used to measure the adsorbed H2 amount. H2 adsorption studies were conducted at room temperature (298 K) in between 0 and 8 bar. A stainless-steel vacuum pressure reactor (± 1.0 μg sensitivity) was used for a precise measurement. Prior to H2 adsorption studies, Fe-BTCs were outgassed for 6 hours at 120 °C.

7.3. Results and Discussion

7.3.1. XRD Analysis

Figure 152 illustrates the XRD patterns of Fe-BTC-1, Fe-BTC-3, and Fe-BTC-5. Single crystal X-ray crystallography analyses showed that micro-sized single crystals were not formed and there were no metallic-iron present.

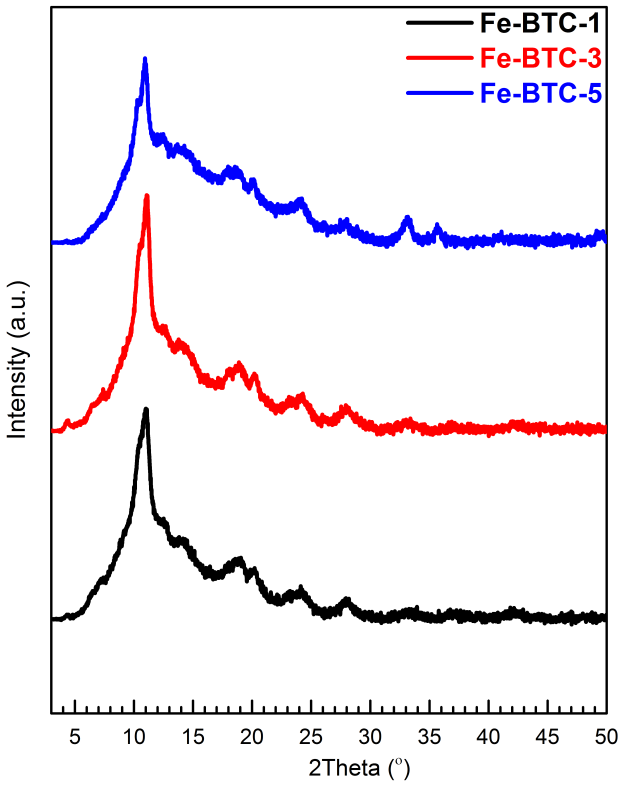

Figure 152. XRD patterns of Fe-BTC-1, Fe-BTC-3, and Fe-BTC-5.

XRD patterns of Fe-BTC-1, Fe-BTC-3, and Fe-BTC-5 matched well with the XRD pattern of Basolite F300. The well matched XRD patterns revealed that by the perturbation assisted nanofusion synthesis strategy Basolite F300 like Fe-BTCs were synthesized successfully.

The broad Bragg peaks and low intensities confirmed that the synthesized Fe-BTCs possess a disordered nature. In addition to the disordered nature of Fe-BTC, nanocrystal building units formed by the perturbation assisted nanofusion synthesis strategy lead to

broadening in the PXRD patterns. Therefore, we have attributed the broadening in the PXRD patterns to the i) disordered nature of Fe-BTC; and ii) the nanosized Fe-BTC crystals.

7.3.2. SEM Images

Figure 153-155 illustrates the SEM images of Fe-BTC-1, Fe-BTC-3, and Fe-BTC-5, respectively.

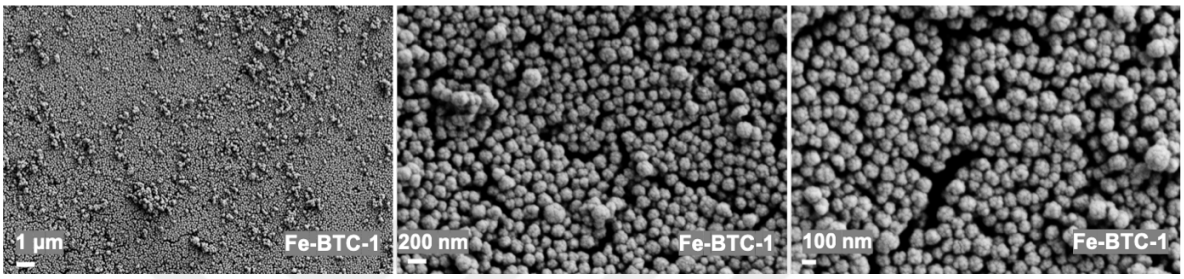

Figure 153. SEM images of Fe-BTC-1.

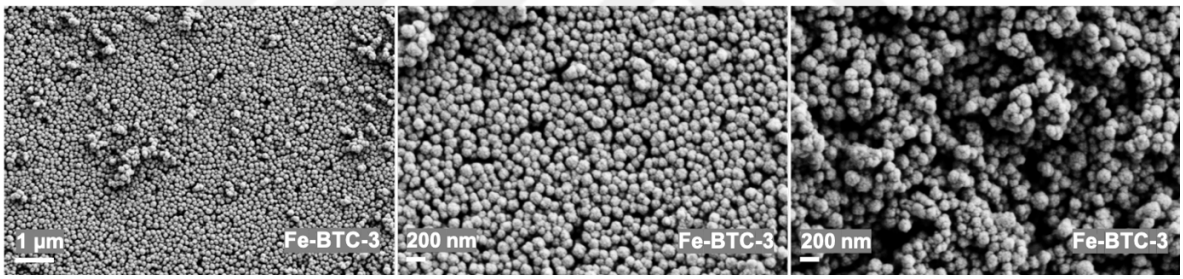

Figure 154. SEM images of Fe-BTC-3.

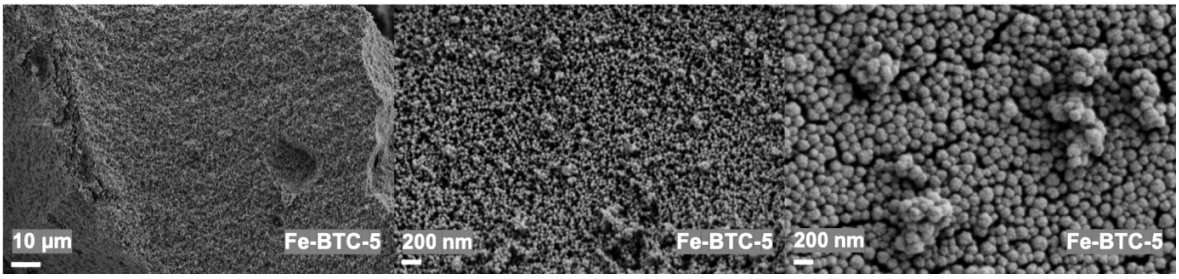

Figure 155. SEM images of Fe-BTC-5.

SEM images of Fe-BTC-1, Fe-BTC-3, and Fe-BTC-5 illustrate that Fe-BTCs synthesized via a perturbation assisted nanofusion synthesis strategy i) have an interconnected highly porous structure, and ii) were formed of aggregated nanosized crystallites.

Vigorous stirring of $FeCl_3 6H_2O$, BTC, and DMF prevented the single crystal formation. SBUs aggregate into nanosized Fe-BTC crystallites which were embedded on an amorphous matrix which can be clearly seen in the SEM images.

The nanosized Fe-BTC crystallites embed on an amorphous matrix and textural mesopores form spontaneously from the self-assembly of the nanosized Fe-BTC crystallites. The amorphous matrix and the interparticle voids created in between the aggregated nanosized Fe-BTCs can be clearly seen in the SEM images of Fe-BTC-1, Fe-BTC-3, and Fe-BTC-5.

7.3.3. N_2 Sorption Isotherms

N_2 sorption isotherms of Fe-BTC-1, Fe-BTC-3 and Fe-BTC-5 are shown in Figure 156-157.

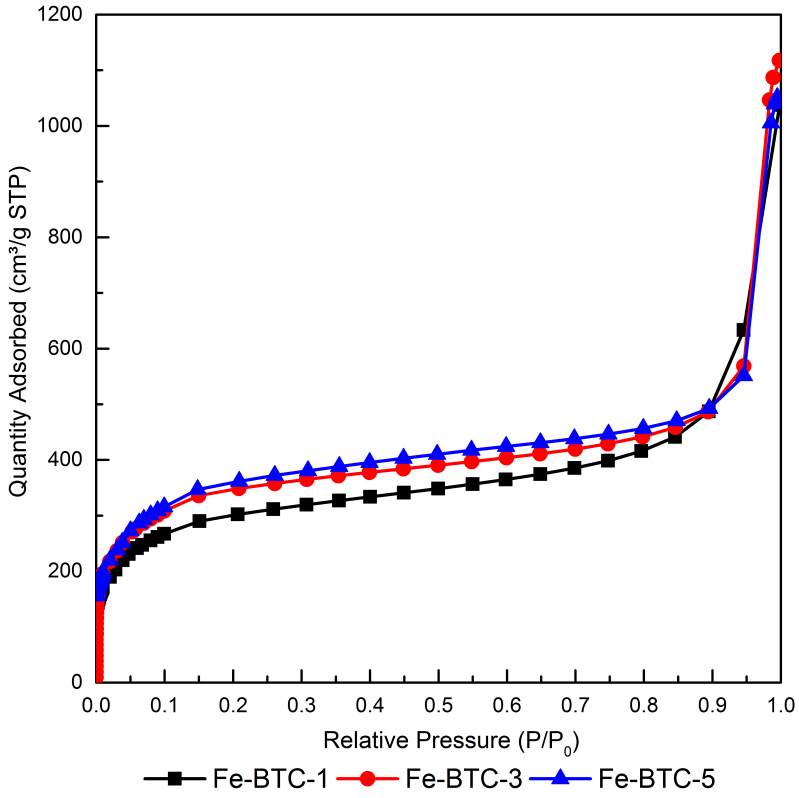

Figure 156. N_2 sorption isotherms of Fe-BTC-1, Fe-BTC-3, and Fe-BTC-5.

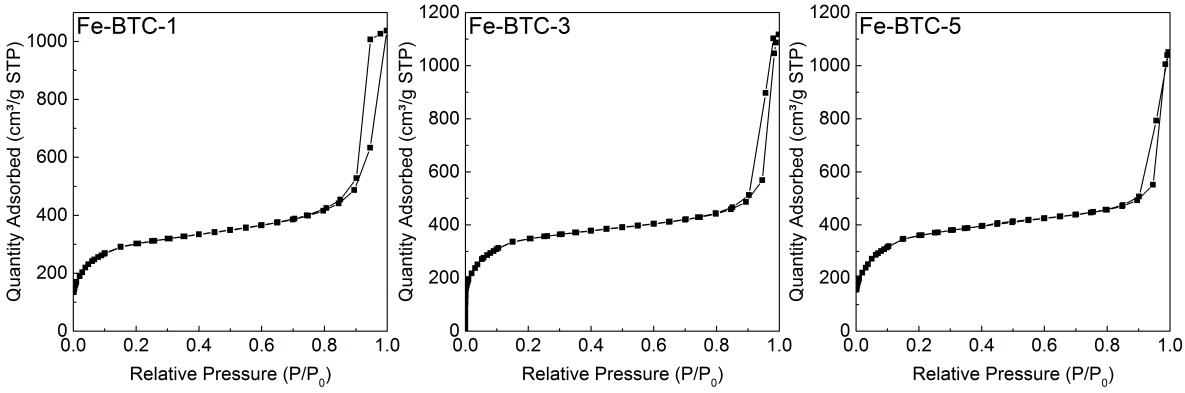

Figure 157. N_2 sorption isotherms of Fe-BTC-1, Fe-BTC-3, and Fe-BTC-5.

N_2 sorption isotherms of hierarchically porous Fe-BTCs synthesized with different Fe:BTC ratio follow the features of IUPAC Type IV isotherms with some microporosity present. High N_2 uptakes at low pressures ($P/P_0 < 0.1$) are attributed to micropores present in the pore structure. Slope observed in between the relative pressures of 0.2 and 0.9 is a consequence of mesopore filling. Lastly, the high N_2 uptakes at pressures close to saturation pressure ($P/P_0 > 0.9$) are a consequence of the mesopores (pore sizes ranging in between 42 to 50 nm) present in the pore structure. Table 49 illustrates the BET surface area (m^2/g), and the total pore volume (cm^3/g) of the synthesized Fe-BTCs.

Table 49. BET surface area (m^2/g) and total pore volume (cm^3/g) of Fe-BTCs

Fe-BTC	BET surface area (m^2/g)	Total pore volume (cm^3/g)
Fe-BTC-1	1139.1±2.1E1	1.29±6.4E-2
Fe-BTC-3	1312.7±1.1E1	1.41±5.7E-2
Fe-BTC-5	1355.9±4.2E1	1.34±2.6E-1

Reported BET surface, and total pore volume of Fe-BTC-1, Fe-BTC-3 and Fe-BTC-5 are higher than those of reported BET surface, and total pore volume of Fe-BTCs (Dhakshinamoorthy, Alvaro, Chevreau, et al., 2012; Dhakshinamoorthy et al., 2011; Dhakshinamoorthy, Alvaro, & Garcia, 2012; X. Hu et al., 2016; Majano et al., 2013; Opanasenko et al., 2013; Torres et al., 2018; Zukal et al., 2015). By synthesizing hierarchically porous Fe-BTCs via a perturbation assisted nanofusion synthesis strategy, hierarchical pores were formed. Introducing hierarchical pores enhanced the BET surface area, and the total pore volume of Fe-BTC.

7.3.4. t-plot Method

t-plot method is used to estimate the micropore volume (Lowell et al., 2004a). t-plots of Fe-BTC-1, Fe-BTC-3, and Fe-BTC-5 can be found in Figure 158 and Table 50 represents the micro- and mesopore areas, fraction of microporosities and micropore volumes estimated by t-plot method.

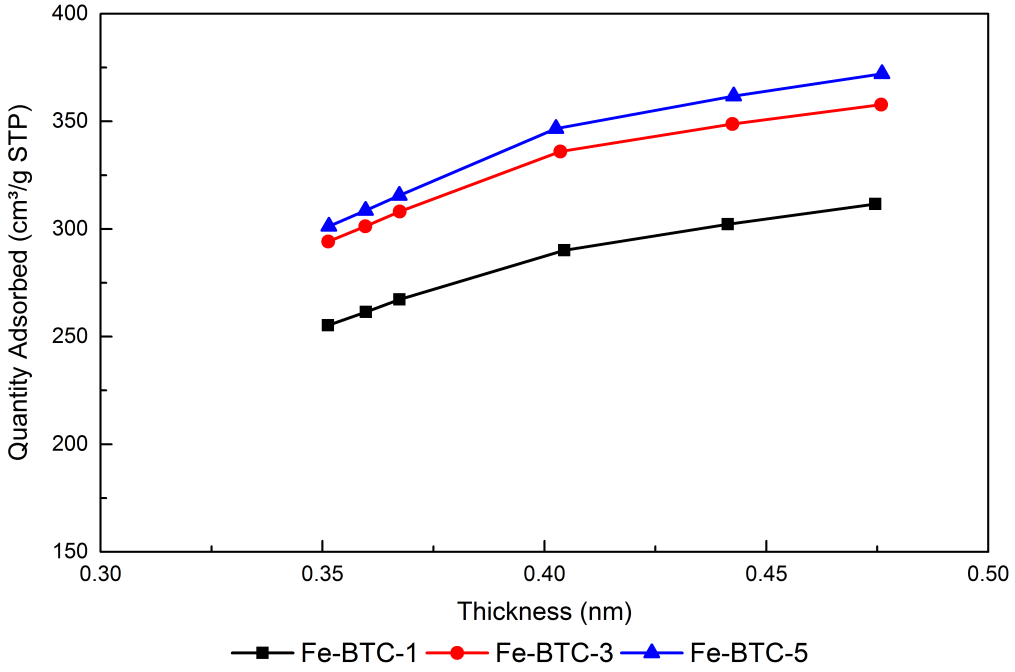

Figure 158. t-plots of Fe-BTC-1, Fe-BTC-3, and Fe-BTC-5.

Table 50. Micro-, and mesopore area, micropore to total pore area fraction and micropore volume estimated by t-plot method

Hierarchically porous Fe-BTCs	Smicro (m^2/g)	Smeso (m^2/g)	Smicro (%)	Vmicro (cm^3/g)
Fe-BTC-1	425.5±5.3E1	713.6±7.4E1	37.4	0.151±2.6-2
Fe-BTC-3	509.6±6.0E-1	803.2±1.2E1	38.8	0.181
Fe-BTC-5	458.7±1.5E2	897.2±7.7	33.8	0.159±7.8E-2

t-plots of Fe-BTC-1, Fe-BTC-3, and Fe-BTC-5 are formed of two linear parts which deviated towards downwards. Deviations illustrated the presence of micropores. Different micropore volumes were estimated for hierarchically porous Fe-BTCs synthesized with

different Fe:BTC ratios and the highest micropore volume belongs to Fe-BTC-3 which is 1.2, and 1.14 times greater than the micropore volume of Fe-BTC-1 and Fe-BTC-5, respectively.

7.3.5. NLDFT Method

Figure 159 shows the incremental pore volume versus pore width plots of Fe-BTC-1, Fe-BTC-3, and Fe-BTC-5 and Table 51 illustrates the pore volumes of narrow micropores, micropores, mesopores, upper mesopores, total pore volume, and fraction of microporosity.

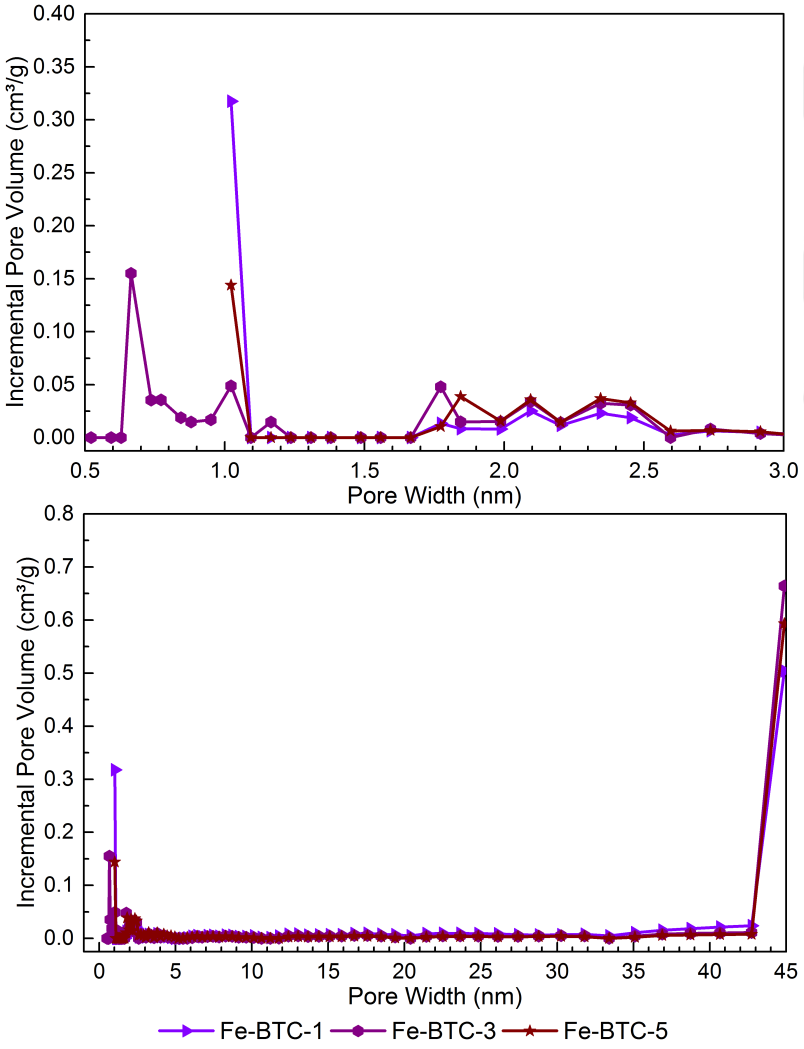

Figure 159. NLDFT plots of Fe-BTC-1, Fe-BTC-3, and Fe-BTC-5.

Table 51. Narrow micro-, micro-, uppermeso-, meso- and total pore volume estimated by NLDFT method

	Vpores <1 nm (cm^3/g)	Vmicro (cm^3/g)	Vuppermeso (cm^3/g)	Vmeso (cm^3/g)	Vtotal (cm^3/g)	Vmicro (%)
Fe-BTC-1	0.318±8.3E-3	0.373±8.1E-3	0.504±8.7E-2	0.917±6.5E-2	1.29±6.4E-2	28.9
Fe-BTC-3	0.326±4.0E-3	0.453±6.3E-3	0.664±4.3E-2	0.957±6.3E-2	1.41±5.7E-2	32.1
Fe-BTC-5	0.367±0.0148	0.468±3.0E-2	0.59±2.8E-1	0.872±2.9E-1	1.34±2.6E-1	34.9

The highest micropore volume belongs to Fe-BTC-5 while the fraction of microporosity of Fe-BTC-3 and Fe-BTC-5 are estimated to be similar. The micropore volume of Fe-BTC-5 is 1.25 and 1.03 times higher than the micropore volume of Fe-BTC-1, and Fe-BTC-3, respectively. Volume of narrow micropores present in Fe-BTC-5 is 1.15 and 1.13 times higher than the volume of narrow micropores present in Fe-BTC-1, and Fe-BTC-3, respectively. The highest total pore volume belongs to Fe-BTC-3 (1.41 cm^3/g) while the lowest total pore volume belongs to Fe-BTC-1.

7.3.6. FTIR Analysis

FTIR spectra of Fe-BTC-1, Fe-BTC-3, and Fe-BTC-5 are provided in Figure 160 while Table 52 shows the FTIR frequencies of Fe-BTCs. FTIR spectra of the synthesized Fe-BTC-1, Fe-BTC-3, and Fe-BTC-5 match well with the FTIR spectrum of the commercial Basolite F300 reported in the literature.

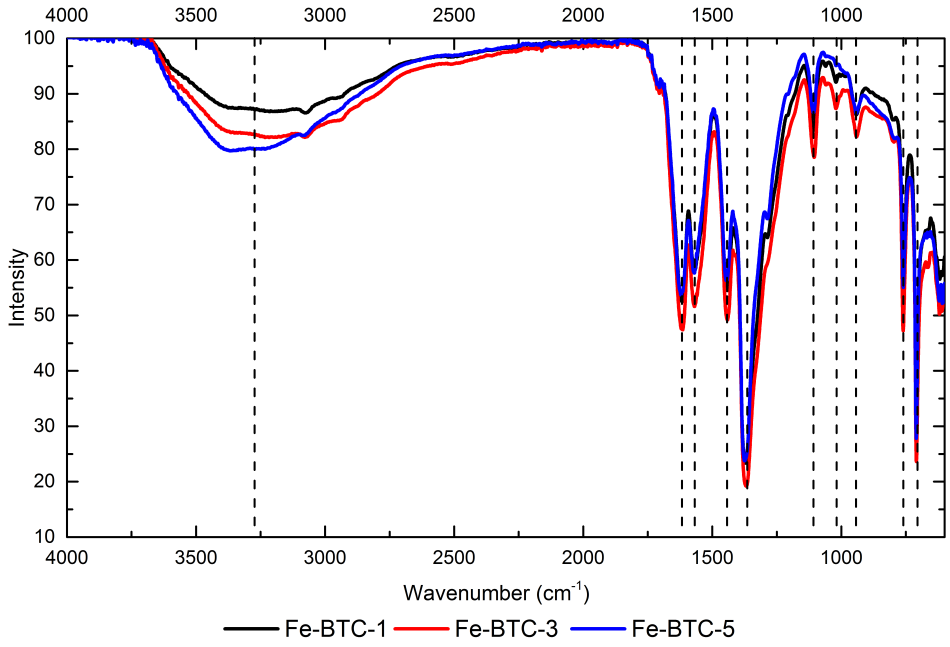

Figure 160. FTIR spectra of Fe-BTC-1, Fe-BTC-3, and Fe-BTC-5.

Table 52. FTIR frequencies of Fe-BTCs

	Fe-BTC-1	Fe-BTC-3	Fe-BTC -5	Assigned mode	Reference
1st	3075 cm^{-1}	3232 cm^{-1}	3367 cm^{-1}	O-H bond stretching	(Torres et al., 2018)
2nd	1616 cm^{-1}	1615 cm^{-1}	1621 cm^{-1}	asymmetric (COO) stretching mode	(Dhumal et al., 2016)
3rd	1569 cm^{-1}	1569 cm^{-1}	1569 cm^{-1}	H_2O bending mode	(X. Hu et al., 2016)
4th	1442 cm^{-1}	1441 cm^{-1}	1445 cm^{-1}	asymmetric (COO) stretching mode	(Dhumal et al., 2016)
5th	1370 cm^{-1}	1367 cm^{-1}	1374 cm^{-1}	symmetric (COO) stretching mode	(Dhumal et al., 2016)
6th	1105 cm^{-1}	1105 cm^{-1}	1107 cm^{-1}	C-O-Fe stretching, skelatal modes of Fe-BTC	(X. Hu et al., 2016)
7th	942 cm^{-1}	941 cm^{-1}	941 cm^{-1}	Trimesate bands	(X. Hu et al., 2016)
8th	761 cm^{-1}	760 cm^{-1}	760 cm^{-1}	Fe-O stretching mode	
9th	709 cm^{-1}	709 cm^{-1}	709 cm^{-1}	Fe-O stretching mode	
10th	618 cm^{-1}	619 cm^{-1}	621 cm^{-1}	Central oxygen in single Fe_3O	(Vuong et al., 2013a)

Broad bands in between 3000 and 3400 cm^{-1} are assigned to OH groups. Peaks at 1370, 1441, 1569, and 1621 cm^{-1} prove that BTC was successfully attached to Fe. The peaks at 1569 and 1621 cm^{-1-} illustrates that Fe sites are coordinated with water molecules. The characteristic peaks of carboxylate symmetric stretching mode, 1375 and 1450 cm^{-1-}, issues a shift to 1369 and 1440 cm^{-1} which is a consequence of bond elongation. The peaks present at 941 and 1105 cm^{-1} indicate that C-H in-plane and out-of-plane bending modes are present in the structure of Fe-BTC-1, Fe-BTC-3, and Fe-BTC-5. The peak at 612 cm^{-1} is attributed

central oxygen in single Fe_3O. The characteristic peaks of Basolite F300 structure, 709 and 760 cm^{-1}, confirm that a Basolite F300 like Fe-BTC was synthesized by the perturbation assisted nanofusion synthesis strategy. Moreover, FTIR spectrum of hierarchically porous Fe-BTCss were compared with the FTIR spectra of $FeCl_3.6H_2O$. None of the peaks observed in the FTIR spectra of $FeCl_3.6H_2O$ (842 cm^{-1}, 1594 cm^{-1}, 2993 cm^{-1}, 3212 cm^{-1}, and 3523 cm^{-1}) were observed in the FTIR spectrum of hierarchically porous Fe-BTCs which proves that there are no metallic iron present.

7.3.7. TGA

Figure 161 illustrates the TGA curves of Fe-BTC-1, Fe-BTC-3, and Fe-BTC-5. A detailed representation of TGA analysis can be found in Table 53 and 54.

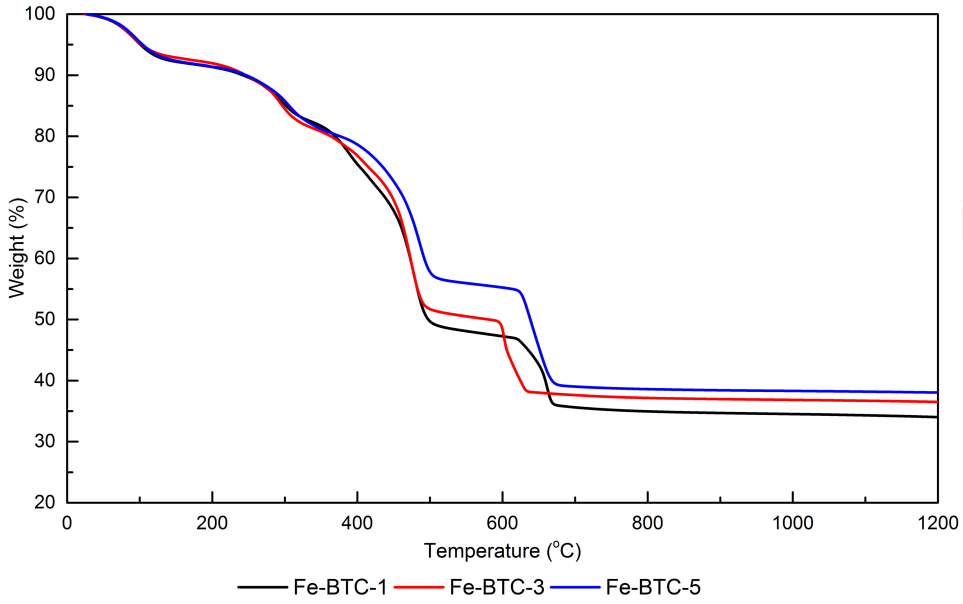

Figure 161. TGA curve of Fe-BTC-1, Fe-BTC-3, and Fe-BTC-5.

Table 53. % mass loss during TGA analysis of Fe-BTC synthesized at 150 °C.

Temperature Range (°C)	Fe-BTC-1 (%)	Temperature Range (°C)	Fe-BTC-3 (%)	Temperature Range (°C)	Fe-BTC-5 (%)
25-179	-8.3	25-168	-7.4	25-178	-8.2
179-334	-9.2	168-342	-11.4	178-374	-11.7
334-556	-34.5	342-547	-30.6	374-570	-24.4
556-776	-13.0	547-754	-13.2	570-766	-17.0

Table 54. Percent residual mass at the end of TGA.

	Fe-BTC-1	Fe-BTC-3	Fe-BTC-5
Residual Mass (%)	35	37.4	38.7

Four main losses occurred when Fe-BTC-1, Fe-BTC-3, and Fe-BTC-5 were heated to 1200 °C under N_2 environment. The first mass loss is a consequence of the removal of adsorbed and coordinated water molecules. The second mass loss is a consequence of the removal of the trapped solvent molecules. The third mass loss occurs as a consequence of BTC decomposition which determines the stability of Fe-BTC structure. The fourth and the last mass loss is a consequence of the decomposition of the carboxylates.

Fe-BTC-1, Fe-BTC-3, and Fe-BTC-5 decomposed at 334, 342, and 374 °C, respectively. The highest thermal stability belongs to Fe-BTC-5 which was synthesized with the least amount of BTC. To the best of our knowledge, Fe-BTC-5 possesses a higher thermal stability than those of Fe-BTC reported in literature, so far (X. Hu et al., 2016; Majano et al., 2013; Torres et al., 2018). Moreover, TGA analysis show that Fe-BTCs synthesized in this study are thermally stable under adsorption process conditions.

7.3.8. H_2 Adsorption Studies

Figure 162 illustrates the H_2 sorption capacities of Fe-BTC-1, Fe-BTC-3, and Fe-BTC-5. The different H_2 sorption capacities of Fe-BTCs synthesized with different Fe:BTC ratio (Fe-BTC-1, Fe-BTC-3, and Fe-BTC-5) are found to be dependent on the pore size distribution and textural properties of Fe-BTC. Langmuir and Freundlich models were

investigated for the best fit and respective isotherm parameters, respective equations, and R^2 values are provided below.

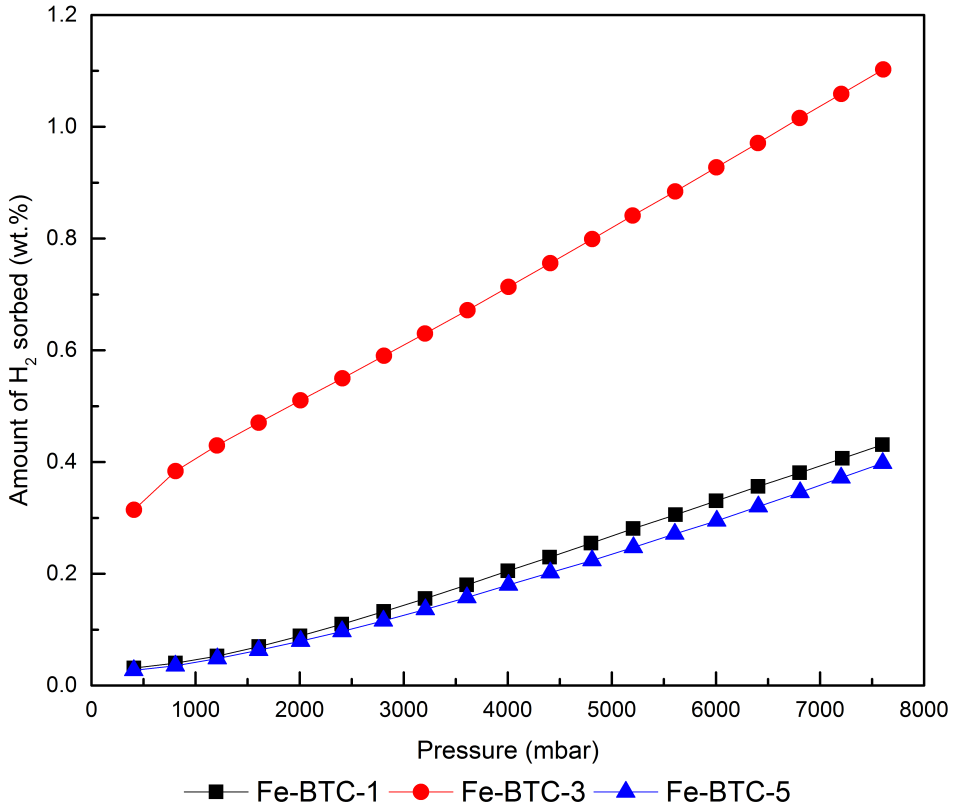

Figure 162. H_2 sorption isotherms (298 K) of Fe-BTC-1, Fe-BTC-3, and Fe-BTC-5.

Langmuir Model:

$$\frac{C_e}{q_e} = \frac{1}{KQ^0} + \frac{C_e}{Q^0} \tag{7.1}$$

Freundlich Model:

$$logq_e = logK_F + \frac{1}{n} logC_e \tag{7.2}$$

Table 55. Respective equations obtained from models

Hierarchically porous Fe-BTCs	Langmuir Model	Freundlich Model
Fe-BTC-1	*y = -0.0835x+4256.9*	*y = 1.0027x-3.5996*
	$R^2 = 0.1534$	$R^2 = 0.9746$
Fe-BTC-3	*y = 0.1428x+453.16*	*y = 0.4454x-1.0347*
	$R^2 = 0.9009$	$R^2 = 0.9639$
Fe-BTC-5	*y = -0.1035x+4819.7*	*y = 1.0068x-3.6643*
	$R^2 = 0.185$	$R^2 = 0.9746$

Table 56. Langmuir and Freundlich isotherm parameters

Hierarchically porous Fe-BTCs	Langmuir	Freundlich
Fe-BTC-1	Q_m= 11.98 mg/g	K_F=2.5E-04 mg/g
	K_a= 1.96E-05 mg-1	η_F= 0.99
	R^2= 0.1534	R^2= 0.9746
Fe-BTC-3	Q_m= 7.0 mg/g	K_F = 9.2E-02 mg/g
	K_a= 3.15E-04 mg-1	η_F = 2.25
	R^2= 0.9009	R^2= 0.9639
Fe-BTC-5	Q_m= 9.66 mg/g	K_F= 2.2E-04 mg/g
	K_a= 2.15E-05 mg-1	η_F= 0.99
	R^2= 0.185	R^2=0.9746

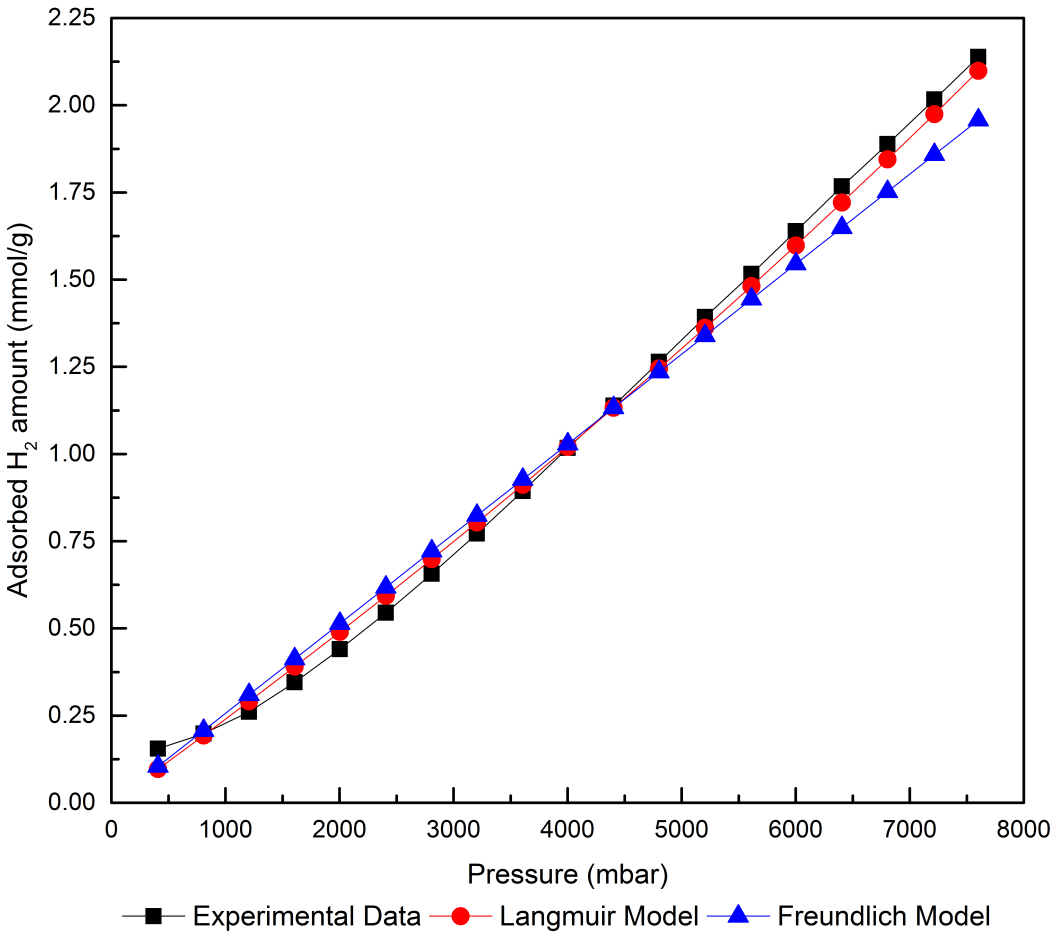

Figure 163. Comparison of the experimental and the estimated data (Fe-BTC-1).

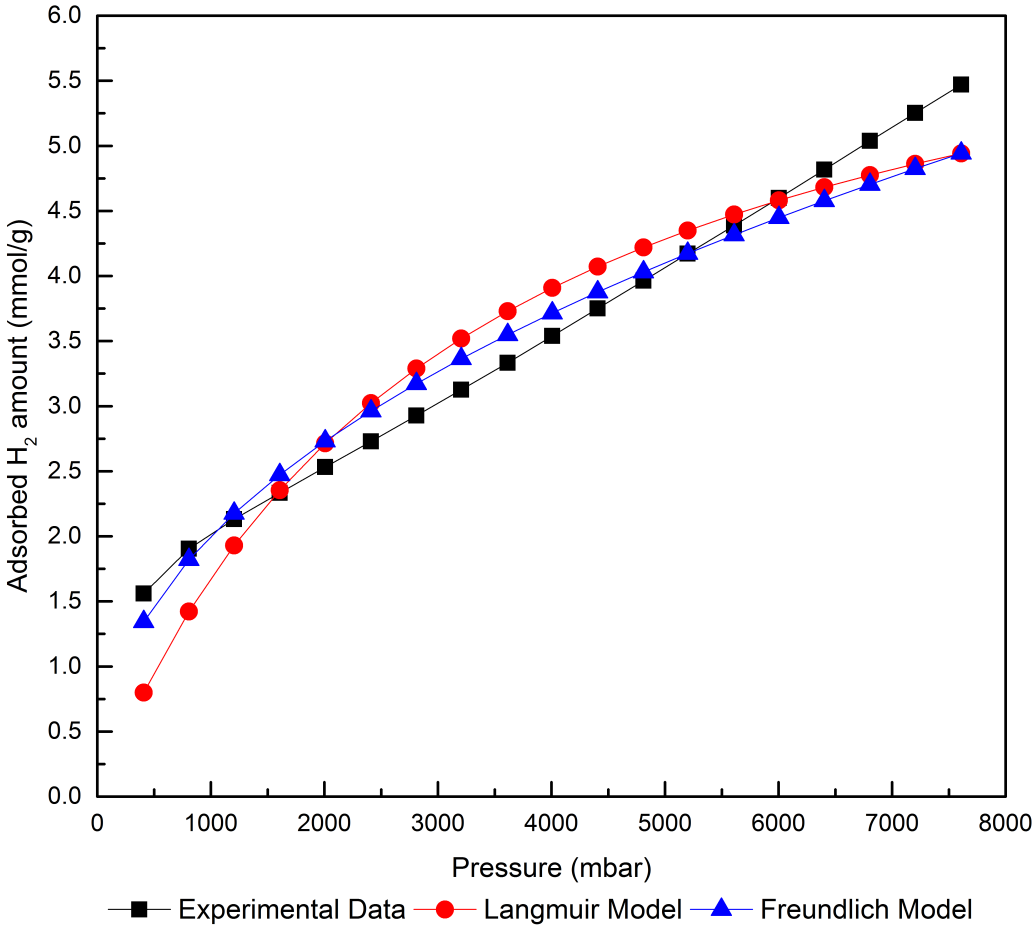

Figure 164. Comparison of the experimental and the estimated data (Fe-BTC-3).

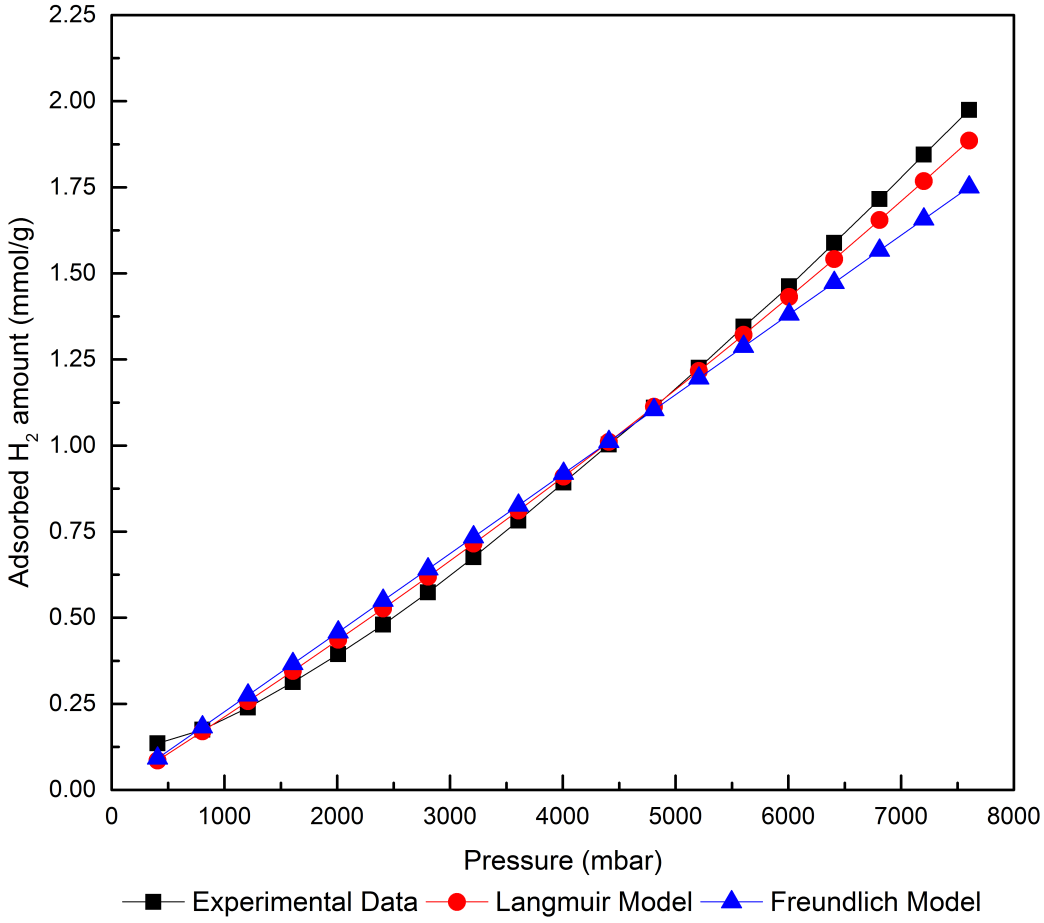

Figure 165. Comparison of the experimental and the estimated data (Fe-BTC-5).

Langmuir and Freundlich isotherm parameters show that Freundlich model describes the H_2 adsorption behavior (at 298 K) of hierarchically porous Fe-BTCs better. However, as the adsorption studies were conducted till 8 bars, the shape of the isotherm may be misleading.

The highest H_2 adsorption capacity belongs to Fe-BTC-3 while Fe-BTC-1 (2.56 times lower), and Fe-BTC-5 (2.82 times lower) possess a significantly lower H_2 adsorption capacities than Fe-BTC-3. The significant differences in H_2 sorption capacities are attributed to different pore size distribution of hierarchically porous Fe-BTCs synthesized with different Fe:BTC ratio. Table 57 illustrates BET surface area, volume of ultramicro-, narrow micro-, micropores and H_2 sorption capacities of Fe-BTC-1, Fe-BTC-3, and Fe-BTC-5 measured at 7.6 bar and 298 K. Figure 166 shows the narrow micro-, and micropore volume of Fe-BTC-1, Fe-BTC-3, and Fe-BTC-5.

Table 57. BET surface area, ultramicro-, narrow micro-, micropore volume, volume fraction of narrow micro- to micropores, and H_2 adsorption capacities of Fe-BTCs

	BET Surface Area (m^2/g)	Vpores < 0.7 nm (cm^3/g)	Vpores < 1 nm(cm^3/g)	Vpores < 2 nm(cm^3/g)	V<1nm/ V<2nm	H_2 adsorption capacity (wt.%) [a]
Fe-BTC-1	1139.1±2.1E1	-	0.318±8.3E-3	0.373±8.1E-3	85.3	0.43
Fe-BTC-3	1312.7±1.1E1	0.19	0.326±4.0E--3	0.453±6.3E-3	71.9	1.10
Fe-BTC-5	1355.9±4.2E1	-	0.367±0.0148	0.468±3.0E-2	78.4	0.39

[a] Measured at 7.6 bar and 298 K

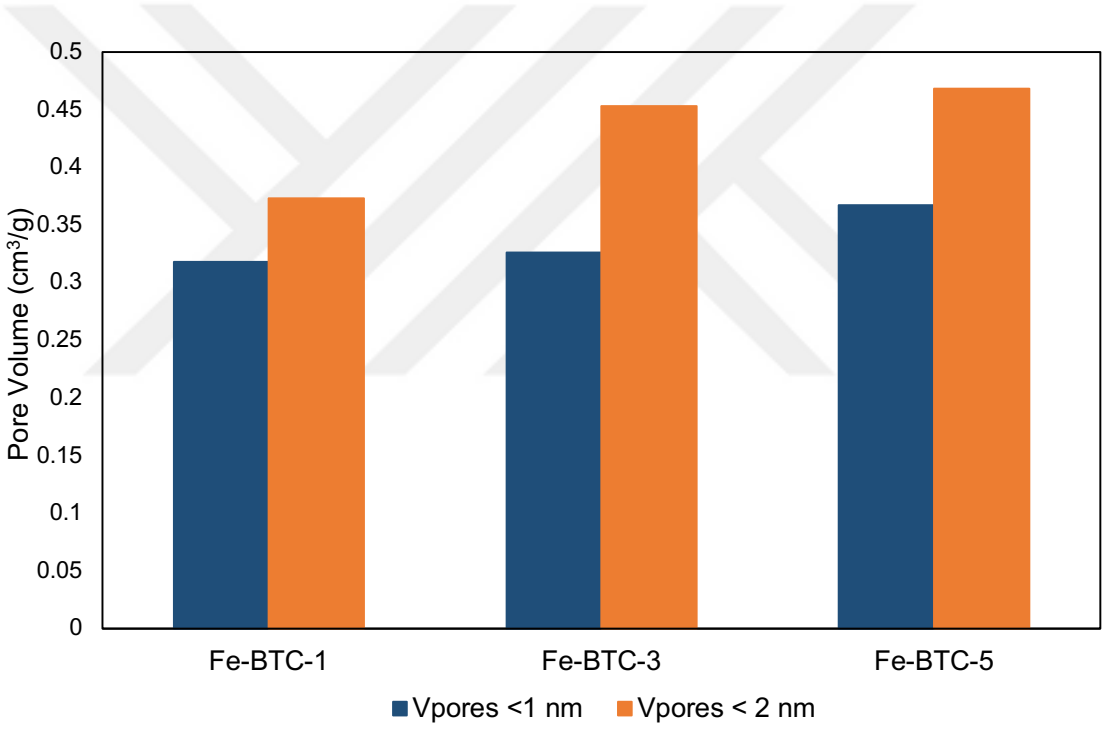

Figure 166. Volume of narrow- and micropores of Fe-BTC-1, Fe-BTC-3, and Fe-BTC-5

Despite its relatively low fraction (71.9%) of narrow micropores (volume of narrow micropores/volume of micropores), Fe-BTC-3 possesses the highest H_2 adsorption capacity among the hierarchically porous Fe-BTCs synthesized in this study. Interestingly, neither the narrow micropore volume nor the micropore volume of Fe-BTC-3 is higher than the narrow micropore volume or the micropore volume of Fe-BTC-5.

Remarkably, among the synthesized hierarchically porous Fe-BTCs, it is Fe-BTC-3 that possesses ultramicropores in its pore structure. Presence of ultramicropores enhances the H_2 adsorption capacity of Fe-BTC-3, and a H_2 adsorption capacity 2.6, and 2.8 times higher than Fe-BTC-1, and Fe-BTC-5 is achieved. This relatively high H_2 adsorption capacity of Fe-BTC-3 indicates the crucial effect of ultramicropores on the adsorbed H_2 amount. Figure 167 compares the H_2 adsorption capacities (7.6 bar and 298 K) and the narrow micropore volumes of Fe-BTC-1, and Fe-BTC-5.

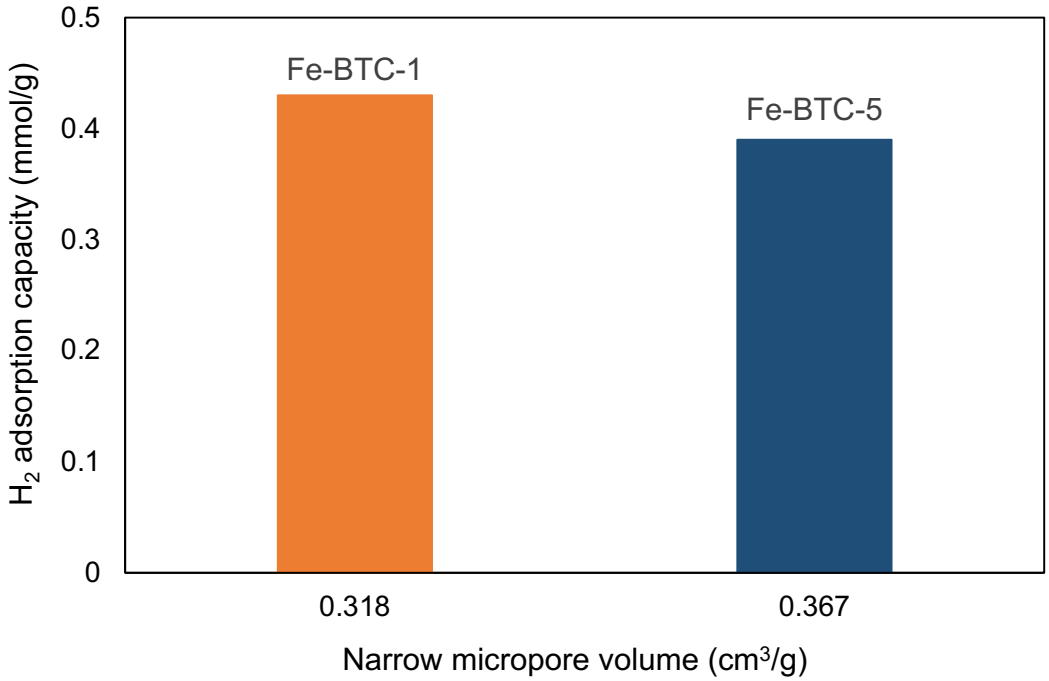

Figure 167. H_2 adsorption capacity (7.6 bar and 298 K) and narrow micropore volume of Fe-BTC-1 and Fe-BTC-5

Fe-BTC-1 which possesses a lower BET surface area (1.19 times), a lower narrow micropore (1.15 times), and a lower micropore volume (1.25 times) than Fe-BTC-5, possesses a H_2 adsorption capacity (0.43 wt.%) 1.1 times greater than Fe-BTC-5 (0.39 wt.%). We have attributed this relatively low H_2 adsorption capacity of Fe-BTC-5 to its lower fraction of narrow micropore volume through the micropore size distribution (narrow micropore volume/micropore volume). As the distribution of narrow micropores through the micropore size distribution becomes narrower, the adsorbed H_2 amount increases. Based on our results, we have attributed the differences in H_2 adsorption capacities to different pore size distributions of Fe-BTC-1, Fe-BTC-3, and Fe-BTC-5. Apparently, it is the pore size that

causes differences in the H_2 adsorption capacity. Revealed by theoretical studies, as pore diameters decrease below 1 nm, van der Waals interaction between the pores and the H_2 molecules strengthen and a higher adsorption potential is achieved (K. Xia, Gao, Wu, Song, & Ruan, 2007). In accordance with Lenard-Jones potential, the highest van der Waals potential is achieved by the pores with pore diameters of 6 to 8 Å (Schlichtenmayer & Hirscher, 2012). On the contrary, theoretical studies illustrate that when hydrogen is adsorbed on wider pores, a hydrogen layer forms on the wells located close to the pore walls and a less dense layer of hydrogen is adsorbed on the center of the pores which results in a lower H_2 adsorption capacity (Becher et al., 2003; Broom et al., 2019; Murray, Dincă, et al., 2009; Barbara Panella et al., 2005a; Schlichtenmayer & Hirscher, 2012, 2016; Schlichtenmayer et al., 2011).

In line with what has been reported in theoretical studies (Becher et al., 2003; Broom et al., 2019; Murray, Dincă, et al., 2009; Barbara Panella et al., 2005a; Schlichtenmayer & Hirscher, 2012, 2016; Schlichtenmayer et al., 2011), our results show that the presence of ultramicropores is the reason why an enhanced H_2 adsorption capacity is observed in Fe-BTC-3. Fe-BTC that has ultramicropores (Fe-BTC-3) in its pore structure possesses a larger adsorption potential and a higher H_2 adsorption capacity than Fe-BTC-1, and Fe-BTC-5. Figure 168 compares the H_2 adsorption capacities (7.6 bar and 298 K) and the narrow micropore volumes of Fe-BTCs. It is clear from Figure 168 that despite the lower narrow micropore volume of Fe-BTC-3, the highest H_2 adsorption capacity belongs to Fe-BTC-3. In line with our results and the theoretical studies conducted by other researchers (Becher et al., 2003; Broom et al., 2019; Murray, Dincă, et al., 2009; Barbara Panella et al., 2005a; Schlichtenmayer & Hirscher, 2012, 2016; Schlichtenmayer et al., 2011), we conclude that the adsorbed H_2 amount depends on: i) the pore size of the sorbent; ii) the presence of ultramicropores; and iii) the volume fraction of narrow micropores to micropores.

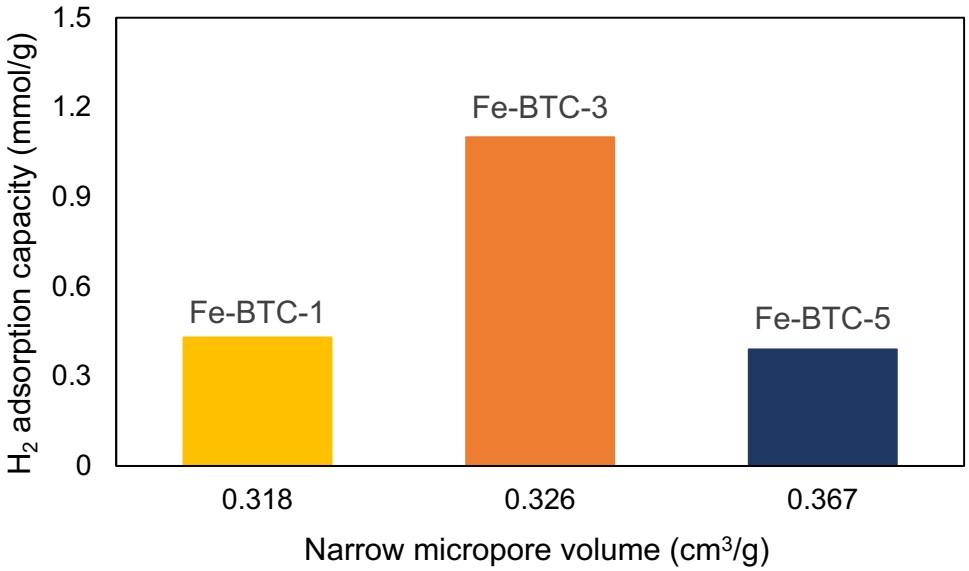

Figure 168. H_2 adsorption capacity (7.6 bar and 298 K) and the narrow micropore volume of Fe-BTCs

It has been reported that physisorption, which is the main adsorption mechanism in MOFs, is affected by the pore size heavily (Dinča et al., 2006; Michael Hirscher & Panella, 2007; Michael Hirscher et al., 2010; Latroche, Surblé, Serre, Mellot-Draznieks, Llewellyn, Lee, Chang, Sung, et al., 2006a; R. E. Morris & Wheatley, 2008; Murray, Dincă, et al., 2009; Barbara Panella et al., 2006, 2008; Schlichtenmayer et al., 2011; Schmitz et al., 2008). Bhatia and Myers showed that 15.1 kJ/mol of energy is thermodynamically needed for an adsorbent to store hydrogen at ambient temperature (Bhatia & Myers, 2006a). However, very weak interactions exist between the physisorbed H_2 molecules and MOFs, and the isosteric heat of adsorption has been found to be in between 4 to 7 kJ/mol (Dinča et al., 2006; R. E. Morris & Wheatley, 2008) meaning that cryogenic temperatures are necessary to adsorb considerable amount of H_2. To increase the isosteric heat of adsorption of H_2 binding at ambient temperature two strategies were suggested: i) forming narrow pores within the framework of MOFs (Dinča et al., 2006; Michael Hirscher & Panella, 2007; Michael Hirscher et al., 2010; Y. H. Hu & Zhang, 2010; Latroche, Surblé, Serre, Mellot-Draznieks, Llewellyn, Lee, Chang, Sung, et al., 2006b; R. E. Morris & Wheatley, 2008; Barbara Panella et al., 2008; Schmitz et al., 2008); and ii) the presence of unsaturated metal sites (Dinča et al., 2006; Dincă & Long, 2005). In one of the studies it was figured out that the desorption temperature increases with the decrease in the pore size (Barbara Panella et al., 2008). Moreover, it was shown that the

desorption temperature and the pore size was directly correlated since the hydrogen adsorbed in the larger pores were desorbed at lower temperatures while the hydrogen adsorbed in the narrower pores were desorbed at higher temperatures (Michael Hirscher et al., 2010; Barbara Panella et al., 2008). Thereof, based on the thermal desorption studies and temperature dependent adsorption isotherm measurements of the researchers, they have concluded that the heat of adsorption of H_2 binding is determined by the pore size (Barbara Panella et al., 2008) and pointed out that the synthesize of a framework with a high specific surface area that possess narrow pores is a challenge to be addressed (Michael Hirscher et al., 2010; Barbara Panella et al., 2008; Schmitz et al., 2008).

In line with what has been addressed and reported in literature, by synthesizing Fe-BTCs via the perturbation assisted nanofusion synthesis strategy, we have introduced both narrow micropores and mesopores to the pore structure. Thereby, the BET surface and the total pore volume of Fe-BTC have been enhanced by 1.6 and 3.1 times, respectively. By introducing ultramicropores and narrow micropores to the pore structure of Fe-BTC-3, the H_2 adsorption capacity has been enhanced by 2.6 times (1.10 wt.% at 7.6 bar and 298 K) and showed experimentally that the presence of ultramicropores influences the adsorbed H_2 amounts, crucially.

7.4. Comparison with Literature

To the best of our knowledge, this research is the first study that reports the H2 adsorption capacity of Fe-BTC at 298 K. By the perturbation assisted nanofusion synthesis strategy and control over textural porosity, an Fe-BTC that possesses ultramicropores in its pore structure were synthesized. Table 58 illustrates the H_2 adsorption capacity of some of those MOFs reported in literature.

Table 58. BET surface area, pore volume, and H_2 adsorption capacity of MOFs reported in literature

MOF	BET Surface Area (m^2/g)	Pore Volume (cm^3/g)	Pressure (bar)	Temperature (K)	H_2 Sorption Capacity	Reference
Fe-BTC-3	1312.7	1.41	1	298	0.43 wt. % (2.1 mmol/g)	This study
Fe-BTC-3	1312.7	1.41	7.6	298	1.10 wt. % (5.47 mmol/g)	This study
MIL-100		1.0	73.3	298	0.15 wt. %	(Latroche, Surblé, Serre, Mellot-Draznieks, Llewellyn, Lee, Chang, Sung, et al., 2006b)
MIL-101 (Cr)		1.9	80.0	298	0.43 wt. %	(Latroche, Surblé, Serre, Mellot-Draznieks, Llewellyn, Lee, Chang, Sung, et al., 2006b)
$Co_2(BDC)_2$ dabco	1595	0.77	10	298	0.03 wt. %	(L. G. Zhu & Xiao, 2008)
HKUST-1	1154		65	298	0.35 wt. %	(Barbara Panella et al., 2006)
ZIF-8			60	298	0.13 wt. %	(W. Zhou et al., 2007)
ZIF-8	1297	1.225	10	298	0.390 mmol/g	(H. Zhou et al., 2015b)
ZIF-8/GO	1247	1.281	10	298	0.364 mmol/g	(H. Zhou et al., 2015b)
Pt@ZIF-8/GO	619	0.586	10	298	0.841 mmol/g	(H. Zhou et al., 2015b)
MOF-5	2296		65	298	0.28 wt. %	(Barbara Panella et al., 2006)
IRMOF-8			30	298	0.4 wt. %	(Dailly et al., 2006)
Co-IRMOF-74	1985	0.86	170	298	0.29 wt. %	(Montes-Andrés, Orcajo, Martos, Botas, & Calleja, 2019)
Ni_{50}Co-IRMOF-74	1913	0.78	170	298	0.39 wt. %	(Montes-Andrés et al., 2019)
MOF-184-Mg	3154		20	298	0.15 wt. %	(Oh et al., 2017)
MOF-184-Ni	2449		20	298	0.11 wt. %	(Oh et al., 2017)

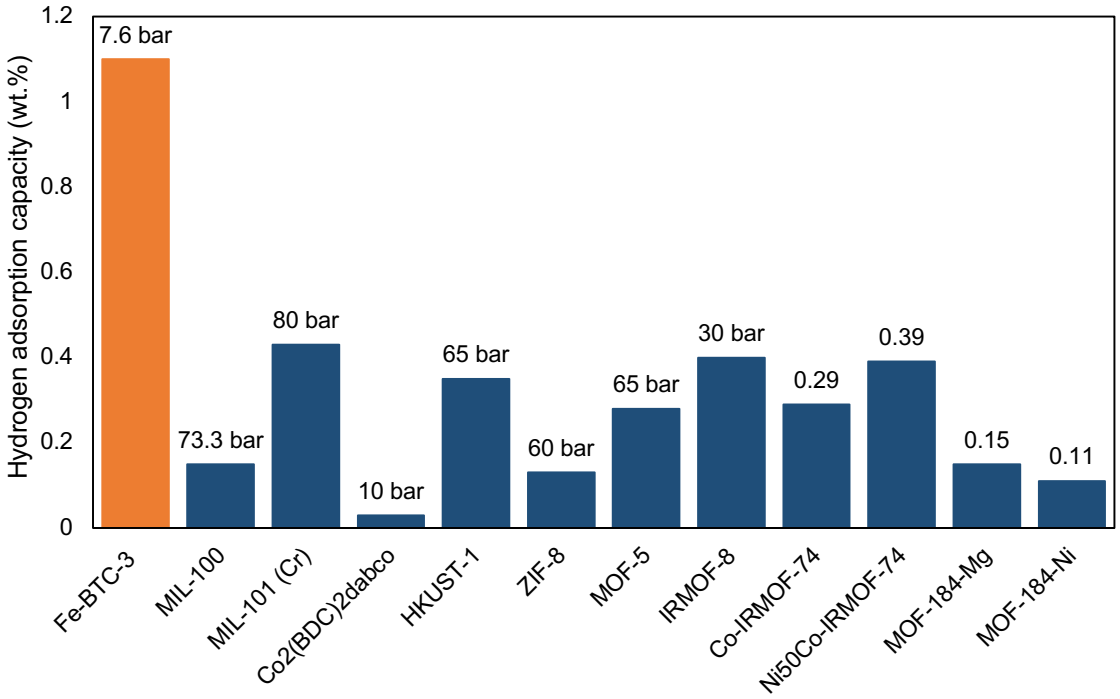

Figure 169. Comparison of H_2 adsorption capacities of Fe-BTC-3 and some of the MOFs reported in literature

By the perturbation assisted nanofusion synthesis strategy and control over textural porosity, a H_2 adsorption capacity (1.10 wt. % at 7.6 bar and 298 K) higher than those of reported MOFs has been achieved. Particularly, the measured H_2 adsorption capacity of MIL-100 at 73.3 bar and 298 K is 0.15 wt.% (Langmuir surface area: 2700 m^2/g) (Latroche, Surblé, Serre, Mellot-Draznieks, Llewellyn, Lee, Chang, Sung, et al., 2006b); the measured H_2 sorption capacity of MIL-101(Cr) at 80 bar and 298 K is 0.43 wt.% (Langmuir surface area: 5500 m^2/g) (Latroche, Surblé, Serre, Mellot-Draznieks, Llewellyn, Lee, Chang, Sung, et al., 2006b); the measured H_2 sorption capacity of $Co_2(BDC)_2dabco$ at 10 bar and 298 K is 0.03 wt.% (BET surface area: 1595 m^2/g, and pore volume. 0.77 cm^3/g) (L. G. Zhu & Xiao, 2008); the measured H_2 sorption capacity of HKUST-1 at 65 bar and 298 K is 0.35 wt. % (BET surface area: 1154 m^3/g) (Barbara Panella et al., 2006); the measured H_2 sorption capacity of ZIF-8 at 60 bar and 298 K is 0.13 wt. % (W. Zhou et al., 2007); the measured H_2 sorption capacity of MOF-5 at 65 bar and 298 K is 0.28 wt. % (BET surface area: 2296 m^3/g) (Barbara Panella et al., 2006); the measured H_2 sorption capacity of IRMOF-8 at 30 bar and 298 K is 0.4 wt. % (Langmuir surface area: 1818 m^2/g) (Dailly et al., 2006).

7.5. Concluding Remarks

The present study reports the H_2 adsorption capacity of hierarchically porous Fe-BTCs that has not been reported yet. A H_2 adsorption capacity (1.10 wt.% is achieved at 7.6 bar and 298 K) higher than those of reported MOFs (MIL-100 (Latroche, Surblé, Serre, Mellot-Draznieks, Llewellyn, Lee, Chang, Sung, et al., 2006b), MIL-101(Cr) (Latroche, Surblé, Serre, Mellot-Draznieks, Llewellyn, Lee, Chang, Sung, et al., 2006b), $Co_2(BDC)_2$dabco (L. G. Zhu & Xiao, 2008), HKUST-1 (Barbara Panella et al., 2006), ZIF-8 (W. Zhou et al., 2007), MOF-5 (Barbara Panella et al., 2006), and IRMOF-8 (Dailly et al., 2006)) has been achieved. By forming hierarchical pores, the highest BET surface area and the total pore volume for Fe-BTC has been reported (Dhakshinamoorthy, Alvaro, Chevreau, et al., 2012; Dhakshinamoorthy et al., 2011; Dhakshinamoorthy, Alvaro, & Garcia, 2012; X. Hu et al., 2016; Majano et al., 2013; Opanasenko et al., 2013; Torres et al., 2018; Zukal et al., 2015).

Herein, by the control of textural porosity via Fe:BTC ratio, an Fe-BTC that has ultramicropores in its pore structure has been synthesized and a BET surface area, and total pore volume that is higher than those of reported Fe-BTCs have been achieved (Dhakshinamoorthy, Alvaro, Chevreau, et al., 2012; Dhakshinamoorthy et al., 2011; Dhakshinamoorthy, Alvaro, & Garcia, 2012; X. Hu et al., 2016; Majano et al., 2013; Opanasenko et al., 2013; Torres et al., 2018; Zukal et al., 2015). Fe-BTC-3 possesses a H_2 adsorption capacity 2.6, and 2.8 times higher than Fe-BTC-1, and Fe-BTC-5, respectively. We have attributed this relatively high H_2 adsorption capacity to the ultramicropores present in its pore structure. Presence of ultramicropores maximizes the van der Waals potential. Thereby, the attraction felt from the surface of the ultramicropore walls increases which causes adsorbed H_2 amount to increase. In the case of Fe-BTC-1 and Fe-BTC-5, despite the relatively low BET surface area, and the relatively low narrow micropore volume of Fe-BTC-1, the H_2 adsorption capacity of Fe-BTC-1 is 1.1 times greater than Fe-BTC-5. The relatively high H_2 adsorption capacity of Fe-BTC-1 in comparison to Fe-BTC-5 is attributed to the narrow distribution of narrow micropores of Fe-BTC-1.

Our results indicate that H_2 adsorption capacity depends on: i) the presence of ultramicropores; and ii) the narrow distribution of narrow micropores (pore diameters smaller than 1 nm) through the micropore size distribution. Based on our results, we have

concluded that higher the ultramicropore volume and the narrower the narrow micropore distribution (pore diameters smaller than 1 nm) through the micropores, the higher will be the adsorbed H_2 amount.

By the control of textural porosity via Fe:BTC ratio, an Fe-BTC that has ultramicropores in its pore structure has been synthesized and a BET surface area, and total pore volume that is higher than those of reported Fe-BTCs have been achieved (Dhakshinamoorthy, Alvaro, Chevreau, et al., 2012; Dhakshinamoorthy et al., 2011; Dhakshinamoorthy, Alvaro, & Garcia, 2012; X. Hu et al., 2016; Majano et al., 2013; Opanasenko et al., 2013; Torres et al., 2018; Zukal et al., 2015). Presence of ultramicropores enhances the H_2 adsorption capacity by 2.6 and 2.8 times and a H_2 sorption capacity that is higher than those of reported MOFs has been reported.

Our results experimentally prove that presence of ultramicropores enhances the H_2 adsorption capacity. Nevertheless, studies should be focused on synthesizing ultramicroporous sorbents to achieve the H_2 storage target set by DOE.

Chapter VIII

Conclusion and future works

8.1. Conclusion

In this Ph.D. thesis, hierarchical porous MOFs and its advantages over the gas adsorption studies have been discussed. It is found that via a perturbation assisted nanofusion synthesis strategy, hierarchical porous MOFs with enhanced BET surface areas, increased pore volumes and improved gas adsorption capacities can be synthesized. In addition, the significance of ultramicropores, and narrow micropores on the gas adsorption capacities have been shown, experimentally.

Perturbation assisted nanofusion synthesis strategy offers a variety of opportunities. Perturbation assisted nanofusion synthesis strategy is a template free synthesis strategy that there is no need to remove the template and thus, the possibility of framework collapse is eliminated. Moreover, by the perturbation assisted nanofusion synthesis strategy a two-pore system is created at which micropores increase the surface area and mesopores enhance the mass transport properties. Additionally, by varying the synthesis temperature and metal to linker ratio, sizes of textural pores can be tuned, finely. For instance, at high synthesis temperatures (> 120 °C), MIL-88B nanorods pack loosely and wider mesopores form while at lower synthesis temperatures (< 120 °C), MIL-88B nanorods pack tightly and narrower pores form. Moreover, in the presence of excess metal salt (a high metal to linker ratio), iron oxide clusters form prior to SBU formation, interparticle voids in between the SBU aggregates widen and wider pores are formed.

Textural porosity provides flexibility to tune the pore size via synthesis temperature and metal to linker ratio. Moreover, by the perturbation assisted nanofusion synthesis strategy, BET surface area and the pore volume are enhanced significantly, and the highest of all the reported BET surface areas and the pore volumes for MIL-88B and Fe-BTC are achieved. Particularly, BET surface areas of MIL-88B and Fe-BTC are enhanced by 2.7 and 1.6 times, respectively while the total pore volumes of MIL-88B and Fe-BTC are enhanced by 4.1, and 3.1 times, respectively.

Besides the improvements achieved in textural properties, by constructing hierarchical pores, gas adsorption performances of hierarchical porous MIL-88B and Fe-BTC are improved, considerably. As reported by Bhatia and Myers, thermodynamically 15.1 kJ/mol of energy is needed to adsorb considerable amount of gas at 298 K (Bhatia & Myers, 2006b). However, the isosteric heat of adsorption values of MOFs range in between 4 to 7 kJ/mol. Reported strategies to date, show promising results with enhancements in gas adsorption capacities. However, achieved gas adsorption capacities are not sufficient enough to meet the DOE target of onboard hydrogen storage. Despite the given efforts, there is still room for improvement for gas adsorption studies conducted at ambient temperature. To increase the isosteric heat of adsorption value of MOFs at ambient temperatures, we synthesized hierarchically porous MOFs and introduced ultramicropores to the pore structure. Forming textural pores and introducing ultramicropores to the pore structure enhanced the gas adsorption capacities of the two MOFs reported in this study. Particularly, CO_2 adsorption capacities of MIL-88B and Fe-BTC are enhanced by 2.1 and 1.6 times, respectively while H_2 adsorption capacities of MIL-88B and Fe-BTC are enhanced by 1.96 and 2.6 times, respectively. The enhanced gas (CO_2 and H_2) adsorption capacities are attributed to: i) the presence of ultramicropores (pore diameters smaller than 0.7 nm), ii) the volume of ultramicropores, iii) the volume of narrow micropores (pore diameters smaller than 1 nm), and iv) the narrow distribution of ultramicropores through the micropore size distribution (high fraction of ultramicopores).

The significance of ultramicropores lies behind their increased binding energies. Revealed by theoretical studies, as pore diameters decrease below 1 nm, van der Waals interactions between the pores and the gas molecules strengthen and higher adsorption capacities can be achieved. Theoretically, the highest gas adsorption capacity can be achieved by pores with pore diameters of 6 to 8 Å which can be explained by Lenard-Jones potential. As the gas molecules and the adsorbent are separated by a long distance, attractive forces dominate while the repulsion forces dominate when the gas molecules and the adsorbent are separated by a short distance. Particularly, theoretical studies show that when hydrogen molecules are adsorbed on wider pores, a hydrogen layer would be formed on the wells located close to the pore walls and a less dense layer of hydrogen would be adsorbed on the center of the pore that minimizes the attraction felt by the pore walls, and thereby H_2 adsorption capacity decreases. In line with what has been reported in theoretical studies, our

results experimentally prove that presence of ultramicropores enhances the gas adsorption capacities, considerably.

We designed and synthesized hierarchical porous MOFs with enhanced BET surface area and pore volume and improved gas adsorption performances. Forming ultramicropores and hierarchical pores has a key role in enhancing the gas adsorption capacities. By experimentally proving the necessity of ultramicropores in gas adsorption studies, we report an effortless, feasible synthesis strategy that can enhance the gas adsorption capacities, considerably and pave the way for the design and use of hierarchical porous MOFs.

8.2. Future work

Hierarchical porous MOFs show promising results in CO_2 and H_2 adsorption studies. However, the following has to be considered for the commercial use of these materials:

It is known that CO_2 adsorption capacities of MOFs decrease in the presence of water molecules as the water molecules compete with CO_2 molecules for the available adsorption sites. Therefore, CO_2 adsorption capacities should be retested in the presence of water.

Moreover, flue gas possesses different kinds of molecules which would compete with CO_2 molecules for the available adsorption sites. CO_2 adsorption capacity of hierarchical porous MOFs should be investigated under flue gas environment.

For the commercial use of hierarchical porous MOFs, mechanical strength of these materials should be tested. MOFs are shaped into pellets prior to their use in commercial applications. Adsorption capacity of hierarchical porous MOF pellets should be retested.

The CO_2/N_2 selectivity of hierarchical porous MOFs were not tested since the scope of this study was limited with the development of hierarchical porous MOFs for enhanced CO_2 and H_2 adsorption capacities (at 298 K). However, isosteric heat of adsorption values of CO_2 and N_2 may provide insight about the performance of selective CO_2/N_2 separation. For further studies, isosteric heat of adsorption values of CO_2 and N_2 should be investigated.

The measured H_2 adsorption capacities of the two hierarchical porous MOFs reported in this study cannot meet the DOE target for onboard hydrogen storage. However, forming ultramicropores enhances the measured H_2 adsorption capacities, considerably. This strategy of forming textural pores should be tested on other MOFs and their H_2 adsorption capacities should be investigated.

BIBLIOGRAPHY

Abanades, J Carlos, & Alvarez, D. (2003). Conversion Limits in the Reaction of CO2 with Lime. *Energy & Fuels*, *17*(2), 308–315. https://doi.org/10.1021/ef020152a

Abanades, J Carlos, Anthony, E. J., Lu, D. Y., Salvador, C., & Alvarez, D. (2004). Capture of CO2 from combustion gases in a fluidized bed of CaO. *AIChE Journal*, *50*(7), 1614–1622. https://doi.org/10.1002/aic.10132

Abanades, Juan Carlos. (2002). The maximum capture efficiency of CO2 using a carbonation/calcination cycle of CaO/CaCO3. *Chemical Engineering Journal*, *90*(3), 303–306. https://doi.org/https://doi.org/10.1016/S1385-8947(02)00126-2

Abdalla, A. M., Hossain, S., Nisfindy, O. B., Azad, A. T., Dawood, M., & Azad, A. K. (2018). Hydrogen production, storage, transportation and key challenges with applications: A review. *Energy Conversion and Management*, *165*(April), 602–627. https://doi.org/10.1016/j.enconman.2018.03.088

Abe, J. O., Popoola, A. P. I., Ajenifuja, E., & Popoola, O. M. (2019). Hydrogen energy, economy and storage: Review and recommendation. *International Journal of Hydrogen Energy*, *44*(29), 15072–15086. https://doi.org/10.1016/j.ijhydene.2019.04.068

Aboudheir, A., Tontiwachwuthikul, P., & Idem, R. (2006). Rigorous model for predicting the behavior of CO2 absorption into AMP in packed-bed absorption columns. In *Industrial and Engineering Chemistry Research*. https://doi.org/10.1021/ie050570d

Adams, R., Carson, C., Ward, J., Tannenbaum, R., & Koros, W. (2010). Metal organic framework mixed matrix membranes for gas separations. *Microporous and Mesoporous Materials*, *131*(1–3), 13–20. https://doi.org/10.1016/j.micromeso.2009.11.035

Adger, N., & Coauthors including Fischlin, A. (2007). Summary for policymakers. *Climate Change 2007: Impacts, Adaptation and Vulnerability. Contribution of Working Group II to the Fourth Assessment Report of the Intergovernmental Panel of Climate Change (IPCC)*, (vii, 973), 7–22. https://doi.org/http://www.ipcc.ch/publications_and_data/ar4/wg2/en/spm.html

Aguey-Zinsou, K.-F., & Ares-Fernández, J.-R. (2010). Hydrogen in magnesium: new perspectives toward functional stores. *Energy & Environmental Science*, *3*(5), 526–543. https://doi.org/10.1039/B921645F

Ahn, C. C., Ye, Y., Ratnakumar, B. V, Witham, C., Bowman, R. C., & Fultz, B. (1998). Hydrogen desorption and adsorption measurements on graphite nanofibers. *Applied Physics Letters*, *73*(23), 3378–3380. https://doi.org/10.1063/1.122755

Ahn, J.-H., Jang, J.-E., Oh, C.-G., Ihm, S.-K., Cortez, J., & Sherrington, D. C. (2006). Rapid Generation and Control of Microporosity, Bimodal Pore Size Distribution, and Surface Area in Davankov-Type Hyper-Cross-Linked Resins. *Macromolecules*, *39*(2), 627–632. https://doi.org/10.1021/ma051152n

Al-Kutubi, H., Gascon, J., Sudhölter, E. J. R., & Rassaei, L. (2015). Electrosynthesis of Metal–Organic Frameworks: Challenges and Opportunities. *ChemElectroChem*, *2*(4), 462–474. https://doi.org/10.1002/celc.201402429

Al-saffar, H. B., Ozturk, B., & Hughes, R. (1997). A Comparison of Porous and Non-Porous Gas-Liquid

Membrane Contactors for Gas Separation. *Chemical Engineering Research and Design*, *75*(7), 685–692. https://doi.org/https://doi.org/10.1205/026387697524182

Alhwaige, A. A., Agag, T., Ishida, H., & Qutubuddin, S. (2013). Biobased chitosan hybrid aerogels with superior adsorption: Role of graphene oxide in CO2 capture. *RSC Advances*, *3*(36), 16011–16020. https://doi.org/10.1039/C3RA42022A

Ameloot, R., Pandey, L., Auweraer, M. Van der, Alaerts, L., Sels, B. F., & De Vos, D. E. (2010). Patterned film growth of metal–organic frameworks based on galvanic displacement. *Chemical Communications*, *46*(21), 3735–3737. https://doi.org/10.1039/C001544J

Ameloot, R., Stappers, L., Fransaer, J., Alaerts, L., Sels, B. F., & De Vos, D. E. (2009). Patterned Growth of Metal-Organic Framework Coatings by Electrochemical Synthesis. *Chemistry of Materials*, *21*(13), 2580–2582. https://doi.org/10.1021/cm900069f

Anbia, M., & Hoseini, V. (2012). Development of MWCNT@MIL-101 hybrid composite with enhanced adsorption capacity for carbon dioxide. *Chemical Engineering Journal*, *191*, 326–330. https://doi.org/https://doi.org/10.1016/j.cej.2012.03.025

Andersson, J., & Grönkvist, S. (2019). Large-scale storage of hydrogen. *International Journal of Hydrogen Energy*, *44*(23), 11901–11919. https://doi.org/10.1016/j.ijhydene.2019.03.063

Ansón, A., Callejas, M. A., Benito, A. M., Maser, W. K., Izquierdo, M. T., Rubio, B., … Martínez, M. T. (2004). Hydrogen adsorption studies on single wall carbon nanotubes. *Carbon*, *42*(7), 1243–1248. https://doi.org/https://doi.org/10.1016/j.carbon.2004.01.038

Araki, S., Kiyohara, Y., Tanaka, S., & Miyake, Y. (2012). Adsorption of carbon dioxide and nitrogen on zeolite rho prepared by hydrothermal synthesis using 18-crown-6 ether. *Journal of Colloid and Interface Science*, *388*(1), 185–190. https://doi.org/https://doi.org/10.1016/j.jcis.2012.06.061

Arenas, J. F., & Marcos, J. I. (1979). Infrared and Raman spectra of phtalate, isophtalate and terephtalate ions. *Spectrochimica Acta Part A: Molecular Spectroscopy*, *35*(4), 355–363. https://doi.org/10.1016/0584-8539(79)80191-9

Arenillas, A., Smith, K. M., Drage, T. C., & Snape, C. E. (2005). CO2 capture using some fly ash-derived carbon materials. *Fuel*, *84*(17), 2204–2210. https://doi.org/https://doi.org/10.1016/j.fuel.2005.04.003

Arévalo-Hidalgo, A. G., Almodóvar-Arbelo, N. E., & Hernández-Maldonado, A. J. (2011). Sr2+–SAPO-34 Prepared via Coupled Partial Detemplation and Solid State Ion Exchange: Effect on Textural Properties and Carbon Dioxide Adsorption. *Industrial & Engineering Chemistry Research*, *50*(17), 10259–10269. https://doi.org/10.1021/ie201083t

Aroonwilas, A., & Veawab, A. (2004). Characterization and Comparison of the CO2 Absorption Performance into Single and Blended Alkanolamines in a Packed Column. *Industrial and Engineering Chemistry Research*. https://doi.org/10.1021/ie0306067

Atchariyawut, S., Feng, C., Wang, R., Jiraratananon, R., & Liang, D. T. (2006). Effect of membrane structure on mass-transfer in the membrane gas–liquid contacting process using microporous PVDF hollow fibers. *Journal of Membrane Science*, *285*(1), 272–281. https://doi.org/https://doi.org/10.1016/j.memsci.2006.08.029

Attia, N. F., Menemparabath, M. M., Arepalli, S., & Geckeler, K. E. (2013). Inorganic nanotube composites based on polyaniline: Potential room-temperature hydrogen storage materials. *International Journal of Hydrogen Energy*, *38*(22), 9251–9262. https://doi.org/10.1016/j.ijhydene.2013.05.049

Aviation – Tracking Transport 2019 – Analysis - IEA. (n.d.). Retrieved July 1, 2020, from https://www.iea.org/reports/tracking-transport-2019/aviation#abstract

Azzouz, A., Nousir, S., Platon, N., Ghomari, K., Shiao, T. C., Hersant, G., … Roy, R. (2013). Truly reversible capture of CO2 by montmorillonite intercalated with soya oil-derived polyglycerols. *International Journal of Greenhouse Gas Control*, *17*, 140–147. https://doi.org/https://doi.org/10.1016/j.ijggc.2013.04.013

Bachu, S. (2000). <Bachu 2000.pdf>, *41*, 953–970.

Bae, T.-H., Hudson, M. R., Mason, J. A., Queen, W. L., Dutton, J. J., Sumida, K., … Long, J. R. (2013). Evaluation of cation-exchanged zeolite adsorbents for post-combustion carbon dioxide capture. *Energy & Environmental Science*, *6*(1), 128–138. https://doi.org/10.1039/C2EE23337A

Bae, Y. S., & Snurr, R. Q. (2011). Development and evaluation of porous materials for carbon dioxide separation and capture. *Angewandte Chemie - International Edition*, *50*(49), 11586–11596. https://doi.org/10.1002/anie.201101891

Bai, B.-C., Kim, J.-G., Im, J.-S., Jung, S.-C., & Lee, Y.-S. (2011). Influence of oxyfluorination on activated carbon nanofibers for CO 2 storage. *Carbon Letters*, *12*(4), 236–242. https://doi.org/10.5714/cl.2011.12.4.236

Bai, S., Liu, J., Gao, J., Yang, Q., & Li, C. (2012). Hydrolysis controlled synthesis of amine-functionalized hollow ethane–silica nanospheres as adsorbents for CO2 capture. *Microporous and Mesoporous Materials*, *151*, 474–480. https://doi.org/https://doi.org/10.1016/j.micromeso.2011.09.014

Balderas-Xicohténcatl, R., Schlichtenmayer, M., & Hirscher, M. (2018). Volumetric Hydrogen Storage Capacity in Metal–Organic Frameworks. *Energy Technology*, *6*(3), 578–582. https://doi.org/10.1002/ente.201700636

Bara, J. E., Carlisle, T. K., Gabriel, C. J., Camper, D., Finotello, A., Gin, D. L., & Noble, R. D. (2009). Guide to CO2 Separations in Imidazolium-Based Room-Temperature Ionic Liquids. *Industrial & Engineering Chemistry Research*, *48*(6), 2739–2751. https://doi.org/10.1021/ie8016237

Bara, J. E., Gabriel, C. J., Hatakeyama, E. S., Carlisle, T. K., Lessmann, S., Noble, R. D., & Gin, D. L. (2008). Improving CO2 selectivity in polymerized room-temperature ionic liquid gas separation membranes through incorporation of polar substituents. *Journal of Membrane Science*, *321*(1), 3–7. https://doi.org/https://doi.org/10.1016/j.memsci.2007.12.033

Barbe, A. M., Hogan, P. A., & Johnson, R. A. (2000). Surface morphology changes during initial usage of hydrophobic, microporous polypropylene membranes. *Journal of Membrane Science*, *172*(1), 149–156. https://doi.org/https://doi.org/10.1016/S0376-7388(00)00338-0

Barker, R. (1973). The reversibility of the reaction CaCO3 ⇄ CaO+CO2. *Journal of Applied Chemistry and Biotechnology*, *23*(10), 733–742. https://doi.org/10.1002/jctb.5020231005

basolite | Sigma-Aldrich. (n.d.). Retrieved August 27, 2019, from https://www.sigmaaldrich.com/catalog/search?term=basolite&interface=All&N=0&mode=partialmax&lang=en&region=TR&focus=product

Bataille, T., Bracco, S., Comotti, A., Costantino, F., Guerri, A., Ienco, A., & Marmottini, F. (2012). Solvent dependent synthesis of micro- and nano- crystalline phosphinate based 1D tubular MOF: structure and CO2 adsorption selectivity. *CrystEngComm*, *14*(21), 7170–7173. https://doi.org/10.1039/C2CE26138C

Batten, S. R., & Robson, R. (1998). Interpenetrating Nets: Ordered, Periodic Entanglement. *Angewandte Chemie International Edition*, *37*(11), 1460–1494. https://doi.org/10.1002/(SICI)1521-3773(19980619)37:11<1460::AID-ANIE1460>3.0.CO;2-Z

Baughman, R. H., Zakhidov, A. A., & de Heer, W. A. (2002). Carbon Nanotubes--the Route Toward Applications. *Science*, *297*(5582), 787 LP – 792. https://doi.org/10.1126/science.1060928

Bazin, P., Morris, R. E., Lavalley, J.-C., McKinlay, A. C., Serre, C., Xiao, B., … Wheatley, P. S. (2013). Nitric Oxide Adsorption and Delivery in Flexible MIL-88(Fe) Metal–Organic Frameworks. *Chemistry of Materials*, *25*(9), 1592–1599. https://doi.org/10.1021/cm304037x

Becher, M., Haluska, M., Hirscher, M., Quintel, A., Skakalova, V., Dettlaff-Weglikovska, U., … Bernier, P. (2003). Hydrogen storage in carbon nanotubes. *Comptes Rendus Physique*, *4*(9), 1055–1062. https://doi.org/10.1016/S1631-0705(03)00107-5

Beckner, M., & Dailly, A. (2016). Hydrogen and methane storage in adsorbent materials for automotive applications. *International Journal of Energy Research*, *40*, 91–99. https://doi.org/10.1002/er.3324

Beldon, P. J., Fábián, L., Stein, R. S., Thirumurugan, A., Cheetham, A. K., & Friščić, T. (2010). Rapid Room-Temperature Synthesis of Zeolitic Imidazolate Frameworks by Using Mechanochemistry. *Angewandte Chemie International Edition*, *49*(50), 9640–9643. https://doi.org/10.1002/anie.201005547

Bellosta von Colbe, J., Ares, J.-R., Barale, J., Baricco, M., Buckley, C., Capurso, G., … Dornheim, M. (2019). Application of hydrides in hydrogen storage and compression: Achievements, outlook and perspectives. *International Journal of Hydrogen Energy*, *44*(15), 7780–7808. https://doi.org/https://doi.org/10.1016/j.ijhydene.2019.01.104

Belof, J. L., Stern, A. C., Eddaoudi, M., & Space, B. (2007). On the Mechanism of Hydrogen Storage in a Metal−Organic Framework Material. *Journal of the American Chemical Society*, *129*(49), 15202–15210. https://doi.org/10.1021/ja0737164

Ben, T., Li, Y., Zhu, L., Zhang, D., Cao, D., Xiang, Z., … Qiu, S. (2012). Selective adsorption of carbon dioxide by carbonized porous aromatic framework (PAF). *Energy & Environmental Science*, *5*(8), 8370–8376. https://doi.org/10.1039/C2EE21935B

Ben, T., Pei, C., Zhang, D., Xu, J., Deng, F., Jing, X., & Qiu, S. (2011). Gas storage in porous aromatic frameworks (PAFs). *Energy & Environmental Science*, *4*(10), 3991–3999. https://doi.org/10.1039/C1EE01222C

Bénard, P., & Chahine, R. (2007). Storage of hydrogen by physisorption on carbon and nanostructured materials. *Scripta Materialia*, *56*(10), 803–808. https://doi.org/https://doi.org/10.1016/j.scriptamat.2007.01.008

Benbellat, N., Gavrilenko, K. S., Le Gal, Y., Cador, O., Golhen, S., Gouasmia, A., … Ouahab, L. (2006). Co(II)-Co(II) paddlewheel complex with a redox-active ligand derived from TTF. *Inorganic Chemistry*, *45*(26), 10440–10442. https://doi.org/10.1021/ic061680v

Bevan, A. I., Züttel, A., Book, D., & Harris, I. R. (2011). Performance of a metal hydride store on the “Ross Barlow” hydrogen powered canal boat. *Faraday Discussions*, *151*(0), 353–367. https://doi.org/10.1039/C0FD00025F

Beyer, M. K., & Clausen-Schaumann, H. (2005). Mechanochemistry: The Mechanical Activation of Covalent Bonds. *Chemical Reviews*, *105*(8), 2921–2948. https://doi.org/10.1021/cr030697h

Bezerra, D. P., Oliveira, R. S., Vieira, R. S., Cavalcante, C. L., & Azevedo, D. C. S. (2011). Adsorption of

CO2 on nitrogen-enriched activated carbon and zeolite 13X. *Adsorption*, *17*(1), 235–246. https://doi.org/10.1007/s10450-011-9320-z

Bhagiyalakshmi, M., Hemalatha, P., Ganesh, M., Mei, P. M., & Jang, H. T. (2011). A direct synthesis of mesoporous carbon supported MgO sorbent for CO2 capture. *Fuel*, *90*(4), 1662–1667. https://doi.org/https://doi.org/10.1016/j.fuel.2010.10.050

Bhagiyalakshmi, M., Lee, J. Y., & Jang, H. T. (2010). Synthesis of mesoporous magnesium oxide: Its application to CO2 chemisorption. *International Journal of Greenhouse Gas Control*, *4*(1), 51–56. https://doi.org/https://doi.org/10.1016/j.ijggc.2009.08.001

Bhatia, S. K., & Myers, A. L. (2006a). Optimum conditions for adsorptive storage. *Langmuir*. https://doi.org/10.1021/la0523816

Bhatia, S. K., & Myers, A. L. (2006b). Optimum Conditions for Adsorptive Storage. *Langmuir*, *22*(4), 1688–1700. https://doi.org/10.1021/la0523816

Bian, S.-W., Baltrusaitis, J., Galhotra, P., & Grassian, V. H. (2010). A template-free, thermal decomposition method to synthesize mesoporous MgO with a nanocrystalline framework and its application in carbon dioxide adsorption. *Journal of Materials Chemistry*, *20*(39), 8705–8710. https://doi.org/10.1039/C0JM01261K

Biswas, S., Grzywa, M., Nayek, H. P., Dehnen, S., Senkovska, I., Kaskel, S., & Volkmer, D. (2009). A cubic coordination framework constructed from benzobistriazolate ligands and zinc ions having selective gas sorption properties. *Dalton Transactions*, (33), 6487–6495. https://doi.org/10.1039/B904280F

Blanchard, L. A., Hancu, D., Beckman, E. J., & Brennecke, J. F. (1999). Green processing using ionic liquids and CO2. *Nature*, *399*(6731), 28–29. https://doi.org/10.1038/19887

Blankenship, T. S., Balahmar, N., & Mokaya, R. (2017). Oxygen-rich microporous carbons with exceptional hydrogen storage capacity. *Nature Communications*, *8*(1). https://doi.org/10.1038/s41467-017-01633-x

Blasig, A., Tang, J., Hu, X., Tan, S. P., Shen, Y., & Radosz, M. (2007). Carbon Dioxide Solubility in Polymerized Ionic Liquids Containing Ammonium and Imidazolium Cations from Magnetic Suspension Balance: P[VBTMA][BF4] and P[VBMI][BF4]. *Industrial & Engineering Chemistry Research*, *46*(17), 5542–5547. https://doi.org/10.1021/ie0616545

Bonelli, B., Onida, B., Fubini, B., Areán, C. O., & Garrone, E. (2000). Vibrational and Thermodynamic Study of the Adsorption of Carbon Dioxide on the Zeolite Na−ZSM-5. *Langmuir*, *16*(11), 4976–4983. https://doi.org/10.1021/la991363j

Boributh, S., Assabumrungrat, S., Laosiripojana, N., & Jiraratananon, R. (2011). A modeling study on the effects of membrane characteristics and operating parameters on physical absorption of CO2 by hollow fiber membrane contactor. *Journal of Membrane Science*, *380*(1), 21–33. https://doi.org/https://doi.org/10.1016/j.memsci.2011.06.029

Boributh, S., Rongwong, W., Assabumrungrat, S., Laosiripojana, N., & Jiraratananon, R. (2012). Mathematical modeling and cascade design of hollow fiber membrane contactor for CO2 absorption by monoethanolamine. *Journal of Membrane Science*, *401–402*, 175–189. https://doi.org/https://doi.org/10.1016/j.memsci.2012.01.048

Bougie, F., & Iliuta, M. C. (2010a). Analysis of regeneration of sterically hindered alkanolamines aqueous solutions with and without activator. *Chemical Engineering Science*, *65*(16), 4746–4750. https://doi.org/https://doi.org/10.1016/j.ces.2010.05.021

Bougie, F., & Iliuta, M. C. (2010b). CO2 Absorption into Mixed Aqueous Solutions of 2-Amino-2-hydroxymethyl-1,3-propanediol and Piperazine. *Industrial & Engineering Chemistry Research*, *49*(3), 1150–1159. https://doi.org/10.1021/ie900705y

Bougie, F., & Iliuta, M. C. (2011). CO2 Absorption in Aqueous Piperazine Solutions: Experimental Study and Modeling. *Journal of Chemical & Engineering Data*, *56*(4), 1547–1554. https://doi.org/10.1021/je1012247

Bougie, F., Lauzon-Gauthier, J., & Iliuta, M. C. (2009). Acceleration of the reaction of carbon dioxide into aqueous 2-amino-2-hydroxymethyl-1,3-propanediol solutions by piperazine addition. *Chemical Engineering Science*, *64*(9), 2011–2019. https://doi.org/https://doi.org/10.1016/j.ces.2009.01.030

Bradshaw, D., El-Hankari, S., & Lupica-Spagnolo, L. (2014). Supramolecular templating of hierarchically porous metal-organic frameworks. *Chemical Society Reviews*, *43*(16), 5431–5443. https://doi.org/10.1039/c4cs00127c

Brandani, F., & Ruthven, D. M. (2004). The Effect of Water on the Adsorption of CO2 and C3H8 on Type X Zeolites. *Industrial & Engineering Chemistry Research*, *43*(26), 8339–8344. https://doi.org/10.1021/ie040183o

Britt, D., Furukawa, H., Wang, B., Glover, T. G., & Yaghi, O. M. (2009). Highly efficient separation of carbon dioxide by a metal-organic framework replete with open metal sites. *Proceedings of the National Academy of Sciences*, *106*(49), 20637 LP – 20640. https://doi.org/10.1073/pnas.0909718106

Broom, D. P., Webb, C. J., Fanourgakis, G. S., Froudakis, G. E., Trikalitis, P. N., & Hirscher, M. (2019). Concepts for improving hydrogen storage in nanoporous materials. *International Journal of Hydrogen Energy*, *44*(15), 7768–7779. https://doi.org/10.1016/j.ijhydene.2019.01.224

Broom, D. P., Webb, C. J., Hurst, K. E., Parilla, P. A., Gennett, T., Brown, C. M., … Hirscher, M. (2016). Outlook and challenges for hydrogen storage in nanoporous materials. *Applied Physics A: Materials Science and Processing*, *122*(3), 1–21. https://doi.org/10.1007/s00339-016-9651-4

Bux, H., Liang, F., Li, Y., Cravillon, J., Wiebcke, M., & Caro, J. (2009). Zeolitic Imidazolate Framework Membrane with Molecular Sieving Properties by Microwave-Assisted Solvothermal Synthesis. *Journal of the American Chemical Society*, *131*(44), 16000–16001. https://doi.org/10.1021/ja907359t

Cai, G., & Jiang, H.-L. (2017a). A Modulator-Induced Defect-Formation Strategy to Hierarchically Porous Metal–Organic Frameworks with High Stability. *Angewandte Chemie International Edition*, *56*(2), 563–567. https://doi.org/10.1002/anie.201610914

Cai, G., & Jiang, H. L. (2017b). A Modulator-Induced Defect-Formation Strategy to Hierarchically Porous Metal–Organic Frameworks with High Stability. *Angewandte Chemie - International Edition*, *56*(2), 563–567. https://doi.org/10.1002/anie.201610914

Cai, X., Lin, J., & Pang, M. (2016). Facile Synthesis of Highly Uniform Fe-MIL-88B Particles. *Crystal Growth and Design*, *16*(7), 3565–3568. https://doi.org/10.1021/acs.cgd.6b00313

Campesi, R., Cuevas, F., Latroche, M., & Hirscher, M. (2010). Hydrogen spillover measurements of unbridged and bridged metal–organic frameworks—revisited. *Physical Chemistry Chemical Physics*, *12*(35), 10457–10459. https://doi.org/10.1039/C0CP00037J

Cao, Y., Ma, Y., Wang, T., Wang, X., Huo, Q., & Liu, Y. (2016). Facile Fabricating Hierarchically Porous Metal-Organic Frameworks via a Template-Free Strategy. *Crystal Growth and Design*, *16*(1), 504–510. https://doi.org/10.1021/acs.cgd.5b01559

Carné-Sánchez, A., Imaz, I., Stylianou, K. C., & Maspoch, D. (2014). Metal-organic frameworks: From molecules/metal ions to crystals to superstructures. *Chemistry - A European Journal*, *20*(18), 5192–5201. https://doi.org/10.1002/chem.201304529

Carpetis, C. (1982). Estimation of storage costs for large hydrogen storage facilities. *International Journal of Hydrogen Energy*. https://doi.org/10.1016/0360-3199(82)90146-X

Carraro, P., Elías, V., Blanco, A. A. G., Sapag, K., Eimer, G., & Oliva, M. (2014). Study of hydrogen adsorption properties on MCM-41 mesoporous materials modified with nickel. *International Journal of Hydrogen Energy*, *39*(16), 8749–8753. https://doi.org/https://doi.org/10.1016/j.ijhydene.2013.12.038

Caskey, S. R., Wong-Foy, A. G., & Matzger, A. J. (2008). Dramatic Tuning of Carbon Dioxide Uptake via Metal Substitution in a Coordination Polymer with Cylindrical Pores. *Journal of the American Chemical Society*, *130*(33), 10870–10871. https://doi.org/10.1021/ja8036096

Centrone, A., Harada, T., Speakman, S., & Hatton, T. A. (2010). Facile Synthesis of Vanadium Metal–Organic Frameworks and their Magnetic Properties. *Small*, *6*(15), 1598–1602. https://doi.org/10.1002/smll.201000773

Centrone, A., Yang, Y., Speakman, S., Bromberg, L., Rutledge, G. C., & Hatton, T. A. (2010). Growth of Metal−Organic Frameworks on Polymer Surfaces. *Journal of the American Chemical Society*, *132*(44), 15687–15691. https://doi.org/10.1021/ja106381x

Chabanon, E., Roizard, D., & Favre, E. (2011). Membrane Contactors for Postcombustion Carbon Dioxide Capture: A Comparative Study of Wetting Resistance on Long Time Scales. *Industrial & Engineering Chemistry Research*, *50*(13), 8237–8244. https://doi.org/10.1021/ie200704h

Chahine, R., & Bose, T. K. (1994). Low-pressure adsorption storage of hydrogen. *International Journal of Hydrogen Energy*, *19*(2), 161–164. https://doi.org/https://doi.org/10.1016/0360-3199(94)90121-X

Chalati, T., Horcajada, P., Gref, R., Couvreur, P., & Serre, C. (2011). Optimisation of the synthesis of MOF nanoparticles made of flexible porous iron fumarate MIL-88A. *Journal of Materials Chemistry*, *21*(7), 2220–2227. https://doi.org/10.1039/C0JM03563G

Chambers, A., Park, C., Baker, R. T. K., & Rodriguez, N. M. (1998). Hydrogen Storage in Graphite Nanofibers. *The Journal of Physical Chemistry B*, *102*(22), 4253–4256. https://doi.org/10.1021/jp980114l

Chen, B., Eddaoudi, M., Hyde, S. T., O'Keeffe, M., & Yaghi, O. M. (2001). Interwoven Metal-Organic Framework on a Periodic Minimal Surface with Extra-Large Pores. *Science*, *291*(5506), 1021 LP – 1023. https://doi.org/10.1126/science.1056598

Chen, B., Eddaoudi, M., Reineke, T. M., Kampf, J. W., O'Keeffe, M., & Yaghi, O. M. (2000). Cu2(ATC)·6H2O: Design of Open Metal Sites in Porous Metal−Organic Crystals (ATC: 1,3,5,7-Adamantane Tetracarboxylate). *Journal of the American Chemical Society*, *122*(46), 11559–11560. https://doi.org/10.1021/ja003159k

Chen, C., Park, D.-W., & Ahn, W.-S. (2013). Surface modification of a low cost bentonite for post-combustion CO2 capture. *Applied Surface Science*, *283*, 699–704. https://doi.org/https://doi.org/10.1016/j.apsusc.2013.07.005

Chen, P., Wu, X., Lin, J., & Tan, K. L. (1999). High H2 uptake by alkali-doped carbon nanotubes under ambient pressure and moderate temperatures. *Science*, *285*(5424), 91–93. https://doi.org/10.1126/science.285.5424.91

Chen, S.-C., Lin, S.-H., Chien, R.-D., & Hsu, P.-S. (2010). Effects of shape, porosity, and operating parameters on carbon dioxide recovery in polytetrafluoroethylene membranes. *Journal of Hazardous Materials*, *179*(1), 692–700. https://doi.org/https://doi.org/10.1016/j.jhazmat.2010.03.057

Chen, S.-C., Lin, S.-H., Chien, R.-D., Wang, Y.-H., & Hsiao, H.-C. (2011). Chemical absorption of carbon dioxide with asymmetrically heated polytetrafluoroethylene membranes. *Journal of Environmental Management*, *92*(4), 1083–1090. https://doi.org/https://doi.org/10.1016/j.jenvman.2010.08.014

Chen, X., Qiao, S., Du, Z., Zhou, Y., & Yang, R. (2013). Synthesis and Characterization of Functional Thienyl-Phosphine Microporous Polymers for Carbon Dioxide Capture. *Macromolecular Rapid Communications*, *34*(14), 1181–1185. https://doi.org/10.1002/marc.201300328

Chen, Y., Hu, Z., Gupta, K. M., & Jiang, J. (2011). Ionic Liquid/Metal–Organic Framework Composite for CO2 Capture: A Computational Investigation. *The Journal of Physical Chemistry C*, *115*(44), 21736–21742. https://doi.org/10.1021/jp208361p

Cheng, H.-M., Yang, Q.-H., & Liu, C. (2001). Hydrogen storage in carbon nanotubes. *Carbon*, *39*(10), 1447–1454. https://doi.org/https://doi.org/10.1016/S0008-6223(00)00306-7

Cheng, H., Chen, L., Cooper, A. C., Sha, X., & Pez, G. P. (2008). Hydrogen spillover in the context of hydrogen storage using solid-state materials. *Energy & Environmental Science*, *1*(3), 338–354. https://doi.org/10.1039/B807618A

Choi, H.-S., & Suh, M. P. (2009). Highly Selective CO2 Capture in Flexible 3D Coordination Polymer Networks. *Angewandte Chemie International Edition*, *48*(37), 6865–6869. https://doi.org/10.1002/anie.200902836

Choi, J.-S., Son, W.-J., Kim, J., & Ahn, W.-S. (2008). Metal–organic framework MOF-5 prepared by microwave heating: Factors to be considered. *Microporous and Mesoporous Materials*, *116*(1), 727–731. https://doi.org/https://doi.org/10.1016/j.micromeso.2008.04.033

Choi, J. H., Kim, Y. E., Nam, S. C., Yun, S. H., Yoon, Y. Il, & Lee, J. H. (2016). CO2 absorption characteristics of a piperazine derivative with primary, secondary, and tertiary amino groups. *Korean Journal of Chemical Engineering*. https://doi.org/10.1007/s11814-016-0180-9

Choi, J. S., Son, W. J., Kim, J., & Ahn, W. S. (2008). Metal-organic framework MOF-5 prepared by microwave heating: Factors to be considered. *Microporous and Mesoporous Materials*, *116*(1–3), 727–731. https://doi.org/10.1016/j.micromeso.2008.04.033

Choi, S., Drese, J. H., & Jones, C. W. (2009a). Adsorbent materials for carbon dioxide capture from large anthropogenic point sources. *ChemSusChem*, *2*(9), 796–854. https://doi.org/10.1002/cssc.200900036

Choi, S., Drese, J. H., & Jones, C. W. (2009b). Adsorbent Materials for Carbon Dioxide Capture from Large Anthropogenic Point Sources. *ChemSusChem*, *2*(9), 796–854. https://doi.org/10.1002/cssc.200900036

Choi, W. J., Min, B. M., Seo, J. B., Park, S. W., & Oh, K. J. (2009). Effect of ammonia on the absorption kinetics of carbon dioxide into aqueous 2-amino-2-methyl-1-propanol solutions. *Industrial and Engineering Chemistry Research*. https://doi.org/10.1021/ie8018438

Chowdhury, P., Bikkina, C., & Gumma, S. (2009). Chowdhury2009, 6616–6621.

Christmann, K., Ertl, G., & Pignet, T. (1976). Adsorption of hydrogen on a Pt(111) surface. *Surface Science*, *54*(2), 365–392. https://doi.org/https://doi.org/10.1016/0039-6028(76)90232-6

Chue, K. T., Kim, J. N., Yoo, Y. J., Cho, S. H., & Yang, R. T. (1995). Comparison of Activated Carbon and Zeolite 13X for CO2 Recovery from Flue Gas by Pressure Swing Adsorption. *Industrial & Engineering Chemistry Research*, *34*(2), 591–598. https://doi.org/10.1021/ie00041a020

Chughtai, A. H., Ahmad, N., Younus, H. A., Laypkov, A., & Verpoort, F. (2015). Metal-organic frameworks: Versatile heterogeneous catalysts for efficient catalytic organic transformations. *Chemical Society Reviews*, *44*(19), 6804–6849. https://doi.org/10.1039/c4cs00395k

Chui, S. S. Y., Lo, S. M. F., Charmant, J. P. H., Orpen, A. G., & Williams, I. D. (1999). A chemically functionalizable nanoporous material [Cu3(TMA)2 (H2O)3](n). *Science*, *283*(5405), 1148–1150. https://doi.org/10.1126/science.283.5405.1148

Chun, H., Jung, H., Koo, G., Jeong, H., & Kim, D.-K. (2008). Efficient Hydrogen Sorption in 8-Connected MOFs Based on Trinuclear Pinwheel Motifs. *Inorganic Chemistry*, *47*(12), 5355–5359. https://doi.org/10.1021/ic800274w

Ciais, P., Sabine, C., Bala, G., Bopp, L., Brovkin, V., Canadell, J., … Thornton, P. (2013). Chapter 6. *Change, IPCC Climate*, 465–570. https://doi.org/10.1017/CBO9781107415324.015

Coppola, A., Salatino, P., Montagnaro, F., & Scala, F. (2014). Reactivation by water hydration of the CO2 capture capacity of a calcium looping sorbent. *Fuel*, *127*, 109–115. https://doi.org/https://doi.org/10.1016/j.fuel.2013.09.059

Corma, A., García, H., & Llabrés I Xamena, F. X. (2010). Engineering metal organic frameworks for heterogeneous catalysis. *Chemical Reviews*, *110*(8), 4606–4655. https://doi.org/10.1021/cr9003924

Cuéllar-Franca, R. M., & Azapagic, A. (2015). Carbon capture, storage and utilisation technologies: A critical analysis and comparison of their life cycle environmental impacts. *Journal of CO2 Utilization*, *9*, 82–102. https://doi.org/10.1016/j.jcou.2014.12.001

Cui, Z., & Demontigny, D. (2013). Part 7: A review of CO2 capture using hollow fiber membrane contactors. *Carbon Management*. https://doi.org/10.4155/cmt.12.73

D'Alessandro, D. M., Smit, B., & Long, J. R. (2010). Carbon dioxide capture: Prospects for new materials. *Angewandte Chemie - International Edition*, *49*(35), 6058–6082. https://doi.org/10.1002/anie.201000431

Dai, Z., & Deng, L. (2016). Membrane absorption using ionic liquid for pre-combustion CO2 capture at elevated pressure and temperature. *International Journal of Greenhouse Gas Control*. https://doi.org/10.1016/j.ijggc.2016.09.001

Dailly, A., Vajo, J. J., & Ahn, C. C. (2006). Saturation of Hydrogen Sorption in Zn Benzenedicarboxylate and Zn Napthalenedicarboxylate. *The Journal of Physical Chemistry B*, *110*, 1099–1101. Retrieved from papers://c438f4a5-b4d4-4968-bf1f-63e00e5cec7c/Paper/p4626

Dash, S. K., Samanta, A. N., & Bandyopadhyay, S. S. (2014). Simulation and parametric study of post combustion CO2 capture process using (AMP+PZ) blended solvent. *International Journal of Greenhouse Gas Control*. https://doi.org/10.1016/j.ijggc.2013.12.003

Davidson, R. (2007). Post-combustion carbon capture from coal fired plants: solvent scrubbing. *Clean Coal Centre*.

Dawodu, O. F., & Meisen, A. (1994). Solubility of Carbon Dioxide in Aqueous Mixtures of Alkanolamines. *Journal of Chemical and Engineering Data*. https://doi.org/10.1021/je00015a034

Dawson, R., Adams, D. J., & Cooper, A. I. (2011). Chemical tuning of CO2 sorption in robust nanoporous organic polymers. *Chemical Science*, *2*(6), 1173–1177. https://doi.org/10.1039/C1SC00100K

Dawson, R., Stöckel, E., Holst, J. R., Adams, D. J., & Cooper, A. I. (2011). Microporous organic polymers for carbon dioxide capture. *Energy & Environmental Science*, *4*(10), 4239–4245. https://doi.org/10.1039/C1EE01971F

de la Casa-Lillo, M. A., Lamari-Darkrim, F., Cazorla-Amorós, D., & Linares-Solano, A. (2002). Hydrogen Storage in Activated Carbons and Activated Carbon Fibers. *The Journal of Physical Chemistry B*, *106*(42), 10930–10934. https://doi.org/10.1021/jp014543m

de Rango, P., Marty, P., & Fruchart, D. (2016). Hydrogen storage systems based on magnesium hydride: from laboratory tests to fuel cell integration. *Applied Physics A*, *122*(2), 126. https://doi.org/10.1007/s00339-016-9646-1

Demessence, A., D'Alessandro, D. M., Foo, M. L., & Long, J. R. (2009). Strong CO2 Binding in a Water-Stable, Triazolate-Bridged Metal−Organic Framework Functionalized with Ethylenediamine. *Journal of the American Chemical Society*, *131*(25), 8784–8786. https://doi.org/10.1021/ja903411w

deMontigny, D., Tontiwachwuthikul, P., & Chakma, A. (2006). Using polypropylene and polytetrafluoroethylene membranes in a membrane contactor for CO2 absorption. *Journal of Membrane Science*, *277*(1), 99–107. https://doi.org/https://doi.org/10.1016/j.memsci.2005.10.024

Demontigny, D., Tontiwachwuthikul, P., & Chakma, A. (2005). Comparing the absorption performance of packed columns and membrane contactors. *Industrial and Engineering Chemistry Research*. https://doi.org/10.1021/ie040264k

Denysenko, D., Grzywa, M., Tonigold, M., Streppel, B., Krkljus, I., Hirscher, M., … Volkmer, D. (2011). Elucidating Gating Effects for Hydrogen Sorption in MFU-4-Type Triazolate-Based Metal–Organic Frameworks Featuring Different Pore Sizes. *Chemistry – A European Journal*, *17*(6), 1837–1848. https://doi.org/10.1002/chem.201001872

Derevschikov, V. S., Veselovskaya, J. V, Kardash, T. Y., Trubitsyn, D. A., & Okunev, A. G. (2014). Direct CO2 capture from ambient air using K2CO3/Y2O3 composite sorbent. *Fuel*, *127*, 212–218. https://doi.org/https://doi.org/10.1016/j.fuel.2013.09.060

Dhakshinamoorthy, A., Alvaro, M., Chevreau, H., Horcajada, P., Devic, T., Serre, C., & Garcia, H. (2012). Iron(iii) metal-organic frameworks as solid Lewis acids for the isomerization of α-pinene oxide. *Catalysis Science and Technology*, *2*(2), 324–330. https://doi.org/10.1039/c2cy00376g

Dhakshinamoorthy, A., Alvaro, M., & Garcia, H. (2011). Atmospheric-Pressure, Liquid-Phase, Selective Aerobic Oxidation of Alkanes Catalysed by Metal–Organic Frameworks, 6256–6262. https://doi.org/10.1002/chem.201002664

Dhakshinamoorthy, A., Alvaro, M., & Garcia, H. (2012). Commercial metal-organic frameworks as heterogeneous catalysts. *Chemical Communications*, *48*(92), 11275–11288. https://doi.org/10.1039/c2cc34329k

Dhakshinamoorthy, A., Alvaro, M., Horcajada, P., Gibson, E., Vishnuvarthan, M., Vimont, A., … Garcia, H. (2012). Comparison of porous iron trimesates basolite F300 and MIL-100(Fe) as heterogeneous catalysts for lewis acid and oxidation reactions: Roles of structural defects and stability. *ACS Catalysis*, *2*(10), 2060–2065. https://doi.org/10.1021/cs300345b

Dhumal, N. R., Singh, M. P., Anderson, J. A., Kiefer, J., & Kim, H. J. (2016). Molecular Interactions of a Cu-Based Metal-Organic Framework with a Confined Imidazolium-Based Ionic Liquid: A Combined

Density Functional Theory and Experimental Vibrational Spectroscopy Study. *Journal of Physical Chemistry C*, *120*(6), 3295–3304. https://doi.org/10.1021/acs.jpcc.5b10123

Díaz, E., Muñoz, E., Vega, A., & Ordóñez, S. (2008). Enhancement of the CO2 Retention Capacity of Y Zeolites by Na and Cs Treatments: Effect of Adsorption Temperature and Water Treatment. *Industrial & Engineering Chemistry Research*, *47*(2), 412–418. https://doi.org/10.1021/ie070685c

Dietzel, P. D. C., Besikiotis, V., & Blom, R. (2009). Application of metal–organic frameworks with coordinatively unsaturated metal sites in storage and separation of methane and carbon dioxide. *Journal of Materials Chemistry*, *19*(39), 7362–7370. https://doi.org/10.1039/B911242A

Dietzel, P. D. C., Johnsen, R. E., Fjellvåg, H., Bordiga, S., Groppo, E., Chavan, S., & Blom, R. (2008). Adsorption properties and structure of CO2 adsorbed on open coordination sites of metal–organic framework Ni2(dhtp) from gas adsorption, IR spectroscopy and X-ray diffraction. *Chemical Communications*, (41), 5125–5127. https://doi.org/10.1039/B810574J

Dillon, A. C., Jones, K. M., Bekkedahl, T. A., Kiang, C. H., Bethune, D. S., & Heben, M. J. (1997). Storage of hydrogen in single-walled carbon nanotubes. *Nature*, *386*(6623), 377–379. https://doi.org/10.1038/386377a0

Dincă, M., Dailly, A., Liu, Y., Brown, C. M., Neumann, D. A., & Long, J. R. (2006). Hydrogen Storage in a Microporous Metal−Organic Framework with Exposed Mn2+ Coordination Sites. *Journal of the American Chemical Society*, *128*(51), 16876–16883. https://doi.org/10.1021/ja0656853

Dinča, M., Dailly, A., Liu, Y., Brown, C. M., Neumann, D. A., & Long, J. R. (2006). Hydrogen storage in a microporous metal-organic framework with exposed Mn2+ coordination sites. *Journal of the American Chemical Society*, *128*(51), 16876–16883. https://doi.org/10.1021/ja0656853

Dincă, M., Han, W. S., Liu, Y., Dailly, A., Brown, C. M., & Long, J. R. (2007). Observation of Cu2+–H2 Interactions in a Fully Desolvated Sodalite-Type Metal–Organic Framework. *Angewandte Chemie International Edition*, *46*(9), 1419–1422. https://doi.org/10.1002/anie.200604362

Dincă, M., & Long, J. R. (2008). Hydrogen Storage in Microporous Metal–Organic Frameworks with Exposed Metal Sites. *Angewandte Chemie International Edition*, *47*(36), 6766–6779. https://doi.org/10.1002/anie.200801163

Dincă, M., & Long, J. R. (2005). Strong H2 binding and selective gas adsorption within the microporous coordination solid Mg3(O2C-C 10H6-CO2)3. *Journal of the American Chemical Society*, *127*(26), 9376–9377. https://doi.org/10.1021/ja0523082

Dincă, M., & Long, J. R. (2007). High-Enthalpy Hydrogen Adsorption in Cation-Exchanged Variants of the Microporous Metal−Organic Framework Mn3[(Mn4Cl)3(BTT)8(CH3OH)10]2. *Journal of the American Chemical Society*, *129*(36), 11172–11176. https://doi.org/10.1021/ja072871f

Dindore, V. Y., Brilman, D. W. F., Geuzebroek, F. H., & Versteeg, G. F. (2004). Membrane–solvent selection for CO2 removal using membrane gas–liquid contactors. *Separation and Purification Technology*, *40*(2), 133–145. https://doi.org/https://doi.org/10.1016/j.seppur.2004.01.014

Dong, J., Wang, X., Xu, H., Zhao, Q., & Li, J. (2007). Hydrogen storage in several microporous zeolites. *International Journal of Hydrogen Energy*, *32*(18), 4998–5004. https://doi.org/https://doi.org/10.1016/j.ijhydene.2007.08.009

Dong, W., Chen, X., & Wu, Y. (2014). TiO2-Doped K2CO3/Al2O3 Sorbents for CO2 Capture. *Energy & Fuels*, *28*(5), 3310–3316. https://doi.org/10.1021/ef500133e

Drage, T. C., Arenillas, A., Smith, K. M., Pevida, C., Piippo, S., & Snape, C. E. (2007). Preparation of carbon dioxide adsorbents from the chemical activation of urea–formaldehyde and melamine–formaldehyde resins. *Fuel*, *86*(1), 22–31. https://doi.org/https://doi.org/10.1016/j.fuel.2006.07.003

Drioli, E., Stankiewicz, A. I., & Macedonio, F. (2011). Membrane engineering in process intensification-An overview. *Journal of Membrane Science*. https://doi.org/10.1016/j.memsci.2011.06.043

Du, M., Li, L., Li, M., & Si, R. (2016). Adsorption mechanism on metal organic frameworks of Cu-BTC, Fe-BTC and ZIF-8 for CO2 capture investigated by X-ray absorption fine structure. *RSC Advances*, *6*(67), 62705–62716. https://doi.org/10.1039/c6ra07582g

Du, N., Park, H. B., Robertson, G. P., Dal-Cin, M. M., Visser, T., Scoles, L., & Guiver, M. D. (2011). Polymer nanosieve membranes for CO2-capture applications. *Nature Materials*, *10*(5), 372–375. https://doi.org/10.1038/nmat2989

Du, X., & Wu, E. (2006). Physisorption of Hydrogen in A, X and ZSM-5 Types of Zeolites at Moderately High Pressures. *Chinese Journal of Chemical Physics*, *19*(5), 457–462. https://doi.org/10.1360/cjcp2006.19(5).457.6

Du, Y., Du, Z., Zou, W., Li, H., Mi, J., & Zhang, C. (2013). Carbon dioxide adsorbent based on rich amines loaded nano-silica. *Journal of Colloid and Interface Science*, *409*, 123–128. https://doi.org/https://doi.org/10.1016/j.jcis.2013.07.071

Duan, J., Yang, Z., Bai, J., Zheng, B., Li, Y., & Li, S. (2012). Highly selective CO2 capture of an agw-type metal–organic framework with inserted amides: experimental and theoretical studies. *Chemical Communications*, *48*(25), 3058–3060. https://doi.org/10.1039/C2CC16231H

Dündar-Tekkaya, E., & Yürüm, Y. (2015). Effect of loading bimetallic mixture of Ni and Pd on hydrogen storage capacity of MCM-41. *International Journal of Hydrogen Energy*, *40*(24), 7636–7643. https://doi.org/https://doi.org/10.1016/j.ijhydene.2015.02.108

Dündar-Tekkaya, E., & Yürüm, Y. (2016). Mesoporous MCM-41 material for hydrogen storage: A short review. *International Journal of Hydrogen Energy*, *41*(23), 9789–9795. https://doi.org/10.1016/j.ijhydene.2016.03.050

Durbin, D. J., & Malardier-Jugroot, C. (2013). Review of hydrogen storage techniques for on board vehicle applications. *International Journal of Hydrogen Energy*, *38*(34), 14595–14617. https://doi.org/10.1016/j.ijhydene.2013.07.058

Düren, T., & Snurr, R. Q. (2004). Assessment of Isoreticular Metal−Organic Frameworks for Adsorption Separations: A Molecular Simulation Study of Methane/n-Butane Mixtures. *The Journal of Physical Chemistry B*, *108*(40), 15703–15708. https://doi.org/10.1021/jp0477856

Dybtsev, D. N., Chun, H., & Kim, K. (2004). Rigid and flexible: A highly porous metal-organic framework with unusual guest-dependent dynamic behavior. *Angewandte Chemie - International Edition*. https://doi.org/10.1002/anie.200460712

Eddaoudi, M., Kim, J., Rosi, N., Vodak, D., Wachter, J., O'Keeffe, M., & Yaghi, O. M. (2002). Systematic Design of Pore Size and Functionality in Isoreticular MOFs and Their Application in Methane Storage. *Science*, *295*(5554), 469 LP – 472. https://doi.org/10.1126/science.1067208

Ello, S., Souza, L. K. C. De, Wickramaratne, N. P., Costa, M. J. F., Costa, C. E. F., & Jaroniec, M. (2013). Enhancement of CO 2 adsorption on phenolic resin-based mesoporous carbons by KOH activation, *5*, 2–8. https://doi.org/10.1016/j.carbon.2013.08.034

Emergence of Metal-Organic Frameworks. (2019, May 6). *Introduction to Reticular Chemistry*. https://doi.org/doi:10.1002/9783527821099.ch1

Energy demand by sector | Energy economics | Home. (n.d.). Retrieved August 22, 2019, from https://www.bp.com/en/global/corporate/energy-economics/energy-outlook/demand-by-sector.html

Environ, E., Sevilla, M., & Fuertes, A. B. (2011). Energy & Environmental Science Sustainable porous carbons with a superior performance for CO 2 capture, *1*(25 C), 1765–1771. https://doi.org/10.1039/c0ee00784f

Fabian San Francisco, CA (United States)], T. [Ardica T., Petrie Menlo Park, CA (United States)], M. [SRI I., Crouch-Baker Menlo Park, CA (United States)], S. [SRI I., & Fong Menlo Park, CA (United States)], H. [SRI I. (2017). *Low-Cost alpha Alane for Hydrogen Storage*. United States. https://doi.org/10.2172/1398788

Fakioğlu, E., Yürüm, Y., & Veziroğlu, T. N. (2004). A review of hydrogen storage systems based on boron and its compounds. *International Journal of Hydrogen Energy*, *29*(13), 1371–1376. https://doi.org/10.1016/j.ijhydene.2003.12.010

Falk-Pedersen, O., Grønvold, M. S., Nøkleby, P., Bjerve, F., & Svendsen, H. F. (2005). CO2 Capture with Membrane Contactors. *International Journal of Green Energy*, *2*(2), 157–165. https://doi.org/10.1081/GE-200058965

Fan, X., Zhang, L., Zhang, G., Shu, Z., & Shi, J. (2013). Chitosan derived nitrogen-doped microporous carbons for high performance CO2 capture. *Carbon*, *61*, 423–430. https://doi.org/https://doi.org/10.1016/j.carbon.2013.05.026

Fang, Q. R., Zhu, G. S., Jin, Z., Ji, Y. Y., Ye, J. W., Xue, M., … Qiu, S. L. (2007). Mesoporous metal-organic framework with rare etb topology for hydrogen storage and dye assembly. *Angewandte Chemie - International Edition*. https://doi.org/10.1002/anie.200700537

Farha, O. K., Özgür Yazaydın, A., Eryazici, I., Malliakas, C. D., Hauser, B. G., Kanatzidis, M. G., … Hupp, J. T. (2010). De novo synthesis of a metal–organic framework material featuring ultrahigh surface area and gas storage capacities. *Nature Chemistry*, *2*(11), 944–948. https://doi.org/10.1038/nchem.834

Farha, O. K., Wilmer, C. E., Eryazici, I., Hauser, B. G., Parilla, P. A., O'Neill, K., … Hupp, J. T. (2012). Designing Higher Surface Area Metal–Organic Frameworks: Are Triple Bonds Better Than Phenyls? *Journal of the American Chemical Society*, *134*(24), 9860–9863. https://doi.org/10.1021/ja302623w

Farrusseng, D., Aguado, S., & Pinel, C. (2009). Metal-organic frameworks: Opportunities for catalysis. *Angewandte Chemie - International Edition*, *48*(41), 7502–7513. https://doi.org/10.1002/anie.200806063

Fauth, D. J., Gray, M. L., Pennline, H. W., Krutka, H. M., Sjostrom, S., & Ault, A. M. (2012). Investigation of Porous Silica Supported Mixed-Amine Sorbents for Post-Combustion CO2 Capture. *Energy & Fuels*, *26*(4), 2483–2496. https://doi.org/10.1021/ef201578a

Felderhoff, M., Weidenthaler, C., von Helmolt, R., & Eberle, U. (2007). Hydrogen storage: the remaining scientific and technological challenges. *Physical Chemistry Chemical Physics*, *9*(21), 2643–2653. https://doi.org/10.1039/B701563C

Feng, B., An, H., & Tan, E. (2007). Screening of CO2 Adsorbing Materials for Zero Emission Power Generation Systems. *Energy & Fuels*, *21*(2), 426–434. https://doi.org/10.1021/ef0604036

Feng, B., Liu, W., Li, X., & An, H. (2006). Overcoming the Problem of Loss-in-Capacity of Calcium Oxide

in CO2 Capture. *Energy & Fuels*, *20*(6), 2417–2420. https://doi.org/10.1021/ef060258w

Feng, C., Wang, R., Zhang, H., & Shi, L. (2011). Diverse morphologies of PVDF hollow fiber membranes and their performance analysis as gas/liquid contactors. *Journal of Applied Polymer Science*, *119*(3), 1259–1267. https://doi.org/10.1002/app.30250

Feng, Z., Jing-Wen, M., Zheng, Z., You-Ting, W., & Zhi-Bing, Z. (2012). Study on the absorption of carbon dioxide in high concentrated MDEA and ILs solutions. *Chemical Engineering Journal*. https://doi.org/10.1016/j.cej.2011.11.066

Férey, G., Latroche, M., Serre, C., Millange, F., Loiseau, T., & Percheron-Guégan, A. (2003). Hydrogen adsorption in the nanoporous metal-benzenedicarboxylate M(OH)(O2C–C6H4–CO2) (M = Al3+, Cr3+), MIL-53. *Chemical Communications*, (24), 2976–2977. https://doi.org/10.1039/B308903G

Fonseca, D. A., Gutierrez, H. R., & Lueking, A. D. (2008). Morphology and porosity enhancement of graphite nanofibers through chemical etching. *Microporous and Mesoporous Materials*, *113*(1–3), 178–186. https://doi.org/10.1016/j.micromeso.2007.11.016

Force, C. (2009). Advanced Post-Combustion CO2 Capture. *Clean Air Task Force*, (April).

Franchi, R. S., Harlick, P. J. E., & Sayari, A. (2005). Applications of Pore-Expanded Mesoporous Silica. 2. Development of a High-Capacity, Water-Tolerant Adsorbent for CO2. *Industrial & Engineering Chemistry Research*, *44*(21), 8007–8013. https://doi.org/10.1021/ie0504194

Franken, A. C. M., Nolten, J. A. M., Mulder, M. H. V, Bargeman, D., & Smolders, C. A. (1987). Wetting criteria for the applicability of membrane distillation. *Journal of Membrane Science*, *33*(3), 315–328. https://doi.org/https://doi.org/10.1016/S0376-7388(00)80288-4

Frankland, S. J. V, & Brenner, D. W. (2001). Hydrogen Raman shifts in carbon nanotubes from molecular dynamics simulation. *Chemical Physics Letters*, *334*(1), 18–23. https://doi.org/https://doi.org/10.1016/S0009-2614(00)01454-8

Friščić, T. (2010). New opportunities for materials synthesis using mechanochemistry. *Journal of Materials Chemistry*, *20*(36), 7599–7605. https://doi.org/10.1039/C0JM00872A

Friščić, T., & Fábián, L. (2009). Mechanochemical conversion of a metal oxide into coordination polymers and porous frameworks using liquid-assisted grinding (LAG). *CrystEngComm*, *11*(5), 743–745. https://doi.org/10.1039/B822934C

Friščić, T., Reid, D. G., Halasz, I., Stein, R. S., Dinnebier, R. E., & Duer, M. J. (2010). Ion- and Liquid-Assisted Grinding: Improved Mechanochemical Synthesis of Metal–Organic Frameworks Reveals Salt Inclusion and Anion Templating. *Angewandte Chemie International Edition*, *49*(4), 712–715. https://doi.org/10.1002/anie.200906583

Frost, H., Düren, T., & Snurr, R. Q. (2006a). Effects of surface area, free volume, and heat of adsorption on hydrogen uptake in metal-organic frameworks. *Journal of Physical Chemistry B*, *110*(19), 9565–9570. https://doi.org/10.1021/jp060433

Frost, H., Düren, T., & Snurr, R. Q. (2006b). Effects of Surface Area, Free Volume, and Heat of Adsorption on Hydrogen Uptake in Metal−Organic Frameworks. *The Journal of Physical Chemistry B*, *110*(19), 9565–9570. https://doi.org/10.1021/jp060433+

Frost, H., & Snurr, R. Q. (2007). Design Requirements for Metal-Organic Frameworks as Hydrogen Storage Materials. *The Journal of Physical Chemistry C*, *111*(50), 18794–18803. https://doi.org/10.1021/jp076657p

Fu, D., Wang, L., Mi, C., & Zhang, P. (2016). Absorption capacity and viscosity for CO2 capture process using high concentrated PZ-DEAE aqueous solution. *Journal of Chemical Thermodynamics*. https://doi.org/10.1016/j.jct.2016.05.022

Fu, D., Zhang, P., & Mi, C. (2016). Effects of concentration and viscosity on the absorption of CO2 in [N1111][Gly] promoted MDEA (methyldiethanolamine) aqueous solution. *Energy*, *101*, 288–295. https://doi.org/https://doi.org/10.1016/j.energy.2016.02.052

Fu, K., Sema, T., Liang, Z., Liu, H., Na, Y., Shi, H., … Tontiwachwuthikul, P. (2012). Investigation of mass-transfer performance for CO2 absorption into diethylenetriamine (DETA) in a randomly packed column. *Industrial and Engineering Chemistry Research*. https://doi.org/10.1021/ie300830h

Fujii, K., Garay, A. L., Hill, J., Sbircea, E., Pan, Z., Xu, M., … Harris, K. D. M. (2010). Direct structure elucidation by powder X-ray diffraction of a metal–organic framework material prepared by solvent-free grinding. *Chemical Communications*, *46*(40), 7572–7574. https://doi.org/10.1039/C0CC02635B

Furukawa, H., Cordova, K. E., O'Keeffe, M., & Yaghi, O. M. (2013). The chemistry and applications of metal-organic frameworks. *Science*. https://doi.org/10.1126/science.1230444

Furukawa, H., Ko, N., Go, Y. B., Aratani, N., Choi, S. B., Choi, E., … Yaghi, O. M. (2010). Ultrahigh Porosity in Metal-Organic Frameworks. *Science*, *329*(5990), 424 LP – 428. https://doi.org/10.1126/science.1192160

Gabelman, A., & Hwang, S. T. (1999). Hollow fiber membrane contactors. *Journal of Membrane Science*. https://doi.org/10.1016/S0376-7388(99)00040-X

Gadiou, R., Saadallah, S.-E., Piquero, T., David, P., Parmentier, J., & Vix-Guterl, C. (2005). The influence of textural properties on the adsorption of hydrogen on ordered nanostructured carbons. *Microporous and Mesoporous Materials*, *79*(1), 121–128. https://doi.org/https://doi.org/10.1016/j.micromeso.2004.10.034

Gallei, E., & Stumpf, G. (1976). Infrared spectroscopic studies of the adsorption of carbon dioxide and the coadsorption of carbon dioxide and water on CaY- and NiY-zeolites. *Journal of Colloid and Interface Science*, *55*(2), 415–420. https://doi.org/https://doi.org/10.1016/0021-9797(76)90051-5

Gangu, K. K., Maddila, S., Mukkamala, S. B., & Jonnalagadda, S. B. (2019). Characteristics of MOF, MWCNT and graphene containing materials for hydrogen storage: A review. *Journal of Energy Chemistry*, *30*, 132–144. https://doi.org/https://doi.org/10.1016/j.jechem.2018.04.012

Gao, C., Chen, S., Quan, X., Yu, H., & Zhang, Y. (2017). Enhanced Fenton-like catalysis by iron-based metal organic frameworks for degradation of organic pollutants. *Journal of Catalysis*, *356*, 125–132. https://doi.org/10.1016/j.jcat.2017.09.015

Gao, J., Yin, J., Zhu, F., Chen, X., Tong, M., Kang, W., … Lu, J. (2016). Integration study of a hybrid solvent MEA-Methanol for post combustion carbon dioxide capture in packed bed absorption and regeneration columns. *Separation and Purification Technology*. https://doi.org/10.1016/j.seppur.2016.04.033

Gao, Y., Zhang, F., Huang, K., Ma, J. W., Wu, Y. T., & Zhang, Z. B. (2013). Absorption of CO2 in amino acid ionic liquid (AAIL) activated MDEA solutions. *International Journal of Greenhouse Gas Control*. https://doi.org/10.1016/j.ijggc.2013.09.019

Garay, A. L., Pichon, A., & James, S. L. (2007). Solvent-free synthesis of metal complexes. *Chemical Society Reviews*, *36*(6), 846–855. https://doi.org/10.1039/B600363J

García-García, P., Moreno, J. M., Díaz, U., Bruix, M., & Corma, A. (2016). Organic-inorganic

supramolecular solid catalyst boosts organic reactions in water. *Nature Communications*, *7*. https://doi.org/10.1038/ncomms10835

García-Holley, P., Schweitzer, B., Islamoglu, T., Liu, Y., Lin, L., Rodriguez, S., … Farha, O. K. (2018). Benchmark Study of Hydrogen Storage in Metal-Organic Frameworks under Temperature and Pressure Swing Conditions. *ACS Energy Letters*, *3*(3), 748–754. https://doi.org/10.1021/acsenergylett.8b00154

García-Payo, M. C., Izquierdo-Gil, M. A., & Fernández-Pineda, C. (2000). Air gap membrane distillation of aqueous alcohol solutions. *Journal of Membrane Science*, *169*(1), 61–80. https://doi.org/https://doi.org/10.1016/S0376-7388(99)00326-9

Garrone, E., Bonelli, B., & Otero Areán, C. (2008). Enthalpy–entropy correlation for hydrogen adsorption on zeolites. *Chemical Physics Letters*, *456*(1), 68–70. https://doi.org/https://doi.org/10.1016/j.cplett.2008.03.014

Gee, A. T., Hayden, B. E., Mormiche, C., & Nunney, T. S. (2000). The role of steps in the dynamics of hydrogen dissociation on Pt(533). *The Journal of Chemical Physics*, *112*(17), 7660–7668. https://doi.org/10.1063/1.481360

Germain, J., Svec, F., & Fréchet, J. M. J. (2008). Preparation of Size-Selective Nanoporous Polymer Networks of Aromatic Rings: Potential Adsorbents for Hydrogen Storage. *Chemistry of Materials*, *20*(22), 7069–7076. https://doi.org/10.1021/cm802157r

Gil, A., Vicente, M. A., & Korili, S. A. (2005). Effect of the Si/Al ratio on the structure and surface properties of silica-alumina-pillared clays. *Journal of Catalysis*, *229*(1), 119–126. https://doi.org/https://doi.org/10.1016/j.jcat.2004.10.013

Global Temperature | Vital Signs – Climate Change: Vital Signs of the Planet. (n.d.). Retrieved July 19, 2020, from https://climate.nasa.gov/vital-signs/global-temperature/

Goeppert, A., Zhang, H., Czaun, M., May, R. B., Prakash, G. K. S., Olah, G. A., & Narayanan, S. R. (2014). Easily Regenerable Solid Adsorbents Based on Polyamines for Carbon Dioxide Capture from the Air. *ChemSusChem*, *7*(5), 1386–1397. https://doi.org/10.1002/cssc.201301114

Gohari-Bajestani, Z., Akhlaghi, O., Yürüm, Y., & Yürüm, A. (2017). Synthesis of anatase TiO2 with exposed (001) facets grown on N-doped reduced graphene oxide for enhanced hydrogen storage. *International Journal of Hydrogen Energy*, *42*(9), 6096–6103. https://doi.org/https://doi.org/10.1016/j.ijhydene.2016.11.069

Gohari Bajestani, Z., Yürüm, A., & Yürüm, Y. (2016). Decoration of graphene sheets with Pd/Al2O3 hybrid particles for hydrogen storage applications. *International Journal of Hydrogen Energy*, *41*(23), 9810–9818. https://doi.org/https://doi.org/10.1016/j.ijhydene.2016.03.201

Goodrich, B. F., de la Fuente, J. C., Gurkan, B. E., Lopez, Z. K., Price, E. A., Huang, Y., & Brennecke, J. F. (2011). Effect of Water and Temperature on Absorption of CO2 by Amine-Functionalized Anion-Tethered Ionic Liquids. *The Journal of Physical Chemistry B*, *115*(29), 9140–9150. https://doi.org/10.1021/jp2015534

Gouedard, C., Picq, D., Launay, F., & Carrette, P. L. (2012). Amine degradation in CO 2 capture. I. A review. *International Journal of Greenhouse Gas Control*. https://doi.org/10.1016/j.ijggc.2012.06.015

Graetz, J, Reilly, J. J., Yartys, V. A., Maehlen, J. P., Bulychev, B. M., Antonov, V. E., … Gabis, I. E. (2011). Aluminum hydride as a hydrogen and energy storage material: Past, present and future. *Journal of Alloys and Compounds*, *509*, S517–S528. https://doi.org/https://doi.org/10.1016/j.jallcom.2010.11.115

Graetz, Jason, & Hauback, B. C. (2013). Recent developments in aluminum-based hydrides for hydrogen storage. *MRS Bulletin*, *38*(6), 473–479. https://doi.org/DOI: 10.1557/mrs.2013.107

Gray, M. L., Champagne, K. J., Fauth, D., Baltrus, J. P., & Pennline, H. (2008). Performance of immobilized tertiary amine solid sorbents for the capture of carbon dioxide. *International Journal of Greenhouse Gas Control*, *2*(1), 3–8. https://doi.org/https://doi.org/10.1016/S1750-5836(07)00088-6

Gray, M. L., Soong, Y., Champagne, K. J., Baltrus, J., Stevens, R. W., Toochinda, P., & Chuang, S. S. C. (2004). CO2 capture by amine-enriched fly ash carbon sorbents. *Separation and Purification Technology*, *35*(1), 31–36. https://doi.org/https://doi.org/10.1016/S1383-5866(03)00113-8

Groen, J. C., Peffer, L. A. A., Moulijn, J. A., & Pérez-Ramírez, J. (2005). Mechanism of hierarchical porosity development in MFI zeolites by desilication: The role of aluminium as a pore-directing agent. *Chemistry - A European Journal*, *11*(17), 4983–4994. https://doi.org/10.1002/chem.200500045

Gruene, P., Belova, A. G., Yegulalp, T. M., Farrauto, R. J., & Castaldi, M. J. (2011). Dispersed Calcium Oxide as a Reversible and Efficient CO2−Sorbent at Intermediate Temperatures. *Industrial & Engineering Chemistry Research*, *50*(7), 4042–4049. https://doi.org/10.1021/ie102475d

Guay, P., Stansfield, B. L., & Rochefort, A. (2004). On the control of carbon nanostructures for hydrogen storage applications. *Carbon*, *42*(11), 2187–2193. https://doi.org/https://doi.org/10.1016/j.carbon.2004.04.027

Gumma, S., Chowdhury, P., & Bikkina, C. (2009). Gas Adsorption Properties of the Chromium-Based Metal Organic Framework MIL-101. *Journal of Physical Chemistry C*, *113*(16), 6616–6621. https://doi.org/10.1021/jp811418r

Guo, D., Thee, H., Da Silva, G., Chen, J., Fei, W., Kentish, S., & Stevens, G. W. (2011). Borate-catalyzed carbon dioxide hydration via the carbonic anhydrase mechanism. *Environmental Science and Technology*. https://doi.org/10.1021/es200590m

Gupta, A., Shervani, S., Amaladasse, F., Sivakumar, S., Balani, K., & Subramaniam, A. (2019). Enhanced reversible hydrogen storage in nickel nano hollow spheres. *International Journal of Hydrogen Energy*, *44*(39), 22032–22038. https://doi.org/10.1016/j.ijhydene.2019.06.090

Gupta, B. K., & Srivastava, O. N. (2000). Synthesis and hydrogenation behaviour of graphitic nanofibres. *International Journal of Hydrogen Energy*, *25*(9), 825–830. https://doi.org/https://doi.org/10.1016/S0360-3199(99)00104-4

Gupta, B. K., & Srivastava, O. N. (2001). Further studies on microstructural characterization and hydrogenation behaviour of graphitic nanofibres. *International Journal of Hydrogen Energy*, *26*(8), 857–862. https://doi.org/https://doi.org/10.1016/S0360-3199(01)00021-0

Gupta, H., & Fan, L.-S. (2002). Carbonation−Calcination Cycle Using High Reactivity Calcium Oxide for Carbon Dioxide Separation from Flue Gas. *Industrial & Engineering Chemistry Research*, *41*(16), 4035–4042. https://doi.org/10.1021/ie010867l

Gupta, K. M., Chen, Y., Hu, Z., & Jiang, J. (2012). Metal–organic framework supported ionic liquid membranes for CO2 capture: anion effects. *Physical Chemistry Chemical Physics*, *14*(16), 5785–5794. https://doi.org/10.1039/C2CP23972H

Gupta, M., Coyle, I., & Thambimuthu, K. (2003). *CO2 Capture Technologies and Opportunities in Canada*.

Gutowski, K. E., & Maginn, E. J. (2008). Amine-Functionalized Task-Specific Ionic Liquids: A Mechanistic Explanation for the Dramatic Increase in Viscosity upon Complexation with CO2 from Molecular

Simulation. *Journal of the American Chemical Society*, *130*(44), 14690–14704. https://doi.org/10.1021/ja804654b

Hairul, N. A. H., Shariff, A. M., & Bustam, M. A. (2017). Process behaviour in a packed absorption column for high pressure CO2 absorption from natural gas using PZ + AMP blended solution. *Fuel Processing Technology*. https://doi.org/10.1016/j.fuproc.2016.11.008

Han, K. K., Ma, L., Zhao, H. M., Li, X., Chun, Y., & Zhu, J. H. (2012). In situ synthesis of SBA-3/cotton fiber composite materials: A hybrid device for CO2 capture. *Microporous and Mesoporous Materials*, *151*, 157–162. https://doi.org/https://doi.org/10.1016/j.micromeso.2011.10.043

Han, K. K., Zhou, Y., Lin, W. G., & Zhu, J. H. (2013). One-pot synthesis of foam-like magnesia and its performance in CO2 adsorption. *Microporous and Mesoporous Materials*, *169*, 112–119. https://doi.org/https://doi.org/10.1016/j.micromeso.2012.11.004

Han, S. S., Deng, W.-Q., & Goddard III, W. A. (2007). Improved Designs of Metal–Organic Frameworks for Hydrogen Storage. *Angewandte Chemie International Edition*, *46*(33), 6289–6292. https://doi.org/10.1002/anie.200700303

Han, S. S., & Goddard, W. A. (2007). Lithium-Doped Metal-Organic Frameworks for Reversible H2 Storage at Ambient Temperature. *Journal of the American Chemical Society*, *129*(27), 8422–8423. https://doi.org/10.1021/ja072599+

Hanikel, N., Prévot, M. S., Fathieh, F., Kapustin, E. A., Lyu, H., Wang, H., … Yaghi, O. M. (2019). Rapid Cycling and Exceptional Yield in a Metal-Organic Framework Water Harvester. *ACS Central Science*, *5*(10), 1699–1706. https://doi.org/10.1021/acscentsci.9b00745

Hanikel, N., Prévot, M. S., & Yaghi, O. M. (2020). MOF water harvesters. *Nature Nanotechnology*, *15*(5), 348–355. https://doi.org/10.1038/s41565-020-0673-x

Harlick, P. J. E., & Sayari, A. (2007). Applications of Pore-Expanded Mesoporous Silica. 5. Triamine Grafted Material with Exceptional CO2 Dynamic and Equilibrium Adsorption Performance. *Industrial & Engineering Chemistry Research*, *46*(2), 446–458. https://doi.org/10.1021/ie060774+

Harries, D. N., Paskevicius, M., Sheppard, D. A., Price, T. E. C., & Buckley, C. E. (2012). Concentrating Solar Thermal Heat Storage Using Metal Hydrides. *Proceedings of the IEEE*, *100*(2), 539–549. https://doi.org/10.1109/JPROC.2011.2158509

Harrison, D. P. (2005). - The role of solids in CO2 capture: A mini review. In E. S. Rubin, D. W. Keith, C. F. Gilboy, M. Wilson, T. Morris, J. Gale, & K. B. T.-G. G. C. T. 7 Thambimuthu (Eds.) (pp. 1101–1106). Oxford: Elsevier Science Ltd. https://doi.org/https://doi.org/10.1016/B978-008044704-9/50114-2

Hartmann, M., Kunz, S., Himsl, D., Tangermann, O., Ernst, S., & Wagener, A. (2008). Adsorptive Separation of Isobutene and Isobutane on Cu3(BTC)2. *Langmuir*, *24*(16), 8634–8642. https://doi.org/10.1021/la8008656

Hasib-ur-Rahman, M., Siaj, M., & Larachi, F. (2010). Ionic liquids for CO2 capture—Development and progress. *Chemical Engineering and Processing: Process Intensification*, *49*(4), 313–322. https://doi.org/https://doi.org/10.1016/j.cep.2010.03.008

Haszeldine, R. S. (2009). Carbon Capture and Storage: How Green Can Black Be? *Science*, *325*(5948), 1647 LP – 1652. https://doi.org/10.1126/science.1172246

Heile, S., Rosenberger, S., Parker, A., Jefferson, B., & McAdam, E. J. (2014). Establishing the suitability of symmetric ultrathin wall polydimethylsiloxane hollow-fibre membrane contactors for enhanced CO2

separation during biogas upgrading. *Journal of Membrane Science*, *452*, 37–45. https://doi.org/https://doi.org/10.1016/j.memsci.2013.10.007

Henke, S., Schneemann, A., Wütscher, A., & Fischer, R. A. (2012). Directing the Breathing Behavior of Pillared-Layered Metal–Organic Frameworks via a Systematic Library of Functionalized Linkers Bearing Flexible Substituents. *Journal of the American Chemical Society*, *134*(22), 9464–9474. https://doi.org/10.1021/ja302991b

Hernández-Huesca, R., Díaz, L., & Aguilar-Armenta, G. (1999). Adsorption equilibria and kinetics of CO2, CH4 and N2 in natural zeolites. *Separation and Purification Technology*, *15*(2), 163–173. https://doi.org/https://doi.org/10.1016/S1383-5866(98)00094-X

Hill, T. L. (1955). Corresponding States in Multilayer Step Adsorption. *The Journal of Physical Chemistry*, *59*(10), 1065–1067. https://doi.org/10.1021/j150532a017

Hirscher, M, Becher, M., Haluska, M., Quintel, A., Skakalova, V., Choi, Y.-M., … Fink, J. (2002). Hydrogen storage in carbon nanostructures. *Journal of Alloys and Compounds*, *330–332*, 654–658. https://doi.org/https://doi.org/10.1016/S0925-8388(01)01643-7

Hirscher, Michael, & Panella, B. (2007). Hydrogen storage in metal-organic frameworks. *Scripta Materialia*, *56*(10), 809–812. https://doi.org/10.1016/j.scriptamat.2007.01.005

Hirscher, Michael, Panella, B., & Schmitz, B. (2010). Metal-organic frameworks for hydrogen storage. *Microporous and Mesoporous Materials*, *129*(3), 335–339. https://doi.org/10.1016/j.micromeso.2009.06.005

Hiyoshi, N., Yogo, K., & Yashima, T. (2005). Adsorption characteristics of carbon dioxide on organically functionalized SBA-15. *Microporous and Mesoporous Materials*, *84*(1), 357–365. https://doi.org/https://doi.org/10.1016/j.micromeso.2005.06.010

Hoff, K. A., Juliussen, O., Falk-Pedersen, O., & Svendsen, H. F. (2004). Modeling and Experimental Study of Carbon Dioxide Absorption in Aqueous Alkanolamine Solutions Using a Membrane Contactor. *Industrial & Engineering Chemistry Research*, *43*(16), 4908–4921. https://doi.org/10.1021/ie034325a

Hong, D.-Y., Hwang, Y. K., Serre, C., Férey, G., & Chang, J.-S. (2009). Porous Chromium Terephthalate MIL-101 with Coordinatively Unsaturated Sites: Surface Functionalization, Encapsulation, Sorption and Catalysis. *Advanced Functional Materials*, *19*(10), 1537–1552. https://doi.org/10.1002/adfm.200801130

Hong, S.-H., Jang, M.-S., Cho, S. J., & Ahn, W.-S. (2014). Chabazite and zeolite 13X for CO2 capture under high pressure and moderate temperature conditions. *Chemical Communications*, *50*(38), 4927–4930. https://doi.org/10.1039/C3CC46313C

Hong, S.-M., Kim, S. H., & Lee, K. B. (2013). Adsorption of Carbon Dioxide on 3-Aminopropyl-Triethoxysilane Modified Graphite Oxide. *Energy & Fuels*, *27*(6), 3358–3363. https://doi.org/10.1021/ef400467w

Horcajada, P., Chalati, T., Serre, C., Gillet, B., Sebrie, C., Baati, T., … Gref, R. (2010a). Porous metal-organic-framework nanoscale carriers as a potential platform for drug deliveryand imaging. *Nature Materials*, *9*(2), 172–178. https://doi.org/10.1038/nmat2608

Horcajada, P., Chalati, T., Serre, C., Gillet, B., Sebrie, C., Baati, T., … Gref, R. (2010b). Porous metal–organic-framework nanoscale carriers as a potential platform for drug delivery and imaging. *Nature Materials*, *9*(2), 172–178. https://doi.org/10.1038/nmat2608

Horcajada, P., Gref, R., Baati, T., Allan, P. K., Maurin, G., Couvreur, P., … Serre, C. (2012). Metal-Organic Frameworks in Biomedicine, *112*, 1232–1268. https://doi.org/10.1021/cr200256v

Horcajada, P., Salles, F., Wuttke, S., Devic, T., Heurtaux, D., Maurin, G., … Serre, C. (2011). How linker's modification controls swelling properties of highly flexible iron(III) dicarboxylates MIL-88. *Journal of the American Chemical Society*, *133*(44), 17839–17847. https://doi.org/10.1021/ja206936e

Horcajada, P., Serre, C., Vallet-Regí, M., Sebban, M., Taulelle, F., & Férey, G. (2006). Metal–Organic Frameworks as Efficient Materials for Drug Delivery. *Angewandte Chemie International Edition*, *45*(36), 5974–5978. https://doi.org/10.1002/anie.200601878

Hou, S., Wu, Y. N., Feng, L., Chen, W., Wang, Y., Morlay, C., & Li, F. (2018). Green synthesis and evaluation of an iron-based metal-organic framework MIL-88B for efficient decontamination of arsenate from water. *Dalton Transactions*, *47*(7), 2222–2231. https://doi.org/10.1039/c7dt03775a

Hu, X., Lou, X., Li, C., Ning, Y., Liao, Y., Chen, Q., … Hu, B. (2016). Facile synthesis of the Basolite F300-like nanoscale Fe-BTC framework and its lithium storage properties. *RSC Advances*, *6*(115), 114483–114490. https://doi.org/10.1039/C6RA22738D

Hu, Y. H., & Zhang, L. (2010). Hydrogen storage in metal-organic frameworks. *Advanced Materials*, *22*(20), 117–130. https://doi.org/10.1002/adma.200902096

Hu, Yingli, Verdegaal, W. M., Yu, S.-H., & Jiang, H.-L. (2014). Alkylamine-Tethered Stable Metal–Organic Framework for CO2 Capture from Flue Gas. *ChemSusChem*, *7*(3), 734–737. https://doi.org/10.1002/cssc.201301163

Hu, Yue, Lin, B., He, P., Li, Y., Huang, Y., & Song, Y. (2015). Probing the Structural Stability of and Enhanced CO2Storage in MOF MIL-68(In) under High Pressures by FTIR Spectroscopy. *Chemistry - A European Journal*, *21*(51), 18739–18748. https://doi.org/10.1002/chem.201502980

Hua, T. Q., & Ahluwalia, R. K. (2011). Alane hydrogen storage for automotive fuel cells – Off-board regeneration processes and efficiencies. *International Journal of Hydrogen Energy*, *36*(23), 15259–15265. https://doi.org/https://doi.org/10.1016/j.ijhydene.2011.08.081

Huang, C.-H., Chang, K.-P., Yu, C.-T., Chiang, P.-C., & Wang, C.-F. (2010). Development of high-temperature CO2 sorbents made of CaO-based mesoporous silica. *Chemical Engineering Journal*, *161*(1), 129–135. https://doi.org/https://doi.org/10.1016/j.cej.2010.04.045

Huang, G., Zhang, F., Zhang, L., Du, X., Wang, J., & Wang, L. (2014). Hierarchical NiFe2O4/Fe2O3 nanotubes derived from metal organic frameworks for superior lithium ion battery anodes. *Journal of Materials Chemistry A*, *2*(21), 8048–8053. https://doi.org/10.1039/C4TA00200H

Huang, H. Y., Yang, R. T., Chinn, D., & Munson, C. L. (2003). Amine-Grafted MCM-48 and Silica Xerogel as Superior Sorbents for Acidic Gas Removal from Natural Gas. *Industrial & Engineering Chemistry Research*, *42*(12), 2427–2433. https://doi.org/10.1021/ie020440u

Huo, S. H., & Yan, X. P. (2012). Metal-organic framework MIL-100(Fe) for the adsorption of malachite green from aqueous solution. *Journal of Materials Chemistry*, *22*(15), 7449–7455. https://doi.org/10.1039/c2jm16513a

IEA, & OECD. (2004). Energy Technology Analysis: Prospects for CO2 Capture and Storage, 1–249. https://doi.org/10.1016/B978-1-85617-710-8.00010-8

Intergovernmental Panel on Climate Change. (2014). *Climate Change 2014 Mitigation of Climate Change*. https://doi.org/10.1017/CBO9781107415416

Intergovernmental Panel on Climate Change, & Intergovernmental Panel on Climate Change. (2015). Drivers, Trends and Mitigation. *Climate Change 2014 Mitigation of Climate Change*, 351–412. https://doi.org/10.1017/cbo9781107415416.011

IPCC. (2005a). IPCC special report on carbon dioxide capture and storage. Prepared by working group III of the Intergovernmental Panel on Climate Change. In *IPCC Special Report on Carbon Dioxide Capture and Storage* (Vol. 2, p. 442). https://doi.org/10.1002/anie.201000431

IPCC. (2005b). IPCC special report on carbon dioxide capture and storage. Prepared by working group III of the Intergovernmental Panel on Climate Change. In *IPCC Special Report on Carbon Dioxide Capture and Storage*. https://doi.org/10.1002/anie.201000431

IPCC. (2018). *Global Warming of 1.5 °C - SR15*. *Ipcc - Sr15*. Retrieved from http://www.ipcc.ch/report/sr15/

Ishibashi, M., Ota, H., Akutsu, N., Umeda, S., Tajika, M., Izumi, J., … Kageyama, Y. (1996). Technology for removing carbon dioxide from power plant flue gas by the physical adsorption method. *Energy Conversion and Management*, *37*(6), 929–933. https://doi.org/https://doi.org/10.1016/0196-8904(95)00279-0

Iyer, M. V, Gupta, H., Sakadjian, B. B., & Fan, L.-S. (2004). Multicyclic Study on the Simultaneous Carbonation and Sulfation of High-Reactivity CaO. *Industrial & Engineering Chemistry Research*, *43*(14), 3939–3947. https://doi.org/10.1021/ie0341911

J. Edler, K., A. Reynolds, P., J. Branton, P., R. Trouw, F., & W. White, J. (1997). Structure and dynamics of hydrogen sorption in mesoporous MCM-41. *Journal of the Chemical Society, Faraday Transactions*, *93*(8), 1667–1674. https://doi.org/10.1039/A607878H

Jacobs, P. A., & Mortier, W. J. (1982). An attempt to rationalize stretching frequencies of lattice hydroxyl groups in hydrogen-zeolites. *Zeolites*, *2*(3), 226–230. https://doi.org/10.1016/S0144-2449(82)80056-0

Jadhav, P. D., Chatti, R. V, Biniwale, R. B., Labhsetwar, N. K., Devotta, S., & Rayalu, S. S. (2007). Monoethanol Amine Modified Zeolite 13X for CO2 Adsorption at Different Temperatures. *Energy & Fuels*, *21*(6), 3555–3559. https://doi.org/10.1021/ef070038y

Jae, Y. C., Kim, J., Sung, H. J., Kim, H. K., Chang, J. S., & Chae, H. K. (2006). Microwave synthesis of a porous metal-organic framework, zinc terephthalate MOF-5. *Bulletin of the Korean Chemical Society*, *27*(10), 1523–1524. https://doi.org/10.5012/bkcs.2006.27.10.1523

Jänchen, J., Möhlmann, D. T. F., & Stach, H. (2007). Water and carbon dioxide sorption properties of natural zeolites and clay minerals at martian surface temperature and pressure conditions. In R. Xu, Z. Gao, J. Chen, & W. B. T.-S. in S. S. and C. Yan (Eds.), *From Zeolites to Porous MOF Materials - The 40th Anniversary of International Zeolite Conference* (Vol. 170, pp. 2116–2121). Elsevier. https://doi.org/https://doi.org/10.1016/S0167-2991(07)81108-6

Jang, D.-I., & Park, S.-J. (2012). Influence of nickel oxide on carbon dioxide adsorption behaviors of activated carbons. *Fuel*, *102*, 439–444. https://doi.org/https://doi.org/10.1016/j.fuel.2012.03.052

Jeon, H. J., Choi, J. H., Lee, Y., Choi, K. M., Park, J. H., & Kang, J. K. (2012). Highly Selective CO2-Capturing Polymeric Organic Network Structures. *Advanced Energy Materials*, *2*(2), 225–228. https://doi.org/10.1002/aenm.201100648

Jeon, H., Min, Y. J., Ahn, S. H., Hong, S.-M., Shin, J.-S., Kim, J. H., & Lee, K. B. (2012). Graft copolymer templated synthesis of mesoporous MgO/TiO2 mixed oxide nanoparticles and their CO2 adsorption capacities. *Colloids and Surfaces A: Physicochemical and Engineering Aspects*, *414*, 75–81. https://doi.org/https://doi.org/10.1016/j.colsurfa.2012.08.009

Jeremias, F., Khutia, A., Henninger, S. K., & Janiak, C. (2012). MIL-100(Al, Fe) as water adsorbents for heat transformation purposes - A promising application. *Journal of Materials Chemistry*, *22*(20), 10148–10151. https://doi.org/10.1039/c2jm15615f

Jhung, S. H., Lee, J.-H., Yoon, J. W., Serre, C., Férey, G., & Chang, J.-S. (2007). Microwave Synthesis of Chromium Terephthalate MIL-101 and Its Benzene Sorption Ability. *Advanced Materials*, *19*(1), 121–124. https://doi.org/10.1002/adma.200601604

Jhung, Sung Hwa, Lee, J.-H., Forster, P. M., Férey, G., Cheetham, A. K., & Chang, J.-S. (2006). Microwave Synthesis of Hybrid Inorganic–Organic Porous Materials: Phase-Selective and Rapid Crystallization. *Chemistry – A European Journal*, *12*(30), 7899–7905. https://doi.org/10.1002/chem.200600270

Jiang, Jing, Zhang, C., & Ai, L. (2016). Hierarchical iron nickel oxide architectures derived from metal-organic frameworks as efficient electrocatalysts for oxygen evolution reaction. *Electrochimica Acta*, *208*, 17–24. https://doi.org/https://doi.org/10.1016/j.electacta.2016.05.008

Jiang, Juncong, Zhao, Y., & Yaghi, O. M. (2016). Covalent Chemistry beyond Molecules. *Journal of the American Chemical Society*. https://doi.org/10.1021/jacs.5b10666

Jiao, J., Cao, J., Xia, Y., & Zhao, L. (2016). Improvement of adsorbent materials for CO2 capture by amine functionalized mesoporous silica with worm-hole framework structure. *Chemical Engineering Journal*, *306*, 9–16. https://doi.org/https://doi.org/10.1016/j.cej.2016.07.041

Jin, Z., Lu, W., O'Neill, K. J., Parilla, P. A., Simpson, L. J., Kittrell, C., & Tour, J. M. (2011). Nano-Engineered Spacing in Graphene Sheets for Hydrogen Storage. *Chemistry of Materials*, *23*(4), 923–925. https://doi.org/10.1021/cm1025188

Jing, Y., Wei, L., Wang, Y., & Yu, Y. (2014). Synthesis, characterization and CO2 capture of mesoporous SBA-15 adsorbents functionalized with melamine-based and acrylate-based amine dendrimers. *Microporous and Mesoporous Materials*, *183*, 124–133. https://doi.org/https://doi.org/10.1016/j.micromeso.2013.09.008

Jones, C. W. (2011). CO 2 Capture from Dilute Gases as a Component of Modern Global Carbon Management . *Annual Review of Chemical and Biomolecular Engineering*. https://doi.org/10.1146/annurev-chembioeng-061010-114252

Jordá-Beneyto, M., Suárez-García, F., Lozano-Castelló, D., Cazorla-Amorós, D., & Linares-Solano, A. (2007). Hydrogen storage on chemically activated carbons and carbon nanomaterials at high pressures. *Carbon*, *45*(2), 293–303. https://doi.org/https://doi.org/10.1016/j.carbon.2006.09.022

Jung, D.-W., Yang, D.-A., Kim, J., Kim, J., & Ahn, W.-S. (2010). Facile synthesis of MOF-177 by a sonochemical method using 1-methyl-2-pyrrolidinone as a solvent. *Dalton Transactions*, *39*(11), 2883–2887. https://doi.org/10.1039/B925088C

Kabbour, H., Baumann, T. F., Satcher Joe H., Saulnier, A., & Ahn, C. C. (2006). Toward New Candidates for Hydrogen Storage: High-Surface-Area Carbon Aerogels. *Chemistry of Materials*, *18*(26), 6085–6087. https://doi.org/10.1021/cm062329a

Kaliva, M., Armatas, G. S., & Vamvakaki, M. (2012). Microporous Polystyrene Particles for Selective Carbon Dioxide Capture. *Langmuir*, *28*(5), 2690–2695. https://doi.org/10.1021/la204991n

Karoor, S., & Sirkar, K. K. (1993). Gas Absorption Studies in Microporous Hollow Fiber Membrane Modules. *Industrial and Engineering Chemistry Research*. https://doi.org/10.1021/ie00016a014

Kaskun, S., & Kayfeci, M. (2018). The synthesized nickel-doped multi-walled carbon nanotubes for

hydrogen storage under moderate pressures. *International Journal of Hydrogen Energy*, *43*(23), 10773–10778. https://doi.org/10.1016/j.ijhydene.2018.01.084

Kato, S., Tsujita, Y., Yoshimizu, H., Kinoshita, T., & Higgins, J. S. (1997). Characterization and CO2 sorption behaviour of polystyrene/polycarbonate blend system. *Polymer*, *38*(11), 2807–2811. https://doi.org/https://doi.org/10.1016/S0032-3861(97)85618-2

Katz, M. J., Mondloch, J. E., Totten, R. K., Park, J. K., Nguyen, S. T., Farha, O. K., & Hupp, J. T. (2014). Simple and Compelling Biomimetic Metal–Organic Framework Catalyst for the Degradation of Nerve Agent Simulants. *Angewandte Chemie International Edition*, *53*(2), 497–501. https://doi.org/10.1002/anie.201307520

Katz, M. J., Moon, S.-Y., Mondloch, J. E., Beyzavi, M. H., Stephenson, C. J., Hupp, J. T., & Farha, O. K. (2015). Exploiting parameter space in MOFs: a 20-fold enhancement of phosphate-ester hydrolysis with UiO-66-NH2. *Chemical Science*, *6*(4), 2286–2291. https://doi.org/10.1039/C4SC03613A

Kaur, M., & Pal, K. (2016). An investigation for hydrogen storage capability of zirconia-reduced graphene oxide nanocomposite. *International Journal of Hydrogen Energy*, *41*(47), 21861–21869. https://doi.org/https://doi.org/10.1016/j.ijhydene.2016.09.129

Kaye, S. S., Dailly, A., Yaghi, O. M., & Long, J. R. (2007a). Impact of Preparation and Handling on the Hydrogen Storage Properties of Zn4O(1,4-benzenedicarboxylate)3 (MOF-5). *J. Am. Chem. Soc.*, *129*(46), 14176–14177.

Kaye, S. S., Dailly, A., Yaghi, O. M., & Long, J. R. (2007b). Impact of Preparation and Handling on the Hydrogen Storage Properties of Zn4O(1,4-benzenedicarboxylate)3 (MOF-5). *Journal of the American Chemical Society*, *129*(46), 14176–14177. https://doi.org/10.1021/ja076877g

Kaye, S. S., & Long, J. R. (2005). Hydrogen Storage in the Dehydrated Prussian Blue Analogues M3[Co(CN)6]2 (M = Mn, Fe, Co, Ni, Cu, Zn). *Journal of the American Chemical Society*, *127*(18), 6506–6507. https://doi.org/10.1021/ja051168t

Kaye, S. S., & Long, J. R. (2007). Hydrogen adsorption in dehydrated variants of the cyano-bridged framework compounds A2Zn3[Fe(CN)6]2·xH2O (A = H, Li, Na, K, Rb). *Chemical Communications*, (43), 4486–4488. https://doi.org/10.1039/B709082J

Kayiran, S. B., Lamari, F. D., & Levesque, D. (2004). Adsorption Properties and Structural Characterization of Activated Carbons and Nanocarbons. *The Journal of Physical Chemistry B*, *108*(39), 15211–15215. https://doi.org/10.1021/jp048169c

Kesanli, B., Cui, Y., Smith, M. R., Bittner, E. W., Bockrath, B. C., & Lin, W. (2004). Highly interpenetrated metal-organic frameworks for hydrogen storage. *Angewandte Chemie - International Edition*. https://doi.org/10.1002/anie.200461214

Keshavarz, P., Fathikalajahi, J., & Ayatollahi, S. (2008). Analysis of CO2 separation and simulation of a partially wetted hollow fiber membrane contactor. *Journal of Hazardous Materials*, *152*(3), 1237–1247. https://doi.org/https://doi.org/10.1016/j.jhazmat.2007.07.115

Khaisri, S., deMontigny, D., Tontiwachwuthikul, P., & Jiraratananon, R. (2009). Comparing membrane resistance and absorption performance of three different membranes in a gas absorption membrane contactor. *Separation and Purification Technology*, *65*(3), 290–297. https://doi.org/https://doi.org/10.1016/j.seppur.2008.10.035

Khan, N. A., Haque, E., & Jhung, S. H. (2010a). Rapid syntheses of a metal–organic framework material Cu3(BTC)2(H2O)3 under microwave: a quantitative analysis of accelerated syntheses. *Physical*

Chemistry Chemical Physics, *12*(11), 2625–2631. https://doi.org/10.1039/B921558A

Khan, N. A., Haque, M. M., & Jhung, S. H. (2010b). Accelerated Syntheses of Porous Isostructural Lanthanide–Benzenetricarboxylates (Ln–BTC) Under Ultrasound at Room Temperature. *European Journal of Inorganic Chemistry*, *2010*(31), 4975–4981. https://doi.org/10.1002/ejic.201000541

Khan, N. A., & Jhung, S. H. (2009). Facile syntheses of metal-organic framework Cu3(BTC)2(H2O)3 under ultrasound. *Bulletin of the Korean Chemical Society*, *30*(12), 2921–2926. https://doi.org/10.5012/bkcs.2009.30.12.2921

Khan, N. A., Kang, I. J., Seok, H. Y., & Jhung, S. H. (2011). Facile synthesis of nano-sized metal-organic frameworks, chromium-benzenedicarboxylate, MIL-101. *Chemical Engineering Journal*, *166*(3), 1152–1157. https://doi.org/https://doi.org/10.1016/j.cej.2010.11.098

Khoobiar, S. (1964). Particle to Particle Migration of Hydrogen Atoms on Platinum—Alumina Catalysts from Particle to Neighboring Particles. *The Journal of Physical Chemistry*, *68*(2), 411–412. https://doi.org/10.1021/j100784a503

Kierzkowska, A. M., Poulikakos, L. V, Broda, M., & Müller, C. R. (2013). Synthesis of calcium-based, Al2O3-stabilized sorbents for CO2 capture using a co-precipitation technique. *International Journal of Greenhouse Gas Control*, *15*, 48–54. https://doi.org/https://doi.org/10.1016/j.ijggc.2013.01.046

Kikkinides, E. S., Yang, R. T., & Cho, S. H. (1993). Concentration and recovery of carbon dioxide from flue gas by pressure swing adsorption. *Industrial & Engineering Chemistry Research*, *32*(11), 2714–2720. https://doi.org/10.1021/ie00023a038

Kim, B.-J., Cho, K.-S., & Park, S.-J. (2010). Copper oxide-decorated porous carbons for carbon dioxide adsorption behaviors. *Journal of Colloid and Interface Science*, *342*(2), 575–578. https://doi.org/https://doi.org/10.1016/j.jcis.2009.10.045

Kim, D. O., Park, J., Ahn, G. R., Jeon, H. J., Kim, J. S., Kim, D. W., … Shin, S. H. (2011). Synthesis of MOF having functional side group. *Inorganica Chimica Acta*, *370*(1), 76–81. https://doi.org/https://doi.org/10.1016/j.ica.2011.01.030

Kim, J., Yang, S.-T., Choi, S. B., Sim, J., Kim, J., & Ahn, W.-S. (2011). Control of catenation in CuTATB-n metal–organic frameworks by sonochemical synthesis and its effect on CO2 adsorption. *Journal of Materials Chemistry*, *21*(9), 3070–3076. https://doi.org/10.1039/C0JM03318A

Kim, K. C. (2018). A review on design strategies for metal hydrides with enhanced reaction thermodynamics for hydrogen storage applications. *International Journal of Energy Research*, *42*(4), 1455–1468. https://doi.org/10.1002/er.3919

Kim, T. K., Lee, K. J., Yuh, J., Kwak, S. K., & Moon, H. R. (2014). Multi-core MgO NPs@C core–shell nanospheres for selective CO2 capture under mild conditions. *New Journal of Chemistry*, *38*(4), 1606–1610. https://doi.org/10.1039/C4NJ00067F

Kim, Y. E., Lim, J. A., Jeong, S. K., Yoon, Y. Il, Bae, S. T., & Nam, S. C. (2013). Comparison of carbon dioxide absorption in aqueous MEA, DEA, TEA, and AMP solutions. *Bulletin of the Korean Chemical Society*. https://doi.org/10.5012/bkcs.2013.34.3.783

Kitagawa, S., Kitaura, R., & Noro, S. (2004). Functional Porous Coordination Polymers. *Angewandte Chemie International Edition*, *43*(18), 2334–2375. https://doi.org/10.1002/anie.200300610

Kladkaew, N., Idem, R., Tontiwachwuthikul, P., & Saiwan, C. (2011). Studies on corrosion and corrosion inhibitors for amine based solvents for CO2 absorption from power plant flue gases containing CO2,

O2 and SO2. *Energy Procedia*, *4*, 1761–1768. https://doi.org/https://doi.org/10.1016/j.egypro.2011.02.051

Klechikov, A. G., Mercier, G., Merino, P., Blanco, S., Merino, C., & Talyzin, A. V. (2015a). Hydrogen storage in bulk graphene-related materials. *Microporous and Mesoporous Materials*, *210*, 46–51. https://doi.org/10.1016/j.micromeso.2015.02.017

Klechikov, A. G., Mercier, G., Merino, P., Blanco, S., Merino, C., & Talyzin, A. V. (2015b). Hydrogen storage in bulk graphene-related materials. *Microporous and Mesoporous Materials*, *210*, 46–51. https://doi.org/https://doi.org/10.1016/j.micromeso.2015.02.017

Klechikov, A., Mercier, G., Sharifi, T., Baburin, I. A., Seifert, G., & Talyzin, A. V. (2015). Hydrogen storage in high surface area graphene scaffolds. *Chemical Communications*, *51*(83), 15280–15283. https://doi.org/10.1039/c5cc05474e

Klimakow, M., Klobes, P., Thünemann, A. F., Rademann, K., & Emmerling, F. (2010). Mechanochemical Synthesis of Metal−Organic Frameworks: A Fast and Facile Approach toward Quantitative Yields and High Specific Surface Areas. *Chemistry of Materials*, *22*(18), 5216–5221. https://doi.org/10.1021/cm1012119

Klontzas, E, Mavrandonakis, A., Froudakis, Carissan, Y., & Klopper, W. (2007). Molecular Hydrogen Interaction with IRMOF-1: A Multiscale Theoretical Study. *The Journal of Physical Chemistry C*, *111*(36), 13635–13640. https://doi.org/10.1021/jp075420q

Klontzas, Emmanouel, Mavrandonakis, A., Tylianakis, E., & Froudakis, G. E. (2008). Improving Hydrogen Storage Capacity of MOF by Functionalization of the Organic Linker with Lithium Atoms. *Nano Letters*, *8*(6), 1572–1576. https://doi.org/10.1021/nl072941g

Klontzas, Emmanouel, Tylianakis, E., & Froudakis, G. E. (2008). Hydrogen Storage in 3D Covalent Organic Frameworks. A Multiscale Theoretical Investigation. *The Journal of Physical Chemistry C*, *112*(24), 9095–9098. https://doi.org/10.1021/jp711326g

Klyamkin, S. N., Chuvikov, S. V., Maletskaya, N. V., Kogan, E. V., Fedin, V. P., Kovalenko, K. A., & Dybtsev, D. N. (2014). High-pressure hydrogen storage on modified MIL-101 metal–organic framework. *International Journal of Energy Research*, *38*, 1562–1570. https://doi.org/10.1002/er.3175

Knowles, G. P., Delaney, S. W., & Chaffee, A. L. (2006). Diethylenetriamine[propyl(silyl)]-Functionalized (DT) Mesoporous Silicas as CO2 Adsorbents. *Industrial & Engineering Chemistry Research*, *45*(8), 2626–2633. https://doi.org/10.1021/ie050589g

Ko, Y. G., Lee, H. J., Oh, H. C., & Choi, U. S. (2013). Amines immobilized double-walled silica nanotubes for CO2 capture. *Journal of Hazardous Materials*, *250–251*, 53–60. https://doi.org/https://doi.org/10.1016/j.jhazmat.2013.01.035

Kohl, A. L., & Nielsen, R. B. (1997). Gas purification 5th ed. *Houston: Gulf Publishing Company*. https://doi.org/10.1016/B978-088415220-0/50009-4

Kong, X.-J., Lin, Z., Zhang, Z.-M., Zhang, T., & Lin, W. (2016). Hierarchical Integration of Photosensitizing Metal–Organic Frameworks and Nickel-Containing Polyoxometalates for Efficient Visible-Light-Driven Hydrogen Evolution. *Angewandte Chemie International Edition*, *55*(22), 6411–6416. https://doi.org/10.1002/anie.201600431

Kong, Y., Jin, L., & Qiu, J. (2013). Synthesis, characterization, and CO2 capture study of micro-nano carbonaceous composites. *Science of The Total Environment*, *463–464*, 192–198. https://doi.org/https://doi.org/10.1016/j.scitotenv.2013.05.050

Kostoglou, N., Tarat, A., Walters, I., Ryzhkov, V., Tampaxis, C., Charalambopoulou, G., … Rebholz, C. (2016). Few-layer graphene-like flakes derived by plasma treatment: A potential material for hydrogen adsorption and storage. *Microporous and Mesoporous Materials*, *225*, 482–487. https://doi.org/https://doi.org/10.1016/j.micromeso.2016.01.027

Kreulen, H., Smolders, C. A., Versteeg, G. F., & van Swaaij, W. P. M. (1993). Microporous hollow fibre membrane modules as gas-liquid contactors Part 2. Mass transfer with chemical reaction. *Journal of Membrane Science*, *78*(3), 217–238. https://doi.org/https://doi.org/10.1016/0376-7388(93)80002-F

Kumar, P. S., Hogendoorn, J. A., Feron, P. H. M., & Versteeg, G. F. (2002). New absorption liquids for the removal of CO2 from dilute gas streams using membrane contactors. *Chemical Engineering Science*, *57*(9), 1639–1651. https://doi.org/https://doi.org/10.1016/S0009-2509(02)00041-6

Kuramoto, K., Fujimoto, S., Morita, A., Shibano, S., Suzuki, Y., Hatano, H., … Takarada, T. (2003). Repetitive Carbonation−Calcination Reactions of Ca-Based Sorbents for Efficient CO2 Sorption at Elevated Temperatures and Pressures. *Industrial & Engineering Chemistry Research*, *42*(5), 975–981. https://doi.org/10.1021/ie0207111

Lachawiec, A. J., Qi, G., & Yang, R. T. (2005). Hydrogen Storage in Nanostructured Carbons by Spillover: Bridge-Building Enhancement. *Langmuir*, *21*(24), 11418–11424. https://doi.org/10.1021/la051659r

Langmi, H W, Walton, A., Al-Mamouri, M. M., Johnson, S. R., Book, D., Speight, J. D., … Harris, I. R. (2003). Hydrogen adsorption in zeolites A, X, Y and RHO. *Journal of Alloys and Compounds*, *356–357*, 710–715. https://doi.org/https://doi.org/10.1016/S0925-8388(03)00368-2

Langmi, Henrietta W, Ren, J., North, B., Mathe, M., & Bessarabov, D. (2014). Hydrogen Storage in Metal-Organic Frameworks: A Review. *Electrochimica Acta*, *128*, 368–392. https://doi.org/https://doi.org/10.1016/j.electacta.2013.10.190

Langmi, Henrietta W, Ren, J., North, B., Mathe, M., & Bessarabov, D. (2017). Electrochimica Acta Hydrogen Storage in Metal-Organic Frameworks : A Review. *Africa*, *128*(2014), 368–392. https://doi.org/10.1016/j.electacta.2013.10.190

Latroche, M., Surblé, S., Serre, C., Mellot-Draznieks, C., Llewellyn, P. L., Lee, J.-H., … Férey, G. (2006). Hydrogen Storage in the Giant-Pore Metal–Organic Frameworks MIL-100 and MIL-101. *Angewandte Chemie International Edition*, *45*(48), 8227–8231. https://doi.org/10.1002/anie.200600105

Latroche, M., Surblé, S., Serre, C., Mellot-Draznieks, C., Llewellyn, P. L., Lee, J. H., … Férey, G. (2006a). Hydrogen storage in the giant-pore metal-organic frameworks MIL-100 and MIL-101. *Angewandte Chemie - International Edition*, *45*(48), 8227–8231. https://doi.org/10.1002/anie.200600105

Latroche, M., Surblé, S., Serre, C., Mellot-Draznieks, C., Llewellyn, P. L., Lee, J. H., … Férey, G. (2006b). Hydrogen storage in the giant-pore metal-organic frameworks MIL-100 and MIL-101. *Angewandte Chemie - International Edition*, *45*(48), 8227–8231. https://doi.org/10.1002/anie.200600105

Leal, O., Bolívar, C., Ovalles, C., García, J. J., & Espidel, Y. (1995). Reversible adsorption of carbon dioxide on amine surface-bonded silica gel. *Inorganica Chimica Acta*, *240*(1), 183–189. https://doi.org/https://doi.org/10.1016/0020-1693(95)04534-1

Leci, C. L. (1996). Financial implications on power generation costs resulting from the parasitic effect of CO2 capture using liquid scrubbing technology from power station flue gases. *Energy Conversion and Management*, *37*(6), 915–921. https://doi.org/https://doi.org/10.1016/0196-8904(95)00277-4

Leclerc, H., Devic, T., Devautour-Vinot, S., Bazin, P., Audebrand, N., Férey, G., … Clet, G. (2011). Influence of the oxidation state of the metal center on the flexibility and adsorption properties of a

porous metal organic framework: MIL-47(V). *Journal of Physical Chemistry C*, *115*(40), 19828–19840. https://doi.org/10.1021/jp206655y

Lee, J. B., Ryu, C. K., Baek, J.-I., Lee, J. H., Eom, T. H., & Kim, S. H. (2008). Sodium-Based Dry Regenerable Sorbent for Carbon Dioxide Capture from Power Plant Flue Gas. *Industrial & Engineering Chemistry Research*, *47*(13), 4465–4472. https://doi.org/10.1021/ie0709638

Lee, J. S., Halligudi, S. B., Jang, N. H., Hwang, D. W., Chang, J. S., & Hwang, Y. K. (2010). Microwave synthesis of a porous metal-organic framework, nickel(II) dihydroxyterephthalate and its catalytic properties in oxidation of cyclohexene. *Bulletin of the Korean Chemical Society*, *31*(6), 1489–1495. https://doi.org/10.5012/bkcs.2010.31.6.1489

Lee, J. Y., Olson, D. H., Pan, L., Emge, T. J., & Li, J. (2007). Microporous Metal–Organic Frameworks with High Gas Sorption and Separation Capacity. *Advanced Functional Materials*, *17*(8), 1255–1262. https://doi.org/10.1002/adfm.200600944

Lee, Jeongyong, Farha, O. K., Roberts, J., Scheidt, K. A., Nguyen, S. T., & Hupp, J. T. (2009). Metal-organic framework materials as catalysts. *Chemical Society Reviews*, *38*(5), 1450–1459. https://doi.org/10.1039/b807080f

Lee, JeongYong, Farha, O. K., Roberts, J., Scheidt, K. A., Nguyen, S. T., & Hupp, J. T. (2009). Metal–organic framework materials as catalysts. *Chemical Society Reviews*, *38*(5), 1450–1459. https://doi.org/10.1039/B807080F

Lee, K.-M., Lim, Y.-H., & Jo, Y.-M. (2012). Evaluation of moisture effect on low-level CO2 adsorption by ion-exchanged zeolite. *Environmental Technology*, *33*(1), 77–84. https://doi.org/10.1080/09593330.2011.551837

Lee, K.-M., Lim, Y.-H., Park, C.-J., & Jo, Y.-M. (2012). Adsorption of Low-Level CO2 Using Modified Zeolites and Activated Carbon. *Industrial & Engineering Chemistry Research*, *51*(3), 1355–1363. https://doi.org/10.1021/ie2013532

Lee, S.-Y., & Park, S.-J. (2011). Effect of platinum doping of activated carbon on hydrogen storage behaviors of metal-organic frameworks-5. *International Journal of Hydrogen Energy*, *36*(14), 8381–8387. https://doi.org/https://doi.org/10.1016/j.ijhydene.2011.03.038

Lee, S.-Y., & Park, S.-J. (2013). Determination of the optimal pore size for improved CO2 adsorption in activated carbon fibers. *Journal of Colloid and Interface Science*, *389*(1), 230–235. https://doi.org/https://doi.org/10.1016/j.jcis.2012.09.018

Lee, S. C., Chae, H. J., Lee, S. J., Park, Y. H., Ryu, C. K., Yi, C. K., & Kim, J. C. (2009). Novel regenerable potassium-based dry sorbents for CO2 capture at low temperatures. *Journal of Molecular Catalysis B: Enzymatic*, *56*(2), 179–184. https://doi.org/https://doi.org/10.1016/j.molcatb.2008.07.007

Lee, S. C., Choi, B. Y., Ryu, C. K., Ahn, Y. S., Lee, T. J., & Kim, J. C. (2006). The effect of water on the activation and the CO2 capture capacities of alkali metal-based sorbents. *Korean Journal of Chemical Engineering*, *23*(3), 374–379. https://doi.org/10.1007/BF02706737

Leliveld, R. G., Ros, T. G., van Dillen, A. J., Geus, J. W., & Koningsberger, D. C. (1999). Influence of Si/Al Ratio on Catalytic Performance of (Co)Mo/Saponite Catalysts. *Journal of Catalysis*, *185*(2), 513–523. https://doi.org/https://doi.org/10.1006/jcat.1999.2529

Lepaumier, H., Picq, D., & Carrette, P. L. (2009). Degradation study of new solvents for CO2 capture in post-combustion. In *Energy Procedia*. https://doi.org/10.1016/j.egypro.2009.01.119

Li, J. L., & Chen, B. H. (2005). Review of CO2 absorption using chemical solvents in hollow fiber membrane contactors. *Separation and Purification Technology*. https://doi.org/10.1016/j.seppur.2004.09.008

Li, J. R., Kuppler, R. J., & Zhou, H. C. (2009). Selective gas adsorption and separation in metal-organic frameworks. *Chemical Society Reviews*, *38*(5), 1477–1504. https://doi.org/10.1039/b802426j

Li, J. R., Ma, Y., McCarthy, M. C., Sculley, J., Yu, J., Jeong, H. K., … Zhou, H. C. (2011). Carbon dioxide capture-related gas adsorption and separation in metal-organic frameworks. *Coordination Chemistry Reviews*, *255*(15–16), 1791–1823. https://doi.org/10.1016/j.ccr.2011.02.012

Li, Lei, Wen, X., Fu, X., Wang, F., Zhao, N., Xiao, F., … Sun, Y. (2010). MgO/Al2O3 Sorbent for CO2 Capture. *Energy & Fuels*, *24*(10), 5773–5780. https://doi.org/10.1021/ef100817f

Li, Liyu, King, D. L., Nie, Z., & Howard, C. (2009). Magnesia-Stabilized Calcium Oxide Absorbents with Improved Durability for High Temperature CO2 Capture. *Industrial & Engineering Chemistry Research*, *48*(23), 10604–10613. https://doi.org/10.1021/ie901166b

Li, P., & Handan Tezel, F. (2007). Adsorption separation of N2, O2, CO2 and CH4 gases by β-zeolite. *Microporous and Mesoporous Materials*, *98*(1), 94–101. https://doi.org/https://doi.org/10.1016/j.micromeso.2006.08.016

Li, T., Sullivan, J. E., & Rosi, N. L. (2013). Design and Preparation of a Core–Shell Metal–Organic Framework for Selective CO2 Capture. *Journal of the American Chemical Society*, *135*(27), 9984–9987. https://doi.org/10.1021/ja403008j

Li, Wei, Jin, X., Huang, F., & Chen, G. Z. (2010). Metal-to-Oxide Molar Volume Ratio: The Overlooked Barrier to Solid-State Electroreduction and a “Green” Bypass through Recyclable NH4HCO3. *Angewandte Chemie International Edition*, *49*(18), 3203–3206. https://doi.org/10.1002/anie.200906833

Li, Wenliang, Shi, H., & Zhang, J. (2014). From Molecules to Materials: Computational Design of N-Containing Porous Aromatic Frameworks for CO2 Capture. *ChemPhysChem*, *15*(9), 1772–1778. https://doi.org/10.1002/cphc.201400064

Li, Y. Y., Han, K. K., Lin, W. G., Wan, M. M., Wang, Y., & Zhu, J. H. (2013). Fabrication of a new MgO/C sorbent for CO2 capture at elevated temperature. *Journal of Materials Chemistry A*, *1*(41), 12919–12925. https://doi.org/10.1039/C3TA12261A

Li, Ye, Wang, L. J., Fan, H. L., Shangguan, J., Wang, H., & Mi, J. (2015). Removal of sulfur compounds by a copper-based metal organic framework under ambient conditions. *Energy and Fuels*, *29*(1), 298–304. https://doi.org/10.1021/ef501918f

Li, Yingjie, Zhao, C., Chen, H., Duan, L., & Chen, X. (2010). Cyclic CO2 capture behavior of KMnO4-doped CaO-based sorbent. *Fuel*, *89*(3), 642–649. https://doi.org/https://doi.org/10.1016/j.fuel.2009.08.041

Li, Yingwei, Yang, F. H., & Yang, R. T. (2007). Kinetics and Mechanistic Model for Hydrogen Spillover on Bridged Metal−Organic Frameworks. *The Journal of Physical Chemistry C*, *111*(8), 3405–3411. https://doi.org/10.1021/jp065367q

Li, Yingwei, & Yang, R. T. (2006a). Hydrogen Storage in Metal−Organic Frameworks by Bridged Hydrogen Spillover. *Journal of the American Chemical Society*, *128*(25), 8136–8137. https://doi.org/10.1021/ja061681m

Li, Yingwei, & Yang, R. T. (2006b). Significantly Enhanced Hydrogen Storage in Metal−Organic Frameworks via Spillover. *Journal of the American Chemical Society*, *128*(3), 726–727.

https://doi.org/10.1021/ja056831s

Li, Yingwei, & Yang, R. T. (2007). Gas Adsorption and Storage in Metal−Organic Framework MOF-177. *Langmuir*, *23*(26), 12937–12944. https://doi.org/10.1021/la702466d

Li, Yingwei, & Yang, R. T. (2008). Hydrogen storage in metal-organic and covalent-organic frameworks by spillover. *AIChE Journal*, *54*(1), 269–279. https://doi.org/10.1002/aic.11362

Li, Z.-Q., Qiu, L.-G., Xu, T., Wu, Y., Wang, W., Wu, Z.-Y., & Jiang, X. (2009). Ultrasonic synthesis of the microporous metal–organic framework Cu3(BTC)2 at ambient temperature and pressure: An efficient and environmentally friendly method. *Materials Letters*, *63*(1), 78–80. https://doi.org/https://doi.org/10.1016/j.matlet.2008.09.010

Li, Z., Cai, N., Huang, Y., & Han, H. (2005). Synthesis, Experimental Studies, and Analysis of a New Calcium-Based Carbon Dioxide Absorbent. *Energy & Fuels*, *19*(4), 1447–1452. https://doi.org/10.1021/ef0496799

Liang, Y., Harrison, D. P., Gupta, R. P., Green, D. A., & McMichael, W. J. (2004). Carbon Dioxide Capture Using Dry Sodium-Based Sorbents. *Energy & Fuels*, *18*(2), 569–575. https://doi.org/10.1021/ef030158f

Liang, Z., Marshall, M., & Chaffee, A. L. (2009). Comparison of Cu-BTC and zeolite 13X for adsorbent based CO2 separation. *Energy Procedia*, *1*(1), 1265–1271. https://doi.org/https://doi.org/10.1016/j.egypro.2009.01.166

Liebl, M. R., & Senker, J. (2013). Microporous Functionalized Triazine-Based Polyimides with High CO2 Capture Capacity. *Chemistry of Materials*, *25*(6), 970–980. https://doi.org/10.1021/cm4000894

Lim, D.-W., Yoon, J. W., Ryu, K. Y., & Suh, M. P. (2012). Magnesium Nanocrystals Embedded in a Metal–Organic Framework: Hybrid Hydrogen Storage with Synergistic Effect on Physi- and Chemisorption. *Angewandte Chemie International Edition*, *51*(39), 9814–9817. https://doi.org/10.1002/anie.201206055

Lim, H., Cha, M. C., & Chang, J. Y. (2012). Preparation of Microporous Polymers Based on 1,3,5-Triazine Units Showing High CO2 Adsorption Capacity. *Macromolecular Chemistry and Physics*, *213*(13), 1385–1390. https://doi.org/10.1002/macp.201200195

Lin, L.-Y., Kuo, J.-T., & Bai, H. (2011). Silica materials recovered from photonic industrial waste powder: Its extraction, modification, characterization and application. *Journal of Hazardous Materials*, *192*(1), 255–262. https://doi.org/https://doi.org/10.1016/j.jhazmat.2011.05.011

Lin, Q., Bu, X., Kong, A., Mao, C., Zhao, X., Bu, F., & Feng, P. (2015). New Heterometallic Zirconium Metalloporphyrin Frameworks and Their Heteroatom-Activated High-Surface-Area Carbon Derivatives. *Journal of the American Chemical Society*, *137*(6), 2235–2238. https://doi.org/10.1021/jacs.5b00076

Lin, S.-H., Chiang, P.-C., Hsieh, C.-F., Li, M.-H., & Tung, K.-L. (2008). Absorption of carbon dioxide by the absorbent composed of piperazine and 2-amino-2-methyl-1-propanol in PVDF membrane contactor. *Journal of the Chinese Institute of Chemical Engineers*, *39*(1), 13–21. https://doi.org/https://doi.org/10.1016/j.jcice.2007.11.010

Lin, S.-H., Hsieh, C.-F., Li, M.-H., & Tung, K.-L. (2009). Determination of mass transfer resistance during absorption of carbon dioxide by mixed absorbents in PVDF and PP membrane contactor. *Desalination*, *249*(2), 647–653. https://doi.org/https://doi.org/10.1016/j.desal.2008.08.019

Lin, S.-H., Tung, K.-L., Chen, W.-J., & Chang, H.-W. (2009). Absorption of carbon dioxide by mixed

piperazine–alkanolamine absorbent in a plasma-modified polypropylene hollow fiber contactor. *Journal of Membrane Science*, *333*(1), 30–37. https://doi.org/https://doi.org/10.1016/j.memsci.2009.01.039

Lin, X., Jia, J., Hubberstey, P., Schröder, M., & Champness, N. R. (2007). Hydrogen storage in metal–organic frameworks. *CrystEngComm*, *9*(6), 438–448. https://doi.org/10.1039/B706207A

Lin, X., Jia, J., Zhao, X., Thomas, K. M., Blake, A. J., Walker, G. S., … Schröder, M. (2006). High H2 Adsorption by Coordination-Framework Materials. *Angewandte Chemie International Edition*, *45*(44), 7358–7364. https://doi.org/10.1002/anie.200601991

Lin, Y., Yan, Q., Kong, C., & Chen, L. (2013). Polyethyleneimine Incorporated Metal-Organic Frameworks Adsorbent for Highly Selective CO2 Capture. *Scientific Reports*, *3*(1), 1859. https://doi.org/10.1038/srep01859

Liu, B., Zou, R.-Q., Zhong, R.-Q., Han, S., Shioyama, H., Yamada, T., … Xu, Q. (2008). Microporous coordination polymers of cobalt(II) and manganese(II) 2,6-naphthalenedicarboxylate: preparations, structures and gas sorptive and magnetic properties. *Microporous and Mesoporous Materials*, *111*(1), 470–477. https://doi.org/https://doi.org/10.1016/j.micromeso.2007.08.024

Liu, C, Fan, Y. Y., Liu, M., Cong, H. T., Cheng, H. M., & Dresselhaus, M. S. (1999). Hydrogen Storage in Single-Walled Carbon Nanotubes at Room Temperature. *Science*, *286*(5442), 1127 LP – 1129. https://doi.org/10.1126/science.286.5442.1127

Liu, Chong, Li, T., & Rosi, N. L. (2012). Strain-Promoted "Click" Modification of a Mesoporous Metal–Organic Framework. *Journal of the American Chemical Society*, *134*(46), 18886–18888. https://doi.org/10.1021/ja307713q

Liu, F.-Q., Li, W.-H., Liu, B.-C., & Li, R.-X. (2013). Synthesis, characterization, and high temperature CO2 capture of new CaO based hollow sphere sorbents. *Journal of Materials Chemistry A*, *1*(27), 8037–8044. https://doi.org/10.1039/C3TA11369H

Liu, H.-K., Tsao, T.-H., Zhang, Y.-T., & Lin, C.-H. (2009). Microwave synthesis and single-crystal-to-single-crystal transformation of magnesium coordination polymers exhibiting selective gas adsorption and luminescence properties. *CrystEngComm*, *11*(7), 1462–1468. https://doi.org/10.1039/B819559E

Liu, J.-L., & Lin, R.-B. (2013). Structural properties and reactivities of amino-modified silica fume solid sorbents for low-temperature CO2 capture. *Powder Technology*, *241*, 188–195. https://doi.org/https://doi.org/10.1016/j.powtec.2013.03.022

Liu, Jiewei, Chen, L., Cui, H., Zhang, J., Zhang, L., & Su, C. Y. (2014). Applications of metal-organic frameworks in heterogeneous supramolecular catalysis. *Chemical Society Reviews*, *43*(16), 6011–6061. https://doi.org/10.1039/c4cs00094c

Liu, Jinchen, Culp, J. T., Natesakhawat, S., Bockrath, B. C., Zande, B., Sankar, S. G., … Johnson, J. K. (2007). Experimental and Theoretical Studies of Gas Adsorption in Cu3(BTC)2: An Effective Activation Procedure. *The Journal of Physical Chemistry C*, *111*(26), 9305–9313. https://doi.org/10.1021/jp071449i

Liu, Jinchen, Lee, J. Y., Pan, L., Obermyer, R. T., Simizu, S., Zande, B., … Johnson, J. K. (2008). Adsorption and Diffusion of Hydrogen in a New Metal−Organic Framework Material: [Zn(bdc)(ted)0.5]. *The Journal of Physical Chemistry C*, *112*(8), 2911–2917. https://doi.org/10.1021/jp710011b

Liu, T., Zhang, Y., Hou, J., Lu, S., Jiang, J., & Xu, M. (2015). High performance mesoporous C@Se

composite cathodes derived from Ni-based MOFs for Li–Se batteries. *RSC Advances*, *5*(102), 84038–84043. https://doi.org/10.1039/C5RA14979G

Liu, W.-J., Jiang, H., Tian, K., Ding, Y.-W., & Yu, H.-Q. (2013). Mesoporous Carbon Stabilized MgO Nanoparticles Synthesized by Pyrolysis of MgCl2 Preloaded Waste Biomass for Highly Efficient CO2 Capture. *Environmental Science & Technology*, *47*(16), 9397–9403. https://doi.org/10.1021/es401286p

Liu, W., Low, N. W. L., Feng, B., Wang, G., & Diniz da Costa, J. C. (2010). Calcium Precursors for the Production of CaO Sorbents for Multicycle CO2 Capture. *Environmental Science & Technology*, *44*(2), 841–847. https://doi.org/10.1021/es902426n

Liu, X., Shen, Z. Q., Xiong, H. H., Chen, Y., Wang, X. N., Li, H. Q., … Tian, Y. Q. (2015). Hierarchical porous materials based on nanoscale metal-organic frameworks dominated with permanent interparticle porosity. *Microporous and Mesoporous Materials*, *204*(C), 25–33. https://doi.org/10.1016/j.micromeso.2014.11.005

Liu, Y.-Y., Zeng, J.-L., Zhang, J., Xu, F., & Sun, L.-X. (2007). Improved hydrogen storage in the modified metal-organic frameworks by hydrogen spillover effect. *International Journal of Hydrogen Energy*, *32*(16), 4005–4010. https://doi.org/https://doi.org/10.1016/j.ijhydene.2007.04.029

Llewellyn, P. L., Bourrelly, S., Serre, C., Vimont, A., Daturi, M., Hamon, L., … Férey, G. (2008). High Uptakes of CO2 and CH4 in Mesoporous Metal—Organic Frameworks MIL-100 and MIL-101. *Langmuir*, *24*(14), 7245–7250. https://doi.org/10.1021/la800227x

Lochan, R. C., & Head-Gordon, M. (2006). Computational studies of molecular hydrogen binding affinities: The role of dispersion forces, electrostatics, and orbital interactions. *Physical Chemistry Chemical Physics*, *8*(12), 1357–1370. https://doi.org/10.1039/B515409J

Lochan, R. C., Khaliullin, R. Z., & Head-Gordon, M. (2008). Interaction of Molecular Hydrogen with Open Transition Metal Centers for Enhanced Binding in Metal-Organic Frameworks: A Computational Study. *Inorganic Chemistry*, *47*(10), 4032–4044. https://doi.org/10.1021/ic701625g

Loiseau, T., Lecroq, L., Volkringer, C., Marrot, J., Férey, G., Haouas, M., … Latroche, M. (2006). MIL-96, a porous aluminum trimesate 3D structure constructed from a hexagonal network of 18-membered rings and μ3-oxo-centered trinuclear units. *Journal of the American Chemical Society*, *128*(31), 10223–10230. https://doi.org/10.1021/ja0621086

López-Maya, E., Montoro, C., Rodríguez-Albelo, L. M., Aznar Cervantes, S. D., Lozano-Pérez, A. A., Cenís, J. L., … Navarro, J. A. R. (2015). Textile/Metal–Organic-Framework Composites as Self-Detoxifying Filters for Chemical-Warfare Agents. *Angewandte Chemie International Edition*, *54*(23), 6790–6794. https://doi.org/10.1002/anie.201502094

Lototskyy, M. V, Tolj, I., Davids, M. W., Klochko, Y. V, Parsons, A., Swanepoel, D., … Linkov, V. (2016). Metal hydride hydrogen storage and supply systems for electric forklift with low-temperature proton exchange membrane fuel cell power module. *International Journal of Hydrogen Energy*, *41*(31), 13831–13842. https://doi.org/https://doi.org/10.1016/j.ijhydene.2016.01.148

Lowell, S., Shields, J. E., Thomas, M. A., & Thommes, M. (2004a). *Characterisation of Porous Solids and Powders*. *Springer Netherlands*. https://doi.org/10.1007/978-1-4020-2303-3

Lowell, S., Shields, J. E., Thomas, M. A., & Thommes, M. (2004b). *Characterisation of Porous Solids and Powders*. *Springer Netherlands*. https://doi.org/10.1007/978-1-4020-2303-3

Lozinska, M. M., Mangano, E., Mowat, J. P. S., Shepherd, A. M., Howe, R. F., Thompson, S. P., … Wright, P. A. (2012). Understanding Carbon Dioxide Adsorption on Univalent Cation Forms of the Flexible

Zeolite Rho at Conditions Relevant to Carbon Capture from Flue Gases. *Journal of the American Chemical Society*, *134*(42), 17628–17642. https://doi.org/10.1021/ja3070864

Lu, C.-M., Liu, J., Xiao, K., & Harris, A. T. (2010). Microwave enhanced synthesis of MOF-5 and its CO2 capture ability at moderate temperatures across multiple capture and release cycles. *Chemical Engineering Journal*, *156*(2), 465–470. https://doi.org/https://doi.org/10.1016/j.cej.2009.10.067

Lu, J.-G., Ji, Y., Zhang, H., & Chen, M.-D. (2010). CO2 Capture Using Activated Amino Acid Salt Solutions in a Membrane Contactor. *Separation Science and Technology*, *45*(9), 1240–1251. https://doi.org/10.1080/01496391003775865

Lu, J.-G., Zheng, Y.-F., & Cheng, M.-D. (2008). Wetting mechanism in mass transfer process of hydrophobic membrane gas absorption. *Journal of Membrane Science*, *308*(1), 180–190. https://doi.org/https://doi.org/10.1016/j.memsci.2007.09.051

Lu, W., Sculley, J. P., Yuan, D., Krishna, R., & Zhou, H.-C. (2013). Carbon Dioxide Capture from Air Using Amine-Grafted Porous Polymer Networks. *The Journal of Physical Chemistry C*, *117*(8), 4057–4061. https://doi.org/10.1021/jp311512q

Lu, Wang, Sun, Li, & Liu. (2005). Absorption of CO2 into Aqueous Solutions of Methyldiethanolamine and Activated Methyldiethanolamine from a Gas Mixture in a Hollow Fiber Contactor. *Industrial & Engineering Chemistry Research*, *44*(24), 9230–9238. https://doi.org/10.1021/ie058023f

Lueking, A., & Yang, R. T. (2003). Hydrogen storage in carbon nanotubes: Residual metal content and pretreatment temperature. *AIChE Journal*, *49*(6), 1556–1568. https://doi.org/10.1002/aic.690490619

Luo, C., Zheng, Y., Ding, N., Wu, Q., Bian, G., & Zheng, C. (2010). Development and Performance of CaO/La2O3 Sorbents during Calcium Looping Cycles for CO2 Capture. *Industrial & Engineering Chemistry Research*, *49*(22), 11778–11784. https://doi.org/10.1021/ie1012745

Luo, W., Guo, D., Zheng, J., Gao, S., & Chen, J. (2016). CO2 absorption using biphasic solvent: Blends of diethylenetriamine, sulfolane, and water. *International Journal of Greenhouse Gas Control*. https://doi.org/10.1016/j.ijggc.2016.07.036

Luo, X., Guo, Y., Ding, F., Zhao, H., Cui, G., Li, H., & Wang, C. (2014). Significant Improvements in CO2 Capture by Pyridine-Containing Anion-Functionalized Ionic Liquids through Multiple-Site Cooperative Interactions. *Angewandte Chemie International Edition*, *53*(27), 7053–7057. https://doi.org/10.1002/anie.201400957

Luo, Y., Li, B., Liang, L., & Tan, B. (2011). Synthesis of cost-effective porous polyimides and their gas storage properties. *Chemical Communications*, *47*(27), 7704–7706. https://doi.org/10.1039/C1CC11466B

Luo, Y., Li, B., Wang, W., Wu, K., & Tan, B. (2012). Hypercrosslinked Aromatic Heterocyclic Microporous Polymers: A New Class of Highly Selective CO2 Capturing Materials. *Advanced Materials*, *24*(42), 5703–5707. https://doi.org/10.1002/adma.201202447

Luzan, S. M., & Talyzin, A. V. (2010). Hydrogen adsorption in Pt catalyst/MOF-5 materials. *Microporous and Mesoporous Materials*, *135*(1), 201–205. https://doi.org/https://doi.org/10.1016/j.micromeso.2010.07.018

Lykourinou, V., Chen, Y., Wang, X.-S., Meng, L., Hoang, T., Ming, L.-J., … Ma, S. (2011). Immobilization of MP-11 into a Mesoporous Metal–Organic Framework, MP-11@mesoMOF: A New Platform for Enzymatic Catalysis. *Journal of the American Chemical Society*, *133*(27), 10382–10385. https://doi.org/10.1021/ja2038003

Ma'mun, S., Svendsen, H. F., Hoff, K. A., & Juliussen, O. (2007). Selection of new absorbents for carbon dioxide capture. *Energy Conversion and Management*, *48*(1), 251–258. https://doi.org/https://doi.org/10.1016/j.enconman.2006.04.007

Ma, Shengqian, Sun, D., Ambrogio, M., Fillinger, J. A., Parkin, S., & Zhou, H.-C. (2007). Framework-Catenation Isomerism in Metal−Organic Frameworks and Its Impact on Hydrogen Uptake. *Journal of the American Chemical Society*, *129*(7), 1858–1859. https://doi.org/10.1021/ja067435s

Ma, Shuangchen, Chen, G., Zhu, S., Wen, J., Gao, R., Ma, L., & Chai, J. (2016). Experimental study of mixed additive of Ni(II) and piperazine on ammonia escape in CO2 capture using ammonia solution. *Applied Energy*. https://doi.org/10.1016/j.apenergy.2016.02.070

Ma, Xiaoliang, Wang, X., & Song, C. (2009). "Molecular Basket" Sorbents for Separation of CO2 and H2S from Various Gas Streams. *Journal of the American Chemical Society*, *131*(16), 5777–5783. https://doi.org/10.1021/ja8074105

Ma, Xiaoyu, Cao, M., & Hu, C. (2013). Bifunctional HNO3 catalytic synthesis of N-doped porous carbons for CO2 capture. *Journal of Materials Chemistry A*, *1*(3), 913–918. https://doi.org/10.1039/C2TA00104G

Mahata, P., Mahata, P., Prabu, M., Prabu, M., Natarajan, S., & Natarajan, S. (2008). Role of Temperature and Time in the Formation of In nite. *Inorganic Chemistry*, *47*(19), 8451–8463.

Majano, G., Ingold, O., Yulikov, M., Jeschke, G., & Pérez-Ramírez, J. (2013). Room-temperature synthesis of Fe-BTC from layered iron hydroxides: The influence of precursor organisation. *CrystEngComm*, *15*(46), 9885–9892. https://doi.org/10.1039/c3ce41366g

Malek, A., Li, K., & Teo, W. K. (1997). Modeling of Microporous Hollow Fiber Membrane Modules Operated under Partially Wetted Conditions. *Industrial and Engineering Chemistry Research*. https://doi.org/10.1021/ie960529y

Mallick, A., Saha, S., Pachfule, P., Roy, S., & Banerjee, R. (2010). Selective CO2 and H2 adsorption in a chiral magnesium-based metal organic framework (Mg-MOF) with open metal sites. *Journal of Materials Chemistry*, *20*(41), 9073–9080. https://doi.org/10.1039/c0jm01125h

Mandal, B. P., & Bandyopadhyay, S. S. (2005). Simultaneous absorption of carbon dioxide and hydrogen sulfide into aqueous blends of 2-amino-2-methyl-1-propanol and diethanolamine. In *Chemical Engineering Science*. https://doi.org/10.1016/j.ces.2005.02.044

Manovic, V., & Anthony, E. J. (2010). CO2 Carrying Behavior of Calcium Aluminate Pellets under High-Temperature/High-CO2 Concentration Calcination Conditions. *Industrial & Engineering Chemistry Research*, *49*(15), 6916–6922. https://doi.org/10.1021/ie901795e

Mansourizadeh, A., & Ismail, A. F. (2009). Hollow fiber gas-liquid membrane contactors for acid gas capture: A review. *Journal of Hazardous Materials*. https://doi.org/10.1016/j.jhazmat.2009.06.026

Mansourizadeh, A, & Ismail, A. F. (2010). Effect of LiCl concentration in the polymer dope on the structure and performance of hydrophobic PVDF hollow fiber membranes for CO2 absorption. *Chemical Engineering Journal*, *165*(3), 980–988. https://doi.org/https://doi.org/10.1016/j.cej.2010.10.034

Mansourizadeh, A, Ismail, A. F., & Matsuura, T. (2010). Effect of operating conditions on the physical and chemical CO2 absorption through the PVDF hollow fiber membrane contactor. *Journal of Membrane Science*, *353*(1), 192–200. https://doi.org/https://doi.org/10.1016/j.memsci.2010.02.054

Mansourizadeh, Amir. (2012). Experimental study of CO2 absorption/stripping via PVDF hollow fiber

membrane contactor. *Chemical Engineering Research and Design*, *90*(4), 555–562. https://doi.org/https://doi.org/10.1016/j.cherd.2011.08.017

Mansourizadeh, Amir, & Ismail, A. F. (2011). A developed asymmetric PVDF hollow fiber membrane structure for CO2 absorption. *International Journal of Greenhouse Gas Control*, *5*(2), 374–380. https://doi.org/https://doi.org/10.1016/j.ijggc.2010.09.007

Mao, S. S., & Chen, X. (2007). Selected nanotechnologies for renewable energy applications. *International Journal of Energy Research*, *31*, 619–636. https://doi.org/10.1002/er.1283

Marco-Lozar, J. P., Kunowsky, M., Suárez-García, F., & Linares-Solano, A. (2014). Sorbent design for CO2 capture under different flue gas conditions. *Carbon*, *72*, 125–134. https://doi.org/https://doi.org/10.1016/j.carbon.2014.01.064

Maroto-Valer, M. M., Tang, Z., & Zhang, Y. (2005). CO2 capture by activated and impregnated anthracites. *Fuel Processing Technology*, *86*(14), 1487–1502. https://doi.org/https://doi.org/10.1016/j.fuproc.2005.01.003

Martavaltzi, C. S., & Lemonidou, A. A. (2008). Development of new CaO based sorbent materials for CO2 removal at high temperature. *Microporous and Mesoporous Materials*, *110*(1), 119–127. https://doi.org/https://doi.org/10.1016/j.micromeso.2007.10.006

Martín, C. F., Stöckel, E., Clowes, R., Adams, D. J., Cooper, A. I., Pis, J. J., … Pevida, C. (2011). Hypercrosslinked organic polymer networks as potential adsorbents for pre-combustion CO2 capture. *Journal of Materials Chemistry*, *21*(14), 5475–5483. https://doi.org/10.1039/C0JM03534C

Mason, J. A., Sumida, K., Herm, Z. R., Krishna, R., & Long, J. R. (2011a). Evaluating metal-organic frameworks for post-combustion carbon dioxide capture via temperature swing adsorption. *Energy and Environmental Science*, *4*(8), 3030–3040. https://doi.org/10.1039/c1ee01720a

Mason, J. A., Sumida, K., Herm, Z. R., Krishna, R., & Long, J. R. (2011b). Evaluating metal-organic frameworks for post-combustion carbon dioxide capture via temperature swing adsorption. *Energy and Environmental Science*, *4*(8), 3030–3040. https://doi.org/10.1039/c1ee01720a

Masoomi, M. Y., Stylianou, K. C., Morsali, A., Retailleau, P., & Maspoch, D. (2014). Selective CO2 Capture in Metal–Organic Frameworks with Azine-Functionalized Pores Generated by Mechanosynthesis. *Crystal Growth & Design*, *14*(5), 2092–2096. https://doi.org/10.1021/cg500033b

Masson-Delmotte, V., Zhai, P., Pörtner, H.-O., Roberts, D. C., Skea, J., Shukla, P. R., … Waterfield, T. (2018). *IPCC, 2018: Summary for Policymakers*. https://doi.org/10.1016/j.oneear.2019.10.025

Mavrandonakis, A., Tylianakis, E., Stubos, A. K., & Froudakis, G. E. (2008). Why Li Doping in MOFs Enhances H2 Storage Capacity? A Multi-scale Theoretical Study. *The Journal of Physical Chemistry C*, *112*(18), 7290–7294. https://doi.org/10.1021/jp7102098

Mavroudi, M., Kaldis, S. P., & Sakellaropoulos, G. P. (2003). Reduction of CO2 emissions by a membrane contacting process☆. *Fuel*, *82*(15), 2153–2159. https://doi.org/https://doi.org/10.1016/S0016-2361(03)00154-6

Mavroudi, M., Kaldis, S. P., & Sakellaropoulos, G. P. (2006). A study of mass transfer resistance in membrane gas–liquid contacting processes. *Journal of Membrane Science*, *272*(1), 103–115. https://doi.org/https://doi.org/10.1016/j.memsci.2005.07.025

Mazloomi, K., & Gomes, C. (2012). Hydrogen as an energy carrier: Prospects and challenges. *Renewable and*

Sustainable Energy Reviews, *16*(5), 3024–3033. https://doi.org/10.1016/j.rser.2012.02.028

McLeod, A., Buzatu, P., Autin, O., Jefferson, B., & McAdam, E. (2015). Controlling shell-side crystal nucleation in a gas–liquid membrane contactor for simultaneous ammonium bicarbonate recovery and biogas upgrading. *Journal of Membrane Science*, *473*, 146–156. https://doi.org/https://doi.org/10.1016/j.memsci.2014.07.063

McNamara, N. D., & Hicks, J. C. (2015). Chelating agent-free, vapor-assisted crystallization method to synthesize hierarchical microporous/mesoporous MIL-125 (Ti). *ACS Applied Materials and Interfaces*, *7*(9), 5338–5346. https://doi.org/10.1021/am508799d

Meng, L.-Y., Meng, W., Chen, T., & Jin, L. Y. (2014). CO2 Adsorption capacity of activated N-doping porous carbons prepared from graphite nanofibers/polypyrrole. *Journal of Applied Polymer Science*, *131*(15). https://doi.org/10.1002/app.40517

Meng, L.-Y., & Park, S.-J. (2012). Effect of exfoliation temperature on carbon dioxide capture of graphene nanoplates. *Journal of Colloid and Interface Science*, *386*(1), 285–290. https://doi.org/https://doi.org/10.1016/j.jcis.2012.07.025

Merel, J., Clausse, M., & Meunier, F. (2008). Experimental Investigation on CO2 Post−Combustion Capture by Indirect Thermal Swing Adsorption Using 13X and 5A Zeolites. *Industrial & Engineering Chemistry Research*, *47*(1), 209–215. https://doi.org/10.1021/ie071012x

Metz, B., Davidson, O., de Coninck, H. C., Loos, M., & Meyer, L. A. (2005). *IPCC, 2005: IPCC Special Report on Carbon Dioxide Capture and Storage.*

Millward, A. R., & Yaghi, O. M. (2005a). Metal-organic frameworks with exceptionally high capacity for storage of carbon dioxide at room temperature. *Journal of the American Chemical Society*, *127*(51), 17998–17999. https://doi.org/10.1021/ja0570032

Millward, A. R., & Yaghi, O. M. (2005b). Metal Organic Frameworks with exceptionally high capacity for storage of CO2, 17998–17999. https://doi.org/10.1021/ja0570032

Millward, A. R., & Yaghi, O. M. (2005c). Metal−Organic Frameworks with Exceptionally High Capacity for Storage of Carbon Dioxide at Room Temperature. *Journal of the American Chemical Society*, *127*(51), 17998–17999. https://doi.org/10.1021/ja0570032

Mishra, A. K., & Ramaprabhu, S. (2012). Palladium nanoparticles decorated graphite nanoplatelets for room temperature carbon dioxide adsorption. *Chemical Engineering Journal*, *187*, 10–15. https://doi.org/https://doi.org/10.1016/j.cej.2011.01.024

Mogri, Z., & Paul, D. R. (2001). Gas sorption and transport in poly(alkyl (meth)acrylate)s. II. Sorption and diffusion properties. *Polymer*, *42*(18), 7781–7789. https://doi.org/https://doi.org/10.1016/S0032-3861(01)00261-0

Møller, K., Sheppard, D., Ravnsbæk, D., Buckley, C., Akiba, E., Li, H.-W., & Jensen, T. (2017). Complex Metal Hydrides for Hydrogen, Thermal and Electrochemical Energy Storage. *Energies*, *10*(10), 1645. https://doi.org/10.3390/en10101645

Montes-Andrés, H., Orcajo, G., Martos, C., Botas, J. A., & Calleja, G. (2019). Co/Ni mixed-metal expanded IRMOF-74 series and their hydrogen adsorption properties. *International Journal of Hydrogen Energy*, *44*(33), 18205–18213. https://doi.org/10.1016/j.ijhydene.2019.05.007

Montoro, C., García, E., Calero, S., Pérez-Fernández, M. A., López, A. L., Barea, E., & Navarro, J. A. R. (2012). Functionalisation of MOF open metal sites with pendant amines for CO2 capture. *Journal of*

Materials Chemistry, *22*(20), 10155–10158. https://doi.org/10.1039/C2JM16770K

Moradi, R., & Groth, K. M. (2019). Hydrogen storage and delivery: Review of the state of the art technologies and risk and reliability analysis. *International Journal of Hydrogen Energy*, *44*(23), 12254–12269. https://doi.org/10.1016/j.ijhydene.2019.03.041

Morris, R. E., & Wheatley, P. S. (2008). Gas storage in nanoporous materials. *Angewandte Chemie - International Edition*, *47*(27), 4966–4981. https://doi.org/10.1002/anie.200703934

Morris, W., Leung, B., Furukawa, H., Yaghi, O. K., He, N., Hayashi, H., … Yaghi, O. M. (2010). A Combined Experimental-Computational Investigation of Carbon Dioxide Capture in a Series of Isoreticular Zeolitic Imidazolate Frameworks. *Journal of the American Chemical Society*, *132*(32), 11006–11008. https://doi.org/10.1021/ja104035j

Mosadegh-Sedghi, S., Brisson, J., Rodrigue, D., & Iliuta, M. C. (2012). Morphological, chemical and thermal stability of microporous LDPE hollow fiber membranes in contact with single and mixed amine based CO2 absorbents. *Separation and Purification Technology*, *96*, 117–123. https://doi.org/https://doi.org/10.1016/j.seppur.2012.05.025

Mosadegh-Sedghi, S., Rodrigue, D., Brisson, J., & Iliuta, M. C. (2014). Wetting phenomenon in membrane contactors – Causes and prevention. *Journal of Membrane Science*, *452*, 332–353. https://doi.org/https://doi.org/10.1016/j.memsci.2013.09.055

Mu, B., Li, F., Huang, Y., & Walton, K. S. (2012). Breathing effects of CO2 adsorption on a flexible 3D lanthanide metal–organic framework. *Journal of Materials Chemistry*, *22*(20), 10172–10178. https://doi.org/10.1039/C2JM15721G

Mueller, U., Puetter, H., Hesse, M., Wessel, H., Schubert, M., Huff, J., & Guzmann, M. (2005). Method for electrochemical production of a crystalline porous metal organic skeleton material.

Mueller, U., Schubert, M., Teich, F., Puetter, H., Schierle-Arndt, K., & Pastré, J. (2006). Metal–organic frameworks—prospective industrial applications. *Journal of Materials Chemistry*, *16*(7), 626–636. https://doi.org/10.1039/B511962F

Mulfort, K. L., & Hupp, J. T. (2007). Chemical Reduction of Metal−Organic Framework Materials as a Method to Enhance Gas Uptake and Binding. *Journal of the American Chemical Society*, *129*(31), 9604–9605. https://doi.org/10.1021/ja0740364

Murray, L. J., Dincă, M., & Long, J. R. (2009). Hydrogen storage in metal–organic frameworks. *Chemical Society Reviews*, *38*(5), 1294–1314. https://doi.org/10.1039/B802256A

Murray, L. J., Dincă, M., & Long, J. R. (2009). Hydrogen storage in metal-organic frameworks. *Chemical Society Reviews*, *38*, 1294–1314. https://doi.org/10.1039/B802256A

NASA/GISS. (2019). Global Temperature | Vital Signs – Climate Change: Vital Signs of the Planet. Retrieved May 13, 2020, from https://climate.nasa.gov/vital-signs/global-temperature/

NASA. (2019). Evidence | Facts – Climate Change: Vital Signs of the Planet. *National Aeronautics and Space Administration (NASA)*. Retrieved from https://climate.nasa.gov/evidence/

NASA. (2020). Carbon Dioxide | Vital signs of the planet. Retrieved May 14, 2020, from https://climate.nasa.gov/vital-signs/carbon-dioxide/

Nguyen, H. L., Hanikel, N., Lyle, S. J., Zhu, C., Proserpio, D. M., & Yaghi, O. M. (2020). A Porous Covalent

Organic Framework with Voided Square Grid Topology for Atmospheric Water Harvesting. *Journal of the American Chemical Society*, *142*(5), 2218–2221. https://doi.org/10.1021/jacs.9b13094

Ni, Z., & Masel, R. I. (2006). Rapid Production of Metal−Organic Frameworks via Microwave-Assisted Solvothermal Synthesis. *Journal of the American Chemical Society*, *128*(38), 12394–12395. https://doi.org/10.1021/ja0635231

Nijkamp, M. G., Raaymakers, J. E. M. J., van Dillen, A. J., & de Jong, K. P. (2001). Hydrogen storage using physisorption – materials demands. *Applied Physics A*, *72*(5), 619–623. https://doi.org/10.1007/s003390100847

Nunes, P., Gomes, A. C., Pillinger, M., Gonçalves, I. S., & Abrantes, M. (2015). Promotion of phosphoester hydrolysis by the ZrIV-based metal-organic framework UiO-67. *Microporous and Mesoporous Materials*, *208*, 21–29. https://doi.org/https://doi.org/10.1016/j.micromeso.2015.01.016

Nwaoha, C., Saiwan, C., Tontiwachwuthikul, P., Supap, T., Rongwong, W., Idem, R., … Benamor, A. (2016). Carbon dioxide (CO2) capture: Absorption-desorption capabilities of 2-amino-2-methyl-1-propanol (AMP), piperazine (PZ) and monoethanolamine (MEA) tri-solvent blends. *Journal of Natural Gas Science and Engineering*. https://doi.org/10.1016/j.jngse.2016.06.002

O'Malley, K., Ordaz, G., Adams, J., Randolph, K., Ahn, C. C., & Stetson, N. T. (2015). Applied hydrogen storage research and development: A perspective from the U.S. Department of Energy. *Journal of Alloys and Compounds*, *645*, S419–S422. https://doi.org/https://doi.org/10.1016/j.jallcom.2014.12.090

Office-of-Energy-Efficiency-&-Renewable-Energy. (2015). Materials-Based Hydrogen Storage | Department of Energy. https://doi.org/DOE/GO-102015-4730

Oh, H., Maurer, S., Balderas-Xicohtencatl, R., Arnold, L., Magdysyuk, O. V., Schütz, G., … Hirscher, M. (2017). Efficient synthesis for large-scale production and characterization for hydrogen storage of ligand exchanged MOF-74/174/184-M (M = Mg2+, Ni2+). *International Journal of Hydrogen Energy*, *42*(2), 1027–1035. https://doi.org/10.1016/j.ijhydene.2016.08.153

Olajire, A. A. (2010). CO2 capture and separation technologies for end-of-pipe applications - A review. *Energy*. https://doi.org/10.1016/j.energy.2010.02.030

Opanasenko, M., Dhakshinamoorthy, A., Shamzhy, M., Nachtigall, P., Horáček, M., Garcia, H., & Čejka, J. (2013). Comparison of the catalytic activity of MOFs and zeolites in Knoevenagel condensation. *Catalysis Science and Technology*, *3*(2), 500–507. https://doi.org/10.1039/c2cy20586f

Ouyang, L., Zhong, H., Li, H.-W., & Zhu, M. (2018). A Recycling Hydrogen Supply System of NaBH4 Based on a Facile Regeneration Process: A Review. *Inorganics*, *6*(1), 10. https://doi.org/10.3390/inorganics6010010

Oveisi, A. R., Khorramabadi-Zad, A., & Daliran, S. (2016). Iron-based metal-organic framework, Fe(BTC): An effective dual-functional catalyst for oxidative cyclization of bisnaphthols and tandem synthesis of quinazolin-4(3H)-ones. *RSC Advances*, *6*(2), 1136–1142. https://doi.org/10.1039/c5ra19013d

Pal, N., & Bhaumik, A. (2013). Soft templating strategies for the synthesis of mesoporous materials: Inorganic, organic–inorganic hybrid and purely organic solids. *Advances in Colloid and Interface Science*, *189–190*, 21–41. https://doi.org/https://doi.org/10.1016/j.cis.2012.12.002

Pan, L., Sander, M. B., Huang, X., Li, J., Smith, M., Bittner, E., … Johnson, J. K. (2004). Microporous Metal Organic Materials: Promising Candidates as Sorbents for Hydrogen Storage. *Journal of the American Chemical Society*, *126*(5), 1308–1309. https://doi.org/10.1021/ja0392871

Panella, B, & Hirscher, M. (2005). Hydrogen Physisorption in Metal–Organic Porous Crystals. *Advanced Materials*, *17*(5), 538–541. https://doi.org/10.1002/adma.200400946

Panella, B, Hirscher, M., Pütter, H., & Müller, U. (2006). Hydrogen Adsorption in Metal–Organic Frameworks: Cu-MOFs and Zn-MOFs Compared. *Advanced Functional Materials*, *16*(4), 520–524. https://doi.org/10.1002/adfm.200500561

Panella, Barbara, Hirscher, M., Pütter, H., & Müller, U. (2006). Hydrogen adsorption in metal-organic frameworks: Cu-MOFs and Zn-MOFs compared. *Advanced Functional Materials*, *16*(4), 520–524. https://doi.org/10.1002/adfm.200500561

Panella, Barbara, Hirscher, M., & Roth, S. (2005a). Hydrogen adsorption in different carbon nanostructures. *Carbon*, *43*(10), 2209–2214. https://doi.org/10.1016/j.carbon.2005.03.037

Panella, Barbara, Hirscher, M., & Roth, S. (2005b). Hydrogen adsorption in different carbon nanostructures. *Carbon*, *43*(10), 2209–2214. https://doi.org/https://doi.org/10.1016/j.carbon.2005.03.037

Panella, Barbara, Hönes, K., Müller, U., Trukhan, N., Schubert, M., Pütter, H., & Hirscher, M. (2008). Desorption studies of hydrogen in metal-organic frameworks. *Angewandte Chemie - International Edition*, *47*(11), 2138–2142. https://doi.org/10.1002/anie.200704053

Pareek, K., Rohan, R., Chen, Z., Zhao, D., & Cheng, H. (2017). Ambient temperature hydrogen storage in porous materials with exposed metal sites. *International Journal of Hydrogen Energy*, *42*(10), 6801–6809. https://doi.org/10.1016/j.ijhydene.2017.01.209

Park, H. H., Deshwal, B. R., Kim, I. W., & Lee, H. K. (2008). Absorption of SO2 from flue gas using PVDF hollow fiber membranes in a gas–liquid contactor. *Journal of Membrane Science*, *319*(1), 29–37. https://doi.org/https://doi.org/10.1016/j.memsci.2008.03.023

Park, H. J., Cheon, Y. E., & Suh, M. P. (2010). Post-synthetic reversible incorporation of organic linkers into porous metal-organic frameworks through single-crystal-to-single-crystal transformations and modification of gas-sorption properties. *Chemistry - A European Journal*, *16*(38), 11662–11669. https://doi.org/10.1002/chem.201001549

Park, J. H., Park, S. H., & Jhung, S. H. (2009). Microwave-syntheses of zeolitic imidazolate framework material, ZIF-8. *Journal of the Korean Chemical Society*, *53*(5), 553–559. https://doi.org/10.5012/jkcs.2009.53.5.553

Park, S.-J., & Lee, S.-Y. (2010). A study on hydrogen-storage behaviors of nickel-loaded mesoporous MCM-41. *Journal of Colloid and Interface Science*, *346*(1), 194–198. https://doi.org/https://doi.org/10.1016/j.jcis.2010.02.047

Pasteur, A. T., Dixon-Warren, S. J., Ge, Q., & King, D. A. (1997). Dynamics of hydrogen dissociation on Pt{100}: Steering, screening and thermal roughening effects. *The Journal of Chemical Physics*, *106*(21), 8896–8904. https://doi.org/10.1063/1.473953

Pellegrini, G., Strube, R., & Manfrida, G. (2010). Comparative study of chemical absorbents in postcombustion CO2 capture. *Energy*. https://doi.org/10.1016/j.energy.2009.08.011

Peng, L., Zhang, J., Xue, Z., Han, B., Sang, X., Liu, C., & Yang, G. (2014a). Highly mesoporous metal-organic framework assembled in a switchable solvent. *Nature Communications*, *5*, 1–7. https://doi.org/10.1038/ncomms5465

Peng, L., Zhang, J., Xue, Z., Han, B., Sang, X., Liu, C., & Yang, G. (2014b). Highly mesoporous metal–organic framework assembled in a switchable solvent. *Nature Communications*, *5*(1), 4465.

https://doi.org/10.1038/ncomms5465

Peng, Y., Krungleviciute, V., Eryazici, I., Hupp, J. T., Farha, O. K., & Yildirim, T. (2013). Methane Storage in Metal–Organic Frameworks: Current Records, Surprise Findings, and Challenges. *Journal of the American Chemical Society*, *135*(32), 11887–11894. https://doi.org/10.1021/ja4045289

Phalak, N., Deshpande, N., & Fan, L.-S. (2012). Investigation of High-Temperature Steam Hydration of Naturally Derived Calcium Oxide for Improved Carbon Dioxide Capture Capacity over Multiple Cycles. *Energy & Fuels*, *26*(6), 3903–3909. https://doi.org/10.1021/ef3003735

Phan, A., Doonan, C. J., Uribe-romo, F. J., Knobler, C. B., Keeffe, M. O., & Yaghi, O. M. (2010). Synthesis, Structure, and Carbon Dioxide Capture Properties of Zeolitic Imidazolate Frameworks. *Accounts of Chemical Research*, *43*(1), 58–67. Retrieved from http://www.ncbi.nlm.nih.gov/pubmed/19877580

Philipp, R., & Fujimoto, K. (1992). FTIR spectroscopic study of carbon dioxide adsorption/desorption on magnesia/calcium oxide catalysts. *The Journal of Physical Chemistry*, *96*(22), 9035–9038. https://doi.org/10.1021/j100201a063

Pichon, A., & James, S. L. (2008). An array-based study of reactivity under solvent-free mechanochemical conditions—insights and trends. *CrystEngComm*, *10*(12), 1839–1847. https://doi.org/10.1039/B810857A

Pires, J., de Carvalho, M. B., Ribeiro, F. R., & Derouane, E. G. (1993). Carbon dioxide in Y and ZSM-20 zeolites: Adsorption and infrared studies. *Journal of Molecular Catalysis*, *85*(3), 295–303. https://doi.org/https://doi.org/10.1016/0304-5102(93)80057-2

Plaza, M. G., Pevida, C., Arenillas, A., Rubiera, F., & Pis, J. J. (2007). CO2 capture by adsorption with nitrogen enriched carbons. *Fuel*, *86*(14), 2204–2212. https://doi.org/https://doi.org/10.1016/j.fuel.2007.06.001

Plaza, M. G., Thurecht, K. J., Pevida, C., Rubiera, F., Pis, J. J., Snape, C. E., & Drage, T. C. (2013). Influence of oxidation upon the CO2 capture performance of a phenolic-resin-derived carbon. *Fuel Processing Technology*, *110*, 53–60. https://doi.org/https://doi.org/10.1016/j.fuproc.2013.01.011

Pommerin, A., Weidenthaler, C., Schüth, F., & Felderhoff, M. (2010). Direct synthesis of pure complex aluminium hydrides by cryomilling. *Scripta Materialia*, *62*(8), 576–578. https://doi.org/https://doi.org/10.1016/j.scriptamat.2009.12.041

Portugal, A. F., Sousa, J. M., Magalhães, F. D., & Mendes, A. (2009). Solubility of carbon dioxide in aqueous solutions of amino acid salts. *Chemical Engineering Science*, *64*(9), 1993–2002. https://doi.org/https://doi.org/10.1016/j.ces.2009.01.036

Prasanth, K. P., Raj, M. C., Bajaj, H. C., Kim, T. H., & Jasra, R. V. (2010). Hydrogen sorption in transition metal modified mesoporous materials. *International Journal of Hydrogen Energy*, *35*(6), 2351–2360. https://doi.org/https://doi.org/10.1016/j.ijhydene.2009.12.134

Prestipino, C., Regli, L., Vitillo, J. G., Bonino, F., Damin, A., Lamberti, C., … Bordiga, S. (2006). Local Structure of Framework Cu(II) in HKUST-1 Metallorganic Framework: Spectroscopic Characterization upon Activation and Interaction with Adsorbates. *Chemistry of Materials*, *18*(5), 1337–1346. https://doi.org/10.1021/cm052191g

Privalova, E. I., Karjalainen, E., Nurmi, M., Mäki-Arvela, P., Eränen, K., Tenhu, H., … Mikkola, J.-P. (2013). Imidazolium-Based Poly(ionic liquid)s as New Alternatives for CO2 Capture. *ChemSusChem*, *6*(8), 1500–1509. https://doi.org/10.1002/cssc.201300120

Proch, S., Herrmannsdörfer, J., Kempe, R., Kern, C., Jess, A., Seyfarth, L., & Senker, J. (2008). Pt@MOF-177: Synthesis, Room-Temperature Hydrogen Storage and Oxidation Catalysis. *Chemistry – A European Journal*, *14*(27), 8204–8212. https://doi.org/10.1002/chem.200801043

Prouzet, E., & Pinnavaia, T. J. (1997). Assembly of Mesoporous Molecular Sieves Containing Wormhole Motifs by a. *Angewandte Chemie International Edition*, *36*, 516–518.

Przepiórski, J., Skrodzewicz, M., & Morawski, A. W. (2004). High temperature ammonia treatment of activated carbon for enhancement of CO2 adsorption. *Applied Surface Science*, *225*(1), 235–242. https://doi.org/https://doi.org/10.1016/j.apsusc.2003.10.006

Puszkiel, J., Garroni, S., Milanese, C., Gennari, F., Klassen, T., Dornheim, M., & Pistidda, C. (2017). Tetrahydroborates: Development and Potential as Hydrogen Storage Medium. *Inorganics*, *5*(4), 74. https://doi.org/10.3390/inorganics5040074

Puxty, G., Rowland, R., & Attalla, M. (2010). Comparison of the rate of CO2 absorption into aqueous ammonia and monoethanolamine. *Chemical Engineering Science*. https://doi.org/10.1016/j.ces.2009.09.042

Pyle, D. S., Gray, E. M. A., & Webb, C. J. (2016). Hydrogen storage in carbon nanostructures via spillover. *International Journal of Hydrogen Energy*, *41*(42), 19098–19113. https://doi.org/10.1016/j.ijhydene.2016.08.061

Qi, Z., & Cussler, E. L. (1985a). Microporous hollow fibers for gas absorption. I. Mass transfer in the liquid. *Journal of Membrane Science*. https://doi.org/10.1016/S0376-7388(00)83149-X

Qi, Z., & Cussler, E. L. (1985b). Microporous hollow fibers for gas absorption. II. Mass transfer across the membrane. *Journal of Membrane Science*. https://doi.org/10.1016/S0376-7388(00)83150-6

Qin, W., Han, L., Bi, H., Jian, J., Wu, X., & Gao, P. (2015). Hydrogen storage in a chemical bond stabilized Co9S8–graphene layered structure. *Nanoscale*, *7*(47), 20180–20187. https://doi.org/10.1039/C5NR06116D

Qiu, L.-G., Li, Z.-Q., Wu, Y., Wang, W., Xu, T., & Jiang, X. (2008). Facile synthesis of nanocrystals of a microporous metal–organic framework by an ultrasonic method and selective sensing of organoamines. *Chemical Communications*, (31), 3642–3644. https://doi.org/10.1039/B804126A

Qiu, L.-G., Xu, T., Li, Z.-Q., Wang, W., Wu, Y., Jiang, X., … Zhang, L.-D. (2008). Hierarchically Micro- and Mesoporous Metal–Organic Frameworks with Tunable Porosity. *Angewandte Chemie International Edition*, *47*(49), 9487–9491. https://doi.org/10.1002/anie.200803640

Rabbani, M. G., & El-Kaderi, H. M. (2011). Template-Free Synthesis of a Highly Porous Benzimidazole-Linked Polymer for CO2 Capture and H2 Storage. *Chemistry of Materials*, *23*(7), 1650–1653. https://doi.org/10.1021/cm200411p

Ramachandran, S., Ha, J.-H., & Kim, D. K. (2007). Hydrogen storage characteristics of metal oxide doped Al–MCM-41 mesoporous materials. *Catalysis Communications*, *8*(12), 1934–1938. https://doi.org/https://doi.org/10.1016/j.catcom.2007.03.029

Ramazani, R., Samsami, A., Jahanmiri, A., Van der Bruggen, B., & Mazinani, S. (2016). Characterization of monoethanolamine + potassium lysinate blend solution as a new chemical absorbent for CO2 capture. *International Journal of Greenhouse Gas Control*. https://doi.org/10.1016/j.ijggc.2016.05.005

Rangwala, H. A. (1996). Absorption of carbon dioxide into aqueous solutions using hollow fiber membrane contactors. *Journal of Membrane Science*, *112*(2), 229–240.

https://doi.org/https://doi.org/10.1016/0376-7388(95)00293-6

Rao, A. B., & Rubin, E. S. (2002). A technical, economic, and environmental assessment of amine-based CO2 capture technology for power plant greenhouse gas control. *Environmental Science and Technology*. https://doi.org/10.1021/es0158861

Rao, C. N. R., Sood, A. K., Subrahmanyam, K. S., & Govindaraj, A. (2009). Graphene: The New Two-Dimensional Nanomaterial. *Angewandte Chemie International Edition*, *48*(42), 7752–7777. https://doi.org/10.1002/anie.200901678

Rao, K. V., Mohapatra, S., Kulkarni, C., Maji, T. K., & George, S. J. (2011). Extended phenylene based microporous organic polymers with selective carbon dioxide adsorption. *Journal of Materials Chemistry*, *21*(34), 12958–12963. https://doi.org/10.1039/C1JM11508A

Rege, S. U., & Yang, R. T. (2001). A novel FTIR method for studying mixed gas adsorption at low concentrations: H2O and CO2 on NaX zeolite and γ-alumina. *Chemical Engineering Science*, *56*(12), 3781–3796. https://doi.org/https://doi.org/10.1016/S0009-2509(01)00095-1

Rehman, A., & Park, S.-J. (2019a). Environmental remediation by microporous carbon: An efficient contender for CO2 and methylene blue adsorption. *Journal of CO2 Utilization*. https://doi.org/10.1016/j.jcou.2019.08.015

Rehman, A., & Park, S. J. (2019b). Tunable nitrogen-doped microporous carbons: Delineating the role of optimum pore size for enhanced CO 2 adsorption. *Chemical Engineering Journal*. https://doi.org/10.1016/j.cej.2019.01.063

Reineke, T. M., Eddaoudi, M., Moler, D., O'Keeffe, M., & Yaghi, O. M. (2000). Large free volume in maximally interpenetrating networks: The role of secondary building units exemplified by TB2(ADB)3[(CH3)2SO]4·16[(CH3)2SO]. *Journal of the American Chemical Society*, *122*(19), 4843–4844. https://doi.org/10.1021/ja000363z

Ren, Jianwei, Langmi, H. W., North, B. C., & Mathe, M. (2014a). Review on processing of metal–organic framework (MOF) materials towards system integration for hydrogen storage. *International Journal of Energy Research*, *39*, 607–620. https://doi.org/10.1002/er.3255

Ren, Jianwei, Langmi, H. W., North, B. C., & Mathe, M. (2014b). Review on processing of metal–organic framework (MOF) materials towards system integration for hydrogen storage. *International Journal of Energy Research*. https://doi.org/10.1002/er

Ren, Jianwei, Musyoka, N. M., Langmi, H. W., Mathe, M., & Liao, S. (2017). Current research trends and perspectives on materials-based hydrogen storage solutions: A critical review. *International Journal of Hydrogen Energy*, *42*(1), 289–311. https://doi.org/10.1016/j.ijhydene.2016.11.195

Ren, Jie, Wu, L., & Li, B.-G. (2012). Preparation and CO2 Sorption/Desorption of N-(3-Aminopropyl)Aminoethyl Tributylphosphonium Amino Acid Salt Ionic Liquids Supported into Porous Silica Particles. *Industrial & Engineering Chemistry Research*, *51*(23), 7901–7909. https://doi.org/10.1021/ie2028415

Rezaei, M., Ismail, A. F., Bakeri, G., Hashemifard, S. A., & Matsuura, T. (2015). Effect of general montmorillonite and Cloisite 15A on structural parameters and performance of mixed matrix membranes contactor for CO2 absorption. *Chemical Engineering Journal*, *260*, 875–885. https://doi.org/https://doi.org/10.1016/j.cej.2014.09.027

Rezaei, M., Ismail, A. F., Hashemifard, S. A., Bakeri, G., & Matsuura, T. (2014). Experimental study on the performance and long-term stability of PVDF/montmorillonite hollow fiber mixed matrix membranes

for CO2 separation process. *International Journal of Greenhouse Gas Control*, *26*, 147–157. https://doi.org/https://doi.org/10.1016/j.ijggc.2014.04.021

Ridha, F. N., Yang, Y., & Webley, P. A. (2009). Adsorption characteristics of a fully exchanged potassium chabazite zeolite prepared from decomposition of zeolite Y. *Microporous and Mesoporous Materials*, *117*(1), 497–507. https://doi.org/https://doi.org/10.1016/j.micromeso.2008.07.034

Riemer, P. W. F., & Ormerod, W. G. (1995). International perspectives and the results of carbon dioxide capture disposal and utilisation studies. *Energy Conversion and Management*. https://doi.org/10.1016/0196-8904(95)00128-Z

Rieth, A. J., Yang, S., Wang, E. N., & Dincă, M. (2017). Record Atmospheric Fresh Water Capture and Heat Transfer with a Material Operating at the Water Uptake Reversibility Limit. *ACS Central Science*, *3*(6), 668–672. https://doi.org/10.1021/acscentsci.7b00186

Ritschel, M., Uhlemann, M., Gutfleisch, O., Leonhardt, A., Graff, A., Täschner, C., & Fink, J. (2002). Hydrogen storage in different carbon nanostructures. *Applied Physics Letters*, *80*(16), 2985–2987. https://doi.org/10.1063/1.1469680

Ritter, N., Senkovska, I., Kaskel, S., & Weber, J. (2011). Intrinsically Microporous Poly(imide)s: Structure−Porosity Relationship Studied by Gas Sorption and X-ray Scattering. *Macromolecules*, *44*(7), 2025–2033. https://doi.org/10.1021/ma102448h

Rochelle, G. T. (2009). Amine Scrubbing for CO2 Capture. *Science*. https://doi.org/10.1126/science.1176731

Rogers, R. D. (2007). Reflections on ionic liquids. *Nature*. https://doi.org/10.1038/447917a

Romanos, J., Beckner, M., Rash, T., Firlej, L., Kuchta, B., Yu, P., … Pfeifer, P. (2012). Nanospace engineering of KOH activated carbon. *Nanotechnology*, *23*(1). https://doi.org/10.1088/0957-4484/23/1/015401

Rongwong, W., Jiraratananon, R., & Atchariyawut, S. (2009). Experimental study on membrane wetting in gas–liquid membrane contacting process for CO2 absorption by single and mixed absorbents. *Separation and Purification Technology*, *69*(1), 118–125. https://doi.org/https://doi.org/10.1016/j.seppur.2009.07.009

Rosi, N. L., Eckert, J., Eddaoudi, M., Vodak, D. T., Kim, J., O'Keeffe, M., & Yaghi, O. M. (2003). Hydrogen Storage in Microporous Metal-Organic Frameworks. *Science*, *300*(5622), 1127 LP – 1129. https://doi.org/10.1126/science.1083440

Roth, E. A., Agarwal, S., & Gupta, R. K. (2013). Nanoclay-Based Solid Sorbents for CO2 Capture. *Energy & Fuels*, *27*(8), 4129–4136. https://doi.org/10.1021/ef302017m

Rowsell, J. L. C., Millward, A. R., Park, K. S., & Yaghi, O. M. (2004). Hydrogen Sorption in Functionalized Metal−Organic Frameworks. *Journal of the American Chemical Society*, *126*(18), 5666–5667. https://doi.org/10.1021/ja049408c

Rowsell, J. L. C., & Yaghi, O. M. (2004a). Metal-organic frameworks: A new class of porous materials. *Microporous and Mesoporous Materials*, *73*(1–2), 3–14. https://doi.org/10.1016/j.micromeso.2004.03.034

Rowsell, J. L. C., & Yaghi, O. M. (2004b). Metal–organic frameworks: a new class of porous materials. *Microporous and Mesoporous Materials*, *73*(1), 3–14. https://doi.org/https://doi.org/10.1016/j.micromeso.2004.03.034

Rowsell, J. L. C., & Yaghi, O. M. (2005). Strategies for hydrogen storage in metal-organic frameworks. *Angewandte Chemie - International Edition*, *44*(30), 4670–4679. https://doi.org/10.1002/anie.200462786

Rowsell, J. L. C., & Yaghi, O. M. (2006a). Effects of Functionalization, Catenation, and Variation of the Metal Oxide and Organic Linking Units on the Low-Pressure Hydrogen Adsorption Properties of Metal−Organic Frameworks. *Journal of the American Chemical Society*, *128*(4), 1304–1315. https://doi.org/10.1021/ja056639q

Rowsell, J. L. C., & Yaghi, O. M. (2006b). Effects of Functionalization, Catenation, and Variation of the Metal Oxide and Organic Linking Units on the Low-Pressure Hydrogen Adsorption Properties of Metal−Organic Frameworks. *Journal of the American Chemical Society*, *128*(4), 1304–1315. https://doi.org/10.1021/ja056639q

Ruminski, A. M., Jeon, K.-J., & Urban, J. J. (2011). Size-dependent CO2 capture in chemically synthesized magnesium oxide nanocrystals. *Journal of Materials Chemistry*, *21*(31), 11486–11491. https://doi.org/10.1039/C1JM11784J

Rzepka, M., Lamp, P., & de la Casa-Lillo, M. A. (1998). Physisorption of Hydrogen on Microporous Carbon and Carbon Nanotubes. *The Journal of Physical Chemistry B*, *102*(52), 10894–10898. https://doi.org/10.1021/jp9829602

Rzepka, M., Lamp, P., & de la Casa-Lillo, M. A. (2002). Physisorption of Hydrogen on Microporous Carbon and Carbon Nanotubes. *The Journal of Physical Chemistry B*, *102*(52), 10894–10898. https://doi.org/10.1021/jp9829602

Sabo, M., Henschel, A., Fröde, H., Klemm, E., & Kaskel, S. (2007). Solution infiltration of palladium into MOF-5: synthesis, physisorption and catalytic properties. *Journal of Materials Chemistry*, *17*(36), 3827–3832. https://doi.org/10.1039/B706432B

Sabouni, R., Kazemian, H., & Rohani, S. (2010). A novel combined manufacturing technique for rapid production of IRMOF-1 using ultrasound and microwave energies. *Chemical Engineering Journal*, *165*(3), 966–973. https://doi.org/https://doi.org/10.1016/j.cej.2010.09.036

Saha, S., Chandra, S., Garai, B., & Banerjee, R. (2012). Carbon dioxide capture by metal organic frameworks. *Indian Journal of Chemistry - Section A Inorganic, Physical, Theoretical and Analytical Chemistry*, *51*(9–10), 1223–1230. https://doi.org/10.1021/cr2003272

Saiwan, C., Supap, T., Idem, R. O., & Tontiwachwuthikul, P. (2011). Part 3: Corrosion and prevention in post-combustion CO2 capture systems. *Carbon Management*, *2*(6), 659–675. https://doi.org/10.4155/cmt.11.63

Sakintuna, B., Lamari-Darkrim, F., & Hirscher, M. (2007). Metal hydride materials for solid hydrogen storage: A review. *International Journal of Hydrogen Energy*, *32*(9), 1121–1140. https://doi.org/10.1016/j.ijhydene.2006.11.022

Salunkhe, R. R., Kaneti, Y. V., Kim, J., Kim, J. H., & Yamauchi, Y. (2016). Nanoarchitectures for Metal–Organic Framework-Derived Nanoporous Carbons toward Supercapacitor Applications. *Accounts of Chemical Research*, *49*(12), 2796–2806. https://doi.org/10.1021/acs.accounts.6b00460

Salvador, C., Lu, D., Anthony, E. J., & Abanades, J. C. (2003). Enhancement of CaO for CO2 capture in an FBC environment. *Chemical Engineering Journal*, *96*(1), 187–195. https://doi.org/https://doi.org/10.1016/j.cej.2003.08.011

Sandrock, G. (1999). A panoramic overview of hydrogen storage alloys from a gas reaction point of view.

Journal of Alloys and Compounds, *293–295*, 877–888. https://doi.org/https://doi.org/10.1016/S0925-8388(99)00384-9

Sandrock, G., & Bowman, R. C. (2003). Gas-based hydride applications: recent progress and future needs. *Journal of Alloys and Compounds*, *356–357*, 794–799. https://doi.org/https://doi.org/10.1016/S0925-8388(03)00090-2

Sanz, R., Calleja, G., Arencibia, A., & Sanz-Pérez, E. S. (2012). Amino functionalized mesostructured SBA-15 silica for CO2 capture: Exploring the relation between the adsorption capacity and the distribution of amino groups by TEM. *Microporous and Mesoporous Materials*, *158*, 309–317. https://doi.org/https://doi.org/10.1016/j.micromeso.2012.03.053

Sanz, R., Martínez, F., Orcajo, G., Wojtas, L., & Briones, D. (2013). Synthesis of a honeycomb-like Cu-based metal–organic framework and its carbon dioxide adsorption behaviour. *Dalton Transactions*, *42*(7), 2392–2398. https://doi.org/10.1039/C2DT32138F

Sarawade, P., Tan, H., & Polshettiwar, V. (2013). Shape- and Morphology-Controlled Sustainable Synthesis of Cu, Co, and In Metal Organic Frameworks with High CO2 Capture Capacity. *ACS Sustainable Chemistry & Engineering*, *1*(1), 66–74. https://doi.org/10.1021/sc300036p

Sartorl, G., & Savage, D. W. (1983). Sterically Hindered Amines for CO2 Removal from Gases. *Industrial and Engineering Chemistry Fundamentals*. https://doi.org/10.1021/i100010a016

Satyapal, S., Filburn, T., Trela, J., & Strange, J. (2001). Performance and Properties of a Solid Amine Sorbent for Carbon Dioxide Removal in Space Life Support Applications. *Energy & Fuels*, *15*(2), 250–255. https://doi.org/10.1021/ef0002391

Schimmel, H. G., Nijkamp, G., Kearley, G. J., Rivera, A., de Jong, K. P., & Mulder, F. M. (2004). Hydrogen adsorption in carbon nanostructures compared. *Materials Science and Engineering: B*, *108*(1), 124–129. https://doi.org/https://doi.org/10.1016/j.mseb.2003.10.091

Schlapbach, L., & Züttel, A. (2001). Hydrogen-storage materials for mobile applications. *Nature*, *414*, 353–358.

Schlapbach, Louis, Schlapbach, L., & Züttel, A. (2001). L. Schlapbach and A. Züttel, Nature, 2001, 414, 353., *414*(May 2016), 353–358. https://doi.org/10.1038/35104634

Schlapbach, Louis, & Züttel, A. (2002). Hydrogen as a Fuel and Its Storage for Mobility and Transport. *MRS Bulletin*, *27*(9), 675–679. https://doi.org/10.1557/mrs2002.220

Schlesinger, M., Schulze, S., Hietschold, M., & Mehring, M. (2010). Evaluation of synthetic methods for microporous metal–organic frameworks exemplified by the competitive formation of [Cu2(btc)3(H2O)3] and [Cu2(btc)(OH)(H2O)]. *Microporous and Mesoporous Materials*, *132*(1), 121–127. https://doi.org/https://doi.org/10.1016/j.micromeso.2010.02.008

Schlichtenmayer, M., & Hirscher, M. (2012). Nanosponges for hydrogen storage. *Journal of Materials Chemistry*, *22*(20), 10134–10143. https://doi.org/10.1039/c2jm15890f

Schlichtenmayer, M., & Hirscher, M. (2016). The usable capacity of porous materials for hydrogen storage. *Applied Physics A: Materials Science and Processing*, *122*(4), 1–11. https://doi.org/10.1007/s00339-016-9864-6

Schlichtenmayer, M., Streppel, B., & Hirscher, M. (2011). Hydrogen physisorption in high SSA microporous materials - A comparison between AX-21-33 and MOF-177 at cryogenic conditions. *International Journal of Hydrogen Energy*, *36*(1), 586–591. https://doi.org/10.1016/j.ijhydene.2010.09.057

Schmitz, B., Müller, U., Trukhan, N., Schubert, M., Férey, G., & Hirscher, M. (2008). Heat of adsorption for hydrogen in microporous high-surface-area materials. *ChemPhysChem*, *9*(15), 2181–2184. https://doi.org/10.1002/cphc.200800463

Scholes, C. A., Qader, A., Stevens, G. W., & Kentish, S. E. (2014). Membrane Gas-Solvent Contactor Pilot Plant Trials of CO2 Absorption from Flue Gas. *Separation Science and Technology*, *49*(16), 2449–2458. https://doi.org/10.1080/01496395.2014.937499

Sedghi, S. M., Brisson, J., Rodrigue, D., & Iliuta, M. C. (2011). Chemical alteration of LDPE hollow fibers exposed to monoethanolamine solutions used as absorbent for CO2 capture process. *Separation and Purification Technology*, *80*(2), 338–344. https://doi.org/https://doi.org/10.1016/j.seppur.2011.05.017

Seo, J. S., Whang, D., Lee, H., Jun, S. I., Oh, J., Jeon, Y. J., & Kim, K. (2000). A Homoquiral metal-organic porous meterial for enentioselective seperation ans catalysis. *Nature*, *404*(April), 982–986. https://doi.org/10.1038/35010088

Seo, Jung Soo, Whang, D., Lee, H., Jun, S. I., Oh, J., Jeon, Y. J., & Kim, K. (2000). A homochiral metal-organic porous material for enantioselective separation and catalysis. *Nature*, *404*(6781), 982–986. https://doi.org/10.1038/35010088

Seo, Y.-K., Hundal, G., Jang, I. T., Hwang, Y. K., Jun, C.-H., & Chang, J.-S. (2009). Microwave synthesis of hybrid inorganic–organic materials including porous Cu3(BTC)2 from Cu(II)-trimesate mixture. *Microporous and Mesoporous Materials*, *119*(1), 331–337. https://doi.org/https://doi.org/10.1016/j.micromeso.2008.10.035

Seo, Y., Jo, S.-H., Ryu, C. K., & Yi, C.-K. (2007). Effects of water vapor pretreatment time and reaction temperature on CO2 capture characteristics of a sodium-based solid sorbent in a bubbling fluidized-bed reactor. *Chemosphere*, *69*(5), 712–718. https://doi.org/https://doi.org/10.1016/j.chemosphere.2007.05.036

Serna-Guerrero, R., Belmabkhout, Y., & Sayari, A. (2010a). Further investigations of CO2 capture using triamine-grafted pore-expanded mesoporous silica. *Chemical Engineering Journal*, *158*(3), 513–519. https://doi.org/https://doi.org/10.1016/j.cej.2010.01.041

Serna-Guerrero, R., Belmabkhout, Y., & Sayari, A. (2010b). Modeling CO2 adsorption on amine-functionalized mesoporous silica: 1. A semi-empirical equilibrium model. *Chemical Engineering Journal*, *161*(1), 173–181. https://doi.org/https://doi.org/10.1016/j.cej.2010.04.024

Serre, C., Bourrelly, S., Vimont, A., Ramsahye, N. A., Maurin, G., Llewellyn, P. L., … Férey, G. (2007). An explanation for the very large breathing effect of a metal-organic framework during CO2adsorption. *Advanced Materials*, *19*(17), 2246–2251. https://doi.org/10.1002/adma.200602645

Sethia, G., & Sayari, A. (2014). Nitrogen-Doped Carbons: Remarkably Stable Materials for CO2 Capture. *Energy & Fuels*, *28*(4), 2727–2731. https://doi.org/10.1021/ef500283e

Sevilla, M., Valle-Vigón, P., & Fuertes, A. B. (2011). N-Doped Polypyrrole-Based Porous Carbons for CO2 Capture. *Advanced Functional Materials*, *21*(14), 2781–2787. https://doi.org/10.1002/adfm.201100291

Shamiri, A., Shafeeyan, M. S., Tee, H. C., Leo, C. Y., Aroua, M. K., & Aghamohammadi, N. (2016). Absorption of CO2 into aqueous mixtures of glycerol and monoethanolamine. *Journal of Natural Gas Science and Engineering*. https://doi.org/10.1016/j.jngse.2016.08.072

Shao, H., He, L., Lin, H., & Li, H.-W. (2018). Progress and Trends in Magnesium-Based Materials for Energy-Storage Research: A Review. *Energy Technology*, *6*(3), 445–458. https://doi.org/10.1002/ente.201700401

Sharma, A., Kaur, S., Mahajan, C. G., Tripathi, S. K., & Saini, G. S. S. (2007). Fourier transform infrared spectral study of N,N′-dimethylformamide- water-rhodamine 6G mixture. *Molecular Physics*, *105*(1), 117–123. https://doi.org/10.1080/00268970601146856

Sharonov, V. E., Okunev, A. G., & Aristov, Y. I. (2004). Kinetics of carbon dioxide sorption by the composite material K2CO3 in Al2O3. *Reaction Kinetics and Catalysis Letters*, *82*(2), 363–369. https://doi.org/10.1023/B:REAC.0000034849.15412.d2

She, L., Li, J., Wan, Y., Yao, X., Tu, B., & Zhao, D. (2011). Synthesis of ordered mesoporous MgO/carbon composites by a one-pot assembly of amphiphilic triblock copolymers. *Journal of Materials Chemistry*, *21*(3), 795–800. https://doi.org/10.1039/C0JM02226H

Sheppard, D. A., & Buckley, C. E. (2008). Hydrogen adsorption on porous silica. *International Journal of Hydrogen Energy*, *33*(6), 1688–1692. https://doi.org/https://doi.org/10.1016/j.ijhydene.2007.12.021

Sheppard, D. A., Maitland, C. F., & Buckley, C. E. (2005). Preliminary results of hydrogen adsorption and SAXS modelling of mesoporous silica: MCM-41. *Journal of Alloys and Compounds*, *404–406*, 405–408. https://doi.org/https://doi.org/10.1016/j.jallcom.2004.09.089

Sherman, B. J., Ciftja, A. F., & Rochelle, G. T. (2016). Thermodynamic and mass transfer modeling of carbon dioxide absorption into aqueous 2-piperidineethanol. *Chemical Engineering Science*. https://doi.org/10.1016/j.ces.2016.07.019

Shiraz, H. G., & Tavakoli, O. (2017). Investigation of graphene-based systems for hydrogen storage. *Renewable and Sustainable Energy Reviews*, *74*, 104–109. https://doi.org/https://doi.org/10.1016/j.rser.2017.02.052

Si, X., Zhang, J., Li, F., Jiao, C., Wang, S., Liu, S., … Xu, F. (2012). Adjustable structure transition and improved gases (H2, CO2) adsorption property of metal–organic framework MIL-53 by encapsulation of BNHx. *Dalton Transactions*, *41*(11), 3119–3122. https://doi.org/10.1039/C2DT12463G

Silva, P., Valente, A. A., Rocha, J., & Almeida Paz, F. A. (2010). Fast Microwave Synthesis of a Microporous Lanthanide−Organic Framework. *Crystal Growth & Design*, *10*(5), 2025–2028. https://doi.org/10.1021/cg900884d

Singh, D., Croiset, E., Douglas, P. L., & Douglas, M. A. (2003). Techno-economic study of CO2 capture from an existing coal-fired power plant: MEA scrubbing vs. O2/CO2 recycle combustion. *Energy Conversion and Management*, *44*(19), 3073–3091. https://doi.org/10.1016/S0196-8904(03)00040-2

Singto, S., Supap, T., Idem, R., Tontiwachwuthikul, P., Tantayanon, S., Al-Marri, M. J., & Benamor, A. (2016). Synthesis of new amines for enhanced carbon dioxide (CO2) capture performance: The effect of chemical structure on equilibrium solubility, cyclic capacity, kinetics of absorption and regeneration, and heats of absorption and regeneration. *Separation and Purification Technology*. https://doi.org/10.1016/j.seppur.2016.05.002

So, M. C., Wiederrecht, G. P., Mondloch, J. E., Hupp, J. T., & Farha, O. K. (2015). Metal–organic framework materials for light-harvesting and energy transfer. *Chemical Communications*, *51*(17), 3501–3510. https://doi.org/10.1039/C4CC09596K

Somorjai, G. A. (1994). The surface science of heterogeneous catalysis. *Surface Science*, *299–300*, 849–866. https://doi.org/https://doi.org/10.1016/0039-6028(94)90702-1

Son, W.-J., Choi, J.-S., & Ahn, W.-S. (2008). Adsorptive removal of carbon dioxide using polyethyleneimine-loaded mesoporous silica materials. *Microporous and Mesoporous Materials*, *113*(1), 31–40. https://doi.org/https://doi.org/10.1016/j.micromeso.2007.10.049

Sreedhar, I., Nahar, T., Venugopal, A., & Srinivas, B. (2017). Carbon capture by absorption – Path covered and ahead. *Renewable and Sustainable Energy Reviews*, *76*, 1080–1107. https://doi.org/https://doi.org/10.1016/j.rser.2017.03.109

Sreenivasulu, B., Gayatri, D. V., Sreedhar, I., & Raghavan, K. V. (2015). A journey into the process and engineering aspects of carbon capture technologies. *Renewable and Sustainable Energy Reviews*. https://doi.org/10.1016/j.rser.2014.09.029

Srinivas, G., Zhu, Y., Piner, R., Skipper, N., Ellerby, M., & Ruoff, R. (2010). Synthesis of graphene-like nanosheets and their hydrogen adsorption capacity. *Carbon*, *48*(3), 630–635. https://doi.org/https://doi.org/10.1016/j.carbon.2009.10.003

Stevens, L., Williams, K., Han, W. Y., Drage, T., Snape, C., Wood, J., & Wang, J. (2013). Preparation and CO2 adsorption of diamine modified montmorillonite via exfoliation grafting route. *Chemical Engineering Journal*, *215–216*, 699–708. https://doi.org/https://doi.org/10.1016/j.cej.2012.11.058

Stocker, T. F., Qin, D., Plattner, G. K., Tignor, M. M. B., Allen, S. K., Boschung, J., … Midgley, P. M. (2013). Climate change 2013 the physical science basis: Working Group I contribution to the fifth assessment report of the intergovernmental panel on climate change. *Climate Change 2013 the Physical Science Basis: Working Group I Contribution to the Fifth Assessment Report of the Intergovernmental Panel on Climate Change*, *9781107057*, 1–1535. https://doi.org/10.1017/CBO9781107415324

Su, F., & Lu, C. (2012). CO2 capture from gas stream by zeolite 13X using a dual-column temperature/vacuum swing adsorption. *Energy & Environmental Science*, *5*(10), 9021–9027. https://doi.org/10.1039/C2EE22647B

Su, F., Lu, C., Kuo, S.-C., & Zeng, W. (2010). Adsorption of CO2 on Amine-Functionalized Y-Type Zeolites. *Energy & Fuels*, *24*(2), 1441–1448. https://doi.org/10.1021/ef901077k

Sun, D., Ma, S., Ke, Y., Collins, D. J., & Zhou, H.-C. (2006). An Interweaving MOF with High Hydrogen Uptake. *Journal of the American Chemical Society*, *128*(12), 3896–3897. https://doi.org/10.1021/ja058777l

Sun, P, Grace, J. R., Lim, C. J., & Anthony, E. J. (2007). The effect of CaO sintering on cyclic CO2 capture in energy systems. *AIChE Journal*, *53*(9), 2432–2442. https://doi.org/10.1002/aic.11251

Sun, Ping, Grace, J. R., Lim, C. J., & Anthony, E. J. (2007). Removal of CO2 by Calcium-Based Sorbents in the Presence of SO2. *Energy & Fuels*, *21*(1), 163–170. https://doi.org/10.1021/ef060329r

Sun, Y., Shen, C., Lai, Q., Liu, W., Wang, D.-W., & Aguey-Zinsou, K.-F. (2018). Tailoring magnesium based materials for hydrogen storage through synthesis: Current state of the art. *Energy Storage Materials*, *10*, 168–198. https://doi.org/https://doi.org/10.1016/j.ensm.2017.01.010

Supasitmongkol, S., & Styring, P. (2010). High CO2 solubility in ionic liquids and a tetraalkylammonium-based poly(ionic liquid). *Energy & Environmental Science*, *3*(12), 1961–1972. https://doi.org/10.1039/C0EE00293C

Surblé, S., Millange, F., Serre, C., Düren, T., Latroche, M., Bourrelly, S., … Férey, G. (2006). Synthesis of MIL-102, a chromium carboxylate metal-organic framework, with gas sorption analysis. *Journal of the American Chemical Society*, *128*(46), 14889–14896. https://doi.org/10.1021/ja064343u

Surblé, S., Serre, C., Mellot-Draznieks, C., Millange, F., & Férey, G. (2006). A new isoreticular class of metal-organic-frameworks with the MIL-88 topology. *Chemical Communications*, (3), 284–286. https://doi.org/10.1039/b512169h

Svante, A. (1896). On the influence of carbonic acid in the air upon the temperature of the ground. *Philosophical Magazine and Journal of Science*, *41*, 237–276.

Svendsen, H. F., Hessen, E. T., & Mejdell, T. (2011). Carbon dioxide capture by absorption, challenges and possibilities. *Chemical Engineering Journal*. https://doi.org/10.1016/j.cej.2011.01.014

Swartzen-Allen, S. L., & Matijevic, E. (1974). Surface and colloid chemistry of clays. *Chemical Reviews*, *74*(3), 385–400. https://doi.org/10.1021/cr60289a004

Tafipolsky, M., Amirjalayer, S., & Schmid, R. (2010). First-principles-derived force field for copper paddle-wheel-based metal-organic frameworks. *Journal of Physical Chemistry C*, *114*(34), 14402–14409. https://doi.org/10.1021/jp104441d

Takagi, H., Hatori, H., Soneda, Y., Yoshizawa, N., & Yamada, Y. (2004). Adsorptive hydrogen storage in carbon and porous materials. *Materials Science and Engineering: B*, *108*(1), 143–147. https://doi.org/https://doi.org/10.1016/j.mseb.2003.10.095

Takagi, H., Hatori, H., Yamada, Y., Matsuo, S., & Shiraishi, M. (2004). Hydrogen adsorption properties of activated carbons with modified surfaces. *Journal of Alloys and Compounds*, *385*(1), 257–263. https://doi.org/https://doi.org/10.1016/j.jallcom.2004.03.139

Tang, J., Sun, W., Tang, H., Radosz, M., & Shen, Y. (2005). Enhanced CO2 Absorption of Poly(ionic liquid)s. *Macromolecules*, *38*(6), 2037–2039. https://doi.org/10.1021/ma047574z

Tang, J., Tang, H., Sun, W., Radosz, M., & Shen, Y. (2005). Poly(ionic liquid)s as new materials for CO2 absorption. *Journal of Polymer Science Part A: Polymer Chemistry*, *43*(22), 5477–5489. https://doi.org/10.1002/pola.21031

Taylor-Pashow, K. M. L., Della Rocca, J., Huxford, R. C., & Lin, W. (2010). Hybrid nanomaterials for biomedical applications. *Chemical Communications*, *46*(32), 5832–5849. https://doi.org/10.1039/c002073g

Taylor-Pashow, K. M. L., Della Rocca, J., Xie, Z., Tran, S., & Lin, W. (2009). Postsynthetic Modifications of Iron-Carboxylate Nanoscale Metal−Organic Frameworks for Imaging and Drug Delivery. *Journal of the American Chemical Society*, *131*(40), 14261–14263. https://doi.org/10.1021/ja906198y

Téllez S., C. A., Hollauer, E., Mondragon, M. A., & Castaño, V. M. (2001). Fourier transform infrared and Raman spectra, vibrational assignment and ab initio calculations of terephthalic acid and related compounds. *Spectrochimica Acta - Part A: Molecular and Biomolecular Spectroscopy*, *57*(5), 993–1007. https://doi.org/10.1016/S1386-1425(00)00428-5

Teter, J., Cazzola, P., & Petropoulos, A. (n.d.). Transport. Retrieved August 22, 2019, from https://www.iea.org/tcep/transport/

Texier-Mandoki, N., Dentzer, J., Piquero, T., Saadallah, S., David, P., & Vix-Guterl, C. (2004). Hydrogen storage in activated carbon materials: Role of the nanoporous texture. *Carbon*, *42*(12), 2744–2747. https://doi.org/https://doi.org/10.1016/j.carbon.2004.05.018

Thomas, K. M. (2007). Hydrogen adsorption and storage on porous materials. *Catalysis Today*, *120*(3), 389–398. https://doi.org/https://doi.org/10.1016/j.cattod.2006.09.015

Thommes, M., Kaneko, K., Neimark, A. V., Olivier, J. P., Rodriguez-Reinoso, F., Rouquerol, J., & Sing, K. S. W. (2015). Physisorption of gases, with special reference to the evaluation of surface area and pore size distribution (IUPAC Technical Report). *Pure and Applied Chemistry*, *87*(9–10), 1051–1069. https://doi.org/10.1515/pac-2014-1117

Tonigold, M., Lu, Y., Bredenkötter, B., Rieger, B., Bahnmüller, S., Hitzbleck, J., … Volkmer, D. (2009). Heterogeneous Catalytic Oxidation by MFU-1: A Cobalt(II)-Containing Metal–Organic Framework. *Angewandte Chemie International Edition*, *48*(41), 7546–7550. https://doi.org/10.1002/anie.200901241

Topologies, M. O. F., Stock, N., & Biswas, S. (2012). Synthesis of Metal-Organic Frameworks (MOFs): Routes to Various, 933–969. https://doi.org/10.1021/cr200304e

Torres, N., Galicia, J., Plasencia, Y., Cano, A., Echevarría, F., Desdin-Garcia, L. F., & Reguera, E. (2018). Implications of structural differences between Cu-BTC and Fe-BTC on their hydrogen storage capacity. *Colloids and Surfaces A: Physicochemical and Engineering Aspects*, *549*(2010), 138–146. https://doi.org/10.1016/j.colsurfa.2018.04.016

Tozzini, V., & Pellegrini, V. (2013). Prospects for hydrogen storage in graphene. *Physical Chemistry Chemical Physics*, *15*(1), 80–89. https://doi.org/10.1039/C2CP42538F

Tranchemontagne, D. J., Hunt, J. R., & Yaghi, O. M. (2008). Room temperature synthesis of metal-organic frameworks: MOF-5, MOF-74, MOF-177, MOF-199, and IRMOF-0. *Tetrahedron*, *64*(36), 8553–8557. https://doi.org/https://doi.org/10.1016/j.tet.2008.06.036

Trickett, C. A., Helal, A., Al-Maythalony, B. A., Yamani, Z. H., Cordova, K. E., & Yaghi, O. M. (2017). The chemistry of metal-organic frameworks for CO2 capture, regeneration and conversion. *Nature Reviews Materials*, *2*(8), 1–16. https://doi.org/10.1038/natrevmats.2017.45

Tripathi, G. N. R., & Sheng, S. J. (1979). Solid-state vibrational spectra and structures of terephthalic acid and the terephthalate ion. *Journal of Molecular Structure*, *57*(C), 21–34. https://doi.org/10.1016/0022-2860(79)80229-X

U.S. Department of Energy. (2015). 3.3 Hydrogen Storage. *Fuel Cell Technologies Office Multi-Year Research, Development, and Demonstration Plan*, (August 2009), 23. Retrieved from https://www.energy.gov/eere/fuelcells/downloads/fuel-cell-technologies-office-multi-year-research-development-and-22

Union, I., Pure, O. F., & Chemistry, A. (1985). *INTERNATIONAL UNION OF PURE COMMISSION ON COLLOID AND SURFACE CHEMISTRY INCLUDING CATALYSIS * REPORTING PHYSISORPTION DATA FOR GAS / SOLID SYSTEMS with Special Reference to the Determination of Surface Area and Porosity*. *Area* (Vol. 57).

United Nations. (2015). *Summary of the Paris Agreement*. *United Nations Framework Convention on Climate Change*. Retrieved from http://bigpicture.unfccc.int/#content-the-paris-agreemen

Vaidya, P. D., & Kenig, E. Y. (2008). Acceleration of CO2 reaction with N,N-Diethylethanolamine in aqueous solutions by piperazine. *Industrial and Engineering Chemistry Research*. https://doi.org/10.1021/ie070783y

Vallet-Regi, M., Rámila, A., del Real, R. P., & Pérez-Pariente, J. (2001). A New Property of MCM-41: Drug Delivery System. *Chemistry of Materials*, *13*(2), 308–311. https://doi.org/10.1021/cm0011559

Valverde, J. M., Sanchez-Jimenez, P. E., & Perez-Maqueda, L. A. (2014). High and stable CO2 capture capacity of natural limestone at Ca-looping conditions by heat pretreatment and recarbonation synergy. *Fuel*, *123*, 79–85. https://doi.org/https://doi.org/10.1016/j.fuel.2014.01.045

Van Der Zwaan, B., & Smekens, K. (2009). CO2 capture and storage with leakage in an energy-climate model. *Environmental Modeling and Assessment*. https://doi.org/10.1007/s10666-007-9125-3

Vinayan, B. P., Nagar, R., & Ramaprabhu, S. (2013). Solar light assisted green synthesis of palladium

nanoparticle decorated nitrogen doped graphene for hydrogen storage application. *Journal of Materials Chemistry A*, *1*(37), 11192–11199. https://doi.org/10.1039/C3TA12016C

Vitillo, J. G., Ricchiardi, G., Spoto, G., & Zecchina, A. (2005). Theoretical maximal storage of hydrogen in zeolitic frameworks. *Physical Chemistry Chemical Physics*, *7*(23), 3948–3954. https://doi.org/10.1039/B510989B

Voskuilen, T. G., Pourpoint, T. L., & Dailly, A. M. (2012). Hydrogen adsorption on microporous materials at ambient temperatures and pressures up to 50 MPa. *Adsorption*, *18*(3), 239–249. https://doi.org/10.1007/s10450-012-9397-z

Vuong, G. T., Pham, M. H., & Do, T. O. (2013a). Direct synthesis and mechanism of the formation of mixed metal Fe 2Ni-MIL-88B. *CrystEngComm*, *15*(45), 9694–9703. https://doi.org/10.1039/c3ce41453a

Vuong, G. T., Pham, M. H., & Do, T. O. (2013b). Synthesis and engineering porosity of a mixed metal Fe2Ni MIL-88B metal-organic framework. *Dalton Transactions*, *42*(2), 550–557. https://doi.org/10.1039/c2dt32073h

Wade, C. R., & Dincă, M. (2012). Investigation of the synthesis, activation, and isosteric heats of CO2 adsorption of the isostructural series of metal–organic frameworks M3(BTC)2 (M = Cr, Fe, Ni, Cu, Mo, Ru). *Dalton Transactions*, *41*(26), 7931–7938. https://doi.org/10.1039/C2DT30372H

Walton, K. S., Abney, M. B., & Douglas LeVan, M. (2006). CO2 adsorption in Y and X zeolites modified by alkali metal cation exchange. *Microporous and Mesoporous Materials*, *91*(1), 78–84. https://doi.org/https://doi.org/10.1016/j.micromeso.2005.11.023

Wang, B., Côté, A. P., Furukawa, H., O'Keeffe, M., & Yaghi, O. M. (2008). Colossal cages in zeolitic imidazolate frameworks as selective carbon dioxide reservoirs. *Nature*, *453*(7192), 207–211. https://doi.org/10.1038/nature06900

Wang, D., Sentorun-Shalaby, C., Ma, X., & Song, C. (2011). High-Capacity and Low-Cost Carbon-Based "Molecular Basket" Sorbent for CO2 Capture from Flue Gas. *Energy & Fuels*, *25*(1), 456–458. https://doi.org/10.1021/ef101364c

Wang, J.-L., Wang, C., & Lin, W. (2012). Metal–Organic Frameworks for Light Harvesting and Photocatalysis. *ACS Catalysis*, *2*(12), 2630–2640. https://doi.org/10.1021/cs3005874

Wang, J., Senkovska, I., Oschatz, M., Lohe, M. R., Borchardt, L., Heerwig, A., … Kaskel, S. (2013). Highly porous nitrogen-doped polyimine-based carbons with adjustable microstructures for CO2 capture. *Journal of Materials Chemistry A*, *1*(36), 10951–10961. https://doi.org/10.1039/C3TA11995E

Wang, K., Shang, H., Li, L., Yan, X., Yan, Z., Liu, C., & Zha, Q. (2012). Efficient CO2 capture on low-cost silica gel modified by polyethyleneimine. *Journal of Natural Gas Chemistry*, *21*(3), 319–323. https://doi.org/https://doi.org/10.1016/S1003-9953(11)60371-X

Wang, L., Stuckert, N. R., & Yang, R. T. (2011). Unique hydrogen adsorption properties of graphene. *AIChE Journal*, *57*(10), 2902–2908. https://doi.org/10.1002/aic.12470

Wang, L., & Yang, R. T. (2008). New sorbents for hydrogen storage by hydrogen spillover – a review. *Energy & Environmental Science*, *1*(2), 268–279. https://doi.org/10.1039/B807957A

Wang, Qiang, Luo, J., Zhong, Z., & Borgna, A. (2011). CO2 capture by solid adsorbents and their applications: current status and new trends. *Energy & Environmental Science*, *4*(1), 42–55. https://doi.org/10.1039/C0EE00064G

Wang, Qingfei, Xia, W., Guo, W., An, L., Xia, D., & Zou, R. (2013). Functional Zeolitic-Imidazolate-Framework-Templated Porous Carbon Materials for CO2 Capture and Enhanced Capacitors. *Chemistry – An Asian Journal*, *8*(8), 1879–1885. https://doi.org/10.1002/asia.201300147

Wang, Qinyu, & Johnson, J. K. (1999). Molecular simulation of hydrogen adsorption in single-walled carbon nanotubes and idealized carbon slit pores. *Journal of Chemical Physics*, *110*(1), 577–586. https://doi.org/10.1063/1.478114

Wang, R., Li, D. F., & Liang, D. T. (2004). Modeling of CO2 capture by three typical amine solutions in hollow fiber membrane contactors. *Chemical Engineering and Processing: Process Intensification*, *43*(7), 849–856. https://doi.org/https://doi.org/10.1016/S0255-2701(03)00105-3

Wang, R., Li, D. F., Zhou, C., Liu, M., & Liang, D. T. (2004). Impact of DEA solutions with and without CO2 loading on porous polypropylene membranes intended for use as contactors. *Journal of Membrane Science*, *229*(1), 147–157. https://doi.org/https://doi.org/10.1016/j.memsci.2003.10.022

Wang, R., Zhang, H. Y., Feron, P. H. M., & Liang, D. T. (2005). Influence of membrane wetting on CO2 capture in microporous hollow fiber membrane contactors. *Separation and Purification Technology*, *46*(1), 33–40. https://doi.org/https://doi.org/10.1016/j.seppur.2005.04.007

Wang, Weilong, Wang, X., Song, C., Wei, X., Ding, J., & Xiao, J. (2013). Sulfuric Acid Modified Bentonite as the Support of Tetraethylenepentamine for CO2 Capture. *Energy & Fuels*, *27*(3), 1538–1546. https://doi.org/10.1021/ef3021816

Wang, Wenjing, & Yuan, D. (2014). Mesoporous carbon originated from non-permanent porous MOFs for gas storage and CO2/CH4 separation. *Scientific Reports*, *4*(1), 5711. https://doi.org/10.1038/srep05711

Wang, X.-F., Zhang, Y.-B., Huang, H., Zhang, J.-P., & Chen, X.-M. (2008). Microwave-Assisted Solvothermal Synthesis of a Dynamic Porous Metal-Carboxylate Framework. *Crystal Growth & Design*, *8*(12), 4559–4563. https://doi.org/10.1021/cg800623v

Wang, Xia, Chen, H., Zhang, L., Yu, R., Qu, R., & Yang, L. (2014). Effects of coexistent gaseous components and fine particles in the flue gas on CO2 separation by flat-sheet polysulfone membranes. *Journal of Membrane Science*, *470*, 237–245. https://doi.org/https://doi.org/10.1016/j.memsci.2014.07.040

Wang, Xianfeng, Akhmedov, N. G., Duan, Y., Luebke, D., & Li, B. (2013). Immobilization of amino acid ionic liquids into nanoporous microspheres as robust sorbents for CO2 capture. *Journal of Materials Chemistry A*, *1*(9), 2978–2982. https://doi.org/10.1039/C3TA00768E

Wang, Xin, Li, X., Ouyang, C., Li, Z., Dou, S., Ma, Z., … Wang, S. (2016). Nonporous MOF-derived dopant-free mesoporous carbon as an efficient metal-free electrocatalyst for the oxygen reduction reaction. *Journal of Materials Chemistry A*, *4*(24), 9370–9374. https://doi.org/10.1039/C6TA03015G

Wang, Xingrui, Li, H., Liu, H., & Hou, X. (2011). AS-synthesized mesoporous silica MSU-1 modified with tetraethylenepentamine for CO2 adsorption. *Microporous and Mesoporous Materials*, *142*(2), 564–569. https://doi.org/https://doi.org/10.1016/j.micromeso.2010.12.047

Wappel, D., Gronald, G., Kalb, R., & Draxler, J. (2010). Ionic liquids for post-combustion CO2 absorption. *International Journal of Greenhouse Gas Control*. https://doi.org/10.1016/j.ijggc.2009.11.012

Wei, J., Zhou, D., Sun, Z., Deng, Y., Xia, Y., & Zhao, D. (2013). A Controllable Synthesis of Rich Nitrogen-Doped Ordered Mesoporous Carbon for CO2 Capture and Supercapacitors. *Advanced Functional Materials*, *23*(18), 2322–2328. https://doi.org/10.1002/adfm.201202764

Wei, L., & Mao, Y. (2016). Enhanced hydrogen storage performance of reduced graphene oxide hybrids with nickel or its metallic mixtures based on spillover mechanism. *International Journal of Hydrogen Energy*, *41*(27), 11692–11699. https://doi.org/https://doi.org/10.1016/j.ijhydene.2016.04.030

Weitkamp, J., Fritz, M., & Ernst, S. (1995). Zeolites as media for hydrogen storage. *International Journal of Hydrogen Energy*, *20*(12), 967–970. https://doi.org/https://doi.org/10.1016/0360-3199(95)00058-L

Wenger, D., Polifke, W., Schmidt-Ihn, E., Abdel-Baset, T., & Maus, S. (2009). Comments on solid state hydrogen storage systems design for fuel cell vehicles. *International Journal of Hydrogen Energy*, *34*(15), 6265–6270. https://doi.org/https://doi.org/10.1016/j.ijhydene.2009.05.072

Wickramaratne, N. P., & Jaroniec, M. (2013). Importance of small micropores in CO2 capture by phenolic resin-based activated carbon spheres. *Journal of Materials Chemistry A*, *1*(1), 112–116. https://doi.org/10.1039/C2TA00388K

Wiersum, A. D., Soubeyrand-Lenoir, E., Yang, Q., Moulin, B., Guillerm, V., Yahia, M. Ben, … Llewellyn, P. L. (2011). An evaluation of UiO-66 for gas-based applications. *Chemistry - An Asian Journal*, *6*(12), 3270–3280. https://doi.org/10.1002/asia.201100201

Wilberforce, T., El-Hassan, Z., Khatib, F. N., Al Makky, A., Baroutaji, A., Carton, J. G., & Olabi, A. G. (2017). Developments of electric cars and fuel cell hydrogen electric cars. *International Journal of Hydrogen Energy*, *42*(40), 25695–25734. https://doi.org/10.1016/j.ijhydene.2017.07.054

Wilke, A., & Weber, J. (2011). Hierarchical nanoporous melamine resin sponges with tunable porosity—porosity analysis and CO2 sorption properties. *Journal of Materials Chemistry*, *21*(14), 5226–5229. https://doi.org/10.1039/C1JM10171D

Willans, C. E., French, S., Anderson, K. M., Barbour, L. J., Gertenbach, J.-A., Lloyd, G. O., … Steed, J. W. (2011). Tripodal imidazole frameworks: Reversible vapour sorption both with and without significant structural changes. *Dalton Transactions*, *40*(3), 573–582. https://doi.org/10.1039/C0DT01011A

Wilson, E. ; Gerard, D. (2007). *Carbon Capture and Sequestration: Integrating Technology, Monitoring and Regulation*. *Carbon Capture and Sequestration: Integrating Technology, Monitoring and Regulation*.

Wirawan, S. K., & Creaser, D. (2006). CO2 adsorption on silicalite-1 and cation exchanged ZSM-5 zeolites using a step change response method. *Microporous and Mesoporous Materials*, *91*(1), 196–205. https://doi.org/https://doi.org/10.1016/j.micromeso.2005.11.047

Wong-Foy, A. G., Matzger, A. J., & Yaghi, O. M. (2006). Exceptional H2 Saturation Uptake in Microporous Metal−Organic Frameworks. *Journal of the American Chemical Society*, *128*(11), 3494–3495. https://doi.org/10.1021/ja058213h

Wu, C., Gao, Q., Hu, J., Chen, Z., & Shi, W. (2009). Rapid preparation, characterization and hydrogen storage properties of pure and metal ions doped mesoporous MCM-41. *Microporous and Mesoporous Materials*, *117*(1), 165–169. https://doi.org/https://doi.org/10.1016/j.micromeso.2008.06.020

Wu, H., Chua, Y. S., Krungleviciute, V., Tyagi, M., Chen, P., Yildirim, T., & Zhou, W. (2013). Unusual and highly tunable missing-linker defects in zirconium metal-organic framework UiO-66 and their important effects on gas adsorption. *Journal of the American Chemical Society*, *135*(28), 10525–10532. https://doi.org/10.1021/ja404514r

Wu, H., Simmons, J. M., Srinivas, G., Zhou, W., & Yildirim, T. (2010). Adsorption Sites and Binding Nature of CO2 in Prototypical Metal−Organic Frameworks: A Combined Neutron Diffraction and First-Principles Study. *The Journal of Physical Chemistry Letters*, *1*(13), 1946–1951. https://doi.org/10.1021/jz100558r

Wu, S. F., & Zhu, Y. Q. (2010). Behavior of CaTiO3/Nano-CaO as a CO2 Reactive Adsorbent. *Industrial & Engineering Chemistry Research*, *49*(6), 2701–2706. https://doi.org/10.1021/ie900900r

Wu, X. B., Chen, P., Lin, J., & Tan, K. L. (2000). Hydrogen uptake by carbon nanotubes. *International Journal of Hydrogen Energy*, *25*(3), 261–265. https://doi.org/https://doi.org/10.1016/S0360-3199(99)00037-3

Wu, Y, Blamey, J., Anthony, E. J., & Fennell, P. S. (2010). Morphological Changes of Limestone Sorbent Particles during Carbonation/Calcination Looping Cycles in a Thermogravimetric Analyzer (TGA) and Reactivation with Steam. *Energy & Fuels*, *24*(4), 2768–2776. https://doi.org/10.1021/ef9012449

Wu, Ye, Chen, X., Dong, W., Zhao, C., Zhang, Z., Liu, D., & Liang, C. (2013). K2CO3/Al2O3 for Capturing CO2 in Flue Gas from Power Plants. Part 5: Carbonation and Failure Behavior of K2CO3/Al2O3 in the Continuous CO2 Sorption–Desorption System. *Energy & Fuels*, *27*(8), 4804–4809. https://doi.org/10.1021/ef400778d

Xi, K., Cao, S., Peng, X., Ducati, C., Vasant Kumar, R., & Cheetham, A. K. (2013). Carbon with hierarchical pores from carbonized metal–organic frameworks for lithium sulphur batteries. *Chemical Communications*, *49*(22), 2192–2194. https://doi.org/10.1039/C3CC38009B

Xia, K., Gao, Q., Wu, C., Song, S., & Ruan, M. (2007). Activation, characterization and hydrogen storage properties of the mesoporous carbon CMK-3. *Carbon*, *45*(10), 1989–1996. https://doi.org/10.1016/j.carbon.2007.06.002

Xia, Y., Yang, Z., & Zhu, Y. (2013). Porous carbon-based materials for hydrogen storage: advancement and challenges. *Journal of Materials Chemistry A*, *1*(33), 9365–9381. https://doi.org/10.1039/C3TA10583K

Xiang, Z., Cao, D., Shao, X., Wang, W., Zhang, J., & Wu, W. (2010). Facile preparation of high-capacity hydrogen storage metal-organic frameworks: A combination of microwave-assisted solvothermal synthesis and supercritical activation. *Chemical Engineering Science*, *65*(10), 3140–3146. https://doi.org/https://doi.org/10.1016/j.ces.2010.02.005

Xiang, Z., Leng, S., & Cao, D. (2012). Functional Group Modification of Metal–Organic Frameworks for CO2 Capture. *The Journal of Physical Chemistry C*, *116*(19), 10573–10579. https://doi.org/10.1021/jp3018875

Xiao, P., Zhang, J., Webley, P., Li, G., Singh, R., & Todd, R. (2008). Capture of CO2 from flue gas streams with zeolite 13X by vacuum-pressure swing adsorption. *Adsorption*, *14*(4), 575–582. https://doi.org/10.1007/s10450-008-9128-7

Xie, L.-H., & Suh, M. P. (2013). High CO2-Capture Ability of a Porous Organic Polymer Bifunctionalized with Carboxy and Triazole Groups. *Chemistry – A European Journal*, *19*(35), 11590–11597. https://doi.org/10.1002/chem.201301822

Xu, A., Yang, A., Young, S., deMontigny, D., & Tontiwachwuthikul, P. (2008). Effect of internal coagulant on effectiveness of polyvinylidene fluoride membrane for carbon dioxide separation and absorption. *Journal of Membrane Science*, *311*(1), 153–158. https://doi.org/https://doi.org/10.1016/j.memsci.2007.12.008

Xu, G., Meng, Z., Liu, Y., Guo, X., Deng, K., Ding, L., & Lu, R. (2019). Porous MOF-205 with multiple modifications for efficiently storing hydrogen and methane as well as separating carbon dioxide from hydrogen and methane. *International Journal of Energy Research*, *43*(13), 7517–7528. https://doi.org/10.1002/er.4631

Xue, Z., Zhang, Z., Han, J., Chen, Y., & Mu, T. (2011). Carbon dioxide capture by a dual amino ionic liquid

with amino-functionalized imidazolium cation and taurine anion. *International Journal of Greenhouse Gas Control*. https://doi.org/10.1016/j.ijggc.2011.05.014

Yaghi, O M, Li, G., & Li, H. (1995). Selective binding and removal of guests in a microporous metal–organic framework. *Nature*, *378*, 703. Retrieved from https://doi.org/10.1038/378703a0

Yaghi, Omar M., Li, H., Davis, C., Richardson, D., & Groy, T. L. (1998). Synthetic Strategies, Structure Patterns, and Emerging Properties in the Chemistry of Modular Porous Solids †. *Accounts of Chemical Research*, *31*(8), 474–484. https://doi.org/10.1021/ar970151f

Yaghi, Omar M, O'Keeffe, M., Ockwig, N. W., Chae, H. K., Eddaoudi, M., & Kim, J. (2003). Reticular synthesis and the design of new materials. *Nature*, *423*(6941), 705–714. https://doi.org/10.1038/nature01650

Yamamoto, Y., Nawa, N., Nishimoto, S., Kameshima, Y., Matsuda, M., & Miyake, M. (2011). Temperature dependence of hydrogen adsorption properties of nickel-doped mesoporous silica. *International Journal of Hydrogen Energy*, *36*(9), 5739–5743. https://doi.org/https://doi.org/10.1016/j.ijhydene.2011.02.010

Yan, L., Dai, P., Wang, Y., Gu, X., Li, L., Cao, L., & Zhao, X. (2017). In Situ Synthesis Strategy for Hierarchically Porous Ni2P Polyhedrons from MOFs Templates with Enhanced Electrochemical Properties for Hydrogen Evolution. *ACS Applied Materials & Interfaces*, *9*(13), 11642–11650. https://doi.org/10.1021/acsami.7b01037

Yan, Q., Lin, Y., Wu, P., Zhao, L., Cao, L., Peng, L., … Chen, L. (2013). Designed Synthesis of Functionalized Two-Dimensional Metal–Organic Frameworks with Preferential CO2 Capture. *ChemPlusChem*, *78*(1), 86–91. https://doi.org/10.1002/cplu.201200270

Yan, S., Fang, M.-X., Zhang, W.-F., Wang, S.-Y., Xu, Z.-K., Luo, Z.-Y., & Cen, K.-F. (2007). Experimental study on the separation of CO2 from flue gas using hollow fiber membrane contactors without wetting. *Fuel Processing Technology*, *88*(5), 501–511. https://doi.org/https://doi.org/10.1016/j.fuproc.2006.12.007

Yang, Hongqun, Xu, Z., Fan, M., Gupta, R., Slimane, R. B., Bland, A. E., & Wright, I. (2008). Progress in carbon dioxide separation and capture: A review. *Journal of Environmental Sciences*, *20*(1), 14–27. https://doi.org/10.1016/S1001-0742(08)60002-9

Yang, Hongwei, Orefuwa, S., & Goudy, A. (2011). Study of mechanochemical synthesis in the formation of the metal–organic framework Cu3(BTC)2 for hydrogen storage. *Microporous and Mesoporous Materials*, *143*(1), 37–45. https://doi.org/https://doi.org/10.1016/j.micromeso.2011.02.003

Yang, J., Sudik, A., Wolverton, C., & Siegel, D. J. (2010). High capacity hydrogen storage materials: attributes for automotive applications and techniques for materials discovery. *Chemical Society Reviews*, *39*(2), 656–675. https://doi.org/10.1039/B802882F

Yang, S., Zhan, L., Xu, X., Wang, Y., Ling, L., & Feng, X. (2013). Graphene-Based Porous Silica Sheets Impregnated with Polyethyleneimine for Superior CO2 Capture. *Advanced Materials*, *25*(15), 2130–2134. https://doi.org/10.1002/adma.201204427

Yartys, V. A., Lototskyy, M. V, Akiba, E., Albert, R., Antonov, V. E., Ares, J. R., … Zhu, M. (2019). Magnesium based materials for hydrogen based energy storage: Past, present and future. *International Journal of Hydrogen Energy*, *44*(15), 7809–7859. https://doi.org/https://doi.org/10.1016/j.ijhydene.2018.12.212

Yazaydin, A. O., Snurr, R. Q., Park, T.-H., Koh, K., Liu, J., LeVan, D. M., … Willis, R. R. (2009). Screening

of Metal-Organic Frameworks for Carbon Dioxide Capture from Flue Gas Using a Combined Experimental and Modeling Approach. *J. Am. Chem. Soc*, *131*, 18198–18199. https://doi.org/10.1017/S0022112081000943

Yazaydin, A. Ö., Snurr, R. Q., Park, T. H., Koh, K., Liu, J., LeVan, M. D., … Willis, R. R. (2009). Screening of metal-organic frameworks for carbon dioxide capture from flue gas using a combined experimental and modeling approach. *Journal of the American Chemical Society*. https://doi.org/10.1021/ja9057234

Ye, Y., Ahn, C. C., Witham, C., Fultz, B., Liu, J., Rinzler, A. G., … Smalley, R. E. (1999). Hydrogen adsorption and cohesive energy of single-walled carbon nanotubes. *Applied Physics Letters*, *74*(16), 2307–2309. https://doi.org/10.1063/1.123833

Yeh, A. C., & Bai, H. (1999). Comparison of ammonia and monoethanolamine solvents to reduce CO2 greenhouse gas emissions. *Science of the Total Environment*. https://doi.org/10.1016/S0048-9697(99)00025-X

Yeon, S.-H., Lee, K.-S., Sea, B., Park, Y.-I., & Lee, K.-H. (2005). Application of pilot-scale membrane contactor hybrid system for removal of carbon dioxide from flue gas. *Journal of Membrane Science*, *257*(1), 156–160. https://doi.org/https://doi.org/10.1016/j.memsci.2004.08.037

Yi, C.-K., Jo, S.-H., Seo, Y., Lee, J.-B., & Ryu, C.-K. (2007). Continuous operation of the potassium-based dry sorbent CO2 capture process with two fluidized-bed reactors. *International Journal of Greenhouse Gas Control*, *1*(1), 31–36. https://doi.org/https://doi.org/10.1016/S1750-5836(07)00014-X

Yi, C.-K., Jo, S. H., Seo, Y., Park, S. D., Moon, K. H., Yoo, J. S., … Ryu, C. K. (2006). CO2 capture characteristics of dry sorbents in a fast fluidized reactor. In H.-K. Rhee, I.-S. Nam, & J. M. B. T.-S. in S. S. and C. Park (Eds.), *New Developments and Application in Chemical Reaction Engineering* (Vol. 159, pp. 501–504). Elsevier. https://doi.org/https://doi.org/10.1016/S0167-2991(06)81643-5

Yi, K. B., Ko, C. H., Park, J.-H., & Kim, J.-N. (2009). Improvement of the cyclic stability of high temperature CO2 absorbent by the addition of oxygen vacancy possessing material. *Catalysis Today*, *146*(1), 241–247. https://doi.org/https://doi.org/10.1016/j.cattod.2008.12.009

Yin, J., Zhang, C., Qin, C., Liu, W., An, H., Chen, G., & Feng, B. (2012). Reactivation of calcium-based sorbent by water hydration for CO2 capture. *Chemical Engineering Journal*, *198–199*, 38–44. https://doi.org/https://doi.org/10.1016/j.cej.2012.05.078

Yoon, M., Srirambalaji, R., & Kim, K. (2012). Homochiral Metal–Organic Frameworks for Asymmetric Heterogeneous Catalysis. *Chemical Reviews*, *112*(2), 1196–1231. https://doi.org/10.1021/cr2003147

Yu, C.-T., & Chen, W.-C. (2014). Hydrothermal preparation of calcium–aluminum carbonate sorbent for high-temperature CO2 capture in fixed-bed reactor. *Fuel*, *122*, 179–185. https://doi.org/https://doi.org/10.1016/j.fuel.2014.01.022

Yu, F.-C., Phalak, N., Sun, Z., & Fan, L.-S. (2012). Activation Strategies for Calcium-Based Sorbents for CO2 Capture: A Perspective. *Industrial & Engineering Chemistry Research*, *51*(4), 2133–2142. https://doi.org/10.1021/ie200802y

Yu, H., Wu, Y.-T., Jiang, Y.-Y., Zhou, Z., & Zhang, Z.-B. (2009). Low viscosity amino acid ionic liquids with asymmetric tetraalkylammonium cations for fast absorption of CO2. *New Journal of Chemistry*, *33*(12), 2385–2390. https://doi.org/10.1039/B9NJ00330D

Yu, Jiaguo, Le, Y., & Cheng, B. (2012). Fabrication and CO2 adsorption performance of bimodal porous silica hollow spheres with amine-modified surfaces. *RSC Advances*, *2*(17), 6784–6791. https://doi.org/10.1039/C2RA21017G

Yu, Juhyon, Guo, M., Muhammad, F., Wang, A., Zhang, F., Li, Q., & Zhu, G. (2014). One-pot synthesis of highly ordered nitrogen-containing mesoporous carbon with resorcinol–urea–formaldehyde resin for CO2 capture. *Carbon*, *69*, 502–514. https://doi.org/https://doi.org/10.1016/j.carbon.2013.12.058

Yuan, D., Zhao, D., Sun, D., & Zhou, H. C. (2010). An isoreticular series of metal-organic frameworks with dendritic hexacarboxylate ligands and exceptionally high gas-uptake capacity. *Angewandte Chemie - International Edition*, *49*(31), 5357–5361. https://doi.org/10.1002/anie.201001009

Yuan, S., Zou, L., Qin, J. S., Li, J., Huang, L., Feng, L., … Zhou, H. C. (2017). Construction of hierarchically porous metal-organic frameworks through linker labilization. *Nature Communications*, *8*(May), 1–10. https://doi.org/10.1038/ncomms15356

Yuan, W., Friščić, T., Apperley, D., & James, S. L. (2010). High Reactivity of Metal–Organic Frameworks under Grinding Conditions: Parallels with Organic Molecular Materials. *Angewandte Chemie International Edition*, *49*(23), 3916–3919. https://doi.org/10.1002/anie.200906965

Yuan, W., Garay, A. L., Pichon, A., Clowes, R., Wood, C. D., Cooper, A. I., & James, S. L. (2010). Study of the mechanochemical formation and resulting properties of an archetypal MOF: Cu3(BTC)2 (BTC = 1,3,5-benzenetricarboxylate). *CrystEngComm*, *12*(12), 4063–4065. https://doi.org/10.1039/C0CE00486C

Yue, M. B., Chun, Y., Cao, Y., Dong, X., & Zhu, J. H. (2006). CO2 Capture by As-Prepared SBA-15 with an Occluded Organic Template. *Advanced Functional Materials*, *16*(13), 1717–1722. https://doi.org/10.1002/adfm.200600427

Yue, Y., Binder, A. J., Song, R., Cui, Y., Chen, J., Hensley, D. K., & Dai, S. (2014). Encapsulation of large dye molecules in hierarchically superstructured metal-organic frameworks. *Dalton Transactions*, *43*(48), 17893–17898. https://doi.org/10.1039/c4dt02516d

Yue, Y., Fulvio, P. F., & Dai, S. (2015). Hierarchical Metal-Organic Framework Hybrids: Perturbation-Assisted Nanofusion Synthesis. *Accounts of Chemical Research*, *48*(12), 3044–3052. https://doi.org/10.1021/acs.accounts.5b00349

Yue, Y., Qiao, Z. A., Fulvio, P. F., Binder, A. J., Tian, C., Chen, J., … Dai, S. (2013a). Template-free synthesis of hierarchical porous metal-organic frameworks. *Journal of the American Chemical Society*, *135*(26), 9572–9575. https://doi.org/10.1021/ja402694f

Yue, Y., Qiao, Z. A., Fulvio, P. F., Binder, A. J., Tian, C., Chen, J., … Dai, S. (2013b). Template-free synthesis of hierarchical porous metal-organic frameworks. *Journal of the American Chemical Society*, *135*(26), 9572–9575. https://doi.org/10.1021/ja402694f

Yue, Y., Zhang, Z., Binder, A. J., Chen, J., Jin, X., Overbury, S. H., & Dai, S. (2015). Hierarchically superstructured Prussian blue analogues: Spontaneous assembly synthesis and applications as pseudocapacitive materials. *ChemSusChem*, *8*(1), 177–183. https://doi.org/10.1002/cssc.201402520

Yurduşen, A., & Yürüm, Y. (2019). A Controlled Synthesis Strategy to Enhance the CO<inf>2</inf> Adsorption Capacity of MIL-88B Type MOF Crystallites by the Crucial Role of Narrow Micropores. *Industrial and Engineering Chemistry Research*, *58*(31). https://doi.org/10.1021/acs.iecr.9b01653

Yurduşen, Aysu, Yürüm, A., & Yürüm, Y. (2019). Engineering MIL-88B crystallites for enhanced H 2 uptake capacity: The role of ultramicropores. *International Journal of Energy Research*. https://doi.org/10.1002/er.5104

Yurduşen, Aysu, Yürüm, A., & Yürüm, Y. (2020a). A remarkable increase in the adsorbed H2 amount: Influence of pore size distribution on the H2 adsorption capacity of Fe-BTC. *International Journal of*

Hydrogen Energy. https://doi.org/10.1016/j.ijhydene.2020.02.202

Yurduşen, Aysu, Yürüm, A., & Yürüm, Y. (2020b). The role of ultramicropores in the CO2 adsorption capacity of Fe–BTC crystallites synthesized with a perturbation-assisted nanofusion synthesis strategy. *CrystEngComm*. https://doi.org/10.1039/C9CE01626K

Yürüm, Y., Taralp, A., & Veziroglu, T. N. (2009a). Storage of hydrogen in nanostructured carbon materials. *International Journal of Hydrogen Energy*, *34*(9), 3784–3798. https://doi.org/10.1016/j.ijhydene.2009.03.001

Yürüm, Y., Taralp, A., & Veziroglu, T. N. (2009b). Storage of hydrogen in nanostructured carbon materials. *International Journal of Hydrogen Energy*, *34*(9), 3784–3798. https://doi.org/https://doi.org/10.1016/j.ijhydene.2009.03.001

Zhang, Fan, Zhao, P., Niu, M., & Maddy, J. (2016). The survey of key technologies in hydrogen energy storage. *International Journal of Hydrogen Energy*, *41*(33), 14535–14552. https://doi.org/10.1016/j.ijhydene.2016.05.293

Zhang, Fumin, Shi, J., Jin, Y., Fu, Y., Zhong, Y., & Zhu, W. (2015). Facile synthesis of MIL-100(Fe) under HF-free conditions and its application in the acetalization of aldehydes with diols. *Chemical Engineering Journal*, *259*, 183–190. https://doi.org/10.1016/j.cej.2014.07.119

Zhang, H.-Y., Wang, R., Liang, D. T., & Tay, J. H. (2008). Theoretical and experimental studies of membrane wetting in the membrane gas–liquid contacting process for CO2 absorption. *Journal of Membrane Science*, *308*(1), 162–170. https://doi.org/https://doi.org/10.1016/j.memsci.2007.09.050

Zhang, H., Goeppert, A., Czaun, M., Prakash, G. K. S., & Olah, G. A. (2014). CO2 capture on easily regenerable hybrid adsorbents based on polyamines and mesocellular silica foam. Effect of pore volume of the support and polyamine molecular weight. *RSC Advances*, *4*(37), 19403–19417. https://doi.org/10.1039/C4RA02145B

Zhang, J., Singh, R., & Webley, P. A. (2008). Alkali and alkaline-earth cation exchanged chabazite zeolites for adsorption based CO2 capture. *Microporous and Mesoporous Materials*, *111*(1), 478–487. https://doi.org/https://doi.org/10.1016/j.micromeso.2007.08.022

Zhang, L., Qu, R., Sha, Y., Wang, X., & Yang, L. (2015). Membrane gas absorption for CO2 capture from flue gas containing fine particles and gaseous contaminants. *International Journal of Greenhouse Gas Control*, *33*, 10–17. https://doi.org/https://doi.org/10.1016/j.ijggc.2014.11.017

Zhang, Q., Xu, Y., Wang, Y., Zhang, H., Wang, Y., Jiao, L., & Yuan, H. (2016). Enhanced hydrogen storage performance of MgH2Ni2P/graphene nanosheets. *International Journal of Hydrogen Energy*, *41*(38), 17000–17007. https://doi.org/https://doi.org/10.1016/j.ijhydene.2016.07.133

Zhang, S., Du, M., Shao, P., Wang, L., Ye, J., Chen, J., & Chen, J. (2018). Carbonic Anhydrase Enzyme-MOFs Composite with a Superior Catalytic Performance to Promote CO 2 Absorption into Tertiary Amine Solution. *Environmental Science and Technology*. https://doi.org/10.1021/acs.est.8b04671

Zhang, T., & Lin, W. (2014). Metal-organic frameworks for artificial photosynthesis and photocatalysis. *Chemical Society Reviews*, *43*(16), 5982–5993. https://doi.org/10.1039/c4cs00103f

Zhang, W., Liu, Y., Lu, G., Wang, Y., Li, S., Cui, C., … Huo, F. (2015). Mesoporous Metal–Organic Frameworks with Size-, Shape-, and Space-Distribution-Controlled Pore Structure. *Advanced Materials*, *27*(18), 2923–2929. https://doi.org/10.1002/adma.201405752

Zhang, X., Fu, K., Liang, Z., Rongwong, W., Yang, Z., Idem, R., & Tontiwachwuthikul, P. (2014).

Experimental studies of regeneration heat duty for CO2 desorption from diethylenetriamine (DETA) solution in a stripper column packed with Dixon ring random packing. *Fuel*. https://doi.org/10.1016/j.fuel.2014.07.057

Zhang, Y., & Wang, R. (2013a). Fabrication of novel polyetherimide-fluorinated silica organic–inorganic composite hollow fiber membranes intended for membrane contactor application. *Journal of Membrane Science*, *443*, 170–180. https://doi.org/https://doi.org/10.1016/j.memsci.2013.04.062

Zhang, Y., & Wang, R. (2013b). Gas–liquid membrane contactors for acid gas removal: recent advances and future challenges. *Current Opinion in Chemical Engineering*, *2*(2), 255–262. https://doi.org/https://doi.org/10.1016/j.coche.2013.03.008

Zhang, Y., & Wang, R. (2014). Novel method for incorporating hydrophobic silica nanoparticles on polyetherimide hollow fiber membranes for CO2 absorption in a gas–liquid membrane contactor. *Journal of Membrane Science*, *452*, 379–389. https://doi.org/https://doi.org/10.1016/j.memsci.2013.10.011

Zhang, Z. (2016). Comparisons of various absorbent effects on carbon dioxide capture in membrane gas absorption (MGA) process. *Journal of Natural Gas Science and Engineering*. https://doi.org/10.1016/j.jngse.2016.03.052

Zhao, B., Su, Y., Tao, W., Li, L., & Peng, Y. (2012). Post-combustion CO 2 capture by aqueous ammonia: A state-of-the-art review. *International Journal of Greenhouse Gas Control*. https://doi.org/10.1016/j.ijggc.2012.05.006

Zhao, C., Chen, X., & Zhao, C. (2010a). Multiple-Cycles Behavior of K2CO3/Al2O3 for CO2 Capture in a Fluidized-Bed Reactor. *Energy & Fuels*, *24*(2), 1009–1012. https://doi.org/10.1021/ef901018f

Zhao, C., Chen, X., & Zhao, C. (2010b). Study on CO2 capture using dry potassium-based sorbents through orthogonal test method. *International Journal of Greenhouse Gas Control*, *4*(4), 655–658. https://doi.org/https://doi.org/10.1016/j.ijggc.2009.12.010

Zhao, D., Timmons, D. J., Yuan, D., & Zhou, H.-C. (2011a). Tuning the Topology and Functionality of Metal−Organic Frameworks by Ligand Design. *Accounts of Chemical Research*, *44*(2), 123–133. https://doi.org/10.1021/ar100112y

Zhao, D., Timmons, D. J., Yuan, D., & Zhou, H. C. (2011b). Tuning the topology and functionality of metal-organic frameworks by ligand design. *Accounts of Chemical Research*, *44*(2), 123–133. https://doi.org/10.1021/ar100112y

Zhao, D., Yuan, D., Sun, D., & Zhou, H. C. (2009). Stabilization of metal-organic frameworks with high surface areas by the incorporation of mesocavities with microwindows. *Journal of the American Chemical Society*, *131*(26), 9186–9188. https://doi.org/10.1021/ja901109t

Zhao, M., Bilton, M., Brown, A. P., Cunliffe, A. M., Dvininov, E., Dupont, V., … Milne, S. J. (2014). Durability of CaO–CaZrO3 Sorbents for High-Temperature CO2 Capture Prepared by a Wet Chemical Method. *Energy & Fuels*, *28*(2), 1275–1283. https://doi.org/10.1021/ef4020845

Zhao, Qiang, Yuan, W., Liang, J., & Li, J. (2013). Synthesis and hydrogen storage studies of metal-organic framework UiO-66. *International Journal of Hydrogen Energy*, *38*(29), 13104–13109. https://doi.org/10.1016/j.ijhydene.2013.01.163

Zhao, Qichao, Wajert, J. C., & Anderson, J. L. (2010). Polymeric Ionic Liquids as CO2 Selective Sorbent Coatings for Solid-Phase Microextraction. *Analytical Chemistry*, *82*(2), 707–713. https://doi.org/10.1021/ac902438k

Zhao, S., Feron, P. H. M., Deng, L., Favre, E., Chabanon, E., Yan, S., … Qi, H. (2016). Status and progress of membrane contactors in post-combustion carbon capture: A state-of-the-art review of new developments. *Journal of Membrane Science*, *511*, 180–206. https://doi.org/https://doi.org/10.1016/j.memsci.2016.03.051

Zhao, W., Zhang, Z., Li, Z., & Cai, N. (2013). Investigation of Thermal Stability and Continuous CO2 Capture from Flue Gases with Supported Amine Sorbent. *Industrial & Engineering Chemistry Research*, *52*(5), 2084–2093. https://doi.org/10.1021/ie303254m

Zhao, X. B., Xiao, B., Fletcher, A. J., & Thomas, K. M. (2005). Hydrogen Adsorption on Functionalized Nanoporous Activated Carbons. *The Journal of Physical Chemistry B*, *109*(18), 8880–8888. https://doi.org/10.1021/jp050080z

Zhao, X., Xiao, B., Fletcher, A. J., Thomas, K. M., Bradshaw, D., & Rosseinsky, M. J. (2004). Hysteretic Adsorption and Desorption of Hydrogen by Nanoporous Metal-Organic Frameworks. *Science*, *306*(5698), 1012 LP – 1015. https://doi.org/10.1126/science.1101982

Zhao, Yi, Shen, Y., Bai, L., Hao, R., & Dong, L. (2012). Synthesis and CO2 Adsorption Properties of Molecularly Imprinted Adsorbents. *Environmental Science & Technology*, *46*(3), 1789–1795. https://doi.org/10.1021/es203580b

Zhao, Yueju, Zhang, J., Han, B., Song, J., Li, J., & Wang, Q. (2011). Metal-organic framework nanospheres with well-ordered mesopores synthesized in an ionic liquid/CO2/surfactant system. *Angewandte Chemie - International Edition*. https://doi.org/10.1002/anie.201005314

Zheng, B., Liu, H., Wang, Z., Yu, X., Yi, P., & Bai, J. (2013). Porous NbO-type metal–organic framework with inserted acylamide groups exhibiting highly selective CO2 capture. *CrystEngComm*, *15*(18), 3517–3520. https://doi.org/10.1039/C3CE26177H

Zheng, B., Yun, R., Bai, J., Lu, Z., Du, L., & Li, Y. (2013). Expanded Porous MOF-505 Analogue Exhibiting Large Hydrogen Storage Capacity and Selective Carbon Dioxide Adsorption. *Inorganic Chemistry*, *52*(6), 2823–2829. https://doi.org/10.1021/ic301598n

Zheng, J., Liu, X., Xu, P., Liu, P., Zhao, Y., & Yang, J. (2012). Development of high pressure gaseous hydrogen storage technologies. *International Journal of Hydrogen Energy*, *37*(1), 1048–1057. https://doi.org/https://doi.org/10.1016/j.ijhydene.2011.02.125

Zheng, Q.-S., Yu, Y., & Zhao, Z.-H. (2005). Effects of Hydraulic Pressure on the Stability and Transition of Wetting Modes of Superhydrophobic Surfaces. *Langmuir*, *21*(26), 12207–12212. https://doi.org/10.1021/la052054y

Zhou, C., & Szpunar, J. A. (2016). Hydrogen Storage Performance in Pd/Graphene Nanocomposites. *ACS Applied Materials & Interfaces*, *8*(39), 25933–25940. https://doi.org/10.1021/acsami.6b07122

Zhou, C., Szpunar, J. A., & Cui, X. (2016). Synthesis of Ni/Graphene Nanocomposite for Hydrogen Storage. *ACS Applied Materials & Interfaces*, *8*(24), 15232–15241. https://doi.org/10.1021/acsami.6b02607

Zhou, H. C., Long, J. R., & Yaghi, O. M. (2012). Introduction to metal-organic frameworks. *Chemical Reviews*, *112*(2), 673–674. https://doi.org/10.1021/cr300014x

Zhou, H., Zhang, J., Zhang, J., Yan, X.-F., Shen, X.-P., & Yuan, A.-H. (2015a). Spillover enhanced hydrogen storage in Pt-doped MOF/graphene oxide composite produced via an impregnation method. *Inorganic Chemistry Communications*, *54*, 54–56. https://doi.org/https://doi.org/10.1016/j.inoche.2015.02.001

Zhou, H., Zhang, J., Zhang, J., Yan, X., Shen, X., & Yuan, A. (2015b). High-capacity room-temperature

hydrogen storage of zeolitic imidazolate framework/graphene oxide promoted by platinum metal catalyst. *International Journal of Hydrogen Energy*, *40*(36), 12275–12285. https://doi.org/10.1016/j.ijhydene.2015.05.199

Zhou, L., Zhou, Y., & Sun, Y. (2004). A comparative study of hydrogen adsorption on superactivated carbon versus carbon nanotubes. *International Journal of Hydrogen Energy*, *29*(5), 475–479. https://doi.org/https://doi.org/10.1016/S0360-3199(03)00092-2

Zhou, W., Wu, H., Hartman, M. R., & Yildirim, T. (2007). Hydrogen and methane adsorption in metal-organic frameworks: A high-pressure volumetric study. *Journal of Physical Chemistry C*, *111*(44), 16131–16137. https://doi.org/10.1021/jp074889i

Zhou, Y., Feng, K., Sun, Y., & Zhou, L. (2003). Adsorption of hydrogen on multiwalled carbon natotubes at 77 K. *Chemical Physics Letters*, *380*(5), 526–529. https://doi.org/https://doi.org/10.1016/j.cplett.2003.09.068

Zhou, Z., Qi, Y., Xie, M., Cheng, Z., & Yuan, W. (2012). Synthesis of CaO-based sorbents through incorporation of alumina/aluminate and their CO2 capture performance. *Chemical Engineering Science*, *74*, 172–180. https://doi.org/https://doi.org/10.1016/j.ces.2012.02.042

Zhu, L. G., & Xiao, H. P. (2008). Gas storages in microporous metal-organic framework at ambient temperature. *Zeitschrift Fur Anorganische Und Allgemeine Chemie*, *634*(5), 845–847. https://doi.org/10.1002/zaac.200700580

Zhu, X., Mahurin, S. M., An, S.-H., Do-Thanh, C.-L., Tian, C., Li, Y., … Dai, S. (2014). Efficient CO2 capture by a task-specific porous organic polymer bifunctionalized with carbazole and triazine groups. *Chemical Communications*, *50*(59), 7933–7936. https://doi.org/10.1039/C4CC01588F

Zhu, Yanwu, Murali, S., Cai, W., Li, X., Suk, J. W., Potts, J. R., & Ruoff, R. S. (2010). Graphene and Graphene Oxide: Synthesis, Properties, and Applications. *Advanced Materials*, *22*(35), 3906–3924. https://doi.org/10.1002/adma.201001068

Zhu, Yu, James, D. K., & Tour, J. M. (2012). New Routes to Graphene, Graphene Oxide and Their Related Applications. *Advanced Materials*, *24*(36), 4924–4955. https://doi.org/10.1002/adma.201202321

Zlotea, C., Campesi, R., Cuevas, F., Leroy, E., Dibandjo, P., Volkringer, C., … Latroche, M. (2010). Pd Nanoparticles Embedded into a Metal-Organic Framework: Synthesis, Structural Characteristics, and Hydrogen Sorption Properties. *Journal of the American Chemical Society*, *132*(9), 2991–2997. https://doi.org/10.1021/ja9084995

Zukal, A., Opanasenko, M., Rubeš, M., Nachtigall, P., & Jagiello, J. (2015). Adsorption of pentane isomers on metal-organic frameworks Cu-BTC and Fe-BTC. *Catalysis Today*, *243*(C), 69–75. https://doi.org/10.1016/j.cattod.2014.07.003

Zukal, A., Pulido, A., Gil, B., Nachtigall, P., Bludský, O., Rubeš, M., & Čejka, J. (2010). Experimental and theoretical determination of adsorption heats of CO2 over alkali metal exchanged ferrierites with different Si/Al ratio. *Physical Chemistry Chemical Physics*, *12*(24), 6413–6422. https://doi.org/10.1039/C001950J

Zuo, W., E, J., & Lin, R. (2018). Numerical investigations on an improved counterflow double-channel micro combustor fueled with hydrogen for enhancing thermal performance. *Energy Conversion and Management*, *159*(January), 163–174. https://doi.org/10.1016/j.enconman.2018.01.017

Zuo, W., Jiaqiang, E., Liu, H., Peng, Q., Zhao, X., & Zhang, Z. (2016). Numerical investigations on an improved micro-cylindrical combustor with rectangular rib for enhancing heat transfer. *Applied Energy*,

184, 77–87. https://doi.org/10.1016/j.apenergy.2016.10.009

Zuo, W., Jiaqiang, E., Liu, X., Peng, Q., Deng, Y., & Zhu, H. (2016). Orthogonal Experimental Design and Fuzzy Grey Relational Analysis for emitter efficiency of the micro-cylindrical combustor with a step. *Applied Thermal Engineering*, *103*, 945–951. https://doi.org/10.1016/j.applthermaleng.2016.04.148

Zuo, W., Li, J., Zhang, Y., & Li, Q. (2019). Multi-factor impact mechanism on combustion efficiency of a hydrogen-fueled micro-cylindrical combustor. *International Journal of Hydrogen Energy*, *45*(3), 2319–2330. https://doi.org/https://doi.org/10.1016/j.ijhydene.2019.11.012

Züttel, A. (2003). Materials for Hydrogen Storage & Separation. *Materials Today*, (May), 24–33.

Züttel, A, Nützenadel, C., Sudan, P., Mauron, P., Emmenegger, C., Rentsch, S., … Kiyobayashi, T. (2002). Hydrogen sorption by carbon nanotubes and other carbon nanostructures. *Journal of Alloys and Compounds*, *330–332*, 676–682. https://doi.org/https://doi.org/10.1016/S0925-8388(01)01659-0

Züttel, Andreas. (2003a). Materials for hydrogen storage. *Materials Today*, *6*(9), 24–33. https://doi.org/10.1016/S1369-7021(03)00922-2

Züttel, Andreas. (2003b). Materials for hydrogen storage. *Materials Today*, *6*(9), 24–33. https://doi.org/https://doi.org/10.1016/S1369-7021(03)00922-2

Züttel, Andreas. (2004). Hydrogen storage methods. *Naturwissenschaften*, *91*(4), 157–172. https://doi.org/10.1007/s00114-004-0516-x

Züttel, Andreas, Remhof, A., Borgschulte, A., & Friedrichs, O. (2010a). Hydrogen: the future energy carrier. *Philosophical Transactions of the Royal Society A: Mathematical, Physical and Engineering Sciences*, *368*(1923), 3329–3342. https://doi.org/10.1098/rsta.2010.0113

Züttel, Andreas, Remhof, A., Borgschulte, A., & Friedrichs, O. (2010b). Hydrogen: The future energy carrier. *Philosophical Transactions of the Royal Society A: Mathematical, Physical and Engineering Sciences*, *368*(1923), 3329–3342. https://doi.org/10.1098/rsta.2010.0113